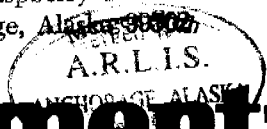


MARINE & COASTAL HABITAT MANAGEMENT  
ALASKA DEPT. OF FISH & GAME  
333 Raspberry Road  
Anchorage, Alaska 99502



# Environmental Assessment of the Alaskan Continental Shelf

Annual Reports of Principal Investigators  
for the year ending March 1979

Volume VIII. Transport



U.S. DEPARTMENT OF COMMERCE  
National Oceanic and Atmospheric Administration



U.S. DEPARTMENT OF INTERIOR  
Bureau of Land Management

VOLUME I	RECEPTORS -- MAMMALS BIRDS
VOLUME II	RECEPTORS -- BIRDS
VOLUME III	RECEPTORS -- FISH, LITTORAL, BENTHOS
VOLUME IV	RECEPTORS -- FISH, LITTORAL, BENTHOS
VOLUME V	RECEPTORS -- MICROBIOLOGY CONTAMINANT BASELINES
VOLUME VI	EFFECTS
VOLUME VII	TRANSPORT
VOLUME VIII	TRANSPORT
VOLUME IX	HAZARDS
VOLUME X	HAZARDS DATA MANAGEMENT

## ARLIS

Alaska Resources  
Library & Information Services  
Anchorage, Alaska

# Environmental Assessment of the Alaskan Continental Shelf

GC  
85.2  
.A4  
E57  
1979  
V.8

Annual Reports of Principal Investigators  
for the year ending March 1979

Volume VIII. Transport

Outer Continental Shelf Environmental Assessment Program  
Boulder, Colorado

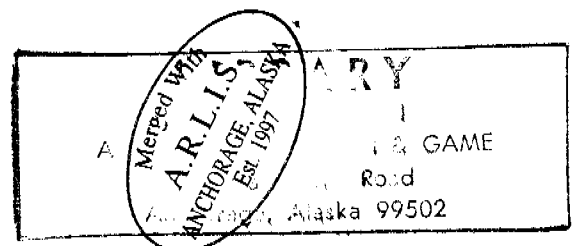
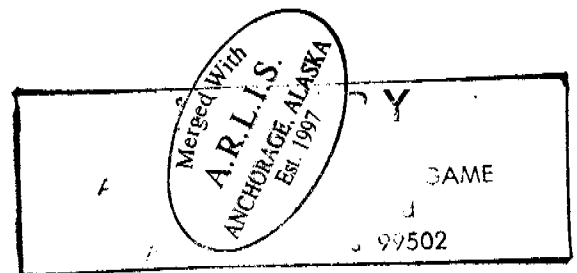
October 1979

## ARLIS

Alaska Resources  
Library & Information Services  
Anchorage, Alaska

U.S. DEPARTMENT OF COMMERCE  
National Oceanic and Atmospheric Administration

U.S. DEPARTMENT OF INTERIOR  
Bureau of Land Management



#### DISCLAIMER

Mention of a commercial company or product does not constitute an endorsement by National Oceanic and Atmospheric Administration. Use for publicity or advertising purposes of information from this publication concerning proprietary products or the tests of such products is not authorized.

#### ACKNOWLEDGMENT

These annual reports were submitted as part of contracts with the Outer Continental Shelf Environmental Assessment Program under major funding from the Bureau of Land Management.



## TRANSPORT

### CONTENTS

<u>RU #</u>	<u>PI - Agency</u>	<u>Title</u>	<u>Page</u>
519	Kozo, T. - Polar Science Center Brown, R. U. of Washington, Seattle, WA	Meteorology of the Alaskan Arctic Coast	1
526	Matthews, J. - Geophysical Inst. U. of Alaska, Fairbanks, AK	Characterization of the Nearshore Hydrodynamics of an Arctic Barrier Island-Lagoon System	57
529	Naidu, A. - Institute of Marine Science, U. of Alaska, Fairbanks, AK	Sources, Transport Pathways, Depositional Sites and Dynamics of Sediments in the Lagoon and Shallow Marine Region, Northern Arctic Alaska	98
531	Mungall, J. - Texas A&M Univ. Whitaker, R. College Station, TX	Oceanographic Processes in a Beaufort Sea Barrier Island-Lagoon System: Numerical Modeling and Current Measurements	182
541/ 550	Muench, R. - Pacific Marine Schumacher, J. Environmental Lab/ Tripp, R. U. of Washington Seattle, WA	Norton Sound/Chukchi Sea Oceanographic Processes (N-COP)	288
562	Kovacs, A. - Cold Regions Research and Engineering Lab, Hanover, NH	Oil Pooling Under Sea Ice	310
567	Coon, M. - Flow Research Co. Pritchard, R. Kent, WA	The Transport and Behavior of Oil Spilled In and Under Sea Ice	354
568	Schultz, L. - ARCTEC, Inc. Cox, J. Columbia, MD	The Transport and Behavior of Oil Spilled In and Under Sea Ice - Task 1	570

ANNUAL REPORT

Contract: 03-5-022-67 to 13

Research Unit: 519

Reporting Period: 1 Apr 78 - 31 Mar 79

Number of Pages: 57

METEOROLOGY OF THE ALASKAN ARCTIC COAST

Thomas L. Kozo  
Research Scientist

R. A. Brown  
Research Scientist

Polar Science Center  
Division of Marine Resources  
University of Washington  
Seattle, Washington 98195

1 April 1979

I. Summary of objectives, conclusions, and implications with respect to OCS oil and gas development.

The objectives of this program were to measure and analyze surface winds, temperature and atmospheric pressures along the Alaskan arctic coast for the purpose of deriving the wind field responsible for near shore (water depths to 20 meters) surface water movement.

Results of this study have shown that the surface wind field in spring and summer is strongly correlated at measuring stations separated by distances up to 100 km. This strong mesoscale correlation implies that a minimum of surface wind measurement points could provide a reasonable data set for coastal current trajectory studies.

Two mesoscale phenomena investigated were sea breeze forcing and mountain barrier baroclinicity. The breeze forcing is an important factor in the summer months while the mountain barrier effect appears to be most significant in the winter months (a season in which no experimental data was collected).

The effect of coastal winds on the summer near-shore circulation has relevance to transport of detritus, biota, spilled oil, and small ice floes. The sea breeze promotes barrier island lagoon flushing, and upwelling by maintaining persistent NE to E surface winds.

II. Introduction

A. General Nature of the Study

This study was designed to measure surface winds and surface atmosphere pressures in the Oliktok-Prudhoe Bay area. These surface winds were to be compared with predicted winds from National Weather Service (NWS) pressure charts. Causes of gross departures from NWS chart predictions were to be investigated and those attributed to mesoscale phenomena were to be examined and possibly modeled.

Measurements made during the 1977 and 1978 field seasons served as input for studies of Simpson Lagoon by Mathews (RU 526), Mungall (RU 531) and Naidu (RU 529).

B. Specific Objectives

This study has specific objectives of:

1. Measurement of surface winds and atmospheric pressures in the Oliktok-Prudhoe Bay area during seasons of interest.

2. Development of a sea breeze model tested with data from the 1976 and 1977 field seasons, to determine the degree and extent of influence seaward from the coastline.

3. Documentation of hydrometeorological extremes such as storm surges.

4. Determination of the degree of influence orographic baroclinicity exerts on coastal surface winds.

5. Comparison of actual winds to geostrophic winds derived from NWS estimates and pressure grids established for this study (see Leavitt, Appendix A).

### C. Relevance to Problems of Petroleum Development

Winds are the principal driving force for surface currents in the nearshore waters of the Alaskan arctic coast. Therefore any attempt to predict current trajectories must include a prediction of the surface wind field. The summer main ice pack edge (offshore several 100 km) serves as a source for small ice floes (roughly 30,000 kg) which are driven into the nearshore region by surface wind and resultant currents. The floes will exhibit movement in the nearshore region influenced by the combined effect of the large scale gradient wind and the sea breeze. Uncovered sea bed pipelines in trenches running from the offshore islands to the coast will be susceptible to ice damage when floes move into shallow water with a northerly velocity component. Oil slicks that may result from the above accident or other types of accidents will also be strongly influenced by the wind regime. Clean-up and containment operations will be made more difficult since local coastal winds will be hard to predict and sea breeze influence will diminish with distance from the coast leading to surface current divergence or convergence effects as a function of large scale winds.

### III. Current State of Knowledge.

The Alaskan arctic coast in contact with the Beaufort Sea has five year-round weather reporting sites but only two are official NWS stations (Class A). These are Pt. Barrow and Barter Island, approximately 540 km apart. Located between Pt. Barrow and Barter Island are two Distant Early Warning (DEW) stations, Lonely and Oliktok and one airport at Deadhorse routinely reporting supplementary data to the NWS but this information is mainly for post analysis and is not incorporated into twice-daily NWS pressure charts. The traditional method of approximating the surface wind from surface pressure field derived geostrophic winds is of limited use since the only surface input data comes from the above two Class A stations. No inland pressure data exists near the Beaufort Coast until south of the Brooks Range and none has been routinely collected in the Beaufort Sea. Kozo (1977) illustrated the increased detail in the pressure field when data from offshore buoys and additional land pressure measuring sites were added to the NWS data set.

Estimation of the surface winds from the synoptic pressure field is further complicated by the existence of an intermittent sea breeze circulation (Kozo, 1977; Moritz, 1977) during the summer months and mountain barrier effects (Schwerdtfeger, 1974) during the winter months. The summer sea breeze circulation is generated by a time varying but always positive land-sea temperature gradient (land temperature greater than the water temperature, Moritz, 1977). This results in a tendency to set up an along-shore component of the surface wind at the coast (a wind from  $90^\circ T \pm 20^\circ$ . Previous work (Kozo, 1977) from

analysis of historical data suggests that the sea breeze occurs approximately 33% of the time in the summer months. The extent of offshore influence is less than 60 km (Hufford, 1979).

Mountain barrier baroclinicity, as explained by Schwerdtfeger (1974), results from a piling up of cold air against the Brooks Range when the atmospheric boundary layer is statically stable. The resultant mesoscale pressure gradient is favorable to westerly winds. The increased frequency of winter west winds recorded at Barter Island (near the Brooks Range) over that recorded at Lonely or Pt. Barrow (both several 100 km from the Brooks Range) is circumstantial evidence of this effect.

#### IV. Study Area.

The study area for the past three years was contained within the latitudes  $69^{\circ}$  N -  $74^{\circ}$  N and longitudes  $143^{\circ}$  W -  $157^{\circ}$  W. In this way, buoy (1976 only) installations within the ice pack, NWS stations at Barrow and Barter Island, DEW sites at Oliktok and Lonely (1976 only), and camps at Umiat and Happy Valley (1976 only) could be used as surface pressure data sources to model the gradient wind fields.

Figure 1 shows the relative positions of the pressure stations (P) within the land-based grid for August 1976, 1977 and 1978. The primary study area is contained within the rectangle A. The area within the rectangle is shown in more detail in Figure 2. The W's and WA's indicate the locations of portable weather stations (MRI's) and small airport weather stations respectively.

Data collection periods for 1976 were Spring (April 27 to June 1) and Summer (August 11 to September 6); for 1977 were Spring (April 25 to June 1) and Summer (July 20 to September 1); and for 1978 were summer only (July 20 to September 1). The summers of 1977 and 1978 focused on measurements near the Simpson Lagoon area.

#### V. Sources, Methods and Rationale of Data Collection.

The previous years of 1976 and 1977 are discussed in Carsey (1977) and Leavitt (1978) respectively.

Data was collected in 1978 in the summer only, from July 20 through September 1. Meteorology Research, Inc. (MRI) mechanical weather stations recorded wind speed, wind direction, and temperature at Cross Island, Cottle Island, and Milne Point. A mesoscale surface pressure triangle was maintained using Weather Measure and Belfort microbarographs at Deadhorse, Umiat, Milne Pt., and Oliktok. These microbarographs were serviced weekly and calibrated with 2 Negretti and Zambra precision digital barometers.

Weekly transportation to the surface pressure stations was provided by Cessna 206's belonging to Jim Helmrich or NARL. Transportation to the MRI stations was provided by NOAA or ERA (Deadhorse) helicopters.

## VI. Results.

### A. 1978

The MRI weather stations recorded average direction, wind run (converted to speed), and temperature on a strip chart. One hour averages of these variables were selected for three-hourly intervals at 00, 03, 06, 09, 12, 15, 18 and 21 hours GMT. Pressure was also reported at three-hourly intervals (from continuous microbarograph output). The pressures were calibrated using Negretti and Zambra precision barometers as transfer standards and then were reduced to sea level pressure using the hypsometric equation, station altitude and mean air temperature. The data has been submitted to the OCS data bank in card form and on magnetic tape. Plots of wind and temperature are presented below in Section VII.

### B. 1976-1978

The following data in this subsection are presented and discussed in Section VII:

1. Histograms of August surface wind speed and direction for 1976, 1977, 1978, and a three-year average.

2. Documentation of the August 1977 negative "storm" surge (note: winds did not reach storm intensities of 22 m/s except in gusts).

3. Monthly percentage differences between the occurrence of north-east-east winds and southwest-west winds at Barter Island, Oliktok, and Lonely (all on the Beaufort Coast).

4. Inversion heights measured with an acoustic sounder in two seasons, Spring (1976) and Summer (1976).

### C. Sea Breeze

Data documenting sea breeze effects and output from a successful sea breeze model run on the University of Washington computer are compared in Section VII.

D. Geostrophic winds have been computed from the NWS surface pressure charts and were compared to geostrophic winds derived from the finer resolution AIDJEX Project buoy pressure array (1976). These in turn were compared to actual measured surface winds. Leavitt discusses the findings in Appendix A.

## VII. Discussion.

### A. 1978 MRI Data

Wind speeds (Figure 3), wind directions (Figure 4), and temperature (Figure 5) from July 15 to September 2, 1978 are shown from Milne Point, Cottle Island, and Cross Island. There is an expected close agreement in wind speed

and direction between stations since their total separation is less than 70 km and Cross Island is only 20 km seaward (within the zone of sea breeze influence, see below). Unfortunately, the Cross Island remote station malfunctioned for two weeks in the beginning of August. The temperature data from these stations also show close correlation. The data presented in the previous 1977 and 1978 annual reports show similar results.

#### B. Histograms

Histograms of surface wind speed and direction (August, Cottle Island) for 1976, 1977, 1978 and a combined average of the three years are presented in Figures 6-9 respectively. There is a persistence of east winds seen in all the figures but August 1977 (Figure 7) shows an unusually high percentage of easterly winds. In this case a six-day storm produced a dominant high speed east wind in the study area (see below, negative storm surge).

The wind speed is 6 m/s or less 60% of the time in August and is from the NE-E 50% of the time. These data compare favorably with the historical August data collected at Oliktok (west end of Simpson Lagoon) and recorded in the OCS Climatic Atlas (Brower et al., 1977).

#### C. Negative "storm" surge.

Figure 7 shows that 90% of the surface winds in August 1977 were from the northeast to east. The gross asymmetry is due to a synoptic event which produced near storm wind speeds that lasted six days (August 8 to August 13, 1977). Examples of prevailing surface winds during the time period were  $85^\circ \pm 5^\circ$  at  $10.5 \text{ m/s} \pm 1 \text{ m/s}$  for 30 hours and  $80^\circ \pm 5^\circ$  at  $12.5 \text{ m/s} \pm 2 \text{ m/s}$  for 75 hours.

These surface wind velocities were responsible for a negative "storm" surge in the Simpson Lagoon area. The decrease in water level due to a net water transport to the right of the prevailing wind (easterly) was documented during the installation of a tide gauge. The gauge float was inside a hollow oil drum in 20 cm of water at 1500 August 9, 1977, with 10 m/s winds. The winds increased to 15 m/s and by 2200 the float was sitting on mud, by 1000 August 10, 1977 a stake in 23 cm of water was dry (winds greater than 15 m/s but less than 20 m/s during this time). By 2200, another stake in 35 cm of water was dry for a net decrease in water depth of 78 cm in 31 hours during which the wind averaged 15 m/s from the east. By 1100 August 11, 1977 the water level increased 58 cm as the wind slowed to 10 m/s. By 1445 with the wind below 10 m/s the water level increased by 16 cm. On August 14, 1977 with east winds of 4 m/s the water level increased 24 cm for a net increase of 98 cm registered off the southwest coast of Pingok Island (Simpson Lagoon) due to the negative surge subsiding. During the storm, wind waves of 1.5 meters (peak to trough) were observed in the lagoon.

The NWS surface pressure charts (Figures 10-15) correlate with the above water level data. Figure 10 (August 7, 1977, 1500 LDST) shows the initial presence of a stationary low pressure center in the Gulf of Alaska. The study area (outlined by dashed lines with an "arrow-head" indicating the Pingok Island position) appeared to be under the influence of an intensifying high

pressure system with easterly winds along the coast, which moved across the top of Alaska and Canada along a trough line that formed by August 9, 1977 (1500 LDST) (Figure 12). The easterly wind's maximum intensity (closest isobaric packing) was seen on August 10, 1977 (1500 LDST) (Figure 13) which was the time of minimum water depth in the lagoon (see above). The anticyclonic flow weakened considerably by 1500 LDST August 12, 1977 (Figure 15) and the water depth increased correspondingly.

D. Monthly percentage differences between NE-E winds and SW-W winds at Barter Island, Oliktok and Lonely.

Figure 16, taken from histograms in the OCS Climatic Atlas, shows a plot of the monthly percentage difference between occurrence of northeast-east winds and southwest-west winds at Barter Island, Oliktok, and Lonely (all on the Beaufort Coast). Positive ( $\Delta\%$ ) implies more east winds than west winds. The months of October through March show a great disparity between Lonely and Barter Island; this is due to the "Mountain Effect" which is eastward deflection of northerly winds by the Brooks Range when the atmospheric boundary layer is statically stable.

In the months of May through August when the sun is above the horizon for more than 20 hours, the land snow cover is gone or depleted, and the land boundary layer is approaching neutral stability, the three coastal stations become very similar. They show an average of northeast-east winds at 3 times the frequency of southwest-west winds. It is obvious that the "Mountain Effect" is minimized during this period (except for mechanical channelling) and the mesoscale thermal effect of the coastline becomes a major influence on the synoptic scale wind in the coastal region.

E. Inversion Heights

Atmospheric inversion heights were measured with an acoustic sounder in two seasons, spring and summer, for 1976. The spring location, Narwhal Island, is less than 20 km from the coast and was surrounded by sea ice (no open water). The summer location was 15 km inland on the tundra between Arco Airport and Deadhorse Airport. Table I shows the average inversion heights recorded in spring and summer. The average for the two seasons of 250 m is evidence that atmospheric pollutants can be trapped in a layer relatively close to the earth's surface.

F. Sea Breezes

1. Experimental Evidence (1976)

Figures 17-19 are two-dimensional least squares fits (TDLSF) plots (Kozo, 1977) of the 0000 GMT (corresponds to 1500 ADST) surface pressure field on days in August 1976 when sea breeze forcing occurred. The surface winds at the five indicated stations are shown using standard NWS notation for the wind velocity arrows (—, short slash  $\equiv$  3-7 knots, / long slash  $\equiv$  8-12 knots). Knots multiplied by .5 are approximately equal to meters per second.

The calculated geostrophic wind for Cottle Island on August 16, 1976 (000 GMT) was .93 m/s from  $188.5^\circ\text{T}$  with a measured surface wind (10 m) of



TABLE I

<u>SPRING LOCATION</u>	<u>NARWHAL ISLAND</u>
<u>Period (1976)</u>	<u>Avg. Inversion Hgt. (m)</u>
14 May-16 May	366
17 May-19 May	323
20 May-22 May	374
23 May-25 May	286
26 May-28 May	192
29 May-31 May	216
1 June-2 June	<u>215</u>
	Avg. 281
<u>SUMMER LOCATION</u>	<u>DEADHORSE</u>
<u>Period (1976)</u>	<u>Avg. Inversion Hgt. (m)</u>
13 Aug-15 Aug	155
16 Aug-18 Aug	212
19 Aug-21 Aug	254
22 Aug-24 Aug	207
25 Aug-27 Aug	189
28 Aug-30 Aug	216
31 Aug-2 Sept	<u>309</u>
	Avg. 220

5.28 m/s from 090°T. Figure 17 and the NWS synoptic chart (not shown) indicates a weak pressure gradient in the Cottle Island area. The land-sea temperature difference from Prudhoe Airport to the coast (15 km) was 15.5°C.

The calculated geostrophic wind for Cottle Island on August 18, 1976 (000 GMT) was 2.14 m/s from 219.2°T with a measured surface wind (10 m) of 3.10 m/s from 105°T. Figure 18 and the NWS synoptic chart (not shown) indicate a weak gradient wind field in the study area. The land-sea temperature difference (Prudhoe Airport to the coast) was 7.8°C.

On August 21, 1976 (000 GMT) the geostrophic wind (calculated) for Cottle Island was 4.48 m/s from 252.1°T while the measured surface wind was 5.30 m/s from 110°T. Figure 19 and the NWS synoptic chart (not shown) indicate a stronger gradient field than on August 18 but a gradual weakening from Oliktok to Barter Island. The land-sea temperature difference from Prudhoe Airport to the coast was 6.7°C.

The TDLSF technique applied for a cubic surface was used twice daily for comparison with NWS surface pressure maps and atmospheric sounding data from Barter Island, both of which are produced for 000 GMT and 1200 GMT. To compare surface winds with the geostrophic winds on a 3-hourly basis the least squares technique was used to fit a linear surface (plane) to pressure data from Prudhoe, Lonely, Umiat and one AIDJEX buoy (closest to coast). These data sites surrounded the experimental area. In this case the two-dimensional polynomial to be solved which gives the best fit to 4 data points is

$$\text{Pressure} \equiv Z(x,y) = a + bx + cy$$

The constants a through c are computed from a 3 x 3 matrix with x the longitude and y the latitude of the respective data site locations. Partial derivatives (with respect to x and y) of the linear pressure polynomial were used to calculate geostrophic velocities. These velocities were first compared to those from the previously mentioned cubic fit (twice daily) and were found to agree ( $\pm 30^\circ$ ) 75% of the observed times.

The linear fit did provide the only continuous comparison (3 hourly) of the geostrophic wind (near Cottle Island) with the 10 meter wind measured at Cottle Island over a two week period in August 1976. Figure 20 shows a combined histogram of the surface wind (solid line) and the computed geostrophic wind (dashed line) for a time segment from August 13 to 23 and August 30 to September 3, 1976. The wind direction is divided into 15° increments with the x-axis indicating the number of samples. Normal planetary boundary layer turning would shift the winds from the southwest quadrant approximately 30° CCW (counterclockwise) from their geostrophic direction. The cross-hatched areas represent simultaneous data. The cross-hatched area under the geostrophic wind curve corresponds to the cross-hatched area under the 10-meter wind curve. The sea breeze has apparently offset the weak geostrophic winds in the boundary layer to produce an average "turning" of 150° CCW.

## 2. Experimental Evidence (1977)

Pilot balloon data was collected in August 1977 on Pingok Island (see Figure 2), the primary experimental site. Early morning and late evening tracking were precluded by fog conditions.

August 15, 1977 data are presented in Figure 21a. The vertical axis is height (m) with the horizontal axes indicated as either wind speed (m/s) or wind direction ( $^{\circ}$ T). The times are in Alaskan Daylight Saving Time (ADST) with 1500 ADST corresponding to 000 GMT the following day, for example. Radiosonde data from 2 launches (1526 and 1810 ADST) indicated the temperature at the top of the ground based inversion layer (200 m) was  $17.5^{\circ}\text{C}$  with a  $5.0^{\circ}\text{C}$  surface temperature. The 1524, 1810, and 1910 pilot balloon profiles show temporal veering of the surface wind vector as expected during times of sea breeze influence and all show abnormal veering of the wind vector with height (greater than  $100^{\circ}$  to the inversion height). The upper level winds at 1524 during the sea breeze maximum were weak (averaging 3 m/s) and should have allowed for its development. The Prudhoe-Coast (P-C) temperature difference (1500 ADST) was  $12.8^{\circ}\text{C}$ .

Figure 21b has August 19, 1977 data labeled as in Figure 21a above. Radiosonde plots (1702 and 2212 ADST) showed a temperature, at the top of the ground based inversion layer (150 m), of  $13^{\circ}\text{C}$  and surface temperature of  $8^{\circ}\text{C}$ . The inversion steepness increased slightly from 1702 to 2212 as the surface temperature decreased. The 1500, 1704, and 1837 profiles (pilot balloon) exhibit backing (counterclockwise turning) of greater than  $90^{\circ}$  through the inversion height with the free stream wind direction changing  $50^{\circ}$  in 3.5 hours. The wind speed above the inversion is relatively weak and again the sea breeze influence is dominant. The P-C temperature difference (1500 ADST) was  $8.9^{\circ}\text{C}$ .

### 3. Time Series Data (surface winds)

Time series of surface wind data from coastal stations and islands were examined with a less conventional technique of spectral analysis than that used for typical speed (scalar) spectra. The technique computes a rotary spectrum as output and is described in detail by Gonella (1972) and utilized to determine the existence of sea breezes by O'Brien and Pillsbury (1974).

Figures 22 and 23 are plots of rotary spectra for August 1976 and 1977 from time series data of surface wind velocities at various stations both inland and offshore. They are semi-log plots with 95% confidence limits (C) and bandwidths (B) indicated. The spectral peaks occurring near -1 cycle/day (24-hour period) are the clockwise-rotating contributions from the sea breeze. The vertical axes are spectral densities ( $[\text{m}^2/\text{s}^2]/[\text{c}/\text{h}]$ ) with the horizontal axes in frequency units of cycles/day.

Figures 22a-d represent spectra for data (1976) collected at Narwhal Island (18 km offshore), Cottle Island (5 km offshore), Tolaktovut (coastal station), and Deadhorse Airport (19 km inland) respectively (see Figure 2). There is a marked asymmetry around the 0 frequency line and all have significant peaks corresponding to the 24-hour period on the negative frequency axis. The peaks related to CW rotation in the Deadhorse (Figure 10d) and Narwhal (Figure 10a) spectra are evidence (O'Brien and Pillsbury, 1974) of sea breeze influence in at least a 37 km band centered on the coastline.

Figures 23a-d are spectra from data (1977) collected at Cross Island (19 km offshore), Cottle Island (5 km offshore), Barter Island (coastal station)

and Deadhorse Airport (19 km inland). Again asymmetry and significant peaks near the -1 cycle/day frequency (24-hour period) can be seen. Cross Island (instead of Narwhal Island) and Deadhorse spectra show sea breeze existence in a 38 km coastal range.

#### 4. Surface Wind Vectors

Two examples of time variation of the local surface wind vector (direction vs. true north, coastal orientation  $25^\circ$  to east-west line) with distance seaward and landward from the coast are presented to illustrate the surface rotation (Figures 24a and b). They have been chosen on days (mentioned above) which exhibited sea breeze characteristics. For August 1976 Narwhal Island was the most seaward site (18 km) while Deadhorse Airport was the most inland site (19 km). August 1977 had Cross Island (19 km) and Deadhorse Airport as the most seaward and most inland sites respectively.

August 17, 1976 (calculated geostrophic wind,  $226.7^\circ T$  and 3.2 m/s, 1500 ADST) is seen in Figure 24a with local wind vectors positions and times as indicated. All five of the sites (E = Narwhal Island, D = Cottle Island, C = Tolaktovut, B = ARCO Airport, A = Deadhorse Airport) had wind vectors that exhibited a CW rotation from 1500 (maximum sea breeze influence) to midnight while the 0900 to 1500 time period had generally CCW surface wind rotation. The computed geostrophic wind direction for midnight was  $137^\circ T$  and 2.2 m/s. The rotation of the computed geostrophic wind was CCW  $110^\circ$  from 1500 to midnight. In this case the geostrophic winds (free stream) were very weak and should have had limited influence on the sea breeze rotation.

August 19, 1977 (Figure 24b) had weak gradient winds of 4 m/s with a relatively constant direction of  $260^\circ T$  from 1205 to 1500. During this time the Cottle Island (D) and Oliktok (C) surface winds rotated CW to become more northerly under the sea breeze influence. Cross Island (E) appears to be under different synoptic situation (located on the NE corner of the data grid) which would account for the morning surface wind direction. By 1837 the geostrophic wind has changed to  $320^\circ T$  in a CW rotation while the surface wind vectors for all stations (except Cross Island) have rotated  $100^\circ$  CW (note: ARCO = B). In this case Deadhorse (A), the most inland station, "felt" the sea breeze effects last.

#### 5. The Sea Breeze Model

Sea breeze characteristics peculiar to the arctic (Kozo, 1978), have been included in a time-dependent, non-linear, two-dimensional numerical model which allows turbulent diffusion of heat and momentum to depend on the local velocity and temperature fields. The arctic sea breeze can be studied by conveniently adjusting the model to simulate experimental data or other possible relevant meteorological circumstances.

Figure 25 represents a right-handed coordinate system and the domain of coverage used in the model. The shoreline is straight and parallel to the y-axis (+ y-axis points west) with no variation in the sea breeze along this direction. The x-axis is normal to the shoreline with the (+) axis pointing north. The z-axis is + upward. This vertical cross-section of the atmosphere

is bounded at the bottom by the earth's surface and at the top by  $z = H$ . A variable horizontal grid has values of  $x = 0, \pm 5 \text{ km}, \pm 10 \text{ km}, \pm 20 \text{ km}, \pm 30 \text{ km}, \pm 40 \text{ km}, \pm 50 \text{ km}, \pm 70 \text{ km}, \pm 90 \text{ km}, \pm 120 \text{ km},$  and  $\pm 150 \text{ km}$ . The lateral boundaries (running north and south) are  $x = \pm D$ . The magnitudes of  $H$  and  $D$  have been chosen so that velocity and temperature changes there are negligible. The vertical distance is subdivided into a surface layer,  $0 \leq z \leq h = 25 \text{ m}$  and a transition layer,  $h \leq z \leq H \approx 1 \text{ km}$  where the eddy fluxes decrease with elevation.

The equations for the wind velocity ( $U$ ), temperature ( $\theta \equiv$  potential temperature), and mixing coefficients ( $K$ ) in the surface layer under neutral to stable conditions ( $Ri \geq 0$ ) are

$$U = \frac{u_*}{k} \left\{ \ln \left( \frac{z+z_0}{z_0} \right) + 4.7\zeta \right\} \quad (1)$$

$$\theta = \frac{\theta_*}{k} \left\{ .74 \ln \left( \frac{z+z_0}{z_0} \right) + 4.7\zeta \right\} + \theta_0 \quad (2)$$

$$K_m \equiv \text{Eddy viscosity} = \frac{u_* k z}{1 + 4.7\zeta} \quad (3)$$

$$K_h \equiv \text{Eddy thermal diffusion} \approx K_m$$

For unstable conditions ( $Ri < 0$ ) the velocity and temperature obey the following relationships:

$$\frac{\partial u}{\partial z} = \frac{u_*}{k} \frac{1}{(z+z_0)} \left\{ 1 - 15\zeta \right\}^{-1/4} \quad (4)$$

$$\frac{\partial \theta}{\partial z} = \frac{\theta_*}{k} \frac{.74}{(z+z_0)} \left\{ 1 - 9\zeta \right\}^{-1/2} \quad (5)$$

while the mixing coefficients ( $K$ ) are defined as

$$K_m = u_* k z \left\{ 1 - 15 Ri \right\}^{1/4} \quad (6)$$

$$K_h = \frac{u_* k z}{.74} \left\{ 1 - 9 Ri \right\}^{1/2} \quad (7)$$

where  $k \equiv$  von Karman's constant,  $u_* \equiv$  friction velocity,  $\theta_* \equiv$  scaling temperature,  $\zeta \equiv$  stability parameter  $= z/L$ , where  $L \equiv$  Obhukov length,  $Ri \equiv$  Richardson number,  $z_0 \equiv$  roughness length and  $\theta_0$  represents the surface temperature. The form of

the  $K$ 's and the velocity and temperature profiles in the surface layer have been taken from Businger et al. (1971).

The prediction equations for the upper layer  $h < z < H$  can be derived from the full momentum equations by assuming that each dependent variable is the sum of a given large scale synoptic component (subscript L) and a mesoscale component due to a sea breeze. Therefore,  $u = u_L + u'$ ,  $v = v_L + v'$ ,  $\theta = \theta_L + \theta'$  etc., where ' denotes the mesoscale component.

$$\frac{\partial u'}{\partial t} + u \frac{\partial u'}{\partial x} + w' \frac{\partial u}{\partial z} = -\frac{RT}{P} \frac{\partial P'}{\partial x} + fv' + \frac{\partial}{\partial z} \left( K_m \frac{\partial u}{\partial z} \right) \quad (8)$$

$$\frac{\partial v'}{\partial t} + u \frac{\partial v'}{\partial x} + w' \frac{\partial v}{\partial z} = -fu' + \frac{\partial}{\partial z} \left( K_m \frac{\partial v}{\partial z} \right) \quad (9)$$

$$\frac{\partial P}{\partial z} = -\frac{P}{RT} g + \frac{g}{R} \frac{P_L}{T_L} \quad (10)$$

$$\frac{\partial \theta'}{\partial t} + u \frac{\partial \theta'}{\partial x} + w' \frac{\partial \theta}{\partial z} = \frac{\partial}{\partial z} \left( K_h \frac{\partial \theta}{\partial z} \right) \quad (11)$$

$$\theta = T \left( \frac{P_0}{P} \right)^{R/C_p} \quad (12)$$

$$\frac{\partial u'}{\partial x} + \frac{\partial w'}{\partial z} = 0 \quad (13)$$

$t$  is time,  $x$ ,  $y$ , and  $z$  are spatial coordinates, and  $u$ ,  $v$ , and  $w$  are the corresponding velocity components in these directions.  $\theta$ ,  $P$ ,  $p$ ,  $T$ ,  $P_0$ ,  $g$ ,  $f$ ,  $R$ , and  $C_p$  are potential temperature, pressure, density, Kelvin temperature, reference pressure, gravitational acceleration, Coriolis parameter, gas constant, and specific heat at constant pressure. All variables are assumed constant in the  $y$ -direction, but a large scale pressure gradient may exist in the  $y$ -direction. The eddy diffusivity terms start at a value equal to that at the top of the lower layer  $z = h$  and decrease to zero at the boundary layer top. The full vertical momentum equation is replaced by the hydrostatic approximation (equation 10) which is reasonable when the ratio of horizontal to vertical grid lengths is  $\geq 3$  (Physick, 1976; and Neumann and Mahrer, 1975). The ratio in the model is greater than 50 for all levels.

The continuity equation (13) is in the incompressible form which is acceptable when the atmospheric motion (sea breeze rarely exceeds 2 km) are confined to a depth which is much less than the scale of density variation in the vertical (scale height  $\sim 8$  km).

The equations (8-11) and (13) are a set of equations which can be integrated numerically if the synoptic scale wind and temperature fields are

given. They are essentially the same as those used by Estoque (1961) except that the expressions for  $K_m$  and  $K_h$  differ and the equation of continuity is not differentiated with respect to  $z$  a second time.

The external boundary conditions at the lateral extremities,  $x = \pm D$ , are:

$$\frac{\partial}{\partial x} (u', v', p', \theta') = w' = 0 \quad (\text{where } D = 150 \text{ km})$$

at the top,  $z = H$  are:

$$p' = u' = v' = T' = \theta' = 0 \quad (\text{excluding } w') \quad (\text{where } H = 1050 \text{ km})$$

with vertical gradients and horizontal gradients of all variables except pressure = 0

and at the earth's surface,  $z = 0$ , are:

$$u = v = w = 0$$

with all horizontal gradients except for pressure = 0 and

$$\theta = \theta(x, t).$$

The initial conditions are  $u' = v' = T' = 0$  at  $t = 0300$  while the large scale velocity, temperature, and pressure fields are specified (see below) and held constant during the integration period.

The internal boundary conditions at  $z = h$  require continuity of the wind velocity and temperature and their respective fluxes. To insure that fluxes in the surface layer are applied at  $z = h + \Delta z$ , the fluxes in the layer from  $z = h$  to  $z = h + \Delta z$  are set equal to those in the surface layer ( $\Delta z = 25 \text{ m}$ ).

The integration is performed in the upper layer ( $h \leq z \leq H$ ) only with the following steps.

a. Using given initial values for  $T'$ ,  $u'$  and  $v'$  at the lowest gridpoint ( $z = h + \Delta z$ ) and the boundary value for temperature at the ground, the values of  $u'$ ,  $v'$ , and  $K$  at  $z = h$  are computed by matching fluxes  $\Delta z$ .  
Note: primes are the disturbance values.

b. Compute the pressure distribution ( $p'$ ) by integrating equation (10) downward from  $z = H$  where  $p' = 0$  using given values of  $T'$ ,  $T_L$  and  $P_L$ .

c. Compute the  $w'$  distribution using equation (13) and the given initial  $u'$  distribution.

- d. Compute  $\frac{\partial u'}{\partial t}$ ,  $\frac{\partial v'}{\partial t}$  and  $\frac{\partial \theta'}{\partial t}$  using equations (8), (9) and (11), respectively.
- e. These result in a new  $u'$ ,  $v'$ , and  $\theta'$  (can be converted to  $T'$ ) depending on the time interval of integration (2 to 5 minutes).
- f. Repeat steps a to e until desired time period is reached.

The surface heating function for the above mentioned arctic conditions with  $+x$  (northward) from the coast over the sea for 150 km and  $-x$  (southward) from the coast over land for 150 km can be written as

(temperatures in Kelvin degrees)

	water $x > 0$
$T = 273$	coastline $x = 0$
$T = 273 + .5 (25) (ARG)$	
$T = 273. + 18 \text{ ARG}$	$x = -5 \text{ km}$
at $z = 0$ $T = 273. + 20 \text{ ARG}$	land $x = -10 \text{ km}$
$T = 273. + 24 \text{ ARG}$	$x = -20 \text{ km}$
$T = 273. + 24 \text{ ARG}$	$x \leq -30 \text{ km}$

where  $ARG = .47 \sin (15 t + 265) + .15 \sin (30 t + 102)$   
 $+ .08 \sin (45 t + 306) + .36$

This is a tri-harmonic fit to Kuo's (1968) surface temperature plot modified for the arctic by keeping the temperature over land  $\geq 273^\circ\text{K}$  for the entire 24 hour period. The maximum temperature gradient at the coast is  $12.5^\circ\text{C}$  at 1500 ADST and reaches  $25^\circ\text{C}$ , 30 km inland.

The large scale temperature field (from radiosonde data), held constant during the integration is represented by a linear increase in temperature from the surface ( $273^\circ\text{K}$ ) to 150 m ( $283^\circ\text{K}$ ) where it is isothermal to 550 m. From 550 on, the temperature has a lapse rate of  $.6^\circ\text{K}/100 \text{ m}$ . These values are the same for each horizontal level in the model from +150 km to -150 km.

The large scale pressure field on 0 synoptic wind days is taken from tables of the U.S. Standard Atmosphere (Berry et al., 1945) to level  $H = 1050 \text{ m}$ . On model runs with a geostrophic wind, a pressure distribution is imposed at each vertical grid level which just balances the given prevailing wind.

The surface roughness  $z_0$  equals  $.001 \text{ m}$  and  $.01 \text{ m}$  for water and land respectively.

## 6. Model Output

- a. u-w Vectors, Velocity and Temperature Contours.

(1) Geostrophic wind  $220^\circ\text{T}$ , at 5 m/s, total velocities and temperature,  $u_L + u'$ ,  $v_L + v'$ ,  $w_L + w'$ , and  $\theta_L + \theta'$ .

The following case shown in Figure 26a-e was chosen to be representative of large scale wind directions and velocities measured during pilot



balloon ascents and inferred from calculated geostrophic winds. This particular direction is one that almost directly opposes sea breeze surface wind direction.

Figure 26a depicts the total u-w plane velocity vectors. The circulation pattern decays with time but unlike the 0 geostrophic wind case progress inland is almost non-existent. Return flow aloft is predominantly due to the southerly geostrophic wind component. The surface flow is from land to sea by 1900.

Isotachs of total u (Figure 26b) are shown, for a 5 m/s geostrophic wind and the PBL heights are superimposed. The boundary layer height over land reaches 750 meters by 1700 but the level over water remains less than 300 m. The isotach core due to the sea breeze and synoptic wind combination remains relatively stationary, with offshore dominance, for the 5 m/s large scale wind inputs. In this case little evidence of a seabreeze would be seen inland beyond 10 km and from 10 km inland to the coast extremely light or null surface winds would exist.

Figure 26c shows that the isotach core of total v remains stationary and offshore. The increased core strength (with time) represents augmented clockwise turning of the total wind vector. This results in flow parallel to the coast since the u component is small by 1900.

The w velocity contours (Figure 26) show a well-developed vertical circulation. The inland penetration of the upward flow maximum is approximately 10 km. The opposing large scale wind has effectively stalled the breeze advance.

The temperature contours ( $^{\circ}\text{C}$ , Figure 26) show a ground-based inversion layer over water from 1500 to 1900 with  $12^{\circ}$  isotherm moving seaward with time due to horizontal temperature advection by the geostrophic wind.

#### b. Surface Wind Vectors.

- (1) Geostrophic wind  $270^{\circ}\text{T}$  at 5 m/s.

The surface wind vectors (Figure 27a) exhibit clockwise turning at model positions  $\pm 30$  km from the coast. Limited effect can be seen at 50 km from the coast and 30 km inland. This type of turning is also seen in the real data from August 19, 1977 (Figure 24b) when geostrophic winds were from  $270^{\circ} \pm 10^{\circ}\text{T}$ .

- (2) Geostrophic wind  $220^{\circ}\text{T}$  at 5 m/s.

The model surface wind vectors (Figure 27b) exhibit clockwise turning from the coast to 30 km at sea where the sea breeze is stalled. Little effect is seen at 50 km offshore while inland 20 km a counterclockwise turning exists by 1700 when the sea breeze approaches and switches to clockwise turning afterward. August 17, 1976 (Figure 24a) and August 15, 1977 (Figure 21a) represent real sea breeze days when the geostrophic wind averaged  $220^{\circ}\text{T}$ . Counterclockwise turning can be seen from 1200 to 1500 as the sea breeze sets up 15 km inland then clockwise turning occurs afterward.

## (3) Geostrophic wind 090°T at 5 m/s.

Minimal turning with time is seen in Figure 27c for a 090°T geostrophic wind. The same thing can be seen in real data from August 14, 1977 (not shown). The surface wind vectors (model) appear to have magnitudes slightly larger than the geostrophic winds aloft for the 5 km seaward (from the coast) to the inland stations.

## c. Simulated Pilot Balloon Data (5 km seaward of the coast; representative of Pingok Island).

Plots of wind velocity vs. height are shown in Figures 28a-c for geostrophic winds of 5 m/s at 270°T, 220°T, 090°T respectively.

## (1) Geostrophic wind 270°T at 5 m/s.

The wind speed (model) profiles (Figure 28a) show a velocity decrease at the inversion height which is coincident with the layer of maximum wind direction change. The 1500 profiles show a backing (counterclockwise turning with height) to 250 m, while the 1900 profiles show a veering (clockwise turning with height) to 250 m. A clockwise turning with time (80° in 3.5 hours) is exhibited by the surface wind vector. Pilot balloon data indicating geostrophic winds from roughly 270° on August 7, 1977 (not shown) shows veering of 200° (up to 250 m) and August 19, 1977 (Figure 21b) shows backing of 140°T (up to 250 m) which are comparable to the turning produced by the model. The real data also show surface clockwise turning with time (80° in 4 hours). The 5 m/s geostrophic wind velocity case (model) shows a slight increase above their respective velocities (bowing out) in the upper level winds from 400 m to 700 m (height). This is attributable to the coast line orientation and weak sea breeze return flow aloft (.5 m/s) adding to the geostrophic wind vector.

## (2) Geostrophic wind 220°T at 5 m/s.

The wind speed (model) profiles (Figure 28b) also show a velocity decrease at the inversion height which again is coincident with the layer of most wind directional change. Both model sets (3 m/s and 5 m/s cases) show a veering up to 250 m which is comparable to real pilot balloon data from August 15, 1977 (figure 21a). A very slight bowing out of the upper level winds (model) again can be attributed to the sea breeze return flow. The clockwise turning with time appears in the real data (70° in four hours) and the model (60° in four hours) at comparable rates.

## (3) Geostrophic wind 090°T at 5 m/s.

The wind direction (model) profiles (Figure 28c) show a normal veering up to 250 m. The wind speed profiles denote the presence of a sea breeze by exhibiting a wind speed increase within the boundary layer (below the inversion) instead of a normal decrease in wind speed. This speed increase within the boundary layer is seen in real data from August 14, 1977 and August 17, 1977 (not shown). A slight speed decrease in the upper level winds from 400 m to

800 m (bowing in), below that of the geostrophic speed, is attributed to weak opposing return flow aloft generated by the sea breeze return circulation. The turning of the surface wind vector with time is negligible both in the model and from the real data for geostrophic winds from approximately 090°T.

c. Rotation and Rotation Rates.

The rotation of ordinary sea and land breeze surface wind vectors has been shown by Haurwitz (1947) to be primarily due to Coriolis forces. In the case of a weak synoptic wind, a complete 360° turn can take place in a diurnal cycle. The summer arctic sea breeze on the Beaufort Coast cannot exhibit 360° (under 0 synoptic wind conditions) turning, since the land remains warmer than the water during the short arctic night. For the study area, a direction from 25°T to 115°T would be the quadrant of influence due to the coastline orientation.

Observations by Defant (1951) and Neumann (1977) indicate that the rate of sea breeze turning is not uniform. The directional change from 1400 LST to 1700 LST during the breeze velocity maximum, is less than that between 0800 and 1100, while turning is more rapid between 2000 and 2300.

Neumann (1977) developed an expression for the rate of turning of a land-sea breeze. He used a coordinate system and notation similar to this model. Letting  $\alpha \equiv \arctan \frac{v}{u}$  with  $\alpha$  measured as the angle between the positive x-axis (north) and the wind, Neumann wrote the  $\frac{\partial \alpha}{\partial t}$  in standard form and substituted the momentum equations arriving at

$$\frac{\partial \alpha}{\partial t} = -f + \frac{1}{v^2} \cdot \left[ \frac{v}{\rho} \frac{\partial P_m}{\partial x} + f(uu_g + vv_g) \right] \quad (14)$$

where  $P_m \equiv$  mesoscale pressure gradient

$u_g \equiv$  geostrophic component perpendicular to the coast

$v_g \equiv$  geostrophic component parallel to the coast

$f \equiv$  Coriolis parameter

$v \equiv u^2 + v^2$

$u \equiv u_g + u_m$ , m denotes mesoscale

$v \equiv v_g + v_m$ , m denotes mesoscale

This expression for rotation rate was tested against model output, and actual data for approximate geostrophic winds from 270°T, 220°T and 90°T at 5 m/s.

The 270°T, 5 m/s geostrophic case (model) exhibits a turning rate of 23.8°/hr clockwise versus 20.5°/hr clockwise, using model output in equation (14). In this case  $u_g = 2.11$  m/s and  $v_g = -4.53$  m/s due to coastline orientation. Actual data taken August 19, 1977 (Figure 21b) shows an approximate surface turning of 22.8° clockwise. In this case  $u_g u$  and  $v_g v$  are both (-),

while  $\frac{\partial p}{\partial x}$  is (+) as usual, therefore the clockwise turning is augmented and approaches that of -f.

The 220°T, 5 m/s geostrophic case (with  $u_g = 4.83$  m/s and  $v_g = -1.29$  m/s due to coastline orientation) has turning in the model from 1500 to 1900 of 13.8°/hr clockwise. The  $\frac{\partial \alpha}{\partial t}$  using model output in equation (14) yields 8.1°/hr clockwise. Data from 0800 August 15, 1977 shows 12.5°/hr clockwise. Again, the mesoscale term is (+) but the u term changes from (-) to (+), which inhibits turning in the late afternoon. Reduced clockwise turning rates result.

The 090°T, 5 m/s geostrophic case (model) showed turning of 1.55°/hr clockwise from 1500-1900, while  $\frac{\partial \alpha}{\partial t}$  using model output in equation (14) with  $u_g = -2.11$  m/s and  $v_g = 4.53$  m/s shows 1.75°/hr clockwise. The large scale (third) term in (14) was (+) and the mesoscale term was (+), which caused the rotation to diminish rapidly. Actual data (not shown) approaching these conditions exhibits turning of approximately 5°/hr clockwise, but this is probably not a true sea breeze turning since wind speeds and directions above the boundary layer changed during the time period.

#### VIII. Conclusions

There is a strong correlation between surface winds (10 m) measured at remote station separations of 200 km or less along the Alaskan Arctic Coast from Lonely to Barter Island (obtained from data presented in this study and Leavitt, 1978). Presently available geostrophic wind calculations from NWS charts are of limited use in estimating the surface wind since simultaneous boundary layer stratification data doesn't exist, and mesoscale influences such as sea breeze forcing in summer and mountain barrier effects in winter are not normally accounted for. The NWS charts themselves (in absence of mesoscale effects) are marginally useful due to lack of data reporting stations north and south of the Beaufort Sea coast resulting in poor resolution and coastal biasing of geostrophic calculations. A possible unreliability of the charts in the arctic has also been mentioned in Rodgers (1978). Therefore for nearshore use (less than 30 km from the coast), a few (6) wind velocity sensors between Barrow and Barter Island could provide the wind data for predicting coastal current velocities and trajectories.

Beyond 30 km at sea, geostrophic wind will be a better estimator of surface winds since the sea breeze influence will be minimal and orographic effects will be diminished. For this part of the shelf, pressure sensor equipped data buoys can be deployed on the main ice pack (200 km from shore) and inland 100 km to maintain a pressure grid with the correct geometry. A combination of coastal wind measurements and pressure measurements in a higher resolution grid could provide a proper data base for studies of oil spill trajectories, upwelling and lagoon flushing.

The major implications of sea breeze forcing along the coast are:

- (1) Maintenance of along shore and offshore surface currents in the nearshore zone which promote lagoon flushing during low synoptic conditions.

(2) Weakening of adverse synoptic wind conditions (those that prevent lagoon flushing) and may eventually offset or neutralize them during the afternoon hours.

(3) Increasing the persistence of upwelling conditions.

(4) Production of wind driven current shears beyond 30 km offshore where synoptic conditions are not influenced by thermal contrasts.

Theoretical evidence for the last effect (surface wind direction) has been demonstrated in model output and data from Hufford (1979) has shown that surface winds at 60 km from the coast are not influenced by the sea breeze. The sea breeze model (running at the University of Washington) can be used to predict surface wind vector rotation from the coast to 50 km at sea under varying synoptic conditions and land-sea thermal contrasts. It has reproduced the pilot balloon measurements for both 270° and 220° synoptic winds. The gross asymmetry in histograms of summer surface wind direction (biased toward E-NE directions) from the study area can be explained by normal synoptic effects augmented by sea breeze forcing.

#### IX. Needs for Further Study

As mentioned in the conclusion, surface wind prediction from geostrophic winds requires a sound pressure grid with reasonable geometry. This has only existed sporadically in the Alaskan arctic. A study of pressure data from two new pressure buoys (one offshore) should be the beginning of a larger coastal buoy program this summer.

The past three years of field work did not include the winter months. In view of the large changes in the histograms of monthly wind directions for Barter Island, Oliktok and Lonely throughout the year, a simultaneous investigation of surface winds and geostrophic winds should be undertaken for December January and February.

A study of sea breeze seaward extent should be made to tie in nearshore current data with outer-shelf current data and to determine its influence on summer nearshore small ice floe trajectories.

A combined inversion height-atmospheric boundary layer study should be initiated at Oliktok DEW site instrumenting their 100 meter tower and using an acoustic sounder to determine atmospheric diffusion parameters and wind profiles under very stable boundary layer conditions near the coast.

#### X. Summary of January-March Quarter.

##### A. Ship or Laboratory Activities

1. Field trip schedule: None undertaken during period.

2. Scientific Party:

Tom Kozo, University of Washington, new Co-principal investigator  
 Roger Andersen, University of Washington, computer programmer  
 and data analyst.

3. Methods:

(a) Field sampling: none

(b) Laboratory analysis:

- 1) Analysis of existing historical data to determine effect of Brooks Range on coastal winds.
- 2) Analysis of 1978 field data.
- 3) Investigation of negative storm surge (August 1977) and correlation to water elevation changes in Simpson Lagoon.
- 4) Numerical modeling of sea breeze system in Simpson Lagoon area and comparison to actual data from August 1976 and 1977.

4. Sample Localities/ship or aircraft tracklines  
 Summer 1978 (July 20 - Sept. 1):

Recording weather stations at Cross Island, Cottle Island and Milne Pt.

Microbarographs at Deadhorse, Oliktok, Umiat and Milne Point.

5. Data Collected or Analyzed

Continuous records of wind speed, wind direction, and temperature at weather station sites.

Continuous records of atmospheric pressure at microbarograph sites.

National Weather Service twice daily surface pressure charts for the 1977 negative storm surge period of August 8 through August 14.

References

- Berry, F. A., E. Bollay, and N. R. Beers, 1973. Handbook of Meteorology, McGraw-Hill, New York, 1068 pp.
- Brower, W. A., H. F. Diaz, A. S. Prechtel, H. W. Searby and J. L. Wise, 1977. Climatic Atlas of the Outer Continental Shelf Waters and Coastal Regions of Alaska, NOAA, NCC, EDS, Asheville, North Carolina, 409 pp.
- Businger, J. A., J. C. Wyngaard, Y. Izumi, and E. F. Bradley, 1971. Flux - profile relationships in the atmospheric surface layer. J. Atmos. Sci. 28, 181-189.
- Carsey, F. D., 1977. Coastal meteorology of the Alaskan Arctic Coast. OCS Contract 03-5-022-671011.
- Defant, F., 1951. Local winds. Compendium of Meteorology. Boston, Massachusetts, Amer. Meteor. Soc., pp. 655-662.
- Estoque, M. A., 1961. A theoretical investigation of the sea breeze. Quart. J. R. Meteor. Soc., 87, 136-146.
- Gonella, J., 1972. A rotary-component method for analysing meteorological and oceanographic vector time series. Deep-Sea Res., 19, 833-846.
- Haurwitz, B., 1947. Comments on the sea-breeze circulation. J. Meteor., 4, 1-8.
- Hufford, G. L., 1979. Personal communication, OCS Office, Anchorage, Alaska.
- Kozo, T. L., 1977. Coastal meteorology of the Alaskan Arctic Coast. P.I. F. Carsey; OCS Contract 03-5-022-671011.
- Kozo, T. L., 1978. Coastal meteorology of the Alaskan Arctic Coast, Appendix, P.I. E. Leavitt. OCS Contract 03-5-022-67 to 13.
- Kuo, H. L., 1968. The thermal interaction between the atmosphere and the earth and propagation of diurnal temperature waves. J. Atmos. Sci., 25, 682-706.
- Leavitt, E., 1978. Coastal meteorology of the Alaskan Arctic Coast. OCS Contract 03-5-022-67 to 13.
- Moritz, R. E., 1977. On a possible sea breeze circulation near Barrow, Alaska. Arctic Alp. Res., 9, 427-431.
- Neumann, J., 1977. On the rotation rate of the direction of sea and land breezes. J. Atmos. Sci., 34, 1913-1917.
- Neumann, J. and Y. Mahrer, 1975. A theoretical study of the lake and land breezes of circular lakes. Mon. Wea. Rev., 103, 474-485.

- O'Brien, J. J. and R. D. Pillsbury, 1974. Rotary wind spectra in a sea breeze regime. J. of App. Meteor., 13, 820-825.
- Physick, W., 1976. A numerical model of the sea-breeze phenomenon over a lake or gulf. J. Atmos. Sci., 33, 2107-2135.
- Rogers, J. C., 1978. Meteorological factors affecting inter-annual variability of summertime ice extent in the Beaufort Sea. Mon. Wea. Rev., 106, 890-897.
- Schwerdtfeger, W., 1974. Mountain barrier effect on the flow of stable air north of the Brooks Range. Climate of the Arctic, Conference Publication of the Geophysical Institute, University of Alaska, Fairbanks. 204-208.



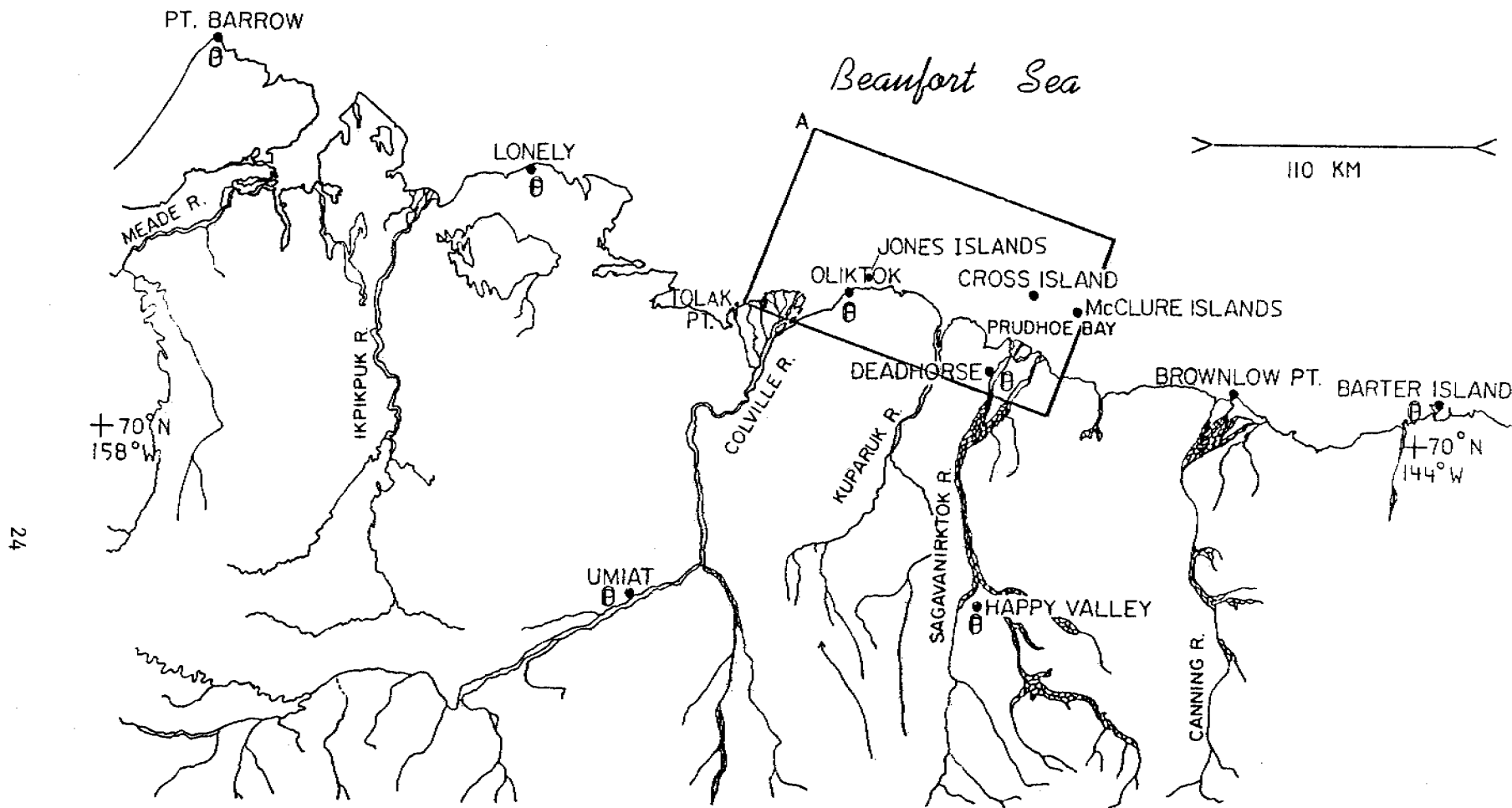


Fig. 1 Locations of atmospheric pressure stations (P) within the land-based grid for 1976, 1977, and 1978 and primary study area. Stations at Lonely and Happy Valley were used in 1976 only.

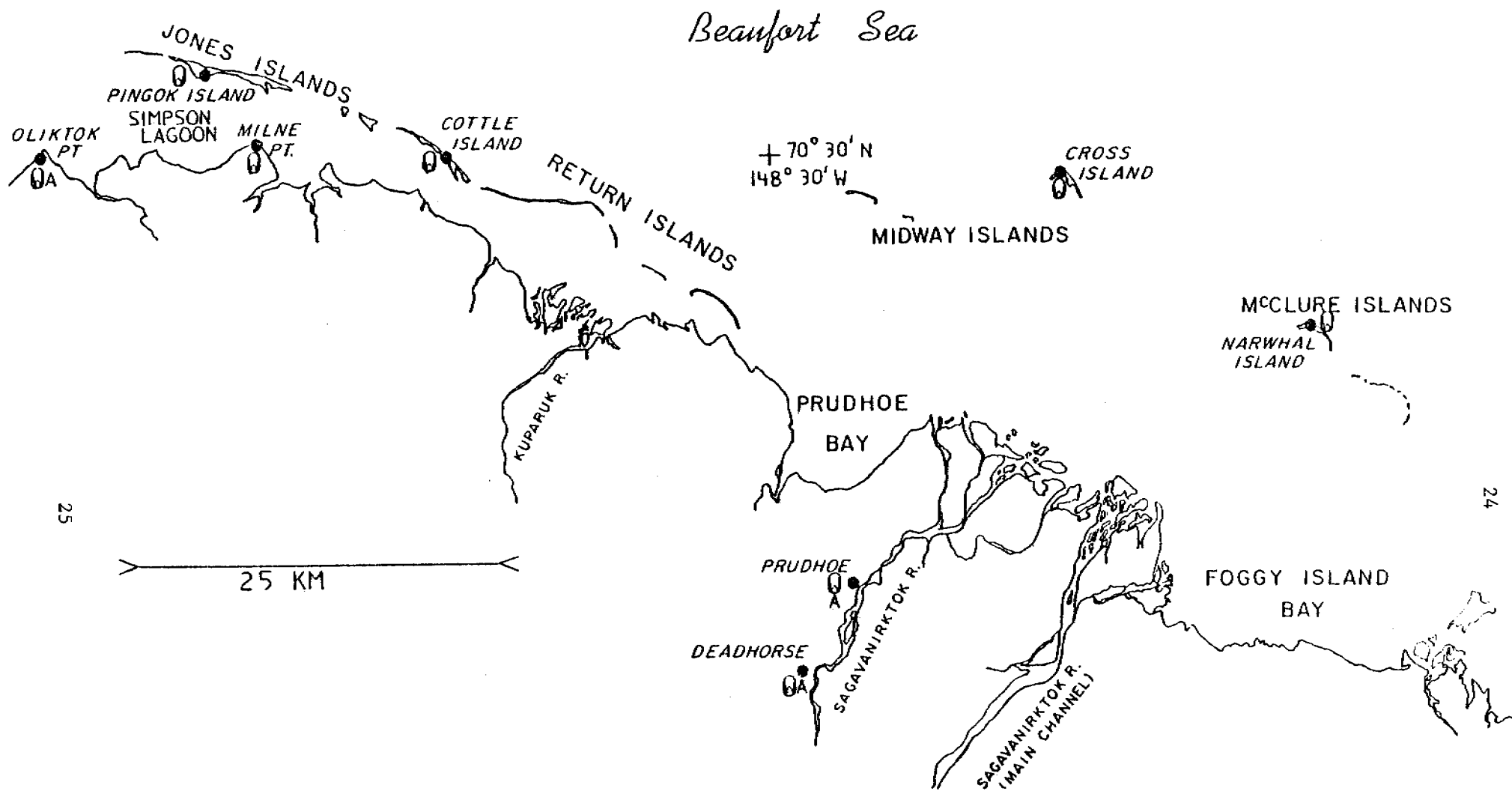


Fig. 2 Primary study area with (W) and (WA) representing mechanical weather stations and airport weather stations respectively.

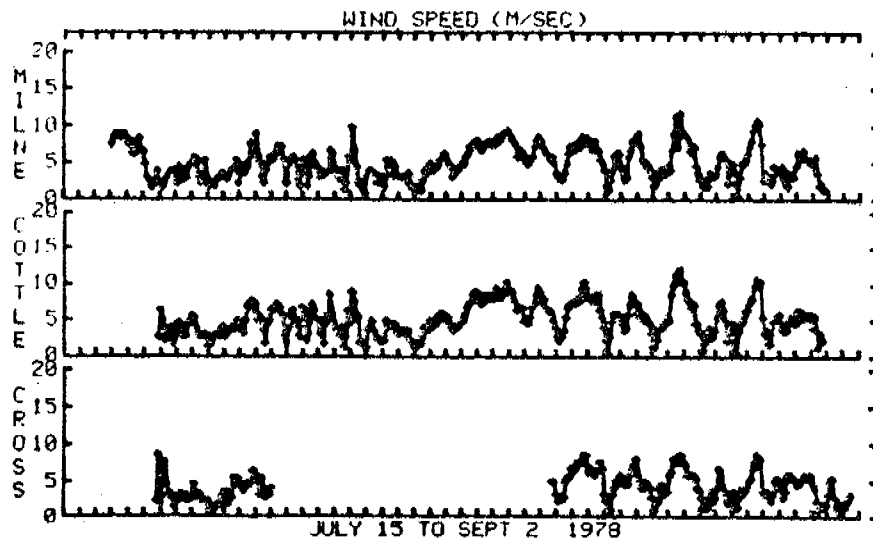


Fig. 3

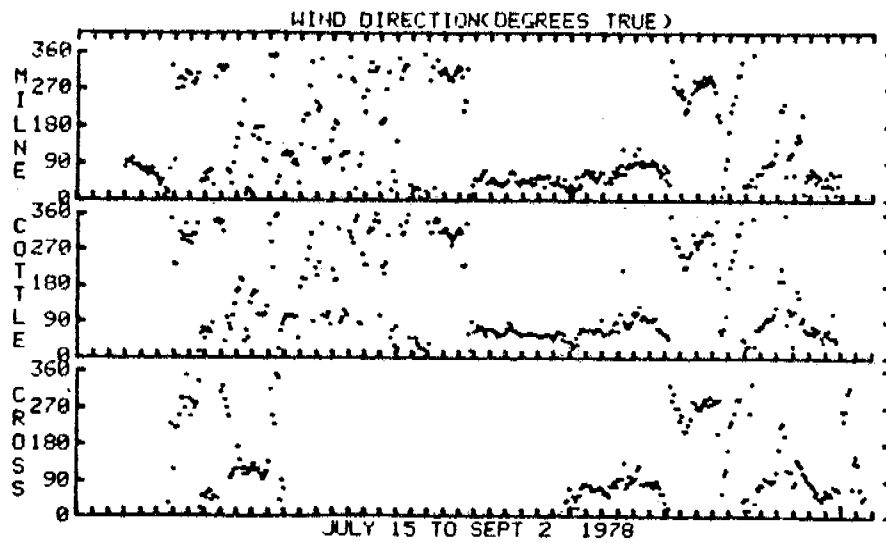


Fig. 4

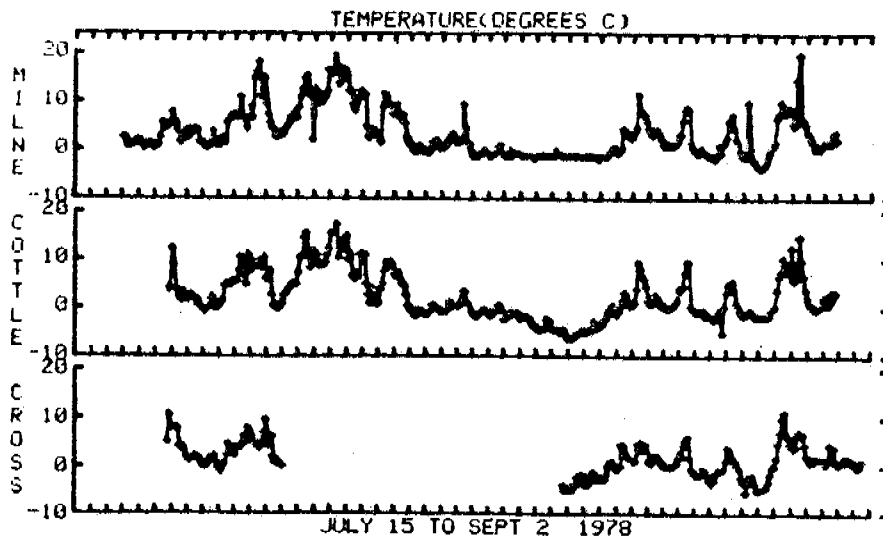


Fig. 5

Figs. 3-5. Comparison of wind speeds, wind directions and temperature from Milne Point, Cottle Island, and Cross Island for July 15 to Sept. 2, 1978. Note: equipment failure caused the gap in the Cross Island data.

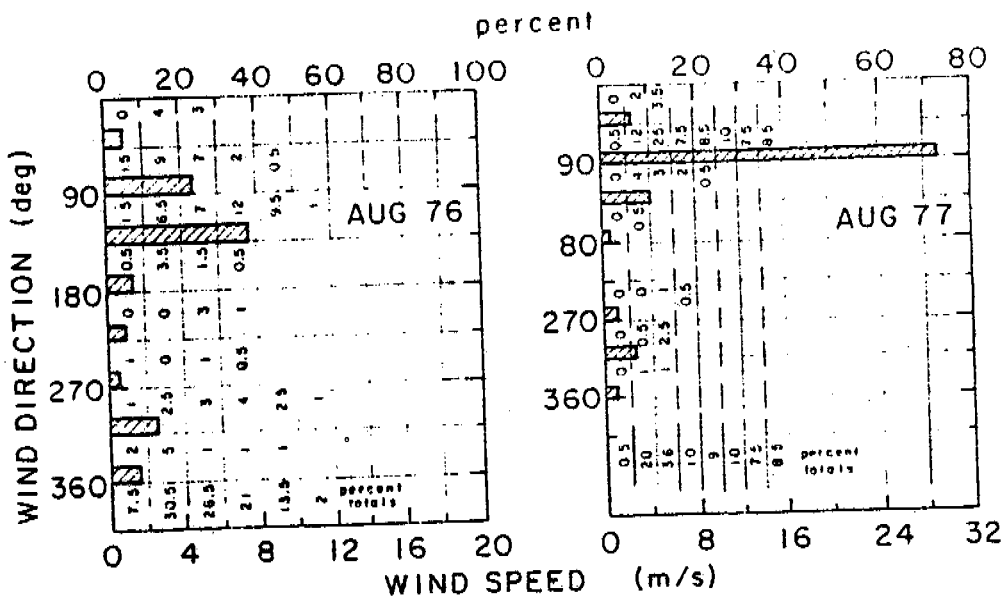


Fig. 6

Fig. 7

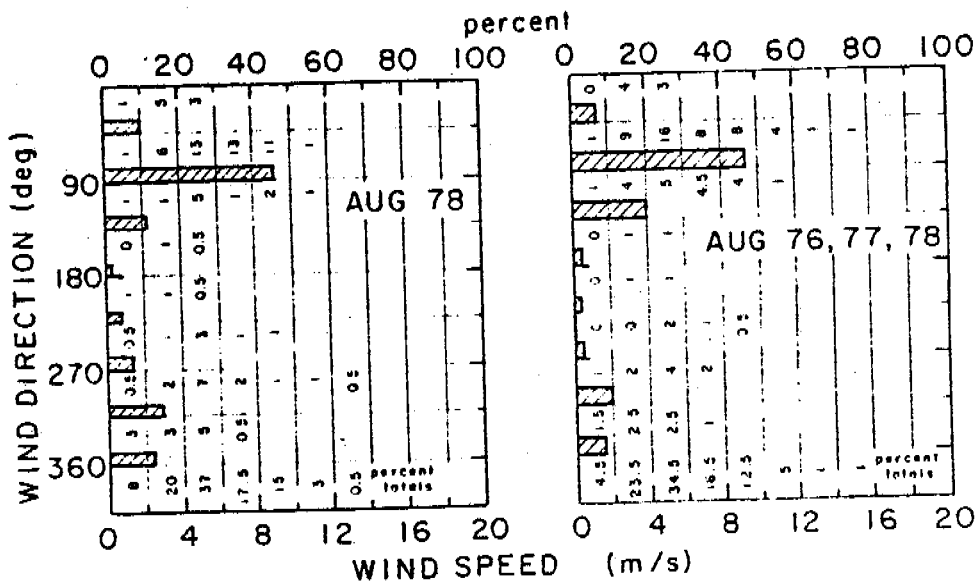


Fig. 8

Fig. 9

Figs. 6-9 Histogram of wind speed and direction for August 1976, 1977, and 1978. (Fig. 9 is 1976, 1977 and 1978 combined).. Note: Direction Frequency—Top Scale—Bars represent % frequency of winds from each direction. Speed frequency—Bottom Scale—Printed numbers are % frequency of wind speeds observed from each direction.

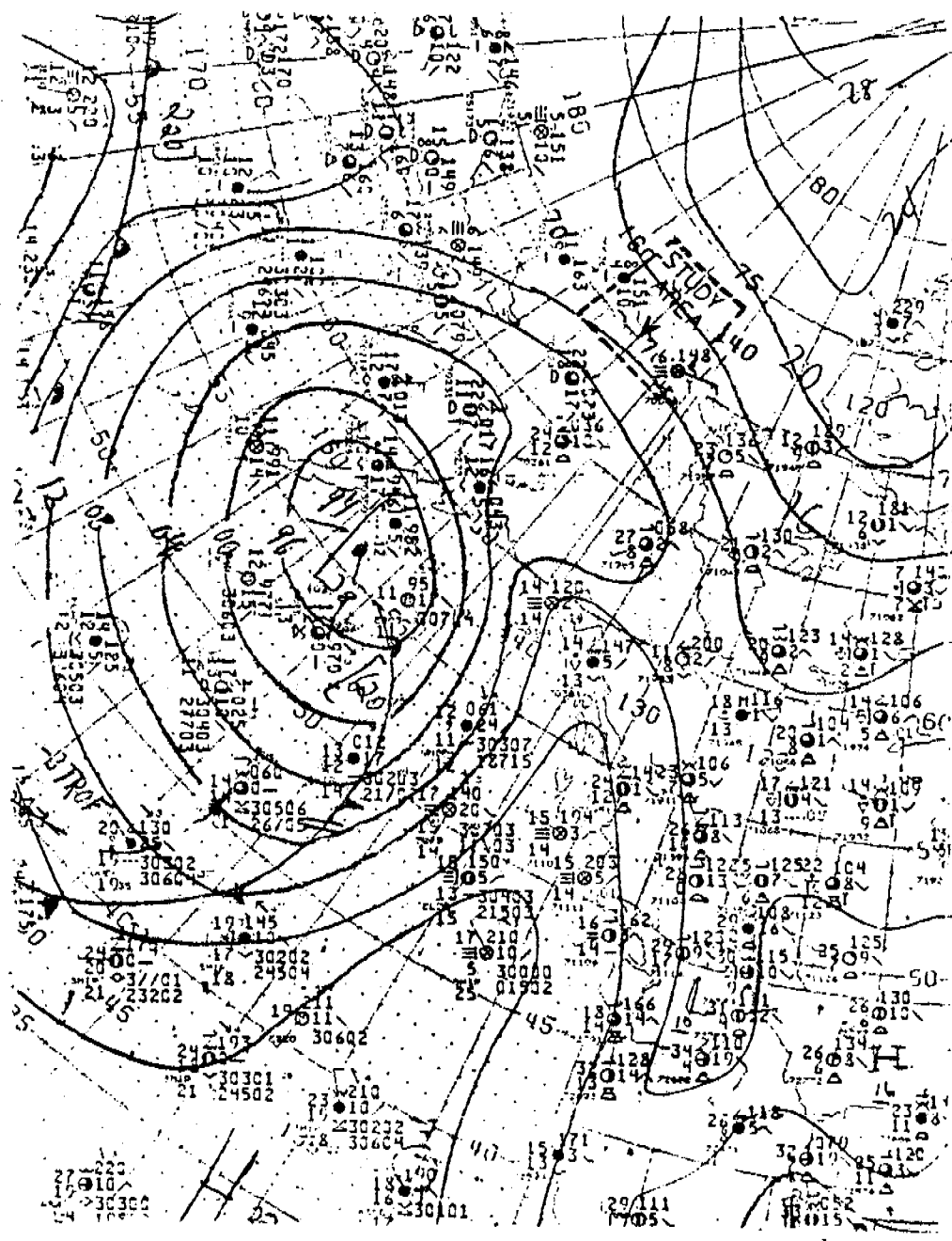


Fig. 10 NWS surface pressure chart for 1500 LDST August 7, 1977. The study area is outlined by dashed lines with an "arrow-head" indicating the Pingok Island position.

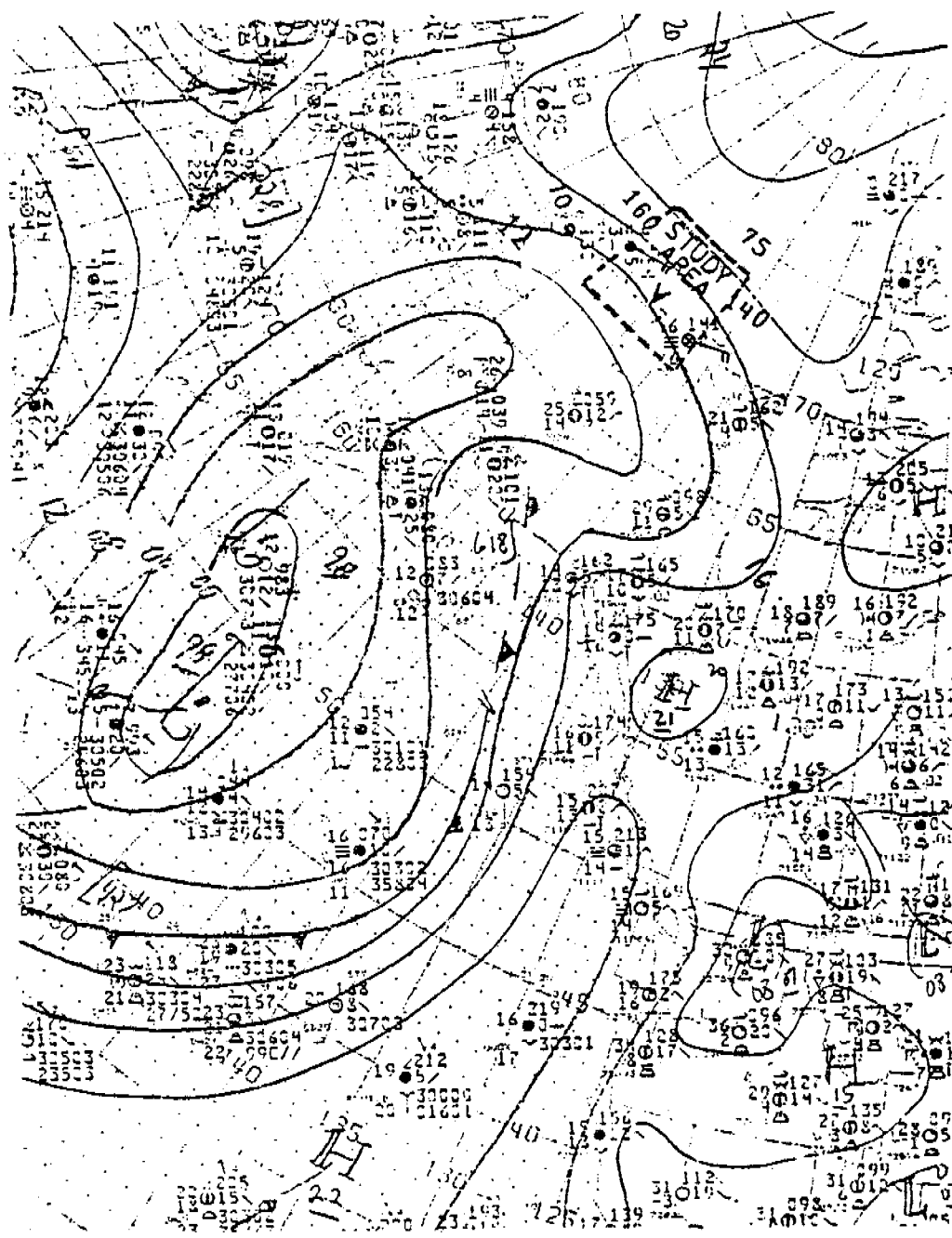


Fig. 11 NWS surface pressure chart for 1500 LDST August 8, 1977. The study area is outlined by dashed lines with an "arrow-head" indicating the Pingok Island position.

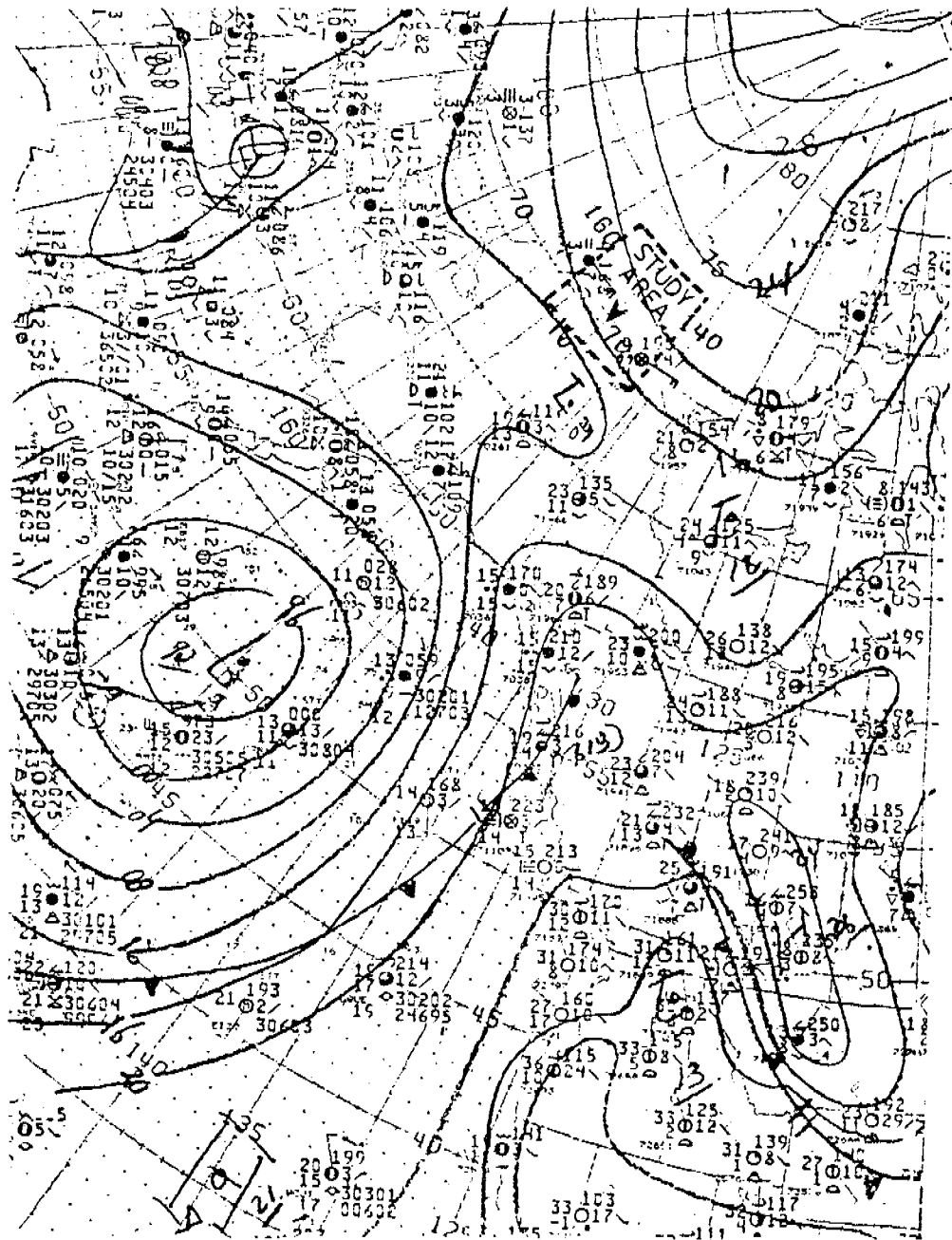


Fig. 12 NWS surface pressure chart for 1500 LDST August 9, 1977. The study area is outlined by dashed lines with an "arrow-head" indicating the Pingok Island position.

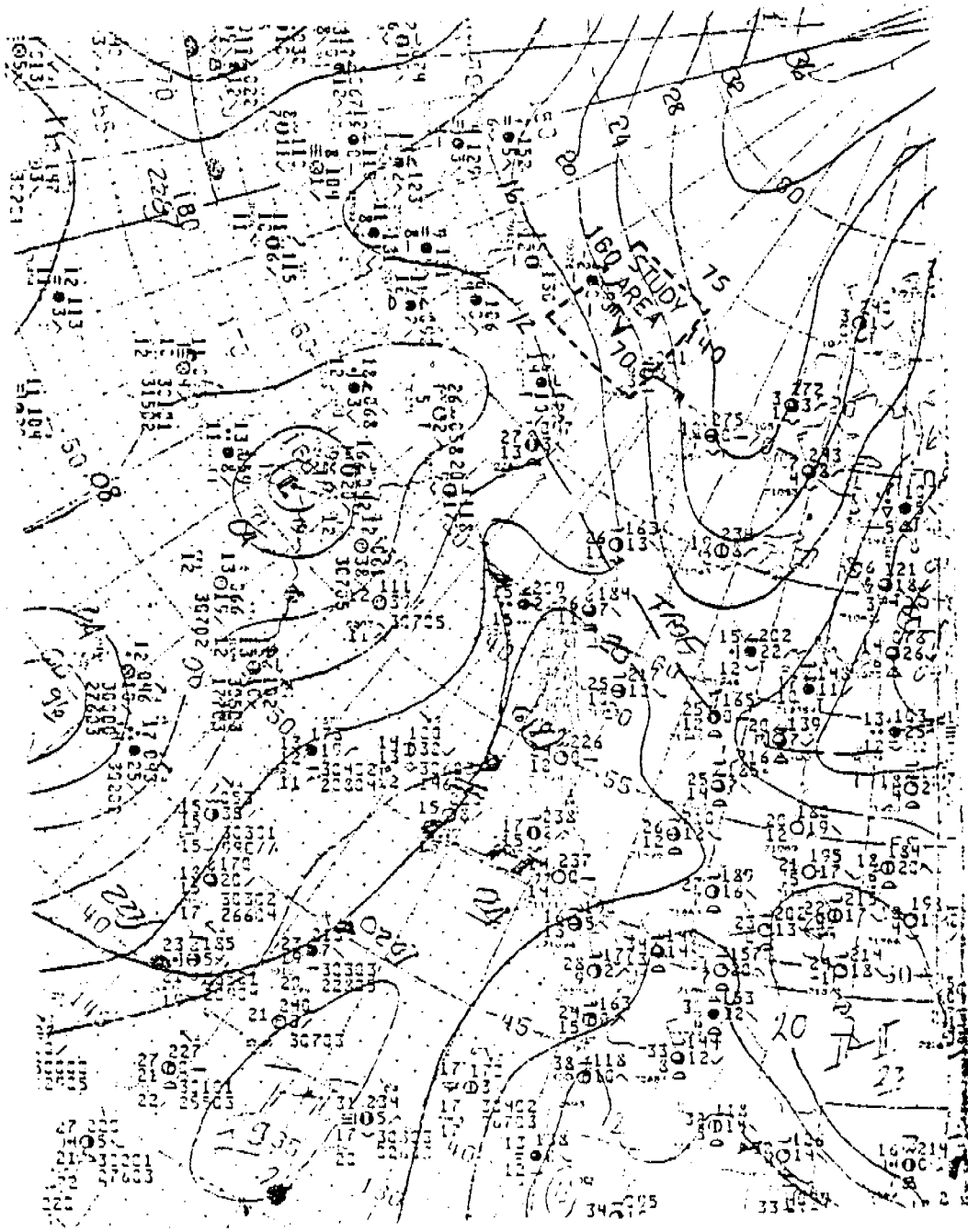


Fig. 13 NWS surface pressure chart for 1500 LDST August 10, 1977. The study area is outlined by dashed lines with an "arrow-head" indicating the Pingok Island position.



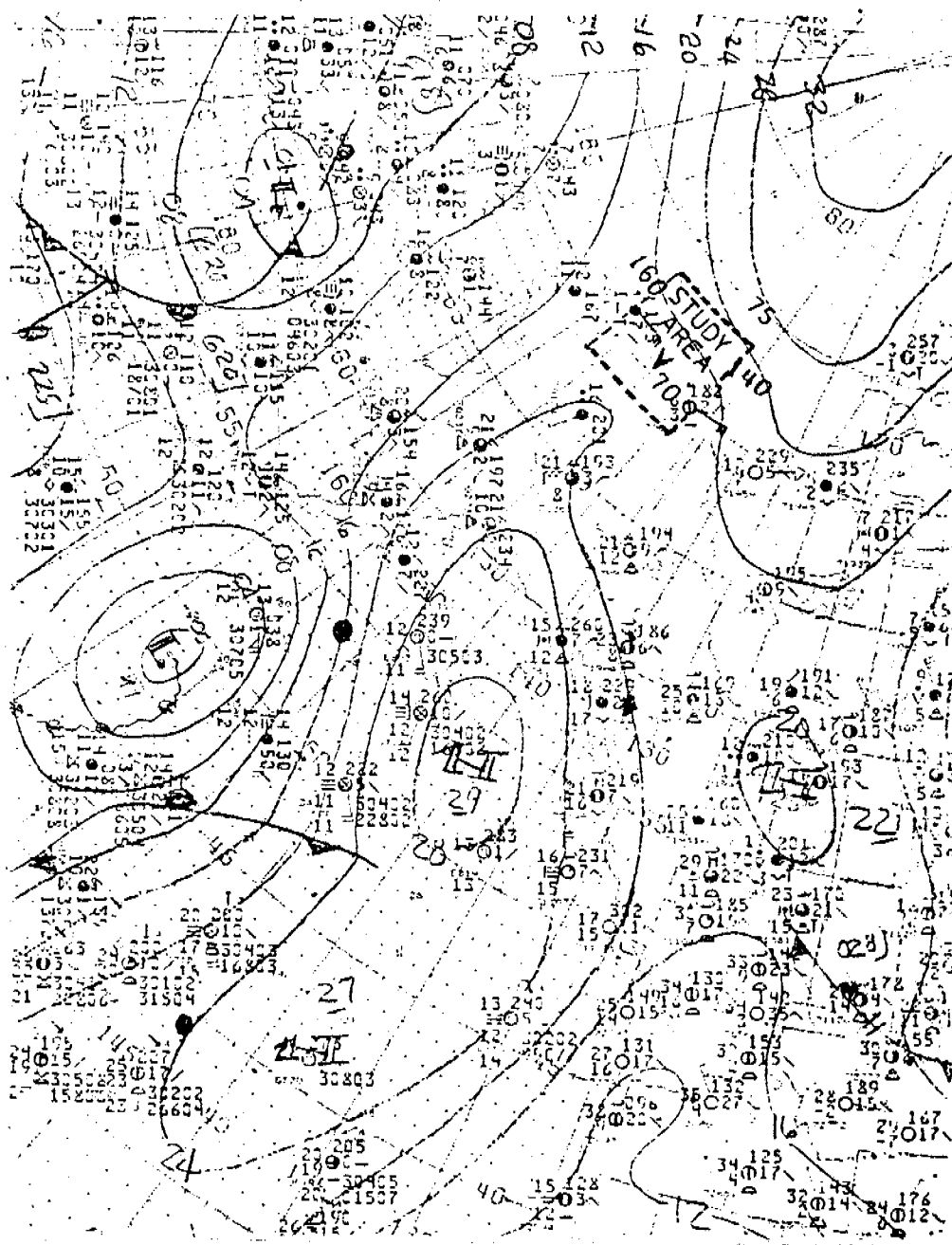


Fig. 14 NWS surface pressure chart for 1500 LDST August 11, 1977. The study area is outlined by dashed lines with an "arrow-head" indicating the Pingok Island position.

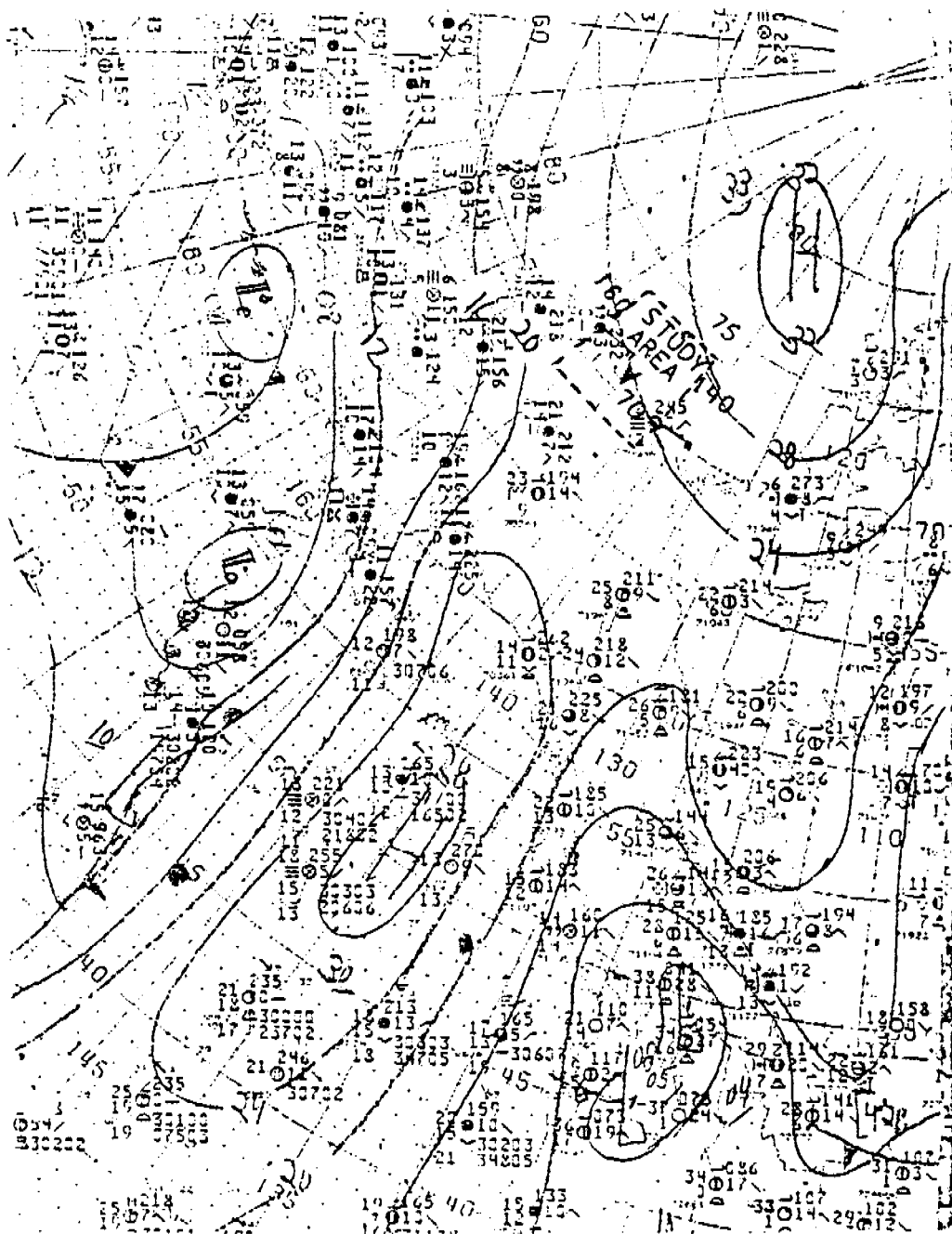


Fig. 15 NWS surface pressure chart for 1500 LDST August 12, 1977. The study area is outlined by dashed lines with an "arrow-head" indicating the Pingok Island position.

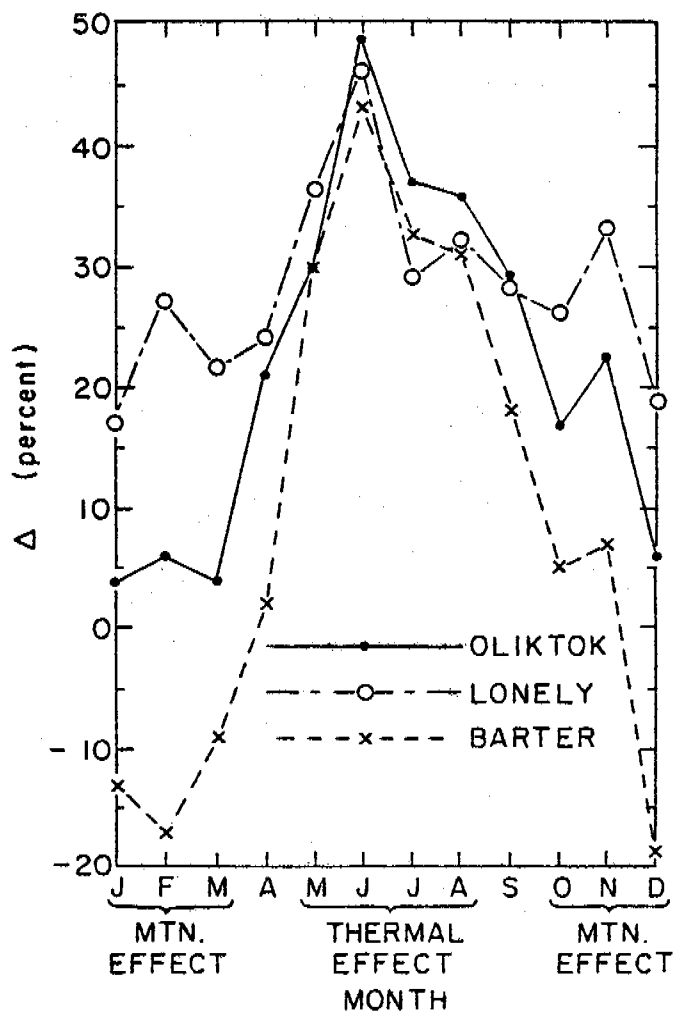


Fig. 16 Monthly percentage difference ( $\Delta\%$ ) between occurrence of NE-E winds and SW-W winds at Barter Island, Oliktok, and Lonely (all on the Beaufort Coast). Positive  $\Delta\%$  implies more east winds than west winds.

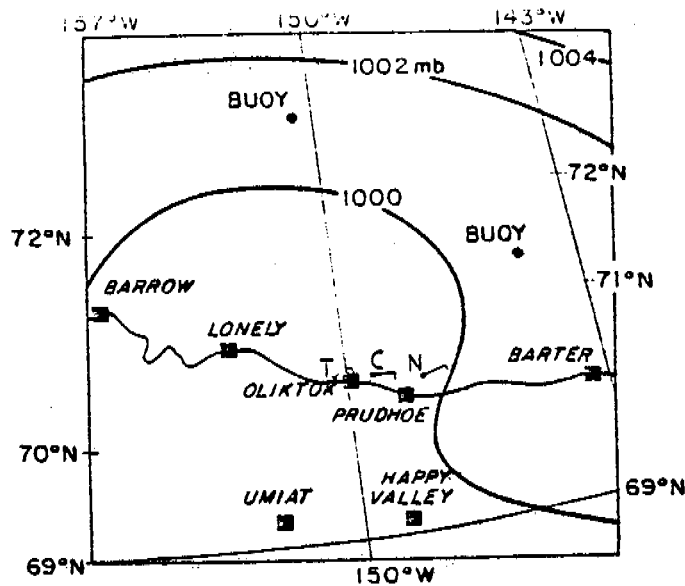


Fig. 17  
August 16, 1976

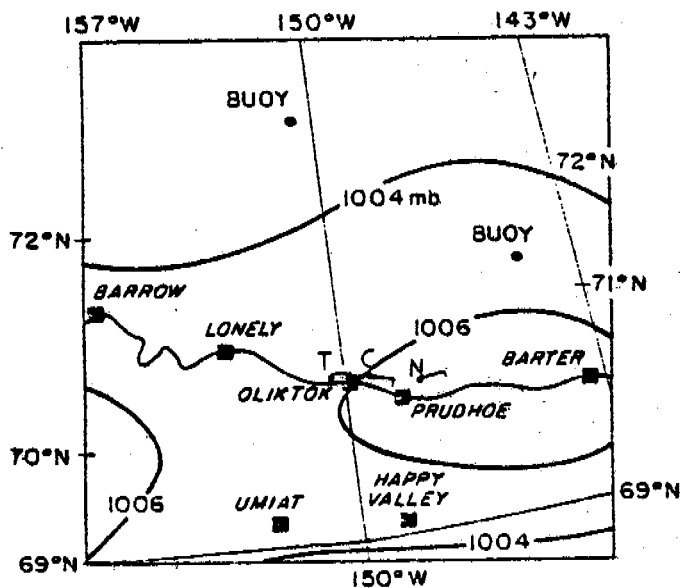


Fig. 18  
August 18, 1976

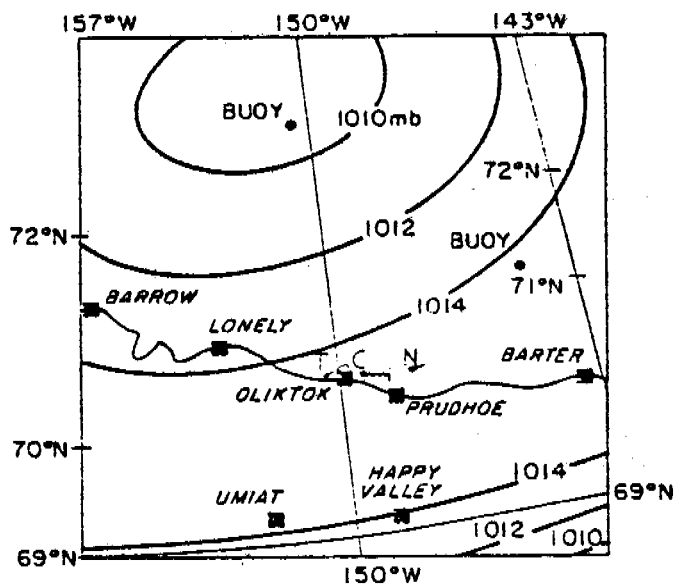


Fig. 19  
August 21, 1976

Fig. 17-19 Two-dimensional least squares fit to surface pressure network on August 16, 18, 21, 1976 (000 GMT). C, N, T represent actual surface wind measurements from Cottle Island, Narwhal Island and Tolaktovut Pt., respectively. (scale 128 km/inch).

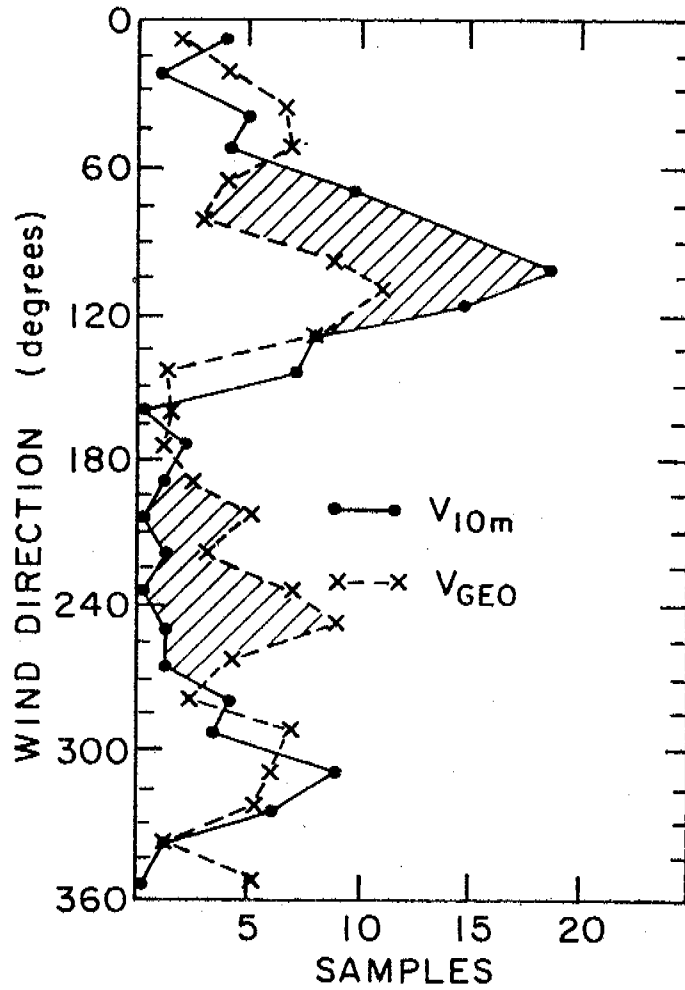


Fig. 20 Comparison of surface winds on Cottle Island (10 meters) with geostrophic winds in August 1976. The wind directions are in 15 degree increments. The actual time period is for August 13 to August 23 and August 30 to September 3, 1976.

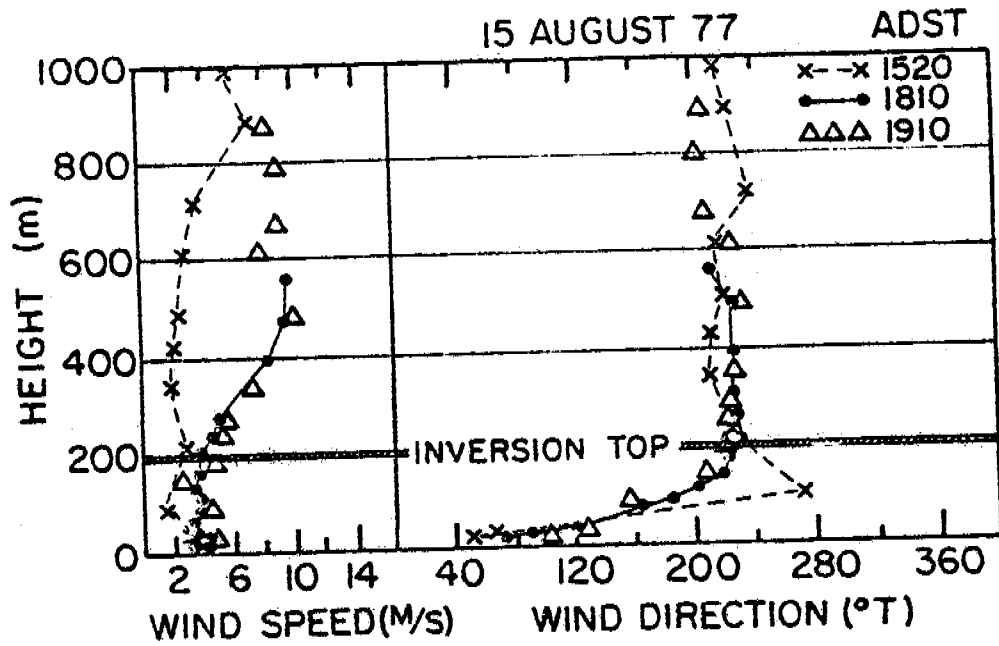


Fig. 21a

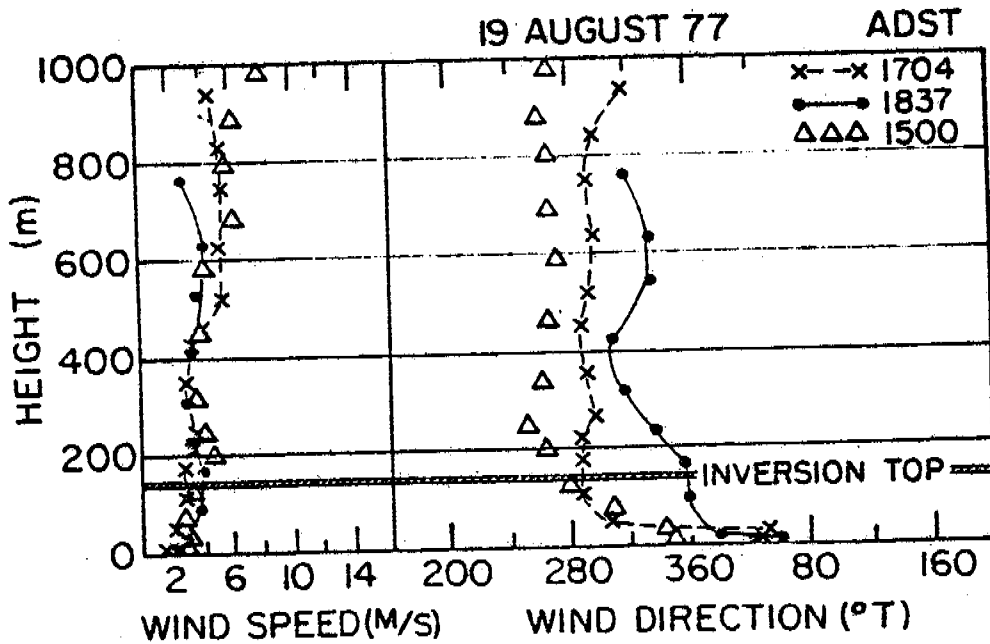


Fig. 21b

Figs. 21a and 21b Pilot balloon derived profiles of wind speed and wind direction for designated times on August 15, 1977 (LDST) and August 19, 1977 (LDST). Top of ground based inversion layer is shown.

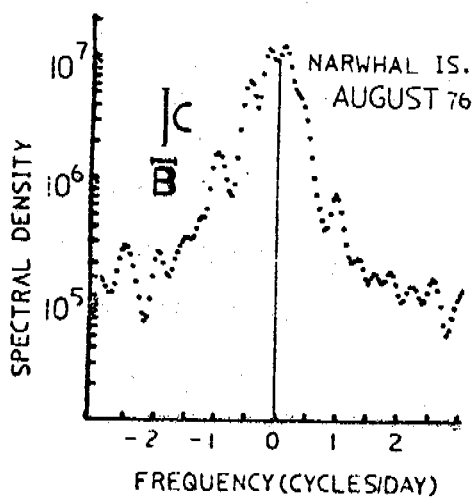


Fig.22a

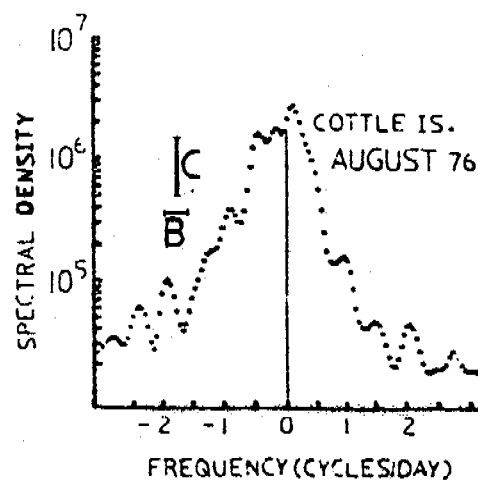


Fig.22b

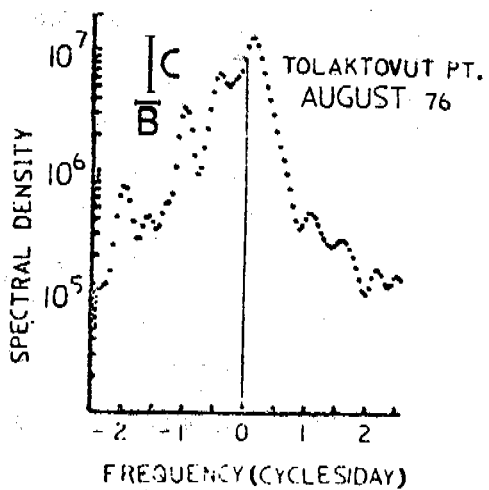


Fig.22c

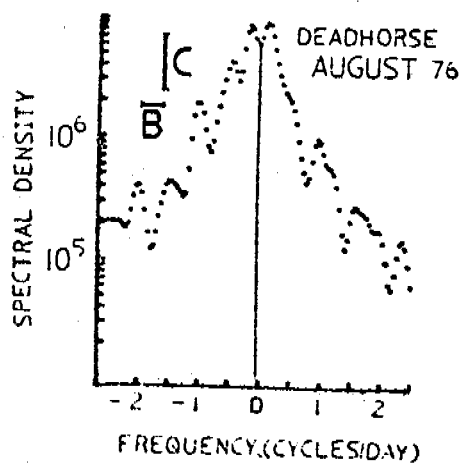


Fig.22d

Figs. 22a-22d Time series rotary spectra of surface wind velocity data for August 1976 collected from Narwhal Island, Cottle Island, Tolaktovut Pt. and Deadhorse.

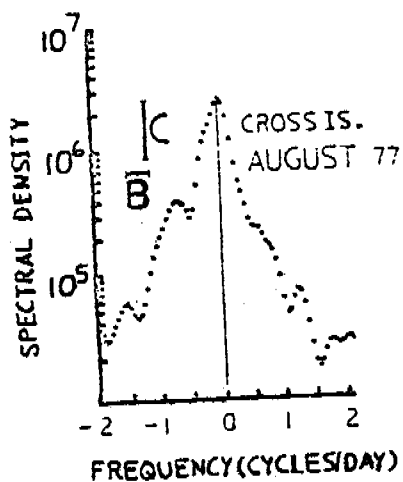


Fig.23a

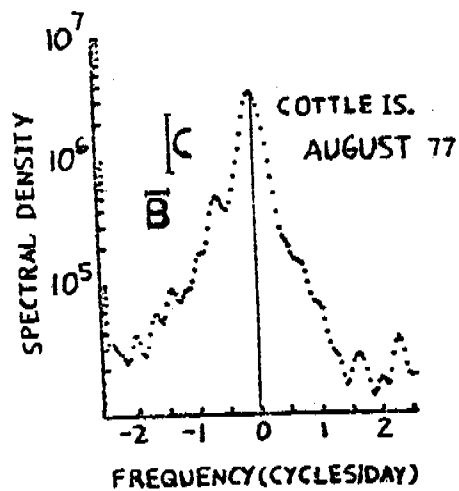


Fig.23b

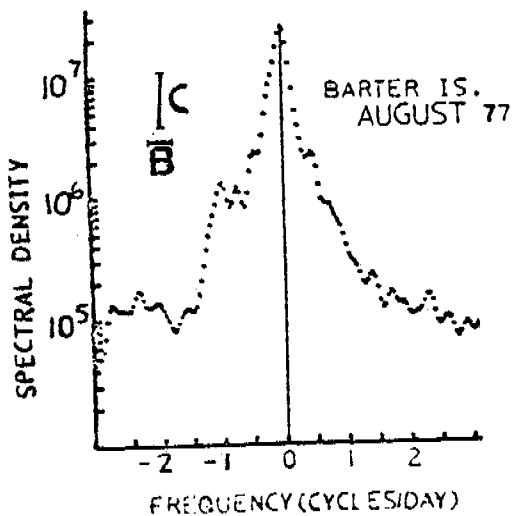


Fig.23c

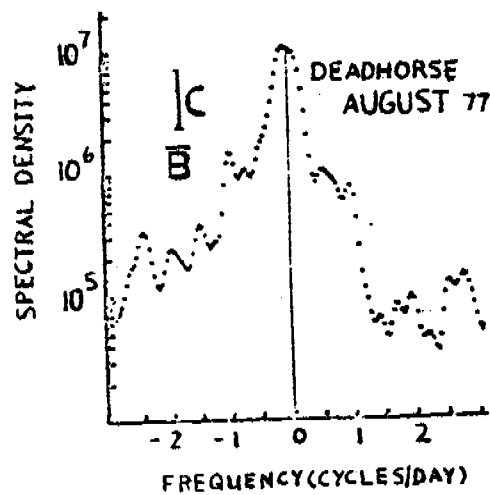


Fig.23d

Figs. 23a-23d Time series rotary spectra of surface wind velocity data for August 1977 from Cross Island, Cottle Island, Barter Island and Deadhorse.



Figs. 24a and 24b Local surface wind vector directions for stations (as referenced below).

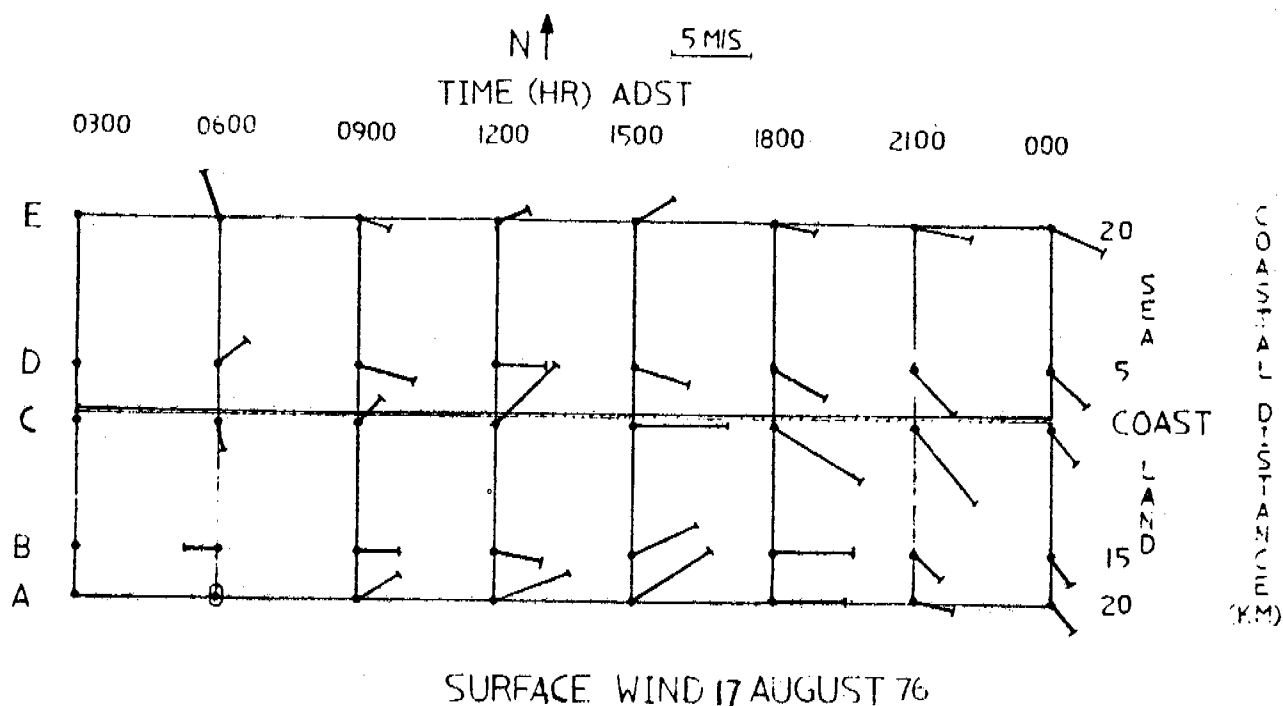


Fig. 24a (E) Narwhal Island; (D) Cottle Island; (C) Tolaktovut; (B) ARCO Airport; (A) Deadhorse Airport

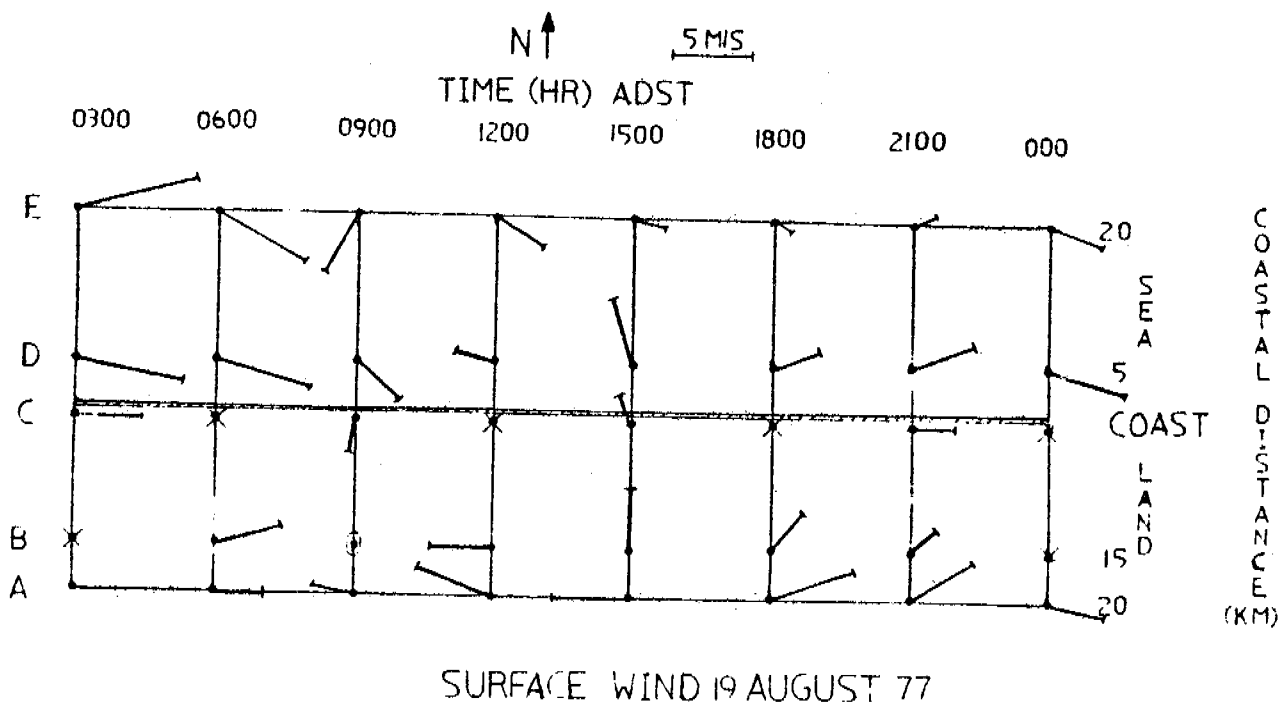


Fig. 24b (E) Cross Island; (D) Cottle Island; (C) Oliktok, (B) ARCO Airport; (A) Deadhorse Airport

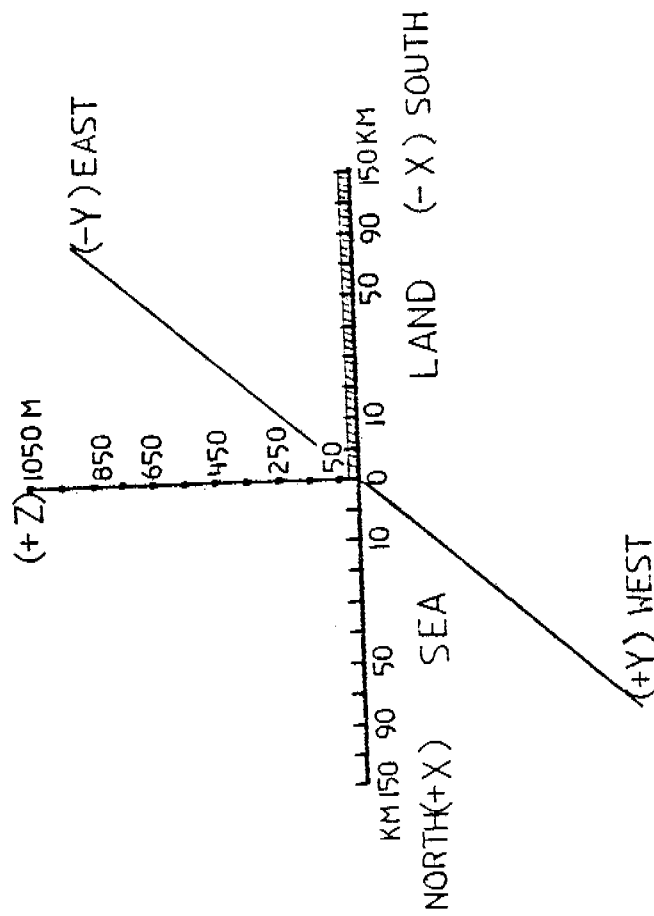


Fig. 25 Sea breeze model coordinate system and x, y, z domains of coverage.

Model Output  
 Geostrophic wind = 5 m/s from 220°T  
 (Pingok Island is 5 km seaward of the coastline)

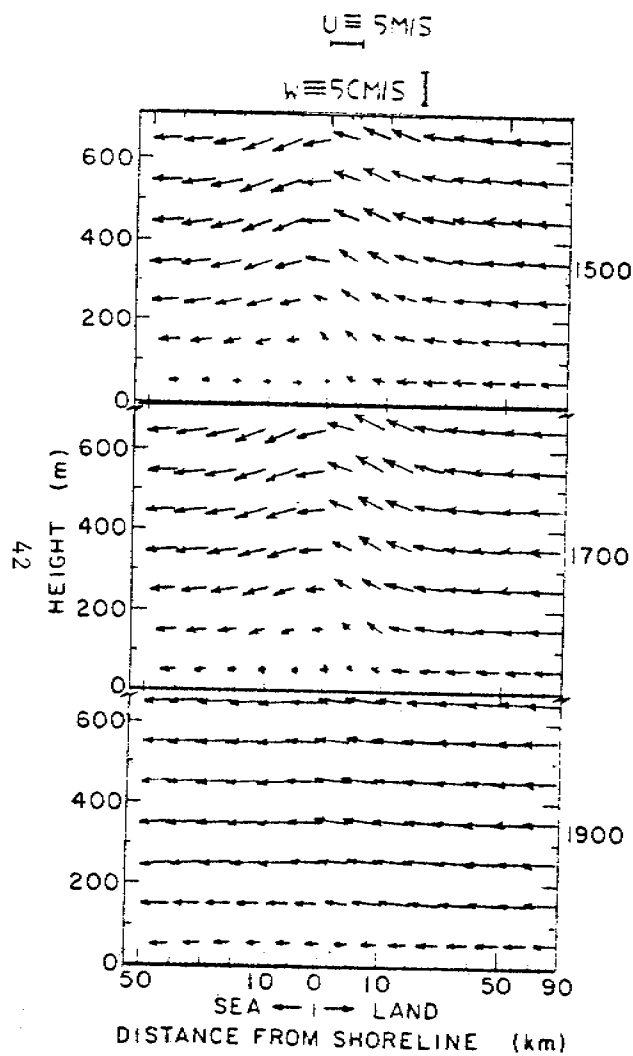


Fig. 26a. Total u-w plane velocity vectors. The u component is perpendicular to the coast and the w is the vertical velocity component.

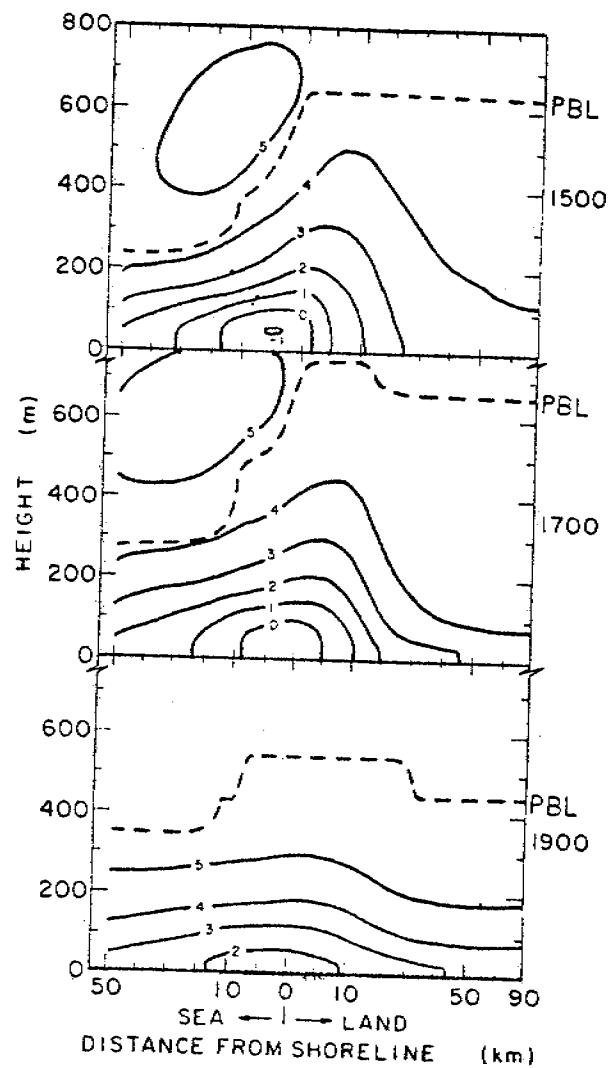


Fig. 26b. Isotachs (m/s) of  $u$  ( $u_L + u'$ ). The  $u$  component is perpendicular to the coast with (-) values representing shoreward flow. The boundary layer height (PBL) is shown as a dashed line.

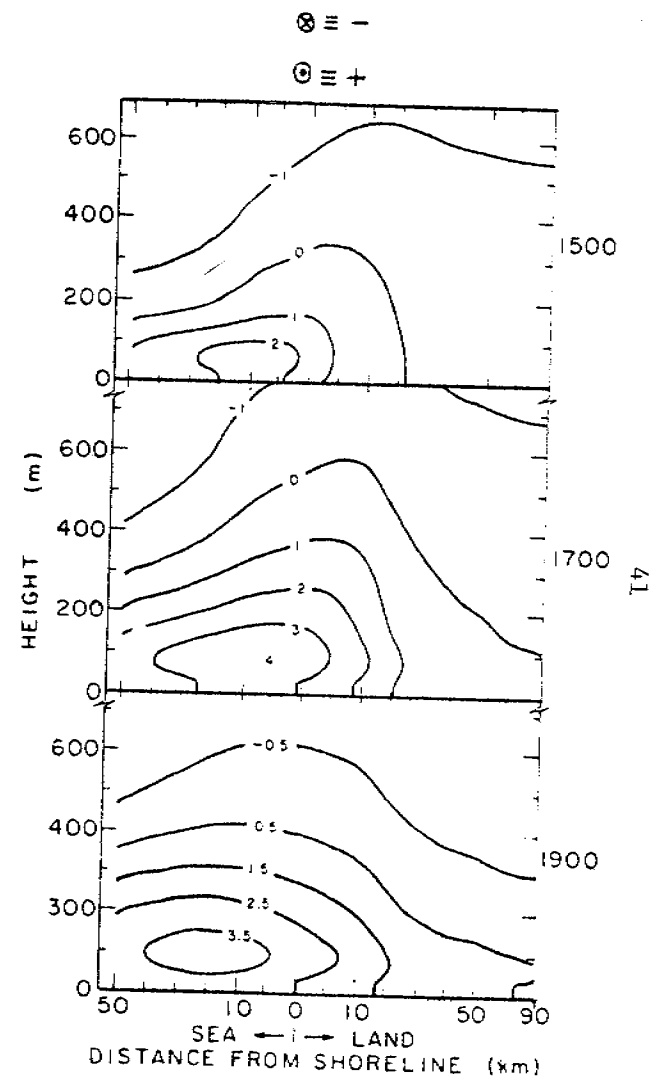


Fig. 26c. Isotachs (m/s) (cross section) of  $v$  ( $v_L + v'$ ). The  $v$  component is parallel to the coast with (-) values representing flow into the figure (west winds).

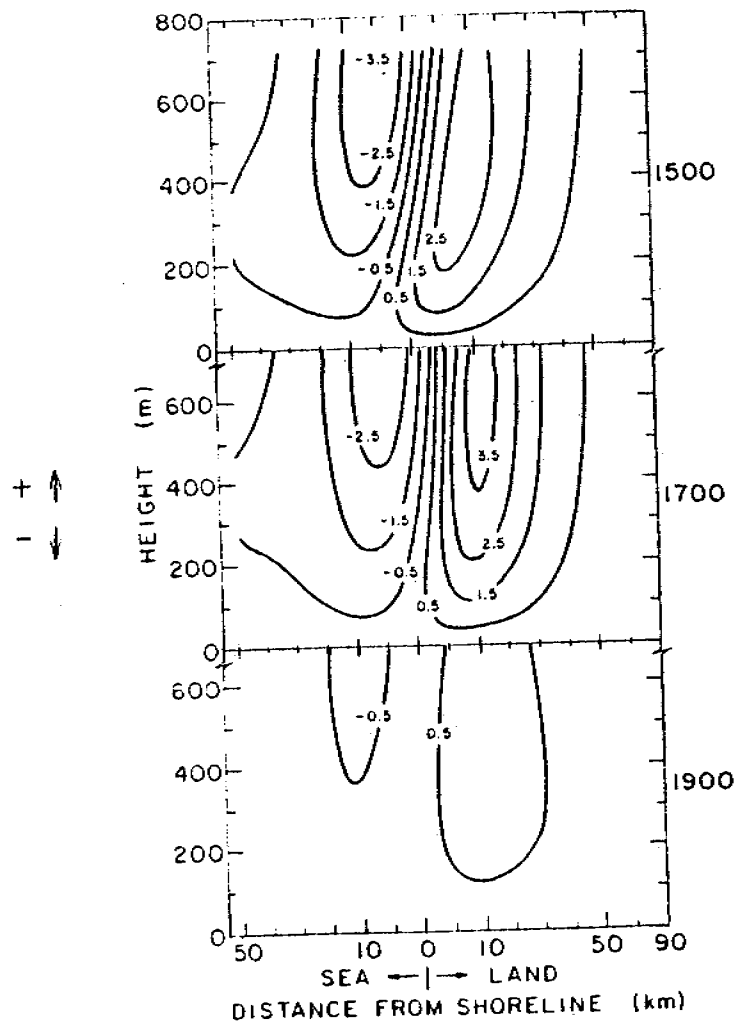


Fig. 26d Model output of isotachs of  $w$  (cm/s) for a geostrophic wind of 5 m/s from  $220^\circ\text{T}$ . The  $w$  component is (+) for upward flow. Pingok Island is 5 km seaward of the coastline.

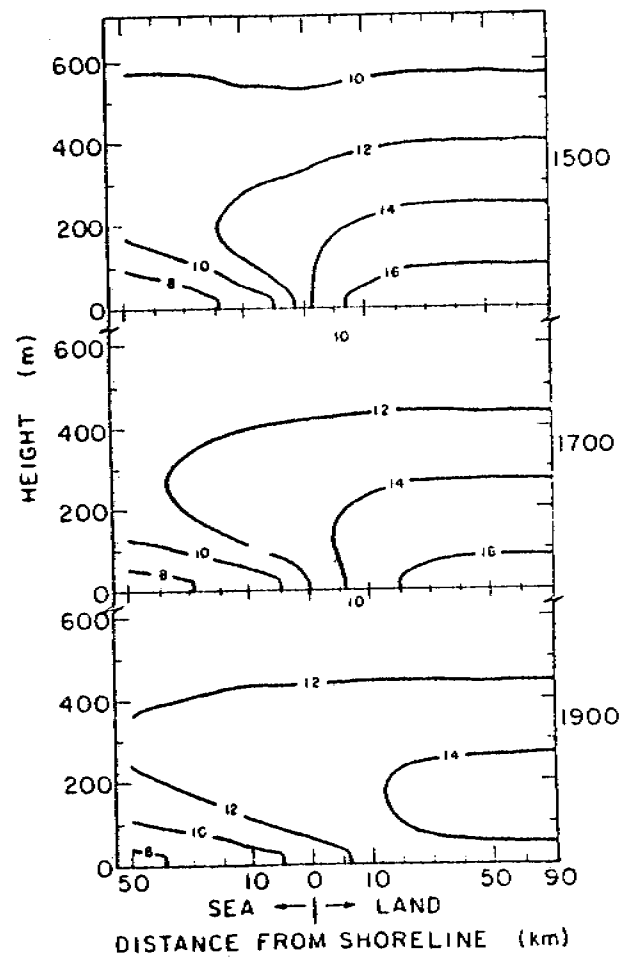


Fig 26e Model output of temperature contours ( $^\circ\text{C}$ ) for a geostrophic wind of 5 m/s from  $220^\circ\text{T}$ . Pingok Island is 5 km seaward of the coastline.

Fig. 27a

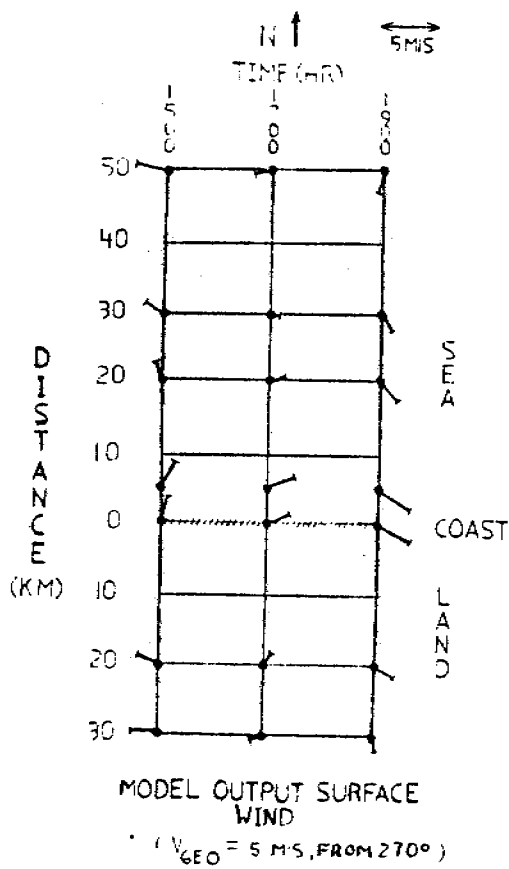


Fig. 27b

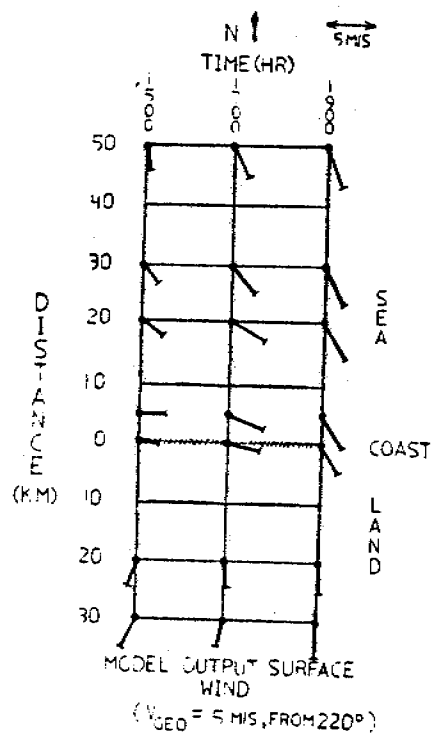
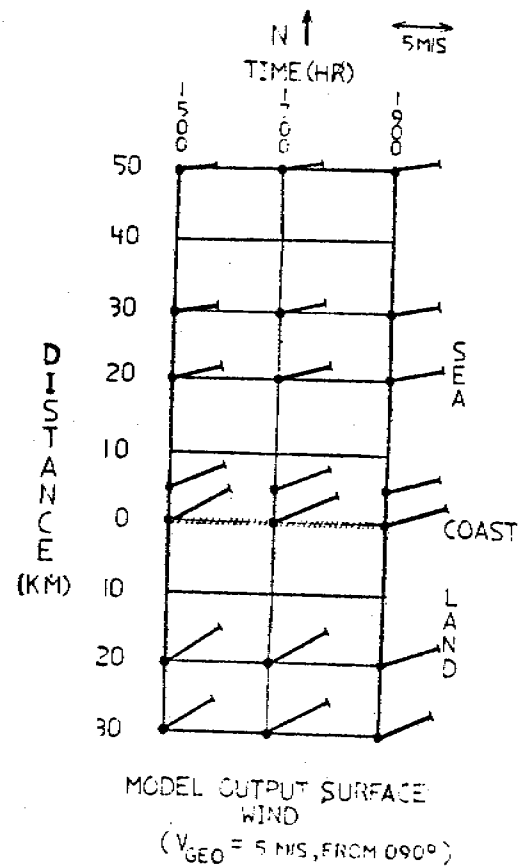
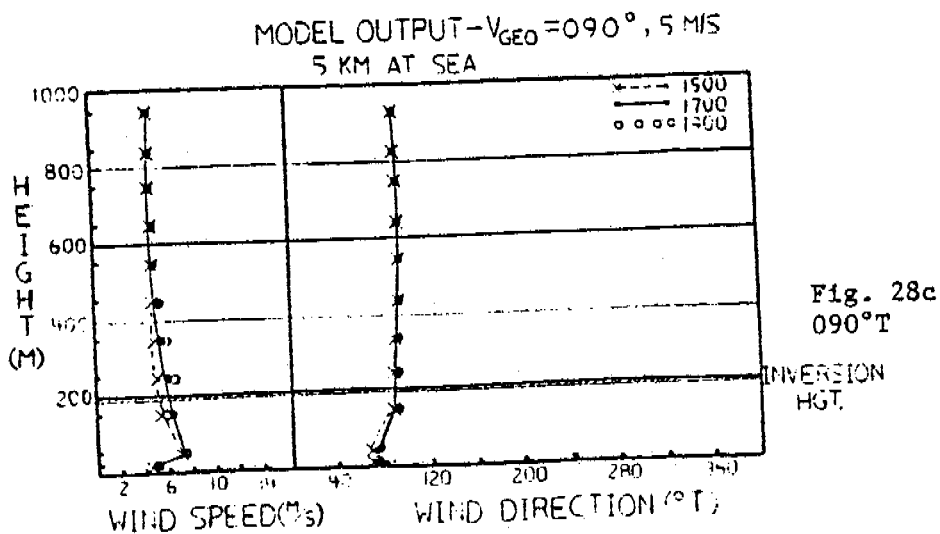
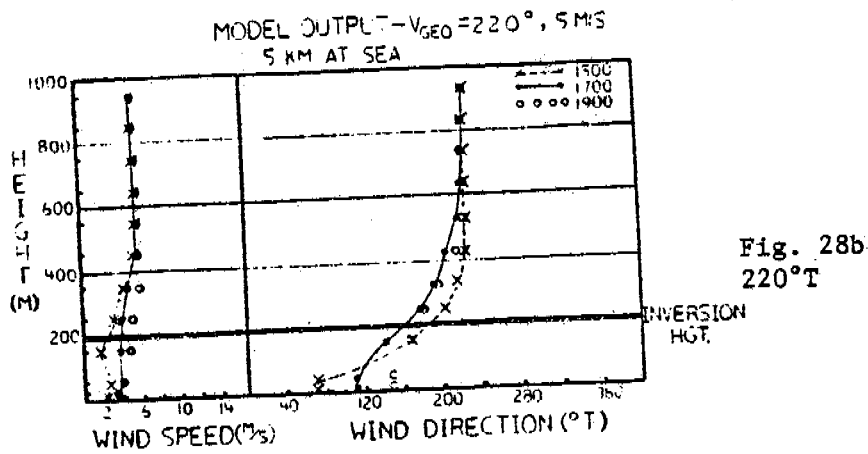
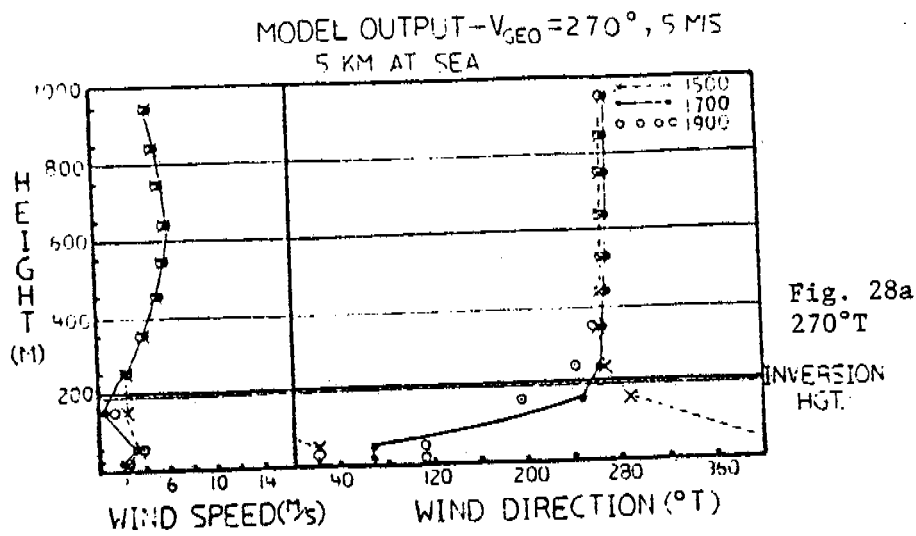


Fig. 27c



Figs. 27a-27c Model output of surface wind vectors for 1500, 1700, 1900 with a geostrophic wind ( $V_{geo}$ ) of 5 m/s from  $270^\circ$ T,  $220^\circ$ T and  $090^\circ$ T (as shown above). Pingok Island is 5 km seaward of the coast.



Figs. 28a-28c Model output of wind speed and wind direction profiles, 5 km from the coast, for the designated times with geostrophic wind ( $v_{geo}$ ) of 5 m/s from 270°T, 220°T and 090°T (as shown above).

Comparison Between Geostrophic Winds Derived from the Standard  
Pressure Measurement Network and the AIDJEX Network.

Eric Leavitt

1. Introduction

Studies of ocean current or ice trajectories require specification of the surface air stress. The normal method is to relate the air stress to the geostrophic wind speed calculated from the gradient of the observed surface pressure field. For example, Thomas and Coon (RU 567, see 1979 annual report) used an historical pressure data set compiled at the National Center for Atmospheric Research (NCAR) to study ice trajectories along the Alaskan North Slope for OCSEAP. They noted (personal communication) that geostrophic wind speeds derived from the NCAR data seemed low compared to surface wind data tabulated in Brower et al. (1977).

During the AIDJEX project surface pressure measurements were made at four manned camps and several data buoys deployed in the Beaufort Sea. Albright (1978) noted that there were large differences in the AIDJEX region between National Weather Service analyses and his analyses using the additional observations. He found pressure differences as large as 14 mb at the location of the manned camps. The accuracy of the NCAR winds is examined by comparing them to the AIDJEX geostrophic winds and to measurements of surface winds at Point Barrow (BRW), Barter Island (BTI) and the AIDJEX manned camps.

2. Data

The time period selected for study was July 20, 1975 (day 201) through March 26, 1976 (day 450). This includes the period during which the largest number of additional pressure sensors were deployed during AIDJEX.

The NCAR data set consists of surface pressures interpolated on a grid spacing of 400 km. Thomas further interpolated the pressures to a spacing of 200 km and then computed the geostrophic wind at the centers of each reduced grid element. Winds for a particular site were calculated by interpolation from this geostrophic grid. Although the NCAR data set included data at 0000 Z and 1200 Z, only 1200 Z data was used in the study by Thomas and Coon and also in this comparison.

Preparation of the AIDJEX pressure maps and calculation of geostrophic winds is described in Albright (1978). The original NMC pressure maps were used to determine pressure values on the border of a 1000 km square centered on the manned camps. A sixth order polynomial was fitted to those values plus observations from NWS stations located within the square and AIDJEX stations. Geostrophic winds were then computed by differentiating the polynomial for specified locations.

Surface winds were measured during AIDJEX at the manned camps from 10 meter towers as described in Leavitt et al. (1978). Values of the surface wind at 1200 Z for BRW and BTI were taken from the monthly weather summaries published by NOAA. These data were less accurate than the AIDJEX surface winds; speeds are reported to the nearest knot, and wind direction is reported to the nearest 10 degrees.

### 3. Comparisons

#### 3a. AIDJEX Camp

Figure 1 is a plot of the frequency of occurrence of surface and geostrophic wind directions at AIDJEX camp Caribou. Thirty degrees was subtracted from the geostrophic winds to approximate the turning of wind direction with height in the planetary boundary layer. (Plots for the other manned stations are



essentially identical.) Plots for the other manned camps show essentially the same good agreement between the two data sets. A bivariate distribution also showed that the two wind directions were in the same sector for 70% of the cases and within plus or minus one sector for 95% of the cases. Albright (1977) reported that a linear relationship fits the two data sets with better than 90% confidence.

Geostrophic wind direction frequencies for NCAR and AIDJEX data are compared in figure 2. Plotted in this fashion the two data sets are not particularly different. The NCAR data shows a larger peak for northwest winds and there is a one sector displacement in the location of the distribution minimums. The NCAR mean wind speed for winds greater than 3 m/s was 7.9 m/s compared to 9.3 m/s for AIDJEX winds but the mean difference in wind direction was only  $-2^\circ$ . However, only 28% of the data points were simultaneously from the same sector and only 80% were from the same sector plus or minus one. The AIDJEX geostrophic and surface winds correlated better with each other than either with the NCAR derived winds.

### 3b. Barter Island Winds

The wind direction distribution for the two geostrophic data sets at BTI is shown in figure 3. The number of west and northwest winds is greater in the AIDJEX data which also displays a greater tendency to a bi-modal distribution. As was the case for the camp data the AIDJEX geostrophic wind speed ( $= 10.5$  m/s) is greater than the NCAR mean ( $= 7.4$  m/s). A comparison of individual values showed that this difference occurred because the NCAR values increasingly underestimate the wind speed as the speed increases.

The surface wind distribution for BTI is plotted in figure 4 and shows a bi-modal distribution that is characteristic for BTI winds, Brower et al. (1977). Several authors have suggested that this is evidence of the influence

of the Brooks range on the flow (e.g., Schwerdtfeger, 1974). The mean direction difference between the surface and geostrophic winds was  $13^\circ$  for AIDJEX and  $5^\circ$  for the NCAR data but this may be biased because the surface winds were only reported to the nearest  $10^\circ$ , ( $20^\circ$  was subtracted from the geostrophic winds plotted in figure 4). Mean wind speeds were 8 m/s, 7.4 m/s and 10.5 m/s for surface, NCAR and AIDJEX winds respectively.

The bivariate distribution for AIDJEX and surface winds is listed in Table 1. There are a significant percentage of cases where the geostrophic wind direction was  $\approx 180^\circ$  different from the surface wind. The NCAR-surface wind distribution showed the same behavior. AIDJEX and surface winds were in the same section 46% and within one adjacent sector 73% of the time. For the NCAR data the numbers were 21% and 51%.

### 3c. Point Barrow

The distribution of geostrophic wind directions at BRW did not show any significant differences between the two data sets. Surface wind distributions calculated assuming  $20^\circ$  at turning are compared to observed BRW surface winds in figure 5. Only relatively small differences are apparent. The bivariate distribution did not reveal significant numbers of  $180^\circ$  direction differences. The AIDJEX-surface winds were from the same sector in 45% of the cases and within one sector in 79%. The NCAR-surface wind numbers were 30% and 65%.

AIDJEX wind speeds were again larger than the NCAR wind speeds, the mean values were 11.4 m/s and 7.4 m/s. The mean surface wind speed was only 5.3 m/s which suggests a systematic error in the AIDJEX values. However, while it is relatively easy to understand how a sparse pressure network can cause the gradient and hence the wind speed to be underestimated, it is difficult to explain a consistent overestimate. This suggests that the reported BRW wind speeds are underestimates of the "true" surface wind speed at least for this comparison.

### 3d. Comparison of winds at BRW and BTI

The bivariate distribution of BRW and BTI surface winds is listed in table 2. The most significant difference between the winds is the large number of northeast and north winds at BRW which are west winds at BTI. The ratios of the mean wind speeds by sector are plotted in table 3. Westerly winds at BTI are considerably speeded up compared to BRW winds. For easterly winds BTI winds are still larger but the difference is less. From the discussion above the significance, if any, of this difference in wind speeds is not clear. The directional differences in winds between the two sites may partially explain the BTI geostrophic-surface directional differences noted in 3b.

### 4. Conclusions

Wind speeds derived by Thomas and Coon from the NCAR data set are underestimated by approximately 25%. The Point Barrow comparison suggests that either the AIDJEX geostrophic wind speeds are too large or that the BRW surface observations are about 20% low relative to measurements at the other stations. This conclusion assumes that the ratio of the surface wind speed measured at  $\approx 10$  m, to the geostrophic wind speed is approximately 0.6. Using this same criterion the Barter Island AIDJEX winds are slightly underestimated since the ratio of BTI surface to geostrophic wind speed was  $\approx 0.8$ .

Mean wind directions from the two geostrophic data sets agreed within a few degrees at all three stations. The average turning between surface and geostrophic was less than  $20^\circ$  for the land stations compared to about  $30^\circ$  (Albright, 1978) for the camp comparison. This could reflect differences in mean boundary layer stratification and is perhaps also affected by the fact that the land stations only report wind direction to the nearest  $10^\circ$

The differences reported here should not seriously affect the conclusions about possible mean oil-in-ice trajectories of Thomas and Coon. There are other variables that were not modelled such as ocean currents, that would have a greater influence on the results. The results do indicate a potential problem for studies of ice dynamics because it is the periods at high wind speeds that will be underestimated most severely by an NCAR type data set. Also, although the direction agrees in the mean, there are large random errors in the wind direction that may be important on shorter time scales.

#### References

- Albright, M. 1977. Geostrophic wind calculations for AIDJEX. Symposium on Sea Ice Processes, University of Washington, Seattle, Washington. To be published by University Press.
- Albright, M. 1978. Construction of atmospheric surface pressure maps from the AIDJEX data set. AIDJEX Bulletin, 39, 111-120.
- Brower, W. A., H. W. Searby, J. L. Wise, H. F. Diaz, A. S. Prechtel. 1977. Climatic Atlas of the Outer Continental Shelf, Vol. III Chukchi-Beaufort Sea. NOAA.
- Leavitt, E., M. Albright and F. Carsey. 1978. Report on the AIDJEX meteorological experiment. AIDJEX Bulletin, 39, 121-148.
- Schwerdtfeger, W. 1974. Mountain barrier effect on flow of stable air north of Brooks Range. Climate of the Arctic. Conference publication, University of Alaska, Fairbanks, Alaska, 204-208.
- Thomas, D. and M. D. Coon. 1979. RU 567 Annual Report to OCSEAP.

Table 1. The bivariate distribution of equivalent AIDJEX and actual wind directions at Barter Island. Twenty degrees was subtracted from the geostrophic direction. Frequencies are listed as percentages of total number of occurrences.

		AIDJEX Equivalent Surface Wind Direction							
		N	NE	E	SE	S	SW	W	NW
Barter Island Surface Wind Direction	N	.5	2.5	.5	.5	0	—	—	—
	NE	.5	4.5	4.5	—	0	.5	.5	—
	E			15.8	3.5	.5	.5	<u>5.0</u>	2.0
	SE				.5	1.0	1.0	1.0	—
	S				1.0	1.0	0	—	—
	SW			2.5	.5	.5	1.0	2.5	1.0
	W	3.0	2.	<u>9.4</u>	.5	—	2.0	17.8	6.9
	NW			.5	.5	—	—	—	1.0

Table 2. Bivariate distribution of surface wind directions at Barter Island and Point Barrow. Frequencies are listed as percentage of total number of occurrences.

		Barter Island Wind Direction							
		N	NE	E	SE	S	SW	W	NW
Point Barrow Wind Direction	N	.6	.6	3.8			.6	5.0	
	NE	.6	1.3	6.9			.6	6.9	
	E		6.3	18.8	1.3		.6	1.3	
	SE			2.5	.6		.6	1.3	.6
	S			.6	.6	1.3	1.9	1.9	
	SW			0	.6	1.3	1.9	4.4	
	W		.6	.6	0		.6	11.9	.6
	NW		.6	1.3	.6			8.1	

Table 3. Ratio of Barter Island to Barrow surface wind speeds by wind direction sector. The ratios were only calculated for sectors with frequencies greater than 1%.

Barrow Wind Direction	Barter Island Wind Direction							
	N	NE	E	SE	S	NW	W	NW
N	—	—	1.32				1.96	
NE	—	.85	1.48				1.56	—
E	—	.99	1.36	1.44			.84	—
SE	—		1.68				1.25	—
S	—				.71	1.18	.79	—
SW	—				.95	1.0	1.53	—
W	—						2.18	—
NW	—		3.13				3.13	—

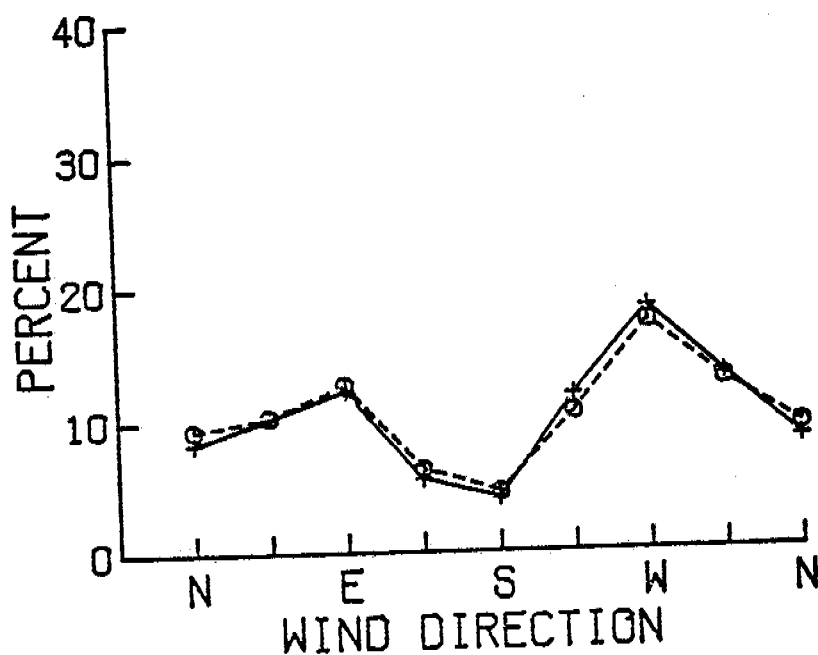


Figure 1. Histogram of surface and AIDJEX geostrophic wind direction frequencies at AIDJEX Camp Caribou. Thirty degrees was subtracted from the geostrophic wind direction to approximate the surface wind direction. Class intervals for this and succeeding plots are 45 degrees and are centered on north, north-east, etc. directions. The symbols are o---o measured surface winds, +---+ geostrophic.

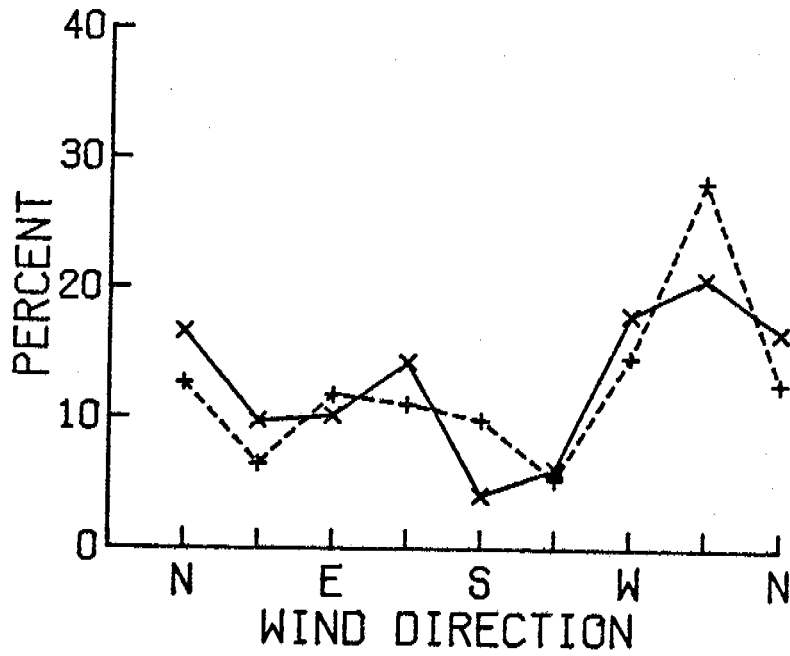


Figure 2. Histogram of NCAR and AIDJEX geostrophic wind direction frequencies for the mean camps position. The symbols are +---+ NCAR, x---x AIDJEX.

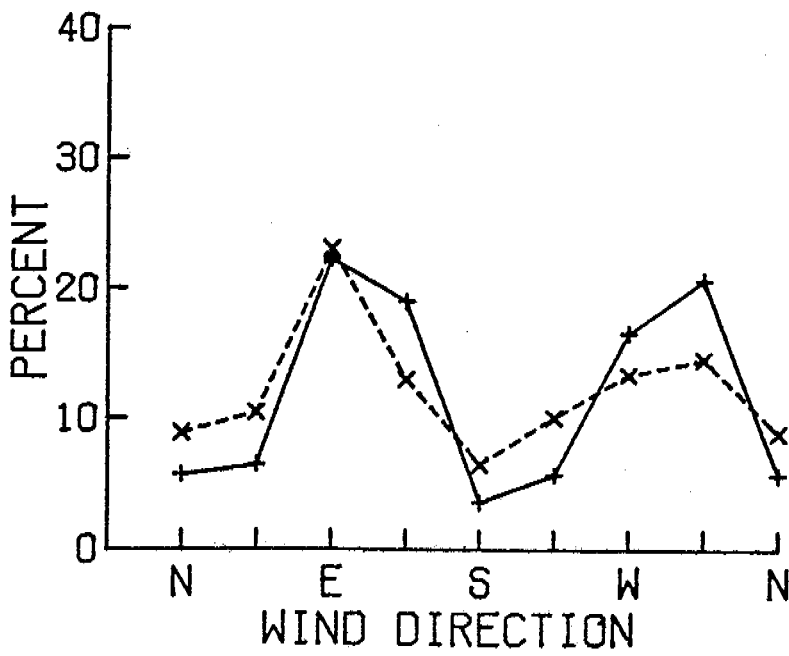


Figure 3. Histogram of NCAR and AIDJEX geostrophic wind direction frequencies at Barter Island. The symbols are x---x NCAR, +---+ AIDJEX.

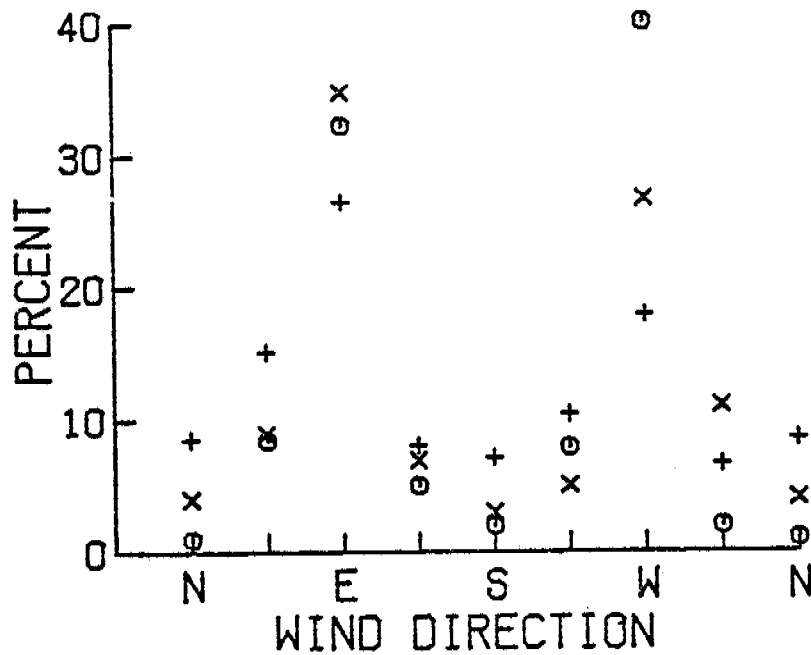


Figure 4. Histogram of surface wind direction frequencies at Barter Island. The symbols are 0 — measured surface winds, X — AIDJEX, + — NCAR. Twenty degrees was subtracted from the geostrophic wind directions to approximate the surface wind directions.

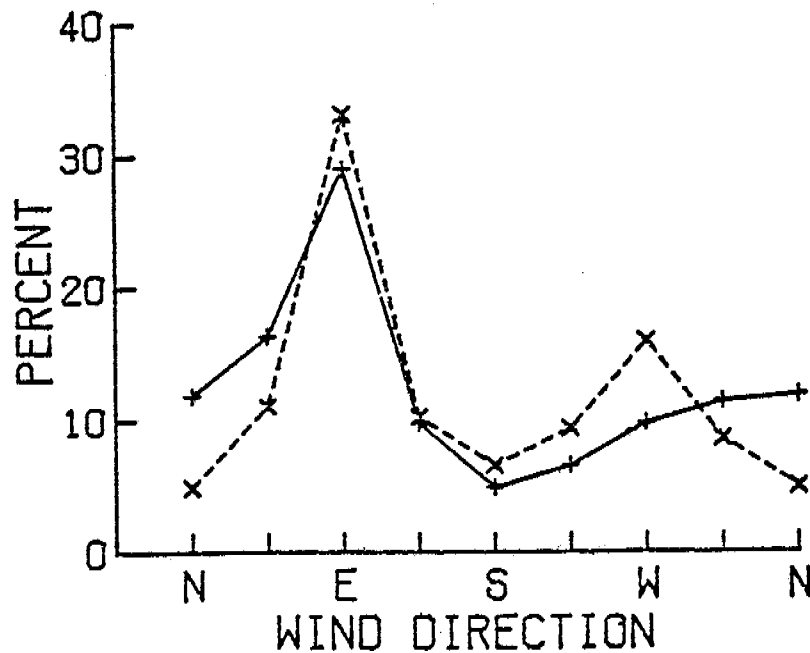


Figure 5. Histogram of geostrophic wind direction frequencies for Point Barrow. The symbols are x — x NCAR, + — + AIDJEX.



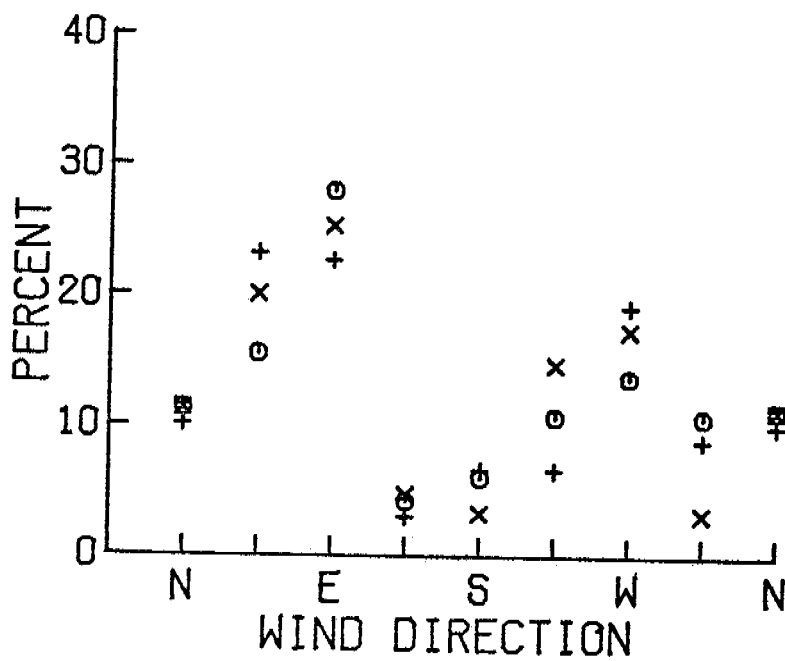


Figure 6. Histogram of surface wind direction frequencies for Point Barrow. Twenty degrees was subtracted from the geostrophic wind directions to approximate the surface wind directions. The symbols are O—measured surface wind, X—NCAR, +—AIDJEX.

ANNUAL REPORT

Contract #03-5-022-56  
Research Unit #526-77  
Task Order # 13  
Reporting Period: 1 April 1978 -  
31 March 1979  
Number of Pages:

CHARACTERIZATION OF THE NEARSHORE HYDRODYNAMICS  
OF AN ARCTIC BARRIER ISLAND-LAGOON SYSTEM

J. B. Matthews  
Geophysical Institute  
University of Alaska  
Fairbanks, Alaska 99701

March 31, 1979

## I. Summary

Data from a Beaufort Sea lagoon system have been briefly examined for the period from before ice break-up to the end of the summer, ice-free season. Water of salinities greater than 40 ‰ and temperatures near -2°C were observed in Egg Island channel in 5 m water under 2 m ice in late May and early June.

The Kuparuk River over-flowed the ice and reached Egg Island channel on June 8, 1979. The channel water remained mainly fresh and cold until July 13. Saline coastal water returned to the channel on that date.

Data from off Beechy Point and Milne Point in August show great consistency between the various stations. Temperatures up to 12°C were observed early in the season when solar radiation was high. Salinities were near 20 ‰ at this time and still showed the influence of coastal runoff.

As August progresses, storms were observed to contribute to the intrusion of cold saline coastal waters into the lagoon. As the freezing season approaches the lagoon waters approached 0°C and salinities rose to 30-32 ‰.

The lagoon waters are wind-driven in the open water season with currents in the same direction as the wind and with 3% the wind speed. 12 m/sec winds during a storm resulted in observed currents in Simpson Lagoon of 40 cm/sec. The sea level changes were about 1 m due to wind set-up whereas tidal ranges are from 10-20 cm. Barometric pressure does not have much influence on sea level during the open water season. Currents under ice were generally less than 10 cm/sec.

## II. Introduction

### A. General nature and scope of the study.

The general scope of the study is to provide physical oceanographic data on the coastal and estuarine regimes of the Beaufort sea shelf. Originally planned as an integral part of the "Beaufort Sea Barrier Island - Lagoon Ecological Processes Studies", Research Unit 467, the project was expanded in FY 79 to include winter studies in the Beaufort Sea. The work is part of two cooperative studies and therefore, involves coordination with several other research units.

This project provides sea level, temperature, salinity, current speed and direction data for stations within the proposed Beaufort Sea lease area. The location of the stations is decided in conjunction with scientists from the other cooperating research units.

### B. Specific Objectives

The overall objective is to determine, over a three-year period, the circulation patterns within a characteristic lagoon system, to estimate flushing times and dispersion characteristics and to attempt to determine the interaction of lagoon waters with the offshore waters, especially with respect to longshore flow and flow between barrier islands. Specific objectives within this overall objective are: 1) to attempt to provide data on physical oceanographic parameters during the spring break-up and develop techniques for this purpose. 2) to provide detailed coverage near Milne Point in support of other programs during the open water

season 3) attempt to broaden the sampling area beyond the Simpson Lagoon and into other parts of the proposed lease area, 4) build on the experience in the preceding work to develop techniques for a winter sampling program within the lease area, 5) extend the winter sampling area into the shear-ice zone in conjunction with Dr. Aagard's (R.U.'s 91 and 151) shelf interaction study.

C. Relevance to Problems of Petroleum Development

The overall ecosystem processes study (R.U. 467), of which this work forms part, addresses only those processes which are anticipated to be impacted by activities related to petroleum development. Water quality and circulation, during both the open-water and ice-covered seasons, are a primary driving mechanisms of the ecosystem. Water quality influences biological growth and migration routes for fish. Water circulation can carry pollutants and nutrients associated with petroleum development. It is influenced by man-made changes to the environment, such as the building of causeways, drilling pads and pipelines in the marine environment. One must know the existing water quality and circulation before oil development begins in order to assess probable impacts resulting from such activities. In short, the project is designed specifically to address problems of petroleum development.

II. Current State of knowledge

Except for the brief ice-free period during summer, circulation and water quality measurements have not been taken in this lease area. The summer data have indicated that the near-shore region is driven by the predominantly easterly winds. We reported, in the previous annual report, that drifter recovery data indicated westward currents of at least 50 cm per second could be sustained over

a 5-day period. If drifters are indicative of the movement of spilled oil, then these data suggest that oil from the lease area could reach Point Barrow, 225 km distant, in a few days if a storm were present.

Data from Simpson Lagoon during July and August 1977 showed traces over water in patches of water of low salinity (15-25 ‰) and higher temperatures (6-10°C). The water moves generally westward with currents in the lagoon of 6-18 cm per sec. Data from satellite photographs confirmed that water with temperatures greater than 7°C is found close to the mainland coast in summer, originates from rivers, and forms boluses and frontal systems near the coast. The coastal water is otherwise composed of water with salinity in the range 30-32 ‰ and temperatures close to 0°C. As the September freeze-up approaches, the water temperatures gradually fall and boluses of warm, brackish water become less marked in extent and frequency until they cease altogether.

No data are available on the processes and circulation of freeze-up or break-up and winter circulation is unknown. Aagaard's (RU 151) work has indicated that Bering Sea water, moving eastwards, occurs year-round at the shelf break. However, the relationship of these water masses to the predominantly westward moving waters found in the shallower lagoons and shelf is not known.

#### IV. Study Area

Figure 1. shows the Beaufort Sea coast study area. It stretches from the eastern edge of the proposed lease area at Flaxman Island to the western edge of Oliktok Point.

V. Sources, Methods and Rationale of Data Collection

Primary logistic support for data collection is by helicopter. This mode of transport is almost mandated by the requirement for year-round operation in the seasonal sea-ice zone. It is cost-effective and practical. Instrument deployment and recovery techniques were described in the previous report. Briefly we have used standard Aanderaa current meters and tide gauges mounted in a special mooring frame designed for water depths of only 1-2 m.

We have further developed the technique so that instruments can be deployed by helicopter. During the open-water season we successfully recovered the instrument package by helicopter. The technique allows for the very rapid deployment and recovery of instruments.

For deployment and recovery during the ice-covered season we have used diver-technicians. We deployed instrument packages through holes in the ice without using divers. The packages are light enough to be deployed by hand. Divers are generally not necessary for deployment. However, we have used divers to service, recover or exchange instruments. Using these methods it is possible to exchange a tide gauge, for example, while still retaining the same mooring and datum. We chose to exchange instruments in late spring, just before break-up, so that at least some data were recovered in the event that the array were lost during the break-up season.

Data from current meters, tide gauges and salinity, temperature and depth sensors are recorded on serial magnetic tape in compatible

formats. The rationale for this is for ease in data processing. We are developing the in-house ability to read, edit, translate and plot these data as part of a data processing system. The system is designed for the rapid, efficient handling of large quantities of oceanographic data.

## VI. Results

Results are presented chronologically. Because extensive field activities have been undertaken throughout the reporting year, we will present only data which has been edited, translated and plotted in our data processing system to data. Detailed examination beyond this has not been possible because of the pressure of field activities.

The first attempt at the winter deployment, and recovery of oceanographic instruments in shallow water under ice was made in May 1978. We chose to deploy a current meter and tide gauge mounted on one of our shallow-water instrument frames in the Egg Island channel (Fig. 1), the deepest channel in the Jones Island chain of barrier islands and the major channel of the Kuparuk River. This site was chosen because it is deep and stable and is a year-round channel for water entering and leaving the Simpson Lagoon-Gwydyr Bay complex. In addition, logistic support was shared with U.S.G.S. workers (Drs. Barnes and Reimnitz). A ditch witch was used to cut two 2-meter long orthogonal slots through which our instrument array was lowered. A 1 meter square diving hole was cut through the 2m-thick ice a few meters from the array. The current meter and tide gauge were left in place for the period 13-26 May 1978. On the latter date the instruments were exchanged. The instruments were exchanged again on 26 July 1978, after ice breakup.



Data from Egg Island Channel for the first 14 days of June are shown in Figure 2. The channel is 5 m deep and the instrument sensors at 4.7 m depth beneath 2 m-thick ice. Salinity drops slowly from over 40 ‰ at the beginning of the month, to 34 ‰ on June 8. On June 8 between 0300 and 0500 hours the salinity fell from 34.6 ‰ to 6.4 ‰. The temperature trace shows a rise from -2°C to 0°C on June 7, 1978 with high temperatures later in the month. The sea level shows normal semi-diurnal tides of approximately 10 cm amplitude until 8 June. The sea-level built-up from 496 cm at 0700 hours on June 8 to 543 cm at 0400 hours on 9 June. The water level fell to less than 500 cm between 10 and 14 June and tidal fluctuations are discernible by 12 June. Currents were 2-5 cm to the south until June 8. Between 0200 and 0300 hours currents increased to 20 cm/sec to the northeast. These currents were sustained for 6 hours when the rotor stopped turning and the direction sensor became fixed.

These results clearly show the spring overflow of the Kuparuk River reaching the barrier islands at Egg Island. The very high salinities in excess of 40 ‰ observed at the beginning of the month are clearly the result of brine exclusion during the winter ice-formation. Data from May 16, the beginning of the record, show salinities of 43.5 ‰ falling slowly to 42.0 ‰ by 26 May. Temperatures recorded during the same period averaged -1.9°C and showed a rise from -1.97 to -1.86°C. These high salinities and low temperatures are confirmed by Schell (RU 537) who observed salinities of 43.5 ‰ to 50 ‰ in Simpson Lagoon and 34 ‰ on the ocean

side of the barrier islands on May 16. A gradient of decreasing salinity seawards from the mainland coast appears to exist. The declining salinity at the bottom of Egg Island channel may indicate that ocean water is mixing with the saline lagoon waters. This mechanism, rather than early river runoff, is suggested by the sluggish 2-5 cm currents flowing southwards, into the channel.

The river overflow began on June 7 and by the early morning hours had reached a peak. Figure 3 shows a satellite photograph taken at 1128 hours on June 8. All North Slope rivers can be seen to have flowed over the ice. The Kuparuk River has overflowed beyond Egg Island and our instrument site. To estimate the volume of the Kuparuk overflow, we measured the area on the satellite photograph. There are approximately 116 sq. km of overflowed water on June 8. If the average depth is 40 cm, based on the sea-level observation in Egg Island Channel, the volume of water is  $4.6 \times 10^7 \text{ m}^3$ .

River runoff data are not available for 1978 at the time of writing. Figure 4 shows the mean runoff figures for the Kuparuk River for the years 1971 through 1975. It is interesting to note that the peak values are 866.5, 886.3 and 877.8 cubic meters/ per second on the 6,7 and 8 June. The peak flow, therefore, occurs with great consistency from year-to-year near these three days. The mean daily volume over these three days is  $7.6 \times 10^7 \text{ m}^3$ . The volume of water seen overflowing the ice in the satellite photograph represents about 60% of the peak daily flow if the 1978 runoff is representative of average conditions.

The progression of breakup in the Beaufort Sea can be followed by reference to Figure 5. The data are from Egg Island channel for the first half of July 1978. Note that temperatures rise to as high as 7°C by July 9. Salinities are for fresh water and sea levels are variable for the same period. Early on July 10 cold water was observed at the instruments and sea levels began to show smooth semi-diurnal tidal characteristics. The salinity rose sharply on 13 July from freshwater to about 23 ‰.

This suggests that the river runoff extended to the bottom of Egg Island channel until 9 July. Subsequently the cold, saline ocean water began to advance up-over. The temperature effect preceded the saline water by about 3 days. It is concluded from these observations that from first river overflow on June 8 to July 9, freshwater filled the Kuparuk River and the lagoon to the barrier islands.

The data sequence can be followed through July 26 in Figure 6. The temperature and salinity at the bottom of Egg Island channel continued to rise until 21 July. Salinity reached about 30 ‰ and temperatures about 6°C. It suggests that the saline wedge of water advanced into the Kuparuk River and lagoon system and was warmed by the 24-hour long solar radiation. The rise in sea level of about 75 cm between 21 and 23 July appears to correspond with the temperature increase. The sea level has been corrected for density and barometric pressure variations. A peak of salinity on 23 July corresponds to a low temperature reading and suggests the intrusion of cold, saline coastal water.

Records for Egg Island are not available for August 1978. Data were taken off Beechy Point (Figure 7) in the western exit from Gwydyr Bay. It is believed that water flows generally westwards along the coast, therefore the Beechy Point station is downstream from the Kuparuk River and Egg Island channel. Figure 8 shows data from the channel off Beechy Point for the first half of August 1978. Note that currents lie in a NW/SE direction, with currents to the west prevailing. At the beginning of August salinities in the range 22-24 ‰ are observed, while temperatures are in the range 14°-18°C. The salinities are lower and the temperatures much higher than those observed in Egg Island channel at the end of the preceding month. This suggests that the Kuparuk River water is the source of water off Beechy Point. From 10 to 14 August strong westerly currents were observed and were accompanied by colder temperatures and high salinities. This suggests that the westerly currents entrained oceanic water into the brackish water. Earlier in the month currents are variable east and westwards. The same water mass probably stayed in the lagoon and passed the instruments several times. This would allow it to warm up in the shallow lagoon. The strong westerly currents are associated with a drop in sea level of about 50 cm over a 3-day period.

Figure 9 shows the data off Beechy Point for the second half of August 1978. The strong westerly currents continued for the first 7 days. The salinity and temperature records show the boluses of saline, cold water which were observed in

1977. On 22 August the currents reversed to flow towards the east. This current change was accompanied by a sea level rise of about 50 cm and prevailed for 3 days. A further short current reversal was observed on 26 August and was accompanied by a smaller sea level change.

The patches of warm, brackish water and cold, saline water were observed in August 1977. The water characteristics are quite different from those observed in June and fully support the contention that as river runoff decreases the coastal water intrudes into the lagoon.

Much could be done with the data presented above, but this has been precluded by field activities. Detailed analysis will continue into the next year. However, since other investigators have worked off Milne Point, data from an array off this point will be presented. Figure 10 shows the station locations.

Figures 11, 12, 13 and 14 show data for North, East, South and West Milne Point Station data for the first two weeks of August 1978. Detailed analysis of these records remains to be done. Notice the coherency of the temperature and salinity records from all four stations. The currents also are consistent, showing variable currents for the first half of the record and strong uniform currents in the last half. The East Milne Point station is strongly influenced by a channel off Bertoncini Island (Figure 10). Thus the currents flow Southwestwards at up to 30 cm/sec. between 9 and 12 August. Winds at Cottle Island (Figure 13) for the same period show strong winds blowing towards

the southwest at up to 9 meters per second. The currents, therefore, flow down wind at 3 to 4% of the wind speed. The South, West and North Milne Point stations show currents of similar speeds to those at East Milne Point station but with directions towards the Northwest. It is believed that the topography influences the direction.

Records of sea level (Figure 11) and barometric pressure (Figure 12) show little correlation. The sea level record has been corrected for water density and barometric pressure, so that it represents a true record of sea level. However, the sea level appears to follow the Cottle Island winds (Figure 13) quite well. The period of strong northeasterly (towards the southwest) winds corresponds to a marked decrease in sea level, lower temperatures and higher salinities.

The data for the second part of August for these same stations are shown in Figures 15, 16, 17 and 18. Here again, there is great coherency between the records of salinity and temperature for the four stations. For the first part of the record from 15 to 22 August great fluctuations in salinity and temperature were observed. These are least marked at South Milne Point station, the station closest to land and most remote from the influence of cold saline ocean water. These fluctuations are coherent with the data from Beechy Point (Figure 9) and suggest that the coastal water of river origin is breaking into small patches, or boluses, separated by ocean water. The current records indicate a westward water movement. The current record from South Milne station is consistent in magnitude but the uniformity in direction suggests that the instrument vane assembly had become fixed due to a mechanical obstruction.

The sea level record (Figure 16) shows a marked increase in sea level from 21 to 23 August. This appears to correspond to the change in wind direction (Figure 17) from winds towards the southwest (northeasterly winds) to winds towards the northeast (southwesterly winds). Onshore winds and currents produce lower sea levels than the offshore winds. Note that the low pressure system passing on 20 August (Figure 15) does not appear in the sea level record as a higher sea level (Figure 16).

## VII. Discussion

The results to date suggest that quite different regimes are active in the ice-covered season from those in the summer, open water season. In late winter, with ice in place, the lagoon has free water only in places deeper than 2 m, the average thickness of the ice. This water has very high salinity, over 40 ‰ in some places, and temperatures near -2°C. It is clearly derived from brine formed during the freezing process. It moves sluggishly with velocities typically less than 10 cm/sec.

River overflow is remarkably consistent from year-to-year and occurs to peak near 6-8 June. The winter accumulation of brine is flushed from the system very rapidly. Our measurements, taken at 5-minute intervals indicated complete flushing of salt water in less than the sampling interval.

The river flow takes place mainly over a 10-day period in early June. However, the lagoon waters appear to retain the

runoff for about one month. Subsequently, saline ocean water appears in the lagoons. The high solar radiation at this time appears to heat the bottom waters to at least 12°C near the coast.

The month of August is marked by the appearances of saline, cold oceanic waters moving in frontal systems through the warmer, brackish waters of the lagoon. The passage of storm systems in August appears to contribute to the mixing of cold oceanic waters into the lagoon waters and the gradual re-establishment of saline water masses.

It has not been possible to carry out detailed analysis of water exchange between the lagoon and ocean waters at this time. However, data analysis will be aimed at quantifying these exchanges using the numerical model of Dr. Mungall (R.U. 531) driven by the observational data presented above.

No data are available on freeze-up processes or winter conditions in the lagoon. The on-going research project is aimed at filling this data gap.

### VIII. Conclusions

The lagoon system changes dramatically from one of extremely high salinity ( $\sim 40$  ‰) and low temperature ( $\sim 2^\circ\text{C}$ ) to one of almost fresh water near its freezing point with the river overflow. The time of river overflow is consistent from year-to-year within a few days. It is believed that currents under the ice are generally less than 10 cm/sec, although more data are required to confirm this.

The lagoon system contains mainly fresh water from river overflow in early June to the time of ice breakup in early July.



Subsequently, the lagoon waters become wind-driven and undergo mixing with coastal waters. Currents generally agree with the numerical model predictions, that they are in the same direction as the wind and about from 3 to 4% of the wind speed. In July, the high incident solar radiation leads to temperatures of at least 12°C in the shallow lagoons.

Storms occur mainly in August and lead to the mixing of cold, saline water with the lagoon waters. The waters are wind-driven at this time. Storm winds of 12 m/s can lead to 40 cm/sec currents in the lagoon, i.e. ~3% of the wind speed. Wind induced sea level changes can be at least 1 m in the lagoons of mean depth of only about 2 m. Diurnal tidal ranges are only 10-20 cm.

By the end of August the lagoon waters reach salinities of ~30 ‰ and the temperatures fall to about 0°C. Winter freeze-up occurs in early September. Data on this latter process and conditions obtaining under the ice in winter are not known at this time.

#### IX. Needs for Further Study

The need for data on winter conditions are presently being obtained, and thus filling a critical need. In addition, data from other lagoon systems along the Beaufort Sea coast are badly needed. There is also a need for data on the shelf region beyond the Barrier Islands in the seasonal sea ice zone. The work of Aagaard (R.U. 91 and 151) has given information on the circulation along the shelf edge, but the relationship of this circulation to the lagoon and coastal waters is not known. In addition, data are available for only one or two years in the Simpson Lagoon. Nothing is known of

the year-to-year variability. Further studies of the type described need to be undertaken for several more years.

The weather and runoff data presented here have been invaluable for understanding coastal processes. The weather service stations are too far from the coast to be representative of coastal conditions. The data provided by Carsey, Kozo and Anderson (R.U. 519) from offshore barrier islands, will need to be repeated. In addition, weather data from stations on the arctic sea ice will be required. Further, the Colville River is the largest on the Alaskan Beaufort sea coast, only the much smaller Kuparuk River is gauged. It is recommended that more north slope rivers be carefully gauged.

X. Summary of January - March Quarter

A. Ship or Laboratory Activities

1. Ship or field trip schedule

a. Dates

(i) 25 Feb. - 7 March 1979

(ii) 10 March - 1 April 1979

b. Name of vessel

None

c. Aircraft

(i) None

(ii) NOAA helicopter

## 2. Scientific Party

### a. Names

(i) J.B. Matthews - University of Alaska,  
Principal Investigator

Garry Meltvedt - University of Alaska,  
Diver-Technician

Bill Kopplin - University of Alaska,  
Diver-Technician

Steve Petersen - University of Alaska,  
Diver-Technician

Clifton Moore - University of Alaska,  
Diver-Technician

(ii) Bill Kopplin - University of Alaska,  
Diver-Technician

Steve Petersen - University of Alaska,  
Diver-Technician

Clifton Moore - University of Alaska,  
Diver-Technician

Kate Persons - University of Alaska,  
Technician

## 3. Methods

### a. Field Sampling

Instrument arrays deployed in November 1978, were located through the arctic ice by means of a pinger locator lowered through ice holes. Dive holes were then cut through the 2-m ice. Subsequently divers replaced the submerged instruments with freshly calibrated and serviced instruments.

b. Laboratory Analysis

Data obtained from instruments deployed in the summer of 1978 were edited, corrected and plotted in preparation for the foregoing annual report.

4. Sample Localities/Ship or Aircraft Tracklines

Figure 19 shows the locations of the instrument sites. The sites off Flaxman Island and Oliktok Point were replaced in deeper water, in the shear zone to link-up with stations deployed by Dr. Aagaard (R.U. 91).

5. Data Collected or Analysed

a. Number and Types of Samples/observations

Data from 8 stations in the Beaufort Sea have been examined. Current speed, direction, salinity and temperature observations were obtained from 8 stations and sea level records from 5 stations.

b. Number and Types of Analyses

Analysis has been restricted to translation and editing of raw data tapes into computer readable formats.

c. Miles of Trackline

None

XI. Auxiliary Material

A. References Used

None

B. Papers in Preparation or Print

J. B. Matthews, Modeling and verification of circulation in an arctic barrier island-lagoon system-an ecosystem process study to be published by Springer Verlag, Heidelberg, W. Germany 1979, 12 pp.

C. Oral Presentation

J. B. Matthews. Circulation modelling and verification in an arctic barrier island-lagoon estuary. Numerical modelling of estuarine physics, keynote address, Hamburg West Germany, August 1978.

D. F. Paskansky and J. B. Matthews, Coastal wind drift during a typical storm. American Geophysical Meeting, ES 59(12): 1091, Dec. 1978.

J. B. Matthews, Spring runoff in an arctic barrier island-lagoon estuary, American Geophysical Union, May 1979.

## FIGURE LEGENDS

- Figure 1. Beaufort Sea study area showing barrier islands, lagoons and rivers.
- Figure 2. Salinity, temperature sea level and current data from a depth of 4.7 m in the 5m-deep, Egg Island channel, June 1-14, 1978.
- Figure 3. Satellite photograph taken 1128 hours local time 8 June 1978 showing rivers overflowing coastal ice.
- Figure 4. Mean Kuparuk River runoff during the month of June for years 1971-5.
- Figure 5. Salinity, temperature and sea level data from 4.7 m depth in the 5m-deep, Egg Island channel July 1-14, 1978.
- Figure 6. Salinity, temperature and sea level data from 4.7 m depth in the 5m-deep Egg Island channel July 15-26, 1978.
- Figure 7. The Beaufort Sea coast line from Prudhoe Bay to Oliktok Point.
- Figure 8. Salinity, temperature, sea level and current data off Beechy Point for the period 1-14 August 1978.
- Figure 9. Salinity, temperature, sea level and current data off Beechy Point for the period 15-28 August 1978.
- Figure 10. Station array off Milne Point August 1978.
- Figure 11. Salinity temperature and current vectors for North Milne Point station and barometric pressure for Milne Point for period 1-14 August 1978.
- Figure 12. Salinity, temperature, current vectors and sea level for East Milne Point station for period 1-14 August 1978.
- Figure 13. Salinity, temperature and current vectors for South Milne Point station and wind sock vectors for Cottle Island for period 1-14 August 1979.
- Figure 14. Salinity, temperature and current vectors for West Milne Point station and sea level at East Milne Point station for period 1-14 August 1978.
- Figure 15. Salinity, temperature and current vectors for North Milne Point station and barometric pressure for Milne Point for period 15-28 August 1978.

- Figure 16. Salinity, temperature, current vectors and sea level for East Milne Point station for period 15-28 August 1978.
- Figure 17. Salinity, temperature and current vectors for South Milne Point station and wind sock vectors for Cottle Island for period 15-26 August 1978.
- Figure 18. Salinity, temperature and current vectors for West Milne Point station and sea level for East Milne Point station for period 15-28 August 1978.

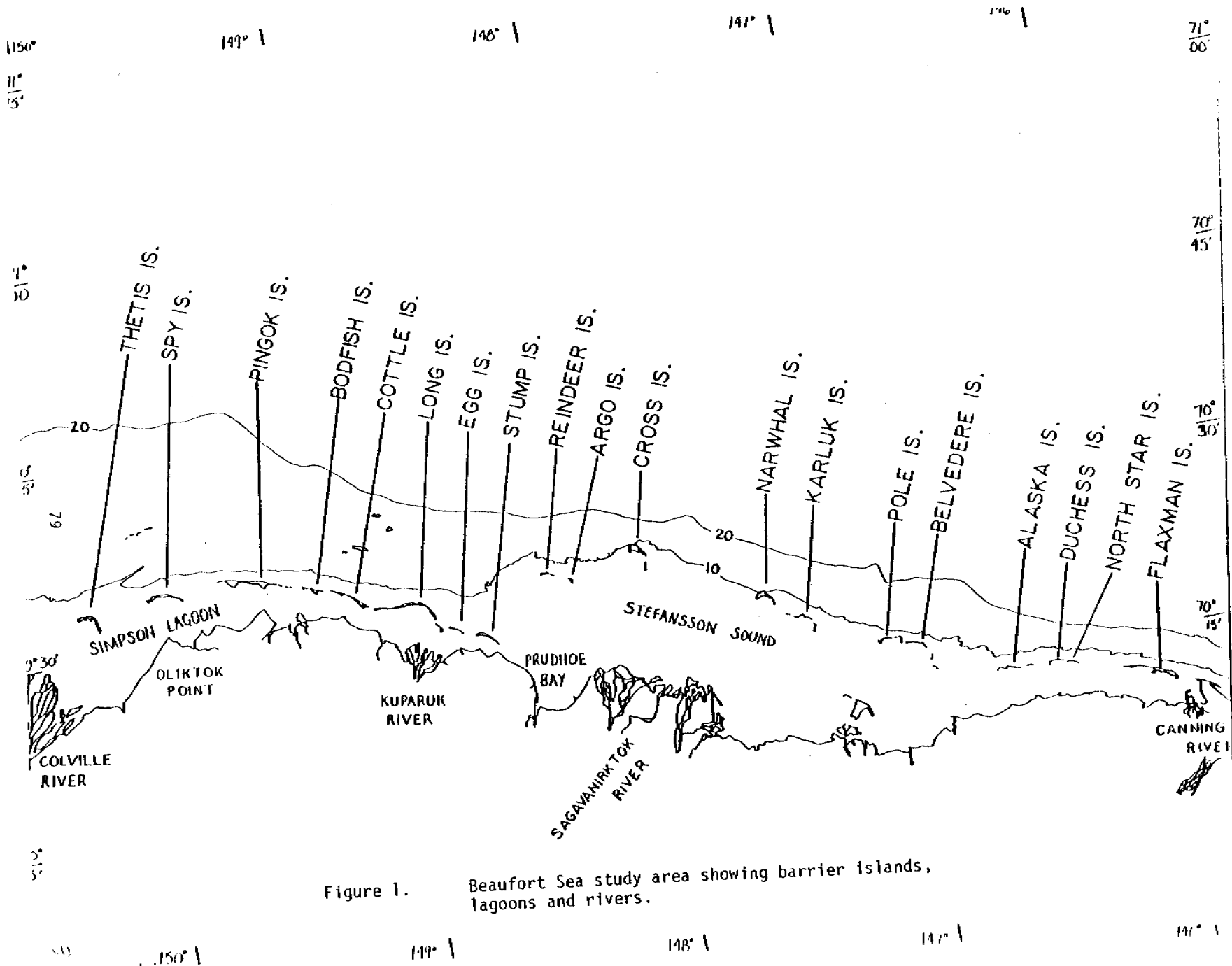


Figure 1. Beaufort Sea study area showing barrier islands, lagoons and rivers.



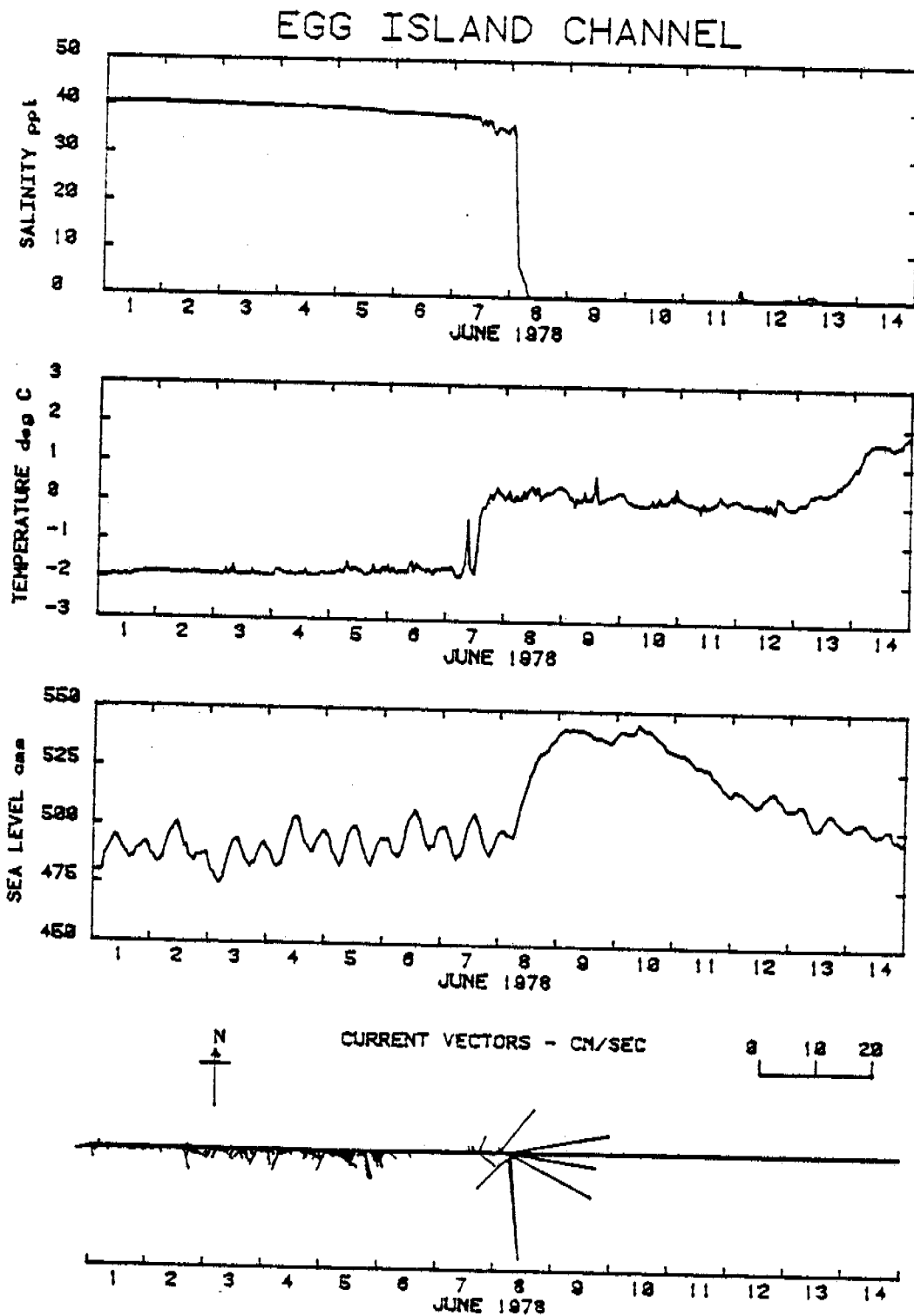


Figure 2. Salinity, temperature sea level and current data from a depth of 4.7 m in the 5m-deep, Egg Island channel, June 1-14, 1978.



Figure 3.

Satellite photograph taken 1128 hours local time  
8 June 1978 showing rivers overflowing coastal ice.

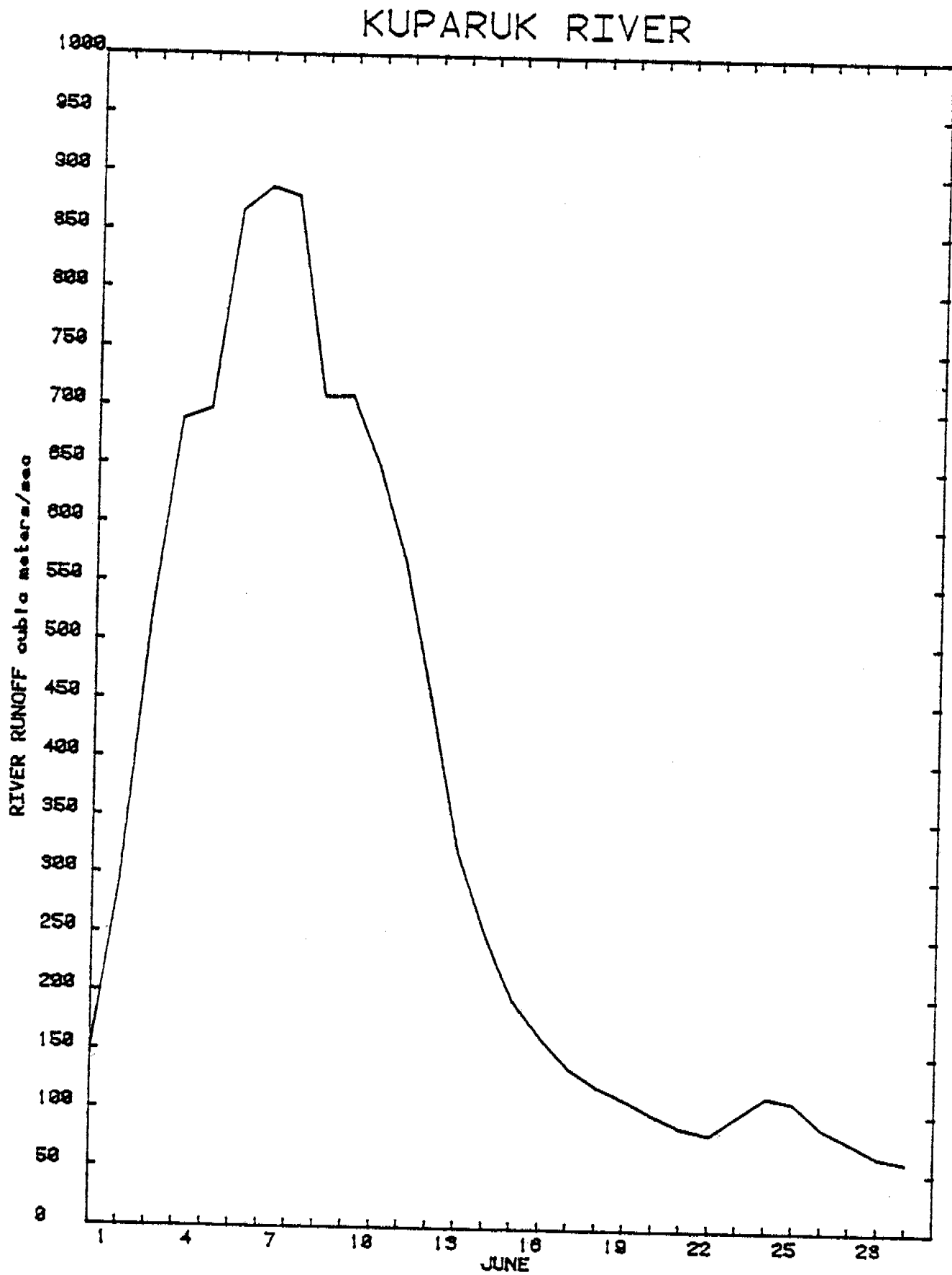


Figure 4. Mean Kuparuk River runoff during the month of June for years 1971-5.

# EGG ISLAND CHANNEL

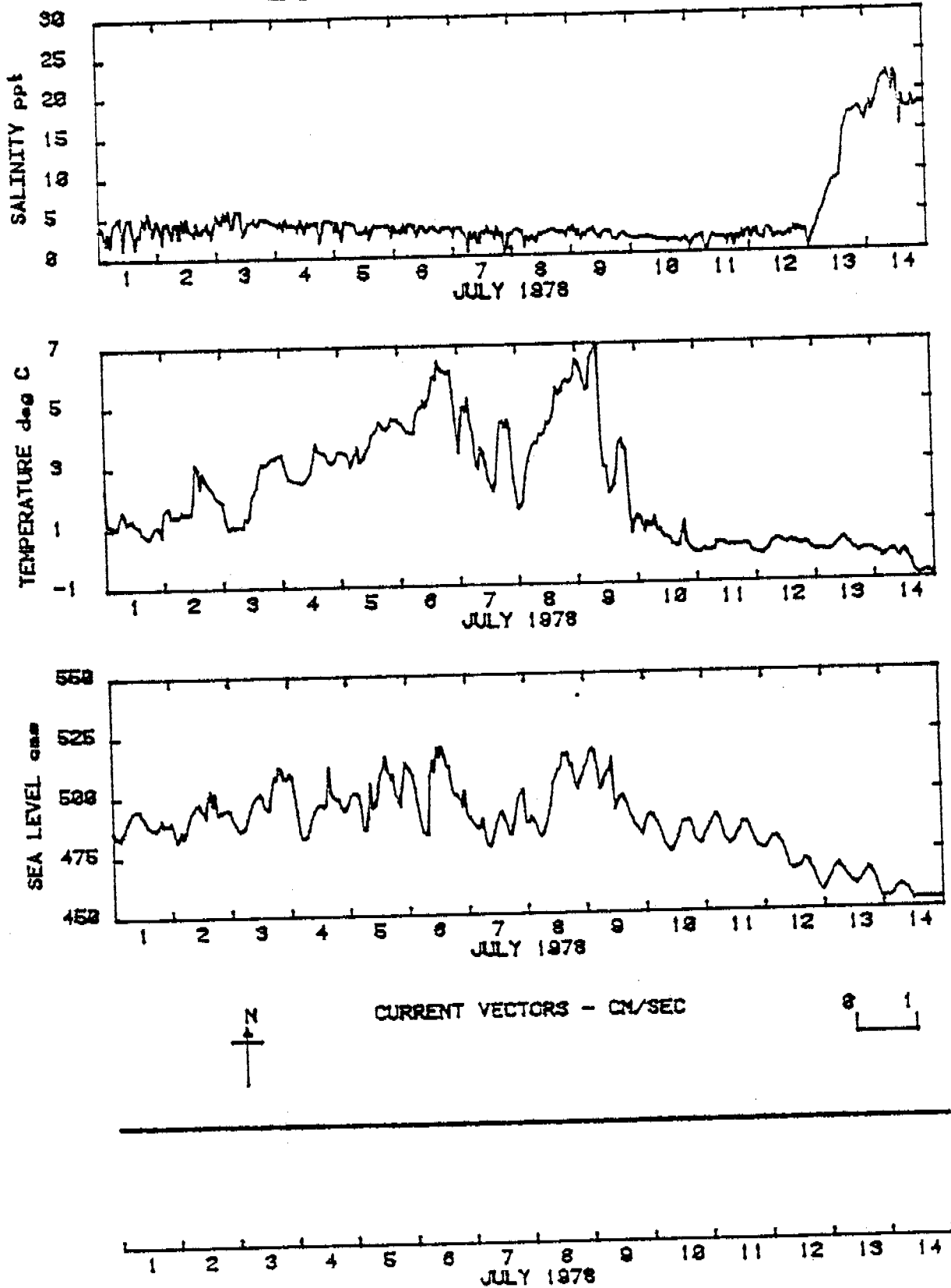


Figure 5. Salinity, temperature and sea level data from 4.7 m depth in the 5m-deep, Egg Island channel July 1-14, 1978.

# EGG ISLAND CHANNEL

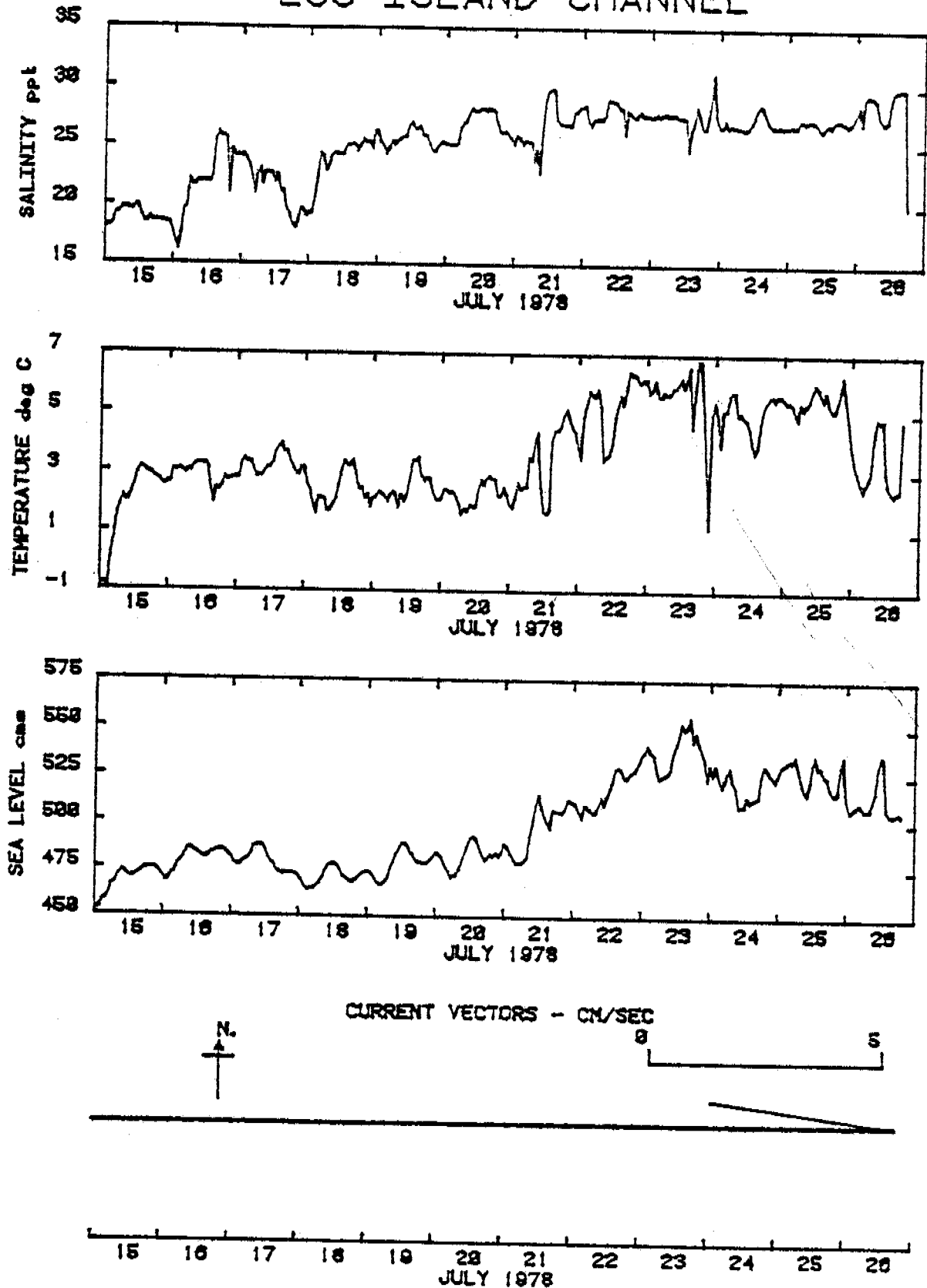


Figure 6. Salinity, temperature and sea level data from 4.7 m depth in the 5m-deep Egg Island channel July 15-26, 1978.

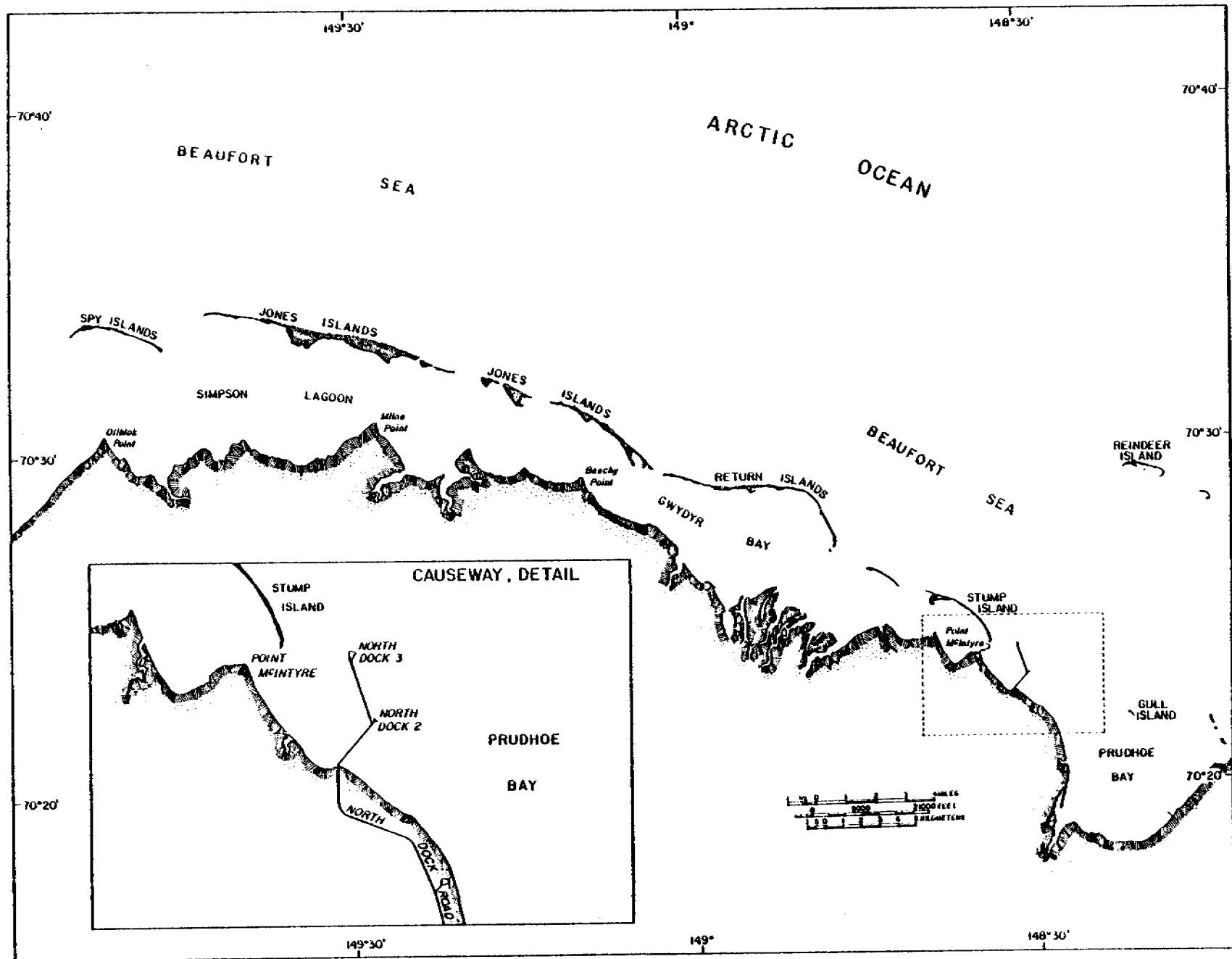


Figure 7. The Beaufort Sea coast line from Prudhoe Bay to Oliktok Point.

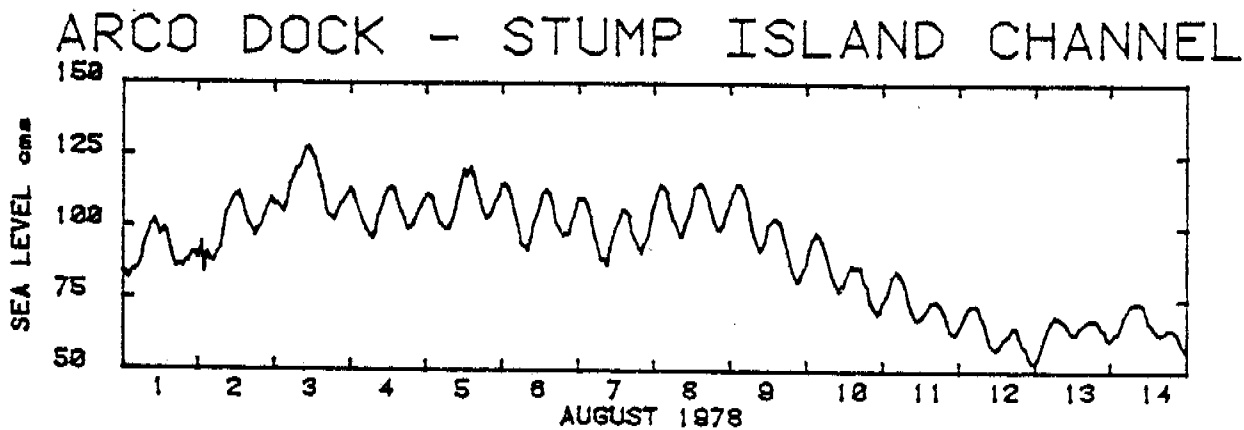
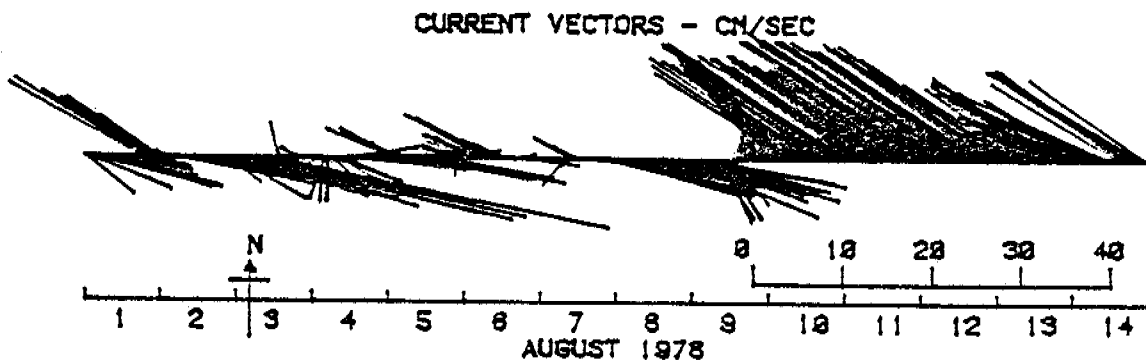
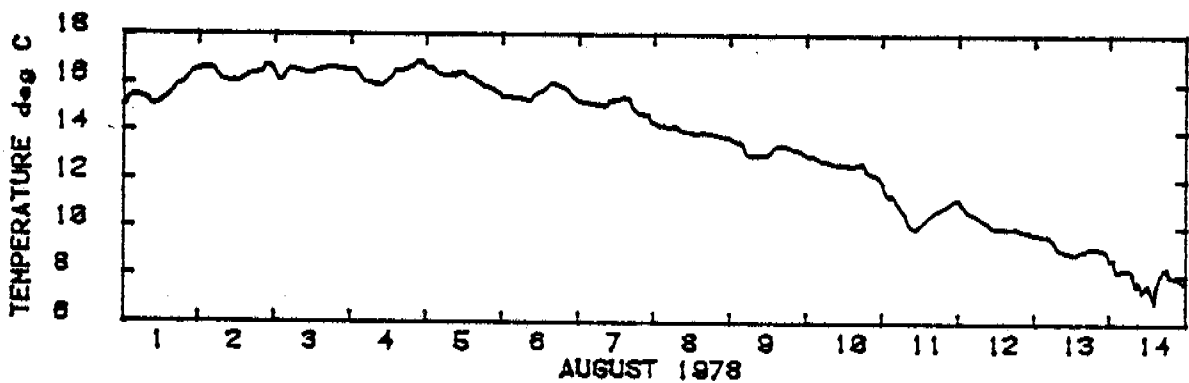
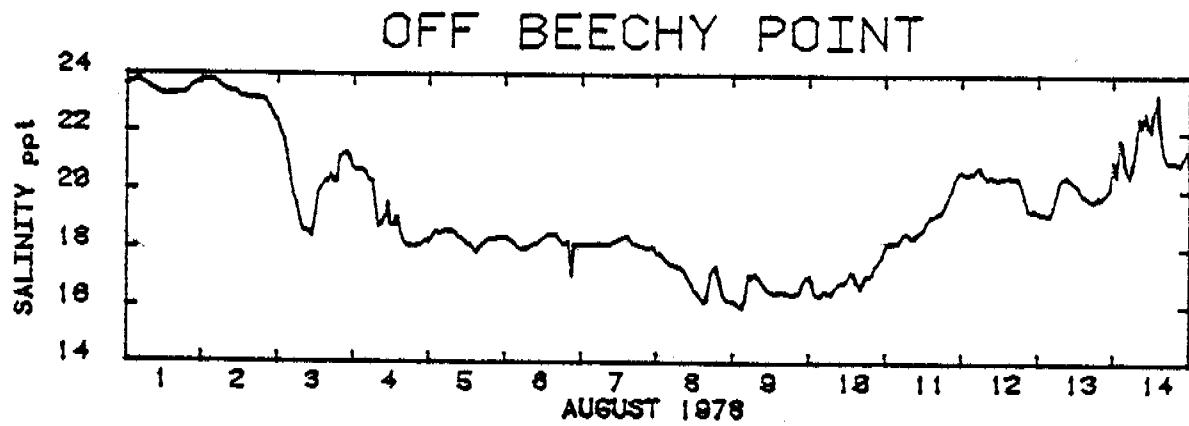
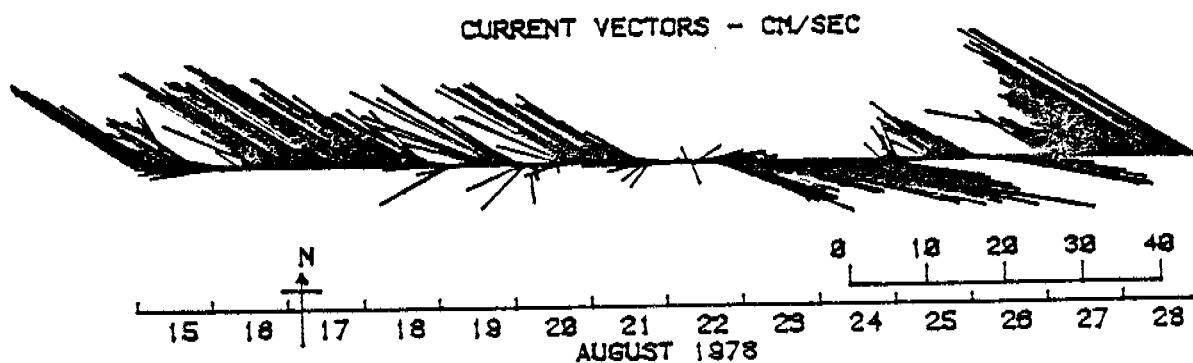
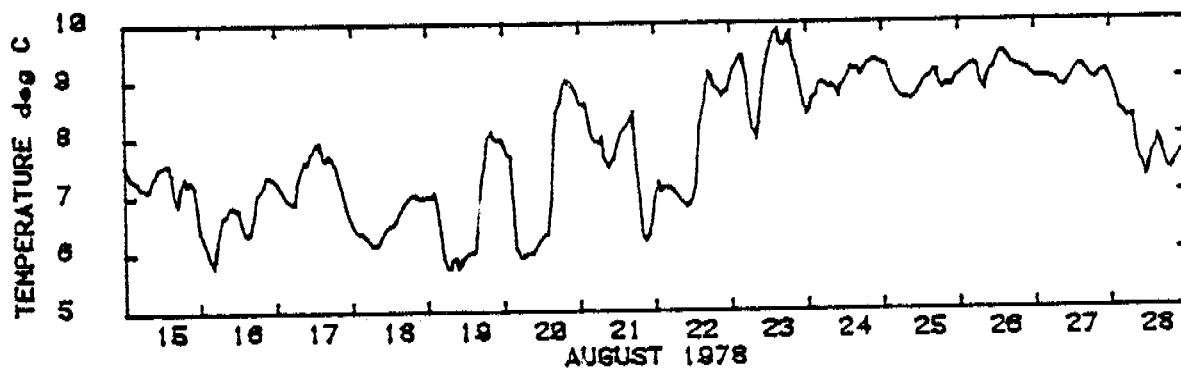
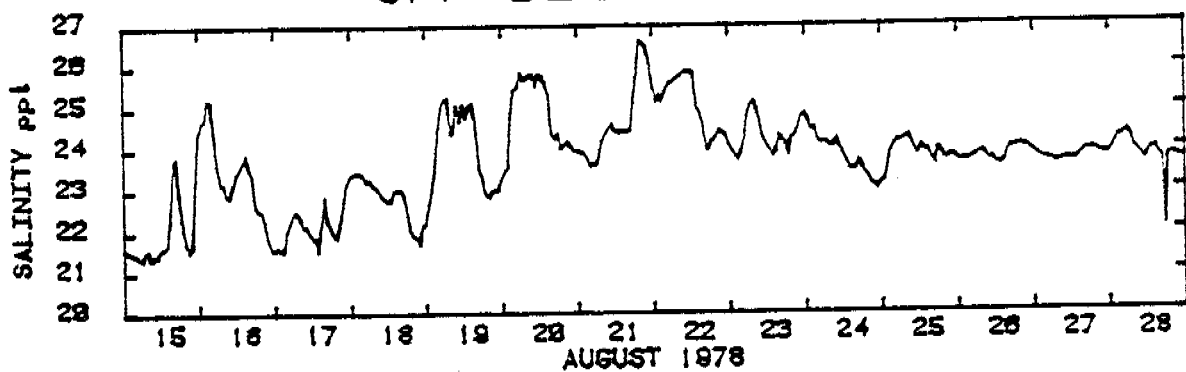


Figure 8. Salinity, temperature, sea level and current data off Beechy Point for the period 1-14 August 1978.

# OFF BEECHY POINT



# ARCO DOCK - STUMP ISLAND CHANNEL

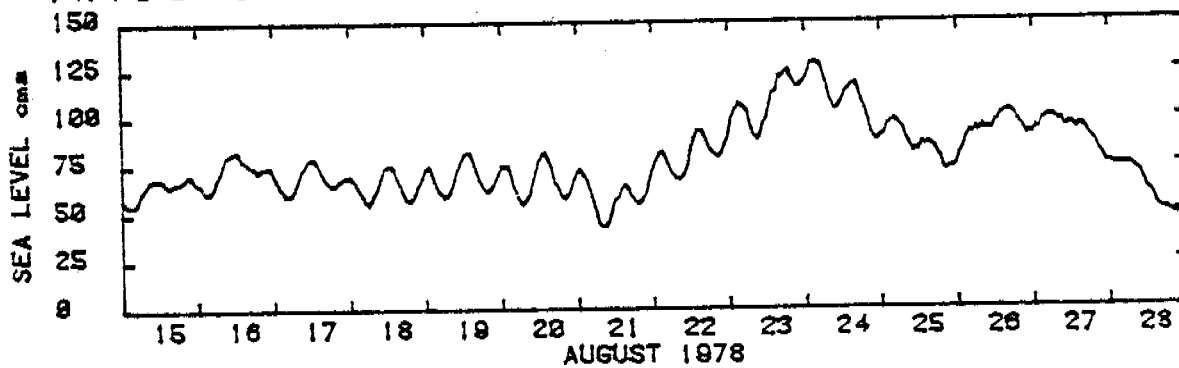


Figure 9. Salinity, temperature, sea level and current data off Beechy Point for the period 15-28 August 1978.



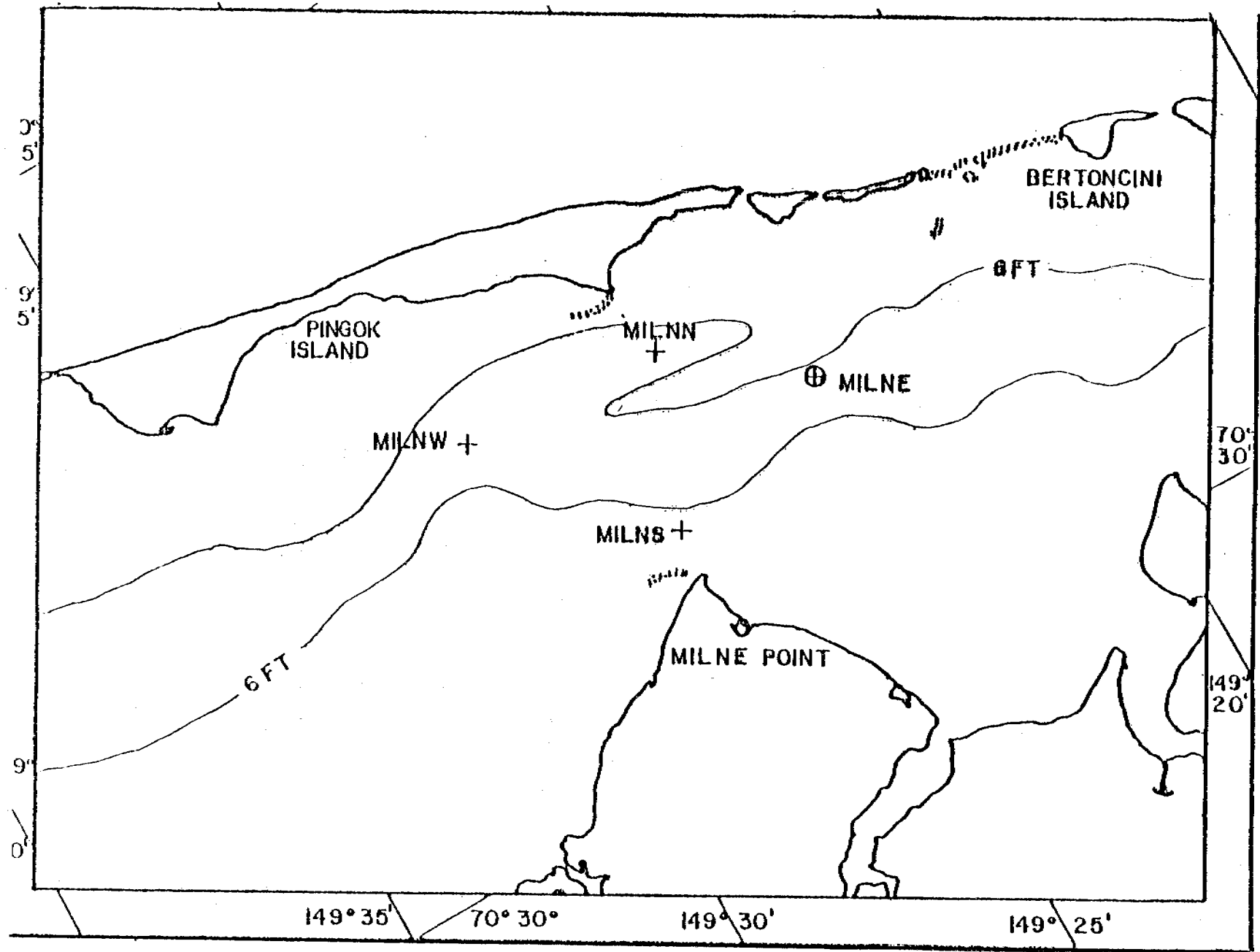
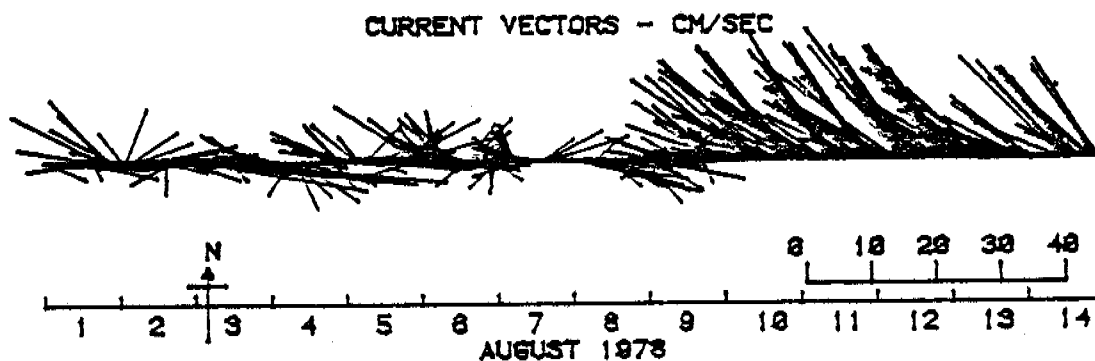
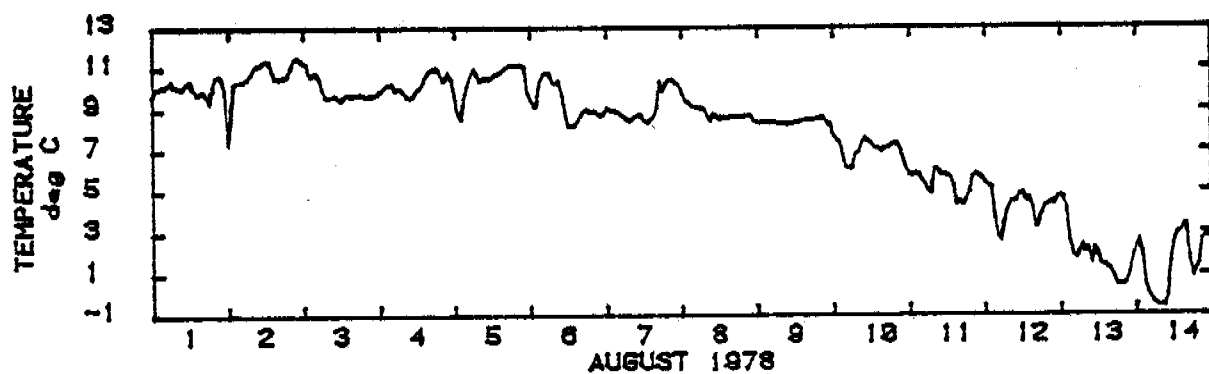
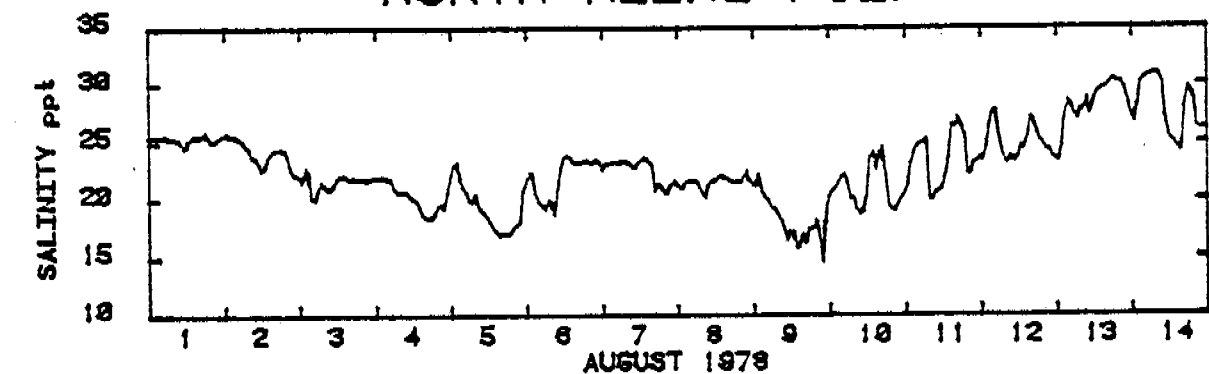


Figure 10. Station array off Milne Point August 1978.

# NORTH MILNE POINT



# EAST MILNE POINT

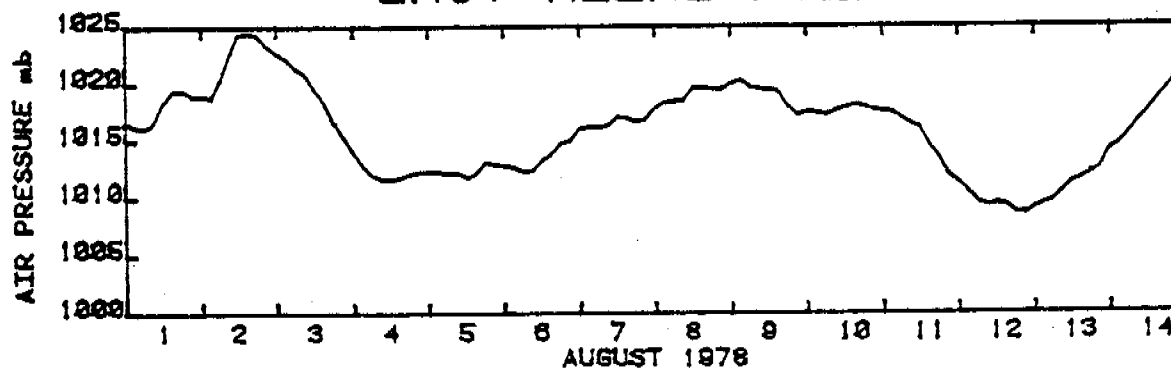


Figure 11. Salinity temperature and current vectors for North Milne Point station and barometric pressure for Milne Point for period 1-14 August 1978.

# EAST MILNE POINT

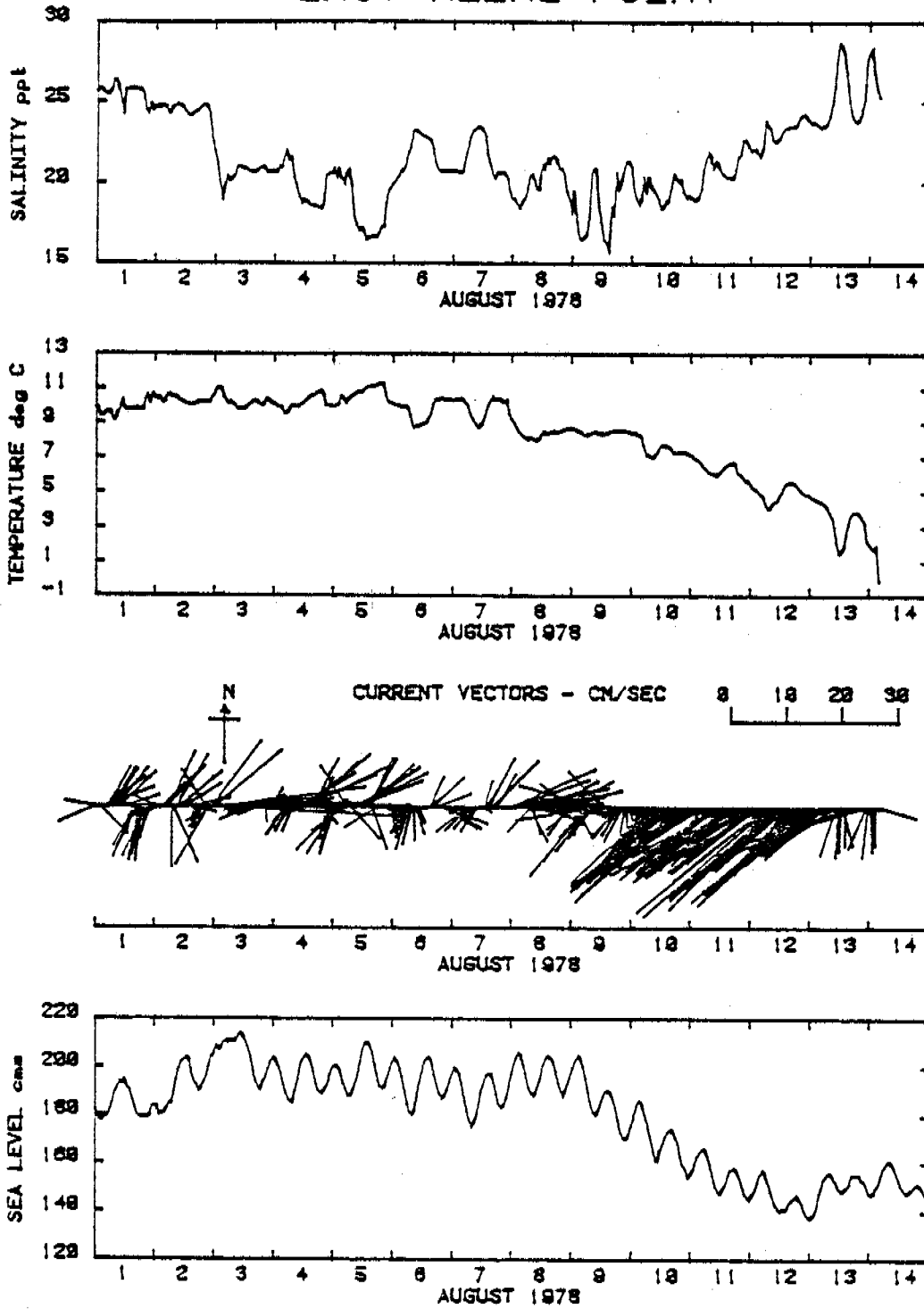
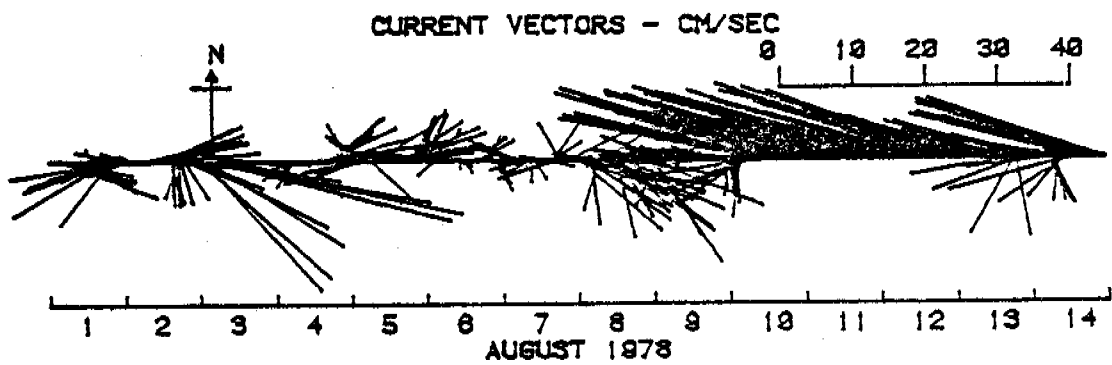
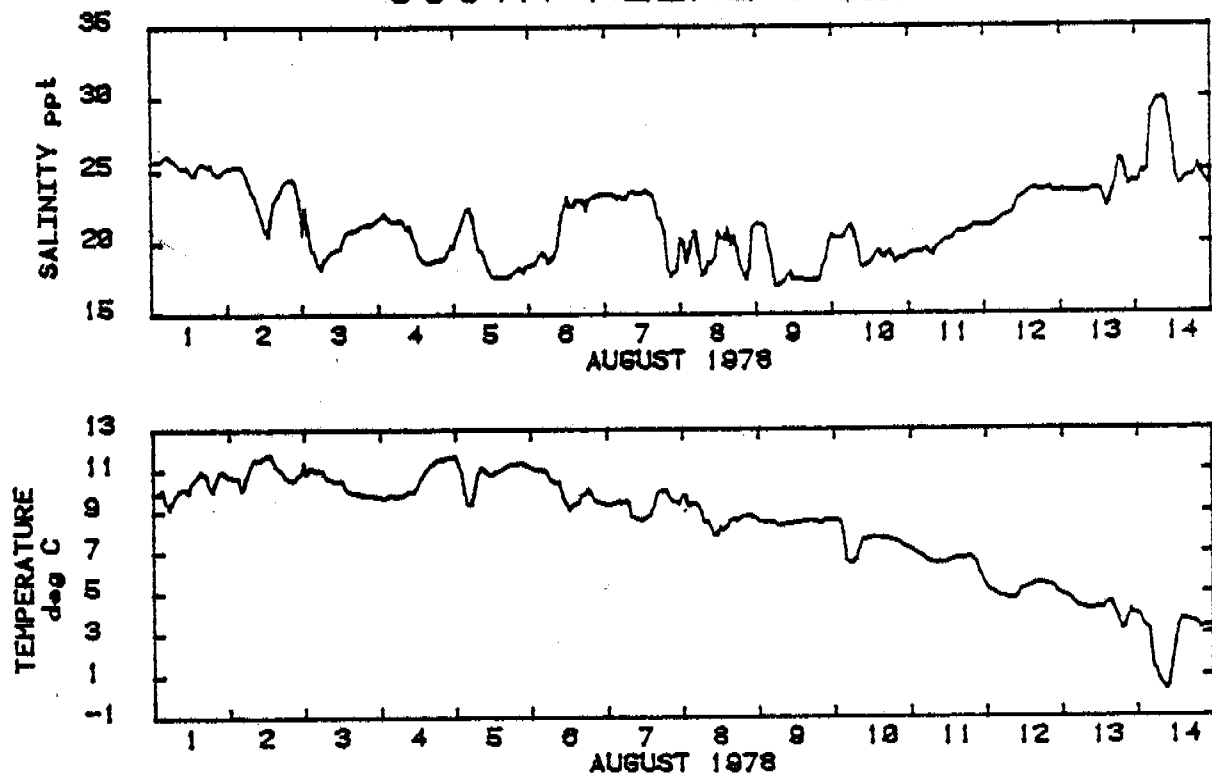


Figure 12. Salinity, temperature, current vectors and sea level for East Milne Point station for period 1-14 August 1978.

# SOUTH MILNE POINT



# COTTLE ISLAND

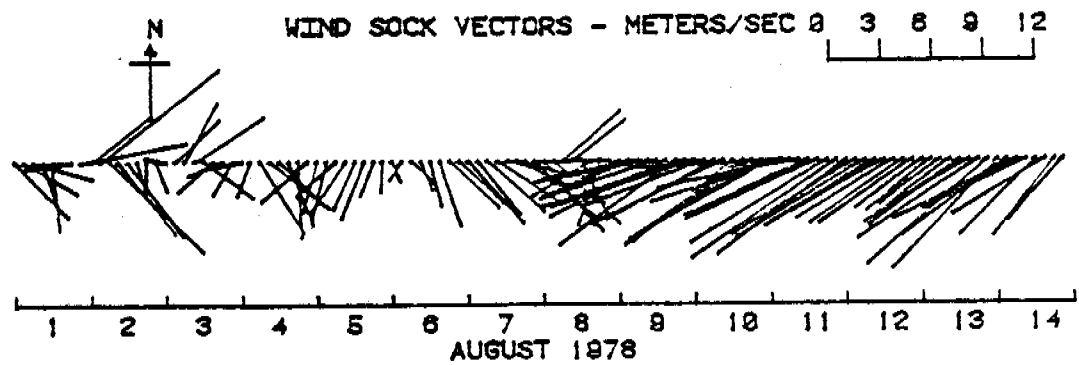


Figure 13. Salinity, temperature and current vectors for South Milne Point station and wind sock vectors for Cottle Island for period 1-14 August 1979.

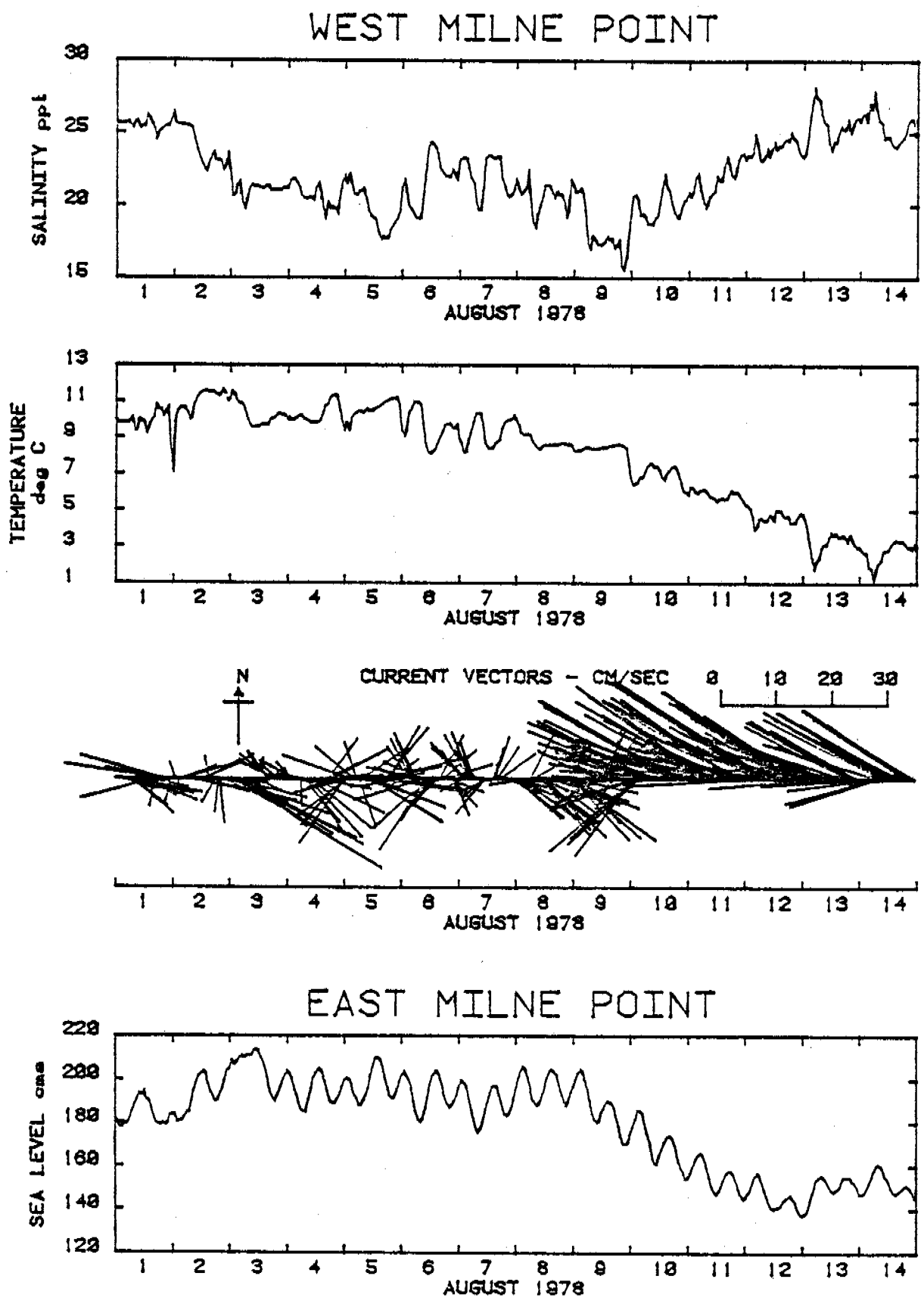


Figure 14. Salinity, temperature and current vectors for West Milne Point station and sea level at East Milne Point station for period 1-14 August 1978.

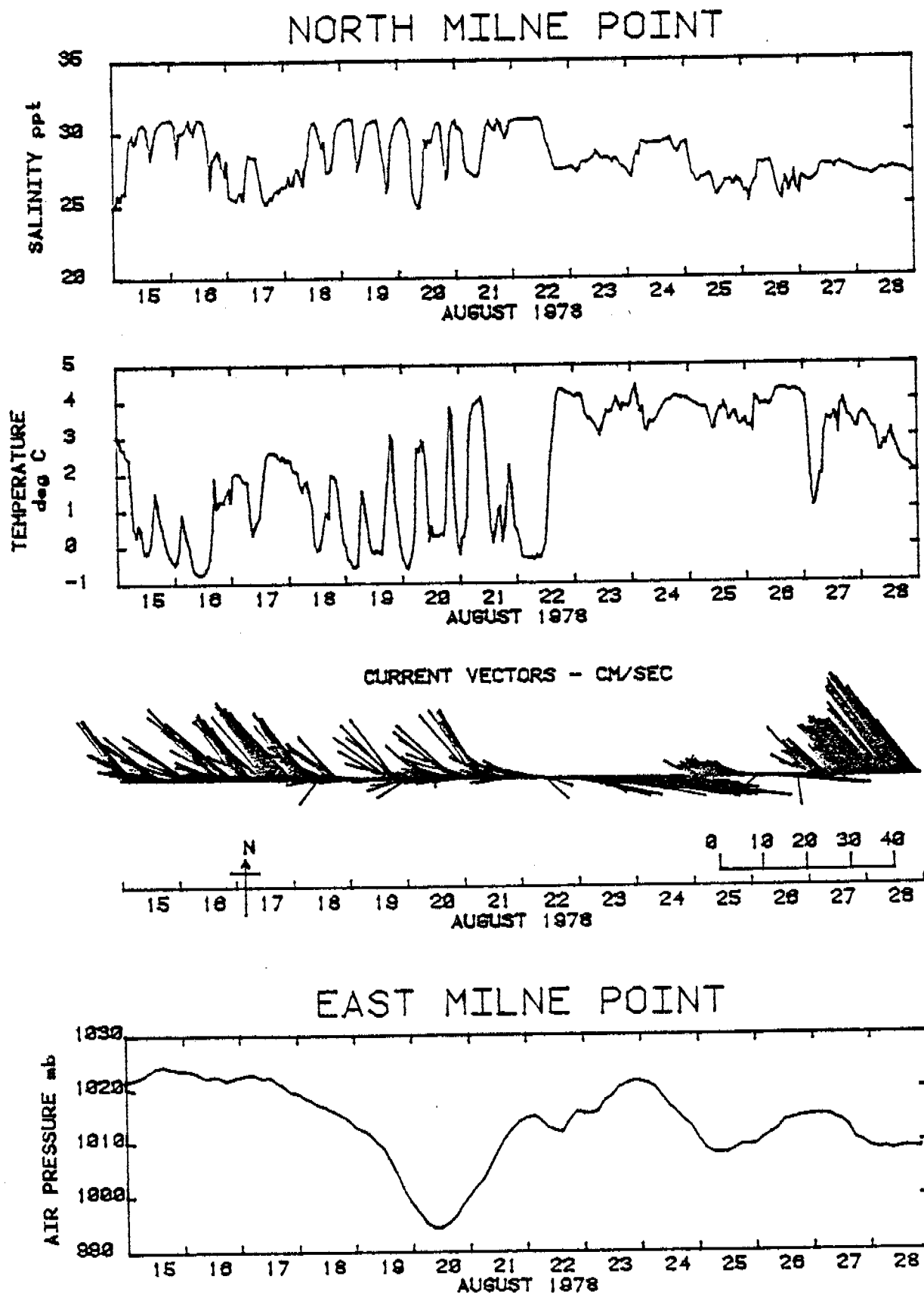


Figure 13. Salinity, temperature and current vectors for North Milne Point station and barometric pressure for Milne Point for period 15-28 August 1978.

# EAST MILNE POINT

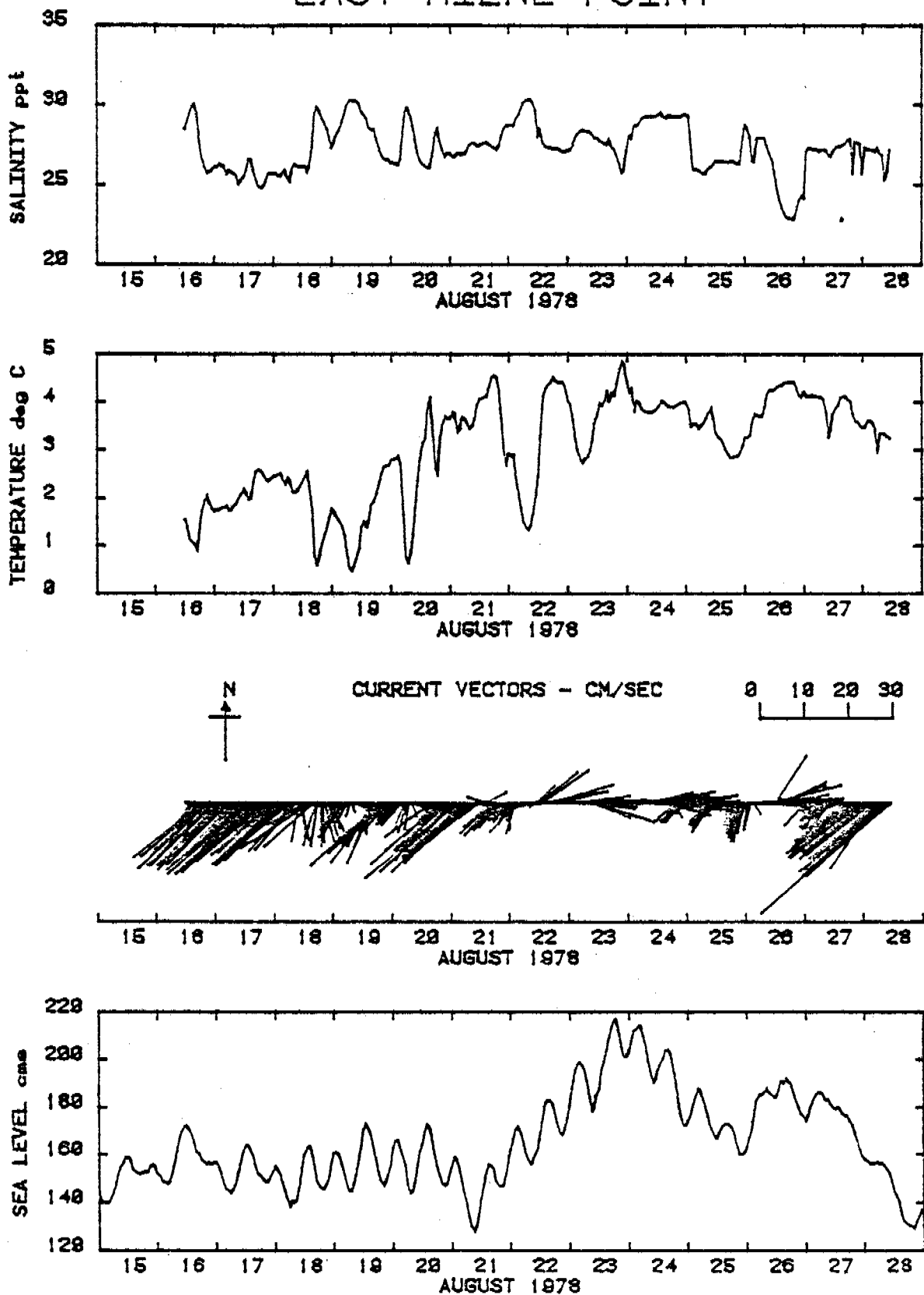


Figure 16. Salinity, temperature, current vectors and sea level for East Milne Point station for period 15-28 August 1978.

# SOUTH MILNE POINT

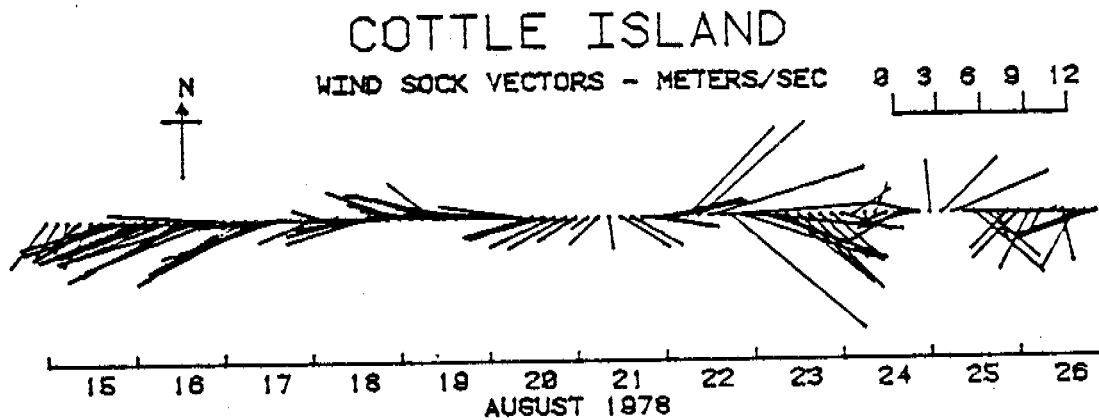
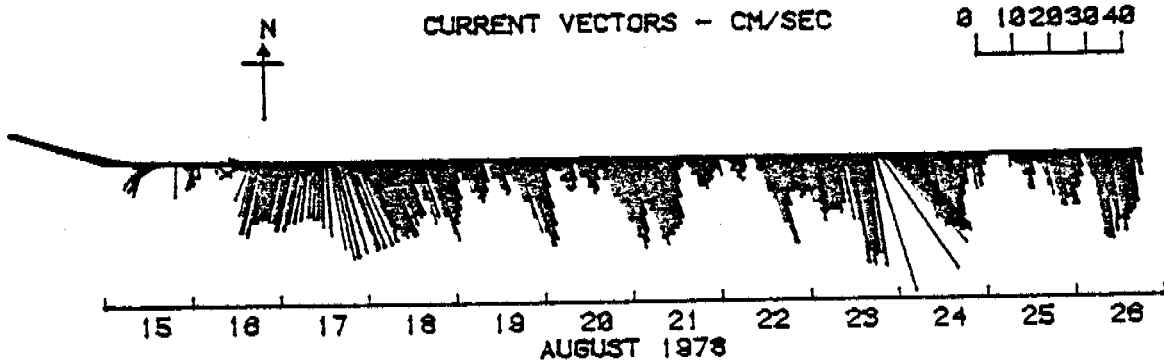
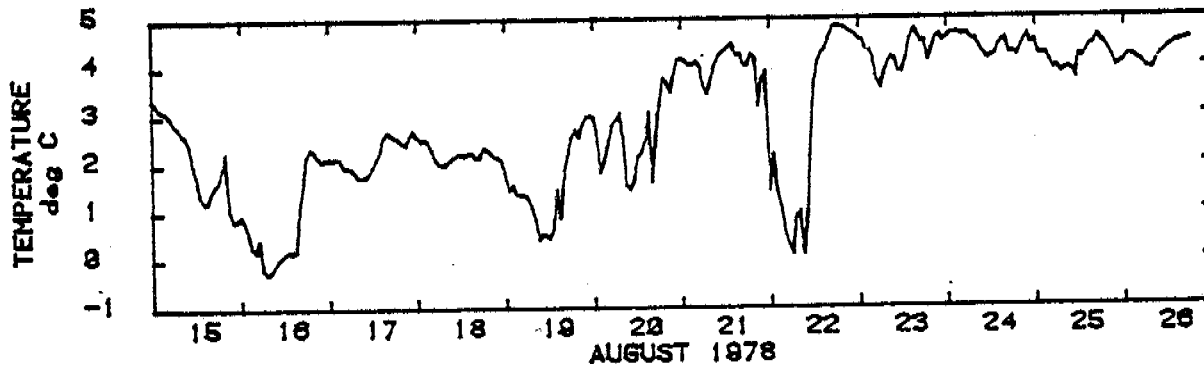
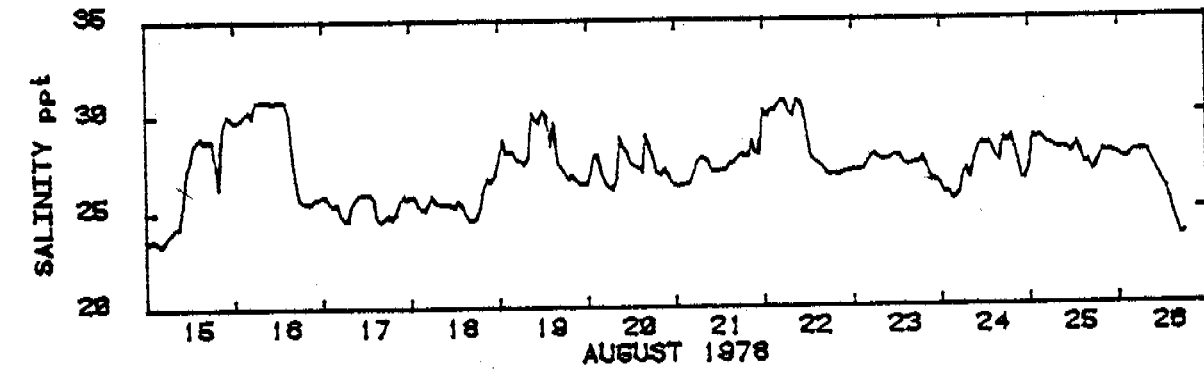


Figure 17. Salinity, temperature and current vectors for South Milne Point station and wind sock vectors for Cottle Island for period 15-26 August 1978.



# WEST MILNE POINT

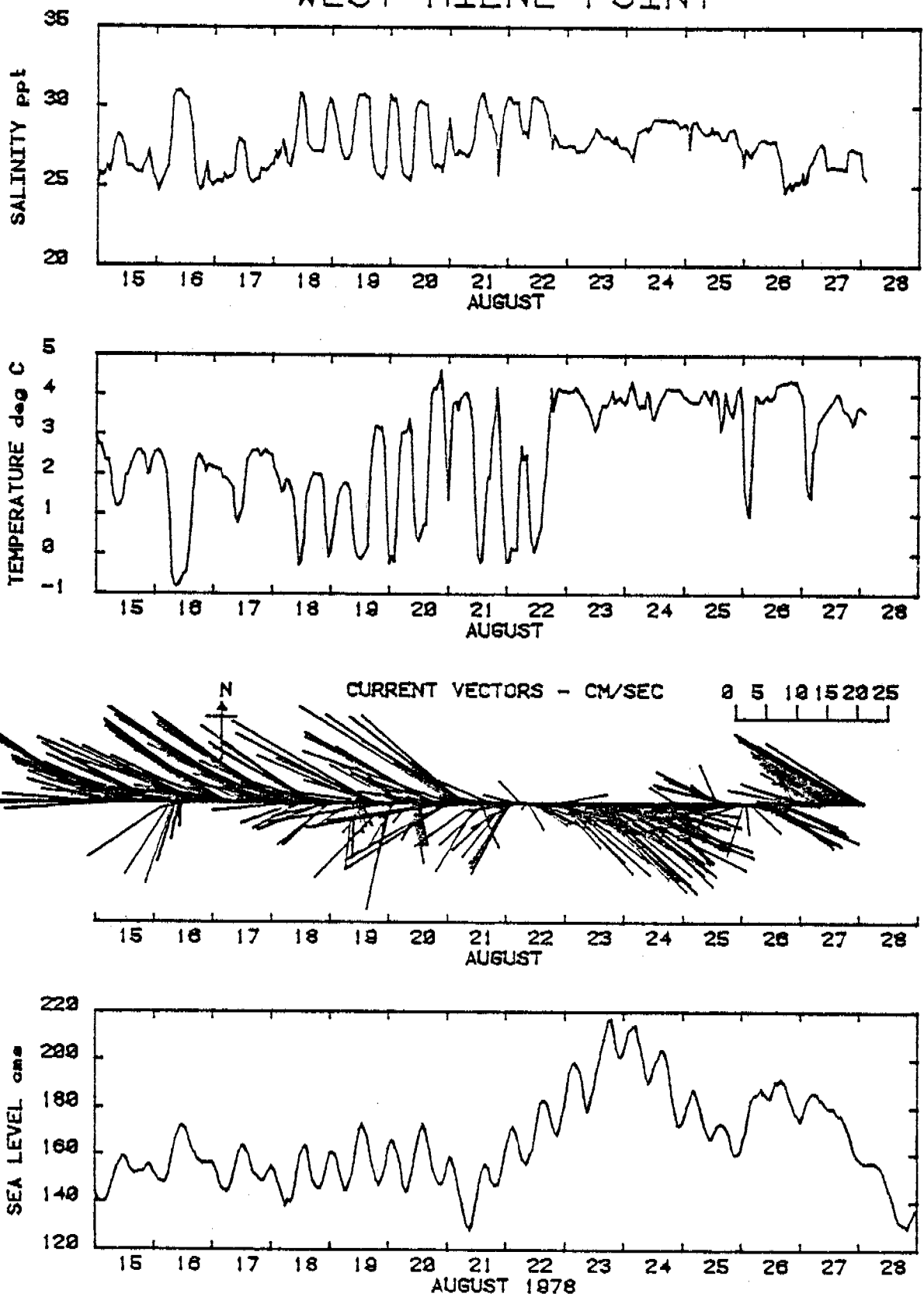


Figure 13. Salinity, temperature and current vectors for West Milne Point station and sea level for East Milne Point station for period 15-28 August 1978.

L6

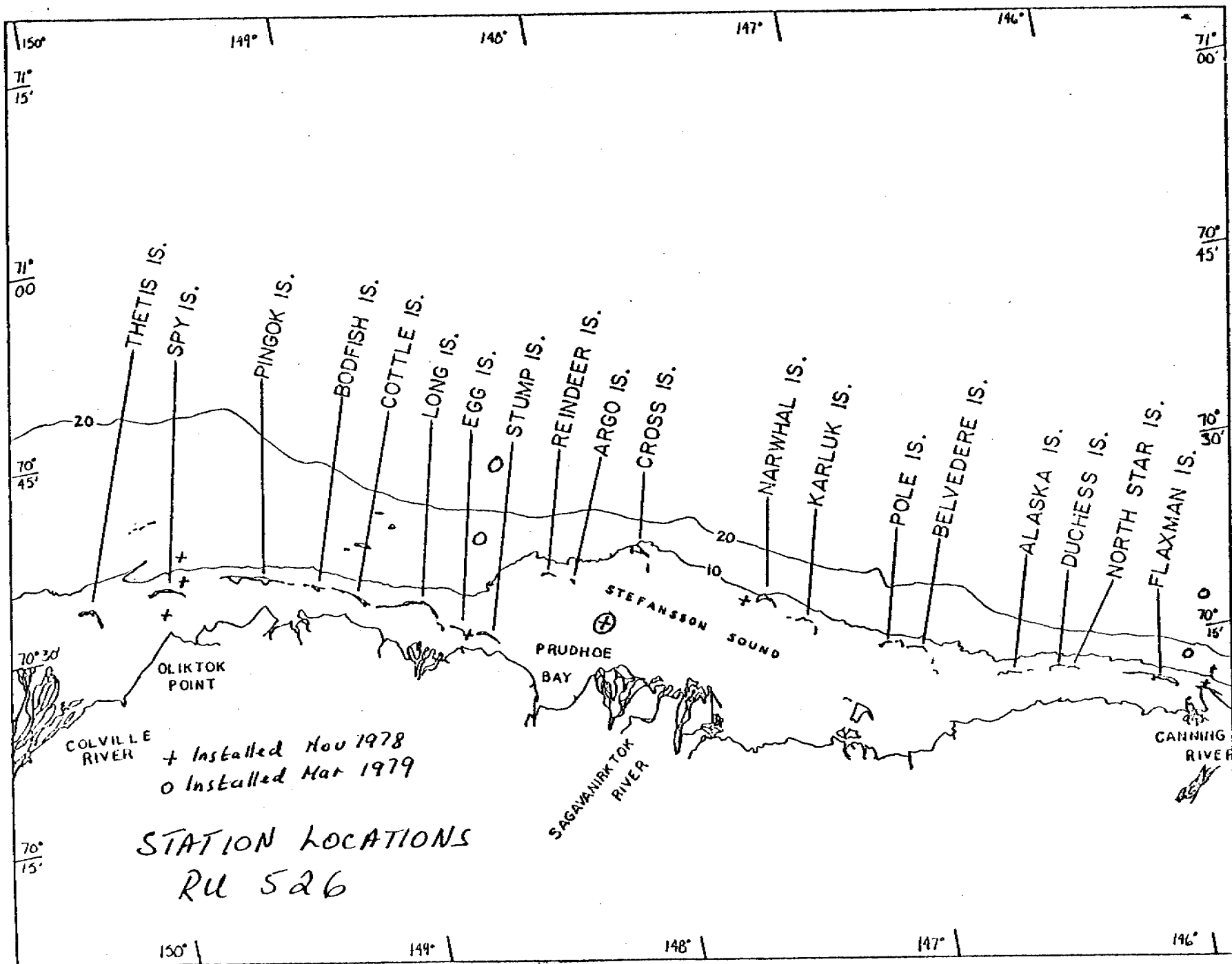


Figure 19.

ANNUAL REPORT

Contract: #03-5-022-56  
Research Unit: #529-77  
Task Order: 33  
Reporting Period: 1/7/78 - 30/3/79  
Number of Pages: 81

SOURCES, TRANSPORT PATHWAYS, DEPOSITIONAL SITES  
AND DYNAMICS OF SEDIMENTS  
IN THE LAGOON AND SHALLOW MARINE REGION, NORTHERN ARCTIC ALASKA

A. Sathy Naidu  
Principal Investigator  
Assistant Professor in Marine Science

Assisted by  
Michael D. Sweeney  
Graduate Student

Institute of Marine Science  
University of Alaska  
Fairbanks, Alaska 99701

March 1979

## TABLE OF CONTENTS

	LIST OF TABLES . . . . .	
	LIST OF FIGURES. . . . .	
I.	SUMMARY OF OBJECTIVES, CONCLUSIONS, AND IMPLICATIONS WITH RESPECT TO OCS OIL AND GAS DEVELOPMENT. . . . .	
II.	INTRODUCTION . . . . .	
	General Nature and Scope of Study. . . . .	
III.	OBJECTIVES . . . . .	
	Relevance to Problems of Petroleum Development . . . . .	
IV.	CURRENT STATE OF KNOWLEDGE . . . . .	
V.	STUDY AREA . . . . .	
VI.	SOURCES, METHODS AND RATIONALE OF DATA COLLECTION. . . . .	
	Field Work and Samples . . . . .	
	Analytical Methods . . . . .	
VII.	RESULTS. . . . .	
	Suspended Particulate Matter . . . . .	
	Sediment Texture . . . . .	
	Possible Sources of Some Arctic Barrier Island Boulder Samples. . . . .	
	Clay Mineralogy. . . . .	
	Carbonate and Organic Carbon Contents in Sediments . . . . .	
	Heavy Metal Chemistry of Sediments . . . . .	
	Lithogenous Versus Nonlithogenous Fractions of Heavy Metals in Sediments. . . . .	
	Correlations Between Chemical, Textural, and Clay Mineral Compositions of Simpson Lagoon Sediments . . . . .	
VIII.	DISCUSSION . . . . .	
	Status of Studies on Sediment Textures . . . . .	
	Stratigraphic Studies on Core Samples. . . . .	
	Origin of Exotic Boulders on the Pingok and Bodfish Islands. . . . .	
	Sediment Dynamics Study. . . . .	
	Clay Mineral Studies . . . . .	
	Sediment Geochemistry. . . . .	

TABLE OF CONTENTS (Continued)

IX. CONCLUSIONS . . . . .

X. NEEDS FOR FURTHER STUDY . . . . .

XI. SUMMARY OF 4TH QUARTER OPERATIONS . . . . .

    Ship or Laboratory Activities . . . . .

REFERENCES. . . . .

APPENDIX. . . . .

LIST OF TABLES

Table I. Weights of suspended particulate matter in the Beaufort Sea . . . . .

Table II. Weights of suspended particles in water samples collected from various regions of the Simpson Lagoon . .

Table III. Weights of suspended particulate matter collected from the surface and 0.9 m below the surface water samples from the Simpson Lagoon, at the SDS tripod station off the Milne Point. . . . .

Table IV. Statistical grain size parameters of Beaufort Sea continental shelf and slope sediments. . . . .

Table V. Statistical grain size parameters of the Simpson Lagoon bottom sediments. . . . .

Table VI. Results of grain size analysis on sediment core samples collected from the continental shelf of the Beaufort Sea, Alaska . . . . .

Table VII. Petrographic compositions and possible sources of boulder samples collected from the lagoonward beaches of the Bodfish and Pingok Islands, north arctic Alaska .

Table VIII. Weighted peak area percentages of clay minerals in the less than 2  $\mu\text{m}$  fraction of the Beaufort Sea and some North Slope river sediments . . . . .

Table IX. Carbonate and organic carbon weight percents of North Alaskan Continental Shelf and Continental Slope sediments retrieved in August, 1977. . . . .

Table X. Concentrations of Mn in the interstitial waters of continental shelf and adjacent lagoon sediments in the Beaufort Sea . . . . .

Table XI. Concentrations of Fe, Mn, Zn, and Cu in acetic acid-hydroxylamine hydrochloride extracts of Beaufort Sea sediments. . . . .

Table XII. Concentrations of Fe, Mn, Zn, Cu, and P in acetic acid-hydroxylamine hydrochloride extracts from Simpson Lagoon sediments . . . . .

LIST OF TABLES (Continued)

- Table XIII. Concentrations of Fe, Mn, Zn, Ni, Cu, Cr, Co, and V in gross sediments from the continental shelf, continental slope, and the deep-sea region of the Beaufort Sea . . . . .
- Table XIV. Concentrations of Zn, Ni, Co, and Cr in gross sediments from the bays, lagoons, and sounds of the coastal region of the Beaufort Sea . . . . .
- Table XV. Concentrations of Fe, Zn, Cu, Ni, Cr, Co, Mn and V in gross sediments of the Simpson Lagoon . . . . .
- Table XVI. Lithogenous and nonlithogenous portions of Fe, Mn, Zn, and Cu in Simpson Lagoon and the Beaufort Sea Continental Shelf, Continental Slope, and Deep-Sea sediments. . . . .
- Table XVII. Correlation coefficients for chemical, textural, and clay mineral compositions of 11 Simpson Lagoon sediments, arctic coast of Northern Alaska . . . . .

LIST OF FIGURES

- Figure 1. Sample locations in Simpson Lagoon . . . . .
- Figure 2. Station locations for Beaufort Sea clay mineral data . . . . .
- Figure 3. Locations of vibrocore sediment samples that have been collected by Drs. P. W. Barnes and E. Reimnitz of the U.S. Geological Survey in 1976 and 1977 . . . . .
- Figures 4a,b. Variation of sediment texture with depth of PWB76 core samples . . . . .
- Figure 5a. Expandable clay mineral distribution in Beaufort Sea surface sediments. . . . .
- Figure 5b. Kaolinite/Chlorite ratio distribution in Beaufort Sea surface sediments. . . . .
- Figure 6. Wind velocity and suspensate concentrations for suspensate sampling times at Milne Point SDS tripod station . . . . .

I. SUMMARY OF OBJECTIVES, CONCLUSIONS AND IMPLICATIONS  
WITH RESPECT TO OCS OIL AND GAS DEVELOPMENT

The major objectives of this program are to understand the dynamics of sedimentation, to characterize benthic substrate habitats, and to elucidate the sources and depositional sites of terrigenous particles in the lagoon and adjacent shelf area of north arctic Alaska. Additional goals of this study include completion of collection of baselines of a suite of heavy metals relative to sediments of the Beaufort Sea, understanding of the geochemical partitioning of the heavy metals in various sediment phases, and estimation of the rate of sedimentation in the above sea.

Compilation of all available data on textural attributes of surficial sediments of the Beaufort Sea has been completed. Very soon a number of maps will be generated to display regional variations in the gross lithology and the various statistical grain size parameters. These maps should be useful to biologists interested in characterizing the benthic habitats of the Beaufort Sea, as well as to geologists who are concerned with elucidation of Holocene depositional history of the Beaufort Sea. Stratigraphic studies of some core samples included lithological and coarse fraction analyses. These studies have assisted to conclude that recently most of the prodeltaic deposits of the Colville River have been free from reworking by ice gouging and/or bioturbation. Coarse-fraction, lithological and structural stratigraphic changes identified in the Simpson Lagoon core suggest that the lagoon has evolved from the coalescing of gradually subsiding coastal lakes and the eventual



inundation of the latter by sea. Attempts are being made to correlate the lagoon evolutionary sequence to the geologic time scale.

The accidental malfunction of the instrumented tripod package of the sediment dynamic sphere (SDS) system struck a serious blow to our sediment dynamic studies. Plans are called for to duplicate the SDS experiments in summer 1979. However, the complementary investigations on the suspensates has offered some interesting data. It would seem that substrate particles in the Simpson Lagoon are periodically resuspended by horizontal oscillatory currents induced by wind generated wave action. The particles thus suspended are generally transported westward in the Simpson Lagoon and the contiguous nearshore open shelf. Results of clay minerals investigations tend to substantiate our earlier conclusions. On the basis of clay mineral dispersal patterns it is possible to elucidate the sources and eventual depositional sites of fine trained terrigenous particles in the lagoons, bays and adjacent shallow-water open shelf regions of the Beaufort Sea. Because of intensive sediment reworking by ice gouging and/or bioturbation it is believed that no definite dispersal patterns of clay minerals in the middle and outer Beaufort Sea shelves are apparent. The exception to the latter is the presence of the Colville River assemblage in a disconnected but extensive patch between Barter Island and the Demarcation Point. It is concluded that this patch represents a relict sediment.

Detailed petrographic studies of several boulder chips suggest that the exotic boulder deposits of the Pingok and Bodfish Islands of the North Slope had their source in the Brooks Range and the contiguous mountain system. A mode of transport other than glaciers is difficult to conceive.

Relative abundances of Fe, Mn, Cu, Ni, Co, Cr, V, Zn and P in the readily mobilized as well as in a few gross sediments have been documented for the Simpson Lagoon and the Beaufort Sea shelf. With the exception of Mn bulk of all metals are fractionated in the crystal lattice of minerals. On basis of correlation coefficient analysis it is concluded that most of the metals are fractionated in the mud fraction of the Simpson Lagoon sediments.

The baseline data on heavy metals in sediments should help in detection of any large scale perturbations in environments that might result from discharge of chemical pollutants into the nearshore areas of the Beaufort Sea. Likewise our baseline lithology maps for the Beaufort Sea, as well as for lagoons and the bays of north arctic Alaska, should serve a useful purpose in detecting any changes in sediment budgets (and by implication benthic habitats) resulting from petroleum-related activities such as dredging, causeway construction and possible gravel/sand exploitation from the above areas. Without an adequate understanding of the sediment budgets, sources and depositional sites of terrigenous particles, and knowledge of dynamics of sedimentation it would be impossible to predict, much less assess, perturbations that might eventually result on the ecosystems by activities related to exploration and exploitation of petroleum in the coastal area of north arctic Alaska.

## II. INTRODUCTION

### General Nature and Scope of Study

This program (Research Unit 529) concerning sedimentological studies is part of a larger interdisciplinary research effort (RU 467), to study the physicochemical and biological processes operative in the barrier island-lagoon ecosystem of the continental margin of the Alaskan Beaufort Sea. Additionally, the general scope of the overall program entails establishment of an ecosystem model which can be put to use in predicting possible impacts resulting from both petroleum exploration and exploitation activities in the barrier island-lagoon complex of the Beaufort Sea coast. Further details on the nature and scope of this study (RU 529) and associated investigations have been enumerated in the original proposal submitted by LGL Ltd.-U.S., Ind. to the OCSEAP office in August 1977. Briefly, the scope of the sedimentological studies (RU 529) includes understanding of the sediment dynamics, delineating benthic substrate habitats, estimating the C, N and P contents in the substrate and suspensate sediments, establishing the alongshore sediment transport directions, completing collection of baseline data on a suite of heavy metals for the Simpson Lagoon and adjacent nearshore environment of the Beaufort Sea.

## III. OBJECTIVES

The overall objectives of this research unit are to understand the sediment dynamics and correlate the transport, resuspension and deposition of sediments as functions of wind-wave-current actions in the lagoon environment of north arctic Alaska. The specific objectives of the study are:

- (i) to define the sources migratory pathways, and depositional sites of terrigenous organic particles, using the assumption that the hydraulic behavior of both fine inorganic particles (e.g. clay minerals) and organic particles are similar.
- (ii) to develop understanding of sediment dynamics in the lagoon environment of north arctic Alaska, considering the Simpson Lagoon as a type area. This objective includes initiating of a study that would eventually lead to the establishment of correlations between wind-wave-current parameters and water turbidity, resuspension and movement of organic and inorganic particles, determination of the critical value of near-bed shear stress for incipient motion of cohesionless sediments under oscillatory wave action.
- (iii) to estimate the contemporary rate of sedimentation in the Simpson Lagoon.
- (iv) to elucidate the sources, transport directions, and depositional sites of sand and clay-size inorganic terrigenous particles.
- (v) to complete mapping of lithological variations in surficial sediments of the continental margin of the Beaufort Sea.
- (vi) to complete establishment of baseline data on first row transition heavy metals.

#### Relevance to Problems of Petroleum Development

The exploitation of the petroleum reserves in the North Slope of Alaska has commenced with the recent flow of oil through the trans-Alaska pipeline. The present trend is towards exploration in the adjacent continental shelf of the Beaufort Sea. As a consequence of the OCS petroleum and gas development activities, the nearshore and the open shelf ecosystem of the Beaufort Sea is bound to be subjected to some degree of anthropogenic perturbations. The industrial activities which most likely will be introduced in this area include the construction of artificial islands and causeways for the use of drilling operations and docking facilities, dredging for maintaining navigation, and the exploitation of gravel and sand deposits

from several possible sources as construction and fill materials. The impact of these activities, as well as others such as a blow-out, inadvertent discharge of cuttings and muds from drilling operations, and accidental oil spills on the nearshore ecosystem are unknown. However, several attempts have been made in postulating the possible socioeconomic scenario and environmental perturbations that might result during the exploration and exploitation of petroleum reserves from the OCS lease areas of the Beaufort Sea (Arnold, 1975; Weller *et al.*, 1977). It is of interest to note that significant changes in the size distributions, benthic and chemical attributes of bottom sediments, as well as on the nearshore bathymetry have already been recognized in the vicinity of Prudhoe Bay, consequent to the building of the new ARCO causeway (Feder *et al.*, 1976; Barnes *et al.*, 1977; Grider *et al.*, 1977).

If the response of the physical environment and biological resources of the continental margin area to petroleum development activities can be properly assessed, or even predicted, it is quite possible that effective measures can be established to protect or enhance existing resources. In recognition of this the BLM-NOAA-OCSEAP Office initiated a comprehensive ecosystem process-response research in the barrier island-lagoon regime of north arctic Alaska. A consolidated research plan was outlined in June 1976, by the LGL Limited, U.S., Inc. who were awarded with the prime contract. Preliminary results of the first year interdisciplinary study, are now becoming available (refer to the 1978 Annual Reports as well as to the subsequent periodic reports submitted by various principal investigators to the OCSEAP Office).

It has become increasingly evident from deliberations at several LGL-sponsored ecosystem modeling workshops, held over the last two years at the University of British Columbia (Vancouver), that the carbon input to the lagoon ecosystem of north arctic Alaska is influenced by terrigenous organic detritus. Seasonal studies in the lagoon regime conducted over a few years by Schell and Alexander (in Alexander *et al.*, 1975), have indicated that the net carbon input in the North Slope lagoon by under-ice and pelagic photosynthesis is low, and that terrestrial peat detritus derived from fluvial discharge and/or coastal bluff erosion would seem to be a relatively more important carbon source for epibenthic organisms often observed in and on the organic detritus that blankets the Simpson Lagoon bottom. It is of further interest to note that the primary food sources of higher trophic organisms (e.g. fishes and birds) in the above lagoon are the epibenthic invertebrates such as mysids, amphipods, isopods, etc. (Truett, 1978). However, importance of the carbon in the terrigenous organic detritus to the lagoon invertebrates, and by implication to the birds and fishes, would seem to depend on several factors, the more critical being the length of time the detritus is exposed to heterotrophic bacterial degradation and to detritivore scavenging. High rate of particulate sedimentation would, of course, preclude the usefulness of the organic detritus as a major carbon source, and vice versa. Additionally, the net amount of particulate organic carbon that would be made available to the Alaskan arctic lagoon detritivores would greatly depend on the volume of terrigenous debris that would be discharged into the lagoon by coastal bluff erosion and/or fluvial discharge. It is conceivable that this terrigenous organic supply can be altered significantly by a number

of possible coastal activities related to petroleum development. Activities such as coastal bluff revetment, causeway construction and dredging operations would eventually change the nearshore sediment budget, which in turn may not only result in a decrease in the net terrigenous organic input into the lagoons but also may modify adversely the deposition-resuspension rates of the organic debris.

One of the questions that was repeatedly raised at the 1977 and 1978 Beaufort Sea Synthesis meeting in Barrow related to the understanding of overall sediment dynamics (including both organic and inorganic particles) in the nearshore area of north arctic Alaska. It was concluded that without an adequate knowledge of the sediment fluxes which would encompass considerations of sources, transport directions, and depositional sites of fine-grained terrigenous particles it would be almost impossible to forecast the fate of soluble and particulate pollutants in the lagoon and shallow marine Alaskan arctic. The importance of clay-sized sediment particles as potential vehicles to transport pollutants is universally well recognized. Additionally, it was concluded at the two meetings that hydrodynamic factors that govern the threshold (minimum current velocity) of coastal sediment movements must also be understood, because of the implication of it in quantitative assessment of changes in sediment budgets resulting from anthropogenic activities (e.g. drilling pad and causeway construction, dredging, etc.). We have no knowledge what the fluxes and mean rate of sedimentation is in the North Slope lagoon and what physicochemical factors can alter the rate. A reasonable concern, as mentioned earlier, has been that any significant disturbance of the contemporary sediment budgets in the shallow lagoons

may eventually lead to the destruction of the lagoon ecosystem of the North Slope area.

Although considerable baseline data on the lithological composition of sediments have been collected for the continental margin of north arctic Alaska - especially under the auspices of the ongoing OCSEAP studies - no serious process-response sedimentological investigations involving extensive data base have ever been undertaken for the above region. A few sediment dynamics studies of a preliminary nature have been conducted along the beaches of the Simpson Lagoon and the Pingok Island by Wiseman *et al.* (1973) and Dygas and Burrell (1976a, 1976b). However, to assume that results of these surf-zone studies may be extrapolated to the adjacent relatively deeper and protected lagoons would seem quite inappropriate. The above investigators made no direct *in situ* measurements of threshold sediment movements. In fact the first system studies on sediment dynamics, involving time-series concomitant wind-wave-current data, in Alaskan waters are those of Cacchione and Drake (1977). It is, therefore, important that sediment dynamics studies in the north Alaskan arctic lagoon be initiated.

Intrinsic to the sediment dynamics studies is the elucidation of the contemporary sources and depositional sites of inorganic sediment particles in north Alaskan arctic nearshore environment. Such an understanding would be very useful in assessing, or even predicting, impact of coastal engineering structures on the trajectories of present littoral sediment transport. Alterations in the nearshore wave-current regime (and by implication the littoral sediment transport directions and depositional sites) as a consequence of causeway and jetty building are



universally well-known. Such alterations generally result in large-scale modification in the erosional-depositional regime of coastal areas, and eventually changes in the associated ecosystems. In the north Alaskan arctic nearshore environment, considerable research has been accomplished to understand the sources and transport directions of fine-grained particles, *via* very detailed analysis of clay minerals (Naidu and Mowatt, 1975; Naidu, 1978). However, relatively little effort has been expended to firmly establish the provenance and net long-term transport directions of sand-sized sediment particles. Several lines of indirect evidence demonstrate that the net along shore sand drift is towards the west. More recently Hopkins (1977) has concluded that the major passes within the Beaufort Sea island chains act as effective obstacles to continuous littoral sediment transport between different island groups. Additionally Hopkins (1977) has suggested that both sand and gravel laterally migrate from one island to another only within individual island groups. Although these observations on sediment transport are interesting, Hopkins' (1977) conclusions need to be substantiated because his data were based chiefly on the lithologic composition of pebbles rather than both pebble petrography and sand grain mineralogy. This constitutes an important data gap which must be filled in order to fully assess impact of activities relative to petroleum exploration and exploitation on the ecosystem of the Beaufort Sea continental margin.

#### IV. CURRENT STATE OF KNOWLEDGE

Within the past nine years or so, considerable research has been accomplished on the processes and products of sedimentation in the continental margin area of the Alaskan Beaufort Sea. A major portion of this research has been accomplished by scientists from three institutions, namely the University of Alaska (Institute of Marine Science), the U.S. Geological Survey (Marine Geology and Alaska Branches, Menlo Park) and the Louisiana State University (Coastal Studies Institute). In a recent OCSEAP report, Naidu (in Burrell, 1977) has compiled a bibliography of sedimentological and related investigations that have been carried out in the Alaskan Beaufort Sea shelf and coastal area. Barnes *et al.* (1977, 1978) have summarized miscellaneous hydrologic and geologic observations as well as characteristics and changing patterns of ice gouging on the Beaufort Sea shelf. The arctic coastal processes and morphology, as studied by the LSU Group, have been condensed in a report by Wiseman *et al.* (1973). Results of more recent investigations, relative to geologic history, sedimentation, mineralogy and geochemistry, supported by the BLM-NOAA environmental program in the Beaufort Sea coastal and shelf areas have been compiled in the 1977 and 1978 OCSEAP Annual and Quaterly Report volumes.

#### V. STUDY AREA

The region of our investigations is confined to the continental margin of the Alaskan Beaufort Sea. However, more intensive study, for barrier island-lagoon ecosystem modeling purpose, has been confined to the Simpson Lagoon area (Fig. 1). The latter region appears to be an



adequately representative type area for ecosystem studies of island-lagoon complex along the Alaskan Beaufort Sea coast. In order to obtain a much wider data base and to assess terrigenous sources and transport directions of sediments along the Beaufort Sea coast, it has been imperative to extend sedimentological work to all the major river systems of the North Slope and to the lagoon environment west of the Simpson Lagoon.

## VI. SOURCES, METHODS AND RATIONALE OF DATA COLLECTION

### Field Work and Samples

Most of the sediment samples for analysis were selected from an archives suite of samples that were collected prior to March 1978 from the Simpson Lagoon (Fig. 1) and the adjacent Beaufort Sea (Fig. 2). Additionally, a few sediment samples were collected in August 1978 in support of the sediment dynamics study. A. S. Naidu and his field assistants, Mr. J. Clough and Mr. J. Haney, spent almost a month in August 1978 collecting sediment and water samples in the Simpson Lagoon and the Beaufort Sea. The lagoon sampling program was operated from the Arctic Project Office Base Camp at Milne Point, whereas the Beaufort Sea sampling was conducted from the ice-breaker USCGC *Northwind*.

In attempting to estimate the rates of sedimentation and to understand the overall geochemistry of elements, gravity core samples were retrieved from the Simpson Lagoon from 4 stations south of the Pingok Island using the R/V *Natchik*. However, the penetration of the 750 lb gravity coring unit was poor in the lagoon and only limited lengths of cores could be retrieved. Samples of a 38 cm long box core and a 75 cm

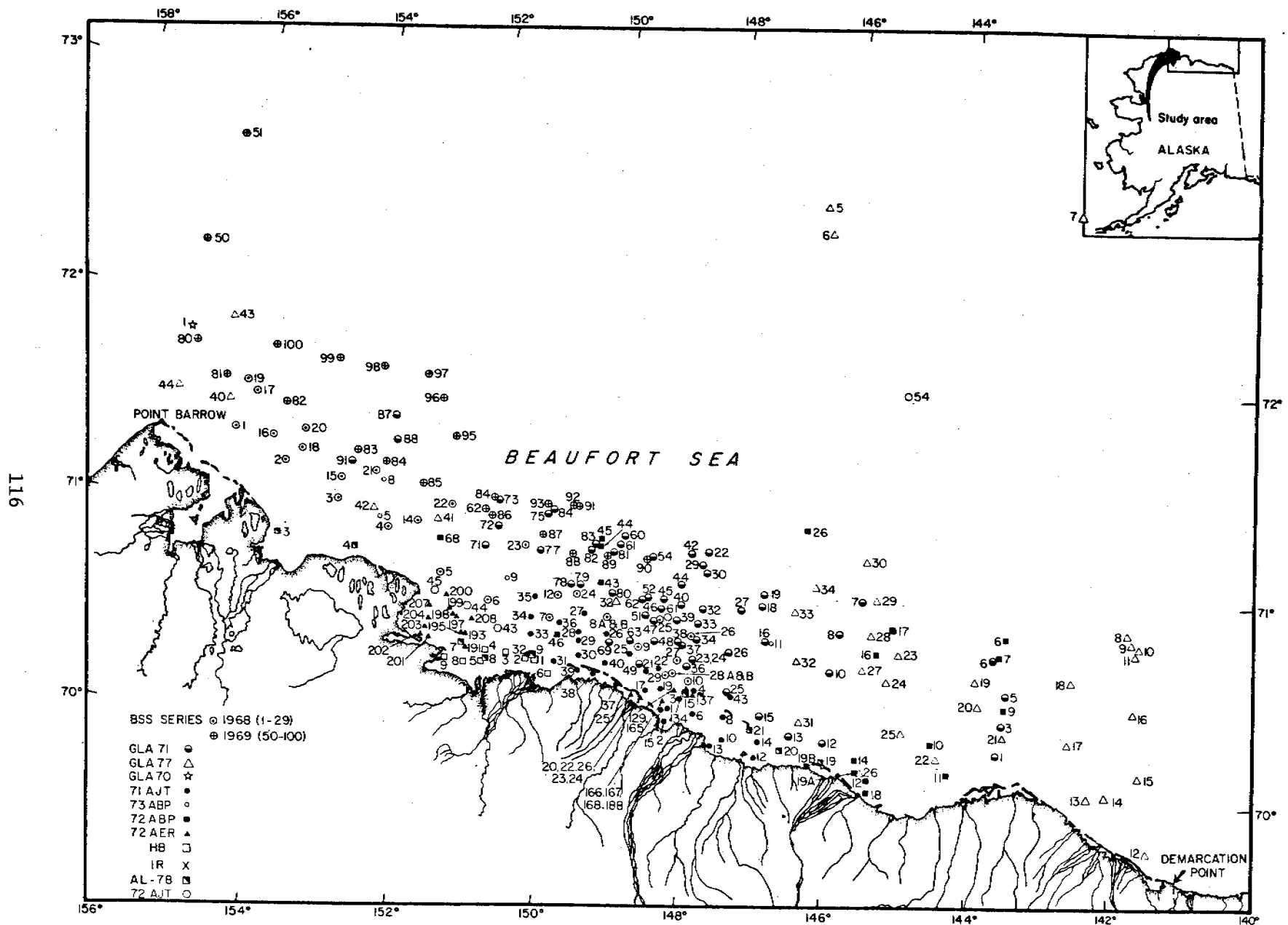


Figure 2. Station locations for Beaufort Sea clay mineral data.

long gravity core were collected in August 1978 from the Colville pro-delta (71°00'N and 149°59.50'W), using the ice-breaker USCGC *Northwind*. The purpose of collecting these samples was to estimate the contemporary rate of sedimentation in the Beaufort Sea continental shelf. All core samples were stored in the original state of retriever in a freezer until they were ready for processing. One centimeter thick continuous sediment sections were subsampled from the top of the box core in the Fairbanks laboratory, and sent to Dr. H. V. Weiss (Naval Ocean System Centre, San Diego) for <sup>210</sup>Pb dating. In case of the lagoon, an entire core length was sent in the original core liner.

To further our knowledge on sediment dynamics in the Simpson Lagoon area, a tripod instrumented package - the Sediment Dynamics Sphere (SDS) - was deployed to an experimentation station in the lagoon. This station was situated between the Milne Point and the eastern Pingok Island (149°27.45'W and 70°32.2'N). The package was transferred from Pt. Barrow to the experimental site, employing the NARL'S *Alumiak* and R/V *Natchik*. The instrumented tripod package was in water from August 12th to September 3, 1978. However, after emplacing it in water there was a major mishap. The drag lines of the tripod were accidentally caught by the balancing anchors of the R/V *Natchik*. As a result of this, the tripod was dragged on the lagoon floor for some distance, which presumably contributed to the ultimate malfunction of the SDS system. Although the SDS unit was eventually uprighted and left in the lagoon for almost 3 weeks, it was disclosed at the end of the experiment and subsequent processing that no long-term time series data had been obtained\*.

Subsequent to the emplacement of the SDS unit, water samples were collected twice daily at the tripod station to monitor concentration of suspensates on a time series basis. The objective of such a monitoring was: (i) to establish an *in situ* field calibration for the nephelometer/transmissometer and (ii) to check if any correlation existed between re-suspension-suspension of inorganic and organic sediment particles in Simpson Lagoon water columns and wind-wave-current parameters. To achieve this objective, one-liter water samples were collected via a Niskin bottle from the surface and from the water depth at which the nephelometer was installed on the tripod (i.e. 0.9 m below the surface). Each of the water samples was filtered at Milne Point base camp, through preweighed Nucleopore filter membranes (0.4  $\mu\text{m}$  pore size). The suspensates thus collected were stored in a freezer until ready for drying and weighing in the Fairbanks laboratory.

At the tripod station substrate sediment samples were periodically collected, using a small hand-operated gravity coring unit from a zodiac boat. The purpose of such a sampling was to obtain a thin layer of the surficial bed-load of the lagoon substrate and correlate the size distribution of such a sample with the wave-current regime prevailing at the time of sample collection. This was part of our sediment dynamic studies. Core samples thus collected were kept intact in the plastic core liners and transferred to the Fairbanks laboratory for textural analysis.

---

\*A detailed report on the sequence of events which led to malfunction of the SDS system was submitted to A. S. Naidu (P.I. of the Project) by Dr. L. H. Larsen, to whom a subcontract was issued to install, gather and process data on the SDS system. Copy of Dr. Larsen's report is appended with this report for information purpose.

A survey of the Pingok and Bodfish islands in the Beaufort Coast of Alaska were made, and samples of large boulders exposed on the lagoonward beaches of these islands were collected. Purpose of this collection was to define the sources and modes of transport of the boulders to the present site.

On August 15 and 16, 1978, when there was satellite coverage of the Simpson Lagoon area, surficial water samples were collected from a number of widely dispersed stations in the lagoon. The purpose of this water sample collection was to analyze concentrations of suspensates in the waters, which would serve as ground truth to interpret sediment plume densities as displayed by LANDSAT images from the coastal regime of the North Slope of Alaska. A total of 20 stations were occupied (Table II) extending from Oliktok Pt. to Beechey Pt. in the Simpson Lagoon. Additionally, 12 stations were occupied in the Beaufort Sea continental shelf during the first phase (August 17-25, 1978) of the USCGC *Northwind* cruise. At each of these stations water samples were collected at various depths (Table I) using a Niskin bottle. Two-litre aliquots of each of the water samples were filtered through pre-weighed Nuclepore filter membranes (pore size: 0.4  $\mu\text{m}$ ). The suspensates were finally washed with distilled water and stored in a freezer.

Splits of all Smith-McIntyre grab samples collected by Mr. Gene Ruff (Oregon State University) during the 1978 USCGC *Northwind* cruise in the Beaufort Sea have been made available to us for textural, clay mineral and organic carbon analyses.



TABLE I  
 WEIGHTS OF SUSPENDED PARTICULATE MATTER IN THE BEAUFORT SEA

Water Samples Were Collected From U.S.C.G.C. Northwind  
 In August 17-24, 1978

Station	Sampling Depth (m)	Suspensate (mg/l)
NW78- 1 (Lat. 71°11'; Long. 150°14')	5	0.27
	25	0.52
	35	0.20
	45	1.16
	45(d)	1.43
NW78- 3 (Lat. 70°58.5'; Long. 149°17')	3	0.41
	20	0.42
	35	0.41
NW78- 4 (Lat. 70°20.9'; Long. 145°59.4')	0	0.66
	15	0.53
	25	0.23
NW78- 5 (Lat. 70°36.2'; Long. 148°20.2')	0	0.82
	9	0.99
	20	0.92
NW78- 6 (Lat. 70°55'; Long. 148°11')	0	1.09
	20	0.46
	35	0.58
NW78- 7 (Lat. 71°05.5'; Long. 149°54')	0	0.55
	10	0.47
	20	0.65
NW78- 8 (Lat. 71°03.6'; Long. 150°52.9')	0	0.53
	10	0.35
	20	2.09
NW78- 9 (Lat. 71°11.1'; Long. 151°51.3')	0	0.83
	10	0.85
	20	0.82
NW78-10 (Lat. 71°05'; Long. 152°51')	0	0.41
	10	1.22
	20	1.37
NW78-11 (Lat. 71°19.8'; Long. 152°47.7')	0	0.39
	20	0.35
	35	1.09
NW78-12 (Lat. 71°21.6'; Long. 152°41.1')	0	0.34
	45	0.94
	90	0.39

## Analytical Methods

The laboratory methods that have been adopted to analyze sediment samples have been elaborately described in the original proposal (OCSEAP RU 529-77). Briefly, the sediment size distribution analysis of the grab and core sections was performed by the usual sieve-pipetting method. Calculation of the conventional statistical grain size parameters was after Folk and Ward (1957), employing the University of Washington (Seattle) SEDAN program with the University of Alaska Honeywell 66/40 computer system.

The clay mineral analysis for the  $<2 \mu\text{m}$  of sediments was accomplished according to the methods elaborated by Naidu *et al.* (1971) and Naidu and Mowatt (1974) using X-ray diffraction technique. For heavy mineral studies, coarse, medium, and fine size grades of sands were considered. The heavy mineral crops in each of the size grades were separated in bromoform (sp. gr. 2.89). Coarse-fraction analyses (Shepard and Moore, 1954) on sections of vibrocore sediments are being conducted under a binocular microscope.

Thin sections were prepared of the boulder chip samples collected from the Pingok and Bodfish islands, and examined under a petrographic microscope to define the rock types.

Each of the Nuclepore filter pads with suspensates were dried in an oven at  $60^{\circ}\text{C}$  and desiccated prior to weighing in a Mettler Balance.

Sediment samples stored in a frozen state were thawed, dried, and two splits of them were taken for geochemical analysis; one for coarse and another for fine powdering. The coarse powder was subjected to Acetic acid-Hydroxylamine hydrochloride extraction to release the

"relatively mobilized" fractions of metals from the sediments (Chester and Hughes, 1967). Portions of the fine-ground sediment powders were taken for analysis of carbonate-bound carbon, total carbon, and a suite of heavy metals in gross sediments. Organic carbon was calculated from the difference between total carbon and carbonate-bound carbon. The total carbon was analyzed in a LECO, TC-12 automatic carbon determinator, whereas the carbonate carbon was determined manometrically (Hülsemann, 1969). Replicate analyses of total and carbonate-bound carbon gave good precision. For total heavy metal analysis sediment powders were taken into solution by HF-HNO<sub>3</sub> acid digestion (Rader and Grimaldi, 1961). From the latter solutions and the acetic acid-hydroxylamine hydrochloride extracts, Fe, Mn, Zn, Cu, Ni, Co, Cr and V were analyzed by atomic absorption spectrophotometry. A Perkin-Elmer Model 603 unit, and Model 360 unit equipped with the model 2100 Graphite Furnace, was used for the heavy metal analysis. Phosphorus in the sediment extracts was analyzed using the molybdate-blue method (Strickland and Parsons, 1965). The frozen interstitial waters samples were first thawed and subsequently analyzed for Mn and P by the techniques mentioned earlier.

Correlation coefficients were calculated for textural, chemical, and mineralogical attributes of Simpson Lagoon sediment samples. A Pearson Product Moment correlation was the method used. The calculations were done on the Alaskan Honeywell 66/40 computer.

## VII. RESULTS

### Suspended Particulate Matter

The weights for the suspended particulate matter collected in August and September, 1978 are listed in Tables I, II and III. In Table I are shown the suspended material weights at each respective sampling depth for stations occupied during the USCGC *Northwind* cruise in the Beaufort Sea from August 17 to 24, 1978. The concentration of particulate matter in the upper 90 m of the water column ranges from 0.20 to 2.1 mg/l.

However, the maximum surface concentration obtained at any NW78 station was 1.1 mg/l. By locating the latitude and longitude of the NW78 station locations one can see that these suspensate samples were taken in waters over the outer continental shelf and out into the deep sea. The particulate densities for NW78 samples indicated above are quite similar to concentrations cited previously for the Beaufort Sea outer continental shelf (greater than 30 m) (Burrell, *et al.*, 1970; Naidu, 1974; Barnes, *et al.*, 1977).

Table II lists the suspensate weights from various areas of Simpson Lagoon. These surface concentrations range from 1.0 to 55 mg/l. The Simpson Lagoon suspensate concentrations are generally five to ten times greater than those in the Beaufort Sea continental shelf. The areal variation within the Lagoon also appears to be much higher than over the shelf.

Satellite imagery confers well with the contrast in suspended loads between nearshore bays and lagoons and the open shelf environment (Tables I, II). Suspensate data collected in Harrison Bay in late

TABLE II

WEIGHTS OF SUSPENDED PARTICLES IN WATER SAMPLES  
COLLECTED FROM VARIOUS REGIONS OF THE SIMPSON LAGOON

Sample #	Date	Time	Station	Water Depth	Suspensates (mg/l)
SL78- 4	8-06-78	12:30 PM	West of Milne Point	Surface	2.71
SL78- 5	8-06-78	1:00 PM	Between Oliktok and Pingok	Surface	1.05
SL78- 6	8-06-78	2:00 PM	South of Pingok Island	Surface	0.89
SL78- 7	8-07-78	NOON	Beechey Point Spit	Surface	6.06
SL78- 8	8-07-78	12:15 PM	South of Cottle Island	Surface	3.36
SL78- 9	8-07-78	1:00 PM	Between Beechey Point and Cottle Island	Surface	7.79
SL78-10	8-09-78	11:00 AM	Mungall's Station	Surface	32.87
SL78-11	8-09-78	11:10 AM	Between Shore and Mungall's Station	Surface	5.61
SL78-13	8-13-78	3:45 PM	Mungall's Station	Surface	30.5
SL78-16	8-14-78	10:45 AM	Mungall's Station	Surface	20.65
SL78-19	8-14-78	4:40 PM	Mungall's Station	Surface	6.96
SL78-22	8-15-78	11:30 AM	Mungall's Station	Surface	9.04
SL78-25	8-15-78	2:30 PM	LGL #2	Surface	6.91
SL78-26	8-15-78	2:30 PM	LGL #1	Surface	6.38
SL78-27	8-15-78	3:00 PM	Mungall's Station	Surface	20.22
SL78-28	8-16-78	4:00 PM	LGL #3	Surface	11.0
SL78-31	8-16-78	4:15 PM	Peat Island Spit	Surface	55.15
SL78-32	8-16-78	PM	200' South of Pingok-Levitt Spit	Surface	16.95
SL78-33	8-16-78	PM	100' South of West Pingok Spit	Surface	5.70
SL78-3	8-16-78	PM	1/2 Mile South of Pingok	Surface	3.90

TABLE III

WEIGHTS OF SUSPENDED PARTICULATE MATTER COLLECTED FROM THE SURFACE  
AND 0.9 m. BELOW THE SURFACE WATER SAMPLES FROM THE SIMPSON  
LAGOON, AT THE SDS TRIPOD STATION OFF THE MILNE POINT  
(LAT. 70° 32.20' N AND LONG. 149° 27.45' W)

Sample #	Date	Time	Location	Water Depth	Suspensates (mg/l)
SL78- 12	8-13-78	3:30 PM	Tripod	Surface	14.35
SL78- 14	8-14-78	10:30 AM	Tripod	0.9m	11.13
SL78- 15	8-14-78	10:30 AM	Tripod	Surface	8.86
SL78- 17	8-14-78	4:30 PM	Tripod	Surface	10.30
SL78- 18	8-14-78	4:30 PM	Tripod	0.9m	8.20
SL78- 20	8-15-78	11:30 AM	Tripod	Surface	7.40
SL78- 21	8-15-78	11:30 AM	Tripod	0.9m	9.90
SL78- 23	8-15-78	2:30 PM	Tripod	Surface	6.01
SL78- 24	8-15-78	2:30 PM	Tripod	0.9m	7.46
SL78- 29	8-16-78	4:00 PM	Tripod	Surface	9.30
SL78- 30	8-16-78	4:00 PM	Tripod	0.9m	8.72
SL78- 35	8-17-78	7:00 PM	Tripod	Surface	6.93
SL78- 36	8-17-78	7:00 PM	Tripod	0.9m	7.61
SL78- 37	8-18-78	6:30 PM	Tripod	Surface	5.27
SL78- 38	8-18-78	6:30 PM	Tripod	0.9m	5.36
SL78- 39	8-19-78	11:45 AM	Tripod	Surface	4.65
SL78- 40	8-19-78	11:45 AM	Tripod	0.9m	4.97
SL78- 41	8-19-78	6:30 PM	Tripod	Surface	3.25
SL78- 42	8-20-78	10:30 AM	Tripod	Surface	6.43
SL78- 43	8-20-78	10:30 AM	Tripod	0.9m	8.95
SL78- 44	8-20-78	6:30 PM	Tripod	Surface	3.90
SL78- 45	8-20-78	6:30 PM	Tripod	0.9m	4.58
SL78- 46	8-21-78	9:45 AM	Tripod	Surface	3.01
SL78- 47	8-21-78	9:45 AM	Tripod	0.9m	2.96
SL78- 48	8-21-78	6:00 PM	Tripod	Surface	3.26
SL78- 49	8-21-78	6:00 PM	Tripod	0.9m	3.04
SL78- 50	8-22-78	10:15 AM	Tripod	Surface	4.93
SL78- 76	8-22-78	10:15 AM	Tripod	0.9m	4.91
SL78- 77	8-23-79	9:15 AM	Tripod	Surface	18.02
SL78- 78	8-23-78	9:15 AM	Tripod	0.9m	14.75
SL78- 79	8-23-78	5:30 PM	Tripod	Surface	20.71
SL78- 80	8-23-78	5:30 PM	Tripod	0.9m	20.60
SL78- 81	8-24-78	9:30 AM	Tripod	Surface	9.63
SL78- 82	8-24-78	9:30 AM	Tripod	0.9m	9.62
SL78- 83	8-24-78	5:30 PM	Tripod	Surface	4.66
SL78- 84	8-24-78	5:30 PM	Tripod	0.9m	4.68
SL78- 85	8-25-78	9:45 AM	Tripod	Surface	7.28
SL78- 86	8-25-78	9:45 AM	Tripod	0.9m	6.61
SL78- 87	8-25-78	6:00 PM	Tripod	Surface	4.61

TABLE III

CONTINUED

Sample #	Date	Time	Location	Water Depth	Suspensates (mg/l)
SL78- 88	8-25-78	6:00 PM	Tripod	0.9m	4.43
SL78- 89	8-26-78	9:30 AM	Tripod	Surface	1.70
SL78- 90	8-26-78	9:30 AM	Tripod	0.9m	2.24
SL78- 91	8-26-78	5:30 PM	Tripod	Surface	2.74
SL78- 92	8-26-78	5:30 PM	Tripod	0.9m	2.71
SL78- 93	8-27-78	10:15 AM	Tripod	Surface	8.51
SL78- 94	8-27-78	10:15 AM	Tripod	0.9m	6.22
SL78- 95	8-27-78	6:00 PM	Tripod	Surface	35.87
SL78- 96	8-27-78	6:00 PM	Tripod	0.9m	26.07
SL78- 97	8-28-78	9:45 AM	Tripod	Surface	4.76
SL78- 98	8-28-78	9:45 AM	Tripod	0.9m	5.84
SL78- 99	8-28-78	5:45 PM	Tripod	Surface	5.03
SL78-100	8-28-78	5:45 PM	Tripod	0.9m	4.71
SL78-201	8-29-78	9:30 AM	Tripod	Surface	3.98
SL78-202	8-29-78	9:30 AM	Tripod	0.9m	3.91
SL78-203	8-29-78	5:15 PM	Tripod	Surface	3.23
SL78-204	8-29-78	5:15 PM	Tripod	0.9m	4.79
SL78-205	8-30-78	9:00 AM	Tripod	Surface	3.40
SL78-206	8-30-78	9:00 AM	Tripod	0.9m	2.91
SL78-207	8-30-78	5:30 PM	Tripod	Surface	3.44
SL78-208	8-30-78	5:30 PM	Tripod	0.9m	3.49
SL78-209	8-31-78	9:15 AM	Tripod	Surface	3.72
SL78-210	8-31-78	9:15 AM	Tripod	0.9m	4.26
SL78-211	8-31-78	5:15 PM	Tripod	Surface	2.95
SL78-212	8-31-78	5:15 PM	Tripod	0.9m	3.01
SL78-213	9-01-78	10:00 AM	Tripod	Surface	2.57
SL78-214	9-01-78	10:00 AM	Tripod	0.9m	2.65
SL78-215	9-02-78	10:15 AM	Tripod	Surface	2.77
SL78-216	9-02-78	10:15 AM	Tripod	0.9m	3.19
SL78-217	9-02-78	5:45 PM	Tripod	Surface	3.09
SL78-218	9-02-78	5:45 PM	Tripod	0.9m	3.11
SL78-219	9-03-78	9:00 AM	Tripod	Surface	4.46
SL78-220	9-03-78	9:00 AM	Tripod	0.9m	3.56

summer 1976 show a distribution of turbidity in the bay quite similar to that shown by a satellite image of the bay in late July, 1974 (Barnes, *et al.*, 1977). The images and suspensate data suggest that in general coastal turbid waters are confined to depths within the 5 m bathymetric line and do not extend much farther seaward than the line of barrier islands.

The satellite photographs also show that the turbidity adjacent to the Colville and Sagavanirktok Deltas is not uniform. A September, 1974 photograph shows that the relatively less turbid river water maintains its identity and almost immediately turns westward upon entering the marine environment staying close to shore. Immediately outside of this relatively clear water is more turbid coastal water. One can see the westward extension but abrupt eastward termination of turbid waters off the two deltas. The clear nature of the river water entering the shallow coastal zone in late summer suggests the origin of the relatively high suspended loads in coastal waters in late summer is the resuspension of bottom sediments derived from very shallow water.

Table III lists the time-series suspensate data taken from a fixed station in Simpson Lagoon. The location is the SDS tripod station off Milne Point and samples were retrieved from the surface and from 0.9 m below the surface depth. Data were collected regularly from August 13, 1978 to September 3, 1978. The following observations can be made concerning the variation of suspensate concentration with time. A general decrease in concentration occurs from August 13 to August 21 going from 15 to 3 mg/l. Two short pulses of high suspended particle concentrations are centered at August 23 and August 27 where suspensates retrieved were



21 and 36 mg/l respectively. Suspensate concentrations generally range between 3 and 6 mg/l between and after these pulses.

In comparison with suspensate data obtained from various parts of Simpson Lagoon (Table II) the single tripod station concentrations show a much lower variability during the thirty day sampling period. In other words, between station variance in the lagoon is greater than within station variance.

#### Sediment Texture

Results of textural analysis and statistical grain size parameter calculations for Beaufort Sea, Simpson Lagoon, and PWB76 core sediment samples are listed in Tables IV, V and VI. Based on Folk and Ward (1957) empirical standards the Beaufort Sea sediments are generally very poorly sorted, can be either slightly negatively or positively skewed, and range between mesokurtic and platykurtic sandy clays and muds (Table IV). A few gravelly, sandy muds are listed also. The Simpson Lagoon sediments, however, are shown to be somewhat less poorly sorted than the Beaufort Sea sediments, very positively skewed, and generally contain leptokurtic to very leptokurtic sandy silts and some silty sands (Table V). The sediments from the coastal lagoon environment are clearly more coarsely textured (sandy) and better sorted, more positively skewed, and contrastingly leptokurtic in comparison to the Beaufort Sea sediments representing a continental shelf environment.

Table VI lists the statistical grain size parameters for the core sections obtained from Dr. Peter W. Barnes of the U.S. Geological Survey in Menlo Park, California. A visual representation of this data is also

TABLE IV

## STATISTICAL GRAIN SIZE PARAMETERS (AFTER FOLK &amp; WARD, 1957) OF BEAUFORT SEA CONTINENTAL SHELF AND SLOPE SEDIMENTS

For Location of Stations Refer to Naidu (1978)

Sample No.	Depth in Meters	% Gravel	% Sand	% Silt	% Clay	Median Size Md	Mean Size $M_z$	Sorting $\delta I$	Skewness $S_{KI}$	Kurtosis $K_G$
GLA77-5	3593	0	3.76	30.39	65.85	9.07	8.76	2.84	-0.13	0.92
GLA77-6	3566	0	0	18.12	81.88	9.78	9.85	2.01	0.01	1.00
GLA77-8	2048	0	1.10	23.08	75.82	9.33	9.22	2.02	-0.07	1.38
GLA77-9	640	0	1.68	26.91	71.41	9.24	9.31	2.22	0.03	0.98
GLA77-10	678	0	0.81	43.39	55.78	8.62	8.74	2.63	0.06	0.82
GLA77-11	406	0	1.15	33.47	65.38	9.21	9.14	2.49	-0.05	0.87
GLA77-12	22	0	33.91	34.99	31.10	6.06	6.44	3.49	0.19	0.69
GLA77-14	35	0	53.07	18.16	28.78	2.93	4.80	3.85	0.63	0.72
GLA77-15	54	0	12.95	22.23	64.82	9.33	8.83	3.36	-0.30	1.25
GLA77-16	118	0	11.22	47.17	41.61	7.33	7.53	3.34	0.03	0.89
GLA77-17	51	0.19	13.71	25.07	61.03	8.99	8.34	3.41	-0.26	0.91
GLA77-18	80	2.67	49.08	17.94	30.31	3.31	5.15	3.74	0.62	0.70
GLA77-19	146	0	11.75	33.19	55.06	8.41	8.13	3.50	-0.18	1.01
GLA77-20	57	3.33	51.42	16.84	28.42	2.85	4.01	4.88	0.29	0.70
GLA77-21	41	0	1.08	34.53	64.39	9.43	9.15	2.58	-0.12	0.78
GLA77-22	32	0	19.69	32.92	47.40	7.68	7.24	3.58	-0.14	0.86
GLA77-23	109	0	18.87	30.65	50.49	8.04	7.30	4.11	-0.28	1.13
GLA77-24	51	10.85	42.49	18.50	28.17	3.27	3.70	4.98	0.09	0.68
GLA77-25	38	3.21	31.40	28.13	37.25	6.32	6.52	4.27	-0.02	0.83
GLA77-26	20	0	51.22	28.38	20.41	3.83	4.67	3.62	0.36	0.85
GLA77-27	54	0	44.46	19.93	35.61	5.65	5.99	4.13	0.09	0.74
GLA77-28	101	0	31.15	27.10	41.75	7.10	6.85	3.60	-0.03	0.68
GLA77-29	521	0	2.07	28.51	69.42	9.19	9.34	2.27	0.06	0.92
GLA77-30	1829	0	1.76	31.05	67.05	8.86	9.12	1.80	0.23	1.11
GLA77-31	28	0.50	23.99	41.34	34.17	6.49	6.86	3.35	0.16	0.77
GLA77-32	42	5.86	40.78	21.64	31.73	5.07	5.56	4.31	0.11	0.81
GLA77-33	66	19.25	41.20	17.87	21.67	2.53	3.38	4.91	0.24	0.79
GLA77-34	1646	0	1.72	38.66	59.63	8.70	8.80	2.44	0.02	1.01
GLA77-35	30	0	11.51	36.72	51.78	8.16	8.19	3.45	-0.10	1.02
GLA77-40	24	0	5.20	55.11	39.68	7.30	7.74	2.96	0.21	0.71
GLA77-42		0	8.76	38.84	52.40	8.17	8.17	3.11	-0.01	0.78

TABLE V

STATISTICAL GRAIN SIZE PARAMETERS (AFTER FOLK & WARD, 1957)  
OF THE SIMPSON LAGOON BOTTOM SEDIMENTS

Data revised since March 1978. Refer to Naidu (1978)  
for sample locations

Sample #	Depth (m)	% Gravel	% Sand	% Silt	% Clay	Md	M <sub>z</sub>	σ <sub>I</sub>	Sk <sub>I</sub>	K <sub>G</sub>
SL877- 1A	1.5	-	80.6	14.5	4.9	2.3	2.8	1.6	.70	3.6
- 1B	1.5	-	88.9	6.6	4.4	2.2	2.3	1.2	.39	4.6
- 1C	1.5	-	86.9	8.2	4.9	2.3	2.3	1.2	.41	4.7
- 1D	1.5	-	83.4	10.2	6.5	2.3	2.75	1.8	.69	5.6
- 1E	1.5	-	82.5	12.0	5.5	2.3	2.75	1.7	.67	4.6
- 2	1.8	-	93.0	3.3	3.7	1.8	1.7	1.2	.28	3.3
3	2.6	-	35.0	45.2	19.8	4.6	5.3	3.2	.32	0.86
4	2.1	-	19.4	56.5	24.1	5.5	6.1	2.9	.30	1.1
5A	1.8	-	35.2	52.8	12.0	4.3	4.8	2.3	.46	1.4
5B	1.8	-	48.9	37.1	14.0	4.0	4.7	2.5	.51	1.4
5C	1.8	-	44.4	42.0	13.6	4.1	4.85	2.4	.54	1.3
5D	1.8	-	48.9	38.6	12.5	4.0	4.7	2.4	.52	1.5
6	2.0	-	31.8	51.0	17.2	4.6	5.2	2.8	.33	1.2
7	0.9	13.3	78.9	3.7	4.1	2.1	1.5	2.3	-.44	2.2
8	0.3	3.2	71.0	17.3	8.5	2.65	2.8	2.8	.18	2.25
9	1.5	-	24.7	54.9	20.4	5.5	5.9	2.9	.27	1.2
11	2.1	-	15.7	65.9	18.4	4.8	5.8	2.65	.52	1.5
12	2.1	-	30.6	52.6	16.8	4.3	5.3	2.7	.52	1.6
13	2.4	-	7.7	79.5	12.8	4.8	5.5	2.0	.58	1.9
14	2.3	-	38.3	47.6	14.1	4.4	4.8	2.7	.30	1.2
15	1.8	2.2	72.7	13.0	12.1	2.3	3.5	3.1	.61	1.9
17	0.6	8.7	67.0	15.0	9.2	2.1	2.6	3.4	.22	2.9
18	0.5	-	54.7	31.0	14.3	3.4	4.5	2.7	.65	1.2
19	3.2	-	67.4	23.4	9.2	2.7	3.5	2.0	.81	1.7
20	2.6	-	85.2	9.0	5.8	2.5	2.7	1.2	.71	6.8
21A	2.9	-	17.0	59.6	23.4	5.6	6.3	2.8	.36	1.1
21B	2.9	-	16.5	61.9	21.6	5.6	6.1	2.7	.32	1.2
21C	2.9	-	22.1	59.5	18.4	5.1	5.6	2.6	.31	1.2
21D	2.9	-	18.0	62.6	19.4	5.3	5.9	2.7	.33	1.3
22	2.4	-	11.0	75.4	13.6	4.8	5.5	2.0	.60	1.6
23	2.4	-	24.8	61.3	13.9	5.0	5.05	2.7	.12	1.8
24	1.5	-	71.8	19.0	9.2	2.55	3.4	2.7	.53	1.7
25A	2.6	-	63.8	26.1	10.1	2.4	3.5	2.6	.71	1.05
25B	2.6	-	66.8	24.8	8.4	2.3	3.4	2.65	.72	1.2
25C	2.6	-	61.9	27.1	11.0	2.6	3.7	2.7	.67	1.0

TABLE V  
CONTINUED

Sample #	Depth (m)	% Gravel	% Sand	% Silt	% Clay	Md	M <sub>z</sub>	σ <sub>I</sub>	Sk <sub>I</sub>	K <sub>G</sub>
SL877-26	2.9	-	20.3	66.7	13.0	4.2	5.2	2.1	.75	1.5
27	3.0	-	19.8	64.3	15.9	4.4	5.3	2.4	.62	1.4
28	2.7	-	14.3	64.9	20.8	5.2	6.0	2.5	.52	1.1
29	2.4	-	22.3	57.3	20.4	5.1	5.7	3.0	.31	1.2
30	1.1	-	78.2	18.1	3.7	2.0	2.5	1.65	.47	1.3
31	2.6	-	10.5	64.2	25.3	6.0	6.6	2.7	.32	1.1
32A	2.3	-	32.6	48.3	19.1	5.2	5.3	3.0	.16	0.84
32B	2.3	-	16.6	58.9	24.5	6.45	6.4	2.8	.02	1.2
32C	2.3	-	26.2	53.6	20.2	5.6	5.6	3.05	.11	0.96
32D	2.3	-	33.6	48.5	17.9	5.3	5.3	3.0	.12	0.83
33	2.1	-	49.2	34.0	16.8	4.3	4.8	3.0	.34	0.83
34	1.5	-	98.2	0.75	1.1	2.0	2.0	.61	.13	1.0
35	2.0	-	44.2	39.4	16.4	4.5	5.1	2.75	.41	0.98
36	2.1	-	39.4	44.0	16.6	4.7	5.05	2.8	.29	0.85
37	2.3	-	37.7	47.6	14.7	4.5	4.9	2.7	.30	1.0
38	2.3	-	26.2	53.8	20.0	5.0	5.4	3.1	.22	1.1
39	2.0	-	35.5	43.0	21.5	4.8	5.2	3.5	.18	0.90
40	1.5	-	69.2	17.3	13.5	2.5	3.7	2.9	.64	1.8
UG-1	0.8	-	56.4	28.5	15.1	3.4	4.4	3.0	.55	1.5

TABLE VI

RESULTS OF GRAIN SIZE ANALYSIS ON SEDIMENT CORE SAMPLES  
COLLECTED FROM THE CONTINENTAL SHELF OF THE BEAUFORT SEA, ALASKA

For Core Locations Refer to Table II in Naidu (1978), and Figure 3

Core Interval	% Gravel	% Sand	% Silt	% Clay	M <sub>d</sub>	M <sub>z</sub>	$\sigma_I$	Sk <sub>I</sub>	K <sub>G</sub>
Core # PWB 76-1									
0-10	0.0	7.06	72.10	20.84	6.19	6.66	2.57	0.28	1.97
10-20	0.0	2.69	69.89	27.42	6.65	7.17	2.34	0.43	1.35
20-30	0.0	3.02	77.38	19.59	5.90	6.32	2.29	0.43	1.38
30-40	0.0	6.46	72.49	21.06	6.02	6.56	2.34	0.42	1.56
40-50	0.0	6.19	73.81	20.00	5.74	6.37	2.26	0.48	1.53
50-60	0.0	1.76	71.51	26.73	6.57	7.21	2.16	0.55	1.32
60-70	0.0	1.85	73.49	24.66	6.54	7.06	2.11	0.50	1.44
70-80	0.0	1.18	76.62	22.20	6.20	6.84	2.11	0.59	1.44
80-90	0.0	6.81	72.33	20.86	6.02	6.40	2.43	0.35	1.36
90-100	0.0	2.55	79.12	18.32	5.68	6.21	2.24	0.51	1.42
100-107	0.0	2.26	76.68	21.06	5.95	6.72	2.23	0.63	1.47

TABLE VI  
CONTINUED

Core Interval	% Gravel	% Sand	% Silt	% Clay	Md	M <sub>Z</sub>	$\sigma_I$	Sk <sub>I</sub>	K <sub>G</sub>
Core # PWB 76-13									
0-10	0.0	67.01	13.81	19.18	3.11	4.89	3.01	0.90	1.09
10-20	0.0	79.30	9.91	10.71	2.96	3.94	2.25	0.90	5.28
20-30	99.81	0.19	0.0	0.0	-2.92	-2.81	0.86	0.18	0.73
30-40	0.0	5.44	36.69	57.87	8.63	9.11	(only mean could be computed)		
40-50	0.0	20.65	39.99	39.96	7.08	7.40	3.80	0.17	0.91
50-60	0.0	53.54	20.57	25.89	3.49	5.38	3.27	0.84	0.81
Core # PWB 76-14									
0-10	0.0	54.28	20.22	25.50	3.56	5.39	3.21	0.83	0.82
10-20	0.0	12.41	46.14	41.45	7.50	7.91	3.33	0.16	1.12
20-30	0.0	3.08	48.76	48.16	7.90	8.46	2.99	0.26	1.01
30-40	0.0	0.98	50.01	49.01	7.93	8.88	(only mean could be computed)		
40-50	0.0	1.02	44.34	54.64	8.29	9.08	(only mean could be computed)		
50-60	0.0	1.55	60.71	37.73	7.31	7.61	2.55	0.26	1.08
60-70	0.0	0.50	47.33	52.17	8.12	8.81	(only mean could be computed)		

TABLE VI

CONTINUED

Core Interval	% Gravel	% Sand	% Silt	% Clay	M <sub>d</sub>	M <sub>z</sub>	$\sigma_I$	Sk <sub>I</sub>	K <sub>G</sub>
Core # PWB 76-16									
0-10	0.0	11.33	55.56	33.10	6.42	7.08	3.13	0.34	0.89
10-20	0.0	11.78	56.56	31.66	6.27	7.00	3.01	0.38	0.95
20-30	0.0	5.39	51.51	43.46	7.53	8.15	(only mean could be computed)		
30-40	0.0	11.28	49.06	39.66	7.34	7.73	3.31	0.18	0.83
40-50	0.0	11.26	51.56	37.08	6.91	7.40	3.14	0.24	0.89
50-60	0.0	30.74	43.14	26.12	5.60	6.11	3.14	0.33	0.86
60-70	0.0	9.89	52.93	37.17	6.97	7.45	3.10	0.23	0.92
70-80	0.0	10.82	54.00	35.18	6.94	7.41	3.04	0.23	1.07
80-90	0.0	9.98	48.78	41.24	7.38	7.64	3.15	0.14	0.94
90-100	0.0	21.18	45.01	33.81	6.61	7.13	3.50	0.24	0.89
100-103	0.0	16.20	51.47	32.33	6.51	7.04	3.13	0.28	0.92

TABLE VI  
CONTINUED

Core Interval	% Gravel	% Sand	% Silt	% Clay	Md	M <sub>z</sub>	$\sigma_I$	Sk <sub>I</sub>	K <sub>G</sub>
Core # PWB 76-18									
0-10	0.0	21.92	55.48	22.60	6.03	6.11	2.93	0.15	1.25
10-20	0.0	58.26	30.78	10.97	3.54	4.44	2.16	0.76	1.20
20-30	0.0	15.24	64.78	19.98	5.76	6.17	2.51	0.37	1.26
30-40	0.0	34.59	43.68	21.73	5.97	6.03	2.93	0.17	0.94
40-50	0.0	41.19	40.91	17.90	4.35	5.38	2.69	0.64	1.09
50-60	0.0	24.46	57.44	18.10	5.34	5.73	2.65	0.34	1.30
60-70	0.0	5.86	69.07	25.07	6.24	6.79	2.54	0.38	1.27
70-80	0.0	15.01	63.06	21.93	5.82	6.31	2.75	0.30	1.47
80-90	0.0	2.05	62.37	35.58	7.09	7.82	2.39	0.47	1.08
90-100	0.0	7.71	56.79	35.50	6.94	7.57	3.02	0.29	0.98
100-110	0.0	9.15	64.53	26.32	6.14	6.77	2.72	0.39	1.14
110-120	0.0	11.63	62.80	25.57	6.17	6.58	2.69	0.36	1.08
120-130	0.0	29.90	56.86	13.25	4.43	5.09	2.20	0.62	1.41
130-140	0.0	15.27	65.16	19.58	5.10	5.98	2.47	0.59	1.25
140-150	0.0	5.05	62.61	32.33	6.92	7.60	2.58	0.37	1.25
150-160	0.0	5.59	65.27	29.14	6.70	7.37	2.55	0.38	1.47
160-170	0.0	9.00	62.69	28.31	6.64	7.27	2.57	0.35	1.59
170-180	0.0	6.83	65.96	27.20	6.53	7.12	2.56	0.37	1.39
180-190	0.0	3.44	67.85	28.72	6.65	7.43	2.28	0.54	1.28



TABLE VI  
CONTINUED

Core Interval	% Gravel	% Sand	% Silt	% Clay	Md	M <sub>z</sub>	$\sigma_I$	Sk <sub>I</sub>	K <sub>G</sub>
Core # PWB 76-19									
0-10	0.0	68.00	22.46	9.54	3.14	4.07	2.31	0.78	1.55
10-20	0.0	87.89	7.20	4.91	2.99	3.09	1.09	0.56	3.74
20-30	0.0	82.39	11.53	6.08	2.98	3.22	1.46	0.67	3.68
30-40	0.0	62.25	28.05	9.70	3.54	4.34	2.15	0.72	1.75
40-50	0.0	31.84	46.37	21.79	5.59	5.82	2.95	0.24	0.97
50-60	0.0	60.67	31.79	7.54	3.60	3.92	1.56	0.66	2.93
60-70	0.0	56.02	34.61	9.37	3.68	4.02	1.83	0.59	2.38
70-80	0.0	53.78	36.84	9.38	3.68	4.22	1.96	0.67	2.26
80-90	0.0	8.63	74.39	16.97	5.68	6.11	2.24	0.41	1.72
90-100	0.0	64.63	25.47	9.90	3.46	3.83	2.01	0.58	2.94
100-105	0.0	72.09	21.64	6.27	3.37	3.53	1.42	0.64	3.27

TABLE VI

CONTINUED

Core Interval	% Gravel	% Sand	% Silt	% Clay	Md	M <sub>z</sub>	$\sigma_I$	Sk <sub>I</sub>	K <sub>G</sub>
Core # PWB 76-20									
0-5	0.0	68.11	24.26	7.63	3.50	3.80	1.58	0.64	2.93
5-10	0.0	54.69	38.45	6.86	3.79	3.86	1.37	0.45	2.57
10-15	0.0	55.49	37.20	7.31	3.82	3.98	1.58	0.55	3.22
15-20	0.0	16.42	68.12	15.46	4.74	5.53	2.31	0.67	1.65
20-25	0.0	41.54	44.99	13.47	4.20	4.98	2.34	0.68	1.72
25-30	0.0	10.91	69.89	19.21	4.95	6.01	2.44	0.67	1.39
30-35	0.0	16.97	64.15	18.88	5.02	5.90	2.60	0.58	1.44
35-40	0.0	47.24	39.66	13.11	4.12	4.85	2.33	0.63	1.47
40-45	0.0	41.85	43.53	14.62	4.17	5.04	2.46	0.66	1.35
45-50	0.0	25.09	57.54	17.37	4.88	5.60	2.63	0.53	1.93
50-55	0.0	24.36	57.50	18.14	5.04	5.74	2.61	0.50	1.31
55-60	0.0	11.70	72.97	15.33	5.03	5.68	2.19	0.58	2.21
60-65	0.0	61.85	28.79	9.37	3.60	4.13	1.91	0.72	2.90
65-70	0.0	27.20	49.66	23.14	5.65	6.32	3.01	0.40	1.04
70-75	0.0	39.55	41.46	18.99	4.50	5.44	2.81	0.59	1.08
75-80	0.0	49.95	36.63	13.43	4.00	4.83	2.32	0.69	1.57
80-85	0.0	36.68	49.80	13.52	4.16	5.04	2.27	0.75	1.80
85-90	0.0	19.33	65.63	15.04	4.31	5.31	2.33	0.78	1.73
90-95	0.0	31.06	56.83	12.10	4.12	4.79	2.17	0.69	2.39
95-100	0.0	21.13	58.64	20.23	5.04	5.96	2.87	0.53	1.24
100-105	0.0	22.55	37.37	20.08	5.45	5.86	2.83	0.36	1.26
105-110	0.0	20.17	60.76	19.07	5.32	5.88	2.68	0.44	1.31
110-115	0.0	32.19	51.30	16.51	4.38	5.30	2.57	0.64	1.34
115-120	0.0	31.40	57.63	10.97	4.37	4.68	2.00	0.49	2.35
120-125	0.0	44.14	45.59	10.27	4.10	4.34	1.89	0.52	3.28

TABLE VI  
CONTINUED

Core Interval	% Gravel	% Sand	% Silt	% Clay	Md	M <sub>z</sub>	$\sigma_I$	Sk <sub>I</sub>	K <sub>G</sub>
Core # PWB 76-23									
0-10	0.0	28.14	51.46	20.13	5.23	5.83	2.85	0.42	1.07
10-20	0.0	20.16	69.03	10.81	4.77	5.12	1.84	0.42	1.80
20-30	0.0	15.82	58.85	25.33	6.08	6.63	2.85	0.33	1.14
30-40	0.0	50.49	36.75	12.77	3.99	4.75	2.32	0.66	2.07
40-50	0.0	14.83	62.88	22.29	5.69	6.47	2.76	0.46	1.31
50-60	Sample not available								
60-70	0.0	24.65	57.78	17.57	4.83	5.59	2.51	0.54	1.23
70-80	0.0	29.11	47.72	23.17	5.56	6.14	2.91	0.39	0.98
80-90	0.0	53.52	35.80	10.67	3.85	4.32	2.00	0.63	2.01
90-100	0.0	45.53	23.66	30.91	4.15	6.39	3.72	0.78	0.60
100-110	0.0	12.88	60.76	26.36	6.46	7.04	2.89	0.31	1.35
110-120	0.0	4.52	75.73	19.76	5.72	6.34	2.25	0.51	1.25
120-130	0.0	24.02	55.35	20.63	4.74	5.60	2.89	0.50	1.45
130-140	0.0	19.51	60.90	19.59	6.52	6.43	3.18	0.06	1.96
140-150	0.0	24.57	45.58	29.86	6.39	6.79	3.59	0.19	0.89

included in Figures 4a and 4b. Core #1 is from Prudhoe Bay (Fig. 3) and from Table VI and Figure 4a one can see little variation in texture with depth. The sediments in core #1 can be described as very poorly sorted, positively skewed, and leptokurtic silt and clayey silt. The cores numbered 13, 14, 16, 18, 19 and 20 represent a linear sequence running perpendicular to the coastline and directly out in front of the Colville River delta (Fig. 3). Core #13 is at a 19 m depth and furthest from the delta whereas core #20 is taken from a 1.5 m water depth and located nearest to the Colville River mouth. By studying Table VI and Figures 4a and 4b one can see a general seaward trend away from the Colville delta of increasing mud content and decrease sand content in the cores. This trend continues away from the delta through core #14. In addition, cores #14 and #18 show a clear decrease in coarseness with depth in the core. However, core #16 shows no such coarsening upward sequence.

In contrast to the lateral fining trend away from the Colville delta source is the lithology of core #13. This most seawardly located core has a rapid reversal of fine to coarse texture from one depth interval to the next and a gravel lens is located in one section of it.

Currently, we are compiling textural data for map plotting by the University of Alaska Honeywell 66/40 computer. Results of these plot analyses were not available for inclusion in this report. These maps will show areal variations in the Beaufort Sea of such textural parameters as % sand, % silt, % clay, mean sediment size, degree of sorting, skewness and kurtosis, and will include all grain size distribution data available to date.

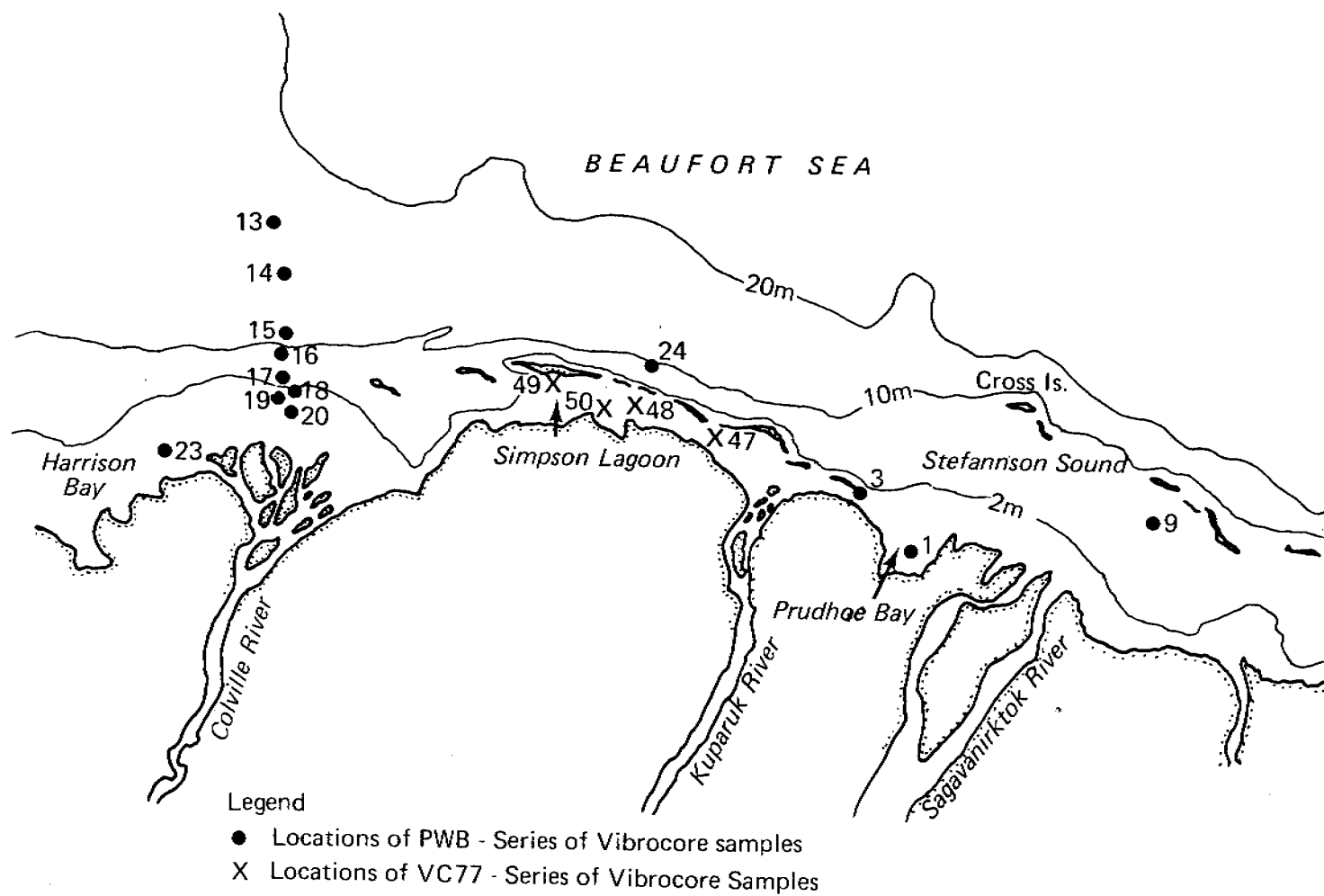


Figure 3. Locations of vibrocore sediment samples that have been collected by Drs. P. W. Barnes and E. Reimtz of the U.S. Geological Survey in 1976 and 1977. Splits of core samples from locations depicted by heavy dots have been provided to us for study.

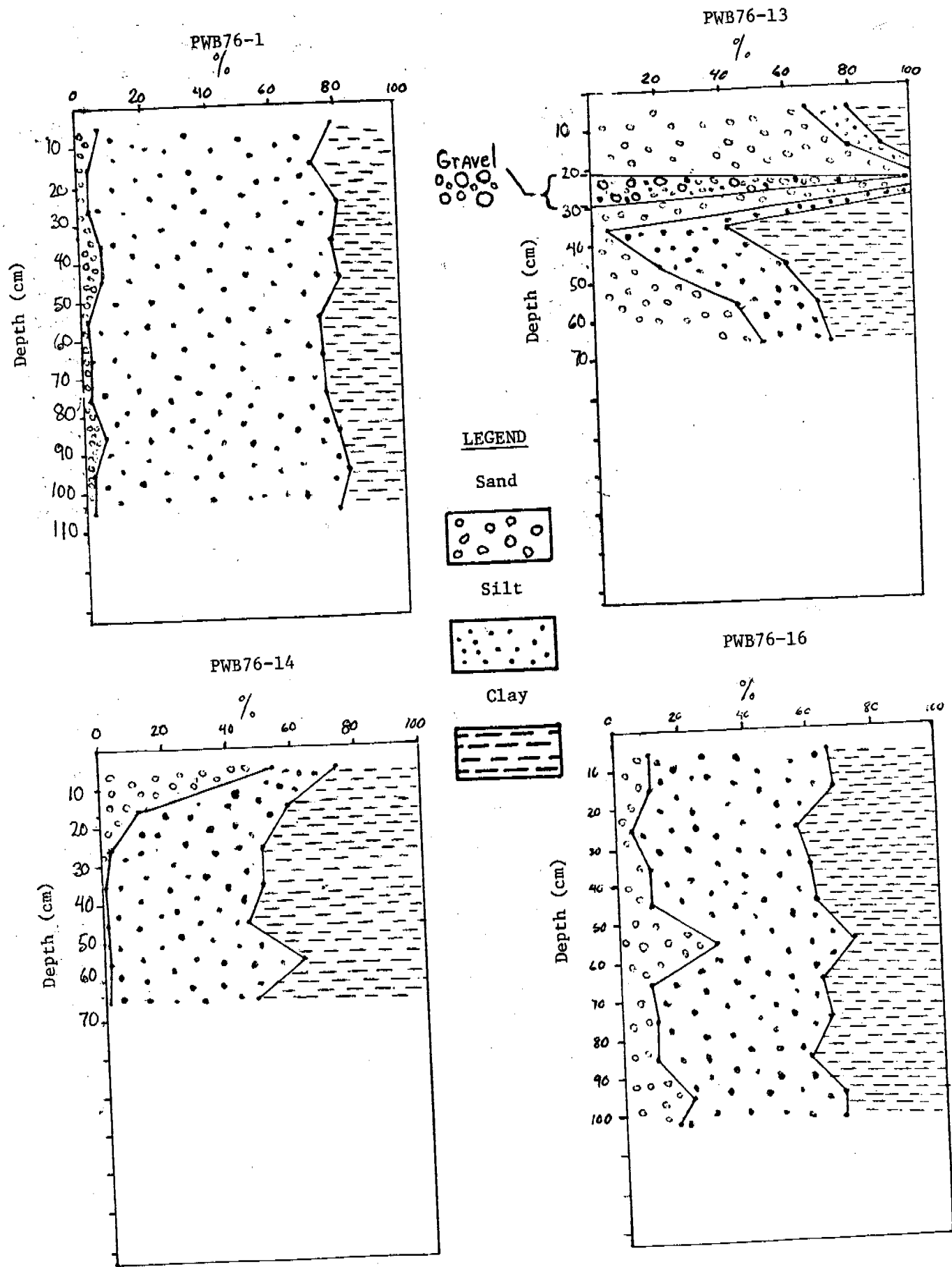


Figure 4a. Variation of sediment texture with depth of PWB76 core samples.

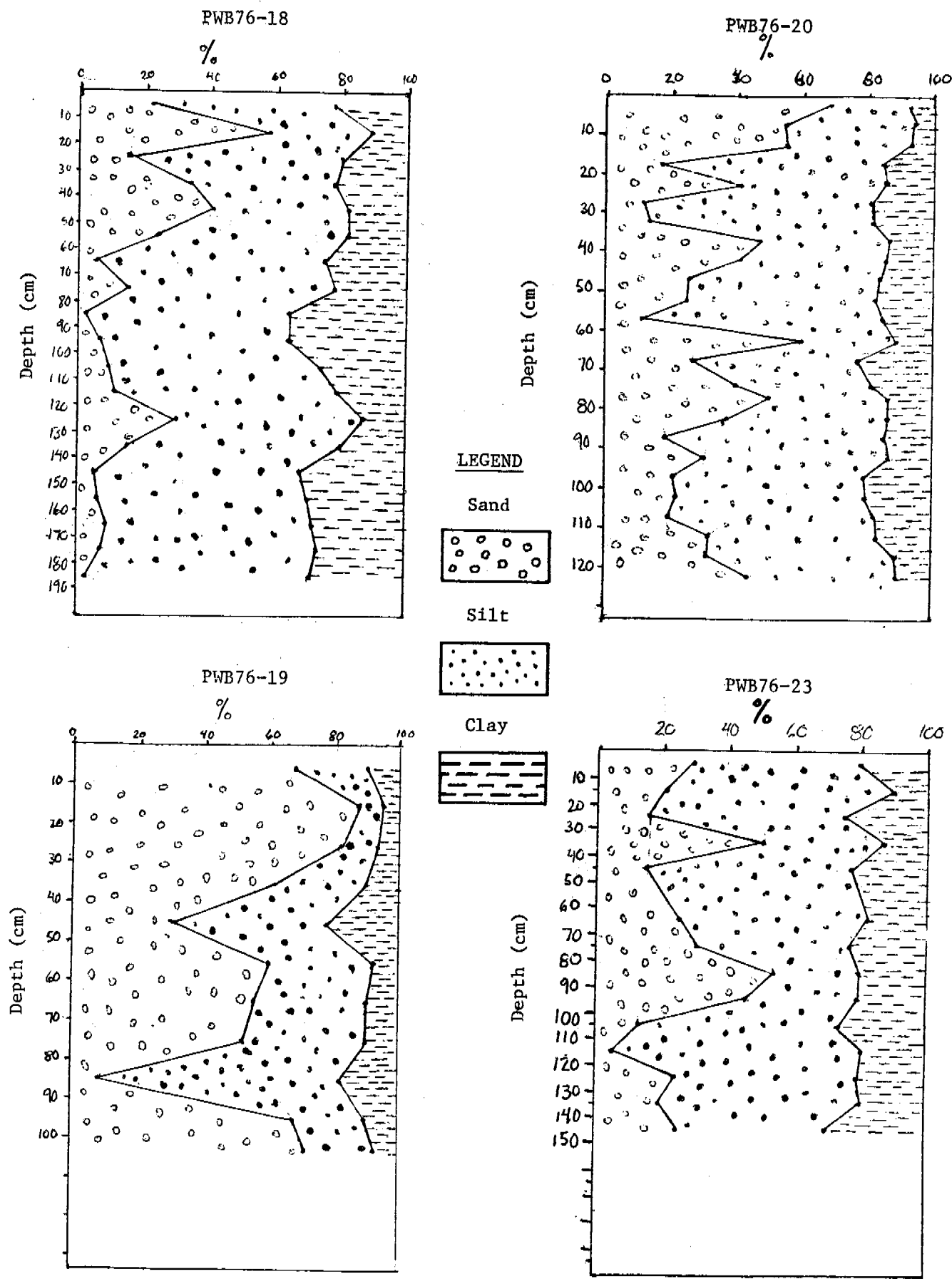


Figure 4b. Variation of sediment texture with depth of PWB76 core samples.

## Possible Sources of Some Arctic Barrier Island Boulder Samples

Table VII shows the lithology of the boulders collected from the lagoonward beaches of Bodfish and Pingok islands on the arctic coast of northern Alaska and inferred sources of the boulders. The data show that there is a possible northern Alaskan source for most of these boulders while a probable north Alaskan source for the rest.

## Clay Mineralogy

Clay mineral results for the less than 2  $\mu\text{m}$  fraction of Beaufort Sea sediment samples and three arctic rivers are listed in Table VIII. The predominate mineral is illite (45-70%). These data were included in the compilation of available clay mineral data for the Beaufort Sea from the last decade. The result of this data synthesis is the distributional pattern of the expandable component and the kaolinite-chlorite ratio in surficial sediments of the Beaufort Sea exhibited in Figures 5a and 5b, respectively. Both figures distinctly show a westward extension along the inner shelf and the coast, in form of a tongue of specific clay minerals. In Figure 5a, the high expandable percentages from the Colville River are seen to move westward from the delta. In Figure 5b, high kaolinite relative to chlorite values seem to extend westward from the Kuparuk and Shaviovik river mouths. Figure 5a also shows that there is a distinct longitudinal patch as well as isolated patches of relatively high expandable clay mineral component in the continental shelf between Barter Island and the Demarcation Point. Figure 5b shows that the distributional pattern of kaolinite/chlorite ratios is quite patchy across the middle and outer continental shelves of the Beaufort Sea.



TABLE VII

PETROGRAPHIC COMPOSITIONS AND POSSIBLE SOURCES  
OF BOULDER SAMPLES COLLECTED FROM THE LAGOONWARD BEACHES  
OF THE BODFISH AND PINGOK ISLANDS, NORTH ARCTIC ALASKA

Sample	Locality	Lithology	Source From Known Rocks Inferred in Northern Alaska		
			Improbable	Possible	Probable
78-9-12-1-A	Bodfish Is.	Metamorphosed granodiorite		X	
78-9-12-1-B	Bodfish Is.	Quartz monzonite		X	?
78-9-12-1-C	Bodfish Is.	Diabase		X	?
78-9-12-1-D	Bodfish Is.	Lithic greywacke			X
78-9-12-1-E	Bodfish Is.	Feldspathic greywacke			X
78-9-12-1-F	Bodfish Is.	Diabase		X	?
78-9-12-1-G	Bodfish Is.	Quartz monzonite		X	?
78-9-12-1-H	Bodfish Is.	Diabase		X	?
78-9-12-1-I	Bodfish Is.	Metamorphosed granodiorite		X	?
78-9-12-1-J	Bodfish Is.	Quartz monzonite		X	?
78-9-12-1-K	Bodfish Is.	Quartz monzonite		X	?
78-9-12-1-L	Bodfish Is.	Quartz		X	?
78-9-12-1-M	Bodfish Is.	Diabase		X	?
78-9-12-1-N	Bodfish Is.	Fine grained diabase	?	X	
78-9-12-1-O	Bodfish Is.	Fine grained diabase		X	
78-9-12-1-P	Bodfish Is.	Diabase		X	?
78-9-12-2-A	Pingok Is. (East End)	Metamorphosed protoclastic quartz monzonite		X	?
78-9-12-2-B	Pingok Is. (East End)	Metamorphosed granodiorite		X	?

TABLE VII

CONTINUED

Sample	Locality	Lithology	Source From Known Rocks Inferred in Northern Alaska		
			Improbable	Possible	Probable
78-9-12-2-C	Pingok Is. (East End)	Diorite	?	X	
78-9-12-2-D	Pingok Is. (East End)	Diabase			X
78-9-12-2-E	Pingok Is. (East End)	Arkosic arenite feldspathic greywacke			X
78-9-12-2-F	Pingok Is. (East End)	Lithic greywacke breccia			X
78-9-12-2-G	Pingok Is. (East End)	Lithic arenite			X
78-9-12-2-H	Pingok Is. (East End)	Lithic arenite			X
78-9-12-3-A	Pingok Is.	Metamorphosed quartz diorite	?	X	
78-9-12-3-B	Pingok Is.	Porphyritic quartz monzonite		X	
78-9-12-3-C	Pingok Is.	Lithic greywacke			X
78-9-12-3-D	Pingok Is.	Diabase		X	?
78-9-12-3-E	Pingok Is.	Basalt	?	X	
78-9-12-3-F	Pingok Is.	Lithic arenite			X
78-9-12-3-G	Pingok Is.	Lithic arenite			X
78-9-12-3-I	Pingok Is.	Basalt	?	X	
78-9-12-3-J	Pingok Is.	Porphyritic basalt	?	X	
78-9-12-3-K	Pingok Is.	Arkosic - lithic arenite			X
78-9-12-3-L	Pingok Is.	Lithic arenite			X
78-9-12-3-M	Pingok Is.	Diabase		X	?
78-9-12-3-N	Pingok Is.	Meta - diabase	?	X	
78-9-12-3-O	Pingok Is.	Metamorphosed quartz diorite	?	X	
78-9-12-3-P	Pingok Is.	Lithic arenite			X

TABLE VIII

WEIGHTED PEAK AREA PERCENTAGES (AFTER BISCAYE, 1965) OF CLAY  
MINERALS IN THE LESS THAN 2  $\mu$ m FRACTION OF THE BEAUFORT SEA  
AND SOME NORTH SLOPE RIVER SEDIMENTS

Refer to Naidu (1978) for Station Locations

Sample	Expandable	Illite	Kaolinite	Chlorite
GLA77-5	9	56	17	18
GLA77-6	10	56	21	23
GLA77-7	9	56	16	19
GLA77-8	6	61	14	19
GLA77-10	11	56	13	20
GLA77-14	22	49	15	14
GLA77-15	16	53	15	16
GLA77-16	8	62	14	16
GLA77-18	10	58	13	19
GLA77-19	13	55	13	19
GLA77-20	11	59	12	18
GLA77-22	19	53	12	16
GLA77-24	14	56	13	17
GLA77-25	14	53	15	18
GLA77-26	8	64	11	17
GLA77-27	15	57	13	15
GLA77-28	12	56	12	20
GLA77-30	8	59	15	18
GLA77-32	12	58	13	17
GLA77-33	8	60	13	19
Canning R. (1)	0	79	4	7
Shaviovik R.	tr	66	15	19
Ugnuravik R. (2)	0	66	11	23

tr = trace

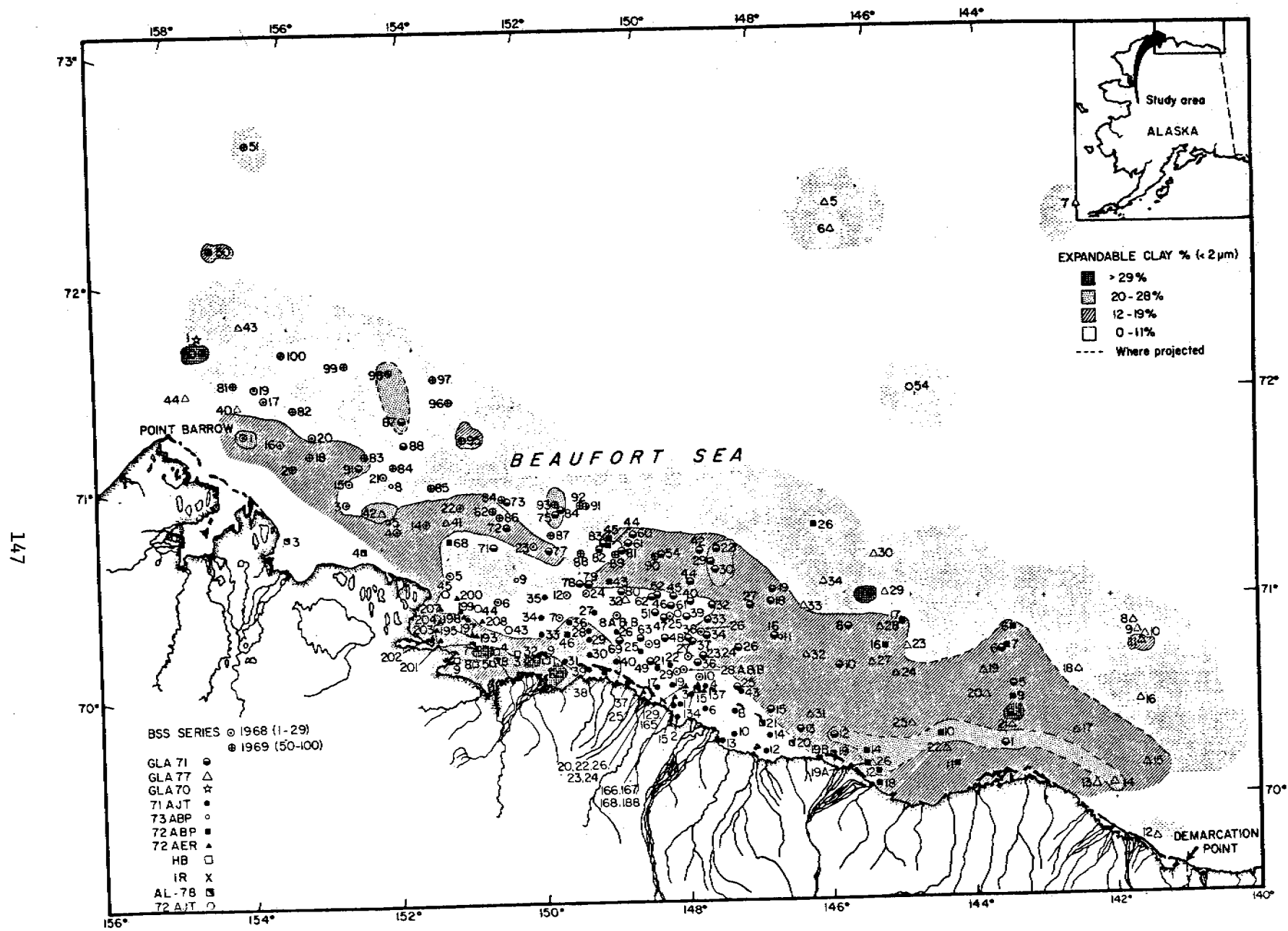


Figure 5a. Expandable clay mineral distribution in Beaufort Sea surface sediments.

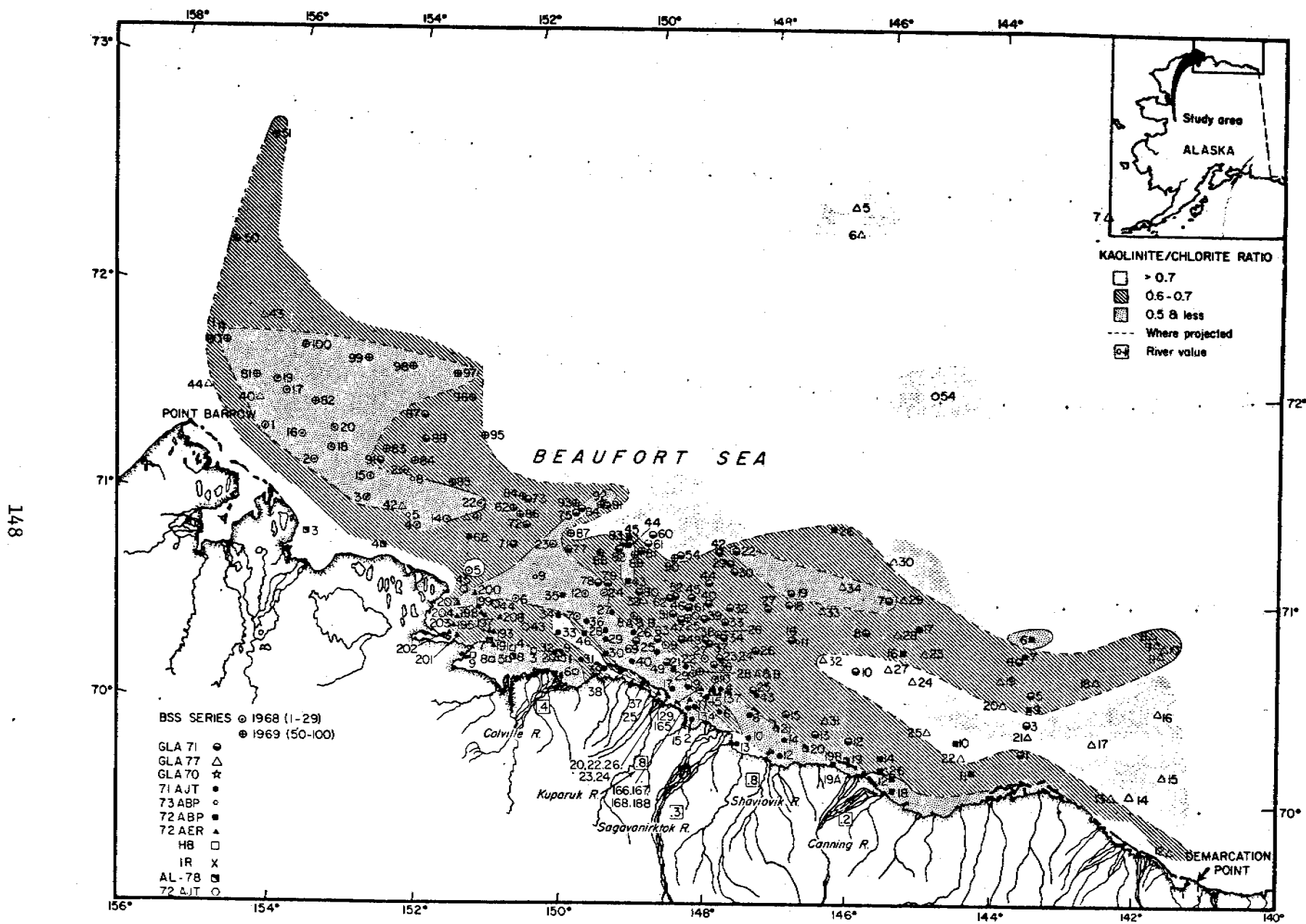


Figure 5b. Kaolinite/chlorite ratio distribution in Beaufort Sea surface sediment.

## Carbonate and Organic Carbon Contents in Sediments

Carbonate and organic carbon percentages in Beaufort Sea sediments are shown in Table IX. Carbonate ranges between 1 and 10% with an average of 4%. Organic carbon ranges between 0.2 and 1.3% and averages 0.7%. As can be seen in Table VII in Naidu (1978), both carbonate and organic carbon are less abundant on the Beaufort Sea continental shelf than in Simpson Lagoon. After plotting these parameters on the standard Beaufort Sea map we hope to have additional interpretations for the distributional pattern in organic carbon.

## Heavy Metal Chemistry of Sediments

Chemical information obtained since March, 1978 for the Beaufort Sea and Simpson Lagoon are shown in Tables X through XV. Table X lists the Mn concentrations in the interstitial waters extracted from some Beaufort Sea and Simpson Lagoon core sections. All the cores show a greater concentration of dissolved Mn below the first few centimeters of the core.

Tables XI and XII list the Fe, Mn, Zn, and Cu concentrations in acetic acid-hydroxylamine hydrochloride extractions of the sediment from the Beaufort Sea and Simpson Lagoon, respectively. Additionally, P concentrations are listed for the Simpson Lagoon data sediment extracts. In the Beaufort Sea average concentrations of metals are about double of those for Simpson Lagoon except for leachable Zn which is relatively more abundant in the lagoon. Also, in Table XI the contrast in extractable element concentrations between the continental shelf, slope and deep-sea sediments is quite apparent.

TABLE IX

CARBONATE AND ORGANIC CARBON WEIGHT PERCENTS OF NORTH ALASKAN CONTINENTAL SHELF AND CONTINENTAL SLOPE SEDIMENTS RETRIEVED IN AUGUST 1977  
(BEAUFORT SEA CRUISE OF USCGC *GLACIER*)

For Location of Stations Refer to Naidu (1978)

Sample No.	Depth in Meters	CO <sub>3</sub> <sup>=</sup>	Organic Carbon	% Sand
GLA-77-5	3593	1.77	0.78	6
GLA-77-6	3566	2.48	0.56	0
GLA-77-7	3566	2.97	0.58	0.08
GLA-77-8	2048	4.27	0.6	1.5
GLA-77-9	640	2.60	NA	2.6
GLA-77-10	678	4.51	0.93	1.2
GLA-77-11	406	3.65	1.06	1.9
GLA-77-12	22	7.32	0.75	42
GLA-77-14	35	6.36	0.71	63
GLA-77-15	54	4.36	0.7	22
GLA-77-16	118	8.05	0.67	15
GLA-77-17	51	4.52	NA	22
GLA-77-18	80	7.08	0.31	59
GLA-77-19	146	6.28	0.76	17
GLA-77-20	57	10.03	0.45	61
GLA-77-22	32	2.18	0.62	26
GLA-77-23	109	3.23	0.83	26
GLA-77-24	51	9.15	0.21	46
GLA-77-25	38	7.69	0.63	41
GLA-77-26	20	5.21	0.84	58
GLA-77-27	54	7.42	0.43	56
GLA-77-28	101	4.36	0.92	40
GLA-77-29	521	5.07	0.63	3.4
GLA-77-30	1829	1.22	NA	2.4
GLA-77-31	28	7.33	NA	30
GLA-77-32	42	8.32	NA	50
GLA-77-33	66	6.82	0.74	46
GLA-77-40	24	5.44	0.96	7.2
GLA-77-42		1.94	1.28	13

NA = Not analyzed

TABLE X

CONCENTRATIONS OF Mn IN THE INTERSTITIAL WATERS OF CONTINENTAL SHELF  
AND ADJACENT LAGOON SEDIMENTS IN THE BEAUFORT SEA

Refer to Naidu (1978) for Sample Locations of the shelf sediments

Station	Core Section (cm)	Mn (ppm)
Beaufort Sea Continental Shelf		
GLA77- 5(a)	0-15	0.83
	15-23	3.6
GLA77- 5(b)	0-15	0.48
	15-27	2.4
GLA77-6	0-13	0.37
	13-24	3.4
	24-34	3.2
GLA77-7	0-9	0.08
	9-18	0.15
	18-27	0.42
	27-36	0.42
GLA77-24	0-8	0.80
	8-17	1.4
GLA77-37	0-10	3.8
	10-20	4.5
Simpson Lagoon		
Between Oliktok Point and Spy Island	0-5	0.95
	5-10	1.76
	10-15	1.0
Between Milne Point and East Pingok Island	0-5	2.7
	5-13	3.4
	13-20	3.0
	20-26	3.6



TABLE XI

CONCENTRATIONS OF IRON, MANGANESE, ZINC AND COPPER IN ACETIC  
ACID-HYDROXYLAMINE HYDROCHLORIDE EXTRACTS (CHESTER & HUGHES, 1967)  
OF BEAUFORT SEA SEDIMENTS

Refer to Naidu (1978) for Stations Locations

Sample #	Depth (m)	Iron $10^4$ $\mu\text{g/g}$	Manganese $\mu\text{g/g}$	Zinc $\mu\text{g/g}$	Copper $\mu\text{g/g}$
GLA77- 5 <sub>1</sub>	3493	0.97	4400	32	22
GLA77- 5 <sub>2</sub>	3593	1.09	4500	34	24
GLA77- 5 <sub>3</sub>	3593	0.98	4550	33	22
GLA77- 7	3566	0.89	2800	31	20
GLA77- 8	2048	0.94	4950	30	15
GLA77-12	22	0.35	139	22	6
GLA77-15	54	0.50	440	25	10
GLA77-17	51	0.60	340	29	9
GLA77-18	80	0.36	515	16	5
GLA77-19	146	0.39	178	28	8
GLA77-22	32	0.41	160	21	7
GLA77-23	109	0.52	344	34	13
GLA77-24	51	0.34	378	14	5
GLA77-25	38	0.27	126	16	5
GLA77-26	20	0.30	119	15	5
GLA77-30	1829	0.85	13100	26	10
GLA77-31	28	0.36	148	19	6
GLA77-32	42	0.27	137	18	6
GLA77-40	24	0.79	309	28	8
GLA77-42	149	0.30	77	22	5
Averages of:					
Shelf (<65m) sediments		0.42	230	21	8
Slope (65-1000 m) sediments		0.36	515	16	5
Deep-Sea (>1000m) sediments		0.95	5717	31	19

TABLE XII

CONCENTRATIONS OF IRON, MANGANESE, ZINC, COPPER, AND PHOSPHORUS IN ACETIC  
ACID-HYDROXYLAMINE HYDROCHLORIDE EXTRACTS (CHESTER & HUGHES, 1967)  
FROM SIMPSON LAGOON SEDIMENTS

Refer to Naidu (1978) for Station Locations

Sample #	Iron $10^4$ $\mu\text{g/g}$	Manganese $\mu\text{g/g}$	Zinc $\mu\text{g/g}$	Copper $\mu\text{g/g}$	Phosphorus $\mu\text{g/g}$
SL877-1	0.11	56	11	Trace	465
2	0.14	94	8	1.1	232
3	0.34	250	32	3.2	454
4	0.60	364	37	5.2	664
5	0.27	180	28	4.5	406
6	0.27	210	39	3.3	376
8	0.12	113	23	1.2	487
9	0.31	360	31	5.2	387
11	0.27	120	44	2.7	532
13	0.41	326	68	4.0	487
14	0.33	228	33	3.3	461
15	0.18	136	37	6.6	399
17	0.16	116	25	6.0	410
18	0.32	55	38	2.4	520
19	0.15	53	16	3.7	382
21	0.43	181	30	3.7	465
22	0.42	159	26	3.7	387
24	0.11	60	20	3.5	454
25	0.27	86	26	2.3	410
27	0.34	158	50	2.6	476
28	0.69	105	21	3.2	941
29	0.35	135	67	4.8	476
30	0.08	49	8	1.4	299
31	0.34	163	30	3.4	487
32	0.24	212	29	4.3	299
33	0.24	212	24	2.6	343
37	0.29	96	40	1.7	476
38	0.27	79	24	4.2	387
40	0.06	61	21	3.8	200
Averages	0.28	152	31	3.4	440

TABLE XIII

CONCENTRATIONS ( $\mu\text{g/g}$ ) OF Fe, Mn, Zn, Cu, Ni, Cr, Co, AND V IN GROSS  
SEDIMENTS FROM THE CONTINENTAL SHELF, CONTINENTAL SLOPE,  
AND THE DEEP-SEA REGION OF THE BEAUFORT SEA

For Sample Locations Refer to Naidu (1978)

Station	Depth (m)	Fe $10^4 \mu\text{g/g}$	Mn	Zn	Cu	Ni	Cr	Co	V
Deep-Sea (>1000m)									
GLA77- 5	3593	4.00	4650	130	40	87	103	70	245
GLA77- 6	3566	4.48	3950	155	45	100	117	70	280
GLA77- 7	3566	3.99	3050	125	42	92	110	66	260
Deep-Sea Average	3575	4.16	3883	137	42	93	110	69	262
Continental Slope (66-1000m)									
GLA77-10	678	3.44	4400	105	25	77	96	52	203
GLA77-16	118	2.59	437	120	19	65	89	41	165
GLA77-18	80	2.32	797	90	20	42	66	26	127
GLA77-23	109	3.08	587	130	30	71	98	54	167
GLA77-42	149	3.02	392	110	18	62	90	42	167
Continental Slope Average	227	2.90	1322	111	22	63	88	43	166
Continental Shelf (<66m)									
GLA77-12	22	2.70	377	110	22	58	86	37	132
GLA77-15	54	3.34	682	130	31	78	98	50	185
GLA77-17	51	3.63	661	150	33	90	108	56	200
GLA77-20	57	3.00	732	108	19	55	70	35	140
GLA77-22	32	2.82	377	115	24	56	84	37	141
GLA77-31	28	2.60	382	115	21	49	80	33	140
GLA77-33	66	2.94	1017	115	30	56	74	34	125
Continental Shelf Average	44	3.00	604	120	26	63	86	40	152

TABLE XIV

CONCENTRATIONS OF ZINC, NICKEL, COBALT AND CHROMIUM IN GROSS SEDIMENTS  
FROM THE BAYS, LAGOONS AND SOUNDS OF THE COASTAL REGION  
OF THE BEAUFORT SEA (EXCLUDING SIMPSON LAGOON AREA).

Refer to Naidu, (1976) for Station Locations, Depths, and  
Other Physical and Chemical Data.

Sample	Zn µg/g	Ni µg/g	Co µg/g	Cr µg/g
HB-1	90	32	20	65
HB-2	85	47	29	100
HB-3	52	21	16	46
HB-4	105	39	22	78
HB-5	74	32	20	59
HB-6	81	29	18	48
HB-7	47	20	18	42
BS70-18	55	32	13	23
BS70-19	37	16	8	20
BS70-21	69	47	21	57
BS70-22	66	43	20	58
BSS-83	72	70	32	112
BSS-84	74	50	28	78
71AER-15	67	38	17	44
72AER-20	43	21	9	25
72AER-22	79	51	20	53
72AER-23	63	38	15	38
72AER-24	55	38	14	37
72AER-25	61	38	14	36
72AER-26	140	84	39	127
72AER-129	83	NA	NA	NA
71AJT-31	94	48	18	53
71AJT-32	43	35	14	30
71AJT-33	82	45	38	108
71AJT-35	90	54	21	56
71AJT-36	70	36	14	30
71AJT-37	107	49	19	45
71AJT-38	69	45	19	43
71AJT-39	106	44	19	49
71AJT-40	109	49	19	49
71AJT-43	100	56	24	58
72AER-29	NA	57	26	NA
71AJT-5	NA	NA	13	30
71AJT-16	NA	NA	20	46
71AJT-20	NA	NA	24	116

TABLE XIV

CONTINUED

Sample	Zn μg/g	Ni μg/g	Co μg/g	Cr μg/g
72AER-134	92	61	30	77
72AER-137	43	21	NA	NA
72AER-166	73	43	17	47
72AER-167	81	NA	NA	NA
72AER-168	82	51	20	52
71AJT-1	63	50	16	32
71AJT-2	90	61	18	54
71AJT-3	46	43	14	32
71AJT-4	53	35	17	36
71AJT-6	71	53	19	32
71AJT-8	70	42	18	42
71AJT-10	54	35	17	31
71AJT-12	109	53	19	50
71AJT-13	97	107	36	70
71AJT-14	89	133	43	88
71AJT-15	91	66	26	44
71AJT-17	128	160	50	115
71AJT-18	214	62	33	87
71AJT-19	64	90	23	43
71AJT-21	47	38	16	34
71AJT-22	71	108	20	42
71AJT-25	242	70	27	30
71AJT-26	30	29	11	21
71AJT-29	47	35	13	32
71AJT-30	55	36	15	34

TABLE XV

CONCENTRATIONS OF IRON, ZINC, COPPER, NICKEL, CHROMIUM, COBALT, MANGANESE, AND VANADIUM  
IN GROSS SEDIMENTS OF THE SIMPSON LAGOON

Refer to Naidu (1978) for Station Locations

Sample	Fe 10 <sup>4</sup> µg/g	Zn µg/g	Cu µg/g	Ni µg/g	Cr µg/g	Co µg/g	Mn µg/g	V µg/g
SL877- 2	0.70	30	9	17	21	9	157	40
SL877- 6	1.70	90	18	44	56	-	397	80
SL877-13	1.95	95	18	46	60	23	502	88
SL877-18	1.40	85	16	42	55	22	175	82
SL877-23	1.55	100	17	42	56	21	407	78
SL877-27	1.84	85	12	48	58	23	317	94
SL877-29	1.92	105	20	43	63	25	313	94
SL877-30	0.65	35	5	19	24	9	137	32
SL877-33	1.22	80	14	39	45	19	347	70
SL877-35	1.51	92	14	40	55	18	267	95
SL877-39	1.63	90	26	45	63	22	242	94
UG-1	1.22	70	13	33	46	15	227	62
Average	1.44	80	15	38	50	19	290	76

Tables XIII, XIV and XV show the total concentrations of Fe, Mn, Zn, Cu, Ni, Cr, Co, and V in Beaufort Sea and Simpson Lagoon sediments. Table XIII clearly shows that the deep-sea sediments are relatively enriched in all elements analyzed as compared to continental shelf deposits. No obvious difference in total elemental abundance is discernable between the continental shelf and slope sediments, however.

In Table XIV are supplementary data on Beaufort Sea coastal sediment samples collected in years previous to 1977. Additional information about these samples is contained in Naidu (1976). The Simpson Lagoon total sediment chemistry is represented in Table XV. In comparing the data from the three environmental regimes represented in the three tables the following generalizations are updated: copper is the least abundant of the metals studied in both Simpson Lagoon and the Beaufort Sea. Zinc and V form an intermediate concentration group between the major constituents of Fe and Mn and the trace elements Cu, Ni, Co, and Cr. For Simpson Lagoon Zn and V have similar concentrations, averaging about 80  $\mu\text{m/g}$ . For the Beaufort Sea V is significantly greater than Zn at all depths. Concentrations of most elements increase from the coastal lagoon environment through the shelf and out into the deep-sea. The greatest increase occurs for Mn which increases from 290  $\mu\text{g/g}$  in the lagoon and shelf sediments to 3800  $\mu\text{g/g}$  in the deep-sea sediments. For the trace elements the order of increasing concentration is  $\text{Cu} < \text{Co} < \text{Ni} < \text{Cr}$ .

These generalizations are not as accurate for the sediments in Table XIV. These samples were taken from several sub-environments along the coast of the Beaufort Sea which should each be treated separately. In the same manner as the textural and clay mineralogical data a synthesis

of the chemical data will be represented by a map of the Beaufort Sea for each element studied. The regional distribution of the elements will be better understood with the completion of these maps.

#### Lithogenous versus Nonlithogenous Fractions of Heavy Metals in Sediments

Table XVI compares the lithogenous and nonlithogenous portions of Fe, Mn, Zn, and Cu in the Simpson Lagoon and Beaufort Sea sediments. Those portions of elements which are extracted in the acetic acid-hydroxylamine hydrochloride treatment are designated as nonlithogenous, whereas the difference between the total content of an element and its nonlithogenous fraction in the sediment is regarded as the lithogenous portion of that element (lattice-held; Chester and Hughes, 1965). Table XVI reveals the fact that except for Mn the major portion of each metal is associated with the lithogenous (within the crystal lattice) fraction of the sediment. One other exception is Zn in Simpson Lagoon. Nonlithogenous Zn in the lagoon averages about 45% of the total Zn content of the sediment. As mentioned above concerning Table XIII there appears to be a contrast between the Simpson Lagoon and the Beaufort Sea sediments in the chemistry of Zn. Whereas most nonlithogenous elemental abundances are shown to be smaller in the lagoon, nonlithogenous Zn generally appears to be in higher concentration in the same sediments. This relationship is even more pronounced in Table XVI by comparing the relatively high nonlithogenous portion (45%) of total Zn contents in Simpson Lagoon sediment versus the much lower (25-30%) fraction offshore.

Manganese itself is quite distinct from all other elements studied in that the nonlithogenous component is on the order of 50% nearshore but



TABLE XVI

LITHOGENOUS (L)<sup>a</sup> AND NONLITHOGENOUS (NL)<sup>b</sup> PORTIONS OF Fe, Mn, Zn, AND Cu CONCENTRATION ( $\mu\text{g/g}$ ) IN SIMPSON LAGOON AND THE BEAUFORT SEA CONTINENTAL SHELF, CONTINENTAL SLOPE, AND DEEP-SEA SEDIMENTS

Station	Fe $10^4$ $\mu\text{g/g}$		Mn		Zn		Cu	
	L	NL	L	NL	L	NL	L	NL
Simpson Lagoon								
SL877- 2	.56	.14	63	94	22	8	7.9	1.1
SL877- 6	1.43	.27	187	210	51	39	14.7	3.3
SL877-13	1.54	.41	176	326	27	68	14.0	3.0
SL877-18	1.08	.32	120	55	47	38	13.6	2.4
SL877-27	1.50	.34	159	158	35	50	9.4	2.6
SL877-29	1.57	.35	178	135	38	67	15.2	4.8
SL877-30	.57	.08	88	49	27	8	3.6	1.4
SL877-33	.98	.24	135	212	56	24	11.4	2.6
UG-1	<u>1.04</u>	<u>.18</u>	<u>129</u>	<u>98</u>	<u>46</u>	<u>24</u>	<u>12.6</u>	<u>0.4</u>
Average	1.14	0.26	137	148	39	36	11.3	2.5
Continental Shelf								
GLA77-12	2.35	.345	238	139	88	22	16	6
GLA77-15	2.85	.495	242	440	105	25	21	10
GLA77-17	3.03	.595	321	340	121	29	24	9
GLA77-22	2.41	.405	217	160	94	21	17	7
GLA77-31	<u>2.25</u>	<u>.355</u>	<u>234</u>	<u>148</u>	<u>96</u>	<u>19</u>	<u>15</u>	<u>6</u>
Average	2.58	.440	250	245	100	23	19	8
Continental Slope								
GLA77-18	1.96	.355	282	515	74	16	15	5
GLA77-23	2.56	.515	243	344	96	34	17	13
GLA77-42	<u>2.72</u>	<u>.295</u>	<u>315</u>	<u>77</u>	<u>88</u>	<u>22</u>	<u>13</u>	<u>5</u>
Average	2.41	.388	280	310	86	24	15	8
Deep-Sea								
GLA77- 5	3.00	1.00	150	4500	97	33	17	23
GLA77- 7	<u>3.10</u>	<u>.890</u>	<u>250</u>	<u>2800</u>	<u>94</u>	<u>31</u>	<u>22</u>	<u>20</u>
Average	3.05	0.95	200	3650	95	32	20	21

<sup>a</sup> Lithogenous is that portion of the total metal content in a sediment which is "lattice-held" and not leachable by the hydroxylamine hydrochloride-acetic acid procedure.

<sup>b</sup> Nonlithogenous refers to that amount of the total metal content leachable by an hydroxylamine hydrochloride-acetic acid treatment of the sediment. (Chester and Hughes, 1965).

rises to as much as 95% of the total content of manganese in the deep-sea sediment.

#### Correlations Between Chemical, Textural, and Clay Mineral Compositions of Simpson Lagoon Sediments

Finally, in Table XVII are presented the correlation coefficients significant at the 90% confidence level for various chemical, textural, and clay mineral compositions for Simpson Lagoon sediments. A Pearson Product Moment correlation was employed in the calculations. The first obvious relationship seen in the table is the very high correlation between many textural and chemical parameters.

The following observations have been made:

1. Textural relationships are such that most chemical components have a strong negative correlation with sand but a strong positive correlation with silt abundance. The exceptions are lithogenous Cu and lithogenous Zn. Additionally, clay abundance has a significant positive correlation with all chemical components except non-lithogenous Mn.
2. Carbonate correlates positively with all chemical components except lithogenous Zn and Cu and nonlithogenous V and P. Note also that the lithogenous component has a larger coefficient than the non-lithogenous component for the elements Fe and Mn.
3. Inter-element correlations:
  - a) Both Fe components and lithogenous Mn have positive correlations with all chemical components except nonlithogenous Mn and lithogenous Zn.
  - b) Nonlithogenous Mn and lithogenous Zn have no significant correlations. Note the opposite behavior of these two elements. Lattice-associated Mn is correlatable with other elements while it is extractable Zn which correlates.
  - c) Except where noted above, both V components and nonlithogenous Zn have positive correlations with all the chemical components. In addition, the nonlithogenous V coefficients are smaller than the lithogenous coefficients for that element.

TABLE XVII

CORRELATION COEFFICIENTS<sup>a</sup> FOR CHEMICAL, TEXTURAL, AND CLAY MINERAL COMPOSITIONS<sup>b</sup> OF 11 SIMPSON LAGOON SEDIMENTS, ARCTIC COAST OF NORTHERN ALASKA

Depth	Sand	Silt	CO <sub>3</sub>	L Fe	NL Fe	L Mn	NL Mn	L Zn	NL Zn	LV	NL V	L Cu	NL Cu	T Ni	T Co	T Cr	NL P
Depth																	
Sand	.983*	-.623	-.917*	-.970*	-.896*	-.945*	-.720	--	-.933*	-.918*	-.686	--	-.788	-.921*	-.902*	-.922*	-.761
Silt	--	--	.890*	.936*	.879*	.902*	.750	--	.923*	.864*	--	--	.776	.868*	.843	.863*	.724
Clay	--	--	.622	.817	.697	.839	--	.706	.692	.865	.717	.823	--	.863*	.868*	.890*	.688
Expand.	--	--	--	--	--	--	--	--	--	--	--	--	--	--	--	--	--
Illite	--	--	--	--	--	--	--	--	--	--	--	--	--	--	--	--	--
Kaol.	--	--	--	--	--	--	--	--	--	--	--	--	--	--	--	--	--
Chlor.	--	--	--	--	--	--	--	--	--	--	--	--	--	--	--	--	--
Org. C.	--	--	--	--	--	--	--	--	--	--	.668	--	--	--	--	--	--
N	--	--	--	--	--	--	--	--	--	--	--	--	--	--	--	--	--
CO <sub>3</sub>	--	--	--	.921*	.806	.928*	.738	--	.861*	.862*	--	--	.831	.854*	.844	.833*	--
L Fe	--	--	--	--	.900	.955*	--	--	.942*	.953*	.799	.758	.784	.927*	.935*	.957*	.782
NL Fe	--	--	--	--	--	.791	--	--	.945*	.956*	.868*	.747	.798	.908*	.951*	.914*	.824
L Mn	--	--	--	--	--	--	.674	--	.851*	.872*	.699	.754	.777	.896*	.908*	.914*	.668
NL Mn	--	--	--	--	--	--	--	--	--	--	--	--	--	--	--	--	--
L Zn	--	--	--	--	--	--	--	--	--	--	--	--	--	--	--	--	--
NL Zn	--	--	--	--	--	--	--	--	--	.909*	.793	.716	.858*	.845*	.913*	.907*	.811
LV	--	--	--	--	--	--	--	--	--	.868*	.776	.752	.752	.971*	.985*	.973*	.836*
NL V	--	--	--	--	--	--	--	--	--	--	.792	.670	.670	.832*	.895*	.877*	.854*
L Cu	--	--	--	--	--	--	--	--	--	--	--	--	--	.756	.796	.831	--
NL Cu	--	--	--	--	--	--	--	--	--	--	--	--	--	.696	.801	.735	--
T Ni	--	--	--	--	--	--	--	--	--	--	--	--	--	--	.971*	.969*	.828
T Co	--	--	--	--	--	--	--	--	--	--	--	--	--	--	--	.978*	.879*
T Cr	--	--	--	--	--	--	--	--	--	--	--	--	--	--	--	--	.886
NL P	--	--	--	--	--	--	--	--	--	--	--	--	--	--	--	--	--

<sup>a</sup> Only coefficients significant at or above 95% confidence level, using a two-tail test Pearson Product Moment Correlation are cited in the Table.

\* These coefficients are significant at or above the 99% confidence level.

<sup>b</sup> The prefix "L" to the heavy metals connotes the lithogenous (lattice-held) portion of each metal in the sediment, whereas the prefix (NL)" connotes nonlithogenous (hydroxylamine hydrochloride-acetic acid leachable) amount of the metals. The prefix "T" connotes the total metal content in the sediment.

Expond., Kaol, Chlor., Org. C, N, and CO<sub>3</sub> are abbreviations for expandable, kaolinite, chlorite, organic carbon, nitrogen, and carbonate respectively.

- d) Keeping in mind the exceptions noted above, the trace elements Cu, Ni, Co, and Cr generally correlate strongly and positively with most chemical components. Note that Cu (both components) has significantly weaker correlations, however.
- e) Similar to Cu, P, although correlating significantly to most chemical parameters enjoys somewhat weaker correlation coefficients.

It should be noted that only the total content of the trace metals Ni, Co and Cr were used in the correlation matrix and therefore no distinction is made as to which component of these elements accounts for the very high inter-element correlation seen between them. Subsequent to this report a more detailed research into relationships brought to light by this matrix will commence. First the nonlithogenous and lithogenous components for Ni, Co and Cr will be distinguished to better understand the extremely high correlations apparent between their total sediment abundance shown in Table XVII.

## VIII. DISCUSSION

### Status of Studies on Sediment Textures

We have just completed compilation of all available data, including those collected this year, on textural attributes of surficial sediments of the Beaufort Sea. These data are in the process of being digitally transferred onto standard OCSEAP maps of the Beaufort Sea. As mentioned earlier the end product will be several maps showing the regional variations in the gross lithology and the various statistical grain size parameters. It is anticipated that preparation of these maps will be completed by the first week of April 1979. Subsequently, we intend to subject all available data to variance analysis. There is a three-fold purpose to generate these maps: (i) to define the benthic

habitats for the Beaufort Sea, (ii) to map shelf areas with potential sources of gravels and sands for construction use, and (iii) to further our understanding of the Holocene depositional history of the Beaufort Sea.

#### Stratigraphic Studies on Core Samples

Examination of the stratigraphy of the unconsolidated cores (Table VI, Figure 4a and 4b) permits inferences on depositional processes prevailing in the Colville Prodeltaic (?) area (Figure 3). It would seem that in the proximal end of the prodelta sediments have been depositing under fluctuating hydrodynamic conditions. This is evident from the presence of alternate bands and laminations of relatively high and low sand contents in cores PWB76-18, 19, 20 and 23. Additionally, it is suggested that in the area of the shelf from where these cores were retrieved reworking of sediments by bioturbation and/or ice gouging has not occurred in recent times. This is inferred from the lack of stratigraphic homogeneity in the four core samples. Reimnitz *et al.* (1972) have shown that disruption of horizontal layering of shelf sediments in the Beaufort Sea (and by implication generation of a homogenous stratigraphic sequence) is a strong evidence of bottom reworking by ice gouging, and vice versa. Barnes *et al.* (1978) have further concluded that the average incision depth of ice-gouging in the Beaufort Sea is 31 cm. This would imply that if the shelf area from which the four cores were collected had been ice gouged then the sediment layering in those cores would have been disrupted. Our conclusions on lack of ice gouging on the four cores are further supported by the recognition of undeformed

laminations and banding by Barnes *et al.* (1977) in the original core sample. However, core PWB76-1 (Figure 4a, Table VI) which was retrieved from the Central Prudhoe Bay (Figure 2) at 3 m water depth consists essentially of homogenous clayey silt with no evidence of sediment layering on basis of textural analysis. This would mean that sediments of the Prudhoe Bay have either not been completely free from reworking by ice gouging, or deposition in the bay has continued under similar hydrodynamic conditions during recent times. The stratigraphy of core PWB76-13 (Table VI, Figure 4a) reflects a relatively complex depositional history at the distal end of the Colville Prodelta (Figure 2). A gravel lens with a few shells between 20-30 cm from the core top most likely represents a paleosedimentary unit deposited under intensified wave reworking. Presence of this distinct gravel lens in the upper core suggests lack of recent ice gouging in the area of the core collection. However, we are quite unsure at this stage whether this gravel lens represents a paleo gravel bar or an old gravel barrier island, or alternatively an old gravel beach section. Presumably through further coarse fraction studies on the entire core criteria could be established to elucidate the sequence of hydrodynamic conditions which culminated in the deposition of the gravel layer.

We have already initiated some research along the lines suggested above. Identification of the progressive changes in lithology, structure and coarse fractions of sediments of a core sample retrieved from the Simpson Lagoon due south of the Pingok Island (core VC77-49 in Figure 2) has provided us with encouraging results pertaining to the lagoon evolution. It is suggestive that the Simpson Lagoon was dominated in

the past by low lying tundra coastal plain with a number of fresh-water coastal lakes very similar to that of the present time. These lakes supported the snail *valvata* and the bivalve *Psidium*. Sometime thereafter it is believed that the lakes got breached and came to be in tidal communication with the sea through tidal channels, as suggested by the presence of marine faunal components such as *Cyrtodaria kurriana*, and species of foraminiferas and ostracods. The breached lakes then got progressively coalesced and eventually inundated by sea water (most likely coincident with continuous subsidence of lake bed resulting from subsurface permafrost melting). The Pingok and the adjacent tundra blanketed islands which presumably represent remnant coastal highlands, delineated the inundated lakes from the open sea to form the present Simpson Lagoon. We hope eventually to correlate the above sequence of events with the geologic time scale.

#### Origin of Exotic Boulders on the Pingok and Bodfish Islands

Results of the detailed petrographic studies on 40 separate samples of boulder chips has enabled us to define the composition of the boulders (Table VII) that are scattered on the lagoonward beaches of the Pingok and Bodfish islands. Based on knowledge of known rock types in the Brooks Range, Davidson, British and Romanzof mountains it would seem most likely that the boulder samples examined by us have their source in the northern arctic Alaskan hinterland. If this is true then does it mean that the transport mode for the boulders was by glaciers (PreWisconsinian?) and that the boulders are in essence residual moraines? Before this proposition is entertained seriously it would be prudent

to bear in mind the suggestion that the arctic coastal plain was most probably not glaciated during the Quaternary (Coulter and others, 1965; Hopkins, 1967). A number of studies have been directed to understand the origin of boulder deposits on the Beaufort Sea continental shelf, and the adjacent barriers and coastal beaches (MacCarthy, 1958; McCulloch, 1967; Naidu and Mowatt, 1974, 1975; Rodeick, 1979; Hopkins, 1978). At this time it would seem that more than one thesis has been proposed to explain the source and origin of the boulder deposits in question. Our studies thus far suggest that the boulders of the Pingok and Bodfish islands probably had their source in the Brooks Range and the contiguous smaller mountain system. However it is not improbable that the exotic boulders observed further east of the above two islands and associated with the Pleistocene Flaxman Formations, as well as some boulders on the Beaufort Sea continental shelf, were ice-rafted from Ellesmere Island vicinity (Naidu and Mowatt, 1974, 1975; Hopkins, 1978) and/or from the Amundsen Gulf region (Rodeick, 1979; Hopkins, 1978). We are extending our petrographic studies on exotic boulder samples to east of the Bodfish Islands, in attempting to better understand origin of boulders in the North Slope coastal region. Presumably a satisfactory answer to the sources and origin of the boulders will provide clues that will aid to the understanding of the late Quaternary depositional history of the Beaufort Sea region.

#### Sediment Dynamics Study

The malfunction of the instrumented tripod package of the SDS System, resulting from an unfortunate accident in the field, was a



serious blow to our sediment dynamics studies initiated in summer 1978. We have planned to rerun the SDS experiments in summer 1979, starting sometime in July. The time-series information gathered by us continuously for 3 weeks on suspensates from water columns at the tripod station and which was meant to complement the SDS experiment, has offered some potentially useful data. The two high pulses of suspensates in both surficial and subsurficial waters recorded for August 23 and 27, 1978 (Table III, Figure 6) correlate strongly with relatively high winds recorded on the same two days (Figure 6) at Milne Point by Mr. Tom Kozo (written communication). On basis of this correlation one would be tempted to conclude that the unusually high suspensate pulses are a result of *in situ* resuspension of the cohesionless lagoon substrate particles by wind induced horizontal oscillatory currents. This would have been an obvious interpretation but for the lack of higher suspensate contents in the subsurface than in the surface water samples (Table III, Figure 6) at the tripod experimental site. An alternate explanation could be that subsequent to resuspension of substrate particles by oscillatory currents the suspensates in the subsurface water columns are diluted by an influx of sea water that is relatively impoverished in suspended particles. It is conceivable that the sea water influx into the lagoon through inter-island channels/inlets would be denser than the lagoon water and thus would be expected to move at flood tide as a subsurface wedge.

Satellite images clearly display that movement of turbid plumes along the nearshore, lagoons and bays of north Alaskan arctic is either in the form of long continuous plumes or disconnected irregular streaks and wedges. With the exception of the Tigvarik Island area where an

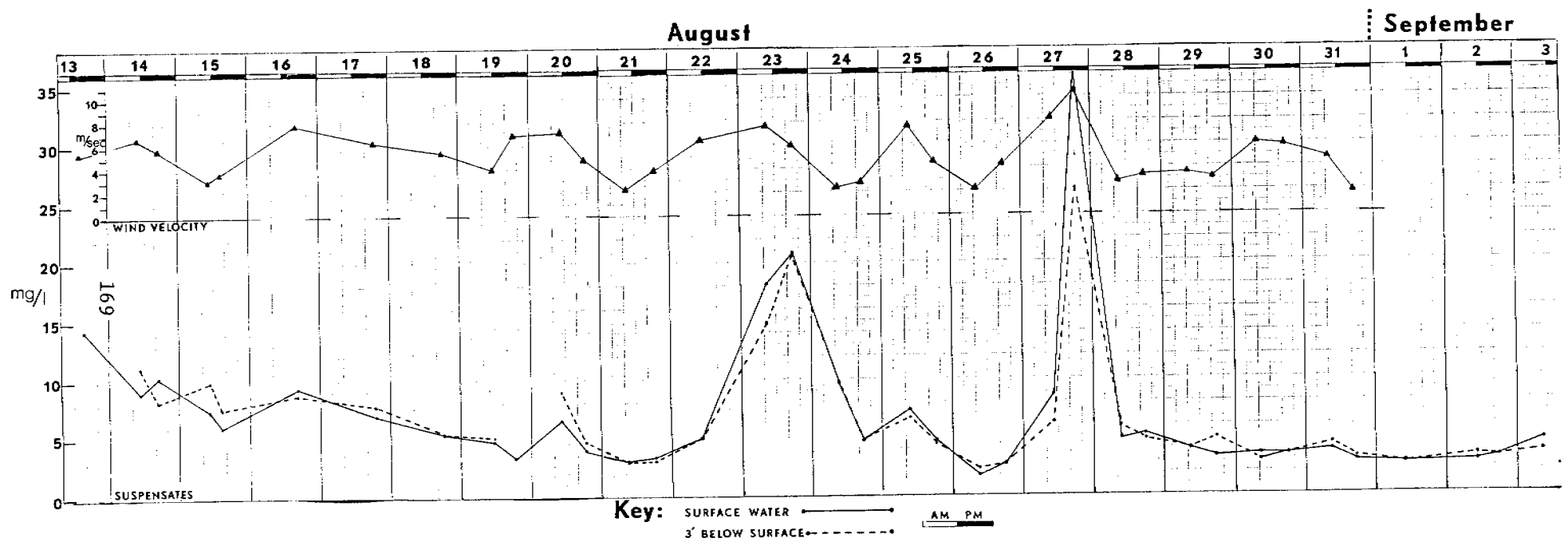


Figure 6. Wind velocity\* and suspensate concentrations for suspensate sampling times at Milne Point SDS tripod station.

\* Average wind speed for the 9 hours prior to the time of the tripod location suspensate sampling.

eastward moving gyre is apparent, along most of the coast the nearshore turbid plume is invariably seen to move westward. The latter water movement is impelled by the prevailing westward littoral currents. However, at this time we are not quite sure whether the tongues of turbid plumes in the lagoons and bays in mid and late summer can be ascribed to fluvial discharge and thermoerosion of coastal bluffs and barriers. No such direct association is apparent from detailed scrutiny of several multi year satellite images, although invariably extensive turbid plumes do occur in the vicinity of large river mouths. It is important to note that comparatively fresh fluvial waters are discharged in late summer from mouths of the major distributary channels, while presence of relatively turbid waters can be delineated off the mouths in the lagoons and bays. Additionally, the lagoon waters extending up to a few meters away from the coastal bluffs and barrier islands are observed to be relatively less turbid than rest of the lagoon. A notable example is the Dease Inlet region. All these observations lead us to suspect that in mid and late summer when the fluvial outflow is low, much of the turbid coastal water is generated by resuspension of the cohesionless substrate particles from shallow-water regions by wave induced agitation. Since the region slightly off the river mouths are generally more shallow than rest of the bays and lagoons relatively high turbid waters are associated with such areas. Subsequent to resuspension the particles are carried westward in the form of a turbid plume.

## Clay Minerals Studies

Results of clay mineral studies conducted this year would seem to substantiate our earlier conclusions (Naidu and Mowatt, 1974, 1975). In the nearshore region of the Beaufort Sea, specially the contiguous area encompassing the lagoons, bays and nearshore open shelf, we can quite confidently infer the sources (relative to various rivers) as well as delineate the depositional sites of clay-sized terrigenous particles. A net westward drift of the fine sized particles which are discharged by the various North Slope rivers are supported by our clay mineral studies. However, elucidation of the sources and understanding of the eventual depositional sites of contemporary clays in the middle and outer continental shelves of the Beaufort Sea, via clay mineral studies, has not been very profitable. This can be attributed to a lack of any clear cut trends in the distributional pattern of clay mineral assemblages throughout the Beaufort Sea. An exception to this, however, is the presence of an extensive but disconnected patch and a few smaller patches with notably high expandable clay minerals in the shelf area between Barter Island and Demarcation Point (Figure 5a). Clay mineral assemblages in these patches correlate well with those of the Colville River. Earlier, on the basis of limited data, we had speculated that findings of the Colville River assemblage thus far east in the Beaufort Sea suggested a contemporary drift of the Colville clays, via the eastward moving water masses in the outer shelf. Although this is still quite conceivable, we are not more inclined to believe that the Colville River assemblage in the east (Figure 5a) is most probably a relict deposit. This conclusion is chiefly based on the

lack of continuity of the Colville assemblage on the east to the Colville River source. The general absence of any regional trend in clay mineral dispersal pattern elsewhere in the middle and outer Beaufort Sea shelves can perhaps be attributed to widescale reworking and thus tendency to homogenize the shelf sediments by the action of ice gouging and/or bioturbation.

#### Sediment Geochemistry

Results of our researches to date on abundances of the various heavy metals and their partitioning patterns in sediments of the Simpson Lagoon are now being synthesized. Correlation coefficient analysis, including lithological, chemical and clay mineralogical data do suggest that the geochemical fractionation patterns of the metals in the Simpson Lagoon and those in the contiguous open shelf are similar. With the exception of Mn large fractions of all metals analyzed are held in the lithogenous component (e.g. lattice of crystals of minerals), which is not readily leachable. In contrast Mn is available in sediments in a easily mobilized phase. Analysis of sediment interstitial waters clearly suggests that post depositional dissolution of Mn in the sub-surface reduced layers is taking place in the Simpson Lagoon. It is also suggested that there is a subsequent upward migration of the dissolved Mn and eventual reprecipitation of it in the oxidized surficial sediment layers. Our analysis of Fe and P in interstitial waters of the lagoon sediments has not been completed as of this report writing. A synthesis of the sediment chemical data should be available within a month or so.

## IX. CONCLUSIONS

Textural and coarse fraction analyses of a few core samples have offered some clues to the understanding of the depositional processes in the Colville Prodeltaic region. It would seem that sediments in the above region are depositing under fluctuating hydrodynamic conditions. The deposits have not been reworked, as in case of most of the adjacent shelf areas, by ice gouging and/or bioturbation. At least one core indicates presence recently of either a shifting gravel bar, or a relict beach or a relict barrier deposit at the distal end of the Colville Prodelta.

Stratigraphic studies of short core samples from the Simpson Lagoon have assisted in the understanding of the lagoon evolution. It would seem most likely that the Simpson Lagoon has evolved from a coastal fresh water lake system. This has probably resulted from a progressive inundation of coastal lakes by the sea.

Investigations on sediment dynamics were greatly hampered because of accidental malfunction of the instrumented tripod package consisting of the sediment dynamic sphere (SDS). We have plans to duplicate the SDS experiment in summer 1979. Nonetheless, time-series data collected on water suspensates strongly suggest that resuspension of cohesionless substrate particles in the Simpson Lagoon is related to horizontal oscillatory currents which are associated with wind-induced waves. At this stage we are not quite sure how turbid water plumes are generated in the North Slope coastal area during mid and late summer. The commonly held notion that the plumes are directly associated with fluvial outflow and/or coastal bluff erosion seems tenuous to believe, based on our

detailed scrutiny of multiyear satellite images. Most likely the turbid plumes are generated by wave turbulence in shoals off river mouths.

This section petrographic studies on 40 samples of boulder chips suggest that almost all exotic boulders on the lagoonward beaches of the Pingok and Bodfish islands were derived from the Brooks Range and the contiguous lesser mountain systems of north arctic Alaska. However, the mode of transport and emplacement of these boulders on the islands remains a matter of speculation. It is attractive to invoke a glacial origin but difficulties are encountered to accept this, considering the possible lack of late Quaternary glaciation in north coastal arctic Alaska. Our future plans call for a detailed petrographic investigation of exotic boulders that occur east of the Bodfish Islands.

Clay mineral studies have proved very useful in identifying the terrigenous sources of fine grained sediment particles, and their eventual depositional sites in the lagoons, bays and adjacent shelf region of the Beaufort Sea. The net westward drift of fine grained sediments are clearly recognizable, via mapping of clay mineral dispersal patterns. However, lack of any definite regional trend in clay mineral distributional pattern have failed us in elucidation of the sources and depositional sites of terrigenous particles in the middle and outer continental shelves of the Beaufort Sea. Lack of such trends is attributed chiefly to reworking of deposited sediments by ice gouging and/or bioturbation. An exception, however, exists in the presence of a well-defined but discontinuous patch of the Colville River clay

mineral assemblage between the Barter Island and the Demarcation Point. This isolated patch is explained to a relict nature of the sediments there.

In conclusion, our geochemical studies clearly show that with the exception of Mn bulk of all other metals investigated are tied to the crystal lattice of minerals. Interstitial water analysis has brought to light that postdepositional Mn dissolution most likely is occurring in the subsurface reduced layers of the Simpson Lagoon sediments. Subsequently, the dissolved Mn appears to migrate upward and get reprecipitated as a hydrate in the upper oxidized layers.

#### X. NEEDS FOR FURTHER STUDY

Our future plans call for duplication of the sediment dynamics experiment in the Simpson Lagoon in summer 1979, and data gathering and analysis of suspensions complementary to that experiment. Additionally, we plan to synthesize all available textural, mineralogical and geochemical data. The ongoing studies on heavy minerals and boulders will be completed to enhance our understanding of sources and mode of transport of sediment particles in the Beaufort Sea nearshore.

#### XI. SUMMARY OF 4th QUARTER OPERATIONS

##### Ship or Laboratory Activities

1. None scheduled
2. Not applicable
3. Methods: Refer to Section for details
4. Not applicable
5. Refer to Section for details



## REFERENCES

- Alexander *et al.* 1975. Environmental studies of an arctic estuarine system. Final Report. U.S. Env. Prot. Agency Rept. 660/3-75-026. 536 p.
- Arnold, K. 1976. Data for State of Alaska socio-economic impact assessment of leasing in the Beaufort Sea. Submitted to the Dept. of Community and Regional Affairs, State of Alaska, Juneau. 1-24 pp.
- Biscaye, P. E. 1965. Mineralogy and sedimentation of recent deep-sea clay in the Atlantic Ocean and adjacent seas and oceans. *Geol. Soc. America Bull.* 76:803-832.
- Barnes, P., E. Reimnitz, D. Drake and L. Toimal. 1977. Miscellaneous hydrologic and geologic observations on the inner Beaufort Sea shelf, Alaska. U.S. Geol. Survey Open File Rept. 77-477 pp.
- Barnes, P. W., D. McDowell, and E. Reimnitz. 1978. Ice gouging characteristics: Their changing patterns from 1975-1977, Beaufort Sea, Alaska. U.S. Geological Survey Open File Report. 78-730. 42 p.
- Burrell, D. C. 1977. Natural distribution of trace heavy metals and environmental background in Alaskan shelf and estuarine areas. Annual Rept. to BLM-OCSEAP Office, Boulder. Inst. Mar. Sci., Univ. Alaska, Fairbanks. 204 p.
- Burrell, D. C., P. J. Kinney, R. S. Hadley and M. E. Arhelger. 1970. Beaufort Sea environmental data, 1968-1969. Inst. Mar. Sci., Univ. Alaska, Fairbanks, R70-20. 270 p.
- Cacchione, D. and D. Drake. 1977. Sediment transport in Norton Sound-Northern Bering Sea, Alaska. Annual Report. In: *Environmental Assessment of the Alaskan Continental Shelf*, Vol. XVIII. NOAA-OCSEAP Office, Boulder, Colorado. 130-158 pp.
- Chester, R. and M. J. Hughes. 1967. A chemical technique for the separation of ferro-manganese minerals, carbonate minerals and absorbed trace elements from pelagic sediments. *Chem. Geol.* 2:249-262.
- Dygas, J. A., R. Tucker and D. C. Burrell. 1972. Geological report on the heavy minerals, sediment transport, and shoreline changes of the barrier islands and coast between Oliktok Point and Beechy Point. In: *Baseline data study of the Alaskan Arctic Aquatic Environment*, P. J. Kinney *et al.* (eds.). Inst. Mar. Sci. Rept. R-72-3, Univ. Alaska, Fairbanks. 61-121 pp.
- Dygas, J. A. and D. C. Burrell. 1976a. Dynamic sedimentological processes along the Beaufort Sea coast of Alaska. In: *Assessment of the Arctic Marine Environment: Selected Topics*, D. W. Hood and D. C. Burrell (eds.), Proc. POAC-75. Inst. Mar. Sci., Univ. Alaska, Fairbanks, Alaska. 189-203 p.

- Dygas, J. A. and D. C. Burrell. 1976b. Response of waves and currents to wind patterns in an arctic lagoon. *In: Assessment of the Arctic Marine Environment: Selected Topics*, D. W. Hood and D. C. Burrell (eds.), Proc-POAC-75. Inst. Mar. Sci., Univ. Alaska, Fairbanks, Alaska. 263-285 pp.
- Feder, H. M., A. S. Naidu, D. Schammel, D. G. Shaw, E. R. Smith and G. W. Smith. 1976. The arctic coastal environment of Alaska, Vol. III. The nearshore marine environment in Prudhoe Bay, Alaska. Inst. Mar. Sci., Rept. R76-7, Univ. Alaska, Fairbanks. 153 p.
- Folk, R. L. and W. C. Ward. 1957. Brazos River bar - a study in the significance of grain size parameters. *J. Sedimentary Petrology* 27:3-26.
- Grider, G. W., Jr., G. A. Robbiliard, and R. W. Firth, Jr. 1977. Final Report on Environmental Studies Associated with the Prudhoe Bay Dock: Coastal Processes and Marine Benthos. Woodward-Clyde Consultants, Anchorage, Alaska. IV85.
- Hülsemann, J. 1966. On the routine analysis of carbonates in unconsolidated sediments. *J. Sedimentary Petrology* 36:622-625.
- Hopkins, D. M. 1977. Shoreline history of Chukchi and Beaufort Seas as an aid to predicting offshore permafrost conditions. Quarterly Rept. to NOAA-OCSEAP, Boulder, October 1977. 7 p.
- Hopkins, D. M. 1978. Offshore permafrost studies, Beaufort Sea, Alaska. Quarterly Rept. to OCSEAP, Environmental Assessment of the Alaskan Continental Shelf, BLM-NOAA. 253-261 pp.
- McCulloch, D. S. 1967. Quarternary geology of the Alaskan shore of Chukchi Sea. *In: The Bering Land Bridge*, D. M. Hopkins, (ed.). Palo Alto, Stanford Univ. Press. 91-120 pp.
- MacCarthy, G. R. 1958. Glacial boulders on the Arctic Coast of Alaska. *Arctic* 11:71-85.
- Mowatt, T. C., A. S. Naidu and N. Veach. 1974. Detailed clay mineralogy of the Colville River and Delta, Northern Arctic Alaska. Alaskan Div. of Geol. and Geophys. Survey's Open File Report, Fairbanks. Rept. 45. 36 pp.
- Naidu, A. S. 1974. Sedimentation in the Beaufort Sea: A synthesis. *In: Marine Geology and Oceanography of the Arctic Seas*, Y. Herman (ed.). Springer-Verlag, N. Y. 173-190 pp.
- Naidu, A. S. 1976. Geologic Studies. *In: The Arctic Coastal Environment of Alaska*, H. M. Feder, D. G. Shaw and A. S. Naidu (eds.). Vol. 1. The nearshore marine environment in Prudhoe Bay, Alaska. Submitted to the Atlantic Richfield Co., Inst. Mar. Sci. Rept. No. R76-3, Univ. Alaska, Fairbanks. 8-36 pp.

- Naidu, A. S. 1978. Sediment characteristics, stability, and origin of the barrier island-lagoon complex, north arctic Alaska. Annual Rept. Submitted to the NOAA-OCSEAP Office, Boulder. 55 p.
- Naidu, A. S. 1978. Sediment characteristics, stability, and origin of the barrier island-lagoon complex, north arctic Alaska. Annual Report OCSEAP Contract #03-022-56, Inst. Mar. Sci., Univ. Alaska, Fairbanks. 55 p.
- Naidu, A. S. and T. C. Mowatt. 1974. Depositional environments and sediment characteristics of the Colville and adjacent deltas, northern arctic Alaska. In: *Deltas Models for Explorations*. M. L. Browssard (ed.). Houston Geol. Soc., Houston, Texas. 284-309 pp.
- Naidu, A. S. and T. C. Mowatt. 1975. Aspects of size distributions, mineralogy, and geochemistry of deltaic and adjacent shallow marine sediments, north arctic Alaska. U.S. E.P.A. Rept. 660:3-75-026, U.S.E.P.A., Corvallis, Oregon. 143-223 pp.
- Naidu, A. S., D. C. Burrell and D. W. Hood. 1971. Clay mineral composition and geologic significance of some Beaufort Sea sediments. *J. Sedimentary Petrology* 41:691-694.
- Rader, L. F. and F. S. Grimaldi. 1961. Chemical analysis for selected minor elements in Pierre Shale. U.S. Geol. Prof. Paper 391-A, A1-A45.
- Reimnitz, E., P. W. Barnes, T. Forgatsch and C. Roderick. 1972. Influence of grounding ice on the arctic shelf of Alaska. *Marine Geology* 13:323-334.
- Shepard, F. P. and D. G. Moore. 1954. Sedimentary environments differentiated by coarse-fraction studies. *Bull. Am. Assoc. Petroleum Geologists* 38: 1792-1802.
- Strickland, J. D. H. and T. R. Parsons. 1965. A Manual of Sea Water Analysis. 2nd ed. Bull. No. 125. *Fish. Res. Bd. Canada*, Ottawa. 47-65 pp.
- Roderick, C. A. 1979. The origin, distribution, and depositional history of gravel deposits on the Beaufort Sea Continental Shelf, Alaska. U.S. Geol. Survey Open File Rept. 79-234, Menlo Park, California. 87 p.
- Truett, J. C. 1978. Beaufort Sea barrier island-lagoon ecological process studies: Overview and synthesis. Annual Rept. Submitted by LGL ltd.-U.S. Inc., Bryan, Texas to the NOAA-OCSEAP Office, Boulder. 86 p.
- Weller, G., D. Norton and T. Johnson. 1977. Environmental impacts of OCS development in northern Alaska. Beaufort Sea Synthesis Report.
- Wiseman, W. J., *et al.* 1973. Alaskan arctic coastal processes and morphology. Tech. Rept. No. 149. Coastal Studies Inst., Louisiana State Univ., Baton Rouge. 171 p.

UNIVERSITY OF WASHINGTON  
SEATTLE, WASHINGTON 98195

Department of Oceanography  
Cable Address: UNWADO

21 September 1978

Dr. A. S. Naidu  
Institute of Marine Science  
O'Neill Building, Room 212  
University of Alaska  
Fairbanks, Alaska 99701

Subject: Interim Report on "Sediment Suspension Studies in Simpson Lagoon."

Dear Dr. Naidu:

The subject of this letter is the documentation of our efforts to obtain data on wave, currents, and sediment concentrations in Simpson Lagoon using the SDS (Sediment Dynamics Sphere) system.

The major difficulties with this experiment were the logistics of operating on the North Slope. It is not the purpose of this letter to criticize but rather to fully document all aspects of the experiment.

Our work began the first week of July 1978. We packed all equipment in crates and performed a complete electronics check of the SDS system, including reading tapes to verify the complete operation of the system. The nephelometer arrived just prior to shipping the system north and was only bench tested. However, the electronics in the SDS system had been checked with dummy inputs so the lack of the nephelometer in a full system check was not a problem.

The full system was shipped from Seattle to Barrow, Alaska on July 15. The shipment arrive in Barrow and was placed on the Alumiak prior to our arrival on July 29, 1978. The SDS was assembled on the deck of the Alumiak on July 30th and 31st.

In the final checkout on 31 July it was noticed that power consumption was too high on the SDS microprocessor. We were not able to isolate the problem element. Because a failure mode for CMOS elements is high power consumption, we decided it best to return the computer to Seattle wherein we would have the equipment to identify the problem elements. It turned out to be a memory chip. This was replaced and the system was brought back to Barrow on 4 August and installed in the tripod. The system operated was operating correctly and programmed to record at 1/2-hour intervals.

It was apparent that we would have difficulties working from the Alumiak because of the small size of the A-frame. We did feel we would be just able to pass the tripod through the A-frame and made plans for the mooring procedure. However, these proved to be unnecessary because the hydraulic system was not

Dr. A. S. Naidu  
21 September 1978  
Page 2

operational. Fortunately, provisions were made to use the R.V. Natchek whose hydraulic system was operating and which had a boom making deployment of the tripod much easier.

The Alumiak carried the tripod to Simpson Lagoon where it was transferred to the Natchek for deployment. Unfortunately, the voyage took much longer than anticipated and I was forced to return to Seattle, leaving my assistant to manage the deployment.

The SDS system was finally placed in the water on 11 August at a depth of about 8 feet in a line between Milne Point and the east end of Jones Island.

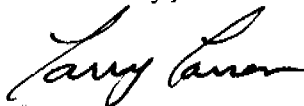
The deployment, however, was not smooth. The system was placed in the water without difficulty; however, following the deployment the Natchek failed to stand clear of the newly deployed instrument and drifted over the tripod toppling it over. With the able help of the personnel at Milne Point Camp the tripod was righted by heroic manpower working from a zodiac.

Because the vessels were unavailable for recovery after 28 August it was decided to attempt a helicopter recovery. Using a chartered helicopter this was accomplished without problem. The unit was not operating when recovered from the water.

The unit was opened when it arrived in Seattle and examined. We found the following. The computer was still operating without flaw. A hecon counter recorded the correct number of samples from the instrument on time until it was back in the laboratory in Seattle. A connector between the computer and the driver board for controlling tape drivers and sensor sampling was pulled out and almost loose. When inserted fully the system operated as it should. We feel that this loose connector caused a loss of data since we had obtained data for only two or three days after the system went into the water. The connector could be pulled loose if the SDS was subjected to a severe shock that shook the circuit boards. Our best guess is that the connector loosened when the tripod was knocked over. In the subsequent days, perhaps due to minor vibrations, the connector loosened to the point that the system no longer sensed the sensors or operated the tape drive.

This analysis is preliminary and a full discussion awaits further testing. We will try to duplicate the problem and also to study all events that led up to the loss of data. Within the next two days the tape will have been fully processed and we will have a measure of the environment in Simpson Lagoon.

Sincerely,



Larry Larsen  
Research Associate Professor

LL:bf

Enclosure

OCS COORDINATION OFFICE  
 University of Alaska  
 ENVIRONMENTAL DATA SUBMISSION SCHEDULE

DATE: March 31, 1979

CONTRACT NUMBER: 03-5-022-56      T/O NUMBER: 33      R.U. NUMBER: 529

PRINCIPAL INVESTIGATOR: Dr. A. S. Naidu

Submission dates are estimated only and will be updated, if necessary, each quarter. Data batches refer to data as identified in the data management plan.

<u>Cruise/Field Operation</u>	<u>Collection Dates</u>		<u>Estimated Submission Dates<sup>1</sup></u>			
	<u>From</u>	<u>To</u>	<u>Batch 1</u>	<u>2</u>	<u>3</u>	<u>4</u>
Archived Samples			None	7/30/79	submitted	10/30/78*
Simpson Lagoon	8/77		submitted	6/30/79	Submitted	10/30/78*
Barrier Islands	8/77		None	6/30/79	None	None
Glacier	8/77	9/6/77	10/30/78*	None	submitted	10/30/78*
Summer '78 Field Season			None	None	6/30/79	None

\* Data awaits coding and keypunching, will be submitted next quarter.

<sup>1</sup> Data Management Plan has been submitted to the Arctic Project Office. We await approval.

Contract # 03-7-022-35182

Research Unit # 531

Reporting Period: March 1, 1978 - March 30, 1979

Oceanographic Processes in a Beaufort Sea  
Barrier Island-Lagoon System:  
Numerical Modeling and Current Measurements

2nd Annual Report

J. C. H. Mungall and R. E. Whitaker

Department of Oceanography  
Texas A&M University  
College Station, TX 77843  
(713) 846-7731

S. D. Pace

Kinnetic Laboratories, Inc.  
One Potrero Street  
Santa Cruz, CA 95060  
(408) 423-6830

April 1979

## CONTENTS

Page

Figures

Tables

Introduction

Investigations: 1978/1979

Numerical Modeling Experiments

- Three-Dimensional Modeling
- Two-Dimensional Modeling
  - A. Scenario Modeling
  - B. Variable-Wind Modeling

1978 Field Season: 20 July 1978-22 August 1978

- Background
- Quasi-Synoptic Surveys
- "Causeway" Studies
- Waves and Currents
- Drifter Studies

Conclusions

References

Appendix A: Annotated Photographic Summary of Field Operations

Appendix B: Printout of Variable-Wind Numerical Model Current  
Components for the Period 0015 20 August 1978 to  
0000 22 August 1978

Appendix C: Data Acquisition Program Listings in North Star BASIC



## FIGURES

Page

- Figure 1. Map of Simpson Lagoon and Prudhoe Bay. The inset shows details of the causeway.
- Figure 2. Typical variation of the eddy viscosity with depth.
- Figure 3. Computed alongshore current field off Milne Point.
- Figure 4. Computed alongshore current field off Point Storkersen.
- Figure 5. Grid schematization for 2-D and 3-D numerical models.
- Figure 6. Beaufort Sea 3-D model surface current field (6.28 m s<sup>-1</sup> from E).
- Figure 7. Beaufort Sea 3-D trajectories (6.28 m s<sup>-1</sup> from E).
- Figure 8. Beaufort Sea 3-D trajectories (6.28 m s<sup>-1</sup> from E).
- Figure 9. Beaufort Sea 3-D trajectories (6.28 m s<sup>-1</sup> from E).
- Figure 10. Beaufort Sea 3-D model surface current field (2.68 m s<sup>-1</sup> from W).
- Figure 11. Beaufort Sea 3-D trajectories (2.68 m s<sup>-1</sup> from W).
- Figure 12. Beaufort Sea 3-D trajectories (2.68 m s<sup>-1</sup> from W).
- Figure 13. Beaufort Sea 3-D trajectories (2.68 m s<sup>-1</sup> from W).
- Figure 14. Beaufort Sea 3-D model surface current field (1.03 m s<sup>-1</sup> from N).
- Figure 15. Beaufort Sea 3-D trajectories (1.03 m s<sup>-1</sup> from N).
- Figure 16. Beaufort Sea 3-D trajectories (1.03 m s<sup>-1</sup> from N).
- Figure 17. Beaufort Sea 3-D trajectories (1.03 m s<sup>-1</sup> from N).
- Figure 18. Beaufort Sea 3-D model surface current field (5.30 m s<sup>-1</sup> from E).
- Figure 19. Beaufort Sea 3-D model surface current field (3.09 m s<sup>-1</sup> from W).
- Figure 20. Beaufort Sea 3-D model surface current field (0.57 m s<sup>-1</sup> from N).
- Figure 21. Beaufort Sea 3-D model surface current field (1.34 m s<sup>-1</sup> from S).

FIGURES (continued)

Page

- Figure 22. Grid scheme for Simpson Lagoon, Alaska. Crosses denote corners of 1 km x 2 km computational rectangles.
- Figure 23. Grid scheme for Simpson Lagoon, Alaska: Scenario One barrier additions.
- Figure 24. Grid scheme for Simpson Lagoon, Alaska: Scenario Two barrier additions.
- Figure 25. Grid scheme for Simpson Lagoon, Alaska: Current printout and current meter locations.
- Figure 26. Simpson Lagoon synoptic survey: 28 July 1978.
- Figure 27. Simpson Lagoon synoptic survey: 5 August 1978.
- Figure 28. Study of salinity differences across Milne Point.
- Figure 29. Milne Point drift currents as computed by microcomputer.
- Figure 30. Drifter trajectory summary.
- Figure 31. Drifter trajectory: buoy 156.
- Figure 32. Drifter triangulation error analysis: buoy 156.
- Figure 33. Drifter trajectory: buoy 157
- Figure 34. Drifter triangulation error analysis: buoy 157.
- Figure 35. Drifter trajectory: buoy 158.
- Figure 36. Drifter triangulation error analysis: buoy 158
- Figure 37. Drifter trajectory: buoy 160.
- Figure 38. Drifter triangulation error analysis: buoy 160.
- Figure 39. Drifter trajectory: buoy 174.
- Figure 40. Drifter triangulation error analysis: buoy 174.
- Figure 41. Hourly winds at Cottle Island during drifter tracking (Source: Roger Andersen).
- Figure 42. Drifter speeds as computed from trajectories.

FIGURES (continued)

Page

- Figure A.1. Living facilities at Prudhoe Bay.
- Figure A.2. Prudhoe Bay temporary check-in facilities.
- Figure A.3. Prudhoe Bay skyline.
- Figure A.4. Landward end of North Dock, Prudhoe Bay.
- Figure A.5. North Dock viewed from the south.
- Figure A.6. North Dock viewed from the north.
- Figure A.7. Close-up of North Dock number 3.
- Figure A.8. Close-up of North Dock number 2.
- Figure A.9. Airlift of electronics hut, Milne Point.
- Figure A.10. Generator and biology huts, Milne Point.
- Figure A.11. Instrument tower, scale in feet.
- Figure A.12. Close-up of EM current sensor.
- Figure A.13. Close-up of EM electronics packages.
- Figure A.14. Wave gauge and current meter displays.
- Figure A.15. Microcomputer data acquisition system.
- Figure A.16. Instrument tower.
- Figure A.17. N.A.R.L. food airdrop.
- Figure A.18. Completion of airdrop.

TABLES

- Table 1. Simpson Lagoon 2-D Modeling Results, Scenario #1
- Table 2. Simpson Lagoon 2-D Modeling Results, Scenario #2

BARRIER ISLAND LAGOON SYSTEM

NUMERICAL MODELING AND CURRENT MEASUREMENTS

Introduction

Simpson Lagoon, the principal study area of this contract, is located on the shore of the north coast of Alaska at approximately  $70^{\circ} 31' N$ ,  $149^{\circ} 15' W$ . The lagoon (see Figure 1), which lies some 10 miles to the west of Prudhoe Bay, is shallow, with depths averaging approximately one meter.

The primary objective of the study is the provision to biological disciplines of the hydrographic data necessary to complement their investigations. This has taken the form of field measurements and of the application of numerical models to the study of Simpson Lagoon and the Beaufort Sea coast.

During most of the study, research has been restricted by mandate to the study of Simpson Lagoon. The reader should be aware however that most of the results and techniques described in this report are applicable to the remainder of the Beaufort Sea coast.

The first year of research (Mungall et al, 1978) covered the period June 1977 through February 1978. Efforts commenced with the two-dimensional numerical modeling of Simpson Lagoon for the purpose of predicting average nearshore and "deep" currents, and the flow of water through the lagoon for a variety of wind cases. These data were made use of in the University of British Columbia/LGL ecological model of Simpson Lagoon. Three-dimensional numerical modeling of the same region was also carried out in order to prepare for questions concerning the detailed flow around the lagoon entrances. A short field season, with Texas A&M personnel being based in Deadhorse, Alaska, led principally to an estimation of the effects of causeways on water temperatures and salinities.

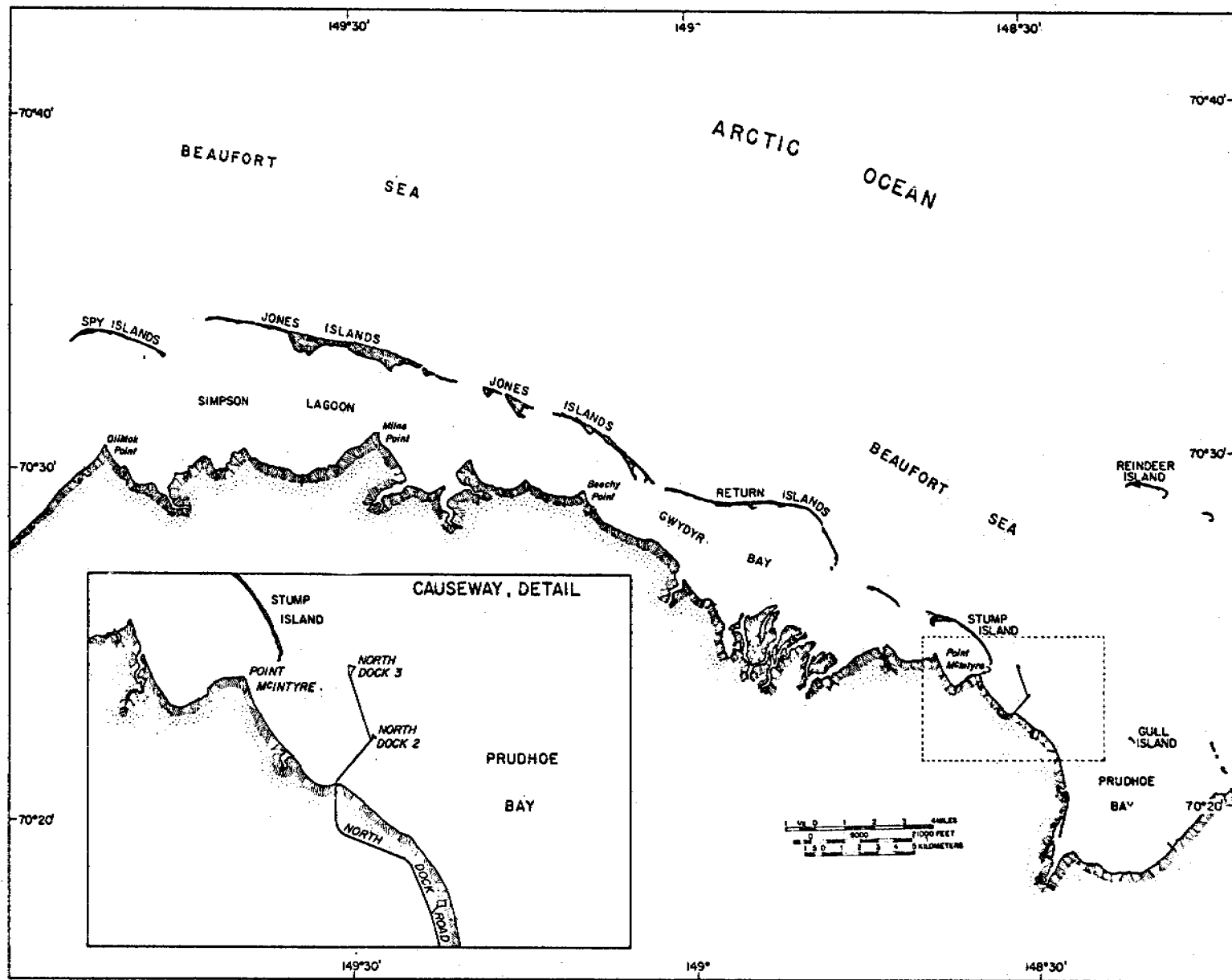


Figure 1. Map of Simpson Lagoon and Prudhoe Bay. The inset shows details of the causeway.

## Investigations: 1978/1979

The investigations to be described here, that is to say conducted since February 1978, have principally been in response to requests for assistance of one type or another; as such, "research" has been kept to a minimum. The work can once again be divided into two areas: modeling and field measurements.

A variety of modeling experiments, described in the following section, have been conducted. The three-dimensional numerical model of Simpson Lagoon was improved, and, after a somewhat unexpected request from the Bureau of Land Management, was applied to the Beaufort Sea coast for the purpose of trajectory computation. Two-dimensional modeling has also continued: studies of Simpson Lagoon have been conducted in order to ascertain the likely effects that certain scenarios involving barrier island changes will have on the lagoon flow regime, and efforts have been directed towards the development of a model of Simpson Lagoon that can respond to the hour-by-hour winds during any given month for which real wind data are available.

The 1978 field season (described in a later section) was planned so as to respond to previous criticisms concerning the lack of physical oceanographers working out of the same camp as the biologists. To this end personnel from Texas A&M were present at the Milne Point camp from 20 July to 22 August 1978. In order to provide other disciplines with timely and accurate data, a small offshore structure was built so as to hold a capacitance wave gauge, an E-M current sensor, and a conductivity/temperature probe. The first two of these sensors were connected through appropriate electronic packages to strip chart recorders and to a micro-processor data acquisition system. In addition

near-synoptic lagoon surveys were carried out by rotary- and fixed-wing aircraft, radio-beacon equipped drifters were tracked by RDF sets, and a small experiment was conducted in order to compare the range of salinities and temperatures to be expected on either side of Milne Point (of relevance to causeway studies). For the possible interest of the reader, an annotated photographic summary depicting life and work in Prudhoe Bay and in the field is shown in Appendix A.

## Numerical Modeling Experiments

### Three-Dimensional Modeling

The three-dimensional Simpson Lagoon model (described in the first annual report) was upgraded by including velocity shear in the vertical eddy viscosity term. An experiment was conducted with

$$A_{kz} = l_0^2 \left| \frac{\partial Q}{\partial z} \right| ,$$

where  $Q$  is the total speed, and the mixing length  $l_0$  is defined as

$$l_0 = k_0 (H-z) z/H ,$$

where  $k_0$  is von Karman's constant,  $H$  is the total mean depth and  $z$  is the elevation above the bottom.

The resulting variation of the eddy viscosity with depth is shown in Figure 2. Figures 3 and 4 show, respectively, the Milne Point and Point Storkersen longshore current cross sections in the vertical. When compared with the corresponding figures (12 and 13) in the first annual report, the effect of the depth-varying eddy viscosity may be seen to have been (for the Milne Point cross section) as one of increasing the rate of decay of velocity with depth. A jet has formed off Point Storkersen in the variable eddy viscosity case, the reason for which is not known.

At the request of the BLM-OCS Anchorage office, the three-dimensional model discussed above was applied to the nearshore Beaufort Sea area in order to obtain surface wind-driven flows for water trajectory studies. The region modeled extended from Brownlow Point (to the east of Flaxman Island) to Oliktok Point (to the east of the Colville river delta). Figure 5 shows the



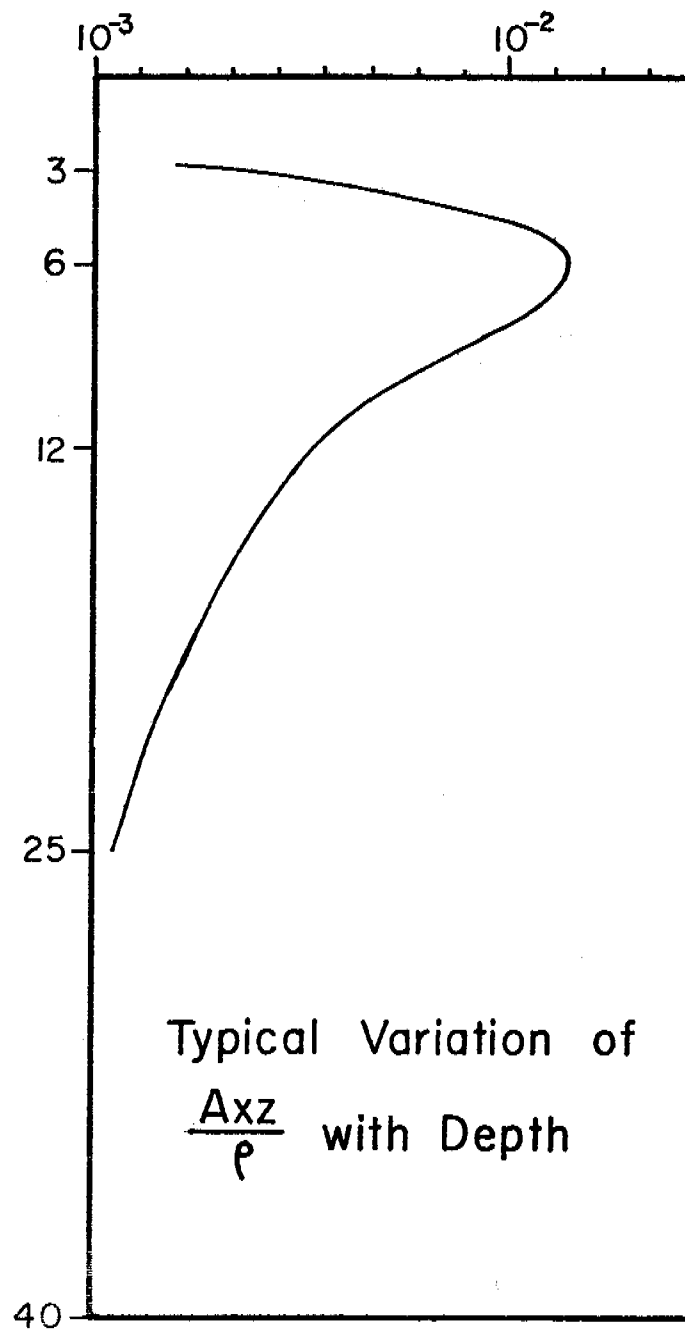


Figure 2. Typical variation of the eddy viscosity with depth.

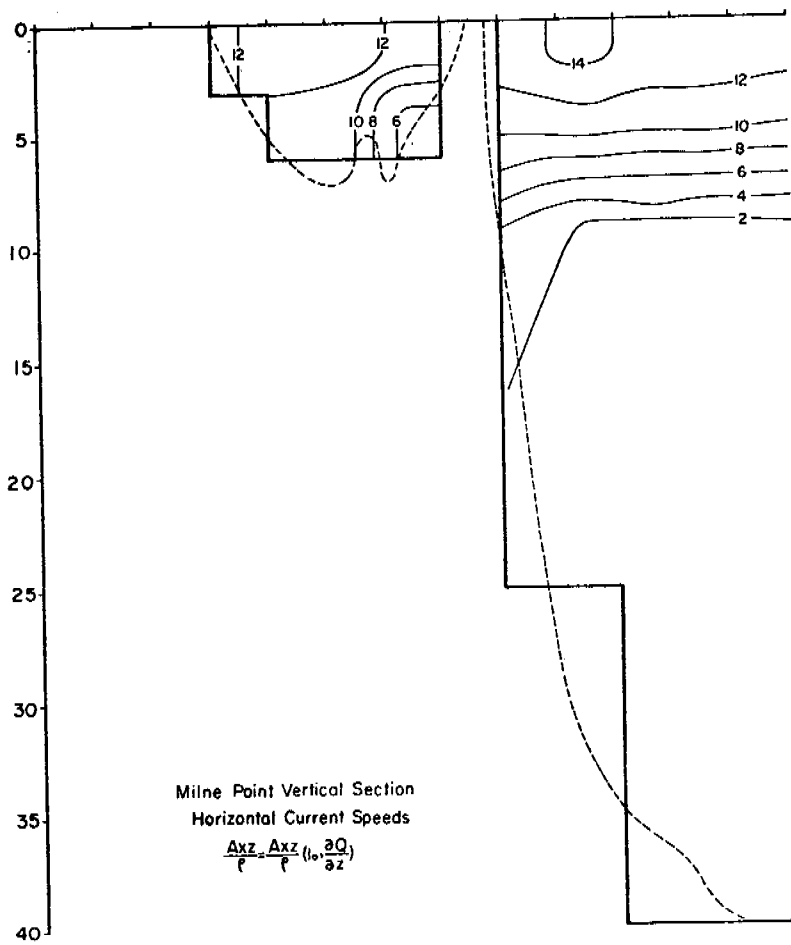


Figure 3. Computed alongshore current field off Milne Point.

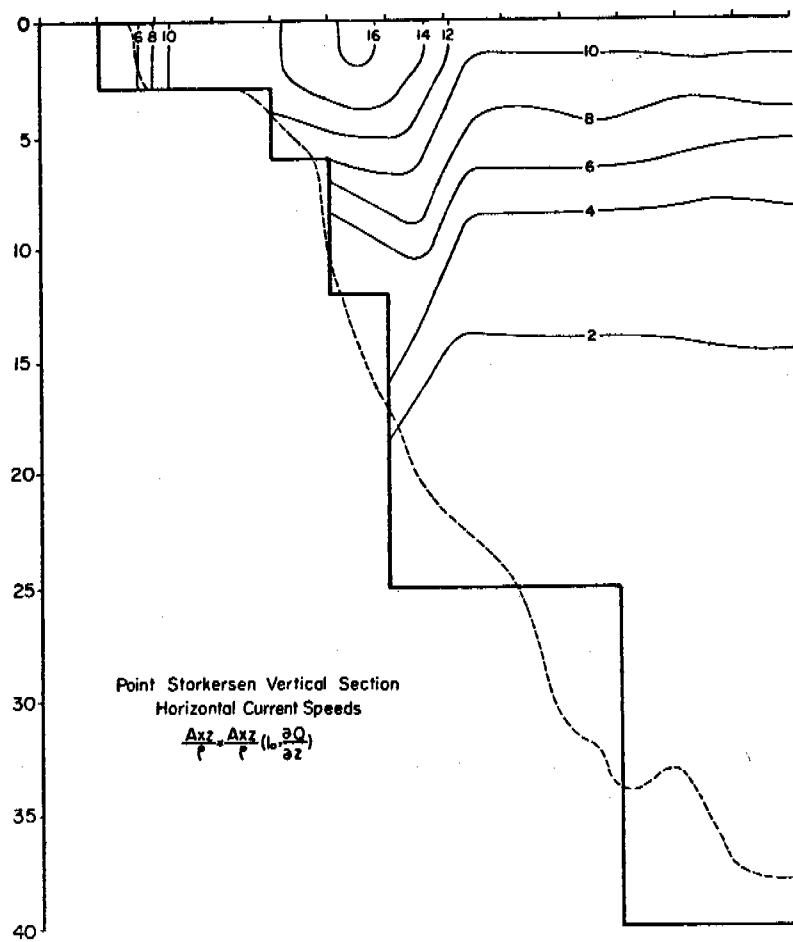


Figure 4. Computed alongshore current field off Point Storkersen.



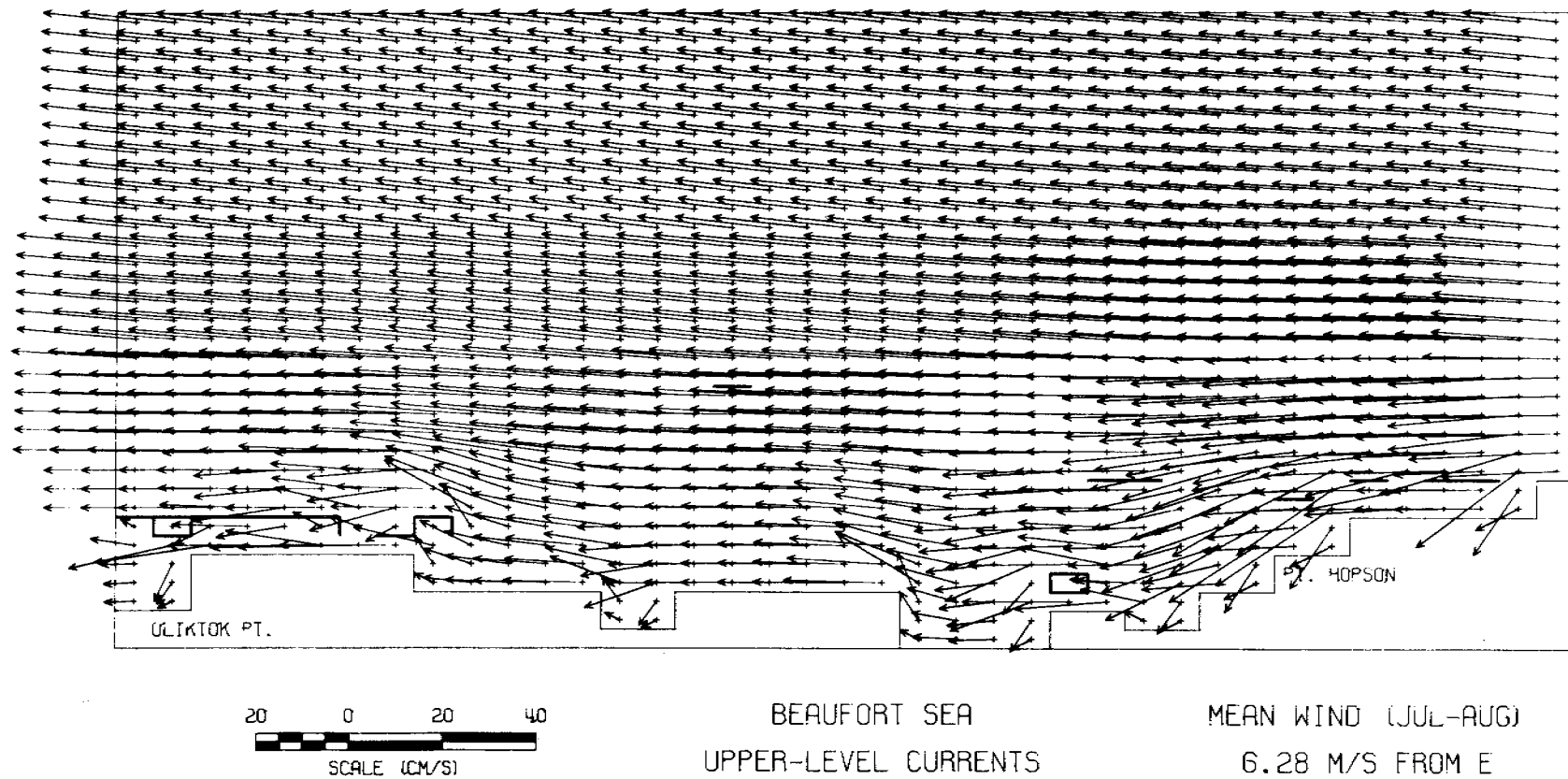


Figure 6. Beaufort Sea 3-D model surface current field  
( $6.28 \text{ m s}^{-1}$  from E).

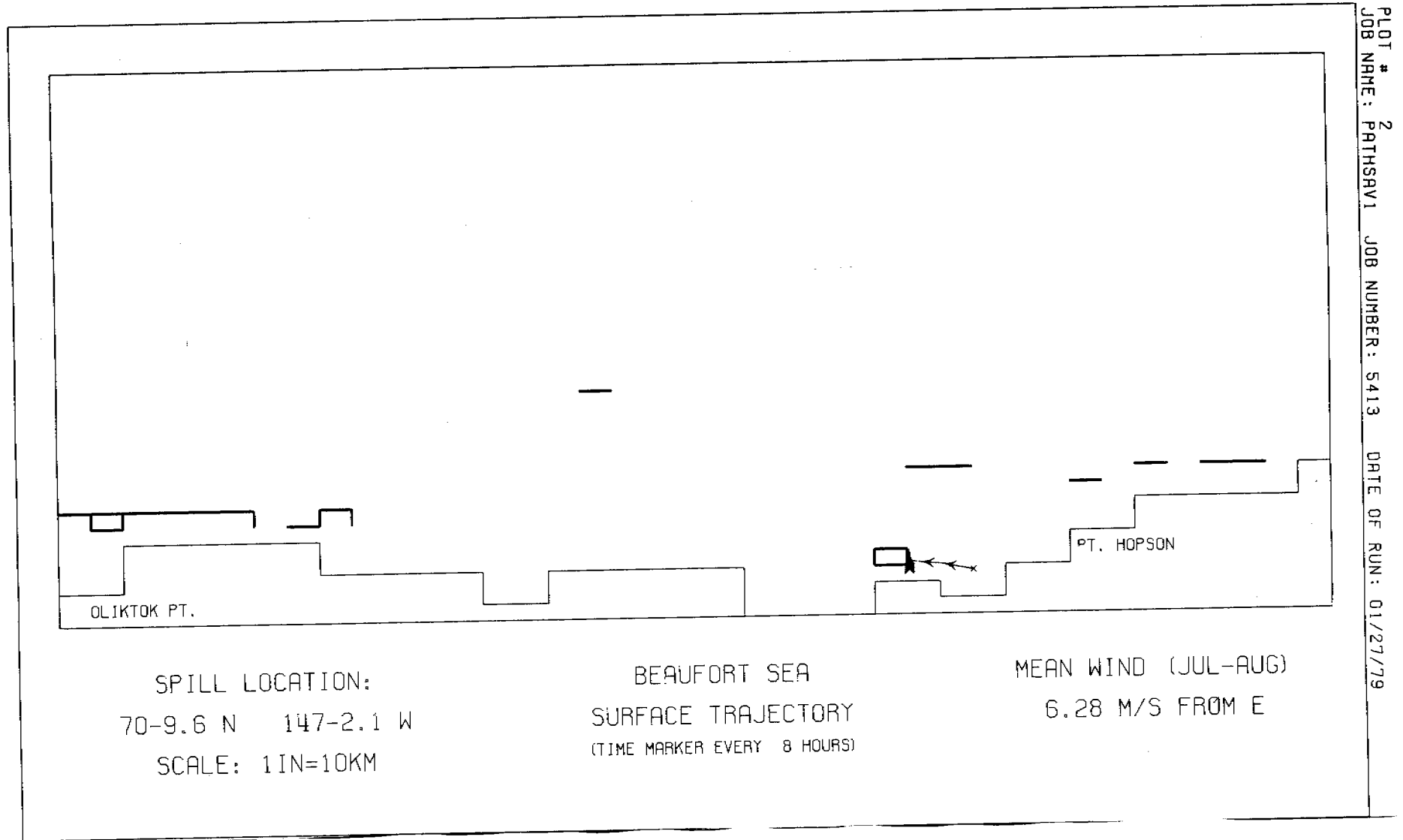


Figure 7. Beaufort Sea 3-D trajectories ( $6.28 \text{ m s}^{-1}$  from E).

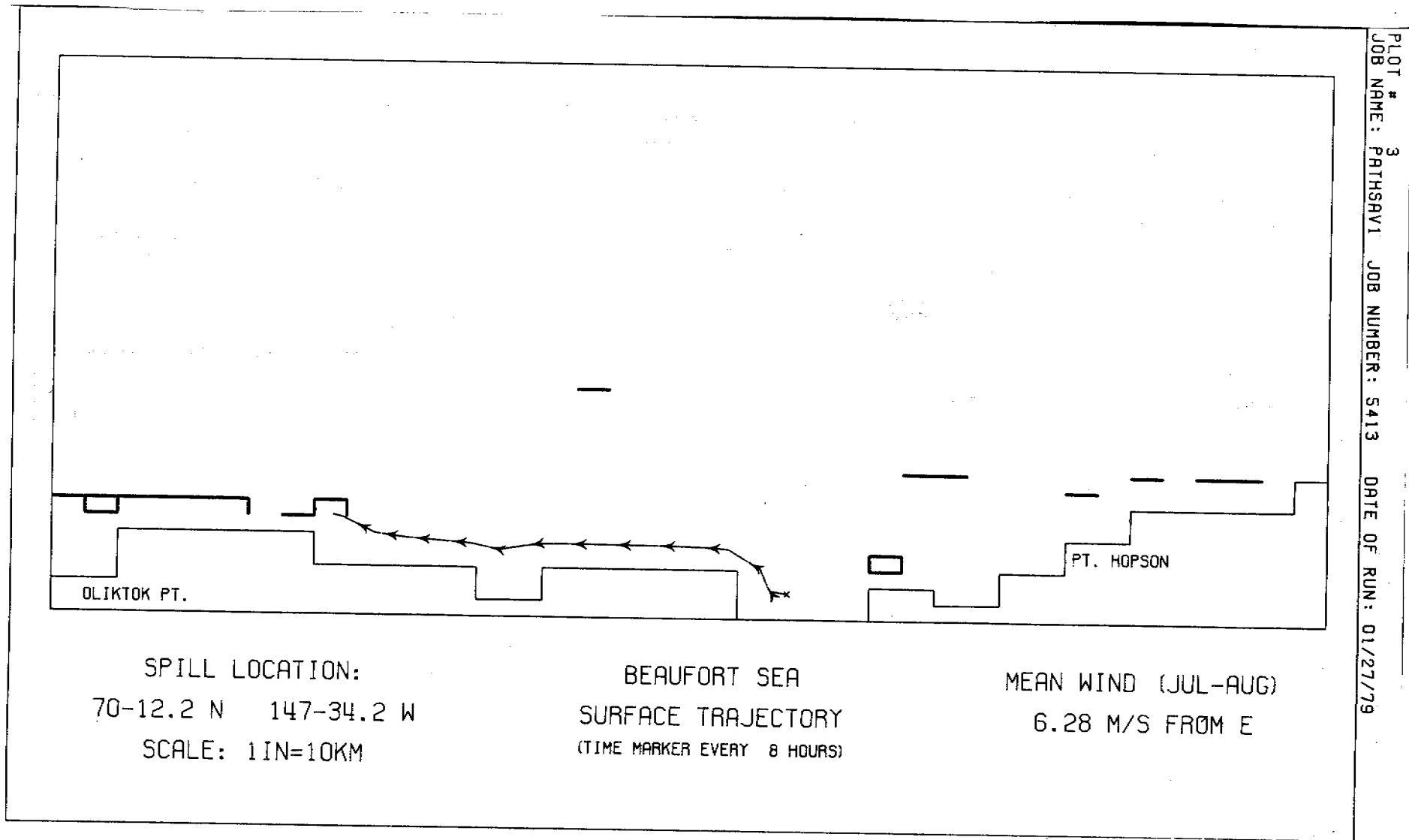


Figure 8. Beaufort Sea 3-D trajectories ( $6.28 \text{ m s}^{-1}$  from E).

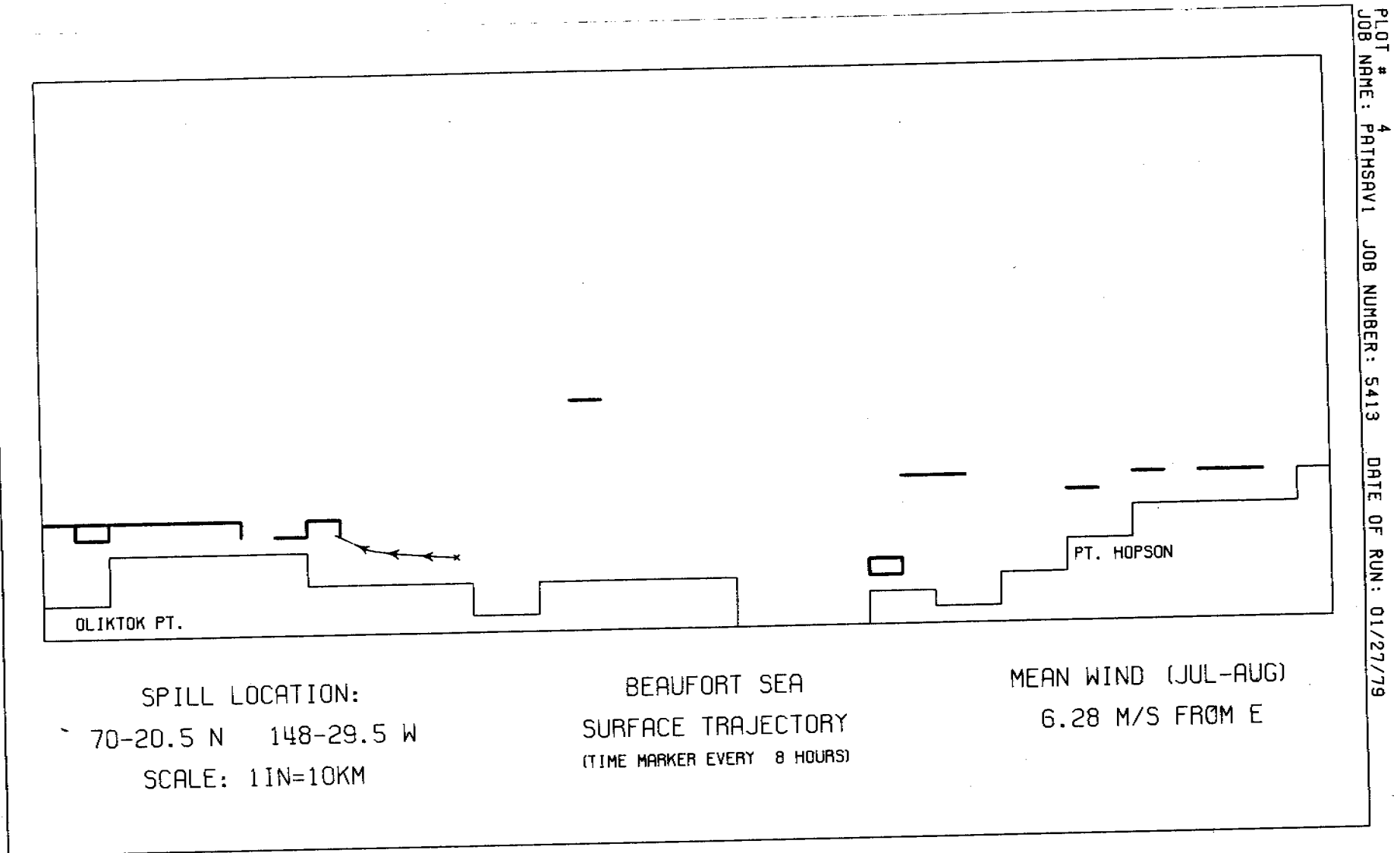
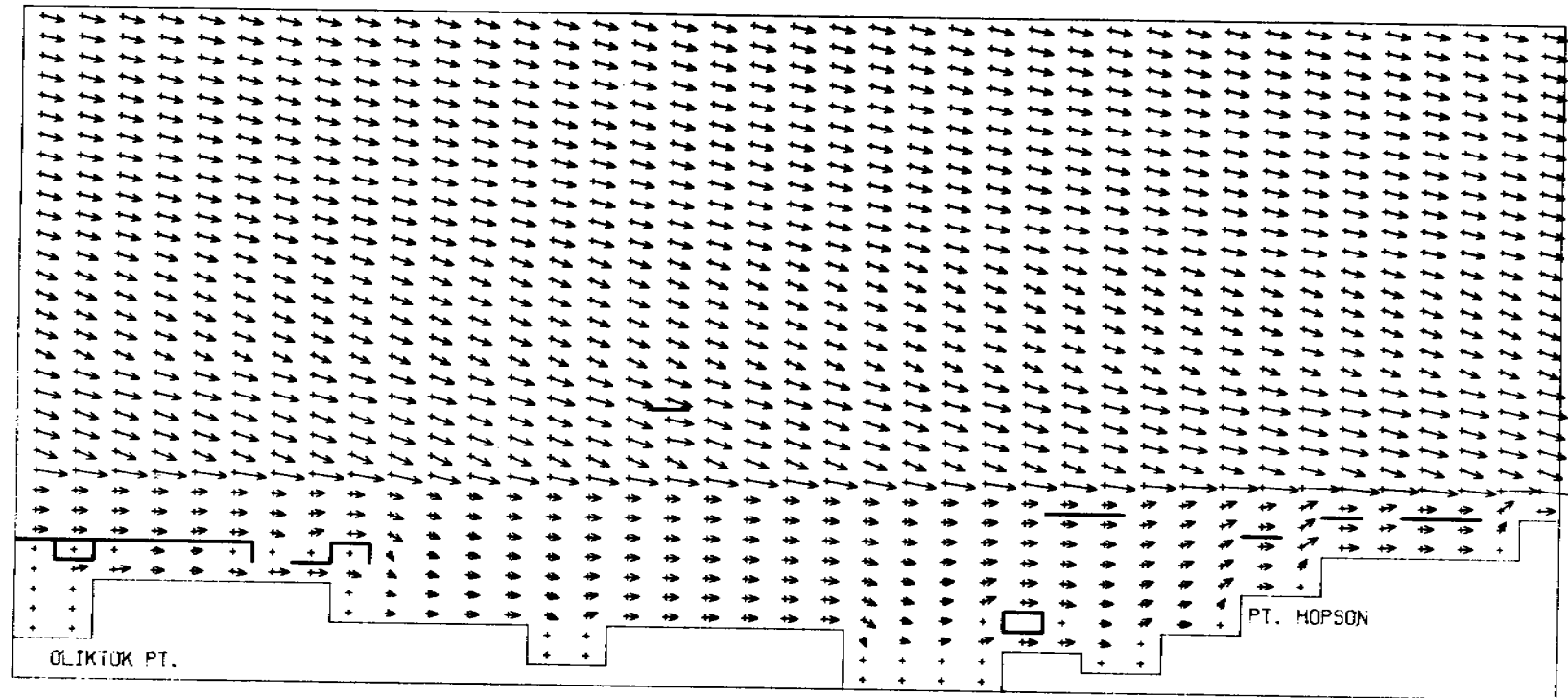


Figure 9. Beaufort Sea 3-D trajectories ( $6.28 \text{ m s}^{-1}$  from E).





20 0 20 40  
SCALE (CM/S)

BEAUFORT SEA  
UPPER-LEVEL CURRENTS

MEAN WIND (JUL-AUG)  
2.68 M/S FROM W

Figure 10. Beaufort Sea 3-D model surface current field  
( $2.68 \text{ m s}^{-1}$  from W).

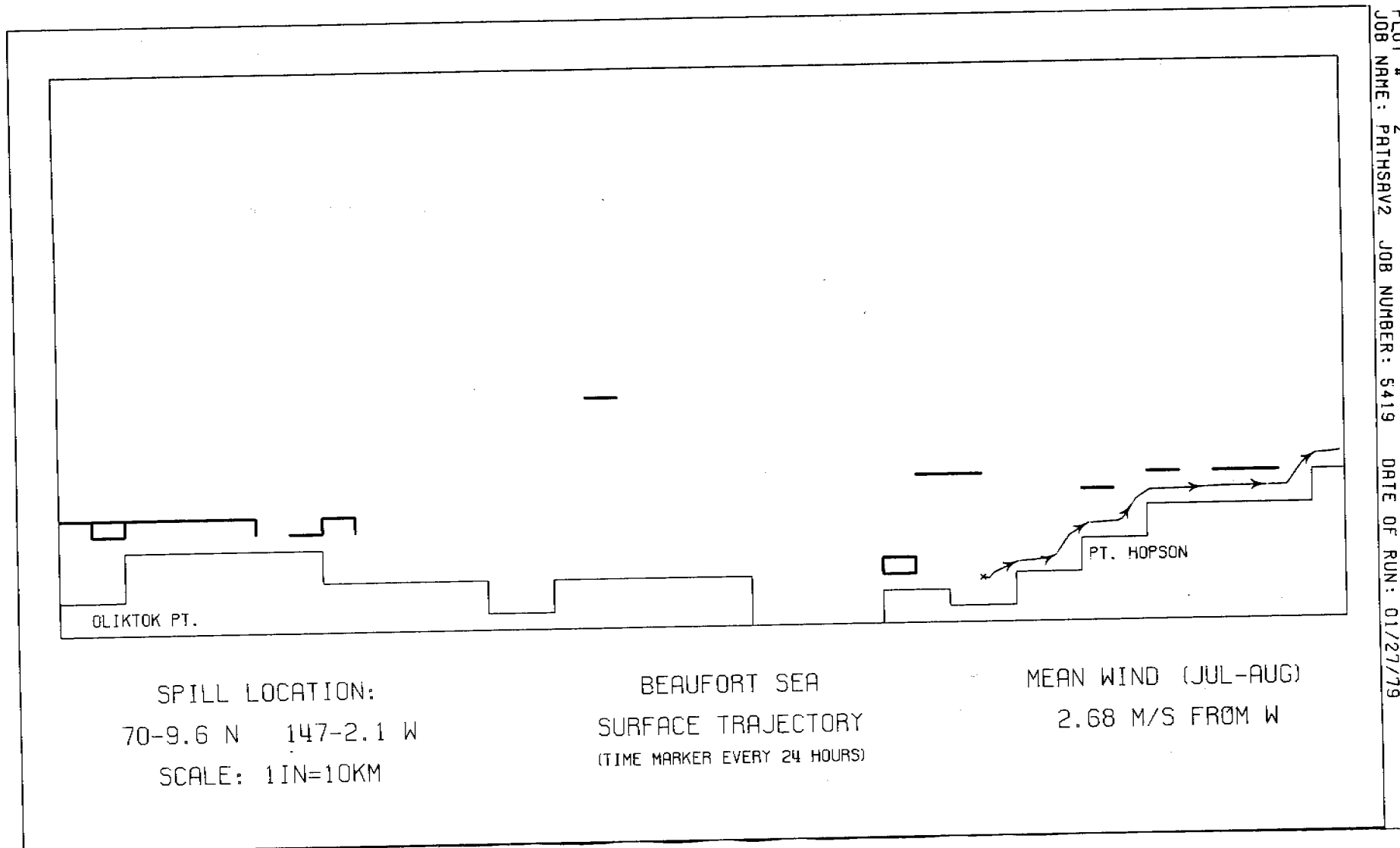
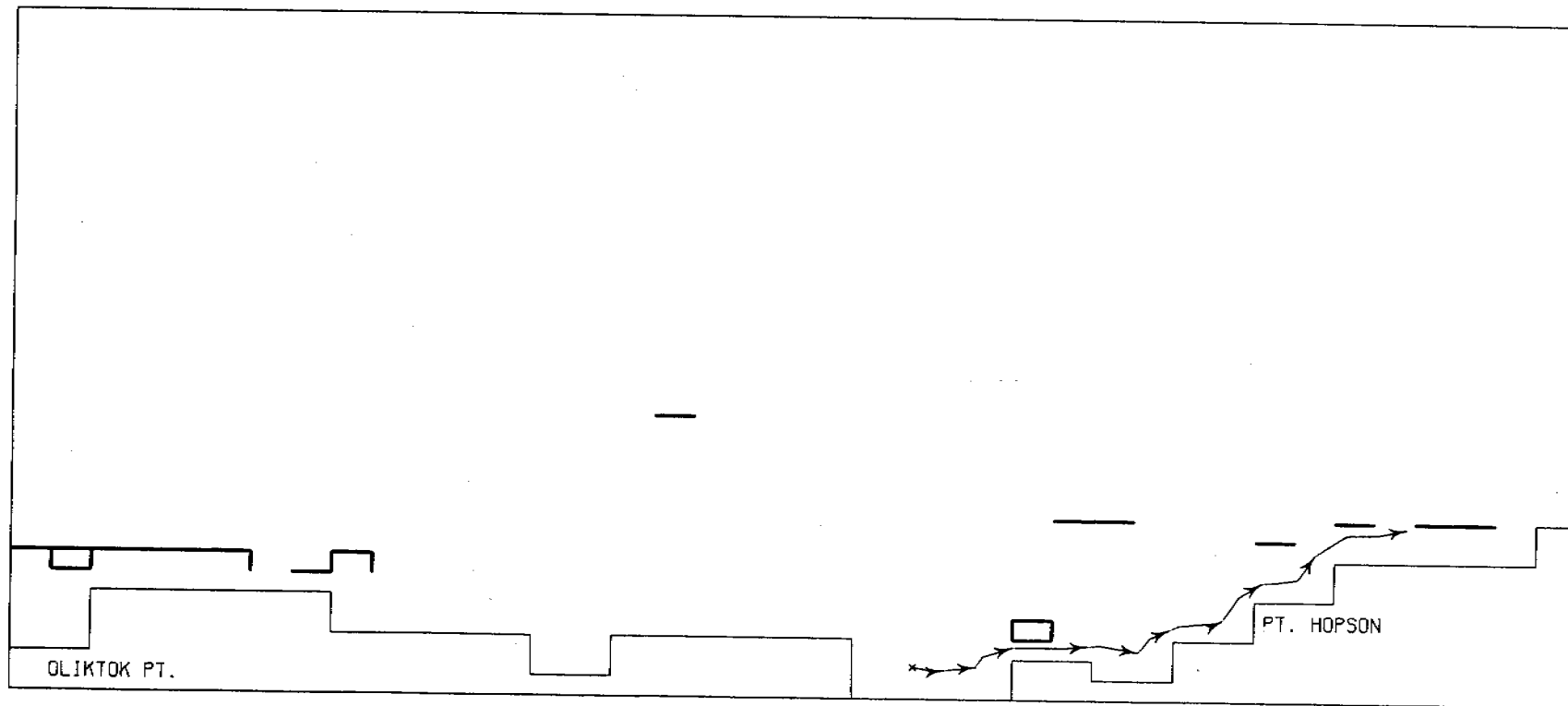


Figure 11. Beaufort Sea 3-D trajectories ( $2.68 \text{ m s}^{-1}$  from W).



SPILL LOCATION:  
 70-12.2 N 147-34.2 W  
 SCALE: 1IN=10KM

BEAUFORT SEA  
 SURFACE TRAJECTORY  
 (TIME MARKER EVERY 24 HOURS)

MEAN WIND (JUL-AUG)  
 2.68 M/S FROM W

Figure 12. Beaufort Sea 3-D trajectories ( $2.68 \text{ m s}^{-1}$  from W).

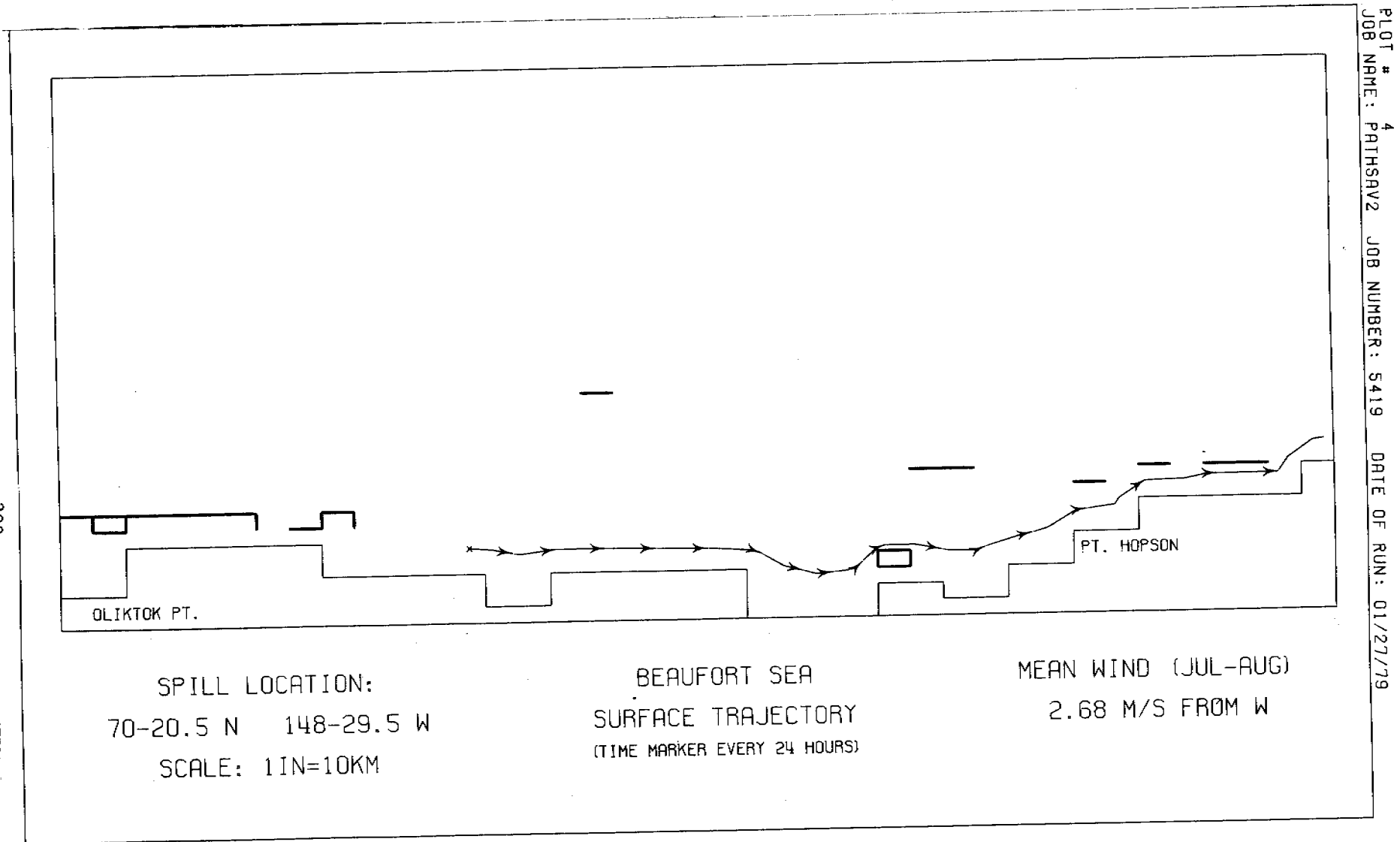


Figure 13. Beaufort Sea 3-D trajectories ( $2.68 \text{ m s}^{-1}$  from W).

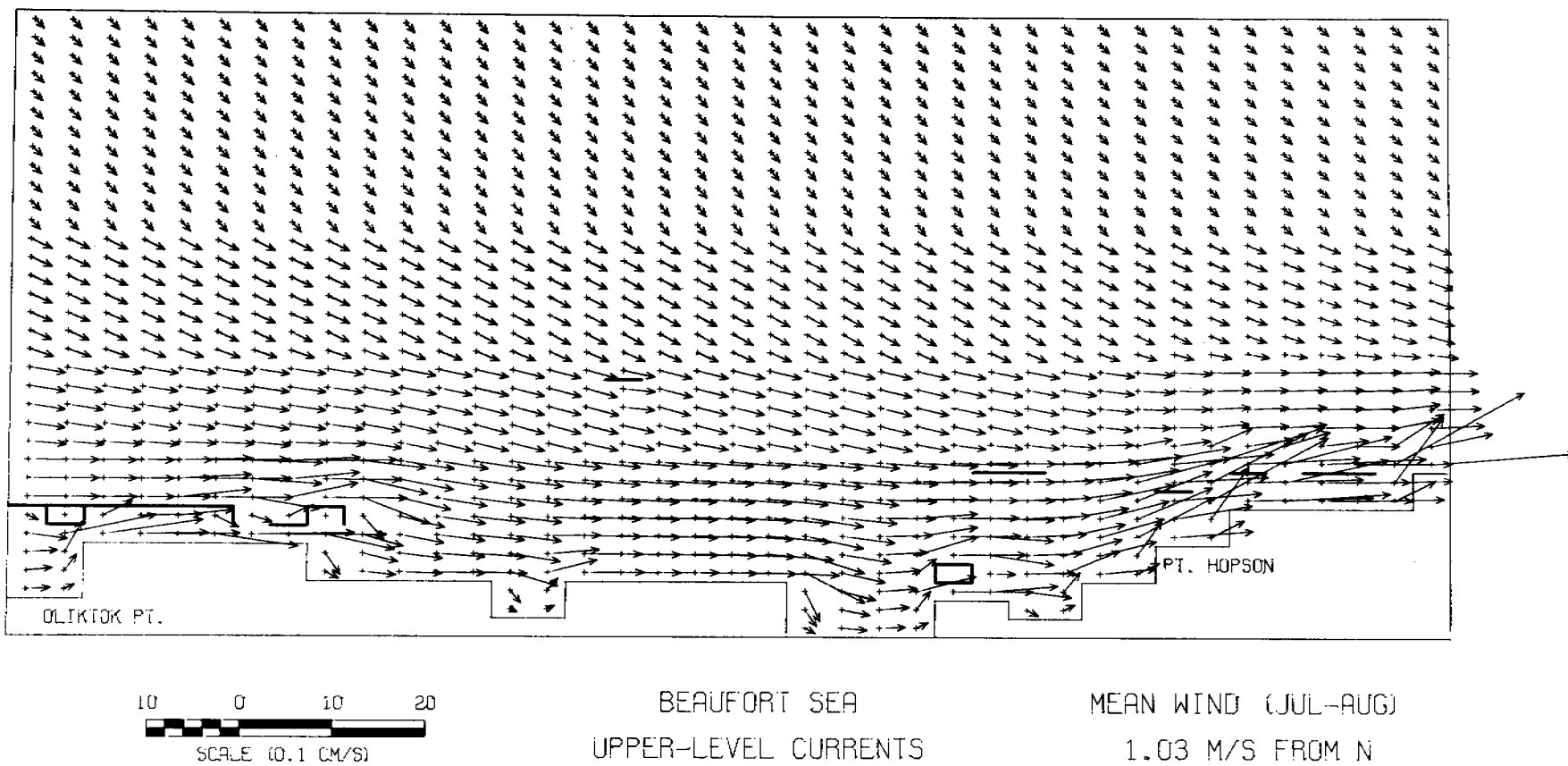


Figure 14. Beaufort Sea 3-D model surface current field  
( $1.03 \text{ m s}^{-1}$  from N).

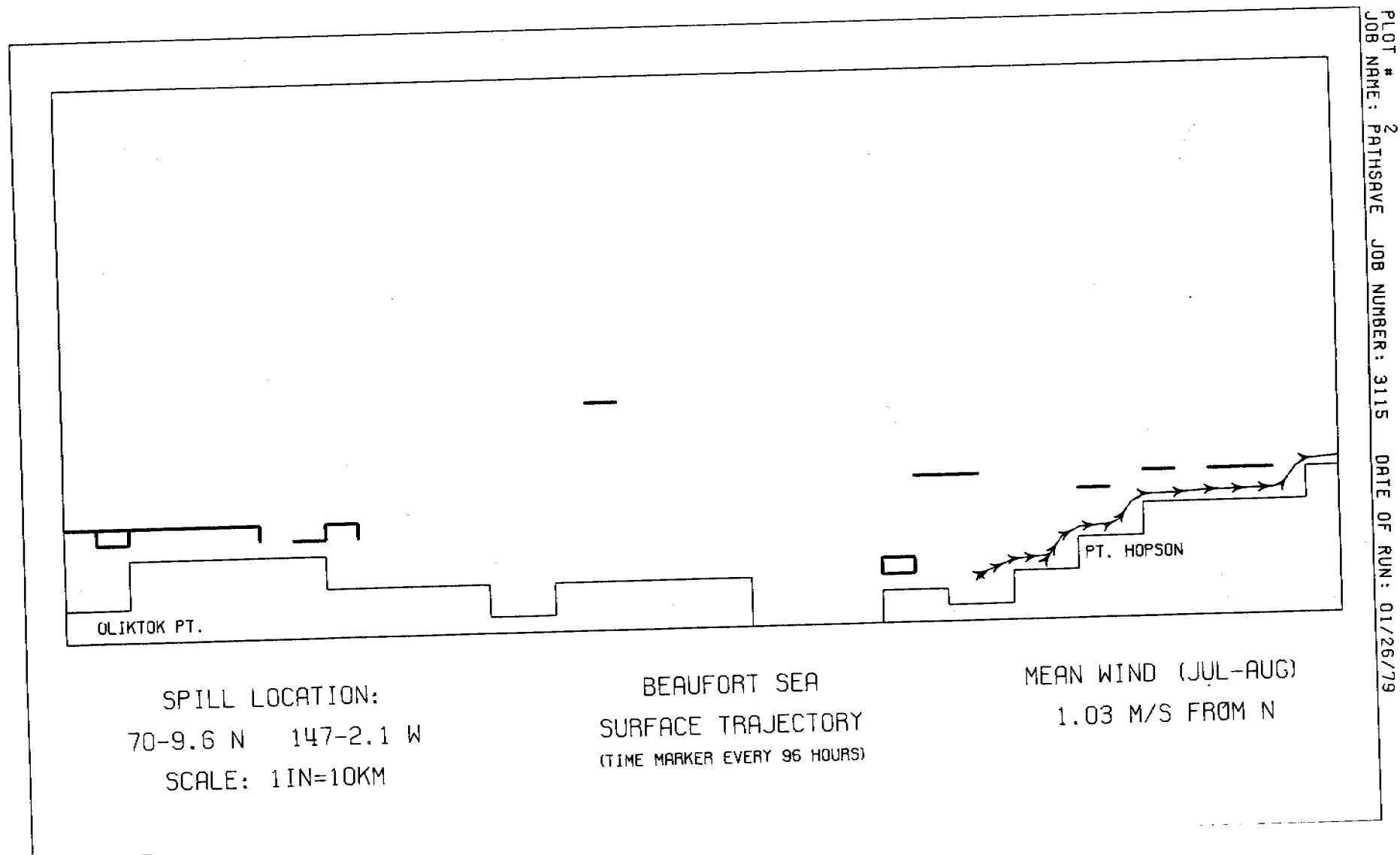


Figure 15. Beaufort Sea 3-D trajectories ( $1.03 \text{ m s}^{-1}$  from N).

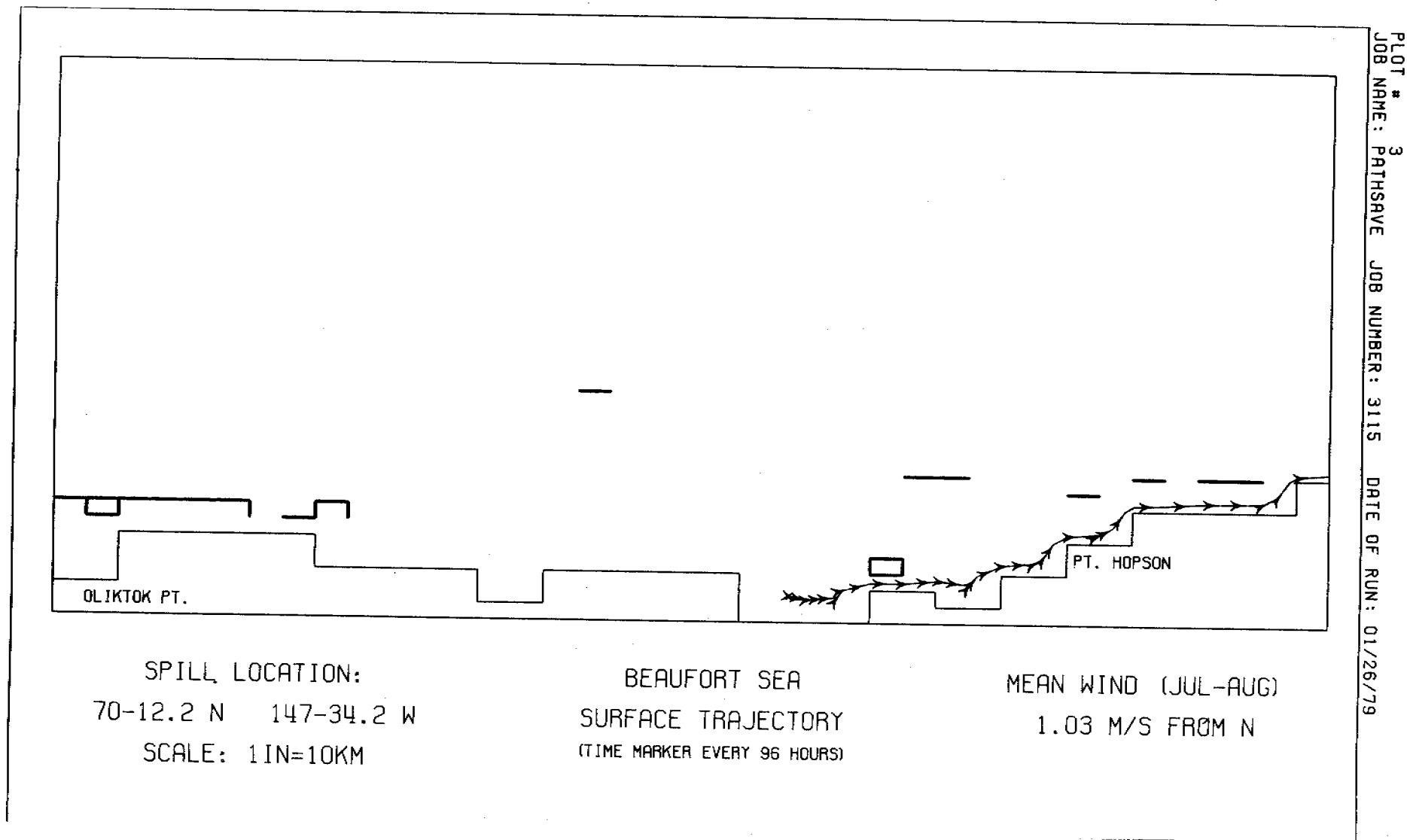


Figure 16. Beaufort Sea 3-D trajectories ( $1.03 \text{ m s}^{-1}$  from N).

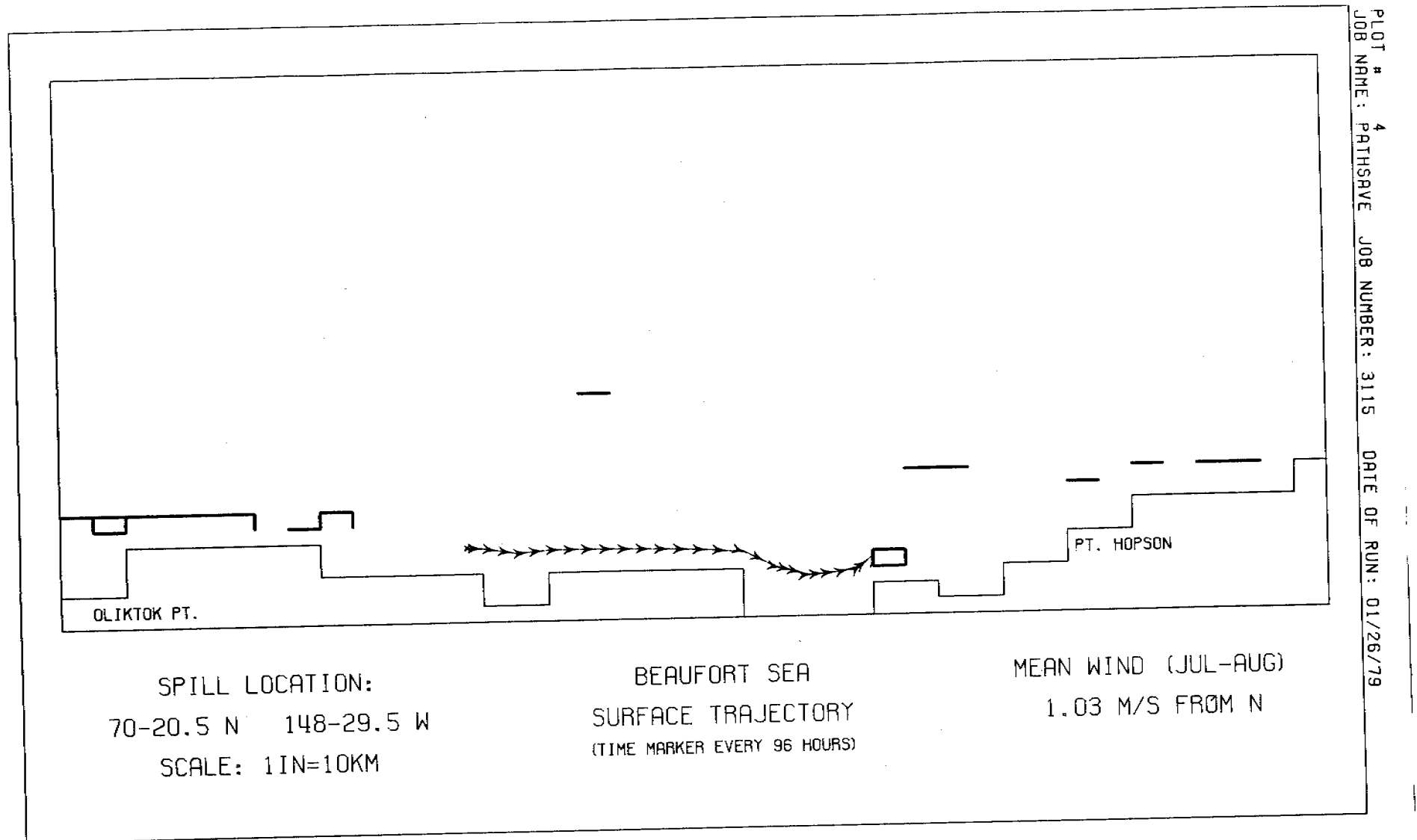


Figure 17. Beaufort Sea 3-D trajectories ( $1.03 \text{ m s}^{-1}$  from N).



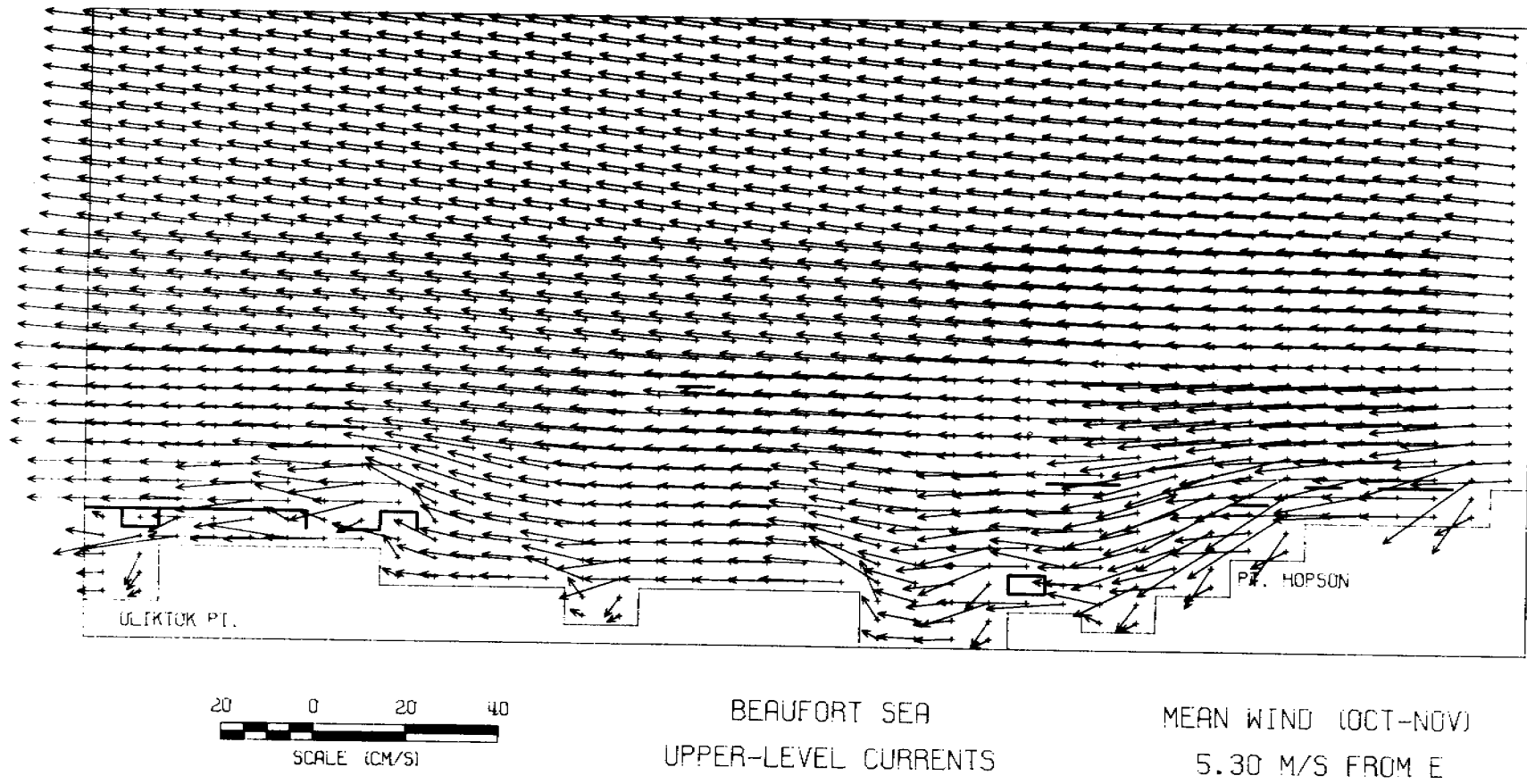


Figure 18. Beaufort Sea 3-D model surface current field  
( $5.30 \text{ m s}^{-1}$  from E).

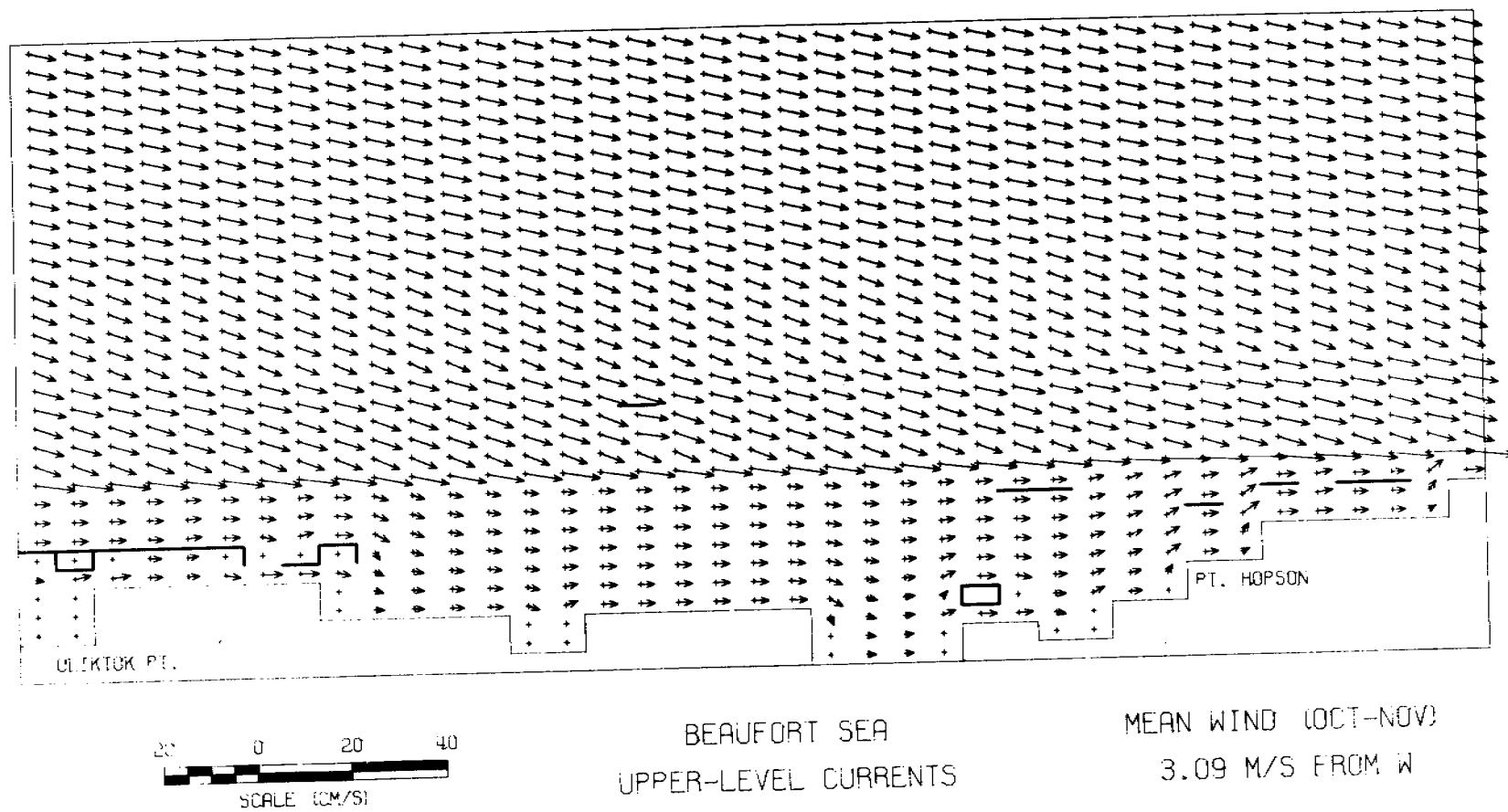
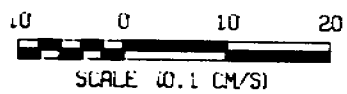
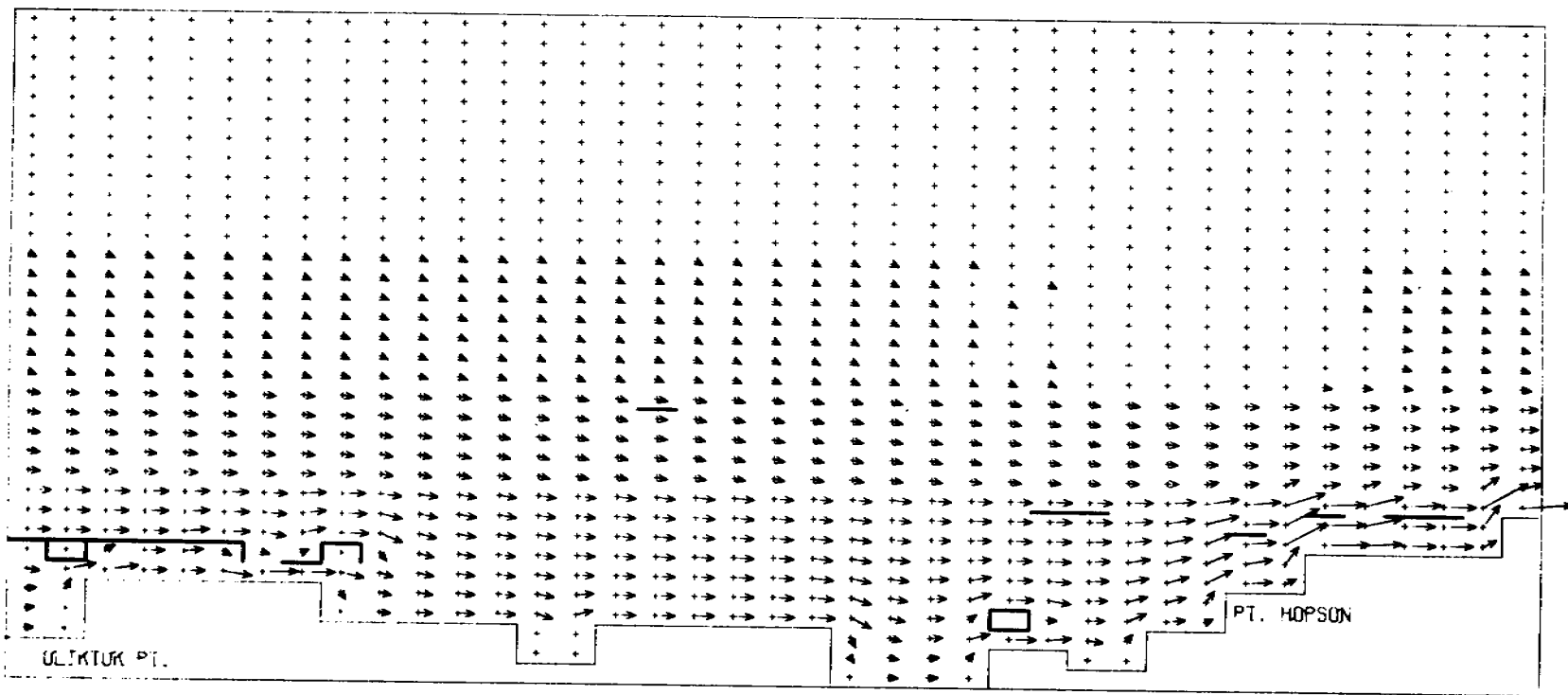


Figure 19. Beaufort Sea 3-D model surface current field  
( $3.09 \text{ m s}^{-1}$  from W).



BEAUFORT SEA  
UPPER-LEVEL CURRENTS

MEAN WIND (OCT-NOV)  
0.57 M/S FROM N

Figure 20. Beaufort Sea 3-D model surface current field,  
( $0.57 \text{ m s}^{-1}$  from N).

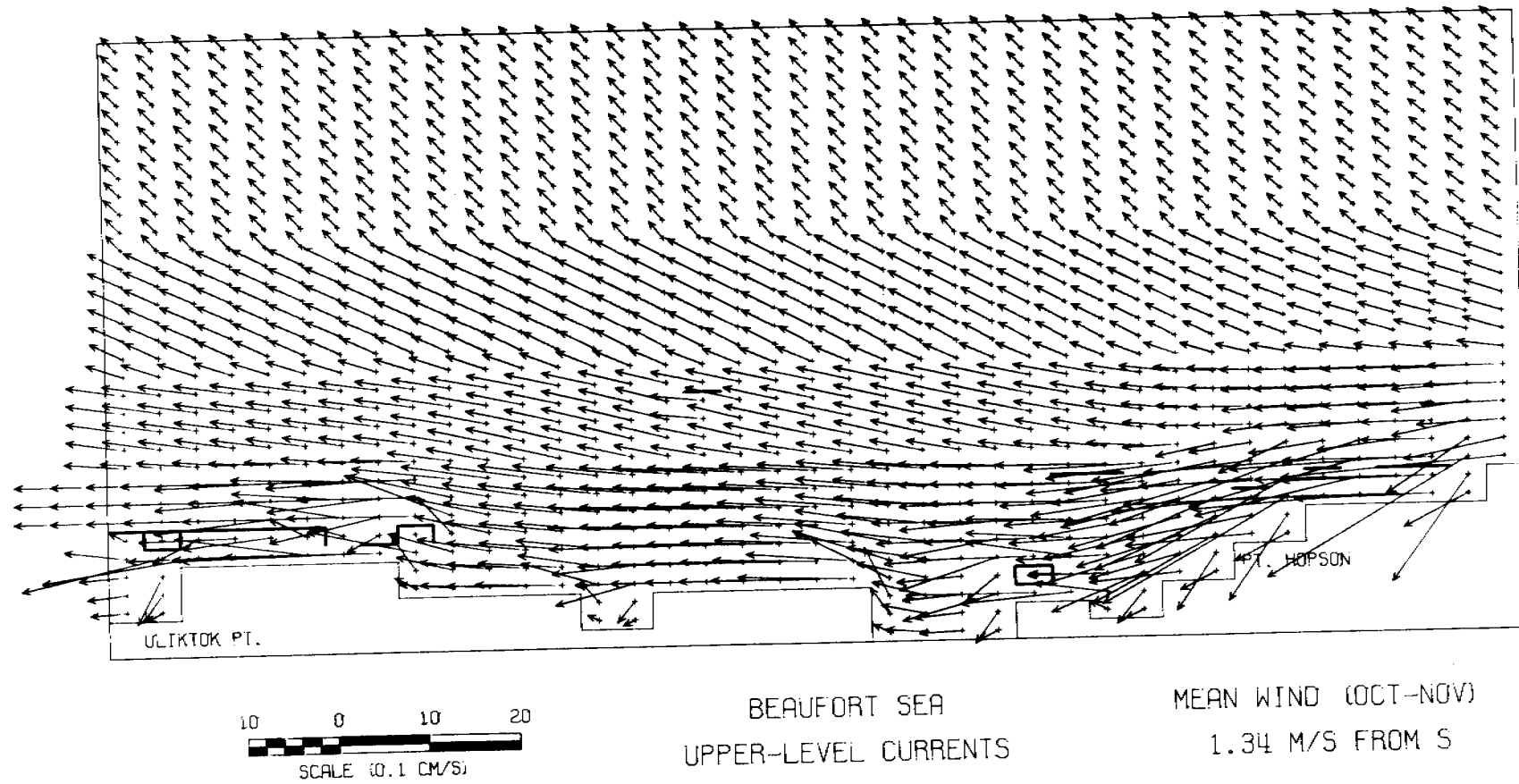


Figure 21. Beaufort Sea 3-D model surface current field  
( $1.34 \text{ m s}^{-1}$  from S).

general location of the region. The grid size used was 4 km x 2 km, with the larger dimension being in the east-west direction. The original grid used for the two-dimensional Beaufort Sea model (a 2 km x 2 km grid) is also shown. Currents were computed for 4 levels, the separation between each level being 5 fathoms.

Average wind speeds were used for the two periods studied: July - August, October-November. The eight wind directions studied were the eight points of the compass. Ten starting points for the trajectories as shown by dots in Figure 5, were specified by BLM-OCS. Some of the results, the unscheduled computation of which caused a severe financial strain on the project, are shown in Figures 6 through 21. It should be noted that owing to the discrete nature of the model and of the requirement for a zero normal current component on every land boundary, it is not in general possible for a water parcel trajectory to go to the shore. When these trajectories are used to provide estimates for oil spill trajectories, it is essential that the spreading nature of an oil spill be taken into account. Furthermore oil may move faster than the currents predicted for the depth-averaged surface layer.

#### Two-Dimensional Modeling

Two-dimensional modeling has chiefly been concentrated on the Simpson Lagoon region. The 1 km x 2 km numerical grid for this region is shown in Figure 22. The model has been described in the first annual report. Numerical experiments with this model have been of two types: scenary studies using steady winds, and verification studies using time-varying winds.

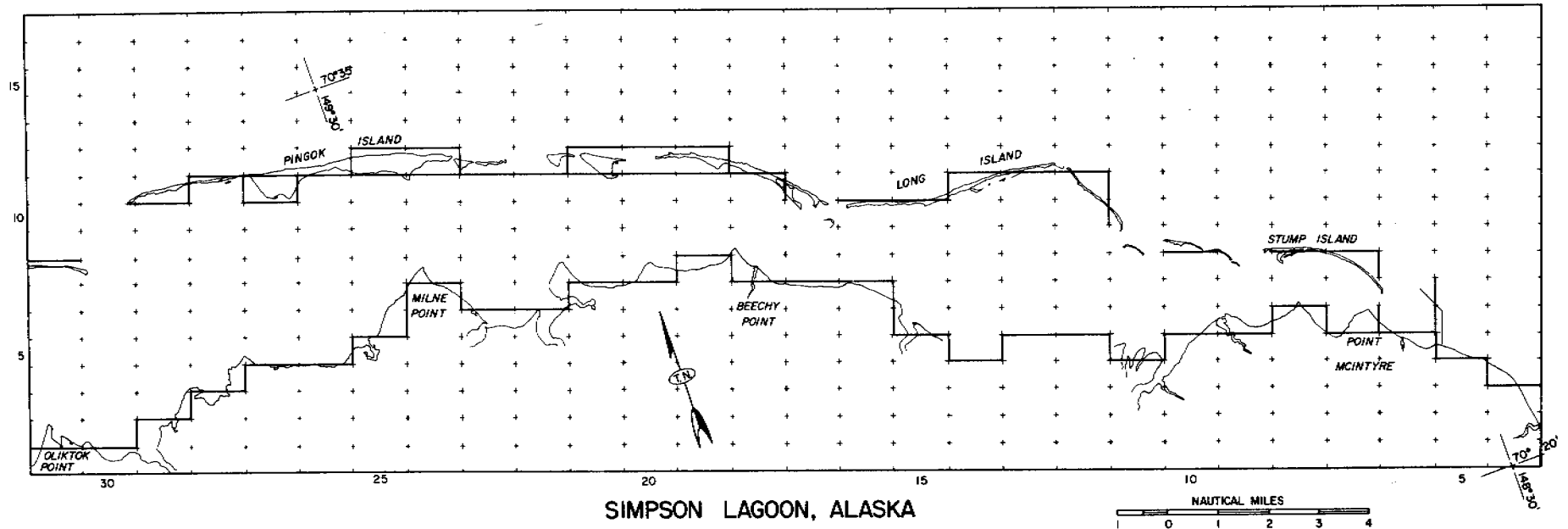


Figure 22. Grid scheme for Simpson Lagoon, Alaska. Crosses denote corners of 1 km x 2 km computational rectangles.

#### A. Scenario Modeling

At the request of LGL (the company responsible for biological investigations) and the Institute of Animal Resource Ecology, University of British Columbia (the group responsible for ecological modeling), studies were undertaken to estimate certain parameters that would prevail were the Simpson Lagoon barrier islands to be altered as a consequence of offshore development. Three parameters were requested: average nearshore currents, average currents in the center of the lagoon, and the rate of flow of water into and out of the lagoon. These parameters were requested for a total of 12 wind conditions for each of two scenarios.

The two scenarios that were arrived at after consultation with members of the oil industry were as follows:

Scenario #1. The barrier islands connected by a road from Point McIntyre on the mainland to the western end of Pingok Island. The deepest lagoon entrance, between Long Island and Egg Island, was assumed to be bridged.

Scenario #2. As for scenario #1, but with an additional causeway (containing a 1 km bridged gap) between Milne Point and Pingok Island.

The alterations that resulted to the original grid are shown in Figures 23 and 24.

As with the original computer runs, described in the first annual report, each computer run was for a period of 8 hours, real time. The steady wind used in each case had superimposed on it a ramp function that

# SCENARIO ONE

XXX DENOTES BARRIERS ADDED TO MODEL

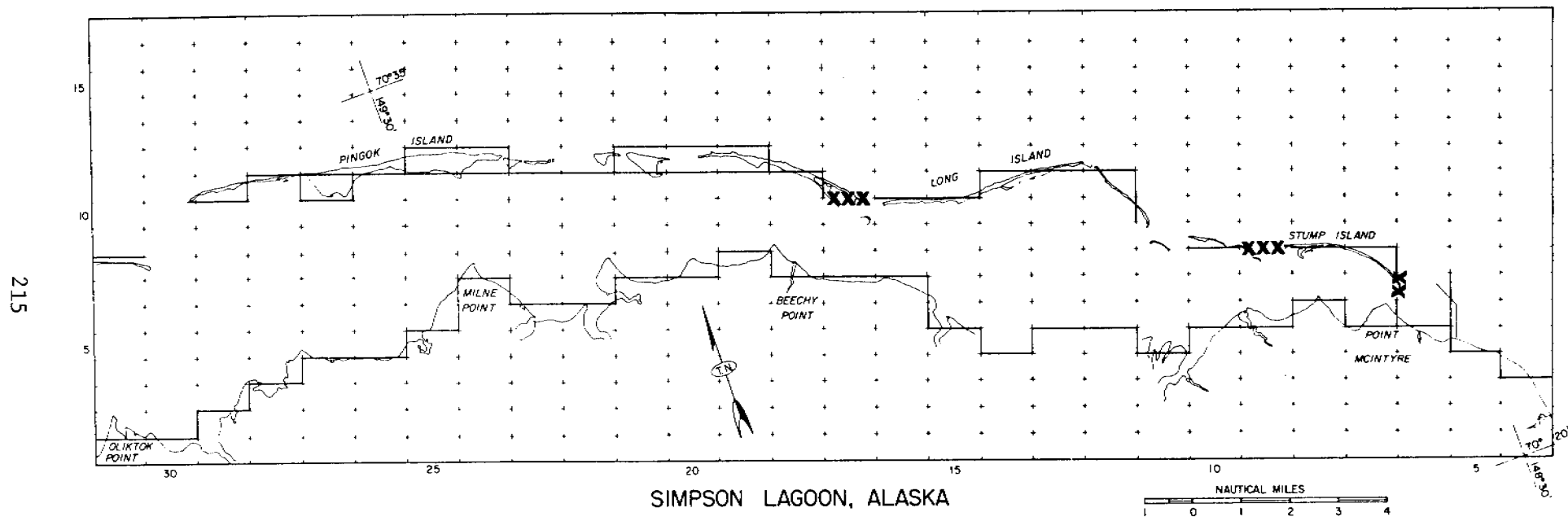


Figure 23. Grid scheme for Simpson Lagoon, Alaska: Scenario One barrier additions.



# SCENARIO TWO

XXX DENOTES BARRIERS ADDED TO MODEL

216

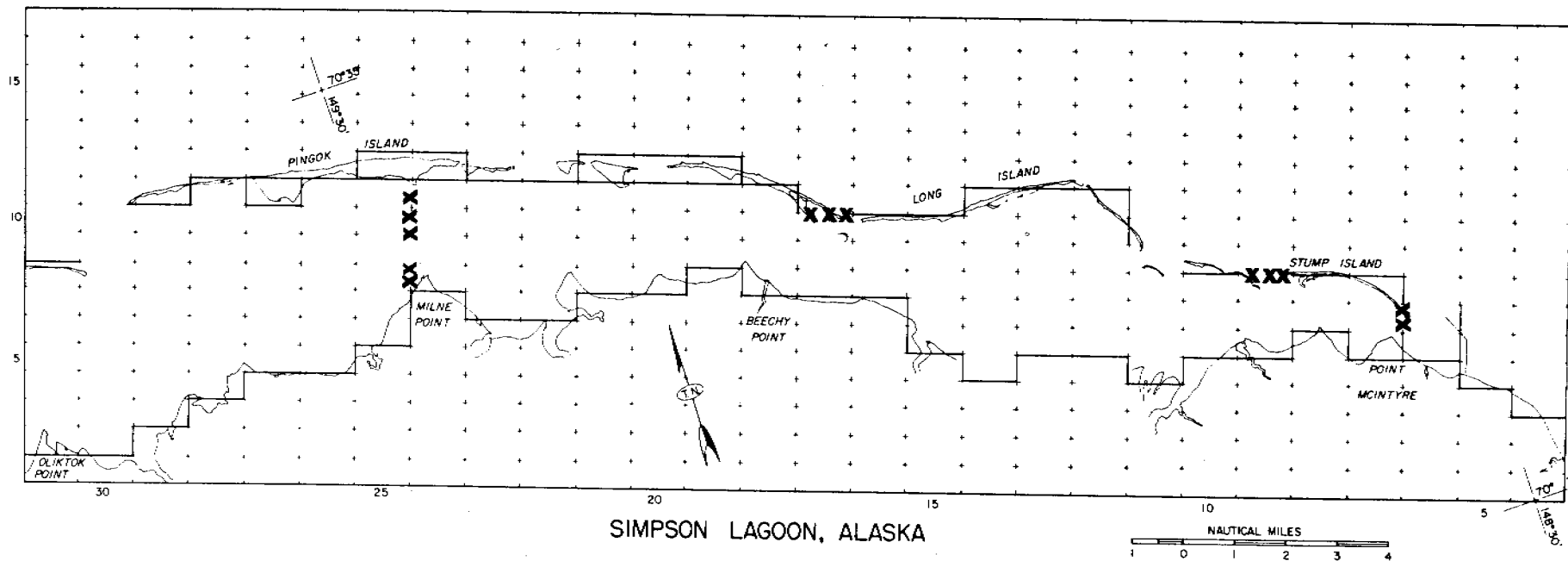


Figure 24. Grid scheme for Simpson Lagoon, Alaska: Scenario Two barrier additions.

resulted in a linear increase of the wind from zero to full speed over 4 hours. Three wind directions were modeled: wind from ENE, WSW, and NW. Although results for wind speeds of 5, 10, 15 and 20 m s<sup>-1</sup> had been requested, economic constraints dictated that runs be made only for the 10 and 20 m s<sup>-1</sup> speeds; the parameter requested could easily be obtained by linear interpolation.

The results of the 12 runs, extended by the inferred values, are shown in Tables 1 and 2; the tables are largely self-explanatory. The tables can be effectively summarized by commenting that, within the rather crude limitations of the modeling undertaken, the effects of scenarios 1 and 2 are, respectively, to reduce the daily flow through the lagoon to 90% and 80% of the values obtained with the original grid (with the causeway but no other man-made changes).

#### B. Variable-Wind Modeling

After discussions with OCSEAP in Boulder, Colorado, funds for an extra month of studies were made available to Kinnetic Laboratories Inc. for the modification and computations necessary to run the two-dimensional numerical model with real, variable winds provided by the University of Washington.

The wind data used (Cottle Island winds) were provided in the form of wind speed and direction measured 3 hours apart during the 1978 summer field season. Upon request, KLI received hourly winds for the period 1200 hrs August 20 to 0000 hrs August 22 1978 --- a period of special interest owing to data from a drifter experiment being available for the same period. The model was thus adapted as follows:

Table 1. Simpson Lagoon 2-D Modeling Results  
Scenario #1

Wind Direction (from)	Wind Speed (ms <sup>-1</sup> )	Exchange Rate (hours)	Lagoon Flow (10 <sup>6</sup> m <sup>3</sup> day <sup>-1</sup> )	Longshore Current (ms <sup>-1</sup> )	Average Current (ms <sup>-1</sup> )
ENE*	5	137.8	54	0.10	0.14
ENE	10	69.8	107	0.19	0.27
ENE*	15	47.7	156	0.27	0.38
ENE	20	36.3	205	0.35	0.48
WSW*	5	130.5	57	0.10	0.14
WSW	10	65.4	114	0.19	0.27
WSW*	15	42.3	176	0.29	0.41
WSW	20	31.4	237	0.39	0.55
NW*	5	100.5	74	0.12	0.18
NW	10	50.3	148	0.23	0.35
NW*	15	31.3	238	0.35	0.53
NW	20	22.7	328	0.47	0.70

\*denotes inferred values

Table 2. Simpson Lagoon 2-D Modeling Results  
Scenario #2

Wind Direction (from)	Wind Speed (ms <sup>-1</sup> )	Exchange Rate (hours)	Lagoon Flow (10 <sup>6</sup> m <sup>3</sup> day <sup>-1</sup> )	Longshore Current (ms <sup>-1</sup> )	Average Current (ms <sup>-1</sup> )
ENE*	5	162.0	46	0.09	0.12
ENE	10	80.0	93	0.17	0.23
ENE*	15	53.9	138	0.25	0.34
ENE	20	41.0	182	0.33	0.44
WSW*	5	155.0	48	0.09	0.12
WSW	10	78.4	95	0.17	0.24
WSW*	15	52.0	143	0.27	0.37
WSW	20	39.2	190	0.36	0.50
NW*	5	122.0	61	0.11	0.15
NW	10	60.8	122	0.21	0.30
NW*	15	39.4	189	0.32	0.47
NW	20	29.2	255	0.42	0.64

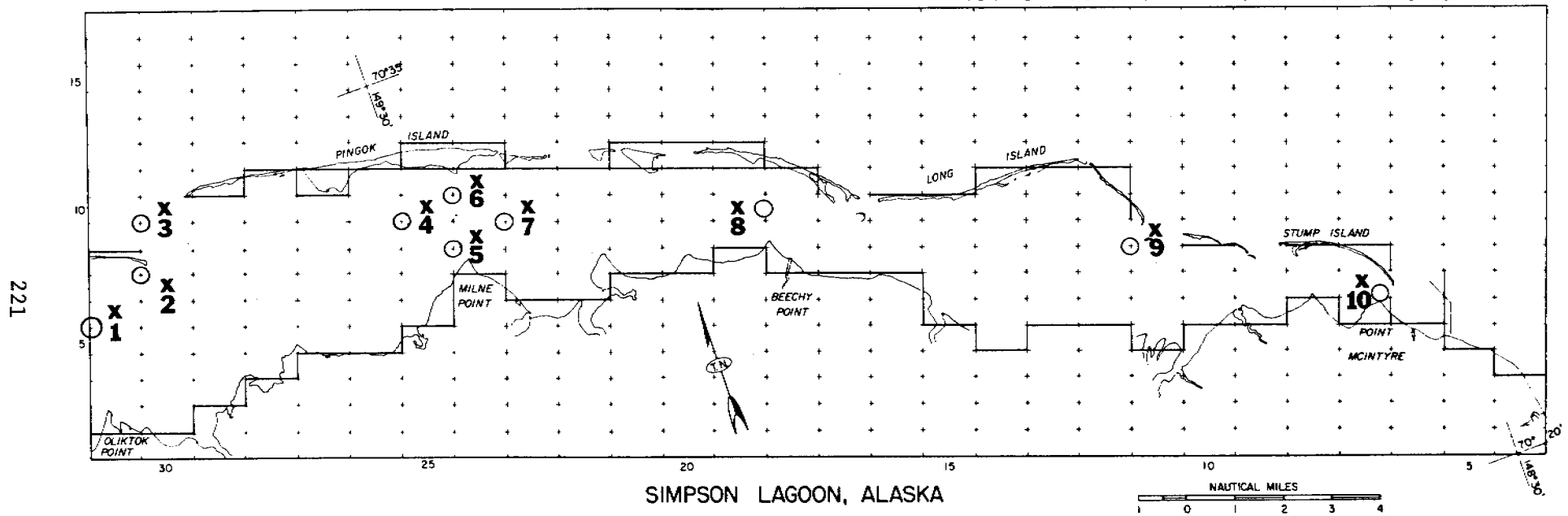
\*denotes inferred values

1. Radiation boundary conditions were used instead of flow-through conditions,
2. The complete Cottle Island August 1978 wind data set was read into the model so that, at will, any period during the month could be selected,
3. An economical "restart" facility was programmed so that the current and height fields generated at the end of one run could be used to start the next run, and
4. Provision was made to provide a punched-card output of the north and east components of the currents at 1/4 hour intervals at selected points.

Following discussions with J.B. Matthews of the University of Alaska, 10 locations were chosen as the locations for which punched-card current output were required. These locations, shown in Figure 25, are those points in the model that are close to current meters. (In Figure 25 the "+" signs denote the corners of computational rectangles --- average currents can only be computed at the center of each rectangle.) The period 0000 hrs August 20 to 0000 hrs August 23 (456 - 504 hours into the month) was modeled in two 24 hour runs. A 4-hour ramp was used for the first run, followed by a smooth restart. A listing of the punched-card output is given in Appendix B (this listing is intended only for the purposes of initial model calibration). The output is largely self-explanatory, with the exception that after the first (time column) the order of the columns corresponds to the numbers shown in Figure 25.

# VARIABLE WIND MODELING STUDY

- x DENOTES CURRENT PRINTOUT LOCATIONS
- o DENOTES CURRENT METER LOCATIONS



221

Figure 25. Grid scheme for Simpson Lagoon, Alaska: Current printout and current meter locations.

An investigation of the current components printed out during the course of the modeling indicates that the Y component of the current changes sign from ~ east to ~ west at 489.75 hrs for locations 5, 6, and 7, and at 489.25 hrs for location 8. Since the wind changed direction at about 487½ hrs (see Figure 42), a response time of some 2 hours is indicated as a preliminary conclusion.

1978 Field Season: 20 July 1978 - 22 August 1978

### Background

It is probably often difficult for people who have not actually visited either Prudhoe Bay or Milne Point to visualize the circumstances under which the research has to be carried out. Operations which may be routine when performed from a well-equipped research vessel or from a location within easy driving distance of a town take on a different significance when one is at the end of a communications link made tenuous by weather, RF noise or lack of transportation. To this end an annotated selection of photographs has been included in Appendix 2. It is hoped that the photographs will help explain the high cost of each Beaufort Sea data point acquired as compared to the cost of those acquired elsewhere.

### Quasi-Synoptic Surveys

Owing to inclement weather, only two hydrographic lagoon surveys were conducted using aircraft. The first survey was made on 28 July 1978 with a float plane. Cottle Island winds for the 24 hours preceding the trip had been predominantly from between NE and ESE with speeds of between 1.8 and 6.7 m s<sup>-1</sup>. Temperatures at the same location had varied between -0.2 °C and 4.8 °C. The lagoon itself was calm throughout the survey, which made it difficult for the pilot to safely judge his height above the water. This problem, along with overheating of the engine after prolonged taxiing, resulted in an incomplete coverage of the stations. The results of the survey are shown in Figure 26. In general temperatures are 1 °C to 2 °C



SIMPSON LAGOON, ALASKA  
OCSEAP R.U. #531

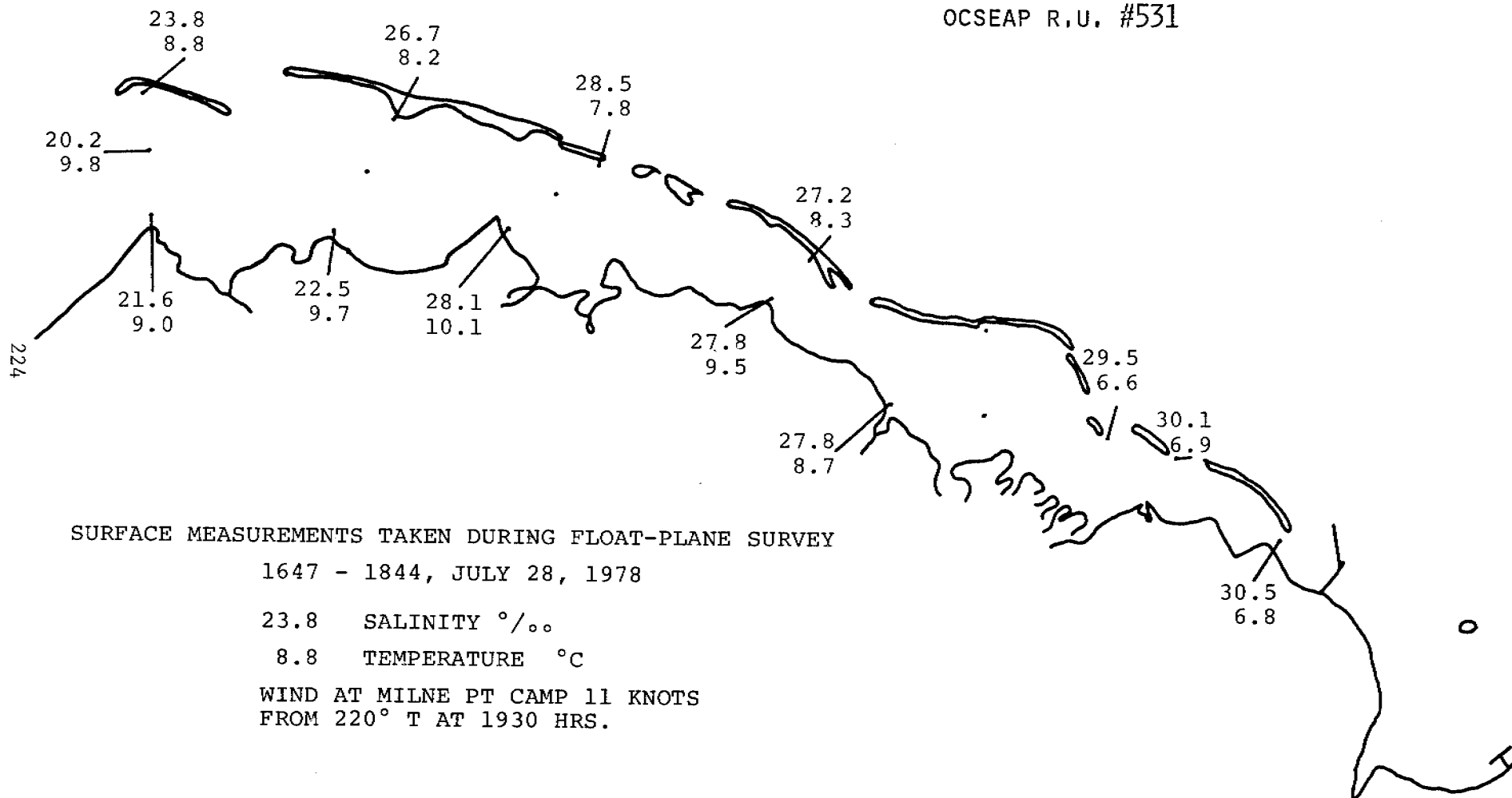


Figure 26. Simpson Lagoon synoptic survey: 28 July 1978.

lower on the seaward side of the lagoon, with the corresponding salinities being up to 4% higher. In general the salinities decrease and temperatures increase with distance towards the west. It would thus appear that the influence of river runoff is increasing with distance towards the west.

The second survey was made on 5 August 1978 using a helicopter. Winds for the previous 24 hours at Cottle Island had been at about  $4 \text{ m s}^{-1}$  from the west, changing to being from the north at 1800 on the 4th. From that time till 1200 on the 5th the winds varied between  $3.1$  and  $3.6 \text{ m s}^{-1}$  from  $0^\circ - 49^\circ$  True. Over the same total period temperatures had dropped from some  $6^\circ \text{C}$  to  $-2^\circ \text{C}$ . The pattern of temperatures and salinities (see Figure 27) is less clear than that of 8 days earlier, however once again temperatures are lower and salinities are generally higher on the seaward side of the lagoon. On the whole, salinities decrease towards the west as with the previous survey, but there is no clear cut correspondence between the temperatures. Probably the shift in the winds has confused the situation.

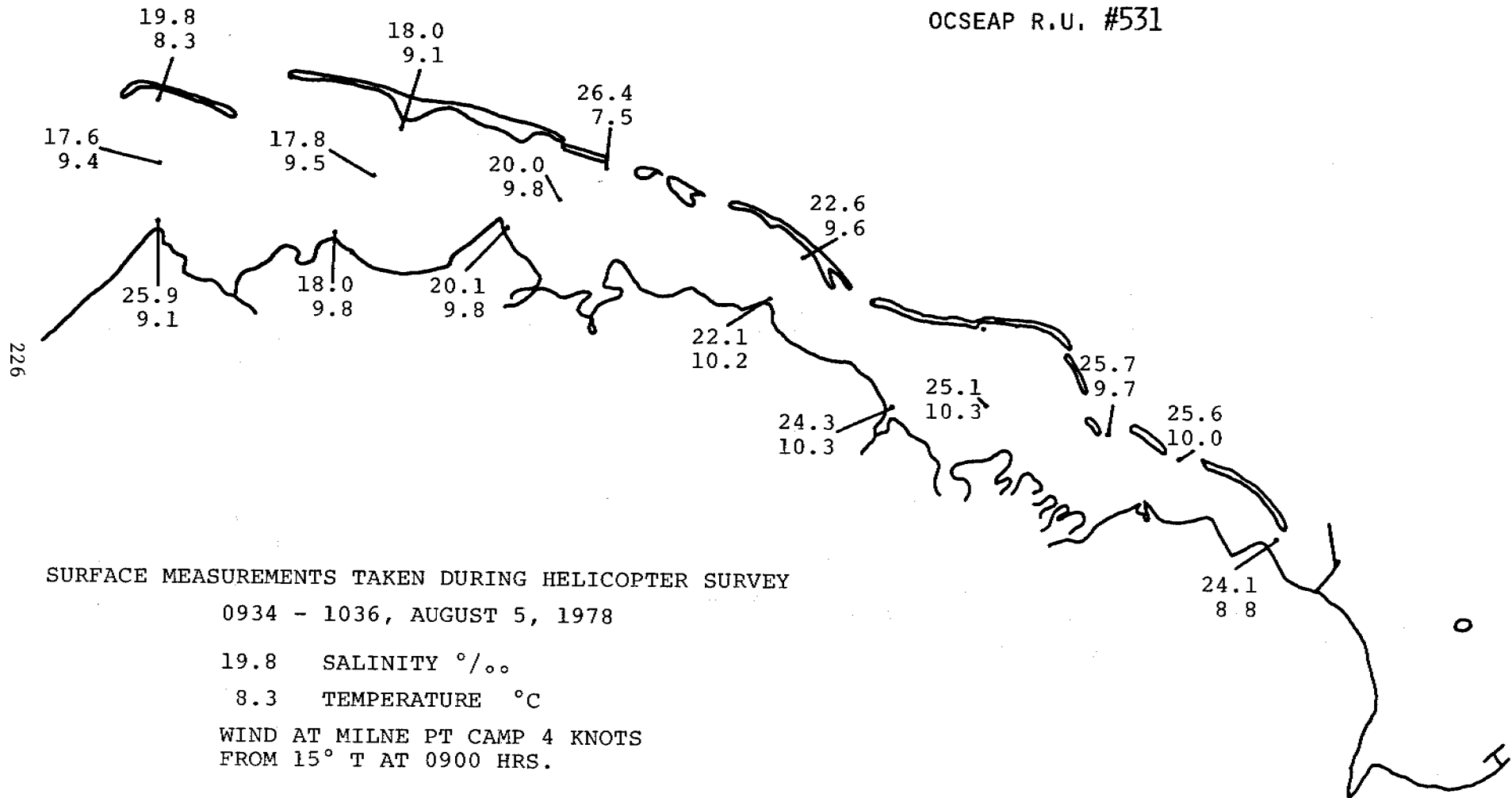
#### "Causeway" Studies

Milne Point, the site of the 1978 summer field season camp, is a likely place for the origin of a causeway, should road access to Pingok Island ever be required. An experiment of limited extent was carried out in order to see if there was any appreciable differences in salinity on either side of Milne Point.

Measurements of salinity were taken over a 2 week period at both the camp and on the west of the point; wind was also measured at the camp. As can be seen in Figure 28, there is little difference between the salinities,

SIMPSON LAGOON, ALASKA

OCSEAP R.U. #531



SURFACE MEASUREMENTS TAKEN DURING HELICOPTER SURVEY

0934 - 1036, AUGUST 5, 1978

19.8 SALINITY ‰

8.3 TEMPERATURE °C

WIND AT MILNE PT CAMP 4 KNOTS  
FROM 15° T AT 0900 HRS.

Figure 27. Simpson Lagoon synoptic survey: 5 August 1978.

NUMBER PERTAINS TO START OF DAY

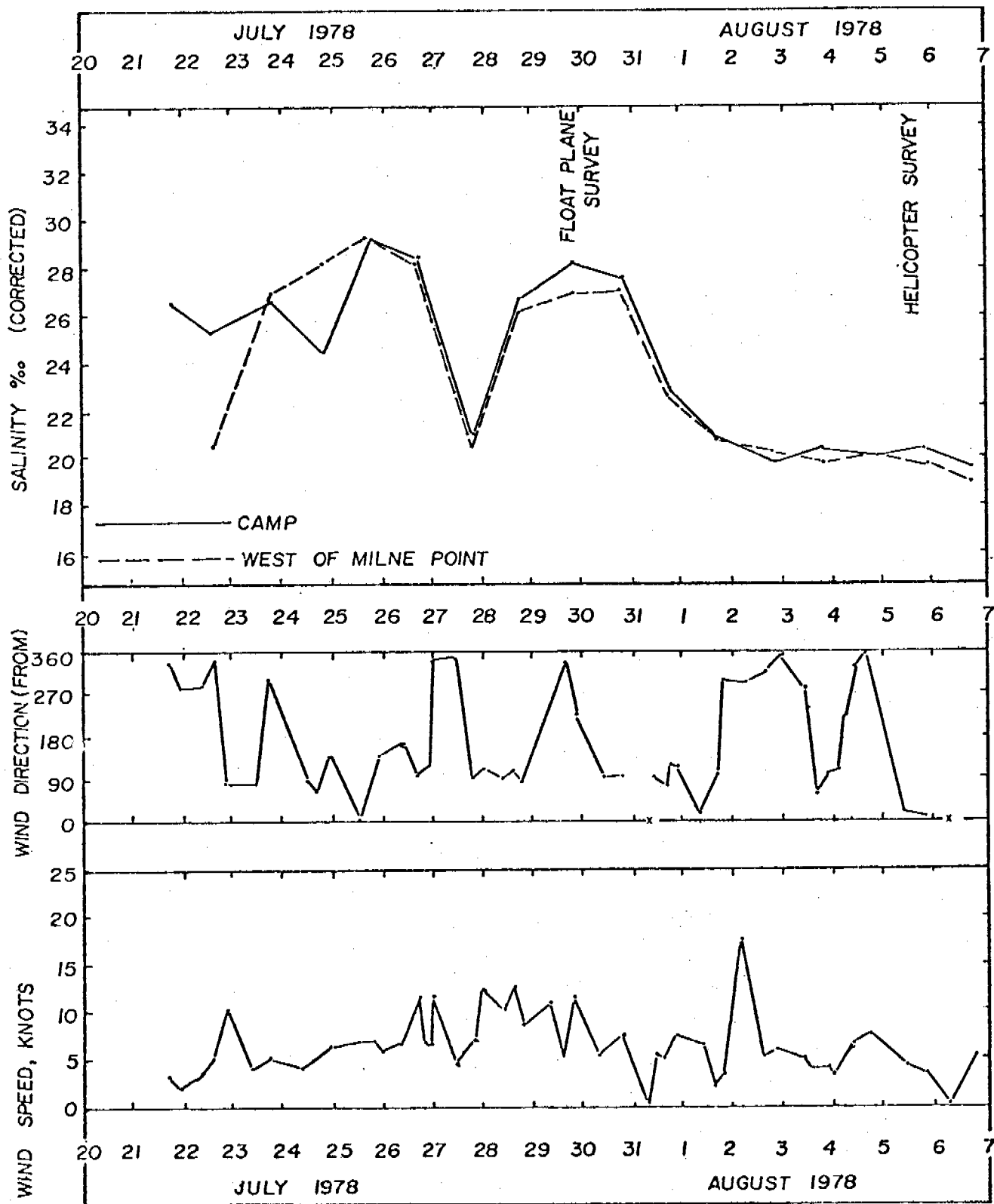


Figure 28. Study of salinity differences across Milne Point.

and the conclusion is reached that should any changes be observed in the future, around a new structure at Milne Point, they are probably caused by it.

### Waves and Currents

In order to provide near real time analyzed hydrographic data to the various scientific disciplines at Milne Point, a current meter and a wave gauge were installed some 50 meters offshore from the camp. The equipment was selected so that data of a quality suitable for detailed analysis could be obtained so as to complement any biological or geomorphological experiments that might be undertaken nearby.

The current meter consisted of a small-size 1½ inch diameter Marsh-McBirney Model 512 electromagnetic (EM) current sensor with a nearby electronics package and power supply. Signals were relayed to shore by land line, to be subsequently processed, displayed on a meter calibrated in  $\text{cm s}^{-1}$ , and ultimately to be recorded both on strip chart recorder and computer disk. The EM current sensor was chosen on account of its rapid response time --- we ordered a version with time constants of 0.1 and 20 seconds. The wave gauge was of the capacitance-type, and was made to order by Specialized Ocean Instruments of Baton Rouge, Louisiana. The central element consisted of a 150 cm teflon-coated wire. Six wave staffs and two readouts were provided, each capable of calibrating or displaying one of three staffs. With the wave gauge came two DC-powered strip chart recorders, one with 2 channels and one with 3 channels.

The current sensor and wave staff were attached to a structure of galvanized pipe in the form of a cube of sides 2 m in length. The current sensor was usually placed 20 cm above the bottom, with the wave staff being

located in the same vertical, some 40 cm above the sensor. The electronic display took place in an insulated hut that had been moved to within 15 m of the lagoon at considerable expense (and some risk) by large helicopter. As originally planned, the primary display and recording was to have been by strip chart recorder. The three-channel recorder was devoted to the two axes of the current sensor and one wave staff; the second recorder was designed so as to be used at a more remote location with two staffs (if necessary), one superimposed on the other to give a combined wave staff height of 3 meters.

As a backup data recording system, but a primary tool for analysis and digitizing, a North Star Horizon II micro-computer was rented from Kinnetic Laboratories, Inc. The computer came equipped with two disk drives (one for the programs, one for the data), a 7-channel A/D board with a resolution of 1 in 256, a TV display, and a clock board capable of supplying time for the purposes of automatically logging the date and time, or for supplying interrupts. Typically the current sensor outputs and the wave display output were sampled at 2/10 s intervals over a period of 102.2 seconds --- generating 512 x 3 data points in all. The information was stored on disk at the end of each period of data collection, and was then analyzed at once for wave spectrum, significant wave height, wave period based on zero crossings, and for drift current. A total of 54 sets of samples were taken between 8 August and 22 August 1978. A listing of the various programs used is given in Appendix C for the sake of completeness. The only analyses conducted so far since leaving the field have been those of the drift currents. The preliminary results are shown roughly sketched in Figure 29 along with winds measured by us at Milne Point. The +X coordinate indicates

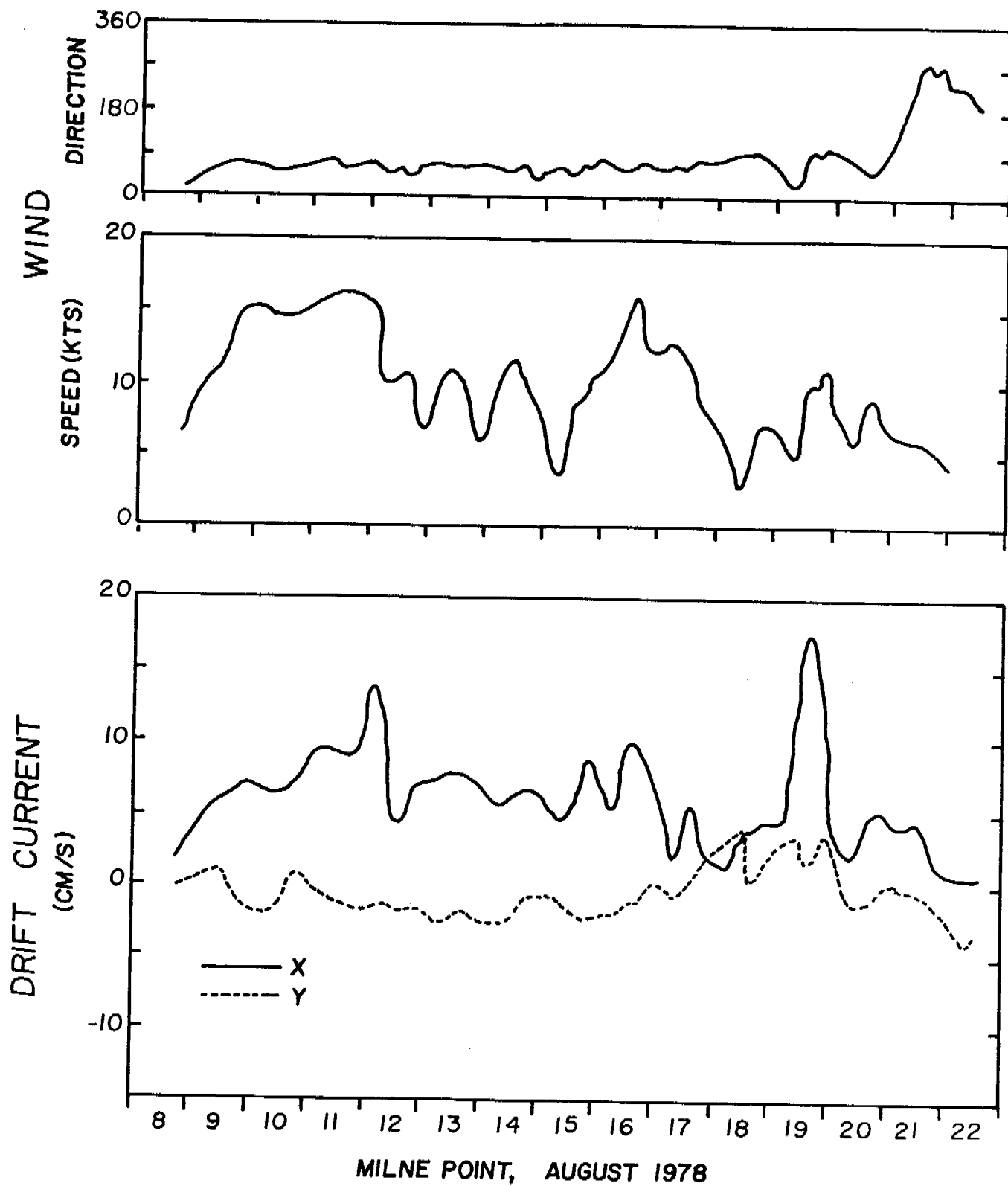


Figure 29. Milne Point drift currents as computed by microcomputer.

a longshore current from the east; the +Y coordinate indicates an onshore current. In almost all cases the current is from the east. The data are capable of yielding interesting data as to wave and current variations, and efforts will be made to complete the analysis as soon as time permits.

#### Drifter Studies

Through the courtesy of Wm. T. Whelan of Telecommunication Enterprises Co., Columbia, MD, and of Reed Armstrong of the National Marine Fisheries Services, Narragansett, RI, we were fortunate enough to have the use of two high frequency ITT-Arionics type DF-4 radio direction finder (RDF) sets. 15 6-MHz radio-beacon equipped drogues were shipped to Milne Point, 5 of which were deployed and tracked through the period 1200 20 August 1978 through 0000 22 August 1978 (one of the drifters unfortunately grounded). The drifters were deployed approximately in the center of Simpson Lagoon and were tracked by RDF sets located at Milne Point camp and at the former Pingok camp.

A summary of the plotted movements of the four drifters is shown in Figure 30. We were fortunate enough to encounter a change of winds from ENE to the west 20 hours into the study --- the drifters thus can be seen moving first towards the west, then towards the east. Plots of the trajectories of each individual drifter, each accompanied by an error analysis, can be seen in Figures 31 through 40. In each of the trajectory plots, S denotes "start", F denotes "finish", and the two circles indicate the locations of the RDF sets. Hourly winds for the period (for Cottle Island) are shown in Figure 41.



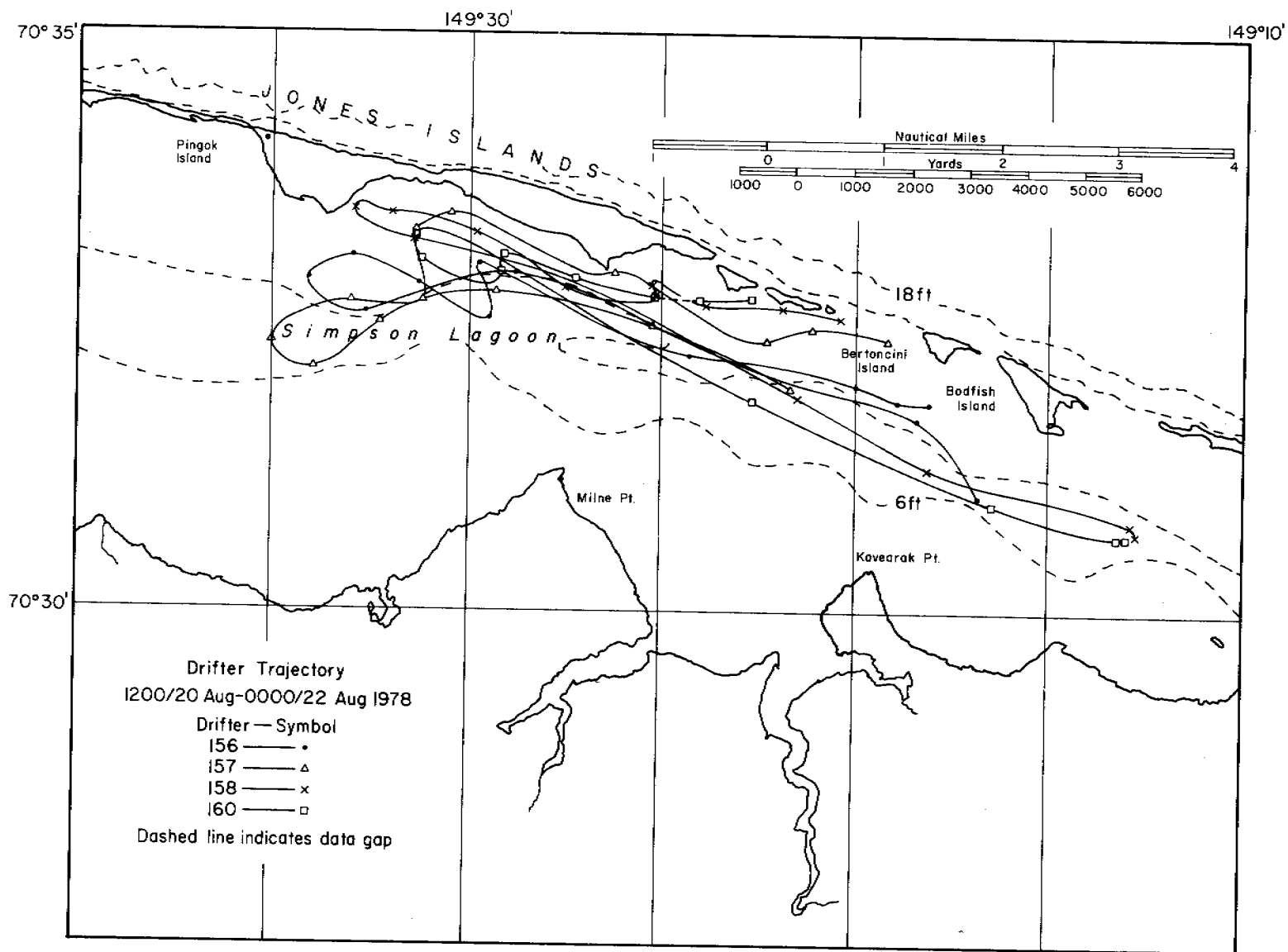


Figure 30. Drifter trajectory summary.

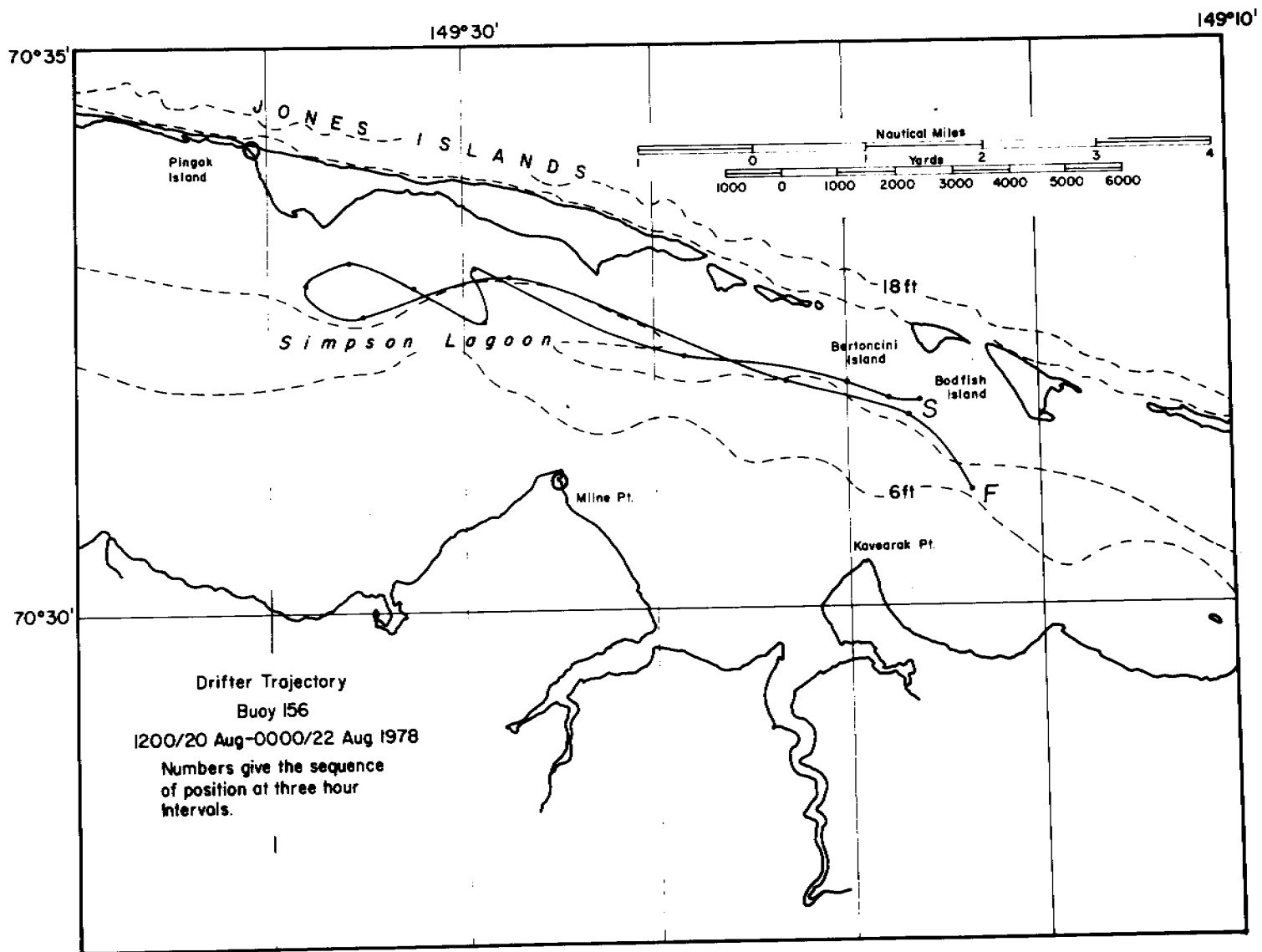


Figure 31. Drifter trajectory: buoy 156.

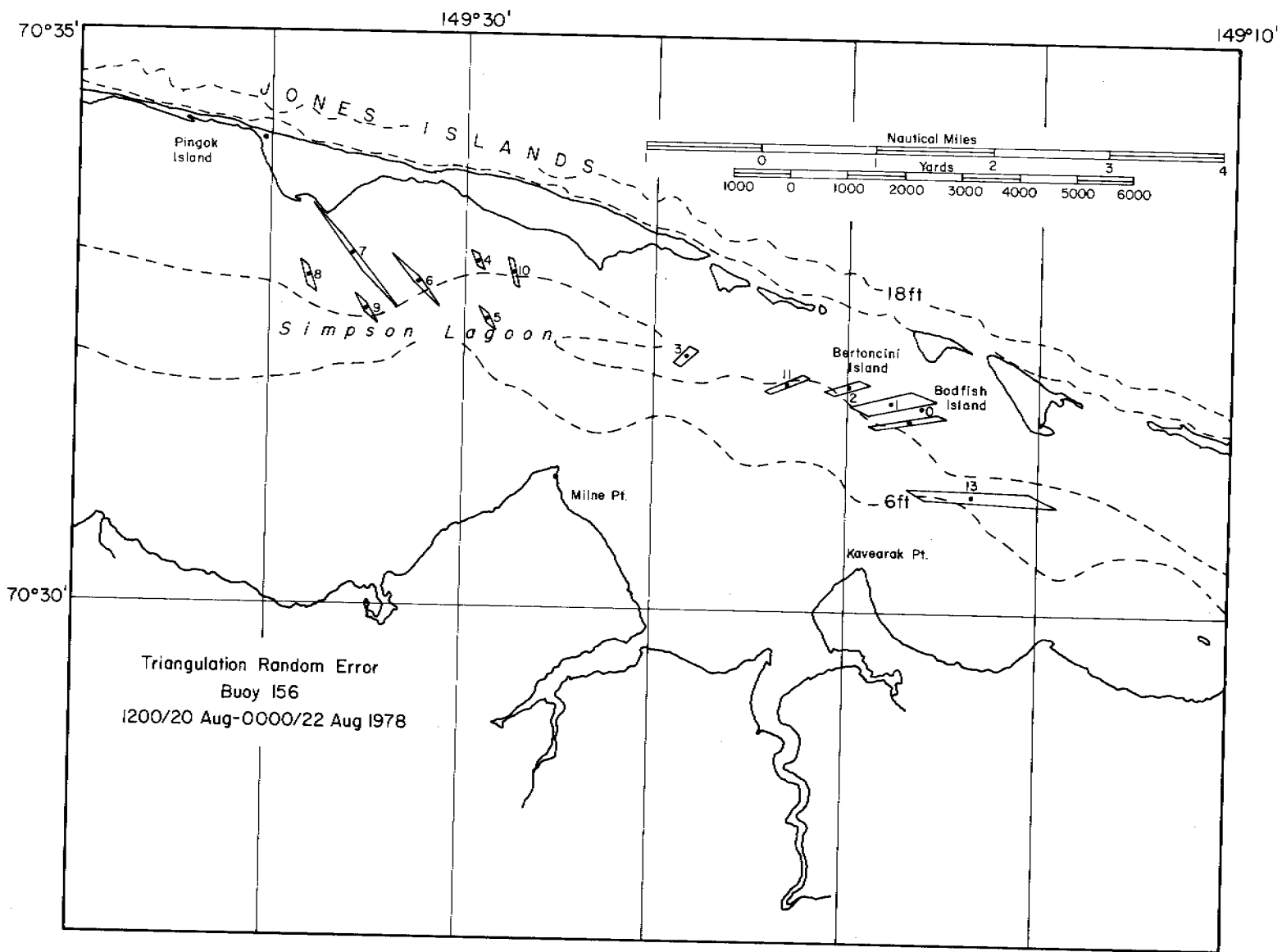


Figure 32. Drifter triangulation error analysis: buoy 156.

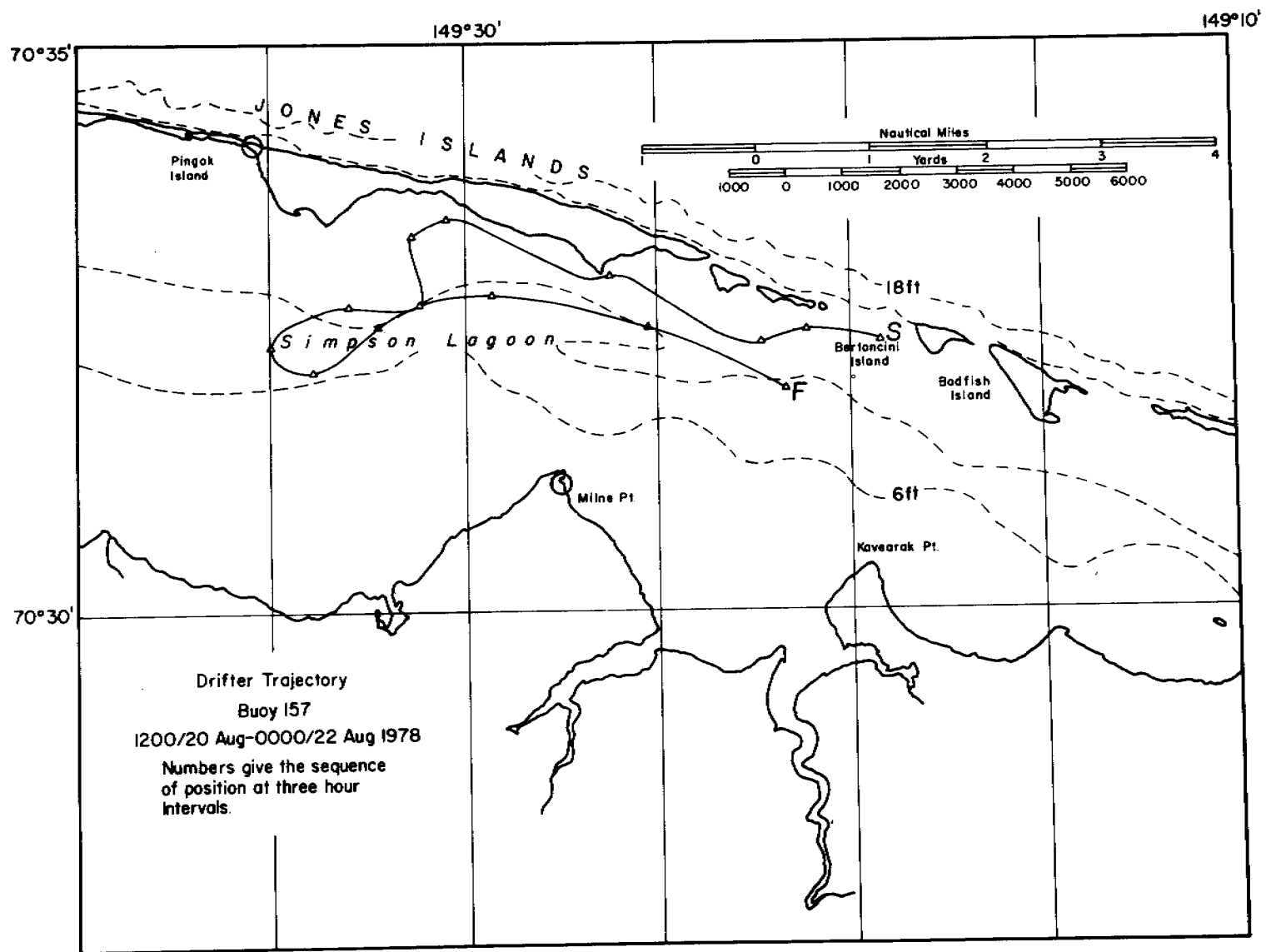


Figure 33. Drifter trajectory: buoy 157

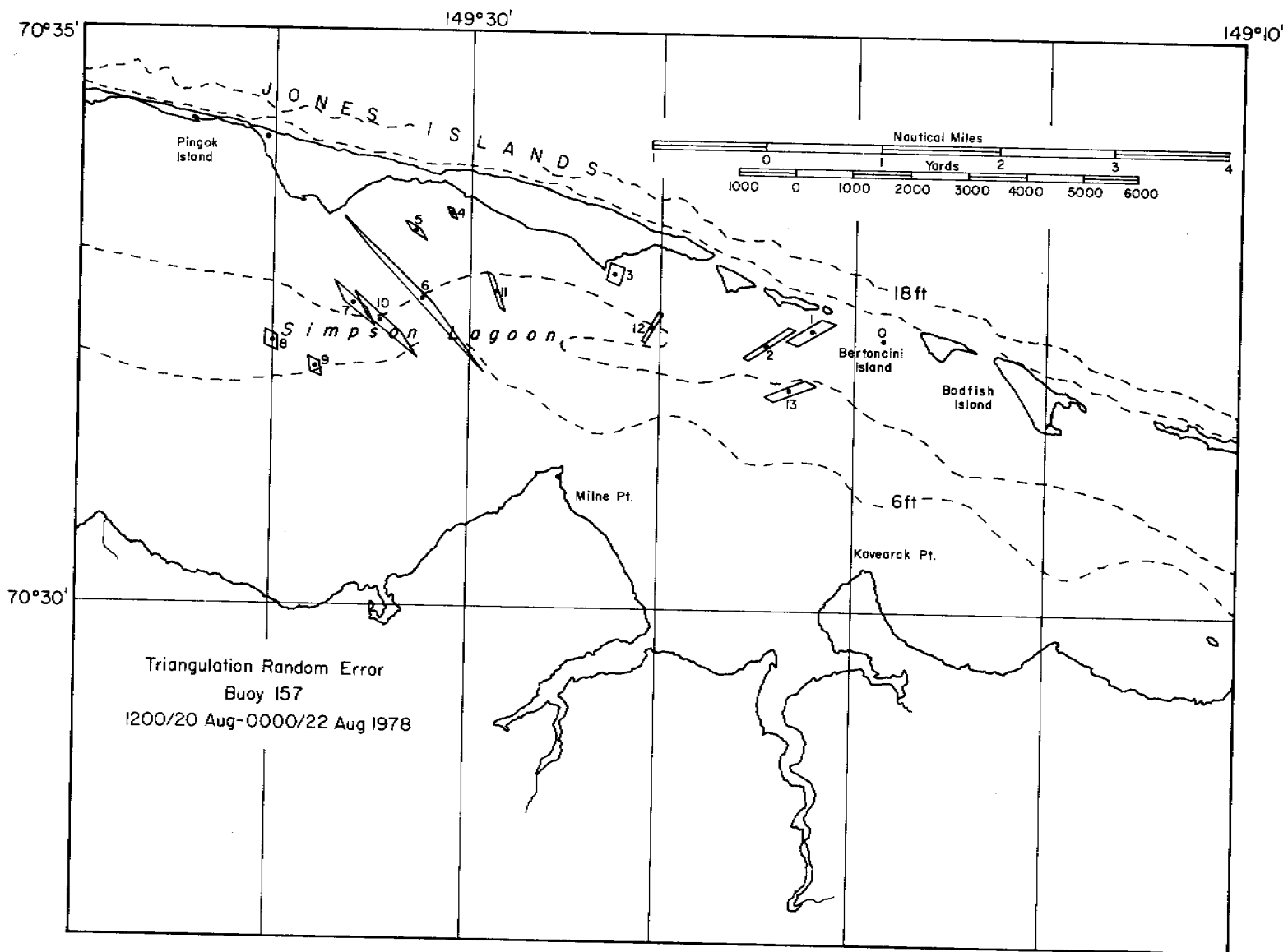


Figure 34. Drifter triangulation error analysis: buoy 157.

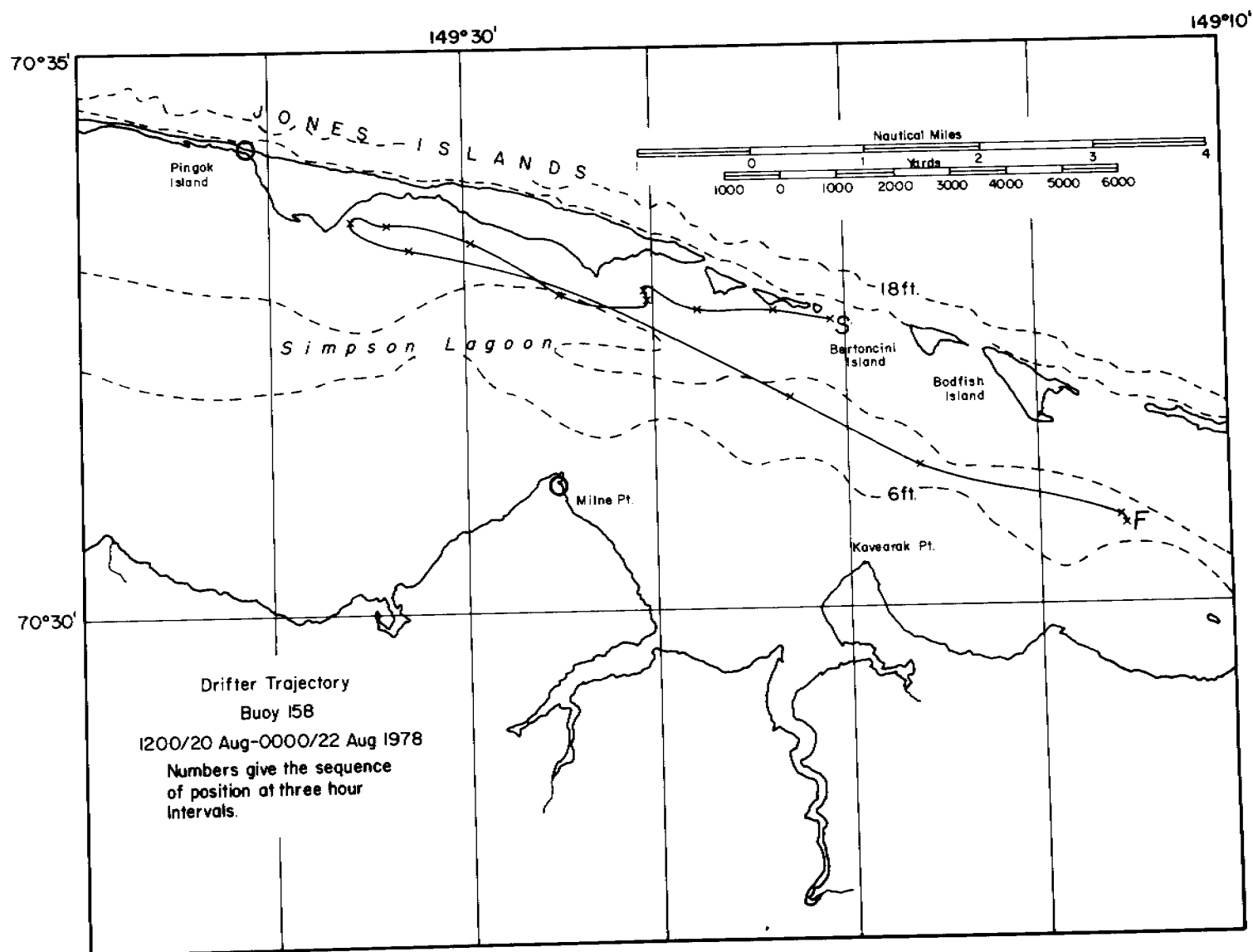


Figure 35. Drifter trajectory: buoy 158.

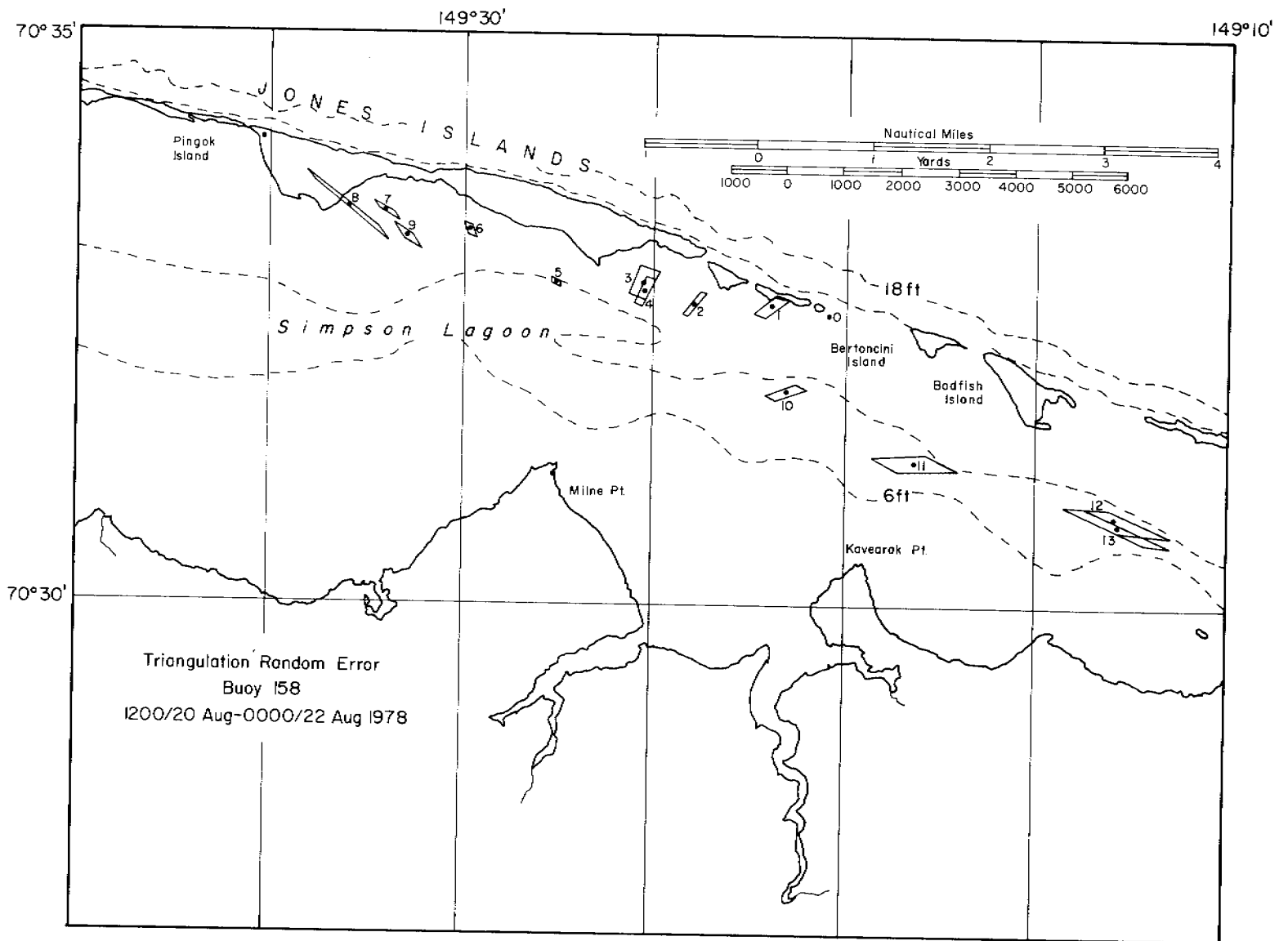


Figure 36. Drifter triangulation error analysis: buoy 158

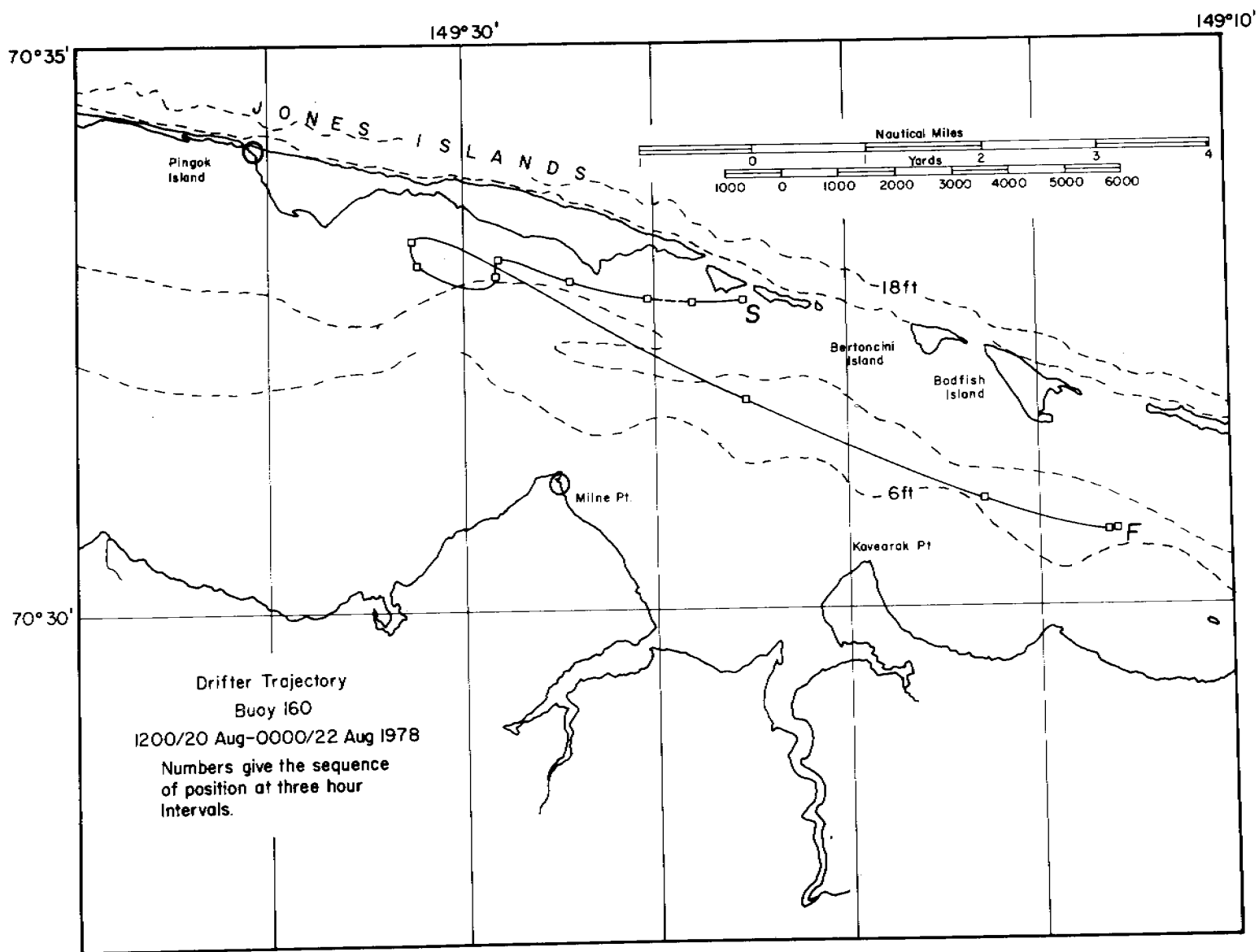


Figure 37. Drifter trajectory: buoy 160.



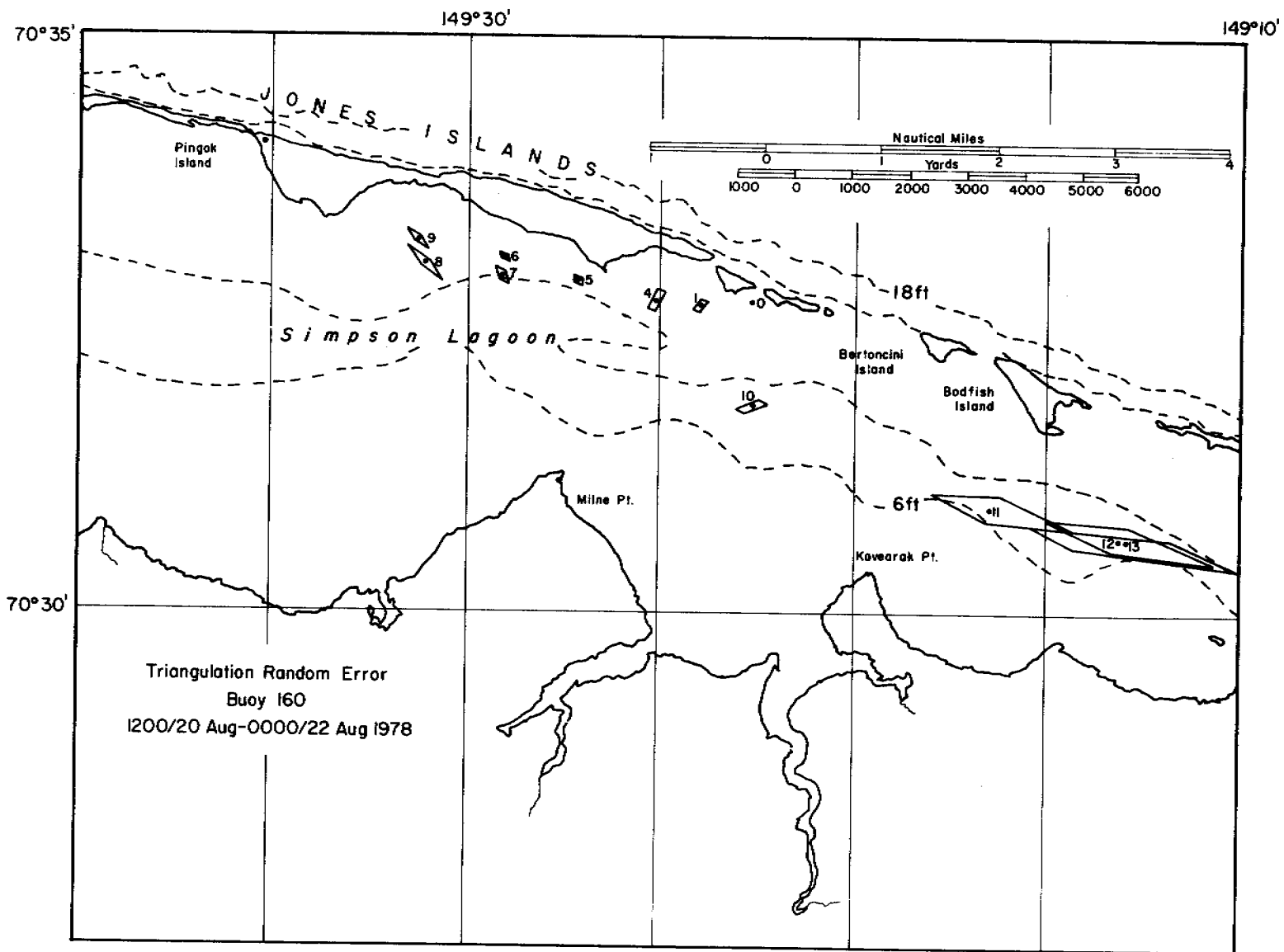


Figure 38. Drifter triangulation error analysis: buoy 160.

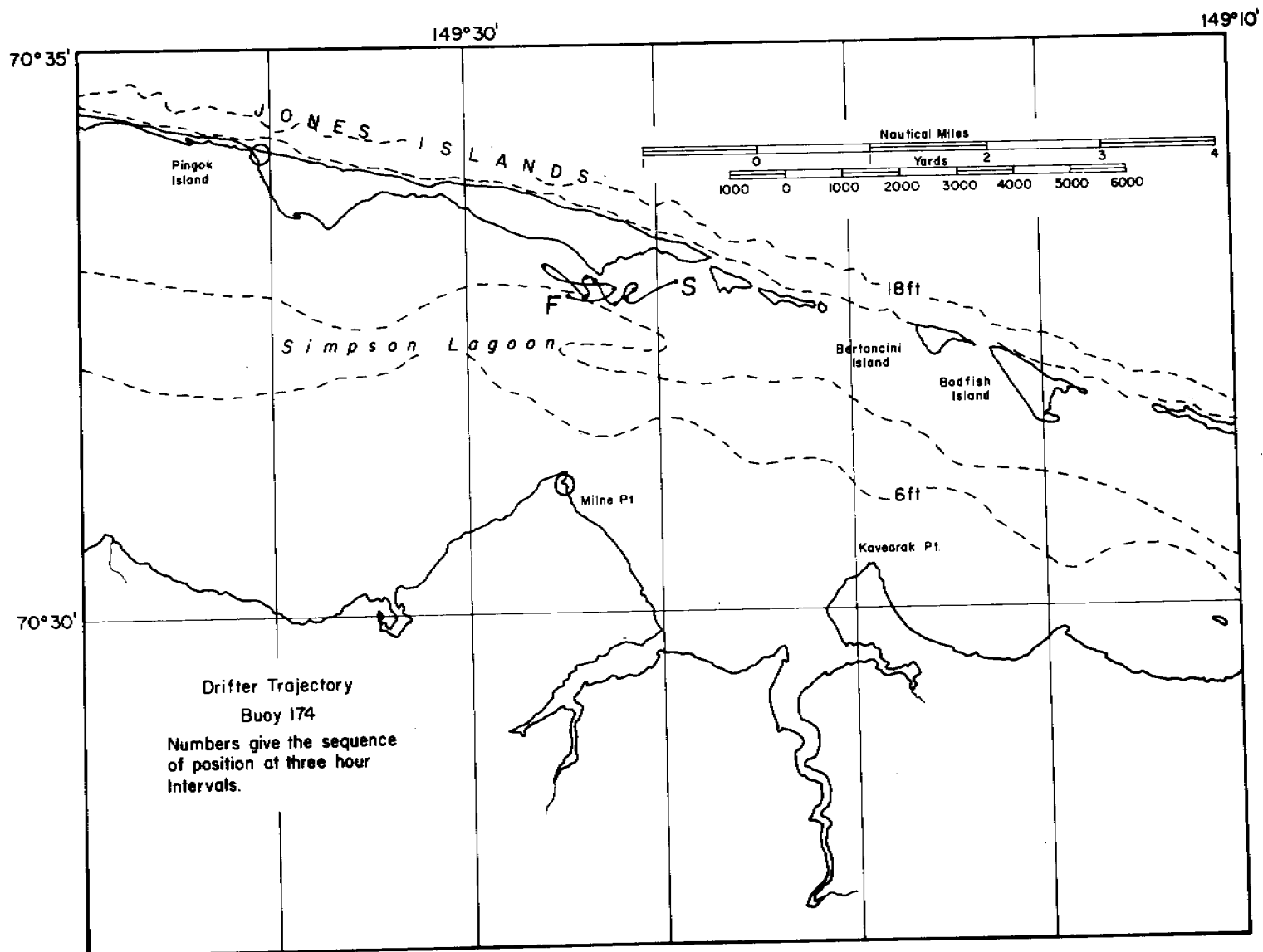


Figure 39. Drifter trajectory: buoy 174.

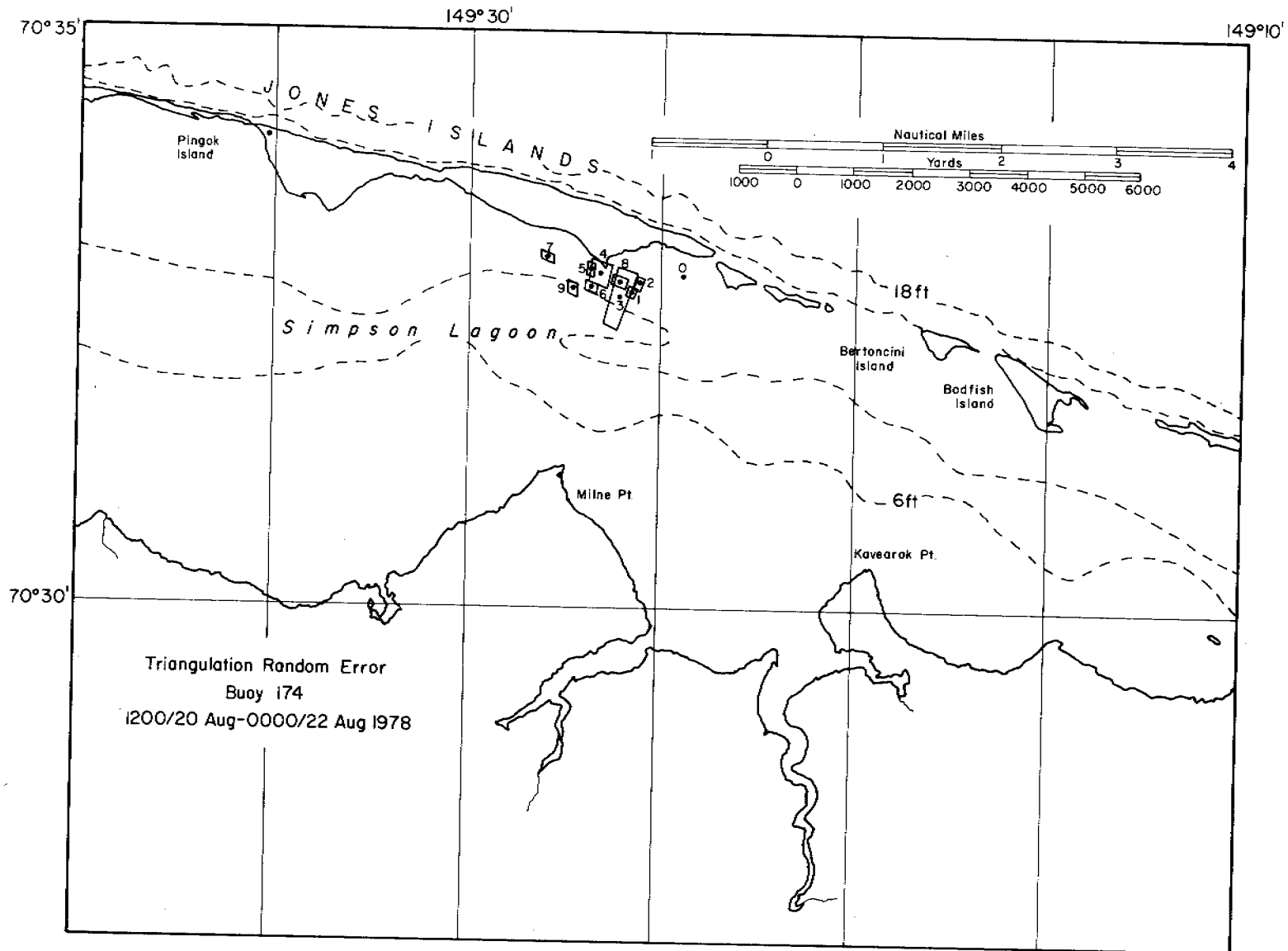


Figure 40. Drifter triangulation error analysis: buoy 174.

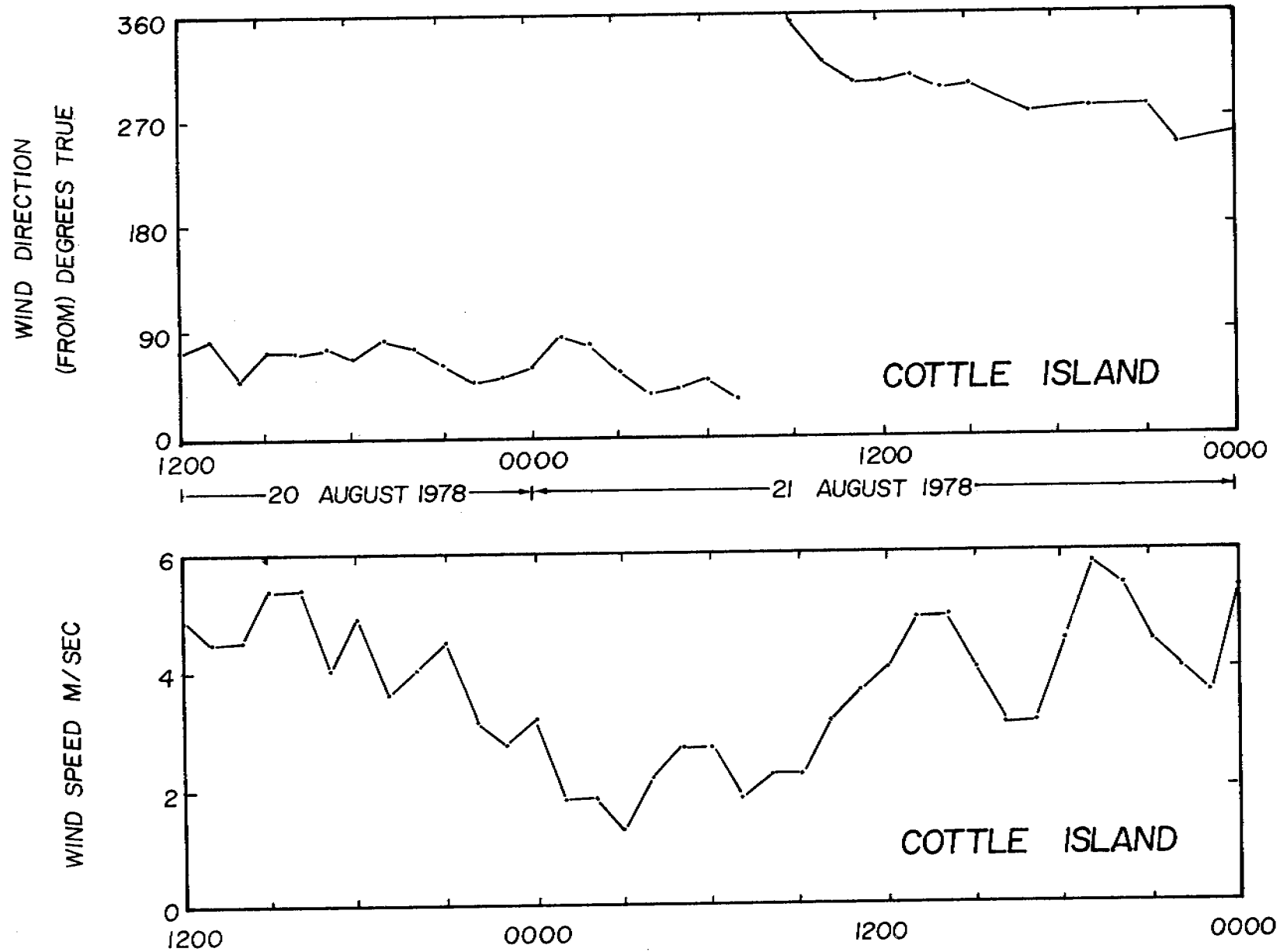


Figure 41. Hourly winds at Cottle Island during drifter tracking  
(Source: Roger Andersen).

A graph of the speeds of three selected drifters is shown in Figure 42. A crude comparison of these speeds, when compared to the wind speeds at the same times, indicates a ratio of drifter speed to wind speed of 0.044. When the total westward and eastward movement of each drifter is compared to the total distance blown by the wind, an approximate calculation results in a ratio of 0.045. These ratios would be slightly increased if westward or eastward components of the wind had been used. These values are slightly greater than the well known 3/100 of the wind speed that one often encounters in engineering literature. Of interest is that the maximum westward excursion of the drifters occurred at 0900 21 August 1978, while the winds measured at Cottle Island changed from blowing from 032 °T at 0700 to blowing from 359 °T at 0800 21 August 1978 --- indicating a response time of the order of 1½ hours or so. This figure can be compared to the 2 hour response time found in the numerical model variable wind modeling, and although both of these numbers are rough, they do tend to support one another. It will be interesting to see the current meter plots being written up by Dr. J. B. Matthews of the University of Alaska.

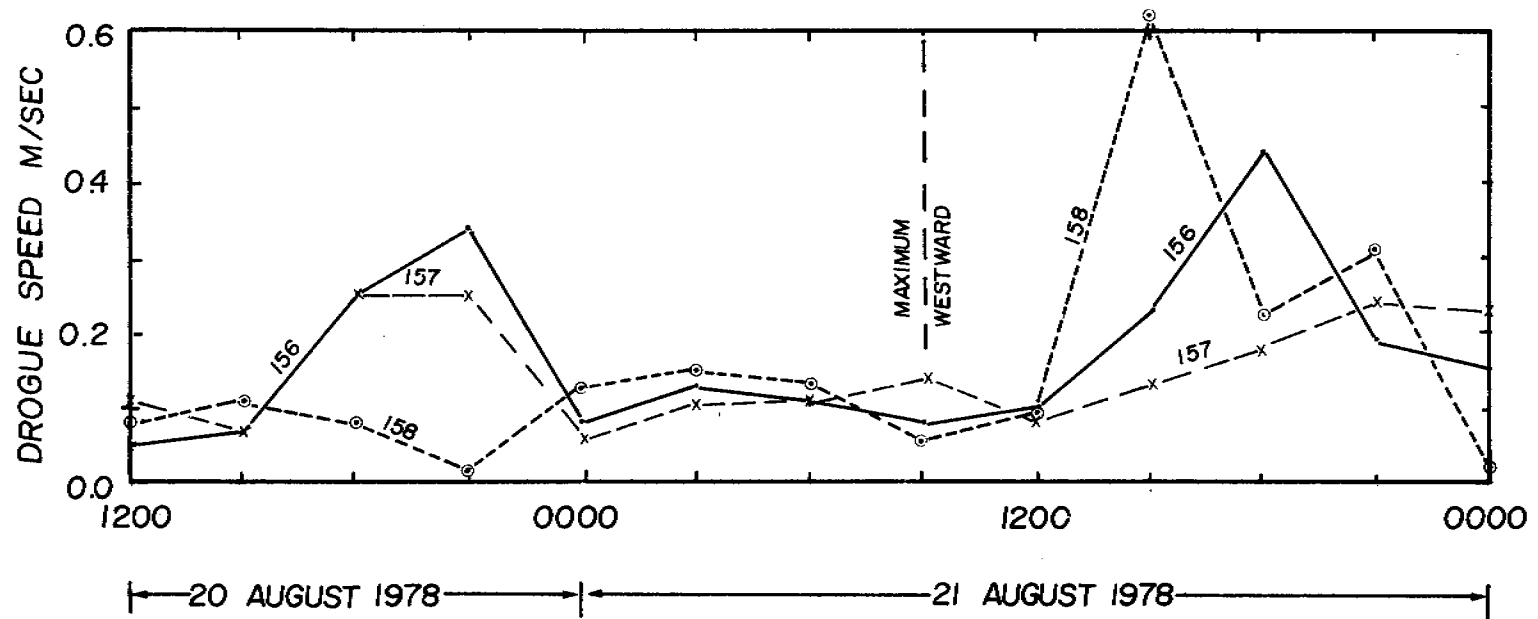


Figure 42. Drifter speeds as computed from trajectories.

## Conclusions

### Modeling

1. The 3-D modeling work has resulted in the generation of a large number of surface layer water parcel trajectories for the Beaufort Sea. These need to be interpreted carefully when they are to be used to indicate likely oil spill trajectories. As example, with a wind from the north, there will be little tendency for water parcels in near-shore (single-layer) parts of the model to move onshore (since there can be no flow across the shore line); oil on the surface however would most likely be blown onto the shore.
2. The 2-D scenario modeling indicates that as long as the two entrances mentioned for Scenario Two are left open, there will be a reduction of about 20% in the volume of water passing through the lagoon per day.
3. The 2-D variable wind preliminary results indicate that the response time of the lagoon to a 180° change in wind direction is of the order of 2 hours.

### Measurements

1. The two surveys show that water on the mainland side of the lagoon is warmer and less salty than that on the barrier island side. In one of the surveys, with easterly winds, most of the lagoon exhibited high salinities (27.0 o/oo) from the causeway to beyond Milne Point.
2. Salinity measurements on either side of Milne Point indicated little difference between their salinities, regardless of the wind direction.
3. 54 sets of Milne Point wave and current data (102 sec each, with a 0.2 second time interval) are available on diskette and await analysis.
4. The drifter experiment indicates a lagoon response time of about 1½ hours, and a relationship between drifter speed and wind speed of 4.5 : 100 or higher.

### Data Gaps

It is felt by this investigator that the data gaps remaining in our knowledge of summer conditions are:

- 1) Movement of coastal water outside the barrier islands (particularly through Harrison Bay).
- 2) Precise effect of causeways on local hydrography, and, if appropriate, how might undesirable effects be mitigated by design changes.

## References

Mungall, J. C. H., R. W. Hann, Jr., D. J. Horne, R. E. Whitaker, and  
C. E. Abel: Oceanographic Processes in a Beaufort Sea Barrier Island-  
Lagoon System: Numerical Modeling and Current Measurements. Annual  
Report RU 531 OCSEAP. Arctic Project. 1978.



## Appendix A

### Annotated Photographic Summary of Field Operations

Figures A.1 through A.4 show scenes from Prudhoe Bay. A modernistic skyline and view of impressive living facilities may mislead the casual observer as to the existence of problems that can impede freedom of movement: temporary check-in facilities in a packing crate and traffic congestion. Figures A.5 through A.8 show several views of the ARCO North Dock. The bend in the causeway is clearly visible in Figures A.5 and A.6. Note in Figure A.6 the large building (probably 6 stories high) being transported by crawler. Such situations cause road blocks for many hours. A close-up of the bend (North Dock #2) is shown in Figure A.8. In the latter photo, scarcely visible, is the NOAA tide gauge at the extreme eastern (left side in the photograph) tip of the dock. An idea of the remarkable activity that can occur during the open water season is clearly shown in Figure A.7. The presence of the technology required for such operations has proved of great convenience to investigators.

Figures A.9 and A.10 show huts at Milne Point. In the former, a one-ton insulated hut (to be used for electronic equipment storage) is moved by large helicopter to the shore. The operation is somewhat hazardous to all involved, since the helicopter is at full load; tent poles become bent by the downdraft. The hut has just cleared the cover of an eskimo ice cave currently being used for food storage. Figure A.10 shows the biology hut (with a bird-watching tower) and the generator/toilet hut that provided AC for the computer, battery chargers, etc. A large herd of caribou is barely visible; the caribou make use of Milne Point to wade conveniently into the sea in an attempt to avoid mosquitoes.

Figures A.11 through A.13 show details of the instrumented platform. The EM current sensor and bottom of the capacitance wave staff can be seen in Figure A.12, while the DC power supply and Marsh-McBirney electronics package is shown in Figure A.13. The scale is in feet. The readouts, strip chart recorder, wave gauge system electronics and an RDF set are visible in Figure A.14. The micro-computer data acquisition system is shown in Figure A.15. (The TV is merely serving as an economical computer readout --- no programs could be received!). It was found that the hut had to be heated to 15 °C for some 15 minutes before the disk drives would work. The completed instrument platform is shown in Figure A.16. The placement of the platform depended on the generous help of the biologists present at the camp.

Investigators at Milne Point had to devote some of their time to maintaining the camp: Figures A.17 and A.18 show the progress and termination of a most professional airdrop of fuel and food, conducted by the Naval Arctic Research Laboratory (at Point Barrow). Figure A.18 was taken looking down from the bird-watching tower as the plane made a final low-level inspection of the successful completion of the task.

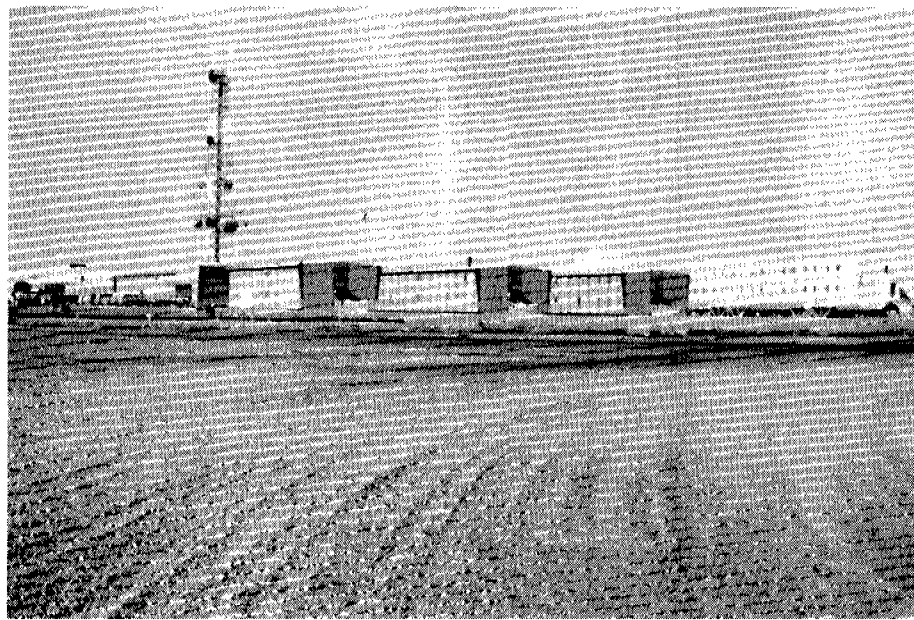


Figure A.1. Living facilities at Prudhoe Bay



Figure A.2. Prudhoe Bay temporary check-in facilities

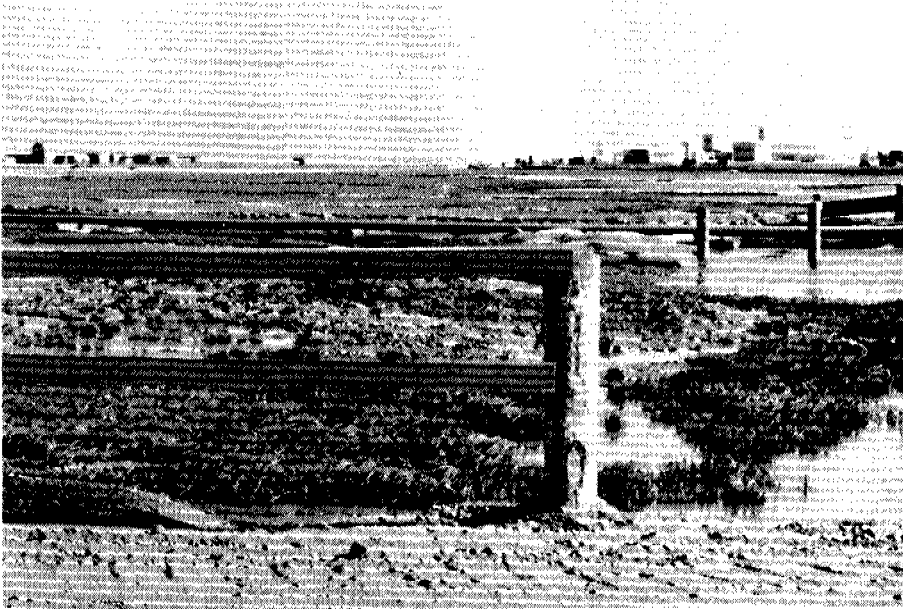


Figure A.3. Prudhoe Bay skyline



Figure A.4. Landward end of North Dock, Prudhoe Bay



Figure A.5. North Dock viewed from the south

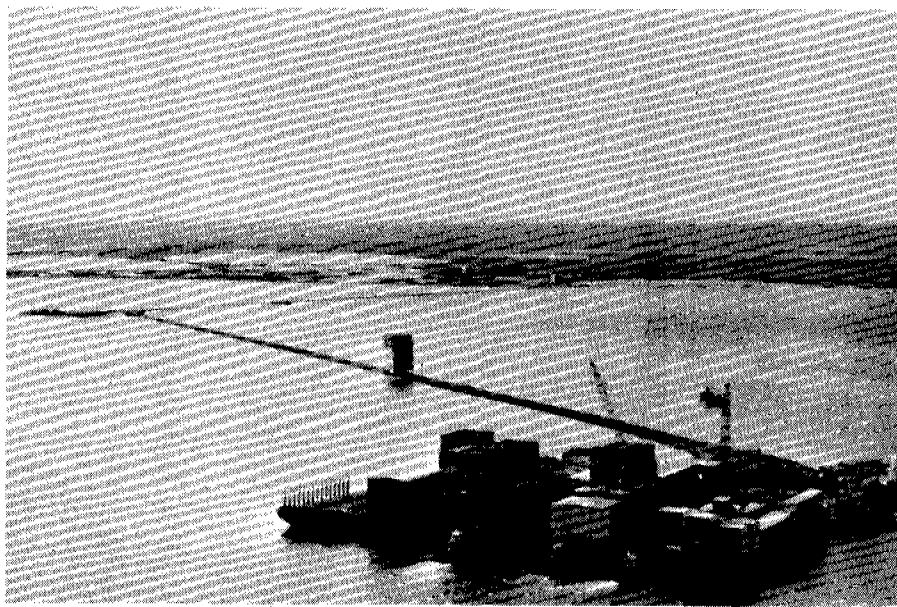


Figure A.6. North Dock viewed from the north

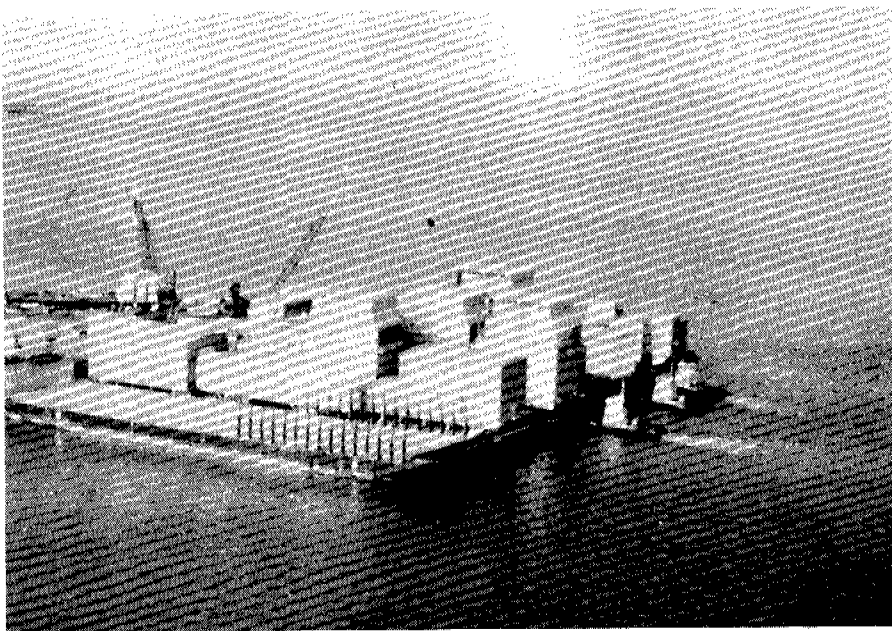


Figure A.7. Close-up of North Dock number 3

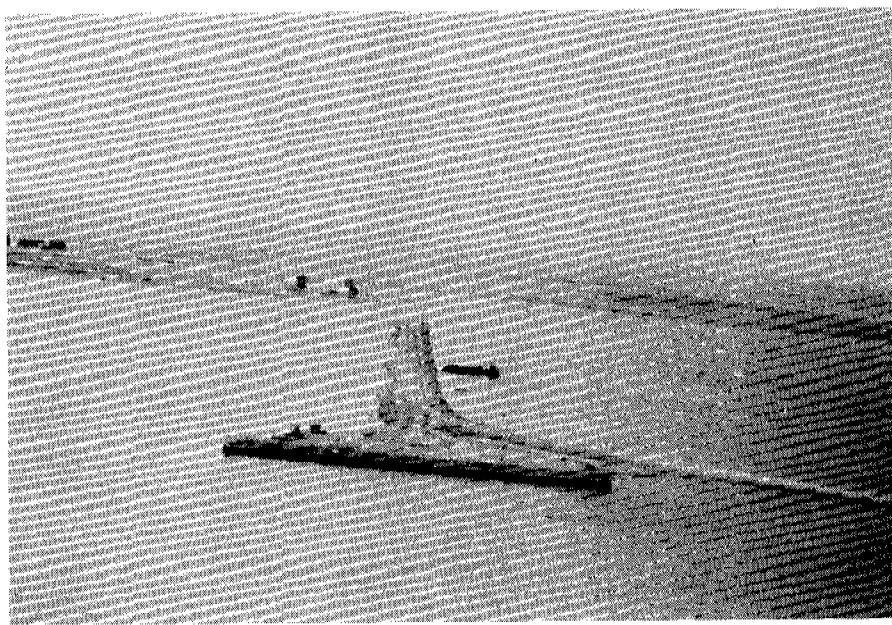


Figure A.8. Close-up of North Dock number 2



Figure A.9. Airlift of electronics hut, Milne Point



Figure A.10. Generator and biology huts, Milne Point



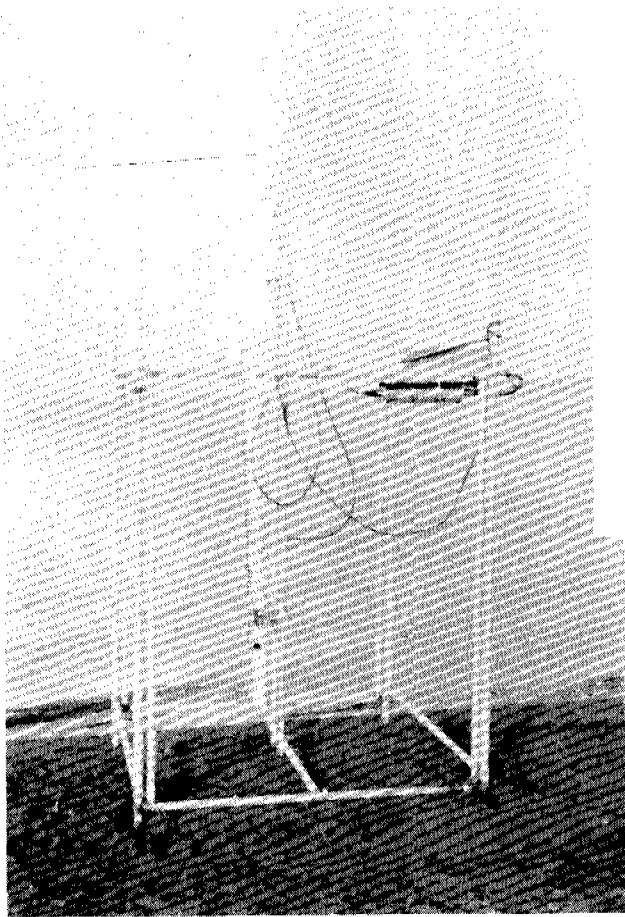


Figure A.11. Instrument tower  
scale in feet

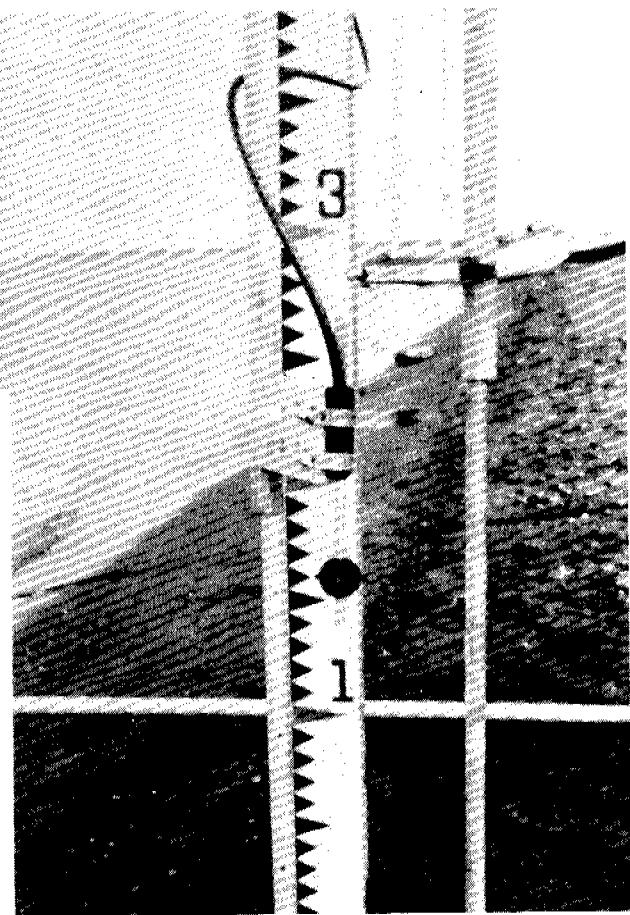


Figure A.12. Close-up of EM  
current sensor



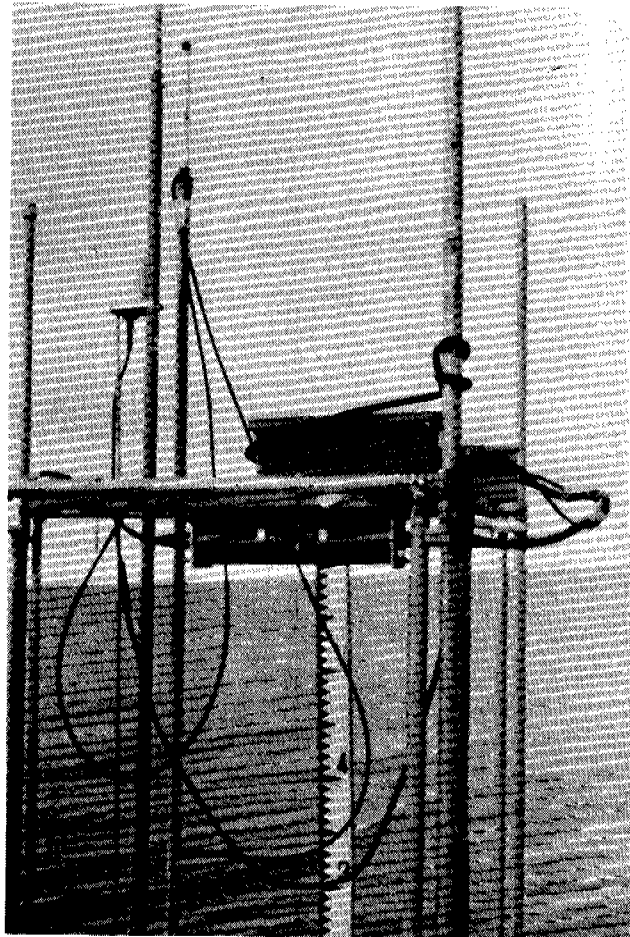


Figure A.13. Close-up of EM  
electronic packages

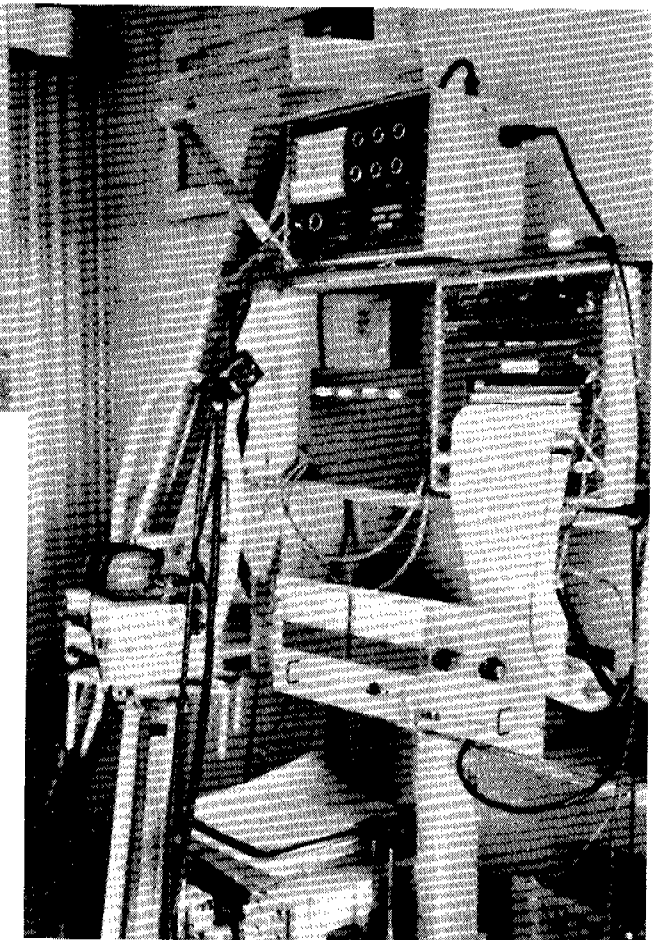


Figure A.14. Wavegauge and  
current meter  
displays

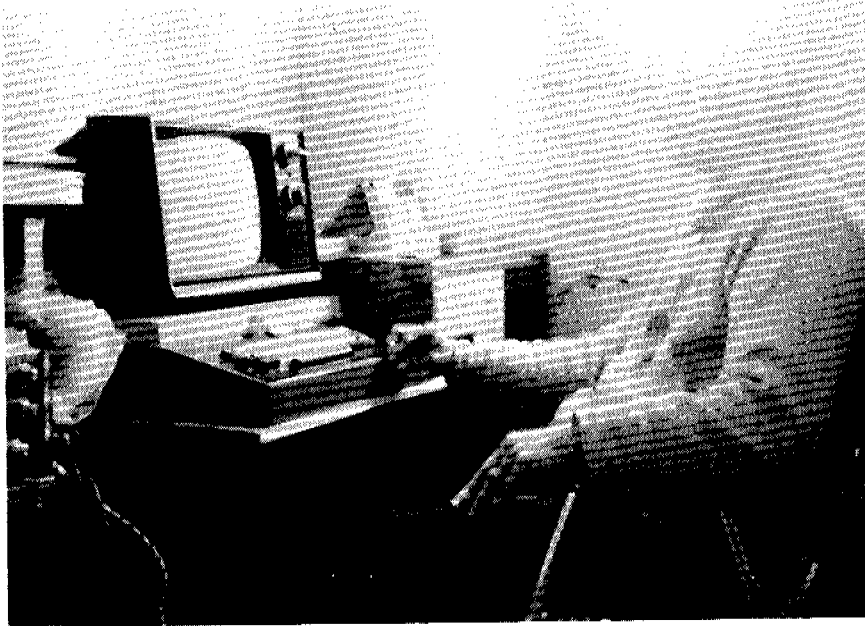


Figure A.15. Microcomputer data acquisition system

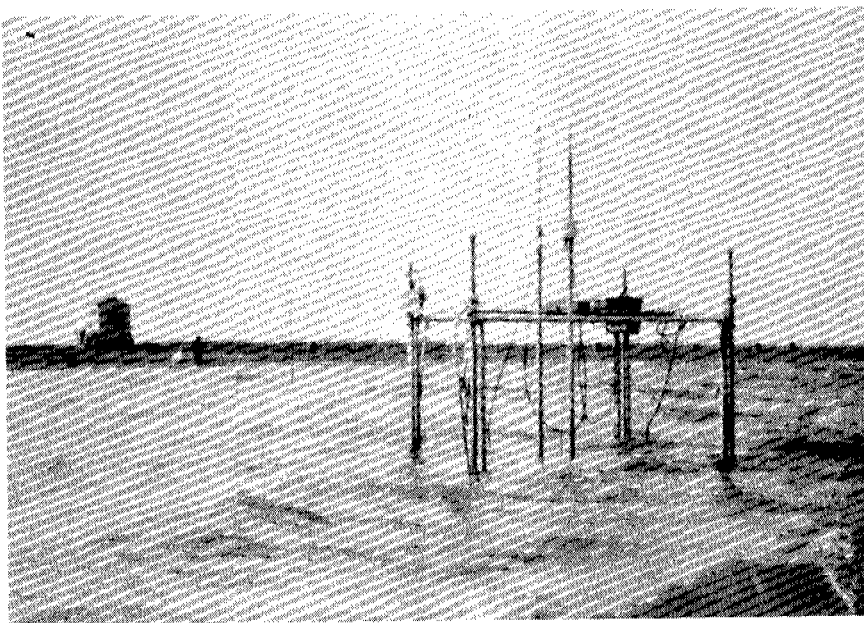


Figure A.16. Instrument tower

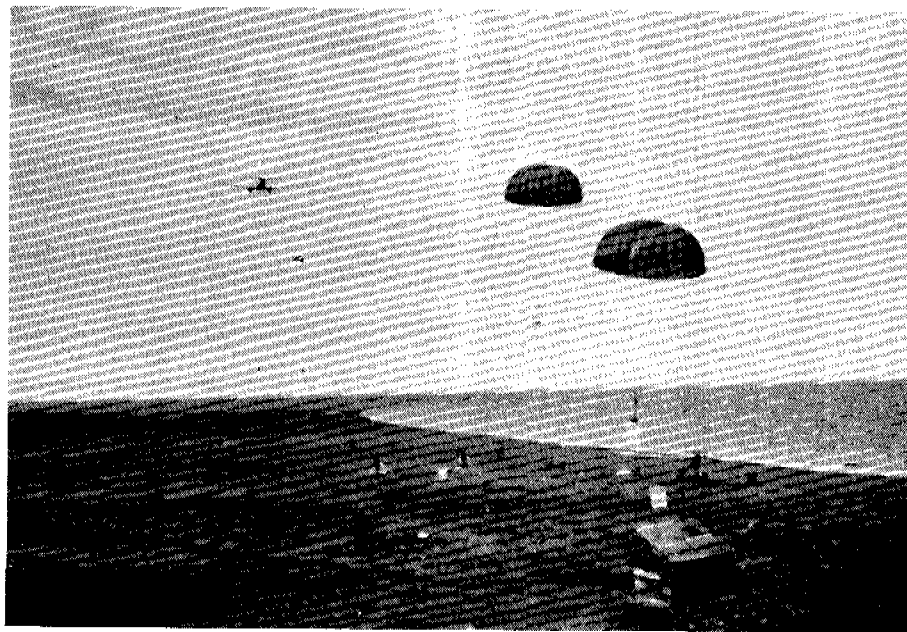


Figure A.17. N.A.R.L. food airdrop

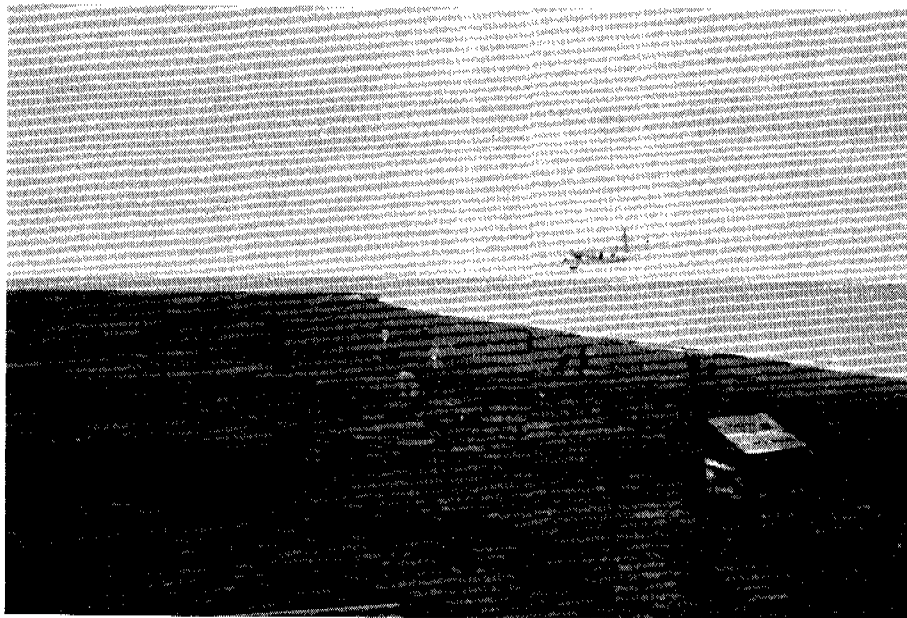


Figure A.18. Completion of airdrop

## Appendix B

Printout of Variable-Wind Numerical Model Current Components  
for the Period 0015 20 August 1978 to 0000 22 August 1978

Please see Figure 25 for the locations (1 through 10, corresponding to columns 2 through 11). Also, please note that the units are decimeters per second, so that, for example 3.17 indicates  $31.7 \text{ cm s}^{-1}$ . The model was spun up from rest.

HOURS AFTER START OF AUGUST 1978. CURRENTS IN DECIMETERS/SEC.  
 FIRST CARD OF PAIR IS TRUE NORTH COMPONENT, SECCND IS TCWARDS EAST

456.25	0.00	0.00	0.00	0.00	0.00	0.00	0.00	0.00	0.00	0.01
456.25	-0.01	-0.01	-0.01	-0.01	-0.01	-0.01	-0.01	-0.01	-0.01	-0.02
456.50	0.02	0.02	0.02	0.01	0.02	0.02	0.02	0.02	0.01	0.06
456.50	-0.04	-0.05	-0.04	-0.05	-0.05	-0.05	-0.05	-0.05	-0.06	-0.09
456.75	0.03	0.03	0.04	0.02	0.05	0.04	0.05	0.05	0.03	0.14
456.75	-0.08	-0.10	-0.10	-0.11	-0.12	-0.11	-0.10	-0.12	-0.13	-0.22
457.00	0.05	0.05	0.06	0.04	0.09	0.08	0.08	0.10	0.05	0.25
457.00	-0.13	-0.16	-0.17	-0.21	-0.22	-0.20	-0.18	-0.22	-0.23	-0.41
457.25	0.07	0.07	0.09	0.07	0.14	0.12	0.13	0.16	0.07	0.39
457.25	-0.19	-0.23	-0.25	-0.33	-0.35	-0.31	-0.29	-0.35	-0.35	-0.65
457.50	0.10	0.09	0.12	0.09	0.21	0.18	0.19	0.23	0.09	0.53
457.50	-0.26	-0.31	-0.34	-0.47	-0.50	-0.44	-0.43	-0.51	-0.48	-0.90
457.75	0.13	0.12	0.15	0.12	0.29	0.24	0.26	0.31	0.12	0.68
457.75	-0.33	-0.39	-0.45	-0.62	-0.66	-0.58	-0.57	-0.70	-0.60	-1.15
458.00	0.16	0.14	0.17	0.15	0.37	0.30	0.33	0.40	0.16	0.82
458.00	-0.41	-0.48	-0.56	-0.78	-0.83	-0.73	-0.73	-0.90	-0.74	-1.39
458.25	0.19	0.17	0.18	0.18	0.46	0.36	0.40	0.50	0.20	0.95
458.25	-0.49	-0.57	-0.68	-0.94	-0.99	-0.87	-0.88	-1.12	-0.88	-1.59
458.50	0.23	0.18	0.18	0.21	0.54	0.43	0.47	0.59	0.24	1.06
458.50	-0.57	-0.67	-0.80	-1.10	-1.15	-1.00	-1.03	-1.34	-1.02	-1.78
458.75	0.26	0.19	0.17	0.24	0.62	0.49	0.54	0.68	0.28	1.16
458.75	-0.65	-0.77	-0.93	-1.25	-1.31	-1.13	-1.18	-1.55	-1.15	-1.94
459.00	0.29	0.20	0.14	0.27	0.70	0.55	0.60	0.76	0.32	1.26
459.00	-0.74	-0.87	-1.06	-1.40	-1.46	-1.25	-1.32	-1.75	-1.29	-2.10
459.25	0.31	0.19	0.09	0.30	0.77	0.60	0.66	0.84	0.34	1.34
459.25	-0.81	-0.96	-1.18	-1.52	-1.58	-1.35	-1.44	-1.93	-1.41	-2.23
459.50	0.32	0.17	0.01	0.32	0.83	0.64	0.70	0.90	0.36	1.39
459.50	-0.86	-1.03	-1.27	-1.62	-1.68	-1.43	-1.54	-2.07	-1.50	-2.32
459.75	0.34	0.14	-0.09	0.34	0.87	0.67	0.74	0.95	0.38	1.42
459.75	-0.91	-1.08	-1.35	-1.69	-1.75	-1.49	-1.61	-2.19	-1.56	-2.38
460.00	0.34	0.11	-0.20	0.35	0.90	0.69	0.76	0.99	0.39	1.45
460.00	-0.94	-1.12	-1.41	-1.73	-1.80	-1.53	-1.67	-2.29	-1.61	-2.43
460.25	0.34	0.07	-0.32	0.35	0.91	0.70	0.78	1.02	0.40	1.46
460.25	-0.96	-1.14	-1.45	-1.74	-1.82	-1.54	-1.70	-2.37	-1.63	-2.44

HOURS AFTER START OF AUGUST 1978. CURRENTS IN DECIMETERS/SEC.  
 FIRST CARD OF PAIR IS TRUE NORTH COMPONENT, SECCND IS TOWARDS EAST

460.50	0.33	0.02	-0.45	0.35	0.91	0.70	0.77	1.03	0.40	1.44
460.50	-0.96	-1.14	-1.46	-1.73	-1.80	-1.53	-1.70	-2.41	-1.63	-2.42
460.75	0.32	-0.03	-0.58	0.35	0.90	0.69	0.77	1.04	0.40	1.42
460.75	-0.95	-1.13	-1.45	-1.69	-1.77	-1.50	-1.68	-2.43	-1.61	-2.38
461.00	0.31	-0.07	-0.70	0.34	0.87	0.67	0.75	1.04	0.39	1.39
461.00	-0.94	-1.12	-1.43	-1.64	-1.72	-1.46	-1.65	-2.44	-1.58	-2.34
461.25	0.30	-0.10	-0.80	0.33	0.84	0.65	0.73	1.04	0.39	1.36
461.25	-0.93	-1.11	-1.41	-1.57	-1.66	-1.41	-1.61	-2.43	-1.56	-2.29
461.50	0.29	-0.14	-0.89	0.32	0.81	0.63	0.71	1.03	0.38	1.34
461.50	-0.92	-1.10	-1.38	-1.51	-1.60	-1.36	-1.56	-2.41	-1.53	-2.25
461.75	0.29	-0.16	-0.97	0.31	0.78	0.61	0.68	1.02	0.37	1.31
461.75	-0.91	-1.08	-1.35	-1.45	-1.54	-1.31	-1.51	-2.39	-1.51	-2.21
462.00	0.28	-0.18	-1.02	0.30	0.75	0.59	0.66	1.01	0.35	1.28
462.00	-0.89	-1.06	-1.32	-1.39	-1.48	-1.27	-1.46	-2.35	-1.49	-2.16
462.25	0.28	-0.19	-1.05	0.29	0.72	0.57	0.64	0.99	0.34	1.26
462.25	-0.89	-1.05	-1.29	-1.34	-1.43	-1.23	-1.42	-2.32	-1.47	-2.13
462.50	0.29	-0.18	-1.06	0.28	0.70	0.56	0.63	0.98	0.33	1.26
462.50	-0.89	-1.06	-1.29	-1.31	-1.40	-1.21	-1.39	-2.29	-1.46	-2.11
462.75	0.29	-0.18	-1.05	0.28	0.69	0.55	0.62	0.97	0.33	1.25
462.75	-0.90	-1.06	-1.29	-1.30	-1.39	-1.20	-1.37	-2.26	-1.46	-2.11
463.00	0.29	-0.17	-1.03	0.28	0.69	0.55	0.62	0.96	0.33	1.26
463.00	-0.90	-1.07	-1.29	-1.30	-1.38	-1.20	-1.36	-2.24	-1.47	-2.11
463.25	0.30	-0.16	-1.00	0.28	0.69	0.55	0.62	0.95	0.32	1.26
463.25	-0.91	-1.08	-1.30	-1.31	-1.39	-1.20	-1.36	-2.21	-1.47	-2.12
463.50	0.31	-0.14	-0.97	0.28	0.70	0.55	0.62	0.94	0.32	1.26
463.50	-0.91	-1.08	-1.31	-1.33	-1.41	-1.21	-1.37	-2.19	-1.47	-2.13
463.75	0.31	-0.13	-0.93	0.28	0.71	0.56	0.63	0.93	0.32	1.27
463.75	-0.92	-1.09	-1.32	-1.34	-1.42	-1.23	-1.38	-2.18	-1.47	-2.14
464.00	0.32	-0.12	-0.90	0.29	0.72	0.56	0.63	0.93	0.32	1.27
464.00	-0.92	-1.09	-1.33	-1.36	-1.44	-1.24	-1.39	-2.17	-1.47	-2.15
464.25	0.32	-0.11	-0.87	0.29	0.72	0.57	0.64	0.93	0.32	1.28
464.25	-0.93	-1.09	-1.34	-1.38	-1.45	-1.25	-1.40	-2.16	-1.47	-2.15
464.50	0.32	-0.10	-0.85	0.29	0.73	0.57	0.64	0.92	0.32	1.28
464.50	-0.93	-1.10	-1.35	-1.39	-1.46	-1.26	-1.41	-2.16	-1.47	-2.16

HOURS AFTER START OF AUGUST 1978. CURRENTS IN DECIMETERS/SEC.  
 FIRST CARD OF PAIR IS TRUE NORTH COMPONENT, SECOND IS TOWARDS EAST

464.75	0.32	-0.10	-0.83	0.30	0.74	0.58	0.65	0.93	0.32	1.29
464.75	-0.93	-1.10	-1.36	-1.40	-1.48	-1.27	-1.41	-2.16	-1.47	-2.17
465.00	0.32	-0.09	-0.81	0.30	0.74	0.58	0.65	0.93	0.33	1.29
465.00	-0.93	-1.10	-1.37	-1.41	-1.48	-1.28	-1.42	-2.16	-1.47	-2.17
465.25	0.32	-0.10	-0.81	0.29	0.74	0.58	0.65	0.92	0.32	1.28
465.25	-0.92	-1.09	-1.36	-1.41	-1.48	-1.27	-1.42	-2.16	-1.47	-2.17
465.50	0.30	-0.11	-0.83	0.29	0.73	0.57	0.64	0.92	0.31	1.27
465.50	-0.90	-1.07	-1.34	-1.40	-1.47	-1.26	-1.40	-2.15	-1.45	-2.14
465.75	0.29	-0.13	-0.87	0.29	0.72	0.57	0.63	0.91	0.30	1.24
465.75	-0.88	-1.05	-1.30	-1.37	-1.44	-1.23	-1.38	-2.12	-1.43	-2.10
466.00	0.28	-0.14	-0.91	0.28	0.70	0.55	0.62	0.90	0.28	1.21
466.00	-0.86	-1.02	-1.26	-1.33	-1.40	-1.20	-1.35	-2.10	-1.41	-2.05
466.25	0.27	-0.15	-0.95	0.27	0.68	0.53	0.60	0.88	0.27	1.17
466.25	-0.84	-1.00	-1.22	-1.28	-1.35	-1.16	-1.32	-2.07	-1.38	-1.99
466.50	0.26	-0.18	-0.98	0.26	0.65	0.52	0.58	0.87	0.26	1.14
466.50	-0.82	-0.98	-1.18	-1.23	-1.30	-1.12	-1.28	-2.04	-1.35	-1.93
466.75	0.25	-0.19	-1.02	0.25	0.63	0.50	0.56	0.85	0.25	1.10
466.75	-0.80	-0.95	-1.14	-1.17	-1.25	-1.08	-1.23	-2.00	-1.32	-1.87
467.00	0.24	-0.20	-1.05	0.24	0.60	0.48	0.54	0.84	0.24	1.06
467.00	-0.78	-0.93	-1.10	-1.12	-1.20	-1.03	-1.18	-1.96	-1.28	-1.81
467.25	0.23	-0.21	-1.07	0.22	0.57	0.46	0.51	0.82	0.22	1.03
467.25	-0.77	-0.91	-1.07	-1.07	-1.15	-0.99	-1.14	-1.91	-1.25	-1.75
467.50	0.22	-0.21	-1.08	0.21	0.55	0.44	0.49	0.79	0.21	0.99
467.50	-0.75	-0.89	-1.03	-1.03	-1.10	-0.95	-1.10	-1.86	-1.22	-1.69
467.75	0.22	-0.22	-1.10	0.20	0.53	0.42	0.48	0.77	0.20	0.95
467.75	-0.74	-0.87	-1.00	-0.99	-1.06	-0.92	-1.06	-1.80	-1.19	-1.63
468.00	0.21	-0.22	-1.10	0.19	0.51	0.41	0.46	0.75	0.19	0.92
468.00	-0.72	-0.85	-0.97	-0.95	-1.02	-0.88	-1.02	-1.75	-1.15	-1.57
468.25	0.21	-0.21	-1.10	0.19	0.49	0.39	0.45	0.73	0.18	0.89
468.25	-0.72	-0.84	-0.95	-0.92	-1.00	-0.85	-0.98	-1.70	-1.12	-1.51
468.50	0.21	-0.20	-1.07	0.18	0.48	0.39	0.44	0.71	0.19	0.87
468.50	-0.72	-0.84	-0.95	-0.90	-0.98	-0.84	-0.97	-1.65	-1.09	-1.48
468.75	0.22	-0.18	-1.03	0.18	0.48	0.38	0.43	0.69	0.19	0.86
468.75	-0.72	-0.84	-0.95	-0.90	-0.98	-0.84	-0.96	-1.62	-1.07	-1.46

HOURS AFTER START OF AUGUST 1978. CURRENTS IN DECIMETERS/SEC.  
 FIRST CARD OF PAIR IS TRUE NORTH COMPONENT, SECCND IS TOWARDS EAST

469.00	0.22	-0.17	-0.99	0.18	0.48	0.39	0.43	0.68	0.20	0.86
469.00	-0.73	-0.84	-0.96	-0.91	-0.98	-0.84	-0.95	-1.59	-1.06	-1.45
469.25	0.23	-0.15	-0.95	0.18	0.49	0.39	0.44	0.67	0.20	0.86
469.25	-0.73	-0.85	-0.97	-0.93	-1.00	-0.85	-0.96	-1.57	-1.05	-1.46
469.50	0.23	-0.13	-0.91	0.18	0.50	0.40	0.44	0.66	0.20	0.87
469.50	-0.74	-0.85	-0.99	-0.95	-1.02	-0.87	-0.97	-1.55	-1.04	-1.47
469.75	0.23	-0.12	-0.87	0.18	0.51	0.40	0.45	0.66	0.21	0.88
469.75	-0.75	-0.86	-1.00	-0.97	-1.04	-0.88	-0.98	-1.54	-1.04	-1.48
470.00	0.24	-0.10	-0.84	0.19	0.52	0.41	0.46	0.66	0.21	0.88
470.00	-0.75	-0.86	-1.02	-1.00	-1.07	-0.90	-1.00	-1.54	-1.03	-1.50
470.25	0.24	-0.09	-0.82	0.19	0.53	0.42	0.47	0.66	0.22	0.89
470.25	-0.75	-0.87	-1.03	-1.01	-1.09	-0.92	-1.01	-1.54	-1.03	-1.50
470.50	0.24	-0.09	-0.80	0.19	0.54	0.42	0.47	0.67	0.22	0.89
470.50	-0.76	-0.87	-1.04	-1.03	-1.10	-0.93	-1.03	-1.55	-1.04	-1.51
470.75	0.24	-0.08	-0.79	0.19	0.55	0.43	0.48	0.67	0.23	0.90
470.75	-0.76	-0.87	-1.05	-1.05	-1.12	-0.94	-1.04	-1.57	-1.04	-1.52
471.00	0.24	-0.08	-0.79	0.20	0.55	0.44	0.48	0.68	0.23	0.91
471.00	-0.76	-0.88	-1.06	-1.06	-1.13	-0.95	-1.05	-1.58	-1.05	-1.53
471.25	0.24	-0.08	-0.79	0.20	0.56	0.44	0.49	0.69	0.23	0.91
471.25	-0.76	-0.88	-1.06	-1.06	-1.14	-0.95	-1.06	-1.60	-1.06	-1.54
471.50	0.23	-0.09	-0.80	0.20	0.56	0.44	0.48	0.69	0.23	0.91
471.50	-0.75	-0.87	-1.05	-1.06	-1.13	-0.95	-1.06	-1.61	-1.06	-1.53
471.75	0.23	-0.09	-0.82	0.19	0.55	0.43	0.48	0.69	0.23	0.90
471.75	-0.74	-0.85	-1.04	-1.05	-1.12	-0.94	-1.05	-1.61	-1.05	-1.52
472.00	0.22	-0.10	-0.84	0.19	0.55	0.43	0.48	0.69	0.23	0.88
472.00	-0.73	-0.84	-1.02	-1.03	-1.11	-0.93	-1.04	-1.61	-1.04	-1.49
472.25	0.22	-0.11	-0.87	0.19	0.54	0.42	0.47	0.69	0.23	0.87
472.25	-0.72	-0.83	-1.00	-1.01	-1.09	-0.91	-1.03	-1.61	-1.02	-1.47
472.50	0.21	-0.12	-0.89	0.18	0.52	0.41	0.46	0.69	0.22	0.85
472.50	-0.71	-0.82	-0.99	-0.98	-1.06	-0.89	-1.01	-1.60	-1.01	-1.44
472.75	0.21	-0.12	-0.91	0.18	0.51	0.40	0.45	0.68	0.22	0.83
472.75	-0.70	-0.81	-0.97	-0.96	-1.04	-0.87	-0.99	-1.59	-1.00	-1.41
473.00	0.20	-0.13	-0.92	0.17	0.50	0.39	0.44	0.67	0.21	0.82
473.00	-0.69	-0.79	-0.95	-0.94	-1.02	-0.85	-0.97	-1.57	-0.99	-1.38



HOURS AFTER START OF AUGUST 1978. CURRENTS IN DECIMETERS/SEC.  
 FIRST CARD OF PAIR IS TRUE NORTH COMPONENT, SECOND IS TOWARDS EAST

473.25	0.20	-0.13	-0.93	0.17	0.49	0.39	0.43	0.66	0.21	0.80
473.25	-0.68	-0.78	-0.94	-0.92	-1.00	-0.83	-0.95	-1.55	-0.97	-1.35
473.50	0.20	-0.13	-0.93	0.16	0.48	0.38	0.42	0.65	0.20	0.78
473.50	-0.67	-0.77	-0.92	-0.89	-0.98	-0.81	-0.93	-1.52	-0.96	-1.32
473.75	0.19	-0.13	-0.94	0.16	0.47	0.37	0.42	0.64	0.20	0.76
473.75	-0.67	-0.76	-0.91	-0.88	-0.96	-0.80	-0.91	-1.50	-0.94	-1.29
474.00	0.19	-0.13	-0.94	0.15	0.46	0.36	0.41	0.63	0.19	0.75
474.00	-0.66	-0.75	-0.90	-0.86	-0.94	-0.78	-0.89	-1.47	-0.92	-1.26
474.25	0.19	-0.13	-0.93	0.15	0.45	0.36	0.40	0.62	0.19	0.73
474.25	-0.65	-0.74	-0.88	-0.84	-0.92	-0.77	-0.88	-1.44	-0.91	-1.24
474.50	0.19	-0.13	-0.92	0.15	0.44	0.35	0.40	0.61	0.19	0.71
474.50	-0.65	-0.74	-0.88	-0.83	-0.91	-0.76	-0.86	-1.42	-0.89	-1.21
474.75	0.19	-0.12	-0.91	0.14	0.44	0.35	0.39	0.59	0.19	0.70
474.75	-0.64	-0.73	-0.87	-0.82	-0.90	-0.75	-0.85	-1.39	-0.87	-1.18
475.00	0.19	-0.12	-0.89	0.14	0.43	0.34	0.38	0.58	0.19	0.69
475.00	-0.63	-0.72	-0.86	-0.81	-0.89	-0.73	-0.83	-1.36	-0.85	-1.16
475.25	0.18	-0.11	-0.87	0.14	0.43	0.34	0.38	0.57	0.19	0.68
475.25	-0.63	-0.71	-0.86	-0.80	-0.88	-0.73	-0.82	-1.34	-0.83	-1.14
475.50	0.18	-0.11	-0.86	0.14	0.42	0.33	0.37	0.56	0.18	0.67
475.50	-0.62	-0.70	-0.85	-0.79	-0.87	-0.72	-0.81	-1.32	-0.82	-1.12
475.75	0.18	-0.10	-0.84	0.13	0.42	0.33	0.37	0.55	0.18	0.66
475.75	-0.62	-0.70	-0.84	-0.79	-0.86	-0.71	-0.80	-1.30	-0.80	-1.11
476.00	0.18	-0.10	-0.83	0.13	0.41	0.33	0.37	0.55	0.18	0.64
476.00	-0.61	-0.69	-0.84	-0.78	-0.85	-0.70	-0.80	-1.28	-0.79	-1.09
476.25	0.18	-0.09	-0.82	0.13	0.41	0.32	0.36	0.54	0.18	0.63
476.25	-0.60	-0.68	-0.83	-0.77	-0.84	-0.70	-0.79	-1.26	-0.78	-1.07
476.50	0.18	-0.09	-0.81	0.13	0.41	0.32	0.36	0.53	0.18	0.62
476.50	-0.59	-0.67	-0.82	-0.76	-0.84	-0.69	-0.78	-1.24	-0.76	-1.05
476.75	0.17	-0.09	-0.80	0.12	0.40	0.32	0.35	0.52	0.18	0.61
476.75	-0.59	-0.66	-0.81	-0.75	-0.83	-0.68	-0.77	-1.22	-0.75	-1.03
477.00	0.17	-0.09	-0.79	0.12	0.40	0.31	0.35	0.52	0.17	0.60
477.00	-0.58	-0.65	-0.80	-0.74	-0.82	-0.67	-0.76	-1.21	-0.74	-1.02
477.25	0.17	-0.08	-0.79	0.12	0.39	0.31	0.35	0.51	0.17	0.59
477.25	-0.57	-0.64	-0.79	-0.73	-0.80	-0.66	-0.74	-1.19	-0.73	-1.00

HOURS AFTER START OF AUGUST 1978. CURRENTS IN DECIMETERS/SEC.  
 FIRST CARD OF PAIR IS TRUE NORTH COMPONENT, SECCND IS TOWARDS EAST

477.50	0.17	-0.08	-0.77	0.12	0.38	0.30	0.34	0.50	0.18	0.58
477.50	-0.55	-0.62	-0.78	-0.71	-0.79	-0.65	-0.73	-1.18	-0.71	-0.97
477.75	0.16	-0.08	-0.75	0.11	0.37	0.29	0.33	0.49	0.18	0.56
477.75	-0.54	-0.60	-0.77	-0.70	-0.77	-0.63	-0.71	-1.15	-0.68	-0.94
478.00	0.16	-0.07	-0.74	0.11	0.36	0.29	0.32	0.48	0.18	0.54
478.00	-0.52	-0.58	-0.75	-0.68	-0.75	-0.61	-0.70	-1.13	-0.66	-0.91
478.25	0.16	-0.07	-0.72	0.11	0.35	0.28	0.31	0.47	0.17	0.53
478.25	-0.51	-0.57	-0.73	-0.65	-0.72	-0.59	-0.68	-1.11	-0.63	-0.89
478.50	0.15	-0.07	-0.70	0.10	0.34	0.27	0.30	0.46	0.17	0.52
478.50	-0.49	-0.55	-0.72	-0.64	-0.70	-0.58	-0.66	-1.08	-0.61	-0.87
478.75	0.15	-0.06	-0.68	0.10	0.33	0.26	0.30	0.45	0.17	0.50
478.75	-0.48	-0.53	-0.70	-0.62	-0.68	-0.56	-0.64	-1.05	-0.59	-0.84
479.00	0.15	-0.06	-0.66	0.10	0.32	0.26	0.29	0.44	0.16	0.49
479.00	-0.46	-0.51	-0.69	-0.60	-0.66	-0.54	-0.62	-1.02	-0.58	-0.82
479.25	0.14	-0.06	-0.65	0.09	0.31	0.25	0.28	0.42	0.15	0.47
479.25	-0.45	-0.50	-0.67	-0.58	-0.64	-0.53	-0.60	-0.99	-0.56	-0.79
479.50	0.14	-0.05	-0.63	0.09	0.30	0.24	0.27	0.41	0.15	0.46
479.50	-0.43	-0.48	-0.65	-0.56	-0.62	-0.51	-0.58	-0.95	-0.54	-0.76
479.75	0.13	-0.05	-0.60	0.09	0.29	0.23	0.26	0.39	0.14	0.44
479.75	-0.41	-0.46	-0.64	-0.55	-0.60	-0.49	-0.56	-0.92	-0.53	-0.74
480.00	0.13	-0.05	-0.59	0.08	0.28	0.23	0.26	0.38	0.13	0.42
480.00	-0.40	-0.44	-0.62	-0.53	-0.58	-0.48	-0.54	-0.89	-0.51	-0.71
480.25	0.13	-0.04	-0.56	0.08	0.27	0.22	0.25	0.37	0.13	0.41
480.25	-0.38	-0.43	-0.60	-0.51	-0.56	-0.46	-0.52	-0.86	-0.49	-0.69
480.50	0.12	-0.04	-0.53	0.08	0.26	0.21	0.24	0.35	0.13	0.39
480.50	-0.37	-0.41	-0.58	-0.49	-0.54	-0.44	-0.50	-0.83	-0.47	-0.56
480.75	0.12	-0.03	-0.51	0.08	0.25	0.20	0.23	0.34	0.12	0.38
480.75	-0.35	-0.39	-0.57	-0.47	-0.52	-0.43	-0.48	-0.80	-0.45	-0.63
481.00	0.12	-0.03	-0.48	0.07	0.24	0.19	0.22	0.33	0.12	0.36
481.00	-0.33	-0.37	-0.55	-0.45	-0.49	-0.41	-0.46	-0.76	-0.42	-0.61
481.25	0.11	-0.02	-0.46	0.07	0.23	0.19	0.21	0.31	0.11	0.35
481.25	-0.31	-0.35	-0.53	-0.43	-0.47	-0.39	-0.44	-0.73	-0.40	-0.58
481.50	0.11	-0.02	-0.43	0.07	0.22	0.18	0.20	0.30	0.11	0.33
481.50	-0.30	-0.33	-0.51	-0.41	-0.45	-0.37	-0.42	-0.70	-0.38	-0.55

HOURS AFTER START OF AUGUST 1978. CURRENTS IN DECIMETERS/SEC.  
 FIRST CARD OF PAIR IS TRUE NORTH COMPONENT, SECOND IS TOWARDS EAST

481.75	0.10	-0.02	-0.40	0.06	0.21	0.17	0.20	0.28	0.10	0.32
481.75	-0.28	-0.31	-0.49	-0.40	-0.43	-0.36	-0.41	-0.67	-0.36	-0.53
482.00	0.10	-0.01	-0.39	0.06	0.21	0.16	0.19	0.27	0.10	0.30
482.00	-0.27	-0.30	-0.47	-0.38	-0.41	-0.34	-0.39	-0.64	-0.34	-0.51
482.25	0.09	-0.01	-0.35	0.06	0.20	0.16	0.18	0.26	0.09	0.29
482.25	-0.25	-0.28	-0.45	-0.36	-0.39	-0.33	-0.37	-0.61	-0.32	-0.48
482.50	0.09	-0.01	-0.34	0.06	0.19	0.15	0.17	0.24	0.09	0.28
482.50	-0.23	-0.26	-0.44	-0.35	-0.37	-0.31	-0.35	-0.58	-0.31	-0.46
482.75	0.09	-0.01	-0.33	0.05	0.18	0.14	0.16	0.23	0.08	0.27
482.75	-0.22	-0.25	-0.42	-0.33	-0.35	-0.30	-0.34	-0.55	-0.29	-0.44
483.00	0.08	-0.00	-0.28	0.05	0.17	0.14	0.16	0.22	0.07	0.25
483.00	-0.21	-0.23	-0.40	-0.31	-0.33	-0.28	-0.32	-0.52	-0.28	-0.42
483.25	0.08	-0.01	-0.29	0.05	0.16	0.13	0.15	0.21	0.07	0.24
483.25	-0.19	-0.22	-0.38	-0.30	-0.32	-0.27	-0.30	-0.50	-0.27	-0.40
483.50	0.07	-0.01	-0.27	0.05	0.15	0.12	0.14	0.20	0.05	0.23
483.50	-0.19	-0.21	-0.36	-0.29	-0.30	-0.26	-0.29	-0.48	-0.26	-0.39
483.75	0.07	-0.01	-0.24	0.05	0.15	0.12	0.14	0.19	0.04	0.23
483.75	-0.18	-0.21	-0.35	-0.28	-0.30	-0.25	-0.28	-0.46	-0.26	-0.39
484.00	0.06	-0.01	-0.29	0.04	0.15	0.12	0.14	0.19	0.04	0.22
484.00	-0.18	-0.20	-0.34	-0.27	-0.29	-0.25	-0.28	-0.45	-0.26	-0.37
484.25	0.06	-0.02	-0.25	0.04	0.14	0.12	0.13	0.18	0.04	0.21
484.25	-0.17	-0.20	-0.32	-0.27	-0.29	-0.24	-0.27	-0.44	-0.26	-0.37
484.50	0.05	-0.02	-0.26	0.04	0.14	0.11	0.13	0.18	0.03	0.21
484.50	-0.17	-0.20	-0.31	-0.27	-0.29	-0.24	-0.27	-0.43	-0.26	-0.36
484.75	0.05	-0.02	-0.32	0.04	0.14	0.11	0.13	0.18	0.03	0.20
484.75	-0.17	-0.20	-0.30	-0.26	-0.29	-0.24	-0.27	-0.43	-0.25	-0.34
485.00	0.05	-0.03	-0.23	0.04	0.14	0.11	0.13	0.18	0.03	0.20
485.00	-0.17	-0.20	-0.29	-0.26	-0.28	-0.23	-0.27	-0.43	-0.25	-0.33
485.25	0.04	-0.03	-0.32	0.04	0.14	0.11	0.13	0.19	0.03	0.20
485.25	-0.18	-0.20	-0.29	-0.26	-0.28	-0.23	-0.26	-0.44	-0.25	-0.34
485.50	0.04	-0.04	-0.34	0.04	0.14	0.11	0.13	0.19	0.03	0.19
485.50	-0.18	-0.21	-0.28	-0.25	-0.28	-0.23	-0.27	-0.45	-0.24	-0.33
485.75	0.04	-0.04	-0.25	0.04	0.14	0.11	0.13	0.19	0.04	0.19
485.75	-0.19	-0.21	-0.28	-0.25	-0.29	-0.23	-0.27	-0.45	-0.24	-0.31

HOURS AFTER START OF AUGUST 1978. CURRENTS IN DECIMETERS/SEC.  
 FIRST CARD OF PAIR IS TRUE NORTH COMPONENT, SECCND IS TOWARDS EAST

486.00	0.04	-0.05	-0.44	0.03	0.14	0.11	0.13	0.19	0.04	0.19
486.00	-0.20	-0.22	-0.28	-0.26	-0.29	-0.24	-0.27	-0.46	-0.24	-0.32
486.25	0.04	-0.05	-0.35	0.03	0.14	0.11	0.13	0.20	0.04	0.19
486.25	-0.20	-0.23	-0.27	-0.26	-0.30	-0.24	-0.27	-0.46	-0.24	-0.31
486.50	0.04	-0.05	-0.33	0.03	0.14	0.11	0.13	0.20	0.05	0.16
486.50	-0.21	-0.22	-0.27	-0.25	-0.30	-0.24	-0.27	-0.46	-0.23	-0.28
486.75	0.04	-0.06	-0.55	0.03	0.13	0.11	0.13	0.19	0.06	0.15
486.75	-0.21	-0.22	-0.27	-0.24	-0.29	-0.23	-0.26	-0.45	-0.21	-0.25
487.00	0.04	-0.06	-0.31	0.02	0.12	0.10	0.12	0.19	0.05	0.14
487.00	-0.21	-0.22	-0.25	-0.23	-0.27	-0.21	-0.25	-0.44	-0.19	-0.24
487.25	0.05	-0.07	-0.48	0.02	0.12	0.10	0.11	0.18	0.05	0.13
487.25	-0.21	-0.23	-0.26	-0.21	-0.26	-0.20	-0.24	-0.42	-0.17	-0.20
487.50	0.05	-0.08	-0.62	0.02	0.11	0.09	0.10	0.17	0.06	0.10
487.50	-0.22	-0.24	-0.25	-0.19	-0.24	-0.18	-0.22	-0.40	-0.16	-0.17
487.75	0.05	-0.09	-0.33	0.01	0.10	0.08	0.10	0.16	0.05	0.10
487.75	-0.23	-0.24	-0.25	-0.18	-0.22	-0.17	-0.20	-0.38	-0.16	-0.16
488.00	0.05	-0.10	-0.72	0.01	0.09	0.08	0.09	0.15	0.04	0.09
488.00	-0.24	-0.26	-0.27	-0.17	-0.21	-0.15	-0.19	-0.35	-0.15	-0.15
488.25	0.05	-0.11	-0.68	0.01	0.09	0.07	0.08	0.14	0.04	0.06
488.25	-0.25	-0.27	-0.25	-0.15	-0.19	-0.14	-0.17	-0.32	-0.14	-0.09
488.50	0.05	-0.13	-0.47	0.00	0.08	0.07	0.08	0.12	0.04	0.04
488.50	-0.26	-0.28	-0.26	-0.14	-0.18	-0.13	-0.16	-0.28	-0.14	-0.06
488.75	0.05	-0.15	-1.00	-0.00	0.07	0.06	0.07	0.10	0.03	0.03
488.75	-0.27	-0.29	-0.28	-0.12	-0.16	-0.11	-0.13	-0.25	-0.13	-0.06
489.00	0.06	-0.16	-0.74	-0.01	0.06	0.05	0.06	0.09	0.02	0.00
489.00	-0.28	-0.30	-0.27	-0.09	-0.13	-0.09	-0.11	-0.22	-0.11	-0.00
489.25	0.06	-0.18	-0.71	-0.01	0.04	0.04	0.04	0.07	0.03	-0.04
489.25	-0.29	-0.31	-0.29	-0.06	-0.10	-0.05	-0.08	-0.18	-0.08	0.08
489.50	0.06	-0.20	-1.27	-0.03	0.02	0.02	0.02	0.05	0.02	-0.06
489.50	-0.29	-0.31	-0.30	-0.02	-0.05	-0.01	-0.04	-0.12	-0.04	0.11
489.75	0.06	-0.21	-0.82	-0.04	-0.00	0.00	0.00	0.02	0.01	-0.11
489.75	-0.29	-0.31	-0.29	0.03	0.00	0.04	0.01	-0.07	0.01	0.18
490.00	0.06	-0.23	-1.01	-0.05	-0.03	-0.02	-0.02	-0.01	0.01	-0.19
490.00	-0.29	-0.31	-0.32	0.09	0.06	0.09	0.07	0.00	0.07	0.34

HOURS AFTER START OF AUGUST 1978. CURRENTS IN DECIMETERS/SEC.  
 FIRST CARD OF PAIR IS TRUE NORTH COMPONENT, SECOND IS TOWARDS EAST

490.25	0.06	-0.26	-1.49	-0.06	-0.06	-0.05	-0.05	-0.05	0.01	-0.26
490.25	-0.28	-0.30	-0.31	0.15	0.13	0.15	0.13	0.09	0.13	0.46
490.50	0.06	-0.28	-0.94	-0.08	-0.09	-0.07	-0.08	-0.10	-0.02	-0.31
490.50	-0.27	-0.28	-0.30	0.22	0.21	0.22	0.20	0.20	0.20	0.53
490.75	0.05	-0.31	-1.35	-0.09	-0.12	-0.10	-0.12	-0.15	-0.04	-0.41
490.75	-0.25	-0.26	-0.32	0.30	0.29	0.29	0.28	0.32	0.29	0.69
491.00	0.04	-0.34	-1.68	-0.10	-0.16	-0.14	-0.15	-0.21	-0.04	-0.51
491.00	-0.24	-0.24	-0.29	0.38	0.38	0.37	0.36	0.45	0.37	0.88
491.25	0.03	-0.37	-1.10	-0.12	-0.21	-0.17	-0.20	-0.27	-0.08	-0.56
491.25	-0.21	-0.21	-0.27	0.47	0.48	0.45	0.45	0.59	0.44	0.94
491.50	0.01	-0.41	-1.66	-0.14	-0.26	-0.21	-0.24	-0.33	-0.12	-0.62
491.50	-0.18	-0.18	-0.29	0.56	0.58	0.54	0.55	0.72	0.53	1.04
491.75	-0.00	-0.44	-1.81	-0.15	-0.31	-0.25	-0.28	-0.39	-0.13	-0.74
491.75	-0.16	-0.15	-0.25	0.66	0.69	0.63	0.64	0.87	0.64	1.25
492.00	-0.02	-0.47	-1.23	-0.17	-0.37	-0.29	-0.33	-0.44	-0.15	-0.81
492.00	-0.12	-0.11	-0.23	0.77	0.79	0.71	0.74	1.00	0.72	1.36
492.25	-0.04	-0.49	-1.87	-0.19	-0.42	-0.33	-0.37	-0.50	-0.20	-0.82
492.25	-0.10	-0.08	-0.25	0.85	0.89	0.79	0.82	1.13	0.79	1.35
492.50	-0.05	-0.51	-1.83	-0.19	-0.45	-0.36	-0.40	-0.54	-0.21	-0.88
492.50	-0.08	-0.06	-0.22	0.92	0.95	0.84	0.89	1.23	0.86	1.48
492.75	-0.06	-0.53	-1.28	-0.20	-0.49	-0.38	-0.42	-0.57	-0.19	-0.93
492.75	-0.07	-0.05	-0.23	0.97	1.00	0.88	0.94	1.31	0.91	1.60
493.00	-0.07	-0.54	-1.96	-0.21	-0.50	-0.39	-0.44	-0.60	-0.22	-0.90
493.00	-0.07	-0.05	-0.26	0.99	1.04	0.90	0.98	1.38	0.92	1.49
493.25	-0.08	-0.54	-1.74	-0.21	-0.52	-0.40	-0.45	-0.62	-0.26	-0.88
493.25	-0.06	-0.04	-0.25	1.01	1.05	0.91	1.00	1.44	0.94	1.46
493.50	-0.08	-0.54	-1.27	-0.21	-0.52	-0.41	-0.46	-0.64	-0.23	-0.95
493.50	-0.06	-0.04	-0.27	1.02	1.06	0.92	1.01	1.48	0.98	1.62
493.75	-0.09	-0.54	-1.97	-0.21	-0.53	-0.41	-0.46	-0.65	-0.22	-0.94
493.75	-0.06	-0.04	-0.31	1.02	1.06	0.92	1.02	1.52	0.99	1.60
494.00	-0.09	-0.54	-1.62	-0.22	-0.53	-0.41	-0.46	-0.67	-0.26	-0.87
494.00	-0.06	-0.04	-0.30	1.02	1.07	0.92	1.03	1.55	0.98	1.43
494.25	-0.09	-0.54	-1.25	-0.22	-0.53	-0.41	-0.47	-0.67	-0.25	-0.92
494.25	-0.06	-0.04	-0.33	1.02	1.07	0.92	1.03	1.57	1.02	1.55

HOURS AFTER START OF AUGUST 1978. CURRENTS IN DECIMETERS/SEC.  
 FIRST CARD OF PAIR IS TRUE NORTH COMPONENT, SECCND IS TCWARDS EAST

494.50	-0.09	-0.53	-1.95	-0.22	-0.53	-0.42	-0.47	-0.68	-0.20	-0.98
494.50	-0.06	-0.04	-0.36	1.02	1.07	0.93	1.04	1.58	1.04	1.68
494.75	-0.09	-0.53	-1.49	-0.22	-0.53	-0.42	-0.47	-0.68	-0.24	-0.90
494.75	-0.06	-0.04	-0.34	1.02	1.07	0.93	1.04	1.60	1.02	1.48
495.00	-0.09	-0.53	-1.25	-0.22	-0.53	-0.42	-0.47	-0.69	-0.27	-0.87
495.00	-0.06	-0.04	-0.37	1.02	1.07	0.93	1.04	1.60	1.03	1.43
495.25	-0.09	-0.52	-1.94	-0.22	-0.53	-0.42	-0.48	-0.69	-0.20	-0.98
495.25	-0.06	-0.04	-0.39	1.02	1.07	0.93	1.04	1.61	1.07	1.69
495.50	-0.09	-0.52	-1.40	-0.22	-0.54	-0.42	-0.48	-0.69	-0.19	-0.95
495.50	-0.05	-0.03	-0.35	1.03	1.08	0.93	1.05	1.62	1.05	1.62
495.75	-0.10	-0.52	-1.28	-0.22	-0.54	-0.43	-0.48	-0.69	-0.27	-0.85
495.75	-0.04	-0.02	-0.37	1.03	1.08	0.94	1.05	1.62	1.03	1.37
496.00	-0.10	-0.52	-1.94	-0.22	-0.54	-0.43	-0.48	-0.70	-0.24	-0.94
496.00	-0.04	-0.02	-0.38	1.04	1.09	0.95	1.06	1.63	1.08	1.59
496.25	-0.10	-0.52	-1.33	-0.23	-0.55	-0.43	-0.49	-0.70	-0.17	-1.02
496.25	-0.03	-0.01	-0.34	1.05	1.10	0.95	1.07	1.64	1.10	1.79
496.50	-0.11	-0.52	-1.34	-0.23	-0.55	-0.44	-0.49	-0.70	-0.24	-0.90
496.50	-0.02	-0.00	-0.37	1.06	1.11	0.96	1.08	1.64	1.05	1.46
496.75	-0.11	-0.53	-1.94	-0.23	-0.56	-0.44	-0.50	-0.71	-0.29	-0.88
496.75	-0.01	0.01	-0.37	1.07	1.12	0.97	1.09	1.65	1.06	1.43
497.00	-0.11	-0.53	-1.26	-0.23	-0.56	-0.44	-0.50	-0.71	-0.19	-1.05
497.00	-0.00	0.01	-0.33	1.08	1.14	0.98	1.09	1.66	1.13	1.84
497.25	-0.12	-0.52	-1.39	-0.23	-0.57	-0.45	-0.50	-0.72	-0.18	-1.00
497.25	0.01	0.02	-0.36	1.10	1.15	0.99	1.10	1.67	1.09	1.70
497.50	-0.12	-0.52	-1.90	-0.23	-0.57	-0.45	-0.51	-0.72	-0.30	-0.85
497.50	0.02	0.03	-0.35	1.11	1.16	1.00	1.11	1.69	1.06	1.33
497.75	-0.12	-0.52	-1.18	-0.24	-0.58	-0.46	-0.51	-0.73	-0.24	-0.99
497.75	0.03	0.04	-0.32	1.12	1.17	1.01	1.12	1.70	1.14	1.70
498.00	-0.12	-0.52	-1.42	-0.24	-0.59	-0.46	-0.52	-0.73	-0.13	-1.10
498.00	0.04	0.06	-0.35	1.13	1.18	1.02	1.13	1.71	1.17	1.95
498.25	-0.13	-0.51	-1.83	-0.24	-0.59	-0.46	-0.52	-0.74	-0.25	-0.90
498.25	0.05	0.06	-0.33	1.13	1.19	1.02	1.14	1.73	1.09	1.43
498.50	-0.13	-0.51	-1.10	-0.24	-0.59	-0.47	-0.52	-0.75	-0.31	-0.89
498.50	0.06	0.07	-0.31	1.14	1.19	1.03	1.15	1.74	1.11	1.43

HOURS AFTER START OF AUGUST 1978. CURRENTS IN DECIMETERS/SEC.  
 FIRST CARD OF PAIR IS TRUE NORTH COMPONENT, SECOND IS TOWARDS EAST

498.75	-0.13	-0.50	-1.45	-0.24	-0.59	-0.47	-0.53	-0.75	-0.15	-1.12
498.75	0.07	0.07	-0.34	1.14	1.20	1.03	1.15	1.75	1.20	2.01
499.00	-0.13	-0.50	-1.76	-0.24	-0.59	-0.47	-0.53	-0.75	-0.15	-1.01
499.00	0.07	0.07	-0.32	1.14	1.20	1.03	1.15	1.76	1.13	1.72
499.25	-0.13	-0.49	-1.03	-0.24	-0.59	-0.47	-0.53	-0.76	-0.33	-0.80
499.25	0.08	0.08	-0.31	1.14	1.20	1.03	1.15	1.76	1.07	1.20
499.50	-0.13	-0.49	-1.48	-0.24	-0.59	-0.47	-0.53	-0.76	-0.23	-1.02
499.50	0.08	0.08	-0.34	1.14	1.19	1.03	1.15	1.77	1.18	1.77
499.75	-0.13	-0.49	-1.68	-0.24	-0.59	-0.47	-0.53	-0.76	-0.08	-1.14
499.75	0.08	0.08	-0.32	1.13	1.19	1.03	1.15	1.77	1.19	2.05
500.00	-0.13	-0.48	-0.98	-0.24	-0.59	-0.47	-0.53	-0.76	-0.25	-0.83
500.00	0.09	0.09	-0.31	1.13	1.19	1.03	1.15	1.77	1.07	1.27
500.25	-0.13	-0.48	-1.53	-0.24	-0.59	-0.47	-0.53	-0.76	-0.31	-0.85
500.25	0.09	0.09	-0.35	1.13	1.19	1.03	1.15	1.78	1.12	1.35
500.50	-0.13	-0.47	-1.61	-0.24	-0.59	-0.47	-0.53	-0.76	-0.08	-1.17
500.50	0.10	0.09	-0.32	1.13	1.19	1.03	1.15	1.78	1.24	2.14
500.75	-0.13	-0.47	-0.95	-0.24	-0.59	-0.47	-0.53	-0.76	-0.10	-0.98
500.75	0.10	0.09	-0.32	1.13	1.19	1.03	1.15	1.78	1.13	1.65
501.00	-0.13	-0.47	-1.57	-0.24	-0.59	-0.47	-0.53	-0.76	-0.33	-0.71
501.00	0.10	0.10	-0.35	1.13	1.19	1.03	1.15	1.78	1.05	1.01
501.25	-0.13	-0.46	-1.53	-0.24	-0.59	-0.47	-0.52	-0.76	-0.17	-1.04
501.25	0.11	0.10	-0.32	1.13	1.19	1.03	1.15	1.78	1.22	1.85
501.50	-0.12	-0.46	-0.93	-0.24	-0.59	-0.47	-0.53	-0.76	0.03	-1.16
501.50	0.11	0.11	-0.32	1.14	1.19	1.03	1.15	1.78	1.23	2.11
501.75	-0.12	-0.45	-1.60	-0.24	-0.59	-0.47	-0.53	-0.76	-0.22	-0.73
501.75	0.12	0.12	-0.34	1.14	1.20	1.03	1.15	1.78	1.06	1.05
502.00	-0.12	-0.45	-1.42	-0.24	-0.59	-0.47	-0.53	-0.76	-0.28	-0.81
502.00	0.13	0.12	-0.31	1.14	1.20	1.03	1.15	1.78	1.15	1.29
502.25	-0.12	-0.44	-0.90	-0.24	-0.59	-0.47	-0.53	-0.76	0.05	-1.21
502.25	0.13	0.13	-0.31	1.14	1.20	1.03	1.16	1.78	1.31	2.27
502.50	-0.11	-0.43	-1.59	-0.24	-0.60	-0.47	-0.53	-0.76	-0.01	-0.92
502.50	0.14	0.14	-0.33	1.14	1.21	1.03	1.16	1.79	1.15	1.52
502.75	-0.11	-0.42	-1.30	-0.24	-0.60	-0.47	-0.53	-0.77	-0.31	-0.62
502.75	0.15	0.15	-0.30	1.14	1.21	1.04	1.16	1.79	1.07	0.82

HOURS AFTER START OF AUGUST 1978. CURRENTS IN DECIMETERS/SEC.  
 FIRST CARD OF PAIR IS TRUE NORTH COMPONENT, SECCND IS TOWARDS EAST

503.00	-0.11	-0.42	-0.86	-0.24	-0.60	-0.47	-0.53	-0.77	-0.06	-1.05
503.00	0.16	0.15	-0.31	1.14	1.21	1.04	1.16	1.79	1.29	1.92
503.25	-0.11	-0.41	-1.57	-0.23	-0.60	-0.47	-0.53	-0.77	0.16	-1.15
503.25	0.17	0.16	-0.33	1.15	1.21	1.04	1.16	1.80	1.28	2.11
503.50	-0.10	-0.40	-1.16	-0.23	-0.60	-0.47	-0.53	-0.77	-0.18	-0.60
503.50	0.19	0.18	-0.29	1.15	1.22	1.04	1.17	1.81	1.05	0.79
503.75	-0.10	-0.39	-0.82	-0.23	-0.60	-0.47	-0.53	-0.78	-0.22	-0.76
503.75	0.20	0.19	-0.30	1.15	1.22	1.04	1.17	1.81	1.19	1.23
504.00	-0.10	-0.38	-1.51	-0.23	-0.60	-0.47	-0.53	-0.78	0.19	-1.22
504.00	0.21	0.20	-0.32	1.15	1.23	1.04	1.17	1.82	1.37	2.34



## Appendix C

### Data Acquisition Program Listings in North Star BASIC

The program listings on the following pages contain the following symbol transposition failures due to the use of a non-ASCII type set:

< has been printed as @

> has been printed as #

^ has been printed as ¢

\ has been printed as 8

The main data acquisition program was written chiefly by C. E. Abel.

```

10 REM DATA ACQUISITION AND ANALYSIS DEMONSTRATION
20 DIM D(2,512),W(2,512),Q(6)
30 DIM C(2,512),A$(80),E(10)
40 PRINT"PROGRAM FOR ACQUISITION AND ANALYSIS"
50 PRINT"OF A REAL SCALAR TIME SERIES"
60 PRINT
70 PRINT"PLEASE DESCRIBE TASK BY RESPONDING"
80 PRINT"TO THE FOLLOWING QUESTIONS:"
90 PRINT"NOTE---#NUMBER OF SAMPLES MUST BE A"
100 PRINT" POWER OF 2 @=512"
110 INPUT"NUMBER OF SAMPLE VALUES"
120 T0=LOG(N1)/LOG(2)+1E-05
130 T1=2*INT(T0)
140 IF T1=N1 THEN 170
150 PRINT"*****NOT A POWER OF 2"
160 GOTO 110
170 IF N1@=512 THEN 200
180 PRINT"*****VALUE TOO LARGE"
190 GOTO 110
200 N0=INT(T0)
210 PRINT"NOTE---#SAMPLING INTERVAL MUST"
220 PRINT" EXCEED .1 SEC."
230 INPUT"SAMPLING INTERVAL IN HUNDREDTHS OF SEC."
240 W7=D9/100
250 IF W7#=.03 THEN 280
260 PRINT"*****SAMPLING INTERVAL TOO SMALL"
270 GOTO 230
280 INPUT" WAVE UNITS CORRESPONDING TO 0 VOLTS"
290 INPUT" WAVE UNITS CORRESPONDING TO 1 VOLT"
300 INPUT"CURRENT UNITS CORRESPONDING TO 1 VOLT"
310 INPUT"WAVE STAFF 0 ELEV ABOVE BOTTOM"
320 PRINT"CURRENT PROBE ELEV ABOVE BOTTOM"
330 INPUT"(IF NO CURRENTS TAKEN, INPUT 999)"
340 INPUT"DISPLAY SAMPLE VALUES(YES/NO)"
350 Q(1)=0
360 IF A$(1,1)="Y" THEN Q(1)=1
370 IF Q(1)=0 THEN 410
380 INPUT"PRINT RATHER THAN PLOT DISPLAY (YES/NO)"
390 Q(6)=0
400 IF A$(1,1)="Y" THEN Q(6)=1
410 INPUT"COMPUTE SPECTRAL ESTIMATE(YES/NO)"
420 Q(2)=0
430 IF A$(1,1)="Y" THEN Q(2)=1
440 INPUT"DISPLAY SPECTRAL ESTIMATE(YES/NO)"
450 Q(3)=0
460 IF A$(1,1)="Y" THEN Q(3)=1
470 INPUT"IS TASK TO BE REPEATED(YES/NO)"
480 Q(4)=0
490 IF A$(1,1)="Y" THEN Q(4)=1
500 IF Q(4)=0 THEN 580

```

?",N1

?",D9

?",S8

?",S9

?",S6

?",E7

?",E6

?",A\$

?",A\$

?",A\$

?",A\$

?",A\$

```

510 INPUT"HOW MANY TIMES                                ?",H0
520 PRINT"IS THERE A DELAY BETWEEN REPETITIONS",
530 INPUT" (YES/NO)?",A$
540 Q(5)=0
550 IF A$(1,1)="Y". THEN Q(5)=1
560 IF Q(5) @#1 THEN GOTO 580
570 INPUT"DELAY IN SECONDS                                ?",D0
580 GOSUB 2830
590 PRINT"BEGIN TASK"
600 IF Q(4)=0 THEN H0=1
610 FOR C0=1 TO H0
620 PRINT"TASK REPETITION #",C0
630 GOSUB 1420
640 IF Q(1)=0 THEN 730
650 PRINT"DISPLAY OF SAMPLED VALUES."
660 PRINT
670 IF Q(6)=0 THEN PRINT" TIME UNITS"
680 IF Q(6)=0 THEN 710
690 PRINT"THERE WILL BE A 1/2 SEC. DELAY"
700 PRINT"AFTER EACH LINE."
710 REM
720 GOSUB 1960
730 IF Q(2)=0 THEN 770
740 S0=-1
750 PRINT"ENTERING SPECTRAL ESTIMATION ROUTINE"
760 GOSUB 1700
770 IF Q(3)=0 THEN 850
780 PRINT"DISPLAY OF SPECTRAL ESTIMATES. THERE"
790 PRINT"WILL BE A 1/2 SEC. DELAY AFTER EACH LINE."
800 PRINT"ONLY VALUES THROUGH THE NYQUIST "
810 PRINT"FREQUENCY ARE DISPLAYED."
820 PRINT
830 IF W(2,1)=0 THEN W(2,1)=1E-60
840 GOSUB 2310
850 IF Q(5)=0 THEN 880
860 W3=D0
870 GOSUB 1650
880 NEXT C0
890 F8=FREE(0)
900 PRINT"BYTES REMAINING FREE= ",F8
910 STOP

```

```

920 REM FFT ALGORITHM FOR COMPLEX SERIES OF
930 REM 2*CN0 POINTS. ARRAYS D(2,2*CN0),W(2,2*CN0)
940 REM ARE DIMENSIONED IN THE CALLING PROGRAM.
950 REM D(1,I),D(2,I) ARE REAL AND IMAGINARY
960 REM PARTS OF INPUT SERIES. TRANSFORM IS
970 REM RETURNED IN D. ASSIGN N0 AND S0
980 REM VALUES IN CALLING ROUTINE. SFT S0=-1
990 REM FOR NORMALIZED FORWARD TRANSFORM, S0=+1 FOR
1000 REM INVERSE OF A NORMALIZED FORWARD TRANSFORM.
1010 N5=2*CN0
1020 N6=N5/2
1030 P1=3.14259
1040 P9=2*P1/N5
1050 FOR J9=1 TO N0
1060 PRINT J9,"/",N0
1070 N7=N5/2*J9
1080 N8=N7
1090 N9=2*(J9-1)
1100 FOR I4=1 TO N9
1110 I5=(I4-1)*N7
1120 T9=I5*P9*S0
1130 W8=COS(T9)
1140 W9=SIN(T9)
1150 FOR K9=1 TO N8
1160 I6=K9+I5
1170 I7=K9+2*I5
1180 I8=I7+N7
1190 I9=I6+N6
1200 W(1,I6)=D(1,I7)+W8*D(1,I8)-W9*D(2,I8)
1210 W(2,I6)=D(2,I7)+W8*D(2,I8)+W9*D(1,I8)
1220 W(1,I9)=D(1,I7)-W8*D(1,I8)+W9*D(2,I8)
1230 W(2,I9)=D(2,I7)-W8*D(2,I8)-W9*D(1,I8)
1240 NEXT K9
1250 NEXT I4
1260 FOR K9=1 TO N5
1270 D(1,K9)=W(1,K9)
1280 D(2,K9)=W(2,K9)
1290 NEXT K9
1300 NEXT J9
1310 IF S0#0 THEN 1330
1320 RETURN
1330 FOR K9=1 TO N5
1340 D(1,K9)=D(1,K9)/N5
1350 D(2,K9)=D(2,K9)/N5
1360 NEXT K9
1370 RETURN

```

```

1380 REM COLLECT DATA FROM A/D CONVERTER AND
1390 REM STORE N DISK FILE N$. DATA ARE ALSO STORED
1400 REM IN ARRAY D FOR COMPUTATION OF SPECTRAL
1410 REM DENSITY ESTIMATES
1420 W3=W7
1430 PRINT"DATA COLLECTION BEGINNING."
1440 GOSUB 2500
1450 REM *** SHOULD =INP(25) ***
1460 REM *** =FNA(M1) FOR TEST ***
1470 FOR M1=1 TO 2CN0
1480 IF W(1,M1)@128 THEN V0= W(1,M1)/50
1490 IF W(1,M1)#=128 THEN V0= (W(1,M1)-256)/50
1500 V0=S8+(S9-S8)*V0
1510 WRITE#0,&W(1,M1)
1520 D(1,M1)=V0
1530 D(2,M1)=0
1540 NEXT M1
1550 FOR M1=1 TO 2CN0
1560 WRITE#0,&C(1,M1)
1570 NEXT M1
1580 FOR M1=1 TO 2CN0
1590 WRITE#0,&C(2,M1)
1600 NEXT M1
1610 CLOSE#0
1620 PRINT"SAMPLE SERIES STORED IN FILE ",N$
1630 RETURN

```

```

1640 REM TIMER ROUTINE, W3=WAIT INTERVAL
1650 N9=INT((W3-.0300)*870)
1660 FOR K1=1 TO N9
1670 NEXT K1
1680 RETURN

```

```
1690 REM SPECTRAL ESTIMATION VIA FFT
1700 Z1=0
1710 Z2=0
1720 K4=2*NO
1730 FOR M2=1 TO K4
1740 Z1=Z1+D(1,M2)
1750 Z2=Z2+D(2,M2)
1760 NEXT M2
1770 Z1=Z1/K4
1780 Z2=Z2/K4
1790 REM REMOVE THE MEAN FROM THE SERIES
1800 FOR M2=1 TO K4
1810 D(1,M2)=D(1,M2)-Z1
1820 D(2,M2)=D(2,M2)-Z2
1830 NEXT M2
1840 F7=1/(K4-1)/W7
1850 GOSUB 1010
1860 FOR M2=1 TO K4
1870 REM FREQUENCIES WRITTEN OVER REAL PART
1880 REM OF W ARRAY
1890 W(1,M2)=(M2-1)*F7
1900 REM SPECTRAL ESTIMATES WRITTEN OVER
1910 REM IMAGINARY PART OF W ARRAY
1920 W(2,M2)=D(1,M2)*2+D(2,M2)*2
1930 NEXT M2
1940 RETURN
```

```

1950 REM DISPLAY SAMPLED FUNCTION
1960 OPEN#0,N$
1970 READ#0,A$
1980 FOR M1=1 TO 8
1990 READ#0,E(M1)
2000 NEXT M1
2010 FOR M1=1 TO 2¢N0
2020 READ#0,&V1
2030 IF V1-@128 THEN V0=V1/50
2040 IF V1#128 THEN V0=(V1-256)/50
2050 C(1,M1)=S8+(S9-S8)*V0
2060 NEXT M1
2070 T7=-10000 %REM MAX V0
2080 R7=10000 %REM MIN V0
2090 FOR M1=1 TO 2¢N0
2100 IF C(1,M1)#T7 THEN T7=C(1,M1)
2110 IF C(1,M1-)@=R7 THEN R7=C(1,M1)
2120 NEXT M1
2130 Z3=(42-16)/(T7-R7)
2140 FOR I3=1 TO 2¢N0
2150 V0=C(1,I3)
2160 T7=(I3-1)*W7
2170 IF Q(6)=1 THEN 2210
2180 S=16+INT((V0-R7)*Z3)
2190 PRINT %6F2,T7,%8F2,V0,TAB(S),"*"
2200 GOTO 2260
2210 PRINT"TIME =",%10F3,T7,TAB(20),
2220 PRINT"SAMPLED VALUE =",%10F3,V0
2230 W3=.5
2240 REM 1/2 SECOND PAUSE FOR EACH LINE
2250 GOSUB 1650
2260 NEXT I3
2270 CLOSE#0
2280 RETURN

```

```

2290 REM DISPLAY SPECTRAL ESTIMATE THROUGH
2300 REM THE NYQUIST FREQUENCY
2310 Z4=0
2320 FOR I3=1 TO INT(2*NO/2+1)
2330 IF W(2,I3)@=Z4 THEN 2360
2340 Z4=W(2,I3)
2350 Z5=I3
2360 NEXT I3
2370 Z3=1/W(1,Z5)
2380 PRINT"PERIOD OF MAXIMUM ENERGY DENSITY = ",Z3
2390 FOR I3=1 TO INT(2*NO/2+1)
2400 Z3=0
2410 IF W(1,I3)#0 THEN Z3=1/W(1,I3)
2420 PRINT"PERIOD =",%10F3,Z3,TAB(20),
2430 PRINT"SPECTRAL ESTIMATE =",%10E3,W(2,I3)
2440 W3=.5
2450 REM 1/2 SECOND PAUSE FOR EACH LINE
2460 GOSUB 1650
2470 NEXT I3
2480 RETURN

```



```

2490 REM CRITICAL TIMING AND SAMPLING SUBROUTINE
2500 T7=INP(53)
2510 S7=INP(52)
2520 R7=INP(51)
2530 Z7=INP(50)
2540 T7=T7-16*INT(T7/16)
2550 S7=S7-16*INT(S7/16)
2560 R7=R7-16*INT(R7/16)
2570 Z7=Z7-16*INT(Z7/16)
2580 W9=0%REM SAMPLING WINDOW IN HUNDREDTHS OF SEC.
2590 Z0=Z7+10*R7+100*S7+1000*T7
2600 PRINT Z0
2610 FOR I=1 TO 20
2620 T7=INP(53)
2630 S7=INP(52)
2640 R7=INP(51)
2650 Z7=INP(50)
2660 T7=T7-16*INT(T7/16)
2670 S7=S7-16*INT(S7/16)
2680 R7=R7-16*INT(R7/16)
2690 Z7=Z7-16*INT(Z7/16)
2700 Z3=Z7+10*R7+100*S7+1000*T7
2710 Z0=Z0-1
2720 D8=Z3-Z0
2730 IF D8=0 THEN D8=D8+6000
2740 IF D9# D8 THEN 2620
2750 Z0=Z3
2760 W(1,I)=INP(25)
2770 C(1,I)=INP(27)%REM X
2780 C(2,I)=INP(26)%REM Y
2790 NEXT I
2800 PRINT Z0
2810 RETURN

```

```

2820 REM FILE HANDLING SUBROUTINE
2830 Q$="WAVE"
2840 P$=" ,2"
2850 M1=1
2860 C$=STR$(M1)
2870 B$=C$(2)
2880 N$=Q$+B$+P$
2890 OPEN#0,N$
2900 READ#0,A$
2910 IF A$(1,2)="99" THEN 3000
2920 PRINT"NEW FILE= ",N$
2930 A$(1,2)="99"
2940 INPUT"LOCATION,NOTES,ETC. (70 CHARACTS.) ?",A$(3,80)
2950 CLOSE#0
2960 OPEN#0,N$
2970 WRITE#0,A$
2980 GOSUB 3100
2990 RETURN
3000 IF M1=20 THEN 3050
3010 PRINT"USED FILE= ",N$
3020 CLOSE#0
3030 M1=M1+1
3040 GOTO 2860
3050 PRINT"ALL FILES FULL"
3060 STOP
3070 RETURN

```

```

3080 REM SUBROUTINE FOR TIME AND OTHER
3090 REM INITIAL CONDITIONS
3100 M4=1000000
3110 M3=0
3120 FOR M1=7 TO 1 STEP -1
3130 M2=INP(53+M1)
3140 M2=M2-16*INT(M2/16)
3150 M3=M3+M2*M4
3160 M4=M4/10
3170 NEXT M1
3180 E(1)=M3
3190 E(2)=2*NO
3200 E(3)=W7*REM TIME INTERVAL
3210 E(4)=S8*REM WAVE 0 VOLT
3220 E(5)=S9*REM WAVE 1 VOLT
3230 E(6)=S6*REM CURRENT 1 VOLT
3240 E(7)=E6*REM CURRENT PROBE ELEV
3250 E(8)=E7*REM WAVE 0 ELEVATION
3260 WRITE#0,E(1),E(2),E(3),E(4),E(5),E(6),E(7),E(8)
3270 RETURN
3280 END

```

```

10 REM TIME IN JULIAN DAYS, HOURS AND MINUTES
20 REM NO SPACES BETWEEN DIGITS
30 M4=1000000
40 M3=0
50 FOR M1=7 TO 1 STEP -1
60 M2=INP(53+M1)
70 M2=M2-16*INT(M2/16)
80 M3=M3+M2*M4
90 M4=M4/10
100 NEXT M1
110 PRINT "TIME (DDHMM) = ",M3
120 END

```

```

10 DIM A$(80)
20 INPUT" FILE NAME ?",N$
30 N$=N$+",2"
40 PRINT N$
50 OPEN#0,N$
60 WRITE#0,A$
70 CLOSE#0
80 STOP

```

```

10 DIM A$(80)
20 N$="WAVE5,2"
30 OPEN#0,N$
40 READ#0,A$
50 PRINT A$(3,60)
60 FOR M1=1 TO 8
70 READ#0,M2
80 PRINT M2
90 NEXT M1-
100 CLOSE#0
110 STOP

```

```

10 REM CALCULATION OF H1/3
20 DIM H(512),P(512),A$(80),E(8)
30 INPUT"FILE NAME"
40 N$=N$+"",2"
50 OPEN#0,N$
60 READ#0,A$
70 PRINT A$
80 FOR M1=1 TO 8
90 READ#0,E(M1)
100 PRINT E(M1)
110 NEXT M1
120 S3=0
130 S8=E(4)
140 S9=E(5)
150 N1=E(2)
160 W7=E(3)
170 FOR M1=1 TO N1
180 READ#0,&V0
190 IF V0@128 THEN H(M1)= V0/50
200 IF V0#128 THEN H(M1)= (V0-256)/50
210 H(M1)=S8+(S9-S8)*H(M1)-5.953125
220 S3=S3+H(M1)
230 NEXT M1
240 E7=E(8)
250 CLOSE#0
260 S4=S3/N1
270 FOR M1=1 TO N1
280 H(M1)=H(M1)-S4
290 NEXT M1
300 REM OBTAIN PEAK VALUES
310 S4=S4+E7
320 PRINT"MEAN SEA LEVEL ABOVE BOTTOM="",S4
330 N2=N1-1
340 N3=0
350 S1=1
360 FOR M1=2 TO N2
370 H1=H(M1)
380 H2=H(M1+1)
390 GOSUB 940
400 IF S2=0 THEN 480
410 IF S2=1 THEN 470
420 IF S1=1 THEN 440
430 GOTO 480
440 N3=N3+1
450 P(N3)=H(M1)
460 GOTO 480
470 S1=1
480 NEXT M1
490 P5=(N1-1)*W7/N3
500 PRINT"PERIOD BASED ON PEAKS="",P5," SEC."

```

```

510 N3=0
520 FOR M1=1 TO N2
530 IF H(M1)*H(M1+1)@0 THEN N3=N3+1
540 NEXT M1
550 P5=(N1-1)*W7/((N3-1)*.5)
560 PRINT"PERIOD BASED ON ZERO CROSSINGS=" ,P5," SEC."
570 REM ARRANGE THE N3 PEAKS IN DESCENDING ORDER
580 PRINT
590 PRINT"ORDERING PROCESS TAKES ABOUT 60 SEC. FOR 256 RECORDS"
600 F1=0
610 IF N3-2*INT(N3/2)=1 THEN 660
620 N3=N3+1
630 REM N3 MUST BE MADE ODD FOR ORDERING ROUTINE
640 P(N3)=-999
650 F1=1
660 F2=0
670 FOR M1=1 TO N3-2 STEP 2
680 IF P(M1)#P(M1+1) THEN 730
690 P1=P(M1)
700 P(M1)=P(M1+1)
710 P(M1+1)=P1
720 F2=1
730 NEXT M1
740 FOR M1=2 TO N3-1 STEP 2
750 IF P(M1)#P(M1+1) THEN 800
760 P1=P(M1)
770 P(M1)=P(M1+1)
780 P(M1+1)=P1
790 F2=1
800 NEXT M1
810 IF F2=1 THEN 660
820 REM PEAKS ARE NOW ORDERED
830 IF F1=1 THEN N3=N3-1
840 N4=INT(N3/3)
850 S3=0
860 FOR M2=1 TO N4
870 S3=S3+P(M2)
880 NEXT M2
890 H3=S3/N4
900 H3=H3*2
910 REM THIS IS TWICE MSL TO AVERAGE PEAK
920 PRINT"SIGNIFICANT WAVE HEIGHT=" ,H3
930 STOP
940 S2=0
950 IF H2#H1 THEN S2=1
960 IF H1#H2 THEN S2=-1
970 RETURN
980 END

```

```

10 REM CURRENT METER CHECK
20 DIM X(512),Y(512),A$(80),E(8)
30 INPUT"FILE NAME           ?",N$
40 N$=N$+"",2"
50 OPEN#0,N$
60 READ#0,A$
70 PRINT A$
80 FOR M1=1 TO 8
90 READ#0,E(M1)
100 PRINT E(M1)
110 NEXT M1
120 S3=0
130 S8=E(4)
140 S9=E(5)
150 N1=E(2)
160 W7=E(3)
170 FOR M1=1 TO N1
180 READ#0,&V0
190 NEXT M1
200 S6=E(6)
210 M7=0
220 PRINT "+X VALUE INDICATES LONGSHORE CURRENT APPROX FROM SE"
230 FOR M1=1 TO N1
240 READ#0,&V0
250 IF V0@128 THEN V1=V0/50
260 IF V0#128 THEN V1=(V0-256)/50
270 X(M1)=S6*V1-2.4
280 M7=M7+X(M1)
290 NEXT M1
300 PRINT "MEAN X= ",M7/N1
310 M7=0
320 PRINT "+Y VALUE INDICATES ONSHORE CURRENT APPROX FROM NE"
330 FOR M1=1 TO N1
340 READ#0,&V0
350 IF V0@128 THEN V1=V0/50
360 IF V0#128 THEN V1=(V0-256)/50
370 Y(M1)=S6*V1-2.4
380 M7=M7+Y(M1)
390 NEXT M1
400 PRINT "MEAN Y= ",M7/N1
410 CLOSE #0

```

```
420 INPUT "TYPE LI (FOR CURRENT PRINTOUT), ELSE NO : ",Z1$
430 IF Z1$(1,2)="LI" THEN 450
440 GOTO 540
450 C7=0
460 FOR M1=1 TO N1
470 C7=C7+1
480 IF C7@23 THEN 520
490 C7=0
500 INPUT "TYPE @CR# FOR MORE ,ELSE N :",C8$
510 IF C8$="" THEN 520 ELSE 540
520 PRINT M1," X= ",X(M1)," Y= ",Y(M1)
530 NEXT M1
540 STOP
550 END
```

```

10 DIM A$(80),E(8)
20 INPUT "FILE NAME ? :",N$
30 OPEN#0,N$
40 READ#0,A$
50 PRINT A$(3,60)
60 FOR M1=1 TO 8
70 READ#0,E(M1)
80 NEXT M1
90 M1=E(1)-INT(E(1)/100)*100
100 H1=E(1)-INT(E(1)/10000)*10000-M1
110 H1=INT(H1/100)
120 J1=INT(E(1)/10000)
130 PRINT TAB(10),"DATE AND TIME (JJJ HH MM) :",
140 PRINT TAB(52),%3I,J1,%3I,H1,%3I,M1
150 PRINT TAB(10),"NUMBER OF SAMPLES :",TAB(51),E(2)
160 PRINT TAB(10),"TIME INTERVAL (SEC) :",TAB(51),E(3)
170 PRINT TAB(10),"WAVE HEIGHT UNITS FOR 0 VOLTS (CMS) :",TAB(51),E(4)
180 PRINT TAB(10),"WAVE HEIGHT UNITS FOR 1 VOLT (CMS) :",TAB(51),E(5)
190 PRINT TAB(10),"CURRENT UNITS FOR 1 VOLT (CMS/SEC) :",TAB(51),E(6)
200 PRINT TAB(10),"CURRENT PROBE ELEVATION (CMS) :",TAB(51),E(7)
210 PRINT TAB(10),"ELEVATION OF BOTTOM OF WAVE STAFF (CMS) :",E(8)
220 CLOSE#0
230 STOP

```



THIRD ANNUAL REPORT

Research Units: 550 (PMEL); 541 (UW)  
Reporting Period: 1 April 1978 -  
31 March 1979

Number of Pages: 8+ Appendices

NORTON SOUND/CHUKCHI SEA OCEANOGRAPHIC  
PROCESSES (N-COP)

R.D. Muench<sup>1</sup>  
J.D. Schumacher<sup>1</sup>  
R.B. Tripp<sup>2</sup>

<sup>1</sup> Pacific Marine Environmental Laboratory  
3711-15th Avenue, N.E.  
Seattle, Washington 98105

<sup>2</sup> Dept. of Oceanography  
Univ. of Washington WB-10  
Seattle, Washington 98195

31 March 1979

## I. Summary

Continuing analysis of field data obtained during prior years is enhancing our understanding of flow in the northern Bering Sea, particularly with regard to subtidal fluctuations. Five current meter moorings deployed during summer 1978 yielded data which will help clarify both the regional tides and some aspects of subtidal circulation in the region between Norton Sound and St. Lawrence Island. These data are being provided as necessary input to the tidal modelling effort being carried out by RU485. Further analysis of the existing field data will address regional tidal behaviour and propagation/forcing of subtidal flow events through the system.

## II. Introduction

### A. General Nature and Scope of Study

The general objective of this work unit is to relate oceanic advective and diffusive processes to potential pollution problems due to OCS petroleum development. This is being accomplished through field activities including moored current measurements and water mass analysis using temperature and salinity observations. The region being considered extends from about the latitude of St. Lawrence Island north as far as the latitude of Cape Lisburne in the Chukchi Sea.

### B. Specific Objectives

1. To quantify the fluctuations in transport of the predominantly northward flow in the system.
2. To correlate fluctuations in transport with synoptic scale variations in meteorological parameters.
3. To verify and define the bifurcation of northward flow that occurs within the Chukchi lease area.
4. To define the temporal and spatial scales of eddies within the system.
5. To define the nearshore hydrography and circulation patterns within Norton and Kotzebue sounds.
6. To provide verification data for modelling of tidal and wind-driven circulation within the Norton Sound lease area (RU-435).

### C. Relevance to Problems of Petroleum Development

Two distinct environmental problems can accompany petroleum development in a marine region; catastrophic spills and chronic or long-term leakage. This research unit addresses both of these problems. The eventual effect of a catastrophic spill depends upon where the spilled oil goes, i.e., its trajectory, how long it takes to get there, and how much diffusion of oil occurs along the trajectory. This study will provide estimates of the trajectories likely to be followed by spilled oil and will furnish an indication of dispersion rates for such oil. Oil introduced into the environment via long-term or chronic leakage is more likely to be dispersed throughout the water column and, possibly, scavenged by suspended particulate matter. The problem then becomes one of understanding net transport of suspended matter, a process related to the advective and diffusive fields within the water column. An understanding of these processes requires, in turn, analysis of the velocity field and its driving mechanisms.

### III. Current State of Knowledge

The first annual report (March 1977) summarized the state of knowledge prior to commencing this study. That report, subsequent reports and Sections VI-VIII of this report update the initial summary.

### IV. Study Area

The study area was initially designated as the southern Chukchi and northern Bering Seas, specifically including Norton and Kotzebue sounds and the Bering Strait. Additionally, during the past two years we have worked on the shelf between the N-COP and B-BOP (Bristol Bay) areas in an attempt to link these two regimes. Physical characteristics of the study area have been discussed in detail in previous annual reports and publications.

### V. Sources, Methods and Rationale of Data Collection

Instrumentation, field and processing methods are identical to those used in the past and are documented in previous reports from this series. Where deviations from standardized methods are significant, they are discussed within the context of the appropriate subregional study.

### VI-VIII. Results, Discussion and Conclusions

#### A. Flow through the Bering Strait system

Continuing analysis has been carried out on current records from the northern Bering Sea and Bering Strait region. Results of this analysis were addressed by a presentation at the Fall 1978 AGU meeting. An abstract is appended hereto.

#### B. Summer circulation in the vicinity of Norton Sound

During the summer of 1978, we deployed four moorings (LD1 to LD4) in Norton Sound to support the tidal model developed by RU485. In addition, we deployed a current meter/pressure gage mooring off Cape Darby. Data from this site will be used to examine the possibility of water piling up along the north shore and to relate interior to exterior flow. Meteorological data from Nome and Unalakleet have been acquired from the National Weather Service and will be incorporated into our data base. These data will be used to relate flow events to meteorological forcing.

The locations of the moorings are shown in Figure 1; TABLE 1 provides a summary and current record statistics. Net flow over the observation period was generally toward the north with speeds between 6 and 14  $\text{cs}^{-1}$ ; however, within Norton Sound, net flow was extremely weak ( $<1.0 \text{cs}^{-1}$ ) and was directed out of the sound. Perturbations about the net flow do occur and such events have been documented before (Muench, Pearson and Tripp 1978; Tripp, Coachman, Aagaard and Schumacher 1978). At times, such perturbations appear to be local events, i.e. they do not

appear at all four of the exterior moorings (e.g. see Figure 2: on 24-25 July, flow reversed at LD1 and 2, but not at 3 or 4). However, at other times (e.g. 8-10 September), flow perturbation occurred at all the moorings then in operation.

As noted above, flow within Norton Sound was weak in a net sense; however, this resulted from directional variability rather than inherently low speeds. As indicated in Figure 2, strong pulses do occur. For example, between 19 and 25 August, the daily mean velocity varied from  $3.0 \text{ cs}^{-1}$  at  $109^{\circ} \text{ T}$  on the 19th, to  $36.6 \text{ cs}^{-1}$  at  $263^{\circ}$  on the 21st, and then  $3.2 \text{ cs}^{-1}$  at  $229^{\circ} \text{ T}$  on the 25th. The record from LD1 indicates a strong pulse on 20 August; at LD2, 3, and 4 this event is not as clear, although some change is evident. These results are preliminary, but suggest that perturbations about the net flow are significant. We suggest that meteorological forcing must be investigated.

TABLE 1

## Mooring Summary and Statistics for Summer 1978 Experiment

Mooring ID Position	Instrument Depth (m)	Observation Period	Speed (cs <sup>-1</sup> ) Max, Min	Mean Temp (°C)		Net (cs <sup>-1</sup> , °T)
				Max	Min	
LD-1 (cm/pg) 62 30.3 166 07.2	10.5	7/22 to 9/14	26.0 99.8 5.6	11.5 13.4 9.8		6.8 at 34
LD-2 (cm/pg) 63 13.2 168 34.8	24.5	7/22 to 9/6	21.5 63.7 6.5	1.9 8.5 -0.1		10.7 at 20
LD-3 (cm) 64 00.3 168 00.2	33.5	7/23 to 9/15	10.5 30.9 1.2	2.0 7.9 0.5		7.9 at 5
LD-4 (cm/pg) 64 46.6 166 49.6	16.5	7/23 to 9/16	19.4 62.4 2.9	10.8 13.4 4.6		13.9 at 324
LD-5 (cm/pg) 64 08.3 163 00.2	20	7/25 to 9/4	19.6 53.8 1.2	7.21 8.25 6.15		0.8 at 309

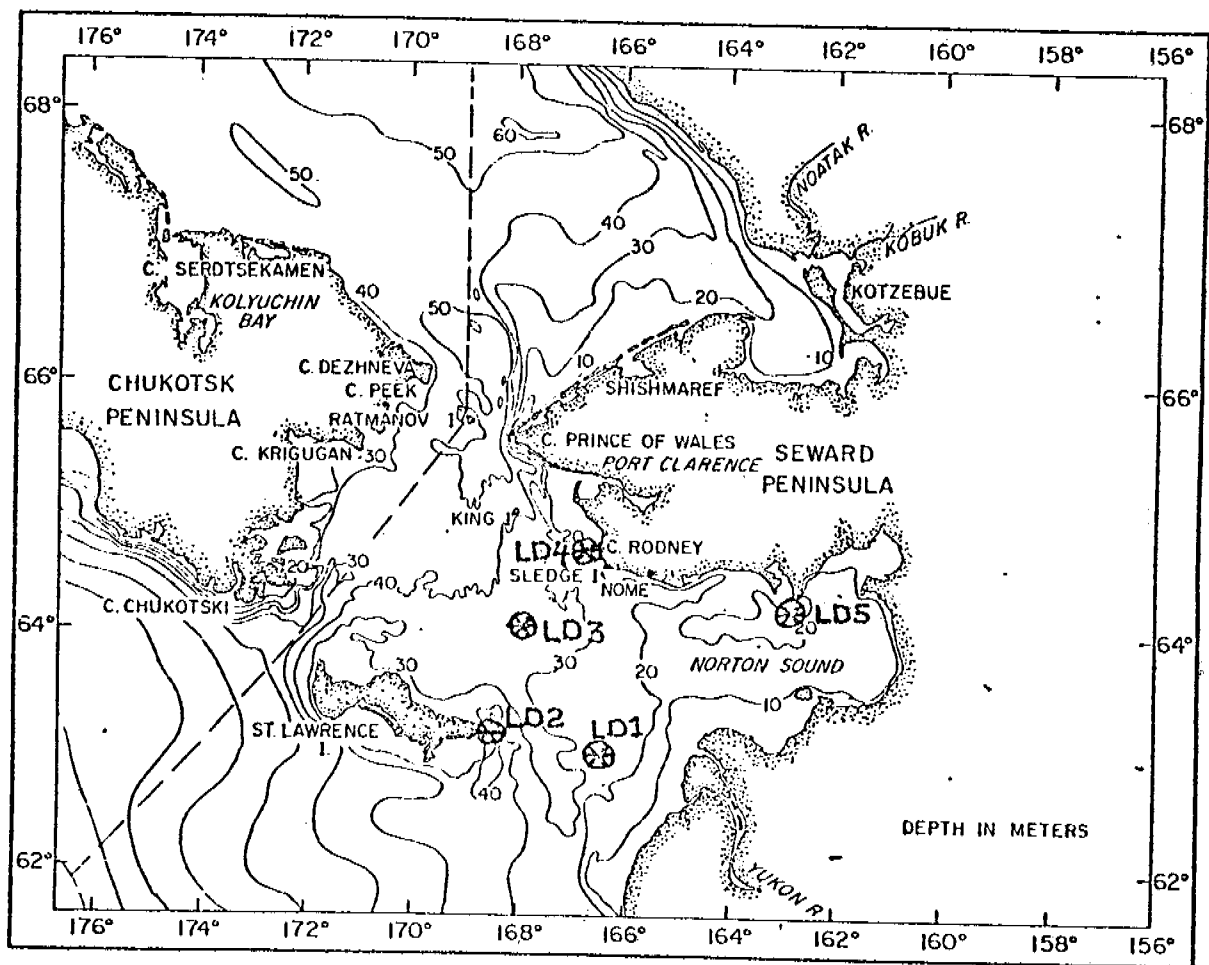


Figure 1. Location of summer 1978 (LD-series) moorings.

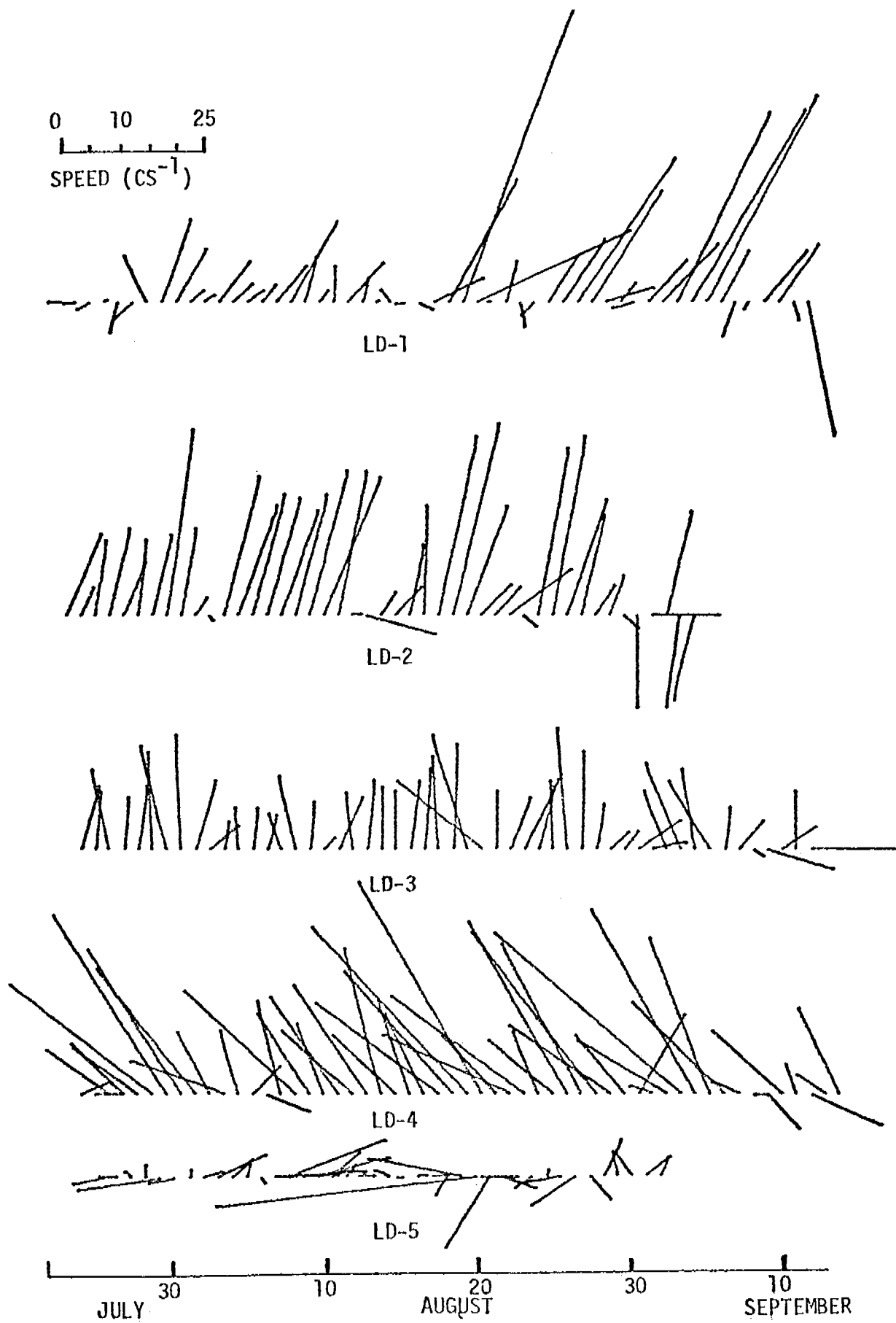


Figure 1. Daily mean current vectors from summer 1978 moorings.



## IX. Needs for Further Study

Further study under this program should concentrate on analyzing data already obtained and trying to understand the phenomena thus revealed. This effort can be fruitfully supplemented by selected field work and by analytical and numerical investigations. Specific points include:

- Examination of the relationship between the N-COP current regime and B-BOP regime to the south.
- Describe and analyze the subtidal current regime.
- Examine, using existing data and additional field data, the effect of ice cover on the near-coastal regions.
- Investigation of the character and dynamics of the Yukon River plume, which will require acquisition of additional field data.

Data are in hand to address most of these topics. Once individual topics have been addressed, synthesis of the regional oceanography should prove feasible and should be undertaken in conjunction with B-BOP synthesis.

## X. Summary of January-March Quarter

No field work was carried out during this quarter.

## XI. Auxiliary Material

### A. References used:

See Section XIC.

### B. Papers in preparation or print:

- Muench, R.D., R.L. Charnell, J.D. Cline & L.K. Coachman 1979. Summer water masses and circulation in Norton Sound, Alaska. (in press as an ERL Technical Report)

### C. Oral presentations:

- Muench, R.D., C. Pearson & R.B. Tripp 1978. Winter currents in the northern Bering Sea and Bering Strait. Eos, Trans. AGU 59(4), 304. (abstract of presentation at Spring 1978 AGU Meeting)
- Tripp, R.B., L.K. Coachman, K. Agaard & J.D. Schumacher 1978. Low frequency components of flow in the Bering Strait system. Eos, Trans. AGU 59(12), 1091. (abstract of presentation at Fall 1978 AGU Meeting)
- Agaard, K. & R.B. Tripp 1978. Saline water on the northern Alaskan shelves. Eos, Trans. AGU 59(12), 1091. (abstract of presentation at Fall 1978 AGU Meeting)

**APPENDIX**

**Extended abstract of presentation made at  
Fall 1978 AGU Meeting**

LOW FREQUENCY COMPONENTS OF FLOW IN  
THE BERING STRAIT SYSTEM

R.B. Tripp, L.K. Coachman, K. Aagaard  
and J.D. Schumacher

This is a joint University of Washington/N.O.A.A. program under the Outer Continental Shelf Environmental Assessment Program (OCSEAP). The purpose of this experiment was to examine the current field during the winter months when the region is generally under the influence of an ice cover.

Figure 1 shows the mooring locations. On each mooring a current meter was placed approximately 10 meters off the bottom to escape damage from the ice ridges during the winter months. These meters are at depths in the ranges of 40-50 meters in the Chukchi Sea, and in the 20-30 meter range in the northern Bering Sea. Norton Sound and Kotzebue Sound meters are slightly shallower.

The lengths of the current meter records varied from 8 to 11 months, starting in August 1976.

The long term means are mostly low (1-6 cm/sec) and to the north. Bering Strait (NC-10) has the largest mean flow at 17 cm/sec.

Table 1

Mooring NC-1	68-15.4N 172-40.6W	Meter depth: 39m
	8/25/76 to 6/17/77	10632 Records

Means:

Speed: 7.57 cm/sec  
Temperature: -1.20°C  
Speed & Direction: 2.91 cm/sec 332.6°

Mooring NC-2      68-29.7N    171-55.3W      Meter depth: 41m  
8/26/76 to 4/4/77      7980 Records

Means:

Speed:            9.62 cm/sec  
Temperature: -0.71°C  
Speed & Direction: 4.37 cm/sec 319.5°

Mooring NC-3      68-44.2N    171-06.2W      Meter depth: 45m  
8/26/76 to 8/7/77      12454 Records

Means:

Speed:            9.15 cm/sec  
Temperature: -0.78°C  
Speed & Direction: 5.51 cm/sec 318°

Mooring NC-4      69-00.7N    169-59.2W      Meter depth: 43m  
8/25/76 to 5/6/77      9160 Records

Means:

Speed:            9.15 cm/sec  
Temperature: -0.80°C  
Speed & Direction: 3.29 cm/sec 351.4°

Mooring NC-6      68-57.2N    168-18.6W      Meter depth: 44.3m  
8/25/76 to 4/20/77      8586 Records

Means:

Speed:            13.07 cm/sec  
Temperature: -0.28°C  
Speed & Direction: 1.05 cm/sec 253.2°

Mooring NC-7      68-55.2N    167-21.3W      Meter depth: 36.3m  
8/24/76 to 6/27/77      11056 Records

Means:

Speed:            13.34 cm/sec  
Temperature: -0.57°C  
Speed & Direction: 2.01 cm/sec 100.6°

Mooring NC-9            66-43.5N    164.08.8W            Meter depth: 14.5m  
                         8/23/76 to 5/9/77            9322 Records

Means:

Speed:            8.38 cm/sec  
Temperature:    0.52°C  
Speed & Direction: 0.92 cm/sec 096.9°

Mooring NC-10           65-45.1N    168-26.8W            Meter depth: 45.6m  
                         8/21/76 to 4/26/77            8915 Records

Means:

Speed:            30.64 cm/sec  
Temperature:    0.02°C  
Speed & Direction: 16.55 cm/sec 010.5°

Mooring NC-14           64.21.6N    165-21.5W            Meter depth: 21.5m  
                         8/21/76 to 6/25/77            11108 Records

Means:

Speed:            18.08 cm/sec  
Temperature:    0.16°C  
Speed & Direction: 2.25 cm/sec 074°

Mooring NC-16           62-37.0N    166.53.2W            Meter depth: 21.0m  
                         9/27/76 to 5/9/77            10714 Records

Means:

Speed:            22.07 cm/sec  
Temperature:    -0.42°C  
Speed & Direction: 4.72 cm/sec 037.9°

Mooring NC-17           62-48.1N    167-27.1W            Meter depth: 22.0m  
                         8/31/76 to 5/16/77            9284 Records

Means:

Speed:            19.95 cm/sec  
Temperature:    -0.32°C  
Speed & Direction: 4.02 cm/sec 099°

However, over the frequency band of one month, there is at least one instance of southerly mean flow at every mooring except NC-10 (Table 2). This does not take into account the moorings in Norton and Kotzebue Sound.

Table 2. North Component (V) cm/sec

Mooring	S	O	N	D	J	F	M	A	M	J	J
NC-1	-2.9	0.6	1.5	5.7	5.1	3.7	3.0	2.3	4.1		
NC-2	1.5	-1.5	0.2	7.7	5.9	5.1	3.1				
NC-3	3.5	-2.5	-0.3	5.4	7.3	4.4	4.9	3.0	4.6	9.5	4.9
NC-4	6.6	0.7	-1.3	2.6	6.5	2.0	4.7	3.9			
NC-6	8.0	3.1	0.8	-12.7	-3.5	-4.5	2.8				
NC-7	4.8	1.5	0.4	-17.7	-3.2	-3.6	-0.1	4.6	3.5		
NC-10	20.4	8.1	16.5	10.9	22.7	14.1	17.3				
NC-16		7.8	3.7	2.2	10.7	3.8	-0.1	-3.0			
NC-17	-0.4	-7.8	-7.5	0.1	6.9	3.2	-0.8	-3.6			

The largest southerly flow (18 cm/sec) in December was at Mooring NC-7. Moorings NC-6 and NC-7 had mean southerly flow over the period December through February. This is probably related to the displacement of the clockwise gyre which is normally located between Cape Lisburne and Icy Cape. This gyre is characterized by lateral gradation from cold and saline (1°C; 32.2‰) in the west, to warm and less saline (4°C; 31.5‰) close to the coast. Perhaps in winter, when very little Alaskan Coastal water, which normally hugs the coast, is present causes the gyre to move westward.

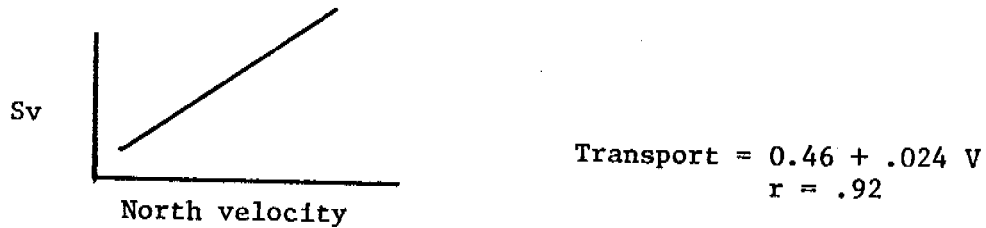
At mooring NC-10 near Bering Strait, the monthly means show no large seasonal variability as claimed by some Soviets (MAKSIMOV).

Table 3

	A	S	O	N	D	J	F	M	A
cm/sec	31	20	8	17	11	23	14	17	0
Sv	1.2	.95	.65	.9	.75	1.0	0.8	0.9	0.4

Connecting mean speeds to transports we have monthly means varying from .65 Sv to 1.2 Sv. The mean of the total record is 0.95 Sv (17 cm/sec).

This conversion was accomplished by taking all our existing cross sections of current measurements for Bering Strait and comparing the site of NC-10 with those measurements.



This indicates fairly well that the greatest variability is on time scales shorter than one month.

In Figure 2 the low frequency bands  $\geq 3$  days show mean 3-day speeds exceeding 60 cm/sec both north and south. This gives transports varying from 2.1 Sv north to 1.0 Sv south. The groups of vectors in one direction show abundant energy in 3 days and longer time scales.

In Figure 3 the 2048 samples were averaged over 7 spectral estimates (7-point running mean and 14 degrees of freedom). All we can say about the various spectra is that they all have larger amounts of energy in 3- and 5-day frequencies and that the shape is very similar in Bering Strait and off Cape Lisburne.

In Figure 4 (Oct. 27 to Nov. 2, 1976) we find that there is some regional coherence on a time scale of 7 days. This event at the end of October, in which the entire system reverses to southerly flow, is the only evidence of this occurrence over an eight-month period.

In Figure 5 (Nov. 3 to Nov. 9, 1976) the system reverses and flows northward. These two figures show the speed on which the system responds to variations in the major during free. Which we suspect to be the north-south pressure gradient.

Figure 6. The temperature profiles of daily averages from September 1, 1976 for all the moorings shows the rapidity in which the system cools. The dates shown are when the temperature drops to  $-1.7^{\circ}\text{C}$ .

The results show: 1) that there is a large phase difference from south to north; 2) the time difference in cooling could be advection from the south, or local breakdown, and turnover in different water depths (south - 30 meters range; north - 50 meters range); 3) the time difference also possible with flushing fresh water from system, which would proceed from south to north and take  $\sim 30$  days.

We feel that we will understand this system somewhat better when we have analyzed the atmospheric data from the shore stations which surround it.

#### Reference

Maksimov, I. V. (1945) Determining the relative volume of the annual flow of Pacific water into the Arctic Ocean through Bering Strait. *Probl. Arktiki*, No. 2, pp. 51-58 (transl.).



Figure 1

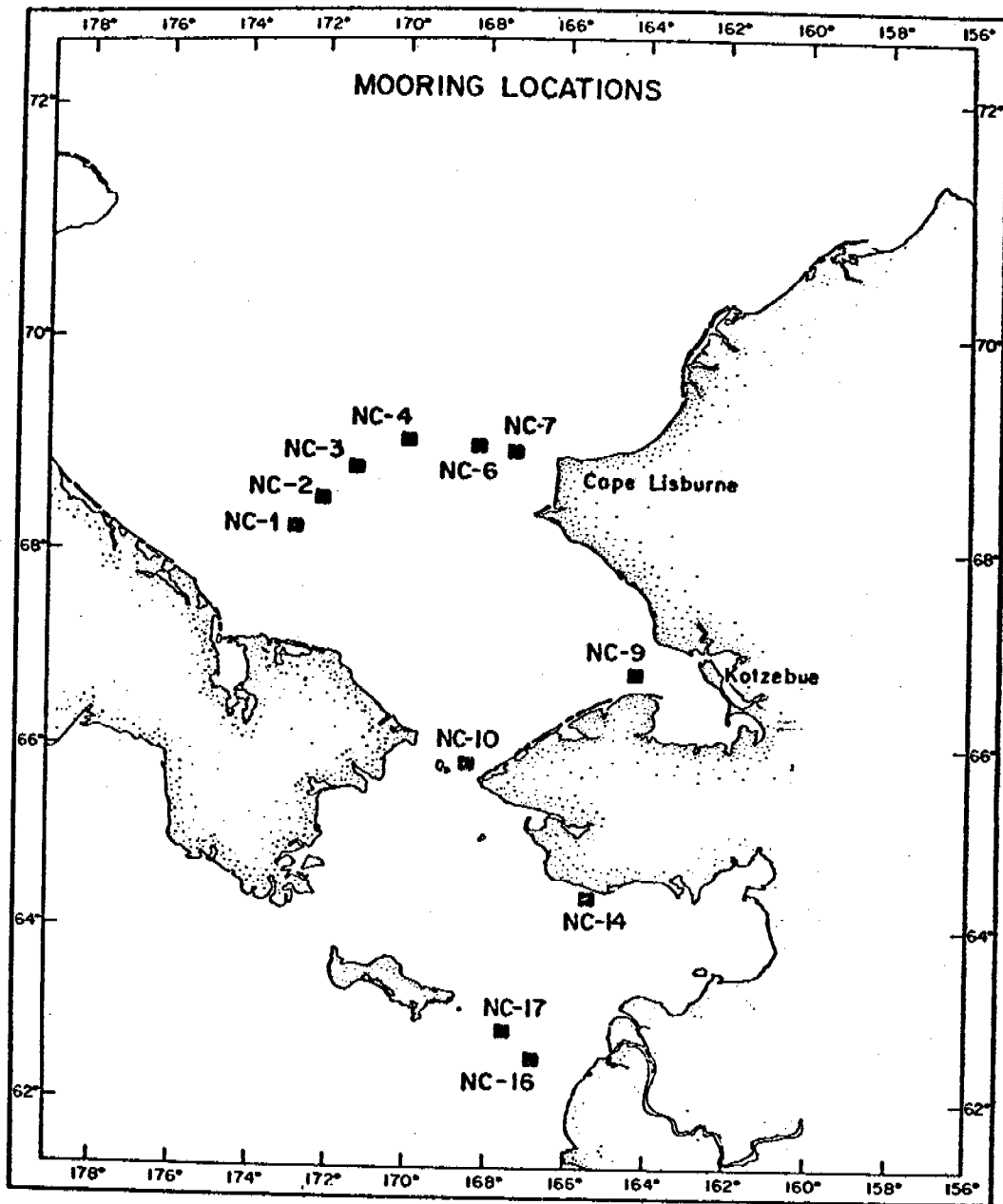
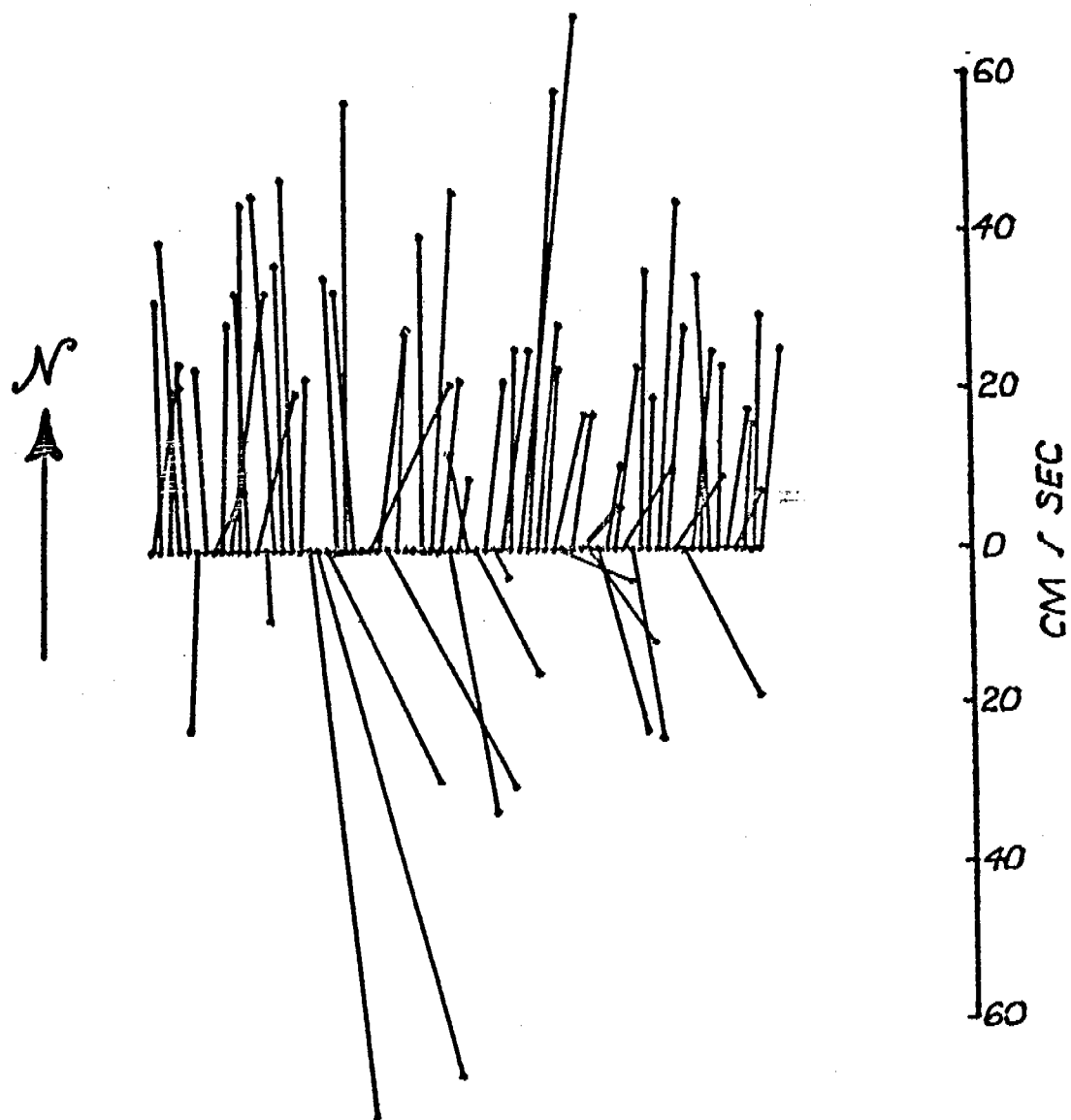


Figure 2



BERING STRAIT CURRENTS  
3 day means 21 AUG 76 to 26 APR 77

Figure 3

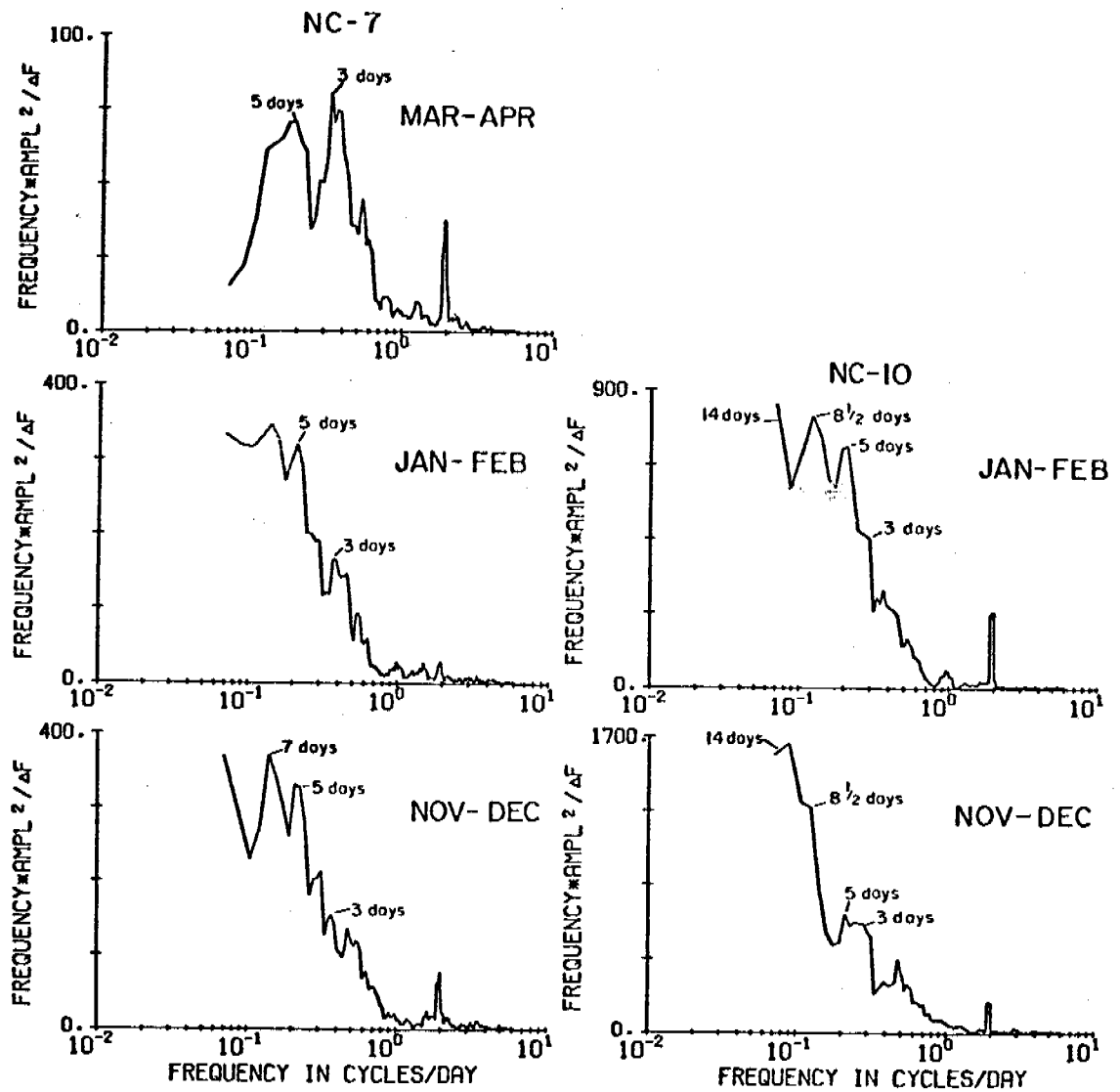


Figure 4

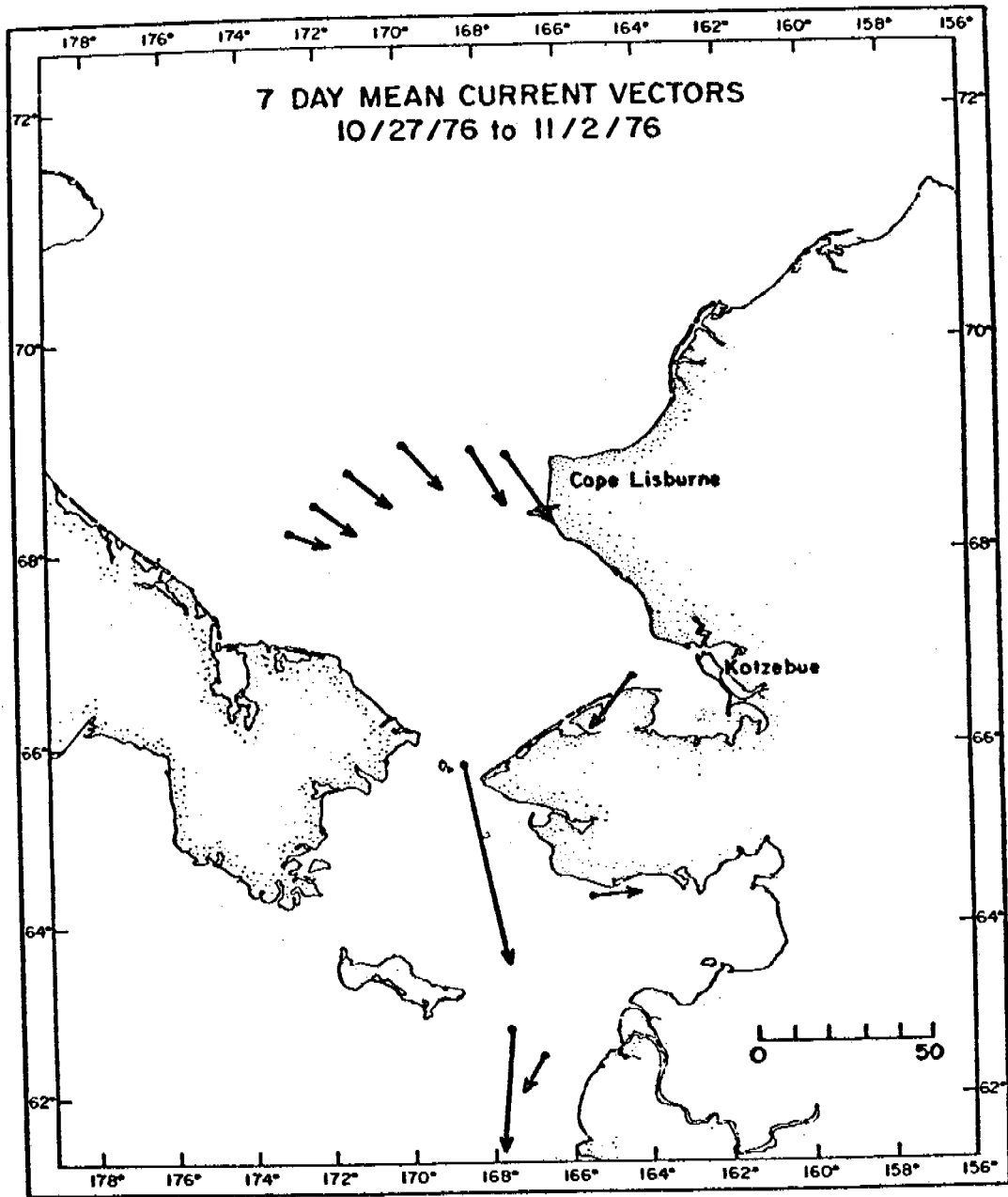


Figure 5

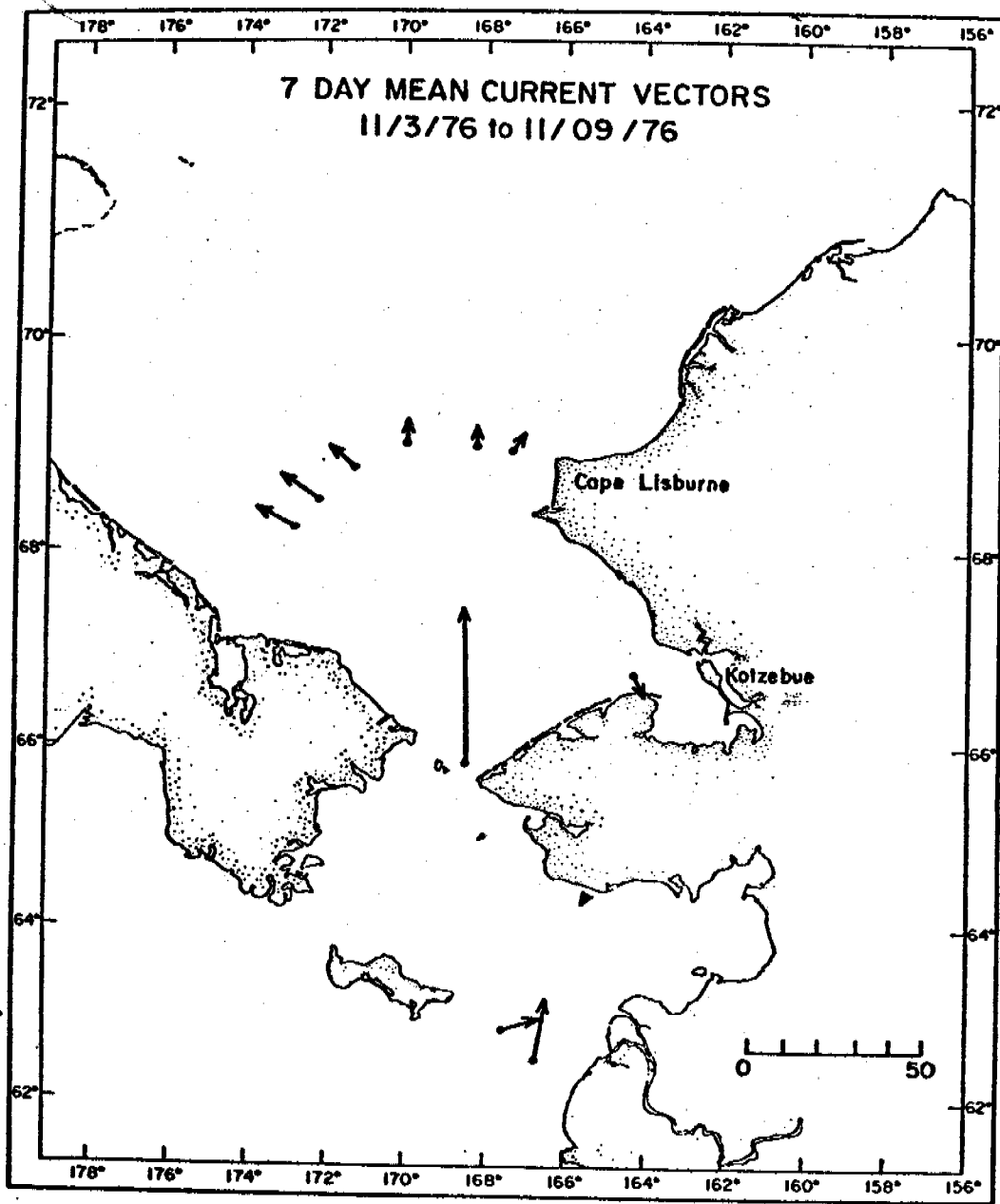
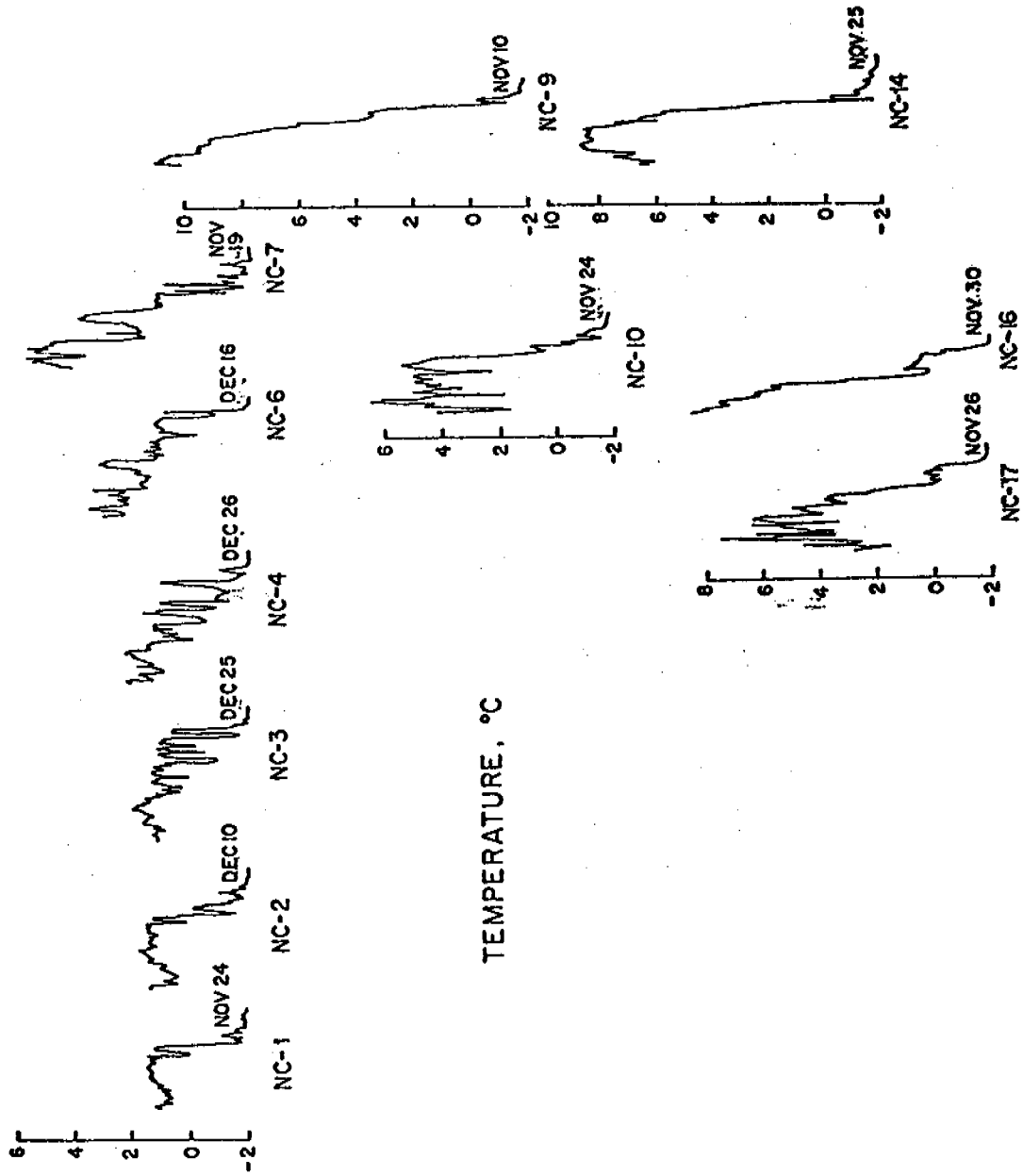


Figure 6



ANNUAL REPORT

R.U. #562 Oil Pooling Under Sea Ice  
NOAA R.D. No. RK-8-0065  
Report Period: 1 April 1978 to 31 March 1979

Oil Pooling Under Sea Ice

Principal Investigator: A. Kovacs

U.S. Army Corps of Engineers  
Cold Regions Research and Engineering Laboratory  
Hanover, N.H. U.S.A.

## I. Summary

The objective of the CRREL study is to:

- a. Determine the cause of the significant relief which exists under the fast ice.
- b. Measure the variations in the relief under fast ice using electromagnetic echo sounding.
- c. Determine if the under-ice relief is a series of individual pockets or consists of long rills.
- d. Estimate the quantity of oil which could pool up in the under-ice depressions should oil be released under the ice cover.
- e. Use impulse radar to study the electromagnetic properties and anisotropy of sea ice.

The data which have been analyzed to date indicate, as expected, that the cause of the mesoscale relief (5 to 50 cm) found under the fast ice in late winter is due to snow cover variation. In short, where the snow depth is greatest the underlying ice sheet is thinnest due to the insulating effect of the snow, which reduces heat transfer to the atmosphere and therefore ice growth. It was found that the volume of oil which could pool in the under-ice pockets existing at our Tigvariak Island study site was of the order of  $31,000 \text{ m}^3/\text{km}^2$ . While this is a very large quantity, it is, after all, only about three times the amount of oil which could be expected to accumulate under a relatively smooth sea ice bottom.



Impulse radar sounding studies confirmed the findings of Kovacs and Morey (1978) that below the transition zone (the first 10 to 40 cm depth) in first year sea ice the "bottom ice" has a preferred horizontal c-axis azimuthal orientation which is aligned with the prevailing current direction. In areas of no current, the c-axes were also found to be horizontal but were randomly oriented.

Initial results from using a polarized radar antenna in the air from the NOAA helicopter indicate that the c-axis anisotropy can be determined from the air. Because this anisotropy is related to current direction, it should be possible to measure, from an airborne platform, the current direction at the ice/water interface.

## II. Introduction

The first year of the CRREL program on Oil Pooling Under Sea Ice centered on the profiling of an 20 x 200 m section of a plowed snow-free runway near Tigvariak Island, and a site north of Reindeer Island. Ice thickness data were obtained in May 1978 using an impulse radar profiling system. The data were displayed on a facsimile recorder and recorded on a magnetic tape recorder for later playback and analysis. From the ice thickness data a contour map was constructed of the ice bottom relief and an assessment of the quantity of oil which could pool in the under-ice relief was made.

The study of sea ice anisotropy centered on the measurement of the electromagnetic properties of sea ice in sites using the impulse radar system.

This program is intended to provide cross-sectional information on the thickness and bottom relief of sea ice. The subsurface topographic data are to provide information for determining the direction that oil discharged under fast ice will flow and the quantity of oil which can be expected to pool up within the under-ice relief.

### III. Current State of Knowledge

The information on undersea ice relief is extremely limited and not well documented. Most ice thickness information consists of spot measurements. These are of no value in assessing under-ice oil pooling potential. Even where profile information exists it generally comprises ice thickness measurements taken along a single traverse of limited length and is therefore of limited value at best.

The data collected during this program have provided meaningful insight into the nature of the undersea ice morphology and the quantity of oil which can be anticipated to accumulate in the under-ice relief should an underice oil release occur. Even so, additional profile information is needed to expand our knowledge of under-ice relief vs. snow cover variation on first year sea ice and of the under-ice relief of multi-year sea ice.

From the anisotropy studies of sea ice obtained using impulse radar we can determine the direction of the current at the ice/water interface and therefore the direction oil will drift should there be an under-ice oil release.

#### IV. Study Area

Sea ice profile information was collected in May 1978 off the northwest side of Tigvariak Island and in March 1979 off the northwest end of the Prudhoe Bay west dock. Location maps showing these sites as well as the sites at which sea ice anisotropy measurements were made are given in attachment A.

#### V. Sources, Methods and Rationale of Data Collection

Ice thickness data were collected using an impulse radar system. The impulse radar used is the same system used by Kovac (1977) in 1976 to profile the thickness of both first and multi-year sea ice. It was from this study that the first assessment of the volume of oil which could pool up under sea ice was made. As a result this profiling system was selected for use in collecting sea ice thickness data for the program on Oil Pooling Under the Sea Ice.

Ice thickness profile information was collected at Tigvariak Island because this site was a representation of an area of deep snow cover and was easily accessible by ice road. The first year sea ice site north of Reindeer Island was chosen for its thin, relatively uniform snow cover. The Prudhoe Bay west dock site was selected because its surface comprised both flat and deformed ice. The deformed ice surface was the result of storm events during fall freezeup.

## VI. Results

### 1. Published reports

- a. Kovacs, A. and R.M. Morey (1978) Radar anisotropy of sea ice due to preferred azimuthal orientation of the horizontal c-axes of ice crystals, J. Geophysical Research, Vol. 83, No. C12.
- b. Kovacs, A. (1978) Remote detection of water under ice-covered lakes on the North Slope of Alaska, Arctic, Dec.
- c. Kovacs, A. (1978) Sea ice thickness profiles and ice bottom contour relief maps, data report for the BLM/NOAA data bank.

### 2. Reports in press

- a. Kovacs, A. and R.M. Morey (1979) Remote detection of a freshwater pool off the Sagavanirktok River Delta, Alaska, Arctic.
- b. Kovacs, A. and R.M. Morey (1979) Anisotropic properties of sea ice in the 50-150 MHz range, J. Geophysical Research.

### 3. Reports in preparation

- a. Kovacs, A. and R.M. Morey, Oil pooling potential under sea ice.

## VII. Conclusions

Our studies have shown that where there is a preferred current direction under sea ice the crystal structure of the ice becomes highly

ordered. This includes a crystal structure with a preferred horizontal c-axis that is oriented parallel with the local current. This ordered structure is a complex anisotropic dielectric which was found to be an effective polarizer of transverse electromagnetic waves. The reason for the polarization has been related to the ordered arrangement of the brine inclusions which are believed to create a unique array of parallel plate wave guides. This arrangement has been shown to reduce or eliminate radar signal reflection from the ice bottom when a linearly polarized radar antenna E-field is oriented perpendicular to the preferred crystal c-axis direction and to allow a maximum signal return when the antenna E-field is aligned parallel with the preferred c-axis azimuth.

Because current effects establish the preferred crystal alignment, the above radar signal phenomenon makes it possible to determine the direction of the preferred current under sea ice remotely. In addition, the fact that large areas of sea ice have a preferred c-axis azimuthal orientation is of great significance to the ice engineer, as c-axis alignment profoundly affects ice strength. For example, Peyton (1966) showed that the unconfined compressive strength of sea ice can be 2-5 times higher when the load is applied parallel rather than perpendicular to the c-axis. This fact must be considered and evaluated in performing sea ice strength tests and in designing offshore structures. Unfortunately, the sea ice research community has been slow to recognize the importance of Peyton's findings.

Our sea ice profiling data from the Tigvariak Island runway site have been partially analyzed, with the following findings. From the ice thickness data we constructed ice thickness cross-sections showing the under-ice relief as depicted in Figure 1. The ice thickness data were also digitized. From this information a contour map of a 150-m-long section of the profiled runway was made. This map is shown in Figure 2. The contour intervals are 5 cm and show only the depth range from 1.5 to 1.65 m. This depth range varies around the mean depth which was found to be 1.56 m. The light shaded areas show relief which is under 1.55 m or areas where oil can be expected to pool up in pockets which are less than the mean depth. The darker shaded areas represent pockets which are less than 1.55 m deep but which may not fill with oil because they are surrounded by deeper ice relief. Chances are, however, that most of these pockets will also fill with oil as the surrounding ice appears to be at the mean ice depth (1.56 m). In other words if the oil reaches this depth under the ice the oil should flow into these depressions as well.

From the digitized data we have determined that the mean depth for 18 parallel traverses 1.1 m apart and 150 m long was 1.56 m with a standard deviation of 0.03 m. We have also found that for the 20 m by 150 m area shown in Figure 2 the quantity of oil which could be expected to pool up in the under-ice pockets which exist above the mean depth is  $0.0320 \text{ m}^3/\text{m}^2$  or  $32,000 \text{ m}^3/\text{km}^2$  with a standard deviation of  $1,580 \text{ m}^3/\text{km}^2$ .

Further analysis of the data in 30-, 60-, 90-, 120- and 150-m-long segments resulted in the findings shown in Table I. This table shows that for ice thickness data from an area 20 m wide by 30 m long the mean depth is not representative of the runway area but that for a length of 60 m or more, a representative mean ice thickness is obtained. An important finding is that a single traverse only 30, 60 or 90 m long is not reliable for determining the surrounding area pocket volume above the mean depth as obtained for that single traverse. For example, the storage volume above the mean depth for each of the 18 30-m-long traverses varied from a high of  $56,300 \text{ m}^3/\text{km}^2$  to a low of  $18,300 \text{ m}^3/\text{km}^2$ . For the 60-m-long segment the volume varied from 20,700 to  $46,800 \text{ m}^3/\text{km}^2$  and for the 90-m-long segment it varied from 25,200 to  $39,800 \text{ m}^3/\text{km}^2$ . Table I shows that with increasing traverse length the standard deviation of the potential storage volume which can be determined from a single traverse decreases.

Table I also shows the mean of the mean pooling volumes for all of the area segments. This mean of  $31,000 \text{ m}^3/\text{km}^2$  represents the storage potential for these area segments at about the 95% confidence level. The tabulated data in Table I are graphically shown in Figure 3. From this graph one can infer that a single traverse profile of 150 m or more down the runway would provide data from which the under-ice storage potential of the area could be determined with a high degree of confidence. However, we do not recommend a single traverse at this time because we do not know the length of individual under-ice pockets.

Our 20-m-wide profile was not wide enough to determine the lateral extent of the pockets traversed. Therefore, until more profile information becomes available that shows the lateral extent of individual under-ice pockets we would advise that three 150 m or longer traverses be made in the form of a 60° triangle.

The above results are representative of a high snow accumulation area. For example the snow depth around the runway site varied from 20 to 46 cm over a distance of 30 m. The mean depth was 33 cm with a standard deviation of 7 cm.

The profile results obtained at the relatively snow-free site north of Reindeer Island showed that the ice bottom was relatively devoid of relief. In other words where no snow depth variation exists the ice bottom will have a relatively uniform depth.

The Tigvariak Island site results can be compared with those of Kovacs (1977) who analyzed a 345-m-long profile at a plowed ice runway site located south of Narwhal Island. The area around this runway had less snow than the Tigvariak Island site and as a result the ice bottom relief was less. The under-ice oil pooling potential for the Narwhal Island runway was found to be  $27,000 \text{ m}^3/\text{km}^2$ . The effect of the thinner snow cover with less surface relief variation resulted in less under ice relief and the lower pocket volume.

The profile information collected to date shows the strong effect of snow cover variation on under-ice relief and therefore oil pooling potential. In short, where a deep snow cover with varying thickness



exists, the under-ice bottom relief is also significant, with large pocket areas above the mean ice thickness depth in which a significant amount of oil could pool should an under-ice oil release occur.

#### VIII. Summary of 4th Quarter Efforts (1 January - 1 April 1979)

##### a. Laboratory Activities

Profiling data collected in May 1978 at the Tigvariak Island runway site were further analyzed. The tentative results have been discussed above.

The two reports listed in Section VI under Reports in Press were written and submitted to journals for their consideration for publication.

##### b. Field Activities

An area 160 m square located northwest of the Prudhoe Bay west dock was plowed free of snow and profiled with the impulse radar system. The results of this field work have not been analyzed to determine under-ice oil pooling potential for this rough ice area.

c. Significant Problems. None.

d. Estimate of Funds Obligated.

As of 31 March \$14,000 remains of \$30,464 FY79 project funds.

#### References

Kovacs, A. (1977) Sea ice thickness profiling and under ice oil entrapment, 9th Annual Offshore Technology Conference, Houston, Texas, OTC2949.

- Kovacs, A. and R.M. Morey (1978) Radar anisotropy of sea ice due to preferred azimuthal orientation of the horizontal c-axes of ice crystals, J. Geophysical Research, Vol. 83, No. C12.
- Peyton, H.R. (1966) Sea ice strength, Rep. UAG R-182, Univ. of Alaska, Fairbanks.

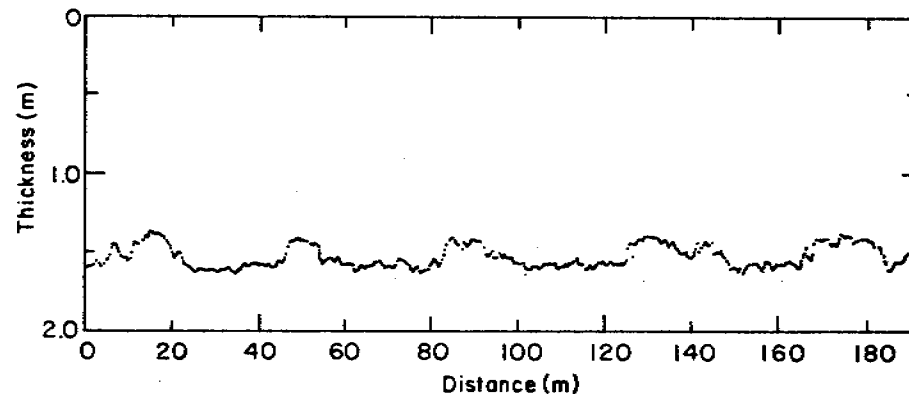


Figure 1. Under-ice relief associated with snow cover thickness variation.

322

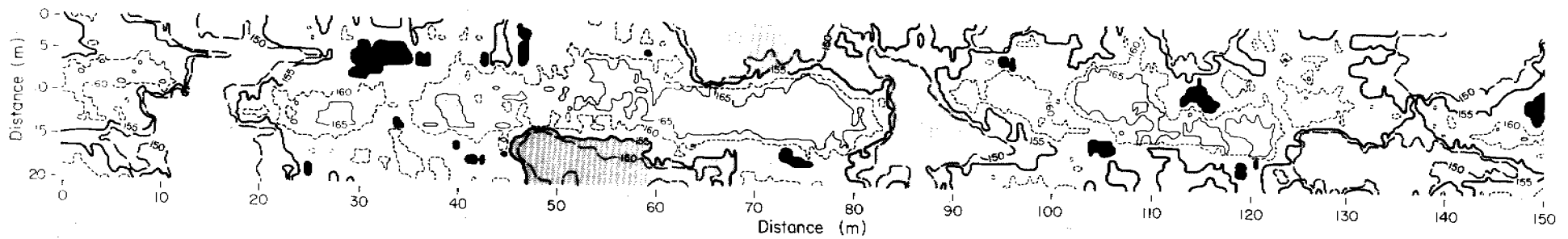


Figure 2. Contour map showing under-ice relief patterns.

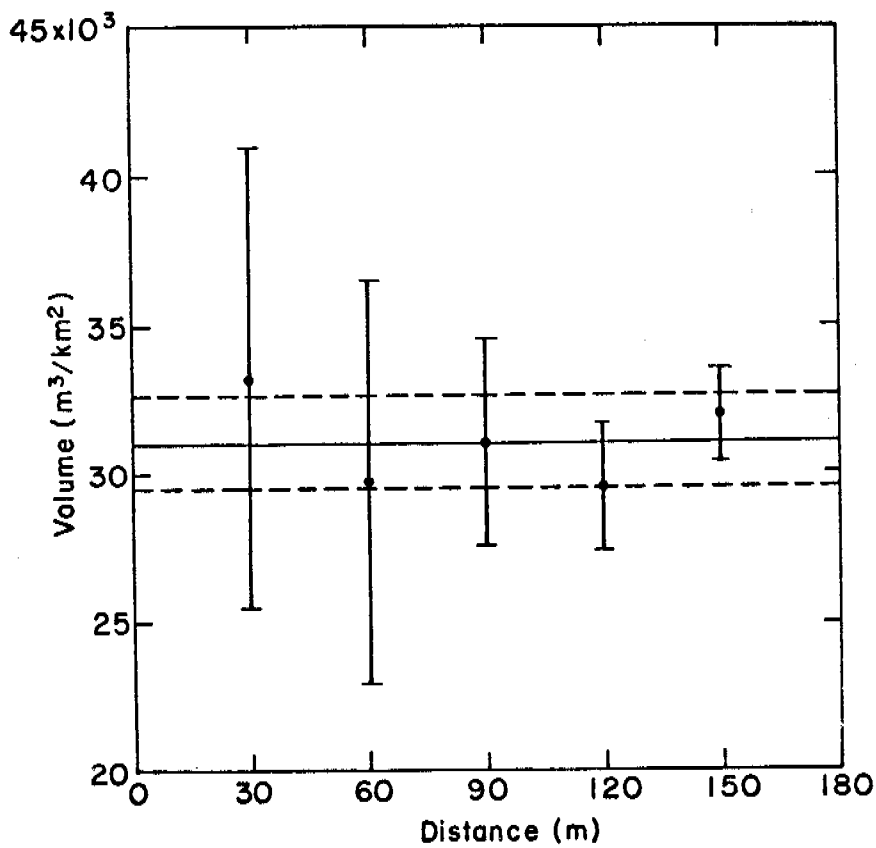


Figure 3. Mean (•) and standard deviation (I) of oil pooling potential under sea ice as determined from 18 traverses 1.1 m apart of 30, 60, 90, 120 and 150-m-long. The solid line across the data is the mean of the means and the dashed line the related standard deviation.

Attachment A

ANISOTROPIC PROPERTIES OF SEA ICE IN THE 50-150 MHz RANGE

by

A. Kovacs<sup>1</sup> and R. M. Morey<sup>2</sup>

January 1979

1. US Army Corps of Engineers Cold Regions Research and Engineering Laboratory, Hanover, New Hampshire, 03755
2. Morey Research Co., B-3 Black Oak Drive, Nashua, New Hampshire 03060

## ABSTRACT

Results of impulse radar studies of sea ice near Prudhoe Bay, Alaska, show that where there is a preferred current direction under the ice cover the crystal structure of the ice becomes highly ordered. This includes a crystal structure with a preferred horizontal c-axis that is oriented parallel with the local current. The radar studies show that this structure behaves as an anisotropic dielectric. The result is that when electromagnetic energy is radiated from a dipole antenna in which the E-field is oriented perpendicular with the c-axis azimuth no bottom reflection is detected. It was also found that the frequency dispersion of anisotropic sea ice varies in the horizontal plane. This is demonstrated by the center frequency of the reflected signal spectrum which is maximum in the preferred c-axis direction and minimum perpendicular to it. In addition it was found that the frequency dispersion is related to the average bulk brine volume of the ice but that the bulk dielectric constant of the ice, as determined from impulse travel time, shows little correlation with the coefficient of anisotropy.

## INTRODUCTION

This study of sea ice anisotropy was a continuation of a program to measure the electromagnetic (EM) properties of sea ice in situ using a remote sensing technique, i.e. impulse radar. The impulse radar used in this study radiated a time domain wavelet of about 14 ns duration. The frequency spectrum of the radiated wavelet is centered at about 125 MHz and the -3 db points of the spectrum are at about 75 MHz and 150 MHz. The same linearly polarized, broadband dipole antenna was used for transmission and reception. After detection and down-conversion, the radar reflection waveforms were recorded on an FM magnetic tape recorder for later playback, computer processing and plotting. A more detailed description of the radar system is contained in Morey (1974) and Campbell and Orange (1974).

Earlier observations and measurements were made in May 1976 and 1977 on the sea ice around Narwhal Island northeast of Prudhoe Bay, Alaska (Kovacs and Morey, 1978). These studies revealed that the crystal structure of sea ice had a c-axis with a preferred azimuthal orientation that was aligned with the under-ice current, and that this oriented structure behaved as an electromagnetic polarizer. The resulting effect was that when the antenna E-field was oriented parallel with the c-axis of the crystal platelets a strong bottom reflection of the radar signal was obtained, but when the E-field was oriented perpendicular to the c-axis no bottom reflection was detected. This report contributes

additional information on the anisotropic EM properties of sea ice near Prudhoe Bay and farther north and east of the previous years' observation sites.

Figure 1 is a map of the Beaufort Sea in the vicinity of Prudhoe Bay showing the station locations at which sea ice crystal, current and radar studies were made in 1976, 1977 and 1978. The field sites (Figures 1a and b) at which impulse radar studies were made in April 1978 (sites 1, 2, 3, 4, WD-1, WD-2, TIG-1, TIG-2 and TIG-3) were primarily chosen to extend and broaden the area of the 1976-77 observations (Figure 1c). The locations of stations 1, 2, 3 and 4 were determined by the use of a precise VLF global navigation system on board the helicopter used for transportation. The locations of the TIG stations were determined by satellite navigation positioning provided by a Geophysical Survey Inc. seismic crew operating in that area. The other (WD) stations were located about 100 m northwest of the Prudhoe Bay West Dock.

#### EXPERIMENTAL PROCEDURE

The measurement procedure at the sites studied was to mark the direction of true north and paint a polar grid on the ice surface, make the radar measurements, and obtain a 7.7-cm-diameter ice core from the center of the grid using a CRREL coring auger. Ice crystal c-axis alignment was determined by visual observation of the ice core structure.

Instantaneous current direction and velocity were measured approximately 10 cm below the bottom of the ice using an electric field current meter.



The temperature of the ice core was measured approximately every 10 cm along the core immediately after withdrawal from the ice sheet. The core was cut into 10-cm sections and bagged for later melt-down and the determination of meltwater salinity. The sea ice brine volume was calculated from the temperature and salinity data.

Radar measurements were made with the radar antenna above the ice surface ( $\approx 1.5$  m). A large metal screen on the ice directly below the antenna (Figure 2) was used to provide a known reference reflection. After the screen was removed, the radar reflection from the top and bottom of the ice was recorded. Additional readings were made at  $30^\circ$  increments. The antenna was then placed on the surface of the ice and the reflection from the ice bottom recorded, again at the same  $30^\circ$  azimuth increments. Radar measurements were made with the antenna on the surface at all stations. However, radar measurements with the antenna elevated were only made at stations 1, 3, WD-1a and WD-2. The ice thickness, c-axis azimuth, current direction, water depth, and radar reflection analysis made at each station are listed in Table I. The preferred c-axis azimuth and current direction (where measured) are also shown in Figure 1.

The two-way time of propagation of the impulse radar signal to and from various reflecting interfaces was measured. The amplitude and wave shape of the reflected signal were analyzed to provide additional information about the material being probed and the nature of the

interfaces. A typical X-Y plot of the impulse radar signal with the antenna elevated is given in Figure 3. This plot shows first the transmit impulse (feed-through from transmitter to receiver), then the reflection from the ice surface, and next the reflection from the ice bottom. The peak-to-peak amplitude of the reflection from the ice surface is used to calculate the apparent dielectric constant  $(\epsilon'_r)^*$  of the ice surface from:

$$\epsilon'_r = \frac{1-p_s^2}{1+p_s^2} \quad (1)$$

here the reflection coefficient of the ice surface ( $p_s$ ) is obtained by dividing the amplitude of the reflected signal from the metal sheet into the amplitude of the ice surface reflection. Table I lists the ice surface reflection amplitude, reflection coefficient and dielectric constant vs. antenna electric field direction for those stations where the measurements were made.

The two-way travel time of the radar signal in the ice and the relative amplitude of the signal reflected at the bottom of the ice were obtained from the X-Y plots of the radar transceived signal. The effective bulk dielectric constant  $\epsilon$  of the sea ice was calculated from:

$$\epsilon = \frac{tc^2}{2D} \quad (2)$$

where  $c$  = impulse radar velocity in free space

$D$  = tape-measured ice thickness - 5 cm

$t$  = two-way travel time (measured from zero crossing to zero crossing as shown in Figure 3)

Five centimeters was subtracted from the measured ice thickness because at the impulse radar frequency used in this study the electromagnetic boundary at the bottom of growing sea ice has been shown to be about this distance above the ice/water interface (Campbell and Orange (1974)). The effective impulse velocity ( $V_e$ ) in the ice was determined from:

$$V_e = \frac{2D}{t} \quad (3)$$

Table I lists the relative bottom reflection amplitude, effective bulk dielectric constant and effective signal velocity in the ice sheet vs. antenna E-field orientation.

#### RESULTS AND DISCUSSION

At stations 1 and 3 the surface dielectric constant varies with antenna azimuth orientation, indicating a small ice surface anisotropy (Table I). As defined by Kovacs and Morey (1978), the coefficient of anisotropy (K) is the ratio of the major-to-minor axis of the polar plot of the reflection amplitude as shown in Figures 4, 5 and 6. All data gathered to date using impulse radar indicate that the surface of sea ice is either not anisotropic in the horizontal plane or only weakly anisotropic.

The average surface dielectric constant and surface brine volume are given in Table II for three stations. Salinity was determined from the meltwater of the top 1 1/2 cm of the ice sheet. The temperature was measured at the 1/2-cm depth. From these measurements the brine volume of the ice was calculated. Figure 7 is a plot of surface brine volume vs. average surface reflection coefficient from Table II. As might be

expected, the coefficient of reflection (and dielectric constant) increases with increasing brine volume since the surface is more conductive at higher brine volume.

Brine volume profiles representative of ice at each study site are shown in Figures 8, 9 and 10. These profiles are fairly typical for first-year ice in that their only striking feature is the sharp increase in brine volume in the lower portions. Note that the brine volume in the top 1/3 of the cores from the Prudhoe Bay West Dock site is less than that of the cores from near Tigvariak Island and sites 1 through 4. This implies that the sea water near the West Dock was less saline during initial freeze-up, presumably as a result of local river flow diluting the near-shore sea water.

The sea ice at the West Dock site was also unique to this study because the upper two-thirds of the ice was composed of fine-grained crystals ( $\approx 15/\text{cm}^2$ ) with random c-axis direction. This fine-grained ice was also quite dirty as shown in Figure 11. The clean sea ice below the dirty ice had a structure composed of long, columnar crystals with small horizontal cross-sectional area ( $\approx 2/\text{cm}^2$ ).

The dirty ice is believed due in part to silt carried to the sea by rivers and to turbulent flow of water in and out of Prudhoe Bay across a shallow zone that rings the outer edge of the bay. As the sea ice grew in thickness the area available for tidal flow between the ice and the bottom became more and more restricted. This resulted in some scouring and the concurrent suspension of fine bed material. When the ice

finally became bottom-fast along the seaward edge of Prudhoe Bay no further scouring occurred. Local coastal currents then quickly removed the silty water. In any event, that a rapid clearing of the water occurred is quite evident in the ice blocks shown in Figure 11.

Ice thickness vs. average brine volume and dielectric constant are given in Table III, where the ice thickness is put into two regimes, i.e. thinner ice (average 1.57 m) and thicker ice (average 1.78 m). A plot of these data shows that the bulk dielectric constant increases with increasing brine volume (Fig. 12). This is to be expected since brine volume is a measure, among other things, of the free liquid in the sea ice. As the amount of liquid in the sea ice increases, the dielectric constant of the bulk sea ice structure (i.e. the proportion of ice, water, salts and air) will increase. For a given average brine volume, the average dielectric depends upon ice thickness, as shown by the two lines in Figure 12. This is because there is relatively more pure ice in the upper portion of the thicker ice as shown in Figures 8, 9 and 10.

As the radar antenna was rotated in the horizontal plane above or on the ice surface, the amplitude of the reflected signal from the bottom of the ice changed, in some cases dramatically. When the antenna E-field was aligned parallel with the preferred horizontal c-axis direction of the ice crystals in the bottom ice layer, a maximum signal return from the "ice bottom" was recorded. But when the antenna was

oriented perpendicular to the preferred c-axis direction the reflected signal was significantly reduced or eliminated. At all locations but the West Dock (WD) site there was very good agreement between preferred c-axis, maximum bottom reflection amplitude, and the instantaneous current direction (Table I). The field results suggest that the under ice short term tidal regime has a negligible effect on the long term current direction at the ice water interface. In other words the mean current affects the orientation of the relatively slow growing crystalline layer at the ice bottom. The fact that our many instantaneous current measurements which were made at various times of the day showed that the ice water interface current was flowing parallel to the preferred crystal c-axis azimuth orientation adds support to the above. This supports the findings of Kovacs and Morey (1978) and Weeks and Gow (1978) - that under-ice currents, typically 1 to 3 cm/sec at our field sites, influence ice growth and cause a preferred crystal c-axis azimuthal alignment parallel with under-ice current direction.

At the West Dock we found from ice core observations that the crystal structure of the sea ice changes over short distances from a structure in which the horizontal c-axes are highly oriented to one in which the c-axis orientation is random. These changes were first observed by moving the radar antenna across the ice surface in 1/2-m increments and observing at each position the radar signal amplitude reflected from the "ice bottom" as the antenna was rotated about its center. Within a

distance of 3.5 m the direction of the maximum reflected signal amplitude would change by as much as  $90^\circ$  between some positions, indicating a varying anisotropic sea ice structure, while at one position no significant amplitude change was noted versus antenna orientation, indicating an isotropic sea ice structure. This randomly varying sea ice structure was noted over a large area and is believed to be the result of under-ice current eddies associated with water flow around the end of the West Dock.

Our impulse radar investigations have shown that sea ice tends to be anisotropic; however, the degree of anisotropy varies considerably, as shown in Table I and Figure 4. In many anisotropic dielectrics, the effective dielectric constant, which determines the velocity of propagation, will change as the E-field of the probing signal is rotated. The mechanism that gives rise to the anisotropy will determine whether or not the dielectric constant will change with rotation of the E-field.

A plot of the normalized reflection amplitude vs. the effective bulk dielectric constant for all of the stations and each antenna azimuth is shown in Figure 13. The variation of the normalized reflection amplitude versus E-field azimuth direction for each station can be an indicator of the anisotropy. One would expect for sea ice that the dielectric constant will increase with decreasing reflection amplitude since less reflected energy implies a more dispersive medium and thus one with a higher dielectric constant. However, there does not seem to be a strong correlation in this direction, as shown in Figure 13.

There are several possible explanations. First, the physical mechanisms that cause the measured electromagnetic anisotropy may not change the bulk dielectric constant of sea ice with E-field orientation. Next, the impulse radar system may not have sufficient resolution or the data analysis techniques may not be accurate enough to produce repeatable results. Finally, near the ice/water interface there may be a strong gradient in the dielectric permittivity so that the reflecting boundary is not well defined electromagnetically. In other words, this boundary reflecting zone, may shift up and down with E-field orientation. The depth to the electromagnetic boundary is inversely proportional to the square root of the dielectric constant. So it is possible that this boundary depth and the bulk dielectric constant change in a unique way with antenna E-field orientation so that no apparent change in the bulk dielectric would be noted because it is currently assumed in our analyses that the depth to the electromagnetic boundary remains constant. If the boundary moves up and down, it would explain why there seems to be little correlation between the coefficient of anisotropy and the difference in bulk dielectric constant (maximum dielectric constant minus minimum dielectric constant for each station) as shown by the scatter in Figure 14.

To help clarify the above let's assume that the bulk dielectric constant of a 1.6-m-thick sheet of sea ice changed from 4 to 5 due to a bulk anisotropy effect. The resultant change in the two-way travel time would be 2.5 ns, provided the electromagnetic boundary remained fixed.



This time change, which is within the accuracy of the radar system, was not observed. But if all the "action" is occurring in the bottom 10% of the ice, then only a 0.25 ns in travel time would take place, which is probably at the limit of the radar system's resolution. If this is the case, then it is possible that the observed sea ice anisotropy is an ice "bottom" phenomenon.

The frequency-dependent nature of the reflected radar signals was also evaluated. For example, the time-amplitude wavelet reflected from the sea ice bottom was stored in a microcomputer and its frequency spectrum was calculated and plotted. The center frequency of the spectrum, as determined by averaging the frequencies at the -3db points obtained from the frequency spectrum plot is plotted vs. E-field orientation in Figures 5 and 6 for stations 1, 2, 3 and 4. As can be seen, the center frequency of the spectrum is maximum in the c-axis direction. This shows that the dispersive properties of sea ice depend on azimuthal direction. Figure 15 is a plot of average brine volume vs. center frequency. As the brine volume increases, the center frequency of the spectrum of the reflected radar signal decreases, indicating that the dispersive properties of sea ice are brine-dependent.

#### CONCLUSIONS

This study reaffirms the findings of Kovacs and Morey (1978), which revealed that highly ordered sea ice, in which the crystal structure has a horizontal c-axis with a preferred azimuthal direction, is a complex,

anisotropic dielectric. This ordered structure is shown to be an effective polarizer of transverse electromagnetic waves. The reason for the polarization has been related to the ordered arrangement of the brine inclusions which are believed to create a unique array of parallel plate wave guides. This arrangement has been shown to reduce or eliminate radar signal reflection from the ice bottom when a linearly polarized radar antenna E-field is oriented perpendicular to the preferred crystal c-axes direction and to allow a maximum signal return when the antenna E-field is aligned parallel with the preferred c-axes azimuth.

In this study it is now shown that in highly ordered sea ice;

- a. the frequency-dispersive properties of the ice vary in the horizontal plane as does the anisotropy,
- b. the dispersion is related to the ice brine volume and
- c. the bulk dielectric constant as measured by impulse two-way travel time does not correlate with the coefficient of anisotropy.

It was also found that where turbulent flow occurs around a dock, no preferred ice crystal c-axes direction is established and it was found that the surface of sea ice has no definite anisotropic trend as determined from reflection measurements.

#### ACKNOWLEDGMENTS

This study was supported by the Office of Naval Research, Project NR 307-393, and in part by the Bureau of Land Management through inter-agency agreement with the National Oceanic and Atmospheric Administration under the Alaska Outer Continental Shelf Environment Assessment Program, RK-8-0065. The helpful discussion by Dr. Steven Arcone concerning electromagnetic propagation in a dispersive media is gratefully acknowledged.

#### REFERENCES

- Campbell, K.J. and A.S. Orange (1974) A continuous profile of sea ice and freshwater ice thickness by impulse radar. Polar Record, Vol. 17.
- Kovacs, A. and R.M. Morey (1978) Radar anisotropy of sea ice due to preferred azimuthal orientation of the horizontal c-axis of ice crystals. J. Geophys. Res., Vol. 83, No. C12.
- Morey, R.M. (1974) Continuous subsurface profiling by impulse radar. Proceedings of Engineering Foundation Conference on "Subsurface Exploration for Underground Excavation and Heavy Construction," American Society of Civil Engineers, N.Y.
- Weeks, W.F. and A.J. Gow (1978) Preferred crystal orientation in the fast ice along the margins of the Arctic Ocean. J. Geophys. Res., Vol. 83, No. C10.

Table . Sea ice property and radar reflection analysis determinations.

Sta.	Ice thick. (m)	Ice surface - Antenna elevated					Ice bottom - Antenna elevated					Ice bottom - Antenna on ice					Water depth (m)						
		Reflection		Max. Diel. const.	Max. refl. dir.	Refl. anisotropy	Reflection		Signal Max.		Refl. anisotropy	Reflection		Signal Max.		C-axis dir.		Current dir.					
		Dir. (V)	Coef.				Dir. (V)	Coef.	Dir. (m/ns)	refl.		Dir. (V)	Coef.	Dir. (m/ns)	refl.				Dir. (V)	Coef.	Dir. (m/ns)	refl.	
1	1.61	0*	5.38	-0.508	9.4																		
		30	5.44	-0.511	9.6																		
		60	5.64	-0.530	10.6	100°	1.1	60	0.08	-0.010	6.5	0.117	60	0.56	-	-							
		90	6.12	-0.580	14.2			90	0.28	-0.032	6.9	0.115	42°	13.6	90	0.33	6.7	0.116	46°	8.1	40°	45°	21.9
		120	5.79	-0.544	11.5			120	0.16	-0.019	6.4	0.118			120	0.25	6.4	0.118					
		150	5.79	-0.544	11.5			150	0.09	-0.015	6.2	0.120			150	0.12	6.2	0.120					
		Avg	-0.536	11.1				Avg	-0.030	6.5	0.117			Avg	6.4	0.118							
2	1.55																						
3	1.83	0	2.70	-0.446	6.8																		
		30	3.01	-0.497	8.9			30	0.20	-0.025	5.2	0.132			30	0.76	5.0	0.134					
		60	3.36	-0.554	12.1			60	0.54	-0.061	5.2	0.131			60	0.71	5.1	0.133					
		90	3.23	-0.533	10.8	70	1.2	90	0.75	-0.089	5.2	0.129	80	4.8	90	1.55	5.2	0.132	80	15.0	90	-	>40
		120	2.99	-0.493	8.7			120	0.41	-0.051	5.5	0.128			120	0.83	5.1	0.133					
		150	2.47	-0.408	5.7			150	0.17	-0.023	5.9	0.123			150	0.20	5.6	0.127					
		Avg	-0.488	8.8				Avg	-0.050	5.4	0.129			Avg	5.3	0.131							
4	1.75																						
WD-1a	1.80	0	2.57	-0.536	11.0																		
		30	2.61	-0.545	11.5																		
		60	2.79	-0.582	14.3																		
		90	2.78	-0.580	14.2	None	None																
		120	2.55	-0.532	10.7																		
		150	2.78	-0.580	14.2																		
WD-1b	1.80																						



Table II. Brine volume of ice surface (upper 2 cm of ice sheet) vs. average ice surface reflection coefficient and dielectric constant.

<u>Sta.</u>	<u>Brine vol (<math>^{\circ}</math>/oo)</u>	<u>Avg refl. coef.</u>	<u>Avg. diel. const.</u>
WD-1a	36	-0.559	12.6
1	34	-0.536	11.1
3	30	-0.488	8.8

Table III. Ice thickness vs. average brine volume, dielectric constant and maximum reflection coefficient.

<u>Sta.</u>	<u>Ice thick. (m)</u>	<u>Avg. brine vol. (<math>^{\circ}</math>/oo)</u>	<u>Avg. diel. const.</u>	<u>Max. ref. amp. (V)</u>
T1G-3	1.60	53	5.9	6.66
2	1.55	65	6.2	2.10
T1G-1	1.53	65	6.3	2.39
1	1.61	74	6.5	0.56
	Avg. 1.57			
WD-1a	1.80	50	4.7	2.73
WD-2	1.74	57	5.2	2.00
3	1.83	62	5.3	1.55
4	1.75	69	5.5	5.95
	Avg. 1.78			

## Figures

- Figure 1. Map of Beaufort Sea in the vicinity of Prudhoe Bay, Alaska, showing station locations at which sea ice crystal, current and radar studies were made in 1976, 1977 and 1978.
- Figure 2. Arrangement used to elevate radar antenna above ice surface. Note azimuth grid under metal screen.
- Figure 3. Example of an X-Y plot of the radar impulse signal obtained when the antenna is elevated above the ice surface (a) and when the antenna is resting on the ice surface (b).
- Figure 4. Polar coordinate plots of radar signal reflection amplitude from the sea ice surface and the ice bottom at site 3 (when the antenna is elevated above the ice surface) and the radar signal reflection amplitude and center frequency from the ice bottom at sites 1 through 4 (when the antenna is on the ice surface) vs. antenna E-field azimuth direction.
- Figure 5. Site 1 polar coordinate plots of radar signal reflection amplitude from the sea ice bottom (a) and ice surface (b) (when the antenna is elevated above the ice surface) and the radar signal reflection amplitude (c) and center frequency (d) from the ice bottom (when the antenna is on the ice surface) vs. antenna E-field azimuth direction.
- Figure 6. Polar coordinate plots of radar signal reflection amplitude from the ice bottom at sites WD1a, WD1b, WD2, Tig. 1, Tig. 2, and Tig. 3 (when the antenna is on the ice surface) vs. antenna E-field azimuth direction.
- Figure 7. Brine volume of ice surface vs. average surface reflection coefficient.
- Figure 8. Brine volume profiles from two cores obtained at the Prudhoe Bay West Dock sites.
- Figure 9. Brine volume profiles from cores obtained at the Tigvariak Island sites.
- Figure 10. Brine volume profiles of cores obtained at sites 1 through 4.
- Figure 11. Ice blocks removed from the ice sheet at the West Dock. Note the uneven interface between the dirty and clean sea ice.
- Figure 12. Average brine volume vs. average dielectric constant as a function of ice thickness.

Figure 13. Coefficient of anisotropy vs. difference in dielectric constant.

Figure 14. Normalized reflection amplitude vs. relative dielectric constant.

Figure 15. Average brine volume vs. center frequency.



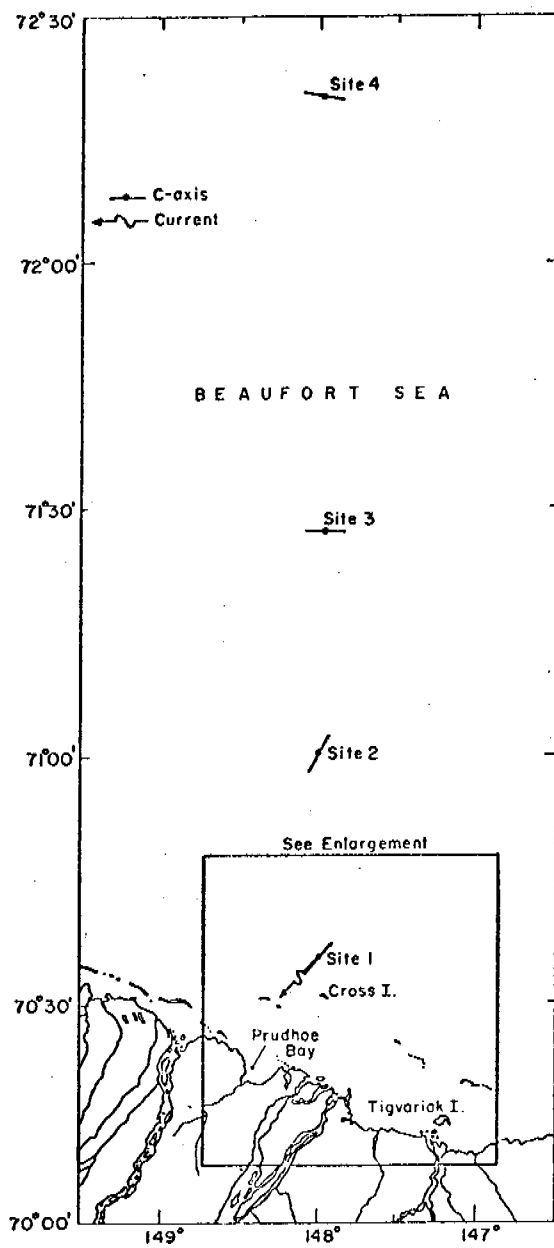


Figure 1(a).

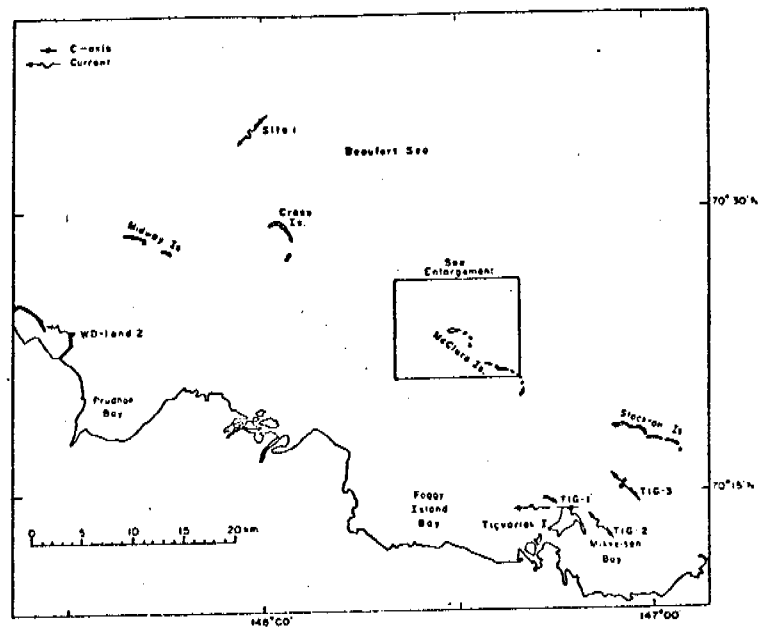


Figure 1(b).

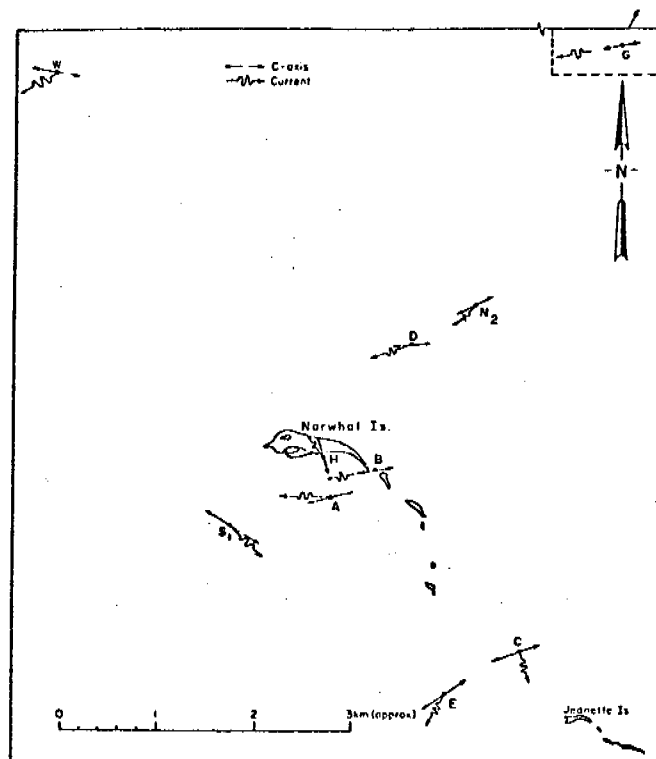


Figure 1(c).

Figure 1. Map of Beaufort Sea in the vicinity of Prudhoe Bay, Alaska, showing station locations at which sea ice crystal, current and radar studies were made in 1976, 1977 and 1978.

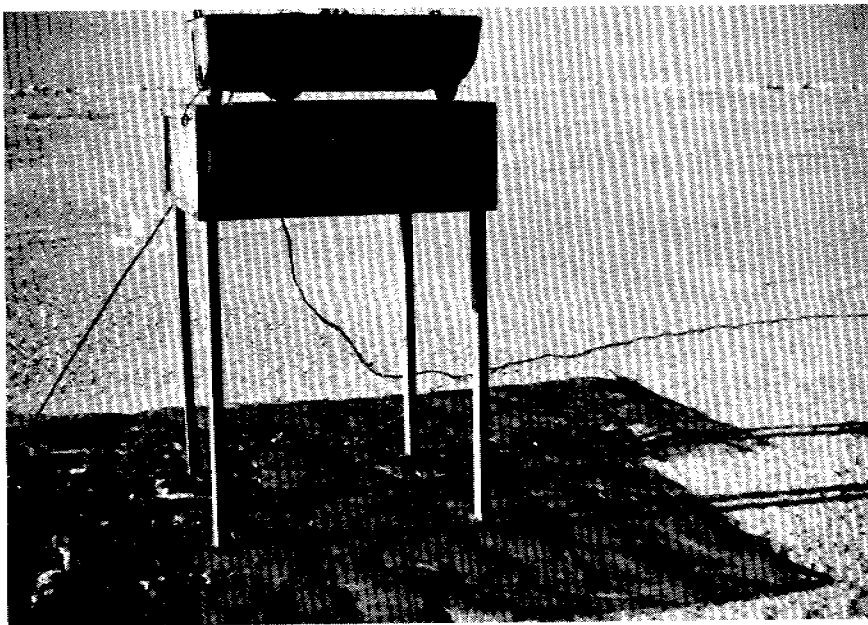


Figure 2. Arrangement used to elevate radar antenna above ice surface. Note azimuth grid under metal screen.

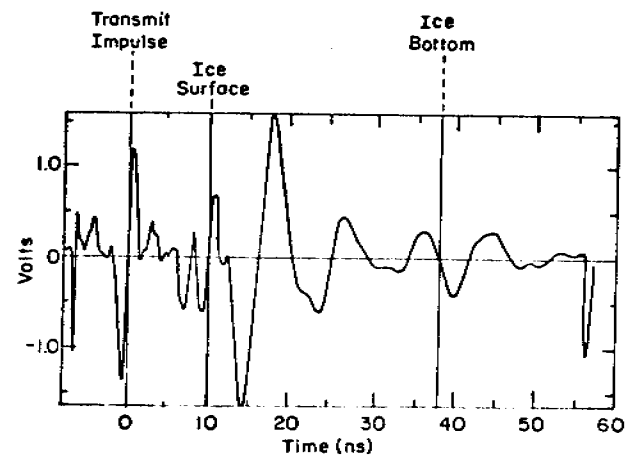


Figure 3 (a).

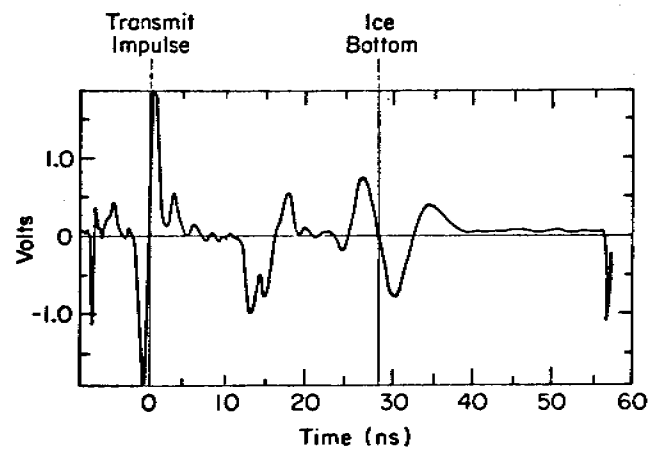


Figure 3 (b).

Figure 3. Example of an X-Y plot of the radar impulse signal obtained when the antenna is elevated above the ice surface (a) and when the antenna is resting on the ice surface (b).

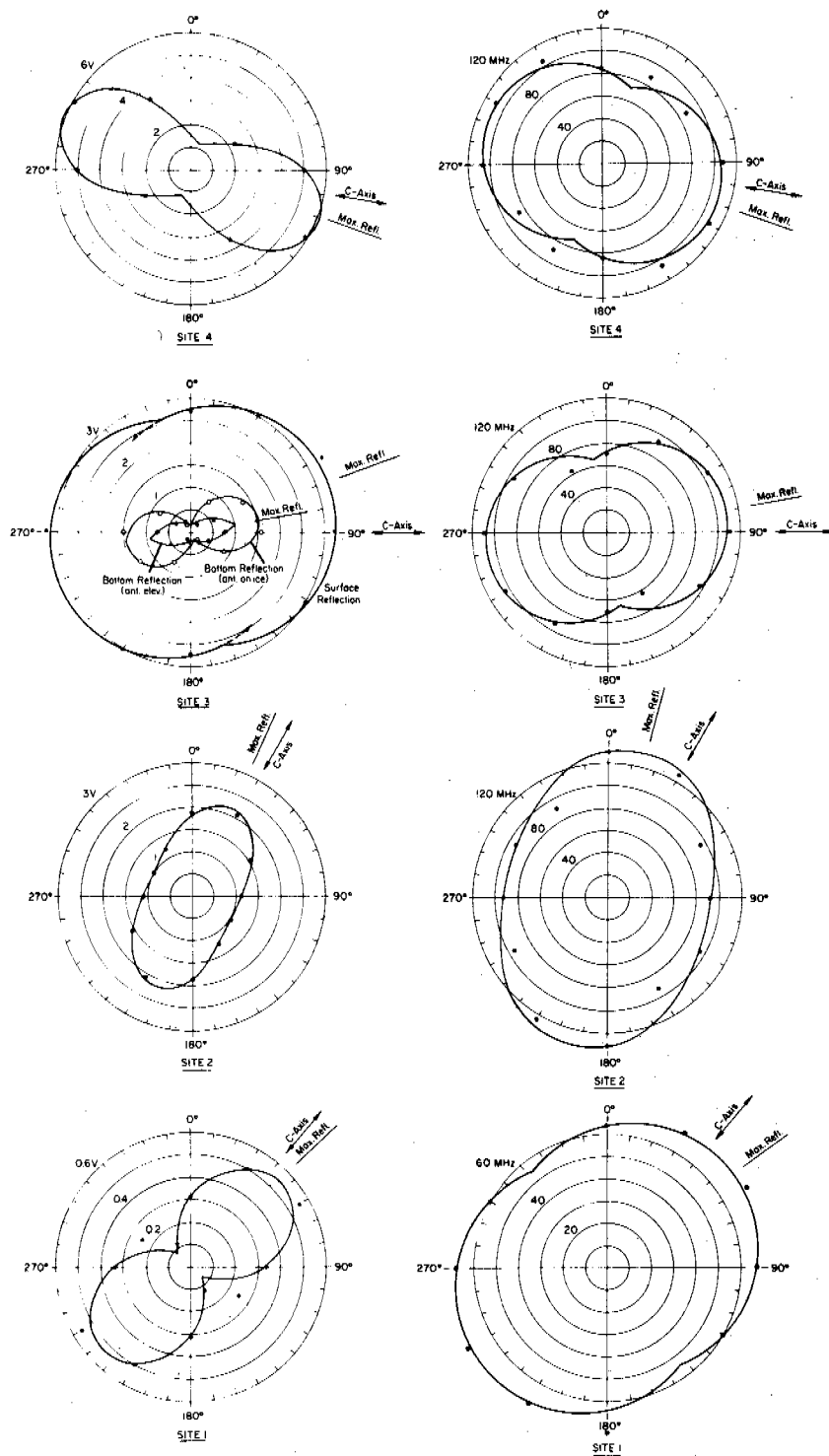


Figure 4. Polar coordinate plots of radar signal reflection amplitude from the sea ice surface and the ice bottom at site 3 (when the antenna is elevated above the ice surface) and the radar signal reflection amplitude and center frequency from the ice bottom at sites 1 through 4 (when the antenna is on the ice surface) vs. antenna E-field azimuth direction.

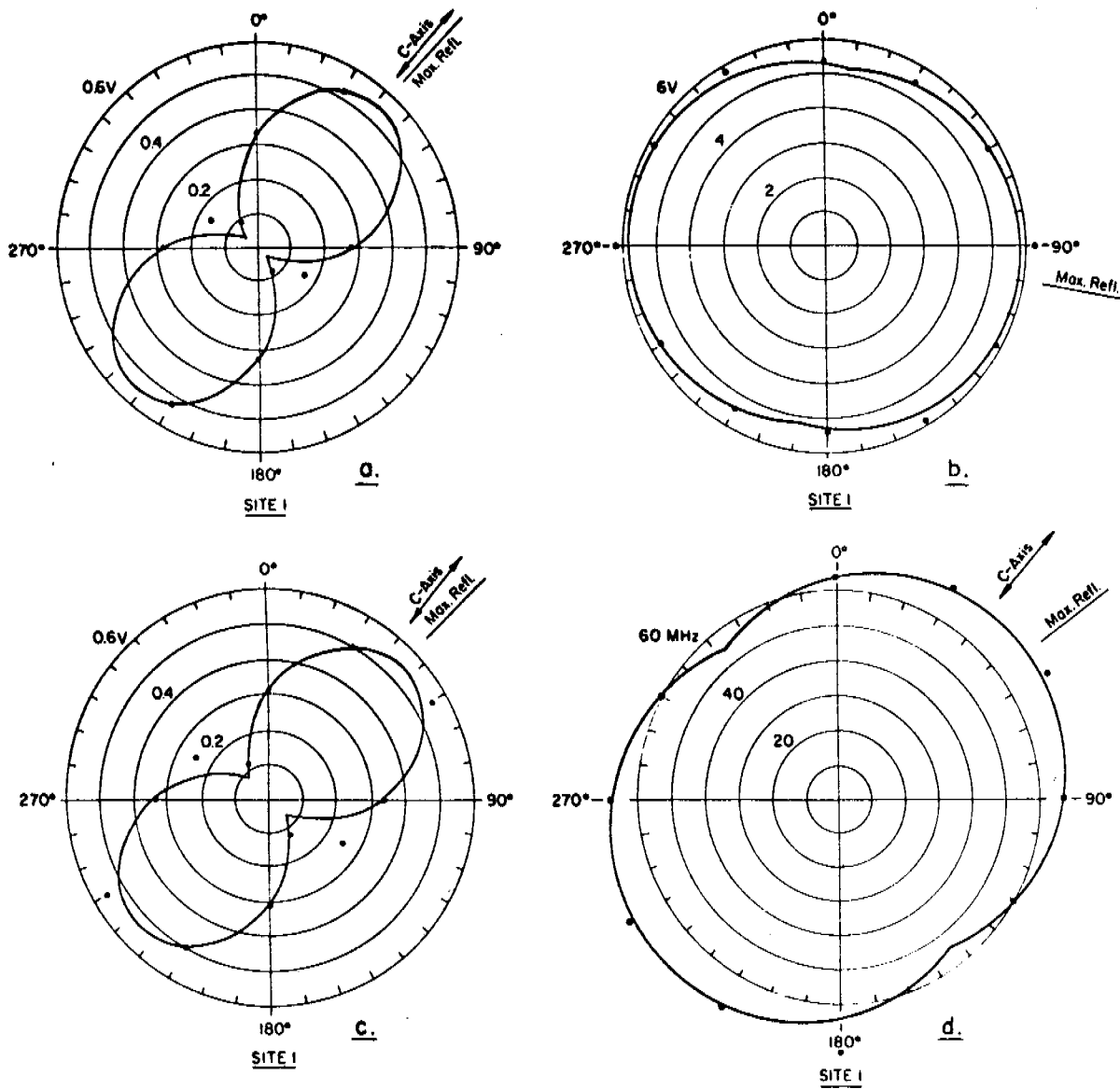


Figure 5. Site 1 polar coordinate plots of radar signal reflection amplitude from the sea ice bottom (a) and ice surface (b) (when the antenna is elevated above the ice surface) and the radar signal reflection amplitude (c) and center frequency (d) from the ice bottom (when the antenna is on the ice surface) vs. antenna E-field azimuth direction.

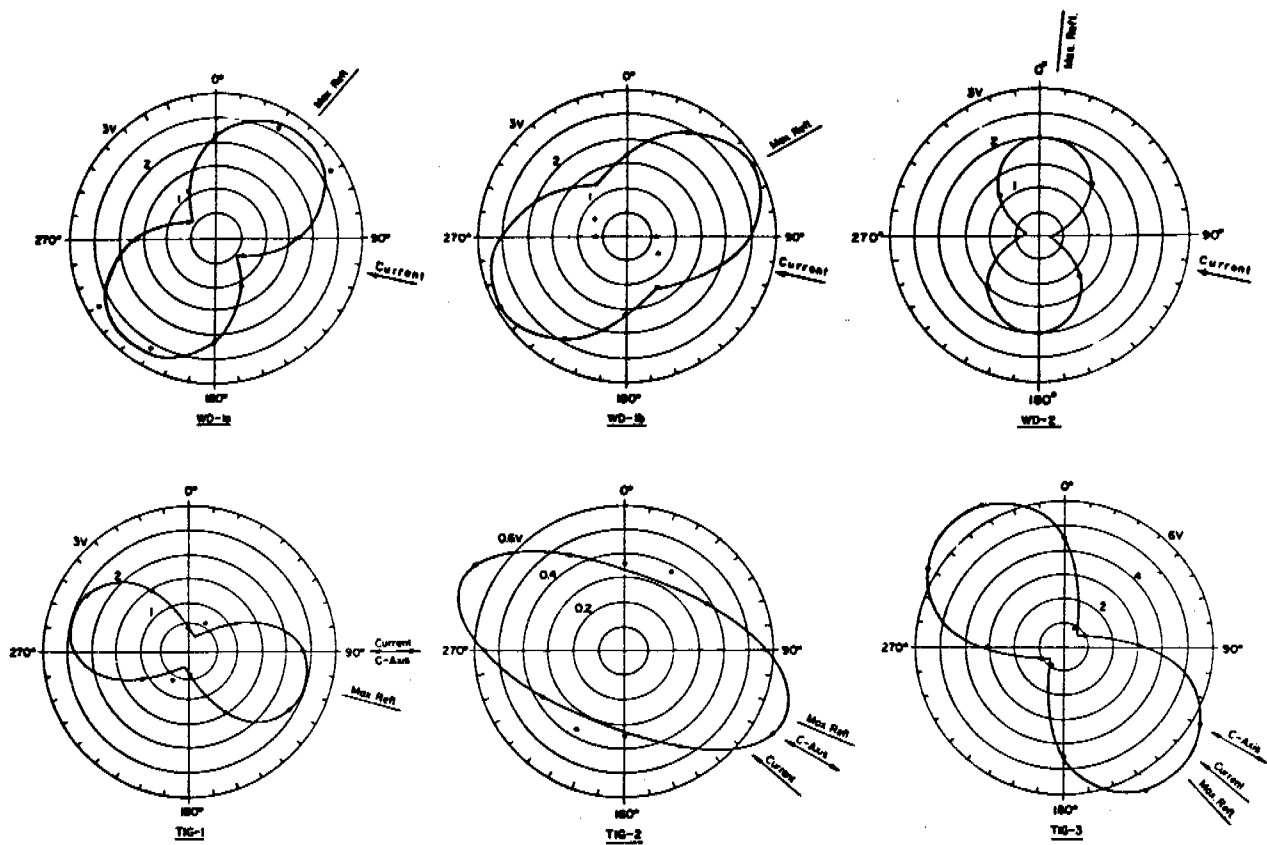


Figure 6. Polar coordinate plots of radar signal reflection amplitude from the ice bottom at sites WD1a, WD1b, WD2, Tig. 1, Tig. 2, and Tig. 3 (when the antenna is on the ice surface) vs. antenna E-field azimuth direction.

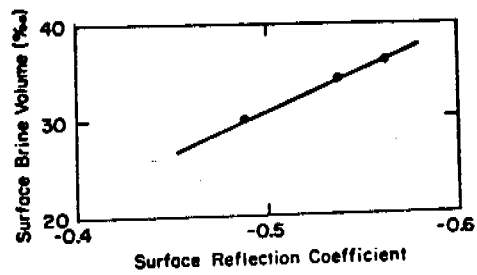


Figure 7. Brine volume of ice surface vs. average surface reflection coefficient.

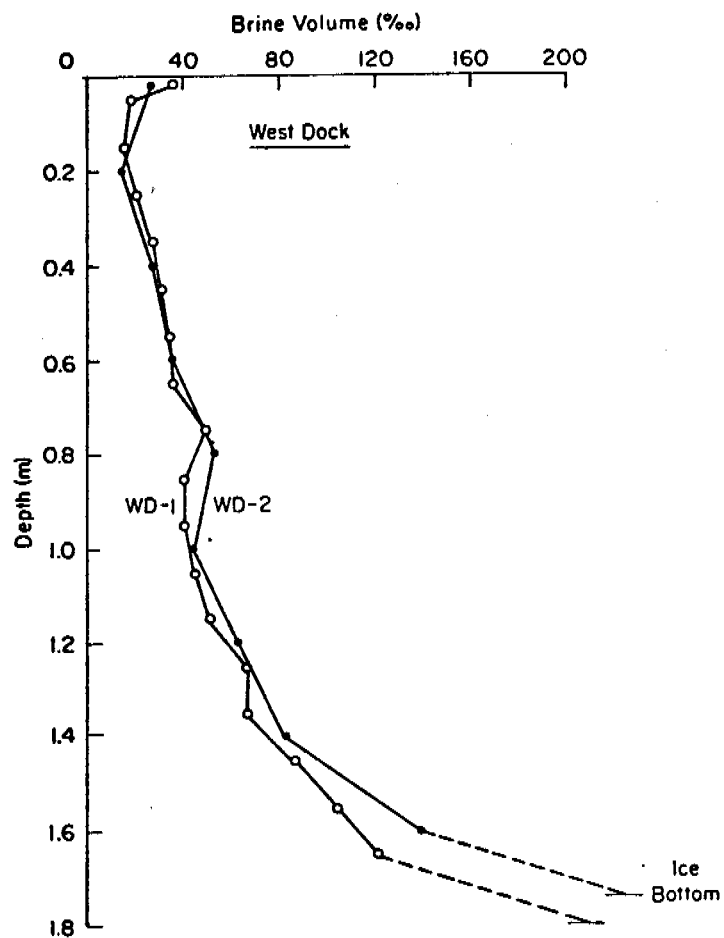


Figure 8. Brine volume profiles from two cores obtained at the Prudhoe Bay West Dock sites.

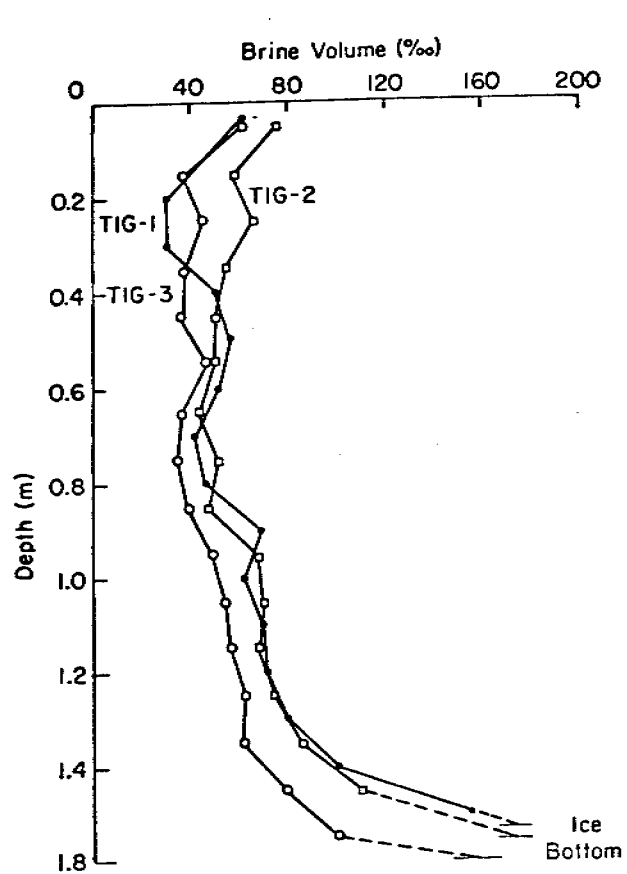


Figure 9. Brine volume profiles from cores obtained at the Tigvariak Island sites.

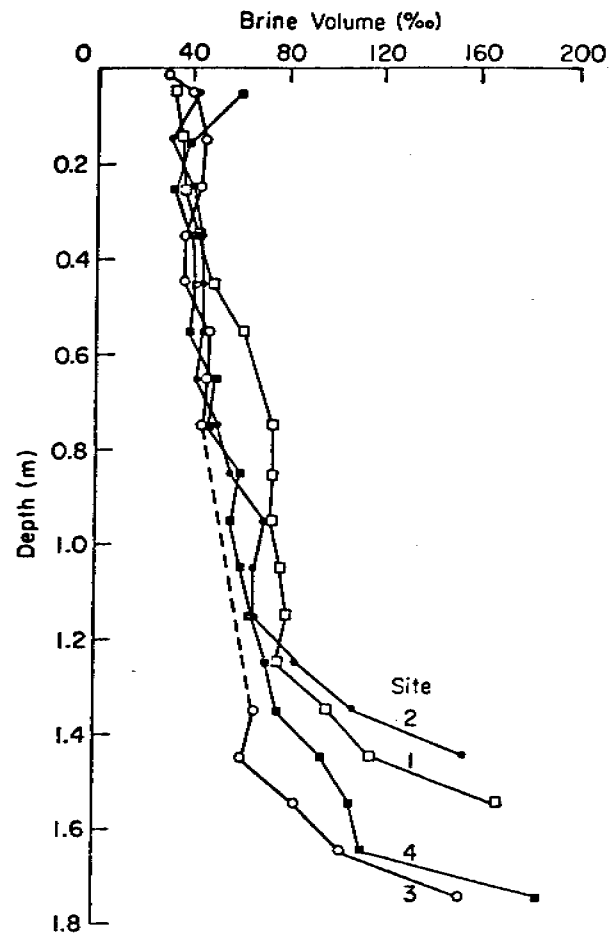


Figure 10. Brine volume profiles of cores obtained at sites 1 through 4.

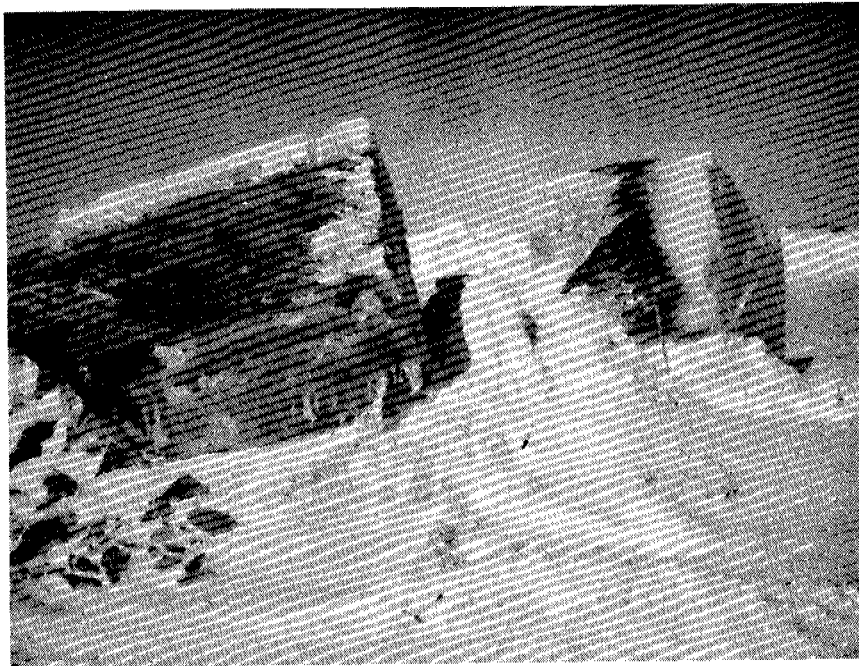


Figure 11. Ice blocks removed from the ice sheet at the West Dock. Note the uneven interface between the dirty and clean sea ice.

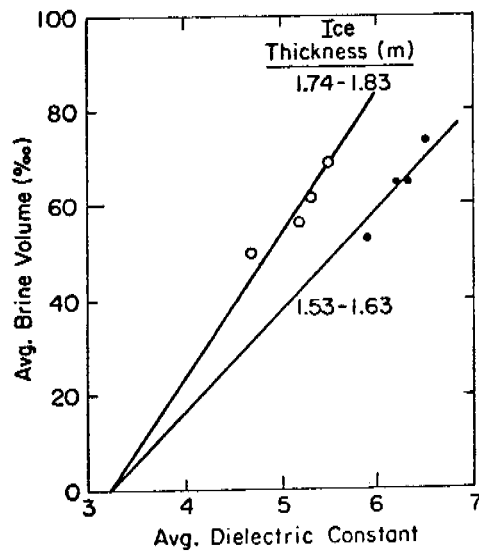


Figure 12. Average brine volume vs. average dielectric constant as a function of ice thickness.



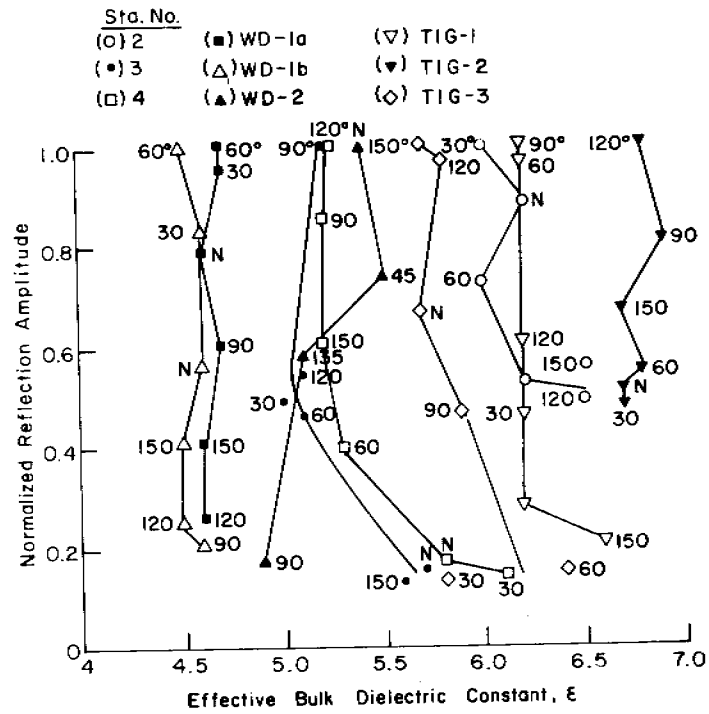


Figure 13. Coefficient of anisotropy vs. difference in dielectric constant.

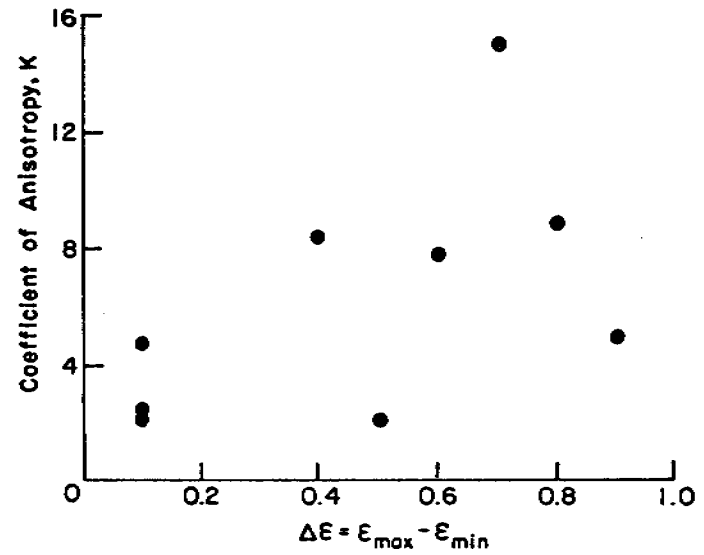


Figure 14. Normalized reflection amplitude vs. relative dielectric constant.

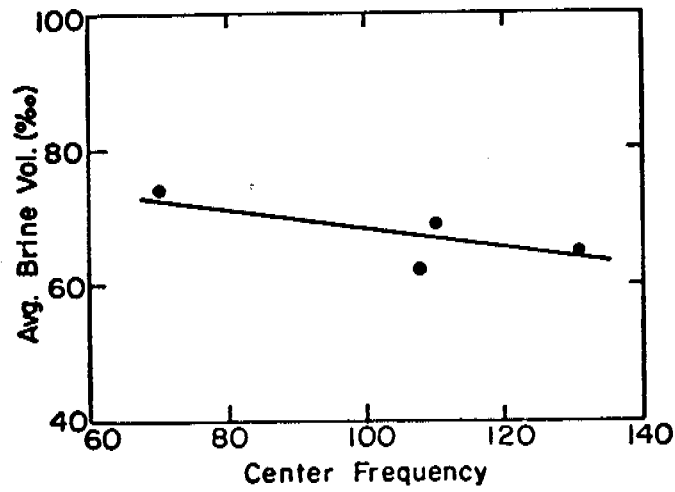


Figure 15. Average brine volume vs. center frequency.

Annual Report  
June 78 - March 79  
Research Unit 567

THE TRANSPORT AND BEHAVIOR OF OIL SPILLED  
IN AND UNDER SEA ICE

M. D. Coon  
R. S. Pritchard

Flow Research Company  
A Division of Flow Industries, Inc.  
21414 - 68th Avenue South  
Kent, Washington 98031  
(206) 854-1370

March 31, 1979

## Table of Contents

Page

### Annual Report

- I. Summary of Objectives
  - II. Introduction
  - III. Current State of Knowledge
  - IV. Study Area
  - V. Sources, Methods and Rationale of Data Collection
  - VI. Results
  - VII. Discussion
  - VIII. Conclusions
  - IX. Need For Further Study
  - X. Summary of Fourth Quarter Operation
- Attached Reports:
- Beaufort and Chukchi Sea Ice Motion
  - Part 1 Pack Ice Trajectories
  - Part 2 Onset of Large Scale Chukchi Sea Ice Breakout
  - Arctic Oil Spill Scenarios - Outline

## Annual Report

### I. Summary of Objectives

The objective of the proposed work is to determine the locations to which oil spilled in or under the ice cover near Prudhoe Bay, Alaska, would be transported, and to determine the behavior of the oil as the ice cover moves and deforms. The work in this research unit is being done in conjunction with that of Research Unit No. 568 conducted by Arctec, Incorporated and with Research Unit No. 562 conducted by CRREL. Arctec is conducting laboratory experiments to determine how oil spreads under sea ice and how oil is incorporated into this ice. The CRREL research consists of field studies to determine the ice thickness profile, and therefore, bottom contour relief which will entrap oil. Two separate tasks have been undertaken by Flow Industries, Inc. The first task is to determine a range of velocity fields which might be taken by the ice cover on the Continental Shelves of the Beaufort and Chukchi Seas by numerical modeling and synthesis of the results from manned and drifting stations. These velocity fields will represent the climatological mean (most probable) and extremes. As part of this task, major breakouts of ice from the Chukchi into the Northern Bering Sea are being analyzed. The second task is for the overall management of the program as well as determining the likely trajectories and destination points of oil in several hypothetical scenarios by combining the relevant information obtained.

### II. Introduction

#### A. General Nature and Scope of Study

To determine the most likely and extreme sea ice motions, the barometric pressure fields, as determined by the U.S. Weather Service for twenty-five years, were used to determine the winds and, through a sea ice dynamics model, the subsequent sea ice motion. This work is discussed in detail in the report "Beaufort and Chukchi Sea Ice Motion - Part I Pack Ice Trajectories" (attached).

The breakout of the sea ice from the Beaufort to the Chukchi Seas has been studied using a rigid plastic model for the behavior of the sea

ice to determine the meteorological conditions under which breakout may occur. This work is discussed in detail in the attached report "Beaufort and Chukchi Sea Ice Motion - Part 2 Onset of Large Scale Chukchi Sea Ice Breakout."

Outlines for twelve scenarios of oil spills in the Prudhoe Bay area are given in the attached report "Arctic Oil Spill Scenarios - Outline". These scenarios can only be outlined at present and will be completed when the work on this Research Unit and Research Units Nos. 568 and 562 have been completed.

#### B. Specific Objectives

The objective of the sea ice velocity study is to produce twelve maps, one for each month, showing the mean and extreme velocities for the last twenty-five years (see report Part I). In the breakout problem, the atmospheric wind and ocean current conditions which control the breakout of sea ice are studied and examples are presented in the report Part II.

#### C. Relevance to Problems of Petroleum Development

Studies of the possible fate of oil spilled in the Prudhoe Bay area can provide for a more environmentally safe exploration and development of possible off-shore oil.

### III. Current State of Knowledge

Past oil spill scenarios for the Arctic have been qualitative in that they have attempted to describe what might happen given the rather sketchy bits of information available. It is the intent of this work to quantify the inputs and subsequent conclusions for oil spill scenarios.

### IV. Study Area: Beaufort and Chukchi Seas

### V. Sources, Methods and Rationale of Data Collection

Data collection was not a part of this Research Unit.

## VI. Results

The results of this work are presented in the attached reports. The results of the sea ice motion study can be summarized by noting that for mean monthly sea ice motions, the steady ocean currents are essentially as important as the winds driving the sea ice. The variations that may occur for a given month, year to year, are controlled by the variations in the winds. These variations for monthly motions, year to year, are about half of the total mean monthly drift. The monthly mean motions due to the winds are presented in twelve figures (Figures 2-13, Part 1 of the attached report) with an obvious westerly trend to the motions throughout most of the year. During the summer months, the motion exhibits a northerly component of motion, with July being the extreme. In general, the mean motions are larger in winter than in summer. This is due, in part, to the winds being more variable in direction during the summer. An examination of the individual monthly trajectories show that more large motions occur during the winter. Also, a pronounced east to west variation in the magnitudes of the means is evident with the larger means occurring in the Chukchi Sea. The breakout of sea ice from the Bering Sea to the Chukchi Sea appears to be related more to the magnitudes of winds and ocean currents than to the strength of the sea ice. When barometric pressure conditions are correct (see Part 2 of the attached report), a combination of northerly winds through the straits and a reversal of the ocean current going north to south through the straits can produce conditions of breakout. These have been documented, and it appears that they can occur a few times each winter.

## VII. Discussion

When the results of this Research Unit and Research Units 562 and 568 are completed, it will be possible to construct meaningful scenarios for the fate of oil spilled under sea ice in the Prudhoe Bay area. The field data on underside ice roughness together with the laboratory studies of how oil moves under rough sea ice will permit a prediction of the area for which an oil spill will spread under the sea ice before it is incorporated into the sea ice. Once the oil has been incorporated into sea ice, the

results from the studies on sea ice motion and breakout will allow a determination of the most likely location of the oil entrapped in ice in subsequent months prior to cleanup.

#### VIII. Conclusions

At this point all conclusions are tentative because the work for the various Research Units involved has not been completed. However, one can tentatively conclude from the laboratory studies that small scale (10 to 20 cm) relief on the bottom of sea ice will contain large volumes of oil. It appears from the field results that this small scale relief is always present on the bottom side of sea ice. Therefore, even a very large volume oil spill will be contained in an area a few kilometers in diameter. During the freezing season, this oil will quickly be incorporated into the ice pack. Subsequently the oil entrapped in the ice will be transported by large scale motions from the Prudhoe Bay area toward Point Barrow and subsequently to the Chukchi Sea. It appears that when the oil entrapped in ice has been incorporated into the pack ice motion, it will not impact the shore but it will be carried west and north of Prudhoe.

#### IX. Need For Further Study

During the conduct of this research, the importance of steady ocean currents has become clear. The mean motion of the sea ice is affected by these ocean currents as much as by winds. It seems extremely important to combine all oceanographic data available to determine the best steady-state ocean currents for the Beaufort and Chukchi Seas. This is not necessarily a part of the work in this research unit, but it is felt that it is a very important work to be done. In reference to sea ice dynamics, the conditions for breakout through the Bering Strait have been determined, however, the study should be continued to determine whether ice which has oil incorporated in it from Prudhoe Bay could possibly be involved in the actual breakout through the Bering Strait. The small scale deformation mechanisms in the region of Prudhoe Bay and how the shorefast ice of the Prudhoe Bay is incorporated into the pack ice needs to be understood before the scenarios can be completed. More work will be required to bring together the data from various research units to complete the oil spill scenarios of this study.



It is felt imperative that a field program involving an oil spill be conducted jointly with Arctec and CRREL to verify the various studies in this program.

X. Summary of Fourth Quarter Operation

A. Ship or Laboratory Activities

1-5. No activity in this research unit.

6. Milestone chart.

All work and reports are ahead of schedule.

B. Problems Encountered/Recommended Changes

None

C. Estimate of Funds Expended

The estimated expenditure under this contract through 31 March 1979 is \$200,000.

**Flow Research No. 133**  
**Beaufort and Chukchi Sea Ice Motion**  
**Part 1. Pack Ice Trajectories**

**By**  
**D. R. Thomas**  
**and**  
**Robert S. Pritchard**

**March 1979**

**Flow Research Company**  
**A Division of Flow Industries, Inc.**  
**21414 - 68th Avenue South**  
**Kent, Washington 98031**  
**(206) 854-1370**

## Table of Contents

Page

1. Introduction
2. Approach
3. Meteorological Data Input
4. Method
5. Results

### References

### Figures

- Appendix I. Daily Free Drift Model of Sea Ice.  
Appendix II. Temporal Averaging in Free Drift.  
Appendix III. Observed Winter Ice Motion.  
Appendix IV. Large Scale Free Drift.

## 1. Introduction

The petroleum industry's anticipated exploration for oil deposits off the north coast of Alaska will involve many new environmental considerations. The permanent ice cover of the Arctic ocean is a feature unique to these offshore areas and is a major factor to be considered in all aspects of the exploratory operation. The ice can exert large forces on structures such as drill rigs, ships, causeways and artificial islands. These structures will be designed to withstand expected loads, but in deeper waters off the coast there will be danger from large floes or ice islands which cannot be designed against. In addition to the hazards due to the ice, the generally hostile environment will tend to magnify the chances of an oil spill due to other accidents. Once an oil spill occurs, for whatever reason, the ice cover will play a major role in the behavior of the oil. There are many facets to this role: dispersion of the oil under and around the ice, incorporation of the oil into the ice and the eventual release of that oil, the transport of oil trapped in the ice and prevention or enhancement of cleanup.

The purpose of this work is to determine where an oil spill could be transported by the motion of the ice cover. This knowledge can be useful to the Federal and Alaska government agencies responsible for evaluating the impact of an oil spill. We would like to point out here that the results of this work are not the best method of keeping track of an oil spill once it has occurred, but it provides a method for predicting where a spill could end up after some period of time. Tracking of an actual oil spill requires wind and current observations and predictions at a particular time as well as day-to-day use of an ice dynamics model to predict motion due to these winds and currents, not a statistical history.

Several articles concerned with the behavior and fate of oil spilled in ice-covered waters have appeared recently (Aagaard, et al. (1978), Cambell and Martin (1973), Martin (1977), NORCOR (1975), Rosenegger (1975), Topham (1975) and Wadhams (1975). These results indicate that when oil is released from the ocean floor it rises and spreads under the ice. The bottom relief of pack ice is able to contain large amounts of oil so that even very large spills under stationary ice will not spread beyond an area of a few km<sup>2</sup>. If the ice is moving, the oil concentration will be less, but it will be spread over a long strip. If the release occurs under smooth shorefast ice, it is felt that the spread of the under ice slick will be limited, even when currents act to spread the oil (Wadhams, 1975). In winter, the oil trapped under the ice will become fixed to the ice by growth of new ice from below. Even during the melt season a major portion of the oil will be

trapped by bottom relief of the ice. Some dispersion of the oil, however, is to be expected during the melt season due to ice melting. Trapped oil will be freed into open water occurring between floes, but this will probably happen over a wide area due to the ice motion and to the time it takes for the ice to melt. In general, oil spilled under ice will be limited in areal extent and is expected to disperse slowly, if at all. Furthermore, it is unlikely that any significant cleanup is possible due to the ice cover. The oil will be transported by the ice and partial or whole release and dispersion will likely occur during subsequent melt seasons. Thus, it is important to be able to predict ice motions for periods up to one year. A minimum resolution of one month is sufficient for accounting for seasonal differences in motion.

Determination of the range of anticipated ice motions requires consideration of many years of data but the amount of ice drift data is limited. Throughout the Beaufort and Chukchi Seas there are only a few data sets (AIDJEX, OCSEAP, U of Wash., APL, and stations IGY-A, ARLIS 1 and 2 and CHARLIE). Of these, only the OCSEAP buoys were located near shore. The total coverage provided by drifting buoys and stations is important for comparison with calculated trajectories, but it is inadequate to define the range of ice motions that may be expected during the lifetime of the Prudhoe Bay offshore oil fields.

Fortunately, there are two bases of information available that allow the historical ice motions to be simulated by mathematical modeling techniques. These are: (i) the availability from NCAR (and NMC) of surface barometric pressure maps over the Arctic Ocean (entire northern hemisphere) daily from 1946 through 1977 (Jenne, 1975), and (ii) an understanding of the ice dynamics behavior and its relationship to barometric pressures developed during the AIDJEX project (Coon, et al. 1974).

Work of the AIDJEX modeling group has demonstrated that daily ice motions may be understood and simulated by considering the balance of horizontal forces on the ice cover (inertia, Coriolis, air stress, water stress, sea surface tilt and ice stress divergence) when the stress is related to the deformation by a plastic model (Pritchard, 1975). Thus the monthly motions may be determined by summing up the daily displacement values. In Appendix I and Appendix II we present results which show that we cannot ignore the nonlinearity of the model and use monthly mean barometric pressures to directly determine monthly ice motions.

In the day to day ice motions it is seen that the largest portion of the ice motion occurs in response to the winds (air stress which is determined from the

surface barometric pressure field), and that ocean currents in the Beaufort Sea apply a steady force that is generally smaller than the air stress. The ice stress also can play a dominant role in controlling ice motions. The magnitude of stresses is limited by a yield strength which is a function of ice conditions. In particular, the yield strength is large when there is not much open water or thin ice present (heavy ice conditions) and the yield strength is small when there is a large amount of open water and thin ice (light ice conditions). Ice yield strengths have been observed to be large enough to prevent ice motions during strong winds ( $6 \text{ ms}^{-1}$ ) acting over a long fetch of 850 km (Pritchard, 1976). On the other hand, yield strength has been observed to be negligible during most of the summer of 1975 (McPhee, 1977a). While the summer of 1975 was considered to have heavy ice conditions in the western Beaufort Sea, with the ice never retreating from Pt. Barrow, enough open water existed for the ice to have little strength away from the shores.

We expect yield strength to be negligible during summer (July through September), to begin to increase in October and to grow throughout the freezing season into June when it drops back to a low value. In addition to seasonal variations of yield strength (or ice conditions), it is expected that comparable variations occur from year to year. During the winter the ice may be relatively strong so that it locks up and does not move or it may be relatively weak so that ice strength is negligible, or anywhere between these extremes. In the summer, after all thin ice has melted, only open water and thick ice remain. If at this time the ice cover converges, eliminating the open water, the strength can be even larger than high winter values. It is unlikely, however, that this condition would prevail for more than a few days so that monthly ice motion would not be dominated by it. In Appendix III we examine the observed ice drift data for the Beaufort Sea during the winter and we do see that for some months and some years, the ice moved very little while at other times, the motion is so large that only negligible ice strength could account for the motion.

In Appendix IV we compare the results of a free drift model in which ice strength is considered to be zero with observed drift motions of the AIDJEX manned camps. We also describe and test a modification of the free drift model which should prove useful during the early freezing season (October through December). Here the winds are averaged over a large area to render negligible the effect of ice stress divergence (Pritchard, 1977).

In the main body of this report we present the results of the simple point free drift model only. During the summer we feel that free drift adequately models

ice motion over time periods of one month. During the rest of the year, free drift accurately represents ice motion for one extreme of ice conditions. The other extreme of very large strengths simply prevents all motion. Questions concerning ice motion when the ice conditions (or strength) aren't extreme remain unanswered. These include how often or under what conditions we can expect less than extreme conditions. We have left these questions for a later phase of the project. Also, we have considered only the motion of the offshore pack ice. Ice motion in the shear or marginal ice zone will be considered later.

In summary, this report presents the expected free drift ice motion and range of motions for the Beaufort and Chukchi Seas. The motions are accurate for light ice conditions which are usual in summer and which occur as an extreme in winter. In the appendices attached to this report, we present some results of work related to the free drift model. In Appendix I, we analyze the non-linearity of the free drift model and the effect of model parameters. Appendix II gives an example of the errors to be expected when temporal averaging is used. The results of an empirical scheme (Zubov, 1943) for estimating ice motion is included. In Appendix III we present the range of observed winter ice motions. A comparison of free drift calculations and observed motions is given in Appendix IV along with a test of the free drift model when area averaged winds are used.

## 2. Approach

The purpose of this work is to define the range of motions that might be expected for oil spilled on ice during the lifetime of Prudhoe Bay oil fields. It is generally accepted that the primary driving forces of the ice cover are the winds and currents. It is also expected that the ice conditions (i.e., the "strength" of the ice cover) can have a dominant influence on how the ice behaves in response to these driving forces. In addition, the geography of the region of interest can have an important affect on the ice response because it can influence both the driving forces (e.g., currents near shore or in the Bering Strait) and the effects of the driving forces (e.g., shorefast ice). Therefore, the ice behavior may differ significantly in different regions and during different times of the year. As the first step in determining ice motions, we separated the region of interest according to expected ice behavior. One important region to consider is the fast ice region along the North coast of Alaska. The importance is obvious since this is where drilling operations will take place. The unique attribute of this region is that the ice motions are very small for much of the year. Work on ice motions in this area is planned for a later phase of the project. Another unique area is the Bering Strait. Because of the funneling effect of the land masses in this area we expect the ice to develop considerable strength and to experience little motion. Some motion does occur though in the form of sporadic breakouts through the straits. This phenomenon is being covered in a separate report. The third region we must consider is the pack ice covered seas where the effects of land are nominal. It is in this area that the ice experiences the greatest range of motion throughout the year. The work described in this report involves the large scale pack ice motion in the Chukchi and Beaufort Seas.

As suggested in the Introduction, our preliminary ideas led us to believe that during the summertime pack ice motions satisfied free drift reasonably accurately. Furthermore, it was anticipated that during the wintertime the strength of the pack ice would be large enough so that essentially no motion would occur because the winds and currents could not exert a load large enough to force the ice to move. During the fall freeze up season from about October through December, it was expected that the ice strength would be increasing gradually and that simplified models similar to free drift models would be adequate to determine the ice motion. During the spring breakup season it was expected that very complicated conditions would exist and that a complete model similar to the AIDJEX ice dynamics model



would be required to define the ice motion at this time. The initial efforts in this work were performed to investigate the validity of the aforementioned assumptions.

It has previously been shown by McPhee (1977a) that free drift is an accurate method of simulating ice motions during the summer in the central Beaufort Sea. We compared free drift simulations with observed motions for the summer of 1975 during which ice conditions were considered to be heavy (see Appendix IV). We found good agreement between free drift and observed motions and concluded that during the summer season free drift would be accurate in its representation.

To demonstrate that during the wintertime ice motions were negligibly small, we examined the available drift station data. The results of this study are presented in Appendix III. It is seen from the results of this study that the assumption is invalid. Ice motions during the wintertime in many years can be just as large as those during the summertime. This result led us to the need for determining winter ice motions by another means.

During the fall freeze up, we expected to use the results of Pritchard (1977) who developed a large scale free drift model that was expected to accurately determine ice velocities when strengths were modest but not insignificant. During 1975 the AIDJEX experiment provided accurate winds as driving forces and accurate observed ice motions to allow a thorough test of this model. The results presented in Appendix IV shows that the model does indeed provide more accurate ice velocities than does the free drift model under equal circumstances, but the amount of improvement is not large enough to warrant using this model. At this time we are unable to determine whether ice conditions were unusually heavy during the Fall of 1975, but in any case, we felt that the assumption could not be depended upon and that an alternate scheme would have to be used to determine ice trajectories during the fall freeze up period.

As can be seen, our preliminary conjecture about winter motion was incorrect. Also, our postulated model for fall ice motions fell short of expectations. While it is theoretically possible to use the full AIDJEX model (or some other model which takes ice strength into account) to simulate ice motions from freeze up through spring break up, the cost of processing 25 years of ice motions this way is prohibitive. As a result, we felt it necessary to redesign our approach to this problem.

The central theme of the modified approach for determining pack ice motion in the Beaufort and Chukchi Seas is to consider the range of motions that might be expected under extreme ice conditions. As mentioned in the introduction, the large

strength or heavy ice condition extreme is easily determined because in that case there can be no ice motion under any expected winds. On the other hand, when ice conditions are light and ice strength is low, we expect the affect of ice stress divergence to be negligible and therefore, the ice will respond in the free drift mode. The work presented in this report deals with the case of free drift. Free drift is considered as an extreme limit to pack ice motion. This extreme is the expected state during the summer, but our results indicate that even during the winter at many times the ice does move in approximately a free drift state.

The requirements of this work are to determine the range of ice motions that could occur during the course of a season, several seasons or a year. We, therefore, felt that it was adequate to resolve motions on monthly intervals. Shorter intervals would provide results so variable, because of the presence of individual storms, that they would have no trends that could be depended upon from one year to the next. If intervals longer than a month had been chosen, we would expect interpolation between points to be inaccurate. Therefore, the main product of this work is a set of monthly displacement fields. With these monthly displacements we will be able to construct trajectories starting at any location at any time of the year and can build up the trajectories for arbitrary intervals.

To determine the free drift of ice during a single month, we first looked into the possibility of using monthly mean winds to drive the model. As suggested in the Introduction, the model of our choice was that balance of air stress, water drag and Coriolis force developed during the AIDJEX experiment. This model is described in Appendix I, and includes the values of drag coefficients that were determined to be accurate in the Beaufort Sea in 1975. The time resolution of this model is one day. To build a monthly trajectory, the procedure is to compute daily average velocity values and accumulate the daily displacements to determine the monthly motion. The response of the model was examined closely in the work presented in Appendix I to determine whether or not monthly mean winds would be adequate to drive the model. Our attempt was to show that the response of the model was approximately linear in which case averaging of the driving force would be accurate. A successful result would reduce the computational cost by a factor of 30.

It was found that speed of the ice is approximately linearly related to the wind, but the direction of ice drift with respect to the orientation of the wind varies strongly with the wind speed. This change in orientation introduces a strong nonlinearity into the response. An example of the result of this nonlinearity is presented in Appendix II. It is seen that nonlinearity in the behavior

creates a very inaccurate response of the model when driven with month-long winds and using the drag coefficients developed in AIDJEX for use with the daily model. The problem is that averaging of the winds reduces the peaks and, therefore, drives the model at a very different orientation than occurs at the higher speeds. As a result, we concluded that the model should be used on a daily basis and monthly displacements determined by superposing daily drift as computed from the daily winds.

The remaining driving force which strongly influences ice motion is the geostrophic ocean currents. While the winds are considered the primary driving force of the ice for time scales of days, the currents can produce equally large motions for time periods of a month or longer. During a month, the winds will generally vary in direction causing the ice to "meander" or wander about. It was observed in 1975 that the net monthly motion ranged from about 20 to 60 percent of the total motion during the month. Meanwhile, during the same month, the current will be making a modest, but nearly constant, contribution towards the ice motion. As a result, we must expect current induced motion to be of the same magnitude as wind driven motion.

Unfortunately, our knowledge of the currents in the Beaufort/Chukchi Seas is limited. The general circulation pattern is known, but quantitative assessment of currents throughout the region is lacking. The best available estimate of currents comes from Newton's (1973) compilation of historical data providing a climatological mean dynamic topography for the Beaufort Sea. These data are not only incomplete in spatial coverage, but do not include the mass of more recent oceanographic observations. The results of the test of free drift presented in Appendix IV indicate that these currents are accurate within 1 cm/sec in the central Beaufort Sea, but we have inadequate checks elsewhere.

Because of the lack of complete and reliable information on the geostrophic ocean currents, we formulated the free drift model in such a way that allows a separate and independent formulation of geostrophic current induced drift. We show in Appendix I that the free drift of sea ice may be decomposed into a part driven by the winds and another part driven by the deep ocean currents. In this work, we have concentrated on determining the component of ice drift caused by winds. As shown in the Methods section, the geostrophic ocean currents are superposed directly on this component of the drift, that is, an exact vector addition of ocean current to the drift shown is appropriate to determine the free drift of the ice cover. It should be remembered that the shear in the mixed layer of the ocean has been accounted

for in our water stress model. We have also shown that mean currents and variations in the current may be superposed directly on the free statistics. Thus, the results of this work are independent of actual currents.

### 3. Meteorological Data Input

Daily sea level pressure (SLP) for the northern hemisphere in the form of digitized grid point values are available at the National Center for Atmospheric Research (Jenne, 1975). SLP data were provided by NCAR for the period 1946 through 1977 on magnetic tapes in packed binary form. Because of the lack of meteorological station input data in the Arctic regions prior to the early 1950's, we felt some doubt about the reliability of the earlier SLP data. Walsh (1978) observed that prior to the early 1950's analysts tended to bias the analyses towards high pressure in the central Arctic. Also, since the early 1950's, a large amount of drift station meteorological data has been available and appears to have been incorporated in the analyses (John Walsh, 1978, personal communication). Therefore, we concluded that the 25 year period beginning in 1953 was the most reliable part of the available data and was sufficient for this study. The only other editing of the data was checking for gross errors. The occasional day of missing data was filled in by linear interpolation. For ease in later computation, the data grid was converted from the NMC octagonal grid (with a spacing of about 400 km in the Beaufort and Chukchi Seas) to a rectangular grid with a spacing of 200 km. A 16 point Bessel central difference interpolation scheme was used to derive the new grid pressure values.

From this pressure grid, geostrophic winds were computed as

$$\vec{U}_g = \frac{-1}{\rho_a f} \vec{k} \times \nabla P \quad (1)$$

where  $\vec{U}_g$  is the geostrophic winds,

$f$  is the Coriolis parameter,

$\rho_a$  is the air density

(see Appendix II for monthly values used)

$\vec{k}$  is the unit vector upward and orthogonal to the plane of motion,

and  $\nabla P$  is the horizontal pressure gradient (average over 200 km square area).

Accuracy of the pressure data, and thus the winds, were checked by comparing the distribution of surface wind speed and direction with the observed winds given in the Climatic Atlas of the Outer Continental Shelf Waters and Coastal Regions of Alaska (1977). Wind direction was compared at Point Barrow and at Barter Island

for most of the year and at Oliktok and Wrangel Island for three months. Wind speed was compared for the same three months (May, July, December) at all four points. The distribution of derived surface wind speeds and directions at Point Barrow for May, July and December is shown in Figure 1. In direction, the derived winds compare quite well with the observed winds. The large easterly peak in observed winds is reflected in the derived winds with occasional shifts to the northeast occurring, especially at Point Barrow. The smaller peak of westerly winds, in particular at Barter Island, is often diminished in the derived wind distribution. At Wrangle Island the directions agree fairly well in May and December, but not as well in July.

In magnitude the derived winds tend to be smaller than observed winds. The average derived surface wind speed at the four points and for three months are from 60- to 90 percent the observed average. The differences are greatest at Barter Island, 30 to 40 percent too low, and least at Wrangel Island, 10 to 25 percent too low. At least part of this greater difference to the East is likely due to the supergradient flow caused by the topography of the Brooks Range, as suggested by Dickey (1961).

Eric Leavitt (1979, personal communications) has compared winds from NCAR SLP data with winds from AIDJEX pressure data and observed winds at the AIDJEX manned camp location for a 250 day period from July, 1975 through March, 1976. During the AIDJEX main experiment, an array of manned camps and buoys measuring location and sea level pressure were scattered throughout the Beaufort Sea. We believe the AIDJEX pressure measurements and resultant winds to be highly accurate (Albright, 1978) and that only the measurement from the manned camps might have been incorporated in the analyses provided by NCAR, due to the time lag in processing the buoy data. As expected, the winds computed from AIDJEX pressure data agree quite well with observed winds. The NCAR derived winds on the other hand, have the same directional distribution as the observed winds, but are smaller in magnitude in the aggregate.

It seems evident then that analysts have historically tended to underestimate the peak pressure gradients in the Arctic regions. Since the amount of underestimation seems to depend upon location and season, and probably wind speed and direction too, we did not feel it was provident to attempt to compensate for the error. While we must be underestimating mean motion and variation, by as much as 25 percent say, the errors are generally within the range of uncertainty of the statistics. We point out also, that when motions and variations due to ocean currents are added to the wind induced motion and variation, the errors in the winds become less important.

In addition to the accuracy en bloc of the derived winds, we checked the day to day difference for one month between geostrophic winds derived from the NCAR pressure data and winds computed from AIDJEX main experiment pressure data. Instead of comparing the winds directly, we looked at the errors in the resultant ice velocities when compared with observed ice velocities (see Appendix IV). During July 1975, the AIDJEX manned camp motions have been determined to be free drift (McPhee, 1977a). Furthermore, the camps were near the center of the Beaufort Gyre at that time so the effects of geostrophic ocean currents were probably small. Conditions were thus ideal for free drift modeling of the ice motion.

Means and standard deviations of daily velocity errors (observed velocity minus modeled velocity) were computed using geostrophic winds from AIDJEX SLP data and NCAR SLP data. For July 1975, the NCAR derived daily ice velocities had a mean approximately equal to, and a standard deviation about twice as large as the daily ice velocities computed using AIDJEX winds. Assuming July 1975 to be representative of the 25 years of data, we conclude that on temporal scales of one month, the winds derived from NCAR data are an adequate approximation to the actual winds.

#### 4. Method

Free drift ice velocities are computed by considering the momentum balance as shown in Appendix I where the forces acting on the ice are air stress, water stress and Coriolis force and sea surface tilt. It is assumed that forces due to ice stress divergence are negligible. This is a valid assumption for the summer and early fall season and for the rest of the year it represents the possible extreme of light ice conditions.

The air stress is related to surface pressure fields as a quadratic drag law with Ekman turning. Values of density  $\rho_a$ , drag coefficient,  $c_a$  and turning angle  $\alpha$  used in this study were derived from AIDJEX data (Albright, 1978, and personal communications). Monthly values of  $\rho_a$  are given in Table I-1, Appendix I. Seasonal values of  $c_a$  and  $\alpha$  are given below in Table 1. Spatial variations of these parameters are not available nor are temporal variations beyond what are given.

Season	$c_a$ ( $\times 10^3$ )	$\alpha$ (degrees)
Summer (July, August, September)	0.9	23
Fall (October, November)	0.83	26
Winter (December, January, February, March)	0.75	30
Spring (April, May, June)	0.83	26

Table 1. Seasonal values of air drag coefficient ( $c_a$ ) and turning angle ( $\alpha$ ).

The water stress is related to ice velocity relative to ocean currents at the bottom of the mixed layer. The oceanic boundary layer is analogous to the atmospheric boundary layer and a quadratic drag law with Ekman turning is also used.

McPhee (1977a) has given values of drag coefficient  $c_w = 0.0055$  and turning angle  $\beta = 23^\circ$ .

As we point out in Appendix IV, data on the geostrophic ocean currents in the Beaufort/Chukchi Sea area are somewhat sparse and certainly not definitive.



We felt the results of this work would be more useful if, in the future when more comprehensive and accurate current data becomes available, the currents could be included. Fortunately, this is easily done. In the form of momentum balance used, we solve for  $\tilde{G}$ , the portion of the ice velocity attributable to the winds. The total free drift ice velocity is then  $\tilde{G} + \tilde{v}_g$  where  $\tilde{v}_g$  is the geostrophic current. Integrating these velocities throughout a day gives daily displacements. Let  $\tilde{x}$  be the daily ice displacement relative to ocean currents and  $\tilde{c}$  be daily displacements of the currents. Total daily displacement is  $\tilde{x} + \tilde{c}$ . During a month of  $M$  days, the total monthly displacement,  $\tilde{W}$ , is

$$\tilde{W} = \sum_{i=1}^M (\tilde{x}_i + \tilde{c}_i) \quad (2)$$

which can be written as

$$\tilde{W} = \tilde{X} + \tilde{C} \quad (3)$$

where  $\tilde{X} = \sum \tilde{x}$  is the monthly relative ice motion and  $\tilde{C} = \sum \tilde{c}$  is the monthly ocean current motion. For a sample of  $N = 25$  years the mean monthly displacement is

$$\bar{\tilde{W}} = \frac{1}{N} \sum \tilde{W} \quad (4)$$

and the standard deviation of monthly displacements is

$$s_w = \left( \frac{1}{N-1} \sum \| \tilde{W} - \bar{\tilde{W}} \|^2 \right)^{1/2} \quad (5)$$

Using the relationship shown in equation (3) and some results of elementary statistics, we can write equations (4) and (5) as

$$\bar{\tilde{W}} = \bar{\tilde{X}} + \bar{\tilde{C}} \quad (6)$$

and

$$S_w = S_x^2 + S_c^2 + 2 \text{cov}(\tilde{X}, \tilde{C})^{1/2} \quad (7)$$

where the covariance is bounded as

$$-S_x S_c \leq \text{cov}(\tilde{X}, \tilde{C}) \leq S_x S_c \quad (8)$$

When ocean currents are constant or nearly constant spatially and temporally throughout the area where ice motion is occurring, then

$$\tilde{C} \approx \bar{C} \quad (9)$$

and

$$S_c \approx 0 \quad (10)$$

so that

$$\bar{W} = \bar{X} + \bar{C} \quad (11)$$

and

$$S_w = S_x \quad (12)$$

If the currents do vary, we see from equations (7) and (8) that the standard deviation of monthly ice motions is bounded by

$$S_w \leq S_x + S_c \quad (13)$$

Equations (6) and (13) show how geostrophic ocean currents affect the expected value and expected variation of monthly ice motion. In Appendix I, we have shown that geostrophic currents may be neglected and relative ice velocity computed. Here we have shown that means and standard deviations of relative ice motion may be computed and then statistics of the currents superposed.

The ice mass per unit area,  $m$ , is  $\rho_i \bar{h}$  where the average ice thickness ( $\bar{h}$ ) is considered constant throughout the region of interest for a month. Monthly values of  $\bar{h}$  are given in Table I-1, Appendix I.

Average daily free drift velocities were computed from the geostrophic wind values at 1200 hours each day. When averaged over a month, and considering the time scales of major atmospheric events, these daily velocities are sufficient for our purposes. The daily velocities were converted to daily displacements and accumulated to form monthly displacements. Air stress, the only position dependent driving force, is computed from the geostrophic winds linearly interpolated at the daily position. Each month's displacement begins at the original grid position. Displacements were computed at nineteen points throughout the Beaufort and Chukchi Seas.

At each of the nineteen grid points and for all 12 months, the mean of 25 years of displacements were formed as

$$\bar{\tilde{x}} = \frac{1}{N} \sum_{i=1}^N \tilde{x}_i \quad (14)$$

where  $\tilde{x}_i = (x_i, y_i)$  is a monthly displacement vector and  $N = 25$ . Rectangular coordinates are used to avoid difficulties inherent in working with azimuths. The variance-covariance matrix at each point for each month was also computed.

$$\tilde{S} = \begin{pmatrix} S_x^2 & S_{xy} \\ S_{xy} & S_y^2 \end{pmatrix} \quad (15)$$

$$S_x^2 = \frac{1}{N-1} \sum (x-\bar{x})^2$$

$$S_y^2 = \frac{1}{N-1} \sum (y-\bar{y})^2$$

$$S_{xy} = \frac{1}{N-1} \sum (x-\bar{x})(y-\bar{y})$$

To show graphically the distribution of monthly displacements, equi-probability ellipses were constructed. A bi-variate normal distribution has the probability density function

$$f(x,y) = \frac{1}{2\pi\sigma_x\sigma_y\sqrt{1-r^2}} e^{-Q/2} \quad (16)$$

where

$$Q = \frac{1}{(1-r^2)} \left[ \frac{(x-\bar{x})^2}{\sigma_x^2} - \frac{2r(x-\bar{x})(y-\bar{y})}{\sigma_x\sigma_y} + \frac{(y-\bar{y})^2}{\sigma_y^2} \right] \quad (17)$$

with mean  $(\bar{x}, \bar{y})$  and correlation  $r$ .

The locus of  $Q = c^2$  ( $c$  is constant) defines an equi-probability ellipse. The probability  $p$  that a random point on the  $x$ - $y$  plane will fall within the ellipse is

$$p = 1 - e^{-c^2/2} \quad (18)$$

We chose to use values of  $p$  equal to 0.5, 0.9 and 0.99. Corresponding values of  $c$  are 1.177, 2.146 and 3.035, respectively.

Actually, a transformation of variables was made to simplify locating the equi-probability ellipses. Morrison (1976), among others, has described the procedure.

First, a translation is made and a new coordinate system defined as

$$\tilde{x} = x_0 - \bar{x}_0 \quad (19)$$

where  $x_0$  refers to the original coordinates and  $\tilde{x}$  now refers to the new. The mean in the new coordinate system is now  $(\bar{\tilde{x}}, \bar{\tilde{y}}) = (0, 0)$ .

The variance-covariance matrix  $\tilde{S}$  is not affected by a linear transformation. The determinant equation

$$|\tilde{S} - \lambda\tilde{I}| = 0 \quad (20)$$

is solved for the characteristic roots (or eigenvalues)  $\lambda_1$  and  $\lambda_2$ , and the equation

$$(\underline{S} - \lambda \underline{I})\underline{e} = 0 \quad (21)$$

is solved for the characteristic vectors (or eigenvectors)  $\underline{e}_1^T = (\cos\alpha, \sin\alpha)$  and  $\underline{e}_2^T = (\cos(\alpha+\pi/2), \sin(\alpha+\pi/2))$  where  $\alpha$  is the angle the first principal axis makes with the x-axis. A rotation of coordinates gives

$$\underline{u} = \underline{x}^T \underline{e}_1 \quad (22)$$

$$\underline{v} = \underline{x}^T \underline{e}_2$$

where the new vector components  $u$  and  $v$  are independent and un-correlated with variances

$$\sigma_u^2 = \lambda_1 \quad (23)$$

$$\sigma_v^2 = \lambda_2 .$$

In this last coordinate system, equation (17) becomes

$$Q = \frac{u^2}{\lambda_1} + \frac{v^2}{\lambda_2} , \quad (24)$$

and when the substitution  $Q = c^2$  is made we have

$$\frac{u^2}{c^2\lambda_1} + \frac{v^2}{c^2\lambda_2} = 1 \quad (25)$$

which is the equation of an ellipse with major and minor axis of length  $2c\sqrt{\lambda_1}$  and  $2c\sqrt{\lambda_2}$ , respectively.

The use of equi-probability ellipses to indicate variability about the mean assumes bi-variate normality. The Central Limit Theorem leads us to expect a near normal distribution of ice motions, but a couple of rough tests were made to confirm this. The quadrant test shows a nearly equal distribution of data among the quadrants with a possible skewness toward the west. A count of the data points

within the 50-, 90- and 99 percent equi-probability ellipses indicates that the data might be more dense near the mean than normality predicts. Since no large and apparent deviations from normality are observed, our assumption of normality is not unreasonable.

## 5. Results

We have decided to present the results of this study in graphical form rather than numerical. One reason for this is that due to all possible sources of error and the rather small sample size ( $n = 25$  years), accuracy beyond that of the plots is unnecessary and unwarranted. A second reason is ease of use, since these results are intended as an aid to developing oil spill scenarios.

In the first set of plots, Figures 2 through 13, we present the monthly mean free drift ice motion fields based upon 25 years of atmospheric data. The 50 percent equi-probability ellipses are shown about the mean vectors (the ensemble average). The most likely free drift ice motion at a particular location is that shown, and about 50 percent of observed motions will lie within the associated ellipse. The major axis of the ellipse lies along the first principal axis and the greatest variability occurs in this direction. We consider the probable trajectory to be any location within the 50 percent ellipse.

The second set of plots, Figures 14 through 25, show the temporal and spatial variability. At three widely separated points, the 50-, 90- and 99-percent equi-probability ellipses are shown. Instead of showing the mean displacements here, we show the 25 displacements making up the sample at each point. By actually showing the elements of the data set, the reader can gain a feeling for the distribution and for the usefulness of our presentation.

Extreme value statistics as such were not computed for the monthly ice displacements due to the lack of an adequate sample. At one point for one month we have 25 ice displacements, only one of which is the extreme. Displacements at nearby points are not independent because of the spatial scale of weather systems which drive the ice. One could perhaps compute extreme value statistics for monthly motions throughout the year. We did not feel this to be necessary. Assuming the motions for the 25 year sample to be representative of the motions to be expected during the life of the Prudhoe Bay oil fields, our 99 percentile ellipses provides lower bounds for the 100-year extreme ice trajectories. It should be remembered that free drift already represents an extreme of ice motion. Generally, large ice motions will produce an increased concentration of ice which tends to resist further motion. Exceptions may occur in the Chukchi Sea when breakout through the Bering Strait occurs, but that problem is not being dealt with in this report.

The 95 percent confidence region for the mean is an elliptic region about 45 percent the size of the 50 percent equi-probability ellipse. The 95 percent confidence limits for the equi-probability ellipses are the elliptical regions  $0.64 D \leq d \leq 2.24 D$  where  $D$  is the distance from the mean to the equi-probability ellipse.

A sample size of 25 is too small to ensure reliable statistics, but we feel some additional information is present in the data and in the results. This is the smooth variation over space and time of the results. The results are also consistent with what is known about the general ice motion in the Beaufort Sea. We, therefore, feel that the region-to-region and month-to-month variations are real and worthy of note.

Looking at the monthly mean motion fields presented in Figures 2 through 13, we see an obvious westerly trend to the motions throughout most of the year. During the summer months the motion exhibits a northerly component of motion with July being the extreme. In fact, the northern most grid points have an average motion almost due east in July.

In general, the winter mean motions are larger than those in summer. This is due in part to the winds being more variable in direction during the summer, but an examination of the individual monthly trajectories shown in Figures 14 through 25 shows that more large motions occur during the winter.

A pronounced east to west variation in the magnitude of the means is also evident. The larger means occur in the Chukchi Sea. During December and January and again during July, the means in the eastern Beaufort Sea are nearly zero. This appears to be a result of directional variability in the winds and motion during these three months. There also appears to be a slight reduction in magnitude of the means as one goes from south to north.

In general, the greatest variability in motion occurs in the east-west direction. Northwest of Point Barrow during the summer is an exception with nearly circular distributions occurring. Our assumption of bi-variate normality appears to be justified in most instances. Some doubtful looking instances are to be expected with sample sizes of 25, but no extreme deviations from normal are evident. A slight skewness to the west appears likely from inspection of Figures 14 through 25.



Sater, et al. (1974) have also computed monthly free drift fields for the Beaufort Sea area. They used atmospheric data for the years 1948-67 along with Zubov's relationship between surface winds and ice motion. In Appendix II we examine the difference between Zubov drift and free drift as we have computed it. Even though these approaches can give very different results, it can be seen that Sater, et al. give displacements in general agreement with ours. Our results give more confidence because AIDJEX drift data have allowed a thorough test of accuracy.

In order to estimate total monthly motion, some measure of geostrophic ocean currents is needed. As a best estimate of the currents, we have used the geostrophic flow taken from a dynamic topography compiled by Newton (1973). These currents, expressed as km/month displacements, are shown in Figure 26. The blank area over most of the region of interest does not indicate zero currents, but lack of information. The accuracy of the currents presented may be questioned too. In Appendix IV where we test the free drift model, we find that the addition of these currents actually increase the error between free drift velocities and observed velocities in the central Beaufort Sea. In areas where long-term currents are unknown, the effect is uncertain. Nevertheless, the currents shown in Figure 25 represent the best available estimates of long-term average currents in the Beaufort Sea.

In Figure 27 we present the results of a twelve-month accumulation of mean free drift beginning October 1. The currents were included in computing the monthly trajectories. The ellipse shown is approximately the 50 percent equi-probability ellipse. We know that for independent random variables the standard deviation of the sum of variables is

$$S_{\Sigma} = \sqrt{\sum_i S_i^2} \quad (26)$$

where the  $S_i$  are standard deviations of monthly displacements. Note that the dimensions of an equi-probability ellipse are a multiple of the standard deviations along the principal axis.

As a first approximation we assume the effects of ocean currents to be constant during a month, in which case currents do not affect the standard deviation of the sum. Since the major axis of the ellipses all lie roughly in the east-west direction, we can apply the above relationship to the major and minor dimensions of the equi-probability ellipses. Figure 28 is the equivalent trajectory beginning June 1.

## References

- Aagaard, K., Atlas, R., Barnes, P., Broad, C., Divoky, G., Martin, S., Naidu, S., Nummedal, D., Pritchard, R., Shaw, D. (1978) "Probable Impacts and Consequences of Oil Development," John J. Burns, editor. In Environmental Assessment of the Alaskan Continental Shelf, Interim Synthesis: Beaufort/Chukchi. National Oceanic and Atmospheric Administration, Environmental Research Laboratories, Boulder, Colorado.
- Abramowitz, M. and Stegun, I. A. (1965) Handbook of Mathematical Functions, Dover New York, p. 892.
- Albright, M. (1978) "Construction of Atmospheric Surface Pressure Maps from the AIDJEX Data Set," AIDJEX Bulletin No. 39, University of Washington, Seattle, Washington, pp. 11-120.
- Cambell, W. J. and Martin, S. (1973) "Oil and Ice in the Arctic Ocean: Possible Large-Scale Interactions," Science, 181, 56-58.
- Climatic Atlas of the Outer Continental Shelf Waters and Coastal Regions of Alaska, Compiled by: William A. Brower, Jr., Henry F. Diaz, Anton S. Prechtel, Harold W. Searby, and James L. Wise. Arctic Environmental Information and Data Center University of Alaska, Anchorage, Alaska; National Climatic Center - Environmental Data Service, Asheville, North Carolina; Vol. III, Chukchi-Beaufort Sea (1977).
- Coon, M. D., Maykut, G. A., Pritchard, R. S., Rothrock, D. A., and Thorndike, A. S. (1974) "Modeling the Pack Ice as an Elastic-Plastic Material," AIDJEX Bulletin No. 24, University of Washington, Seattle, Washington, pp. 1-105.
- Dickey, Woodrow W. (1961) "A Study of a Topographic Effect on Wind in the Arctic," J. of Meteorology, 18, pp. 790-803.
- Dunbar, M. and Wittman, W. I. (1963) "Some Features of Ice Movement in the Arctic Basin," Proceedings Arctic Basin Symposium, Arctic Institute of North America, Washington, D.C., pp. 90-104.
- Jenne, R. L. (1975) "Data Sets for Meteorological Research," NCAR Technical Note TN/1A-III.
- Leavitt, E., Albright, M., and Baumann, R. (1978a) "Variation in Planetary Boundary Layer Parameters Observed during AIDJEX," AIDJEX Bulletin No. 39, University of Washington, Seattle, Washington, pp. 149-163.
- Leavitt, E., Albright, M., and Carsey (1978b) "Report on the AIDJEX Meteorological Experiment," AIDJEX Bulletin No. 39, University of Washington, Seattle, Washington, pp. 121-147.
- Lewis, E. L. (1976) "Oil in Sea Ice," Pacific Marine Science Report 76-12.
- Martin, S. (1977) "The Seasonal Variation of Oil Entrainment in First Year Arctic Sea Ice: A Comparison of NORCOR/OCS Observations," Department of Oceanography Special Report Number 71, a Report from BLM/NOAA Contract No. 03-5-022-67, Task Order No. 6, Research Unit No. 87.

## References (Cont.)

- McPhee, M. (1977a) "An Analysis of Pack Ice Drift in Summer." A symposium on Sea Ice Processes and Models, Preprints, Vol. I, University of Washington, Seattle, Washington, pp. 240-250.
- McPhee, M. G. (1977b) "A Simulation of Inertial Oscillations Observed in the Drift of Manned Ice Stations," AIDJEX Bulletin No. 39, University of Washington, Seattle, Washington, pp. 65-85.
- McPhee, M. G. (1978a) "The Effect of the Oceanic Boundary Layer on the Mean Drift of Pack Ice: Application of a Simple Model," AIDJEX Bulletin No. 39, University of Washington, Seattle, Washington, pp. 1-32.
- McPhee, M. G. (1978b) AIDJEX Oceanographic Data Report, AIDJEX Bulletin No. 39, University of Washington, Seattle, Washington, pp. 33-78.
- Morrison, Donald F. (1976) Multivariate Statistical Methods, 2nd ed., McGraw-Hill Book Company, New York.
- Newton, J. L. (1973) "The Canada Basin: Mean Circulation and Intermediate Scale Flow Features," Ph.D. Thesis, University of Washington, Seattle, Washington.
- NORCOR Engineering and Research Limited (1975) "The Interaction of Crude Oil with Arctic Sea Ice," Beaufort Sea Technical Report No. 27.
- Pritchard, R. S. (1975) "An Elastic-Plastic Constitutive Law for Sea Ice," Trans., ASME 97; J. Appl. Mech. 42 (Ser. E, No. 2).
- Pritchard, R. S. (1976) "An Estimate of the Strength of Arctic Pack Ice," AIDJEX Bulletin No. 34, University of Washington, Seattle, Washington, pp. 94-113.
- Pritchard, R. S. (1977) "The Effect of Strength on Simulation of Sea Ice Dynamics," Proceedings of the Fourth International Conference on Port and Ocean Engineering Under Arctic Conditions.
- Pritchard, R. S., Coon, M. D., and McPhee, M. G. (1977) "Simulation of Sea Ice Dynamics During AIDJEX," Journal of Pressure Vessel Technology, 99, No. 3, pp. 491-497.
- Pritchard, R. S. and Thomas, D. R. (1978) "Response of Sea Ice to One-Dimensional Driving Forces and Boundary Perturbations," AIDJEX Bulletin No. 38, University of Washington, Seattle, Washington, pp. 53-94.
- Rosenegger, L. W. (1975) "The Movement of Oil Under Sea Ice," Beaufort Sea Technical Report No. 28.
- Ruby, C. H., Ward, L. G., Fischer, I. A. and Brown, P. J. (1977) "Buzzards Bay Oil Spill - An arctic Analogue," Fourth International Conference on Port and Ocean Engineering Under Arctic Conditions.
- Sater, J. E., Walsh, J. E. and Wittmann, W. I. (1974) "Impingement of Sea Ice on the North Coast of Alaska," Proceedings of a Symposium on Beaufort Sea Coast and Shelf Research, John C. Reed and John E. Sater, editors, Arctic Institute of North America, Arlington, Virginia.

#### References (Cont.)

- Thorndike, A. S., Rothrock, D. A., Maykut, G. A. and Colony, R. (1975) "The Thickness Distribution of Sea Ice," Journal of Geophysical Research, Vol. 80, No. 33, pp. 4501-4513.
- Topham, D. R. (1975) "Hydrodynamics of an Oil Well Blowout," Beaufort Sea Technical Report No. 33.
- Wadhams, P. (1975) "Sea Ice Morphology in the Beaufort Sea," Beaufort Sea Technical Report No. 36.
- Wadjams, P. and Horne R. J. (1978) "An Analysis of Ice Profiles Obtained by Submarine Sonar in the AIDJEX Area of the Beaufort Sea," Scott Polar Research Institute, Technical Report 78-1.
- Walsh, John E. (1978) "Temporal and Spatial Scales of the Arctic Circulation," Mon. Weather Review, Vol. 106, No. 11, pp. 1532-1544.
- Zubov, N. N. (1943) Arctic Sea Ice. Translated by Naval Oceanographic Office and American Meteorological Society under contract to Air Force/Cambridge Research Center, 1963. Published by Naval Electronics Laboratory (San Diego).

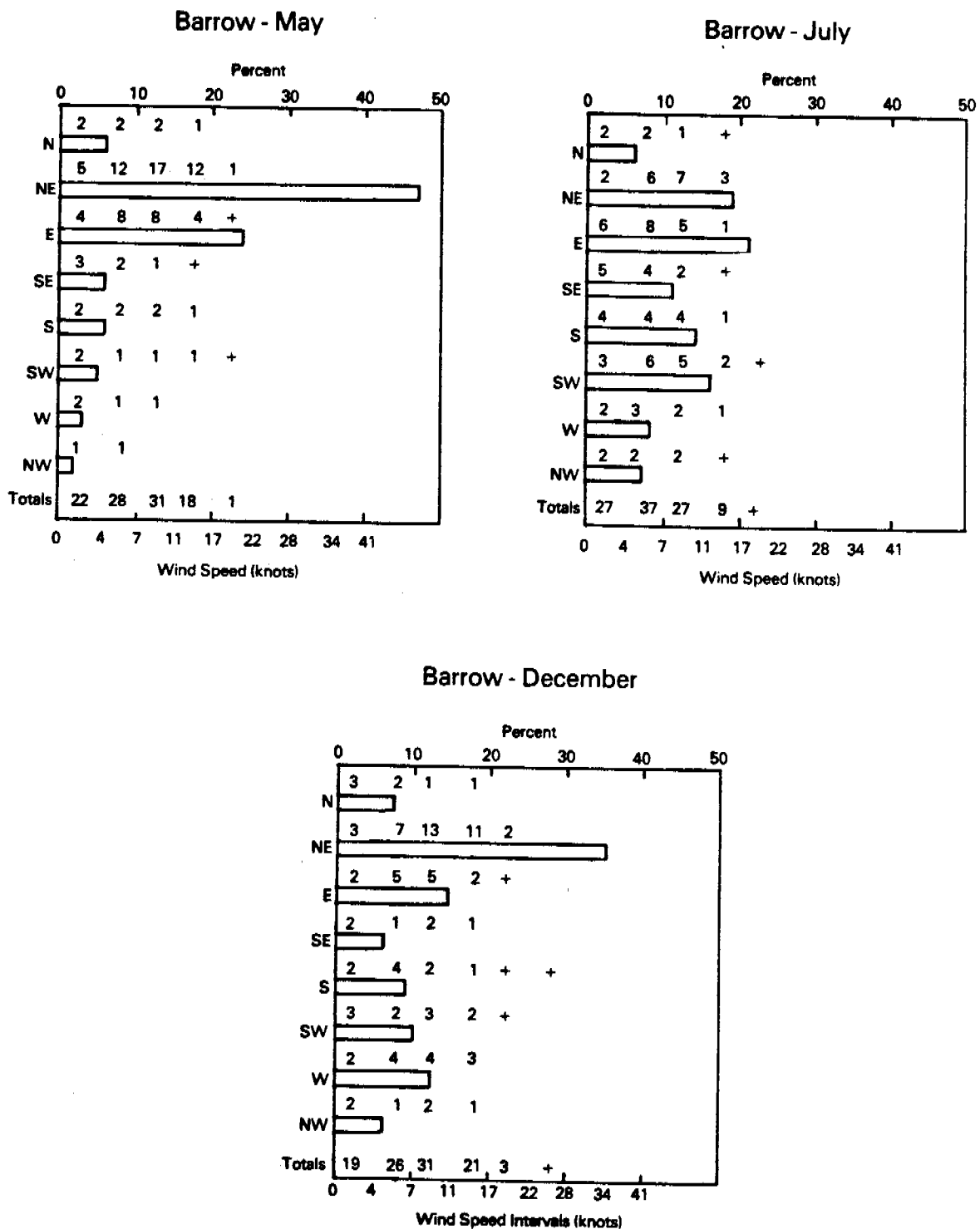


**Figure 1. Distribution of Derived Surface Wind Speed and Direction at Point Barrow for May, July and December.**

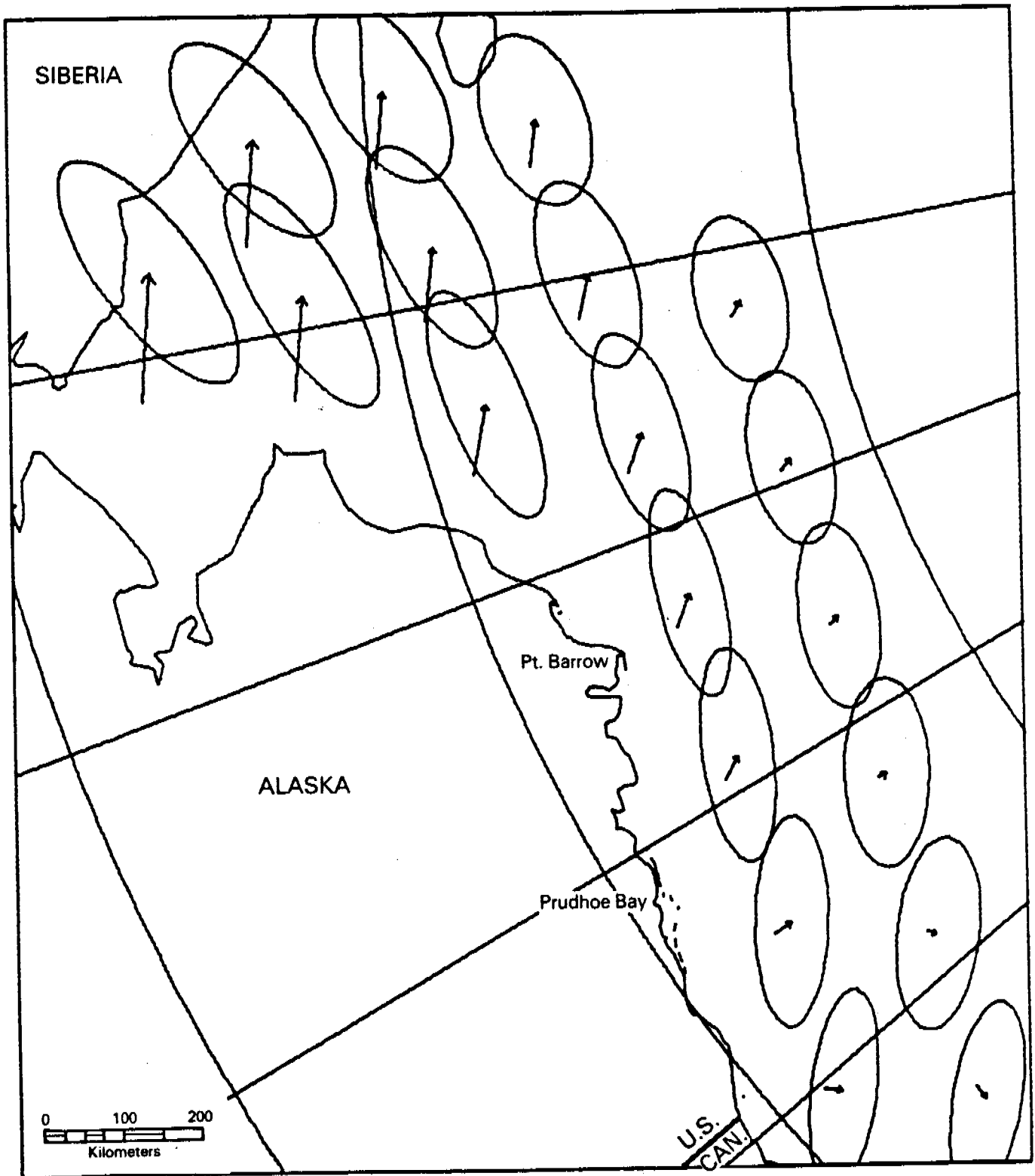


**Figure 2. Mean Free Drift Ice Displacement and Mean Error Ellipses for January.**

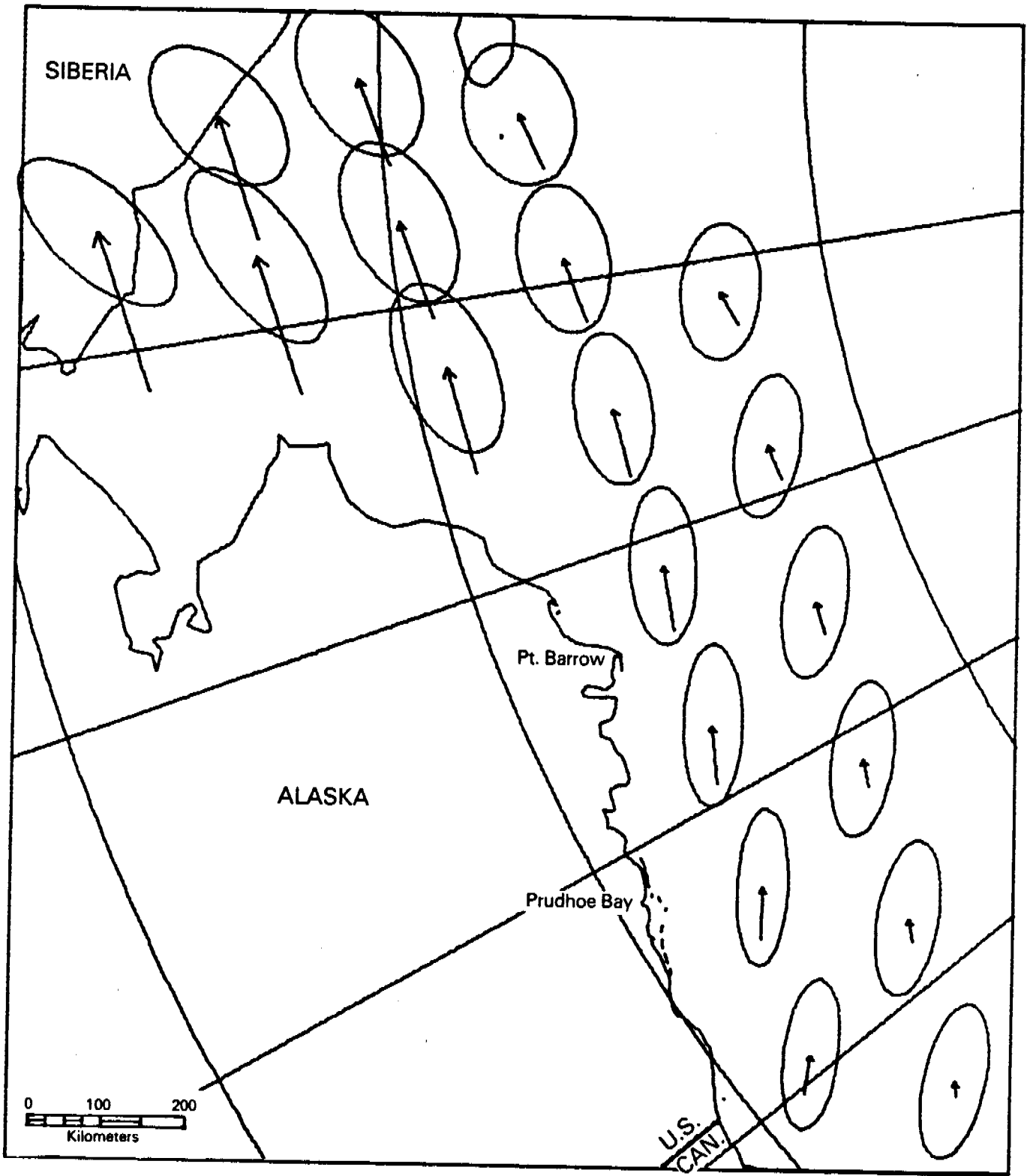


**Figure 3. Mean Free Drift Ice Displacement and Mean Error Ellipses for February.**

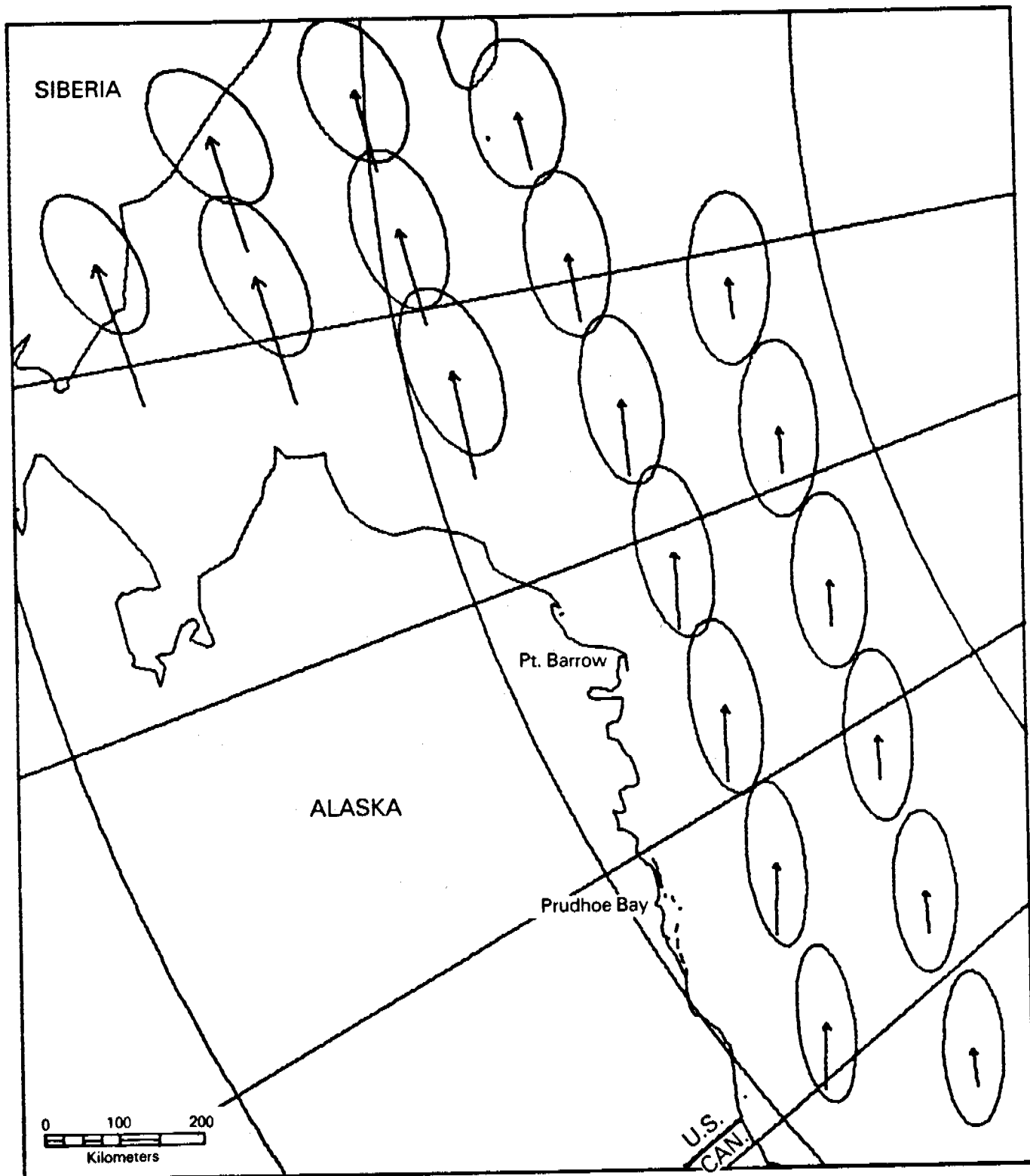


**Figure 4. Mean Free Drift Ice Displacement and Mean Error Ellipses for March.**



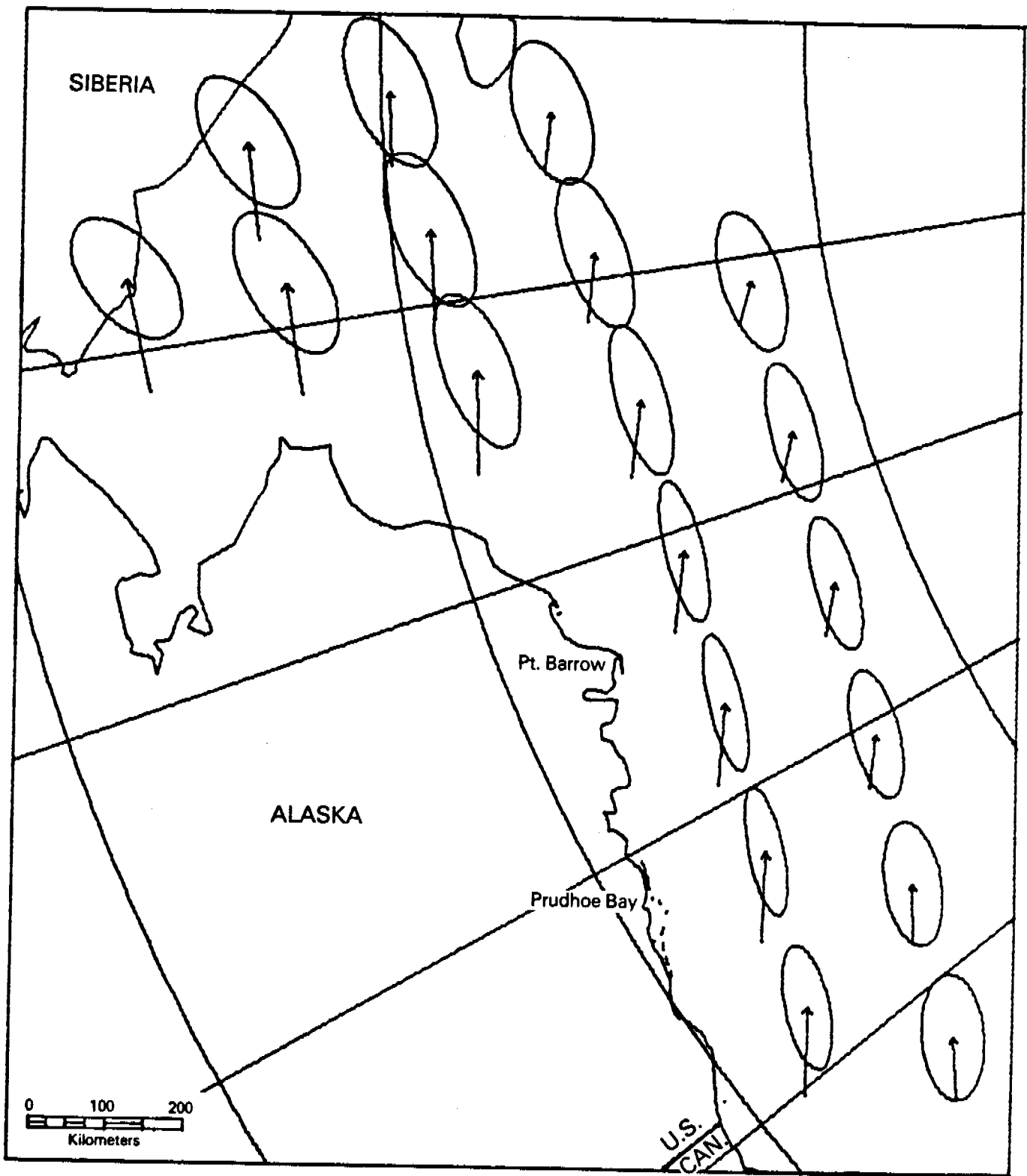


Figure 5. Mean Free Drift Ice Displacement and Mean Error Ellipses for April.

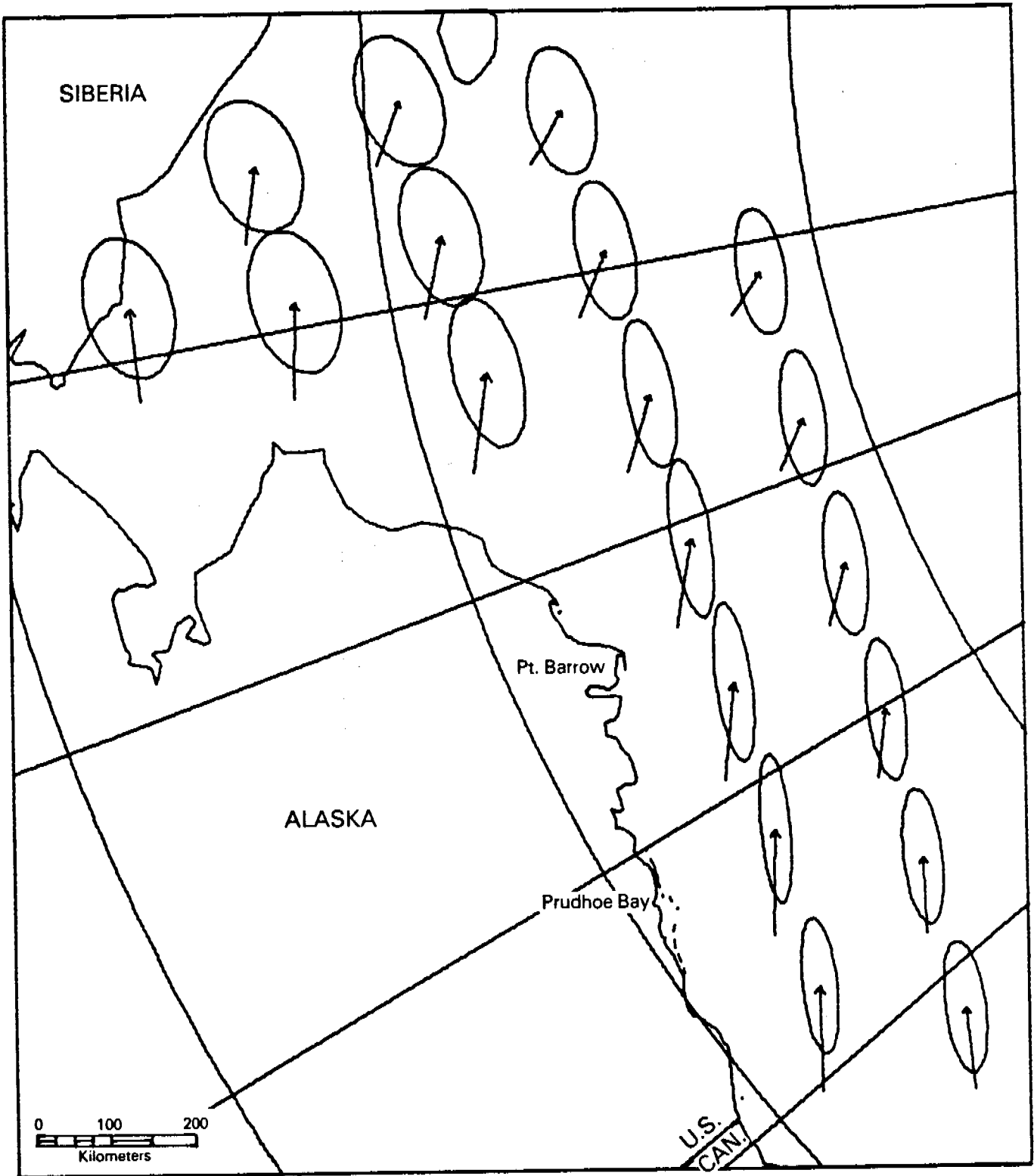
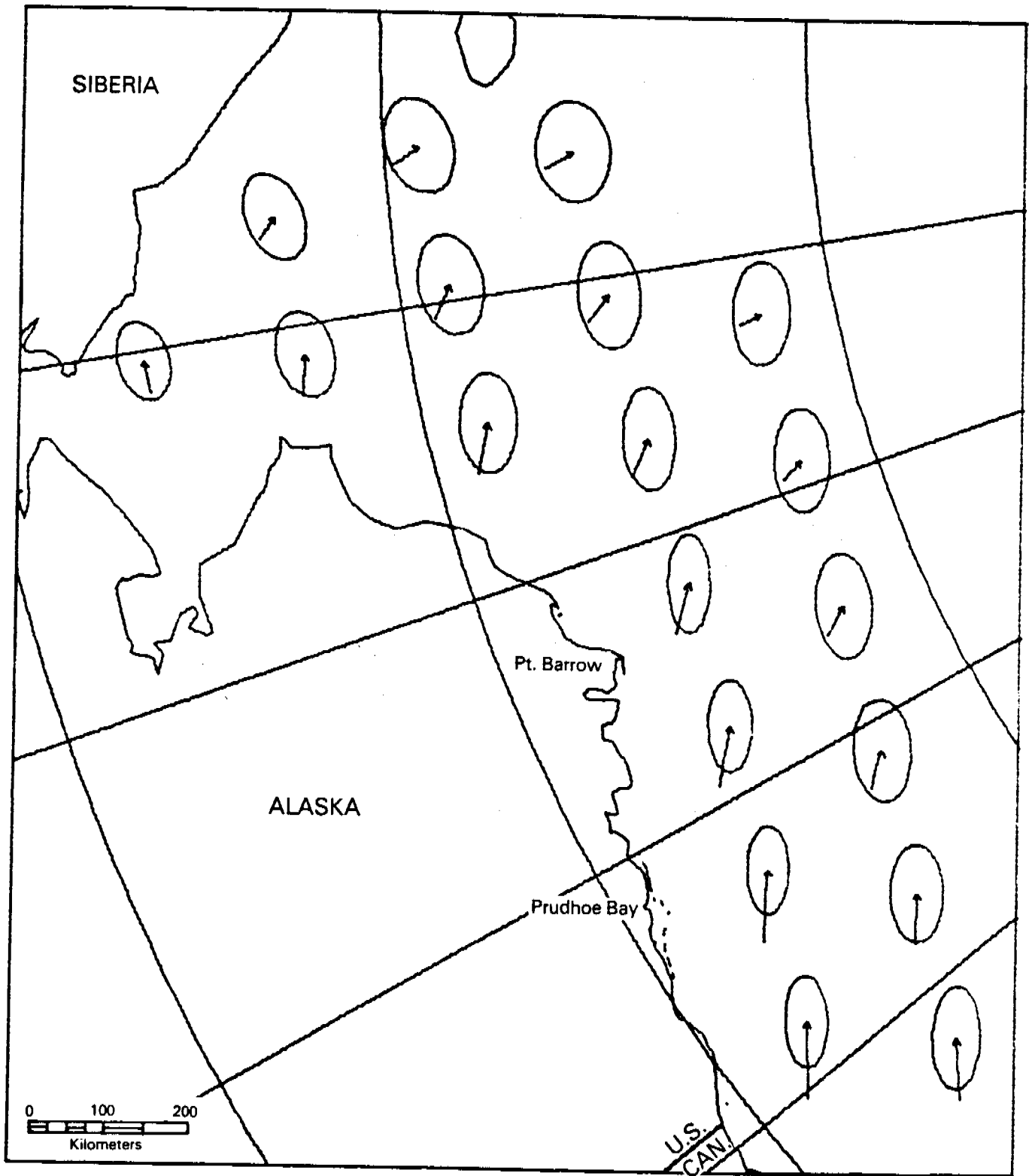


Figure 6. Mean Free Drift Ice Displacement and Mean Error Ellipses for May.



**Figure 7. Mean Free Drift Ice Displacement and Mean Error Ellipses for June.**

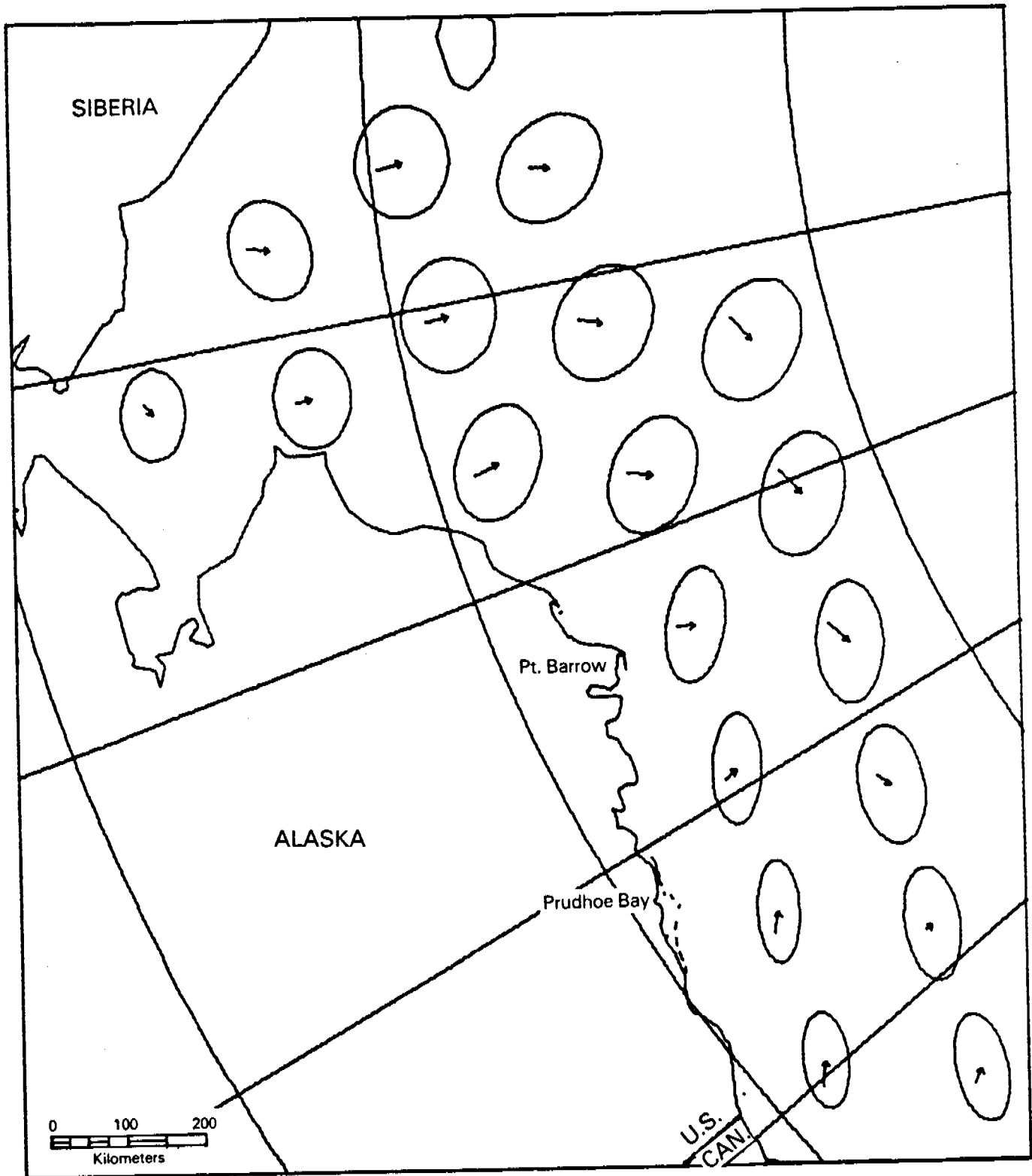


Figure 8. Mean Free Drift Ice Displacement and Mean Error Ellipses for July.

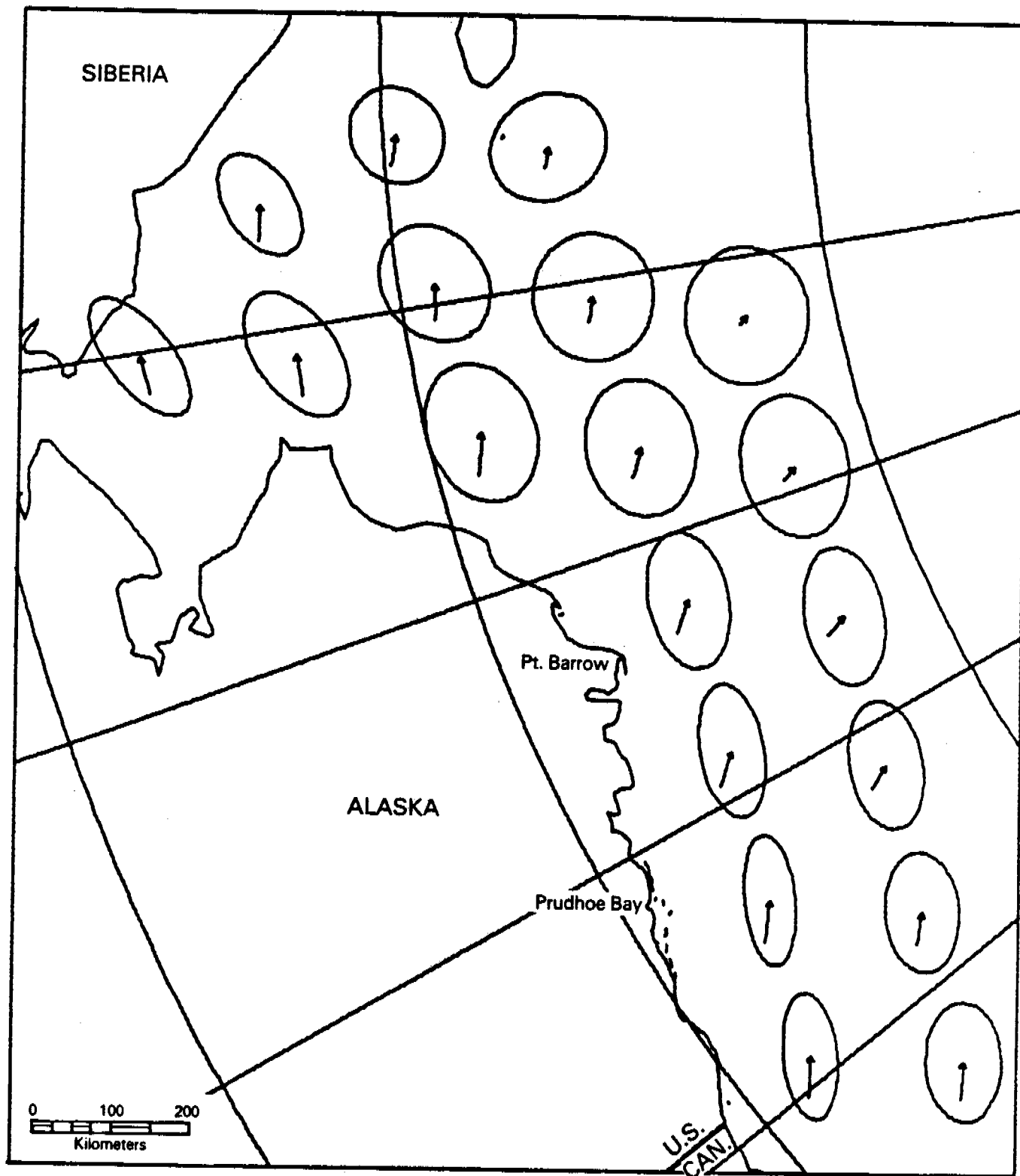


Figure 9. Mean Free Drift Ice Displacement and mean Error Ellipses for August.

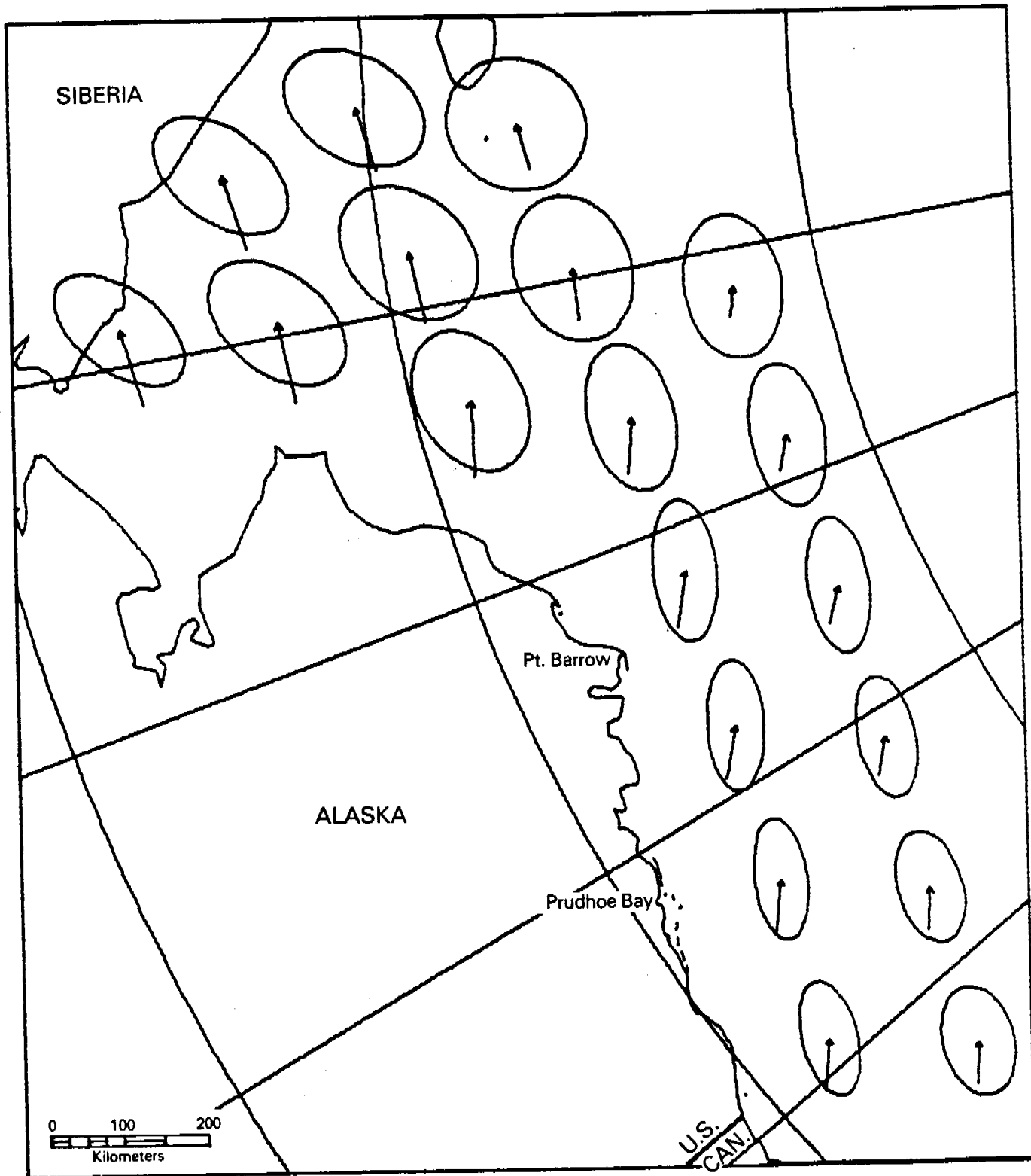


Figure 10. Mean Free Drift Ice Displacement and Mean Error Ellipses for September.

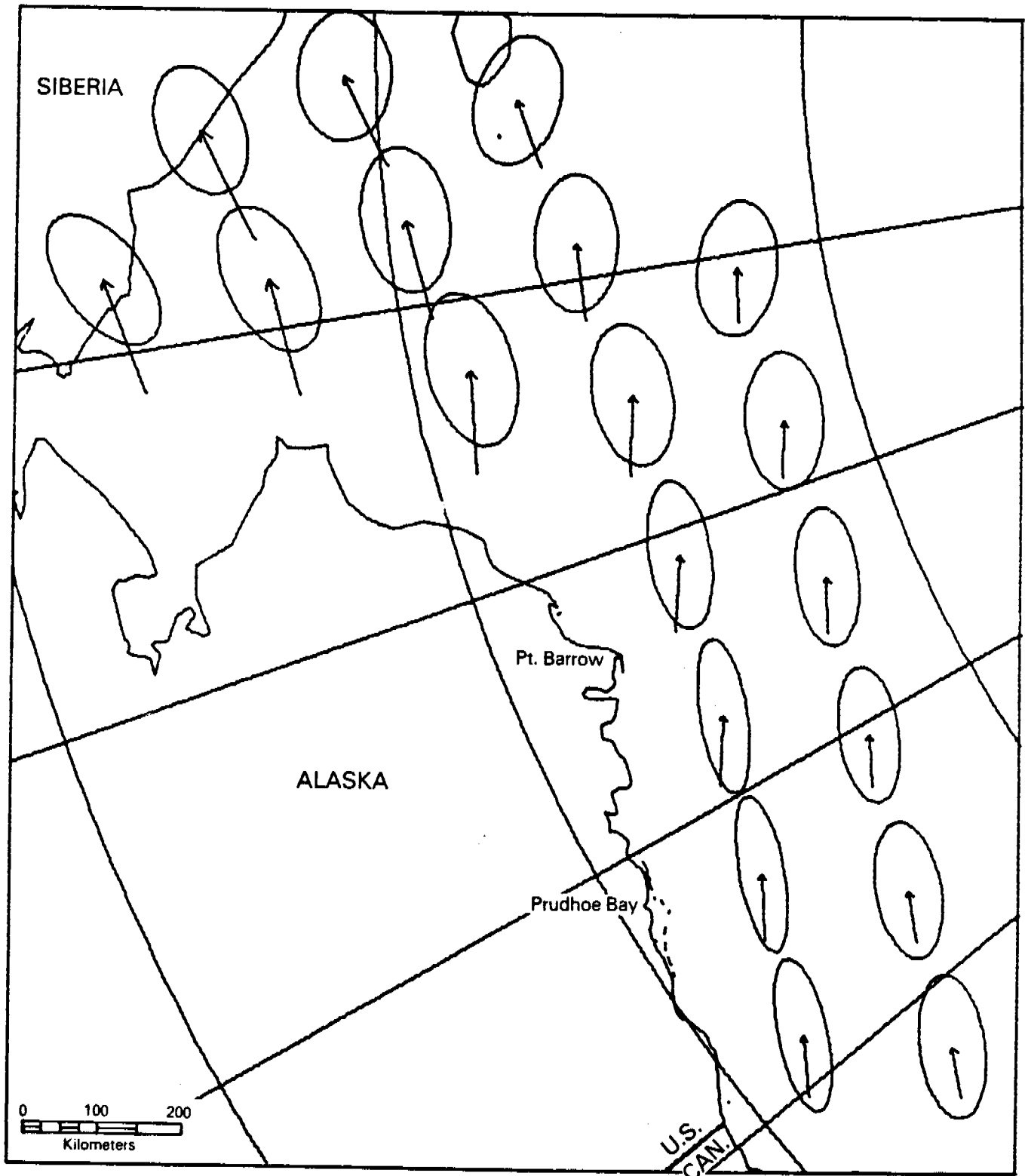


Figure 11. Mean Free Drift Ice Displacement and Mean Error Ellipses for October.

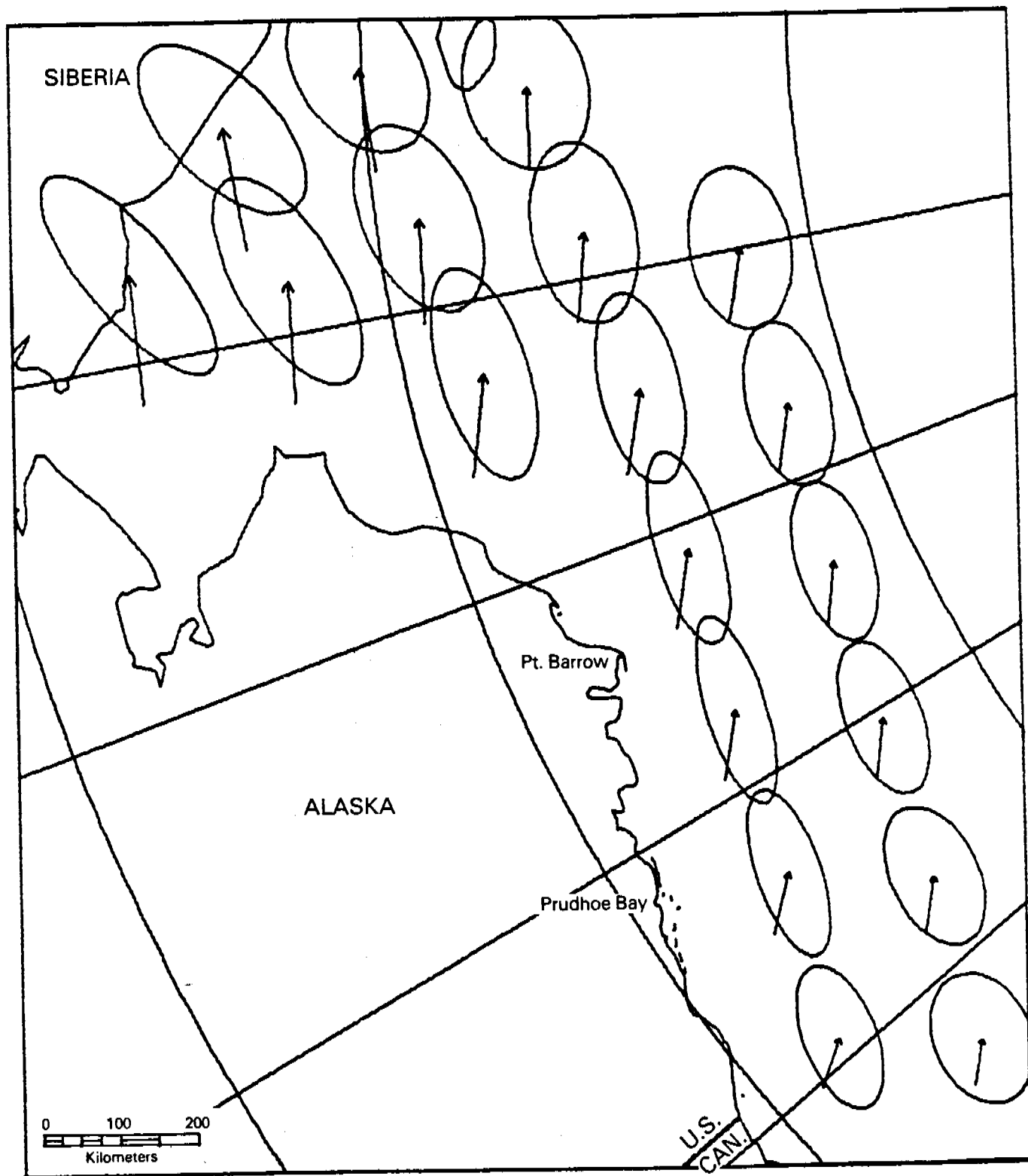


Figure 12. Mean Free Drift Ice Displacement and Mean Error Ellipses for November.



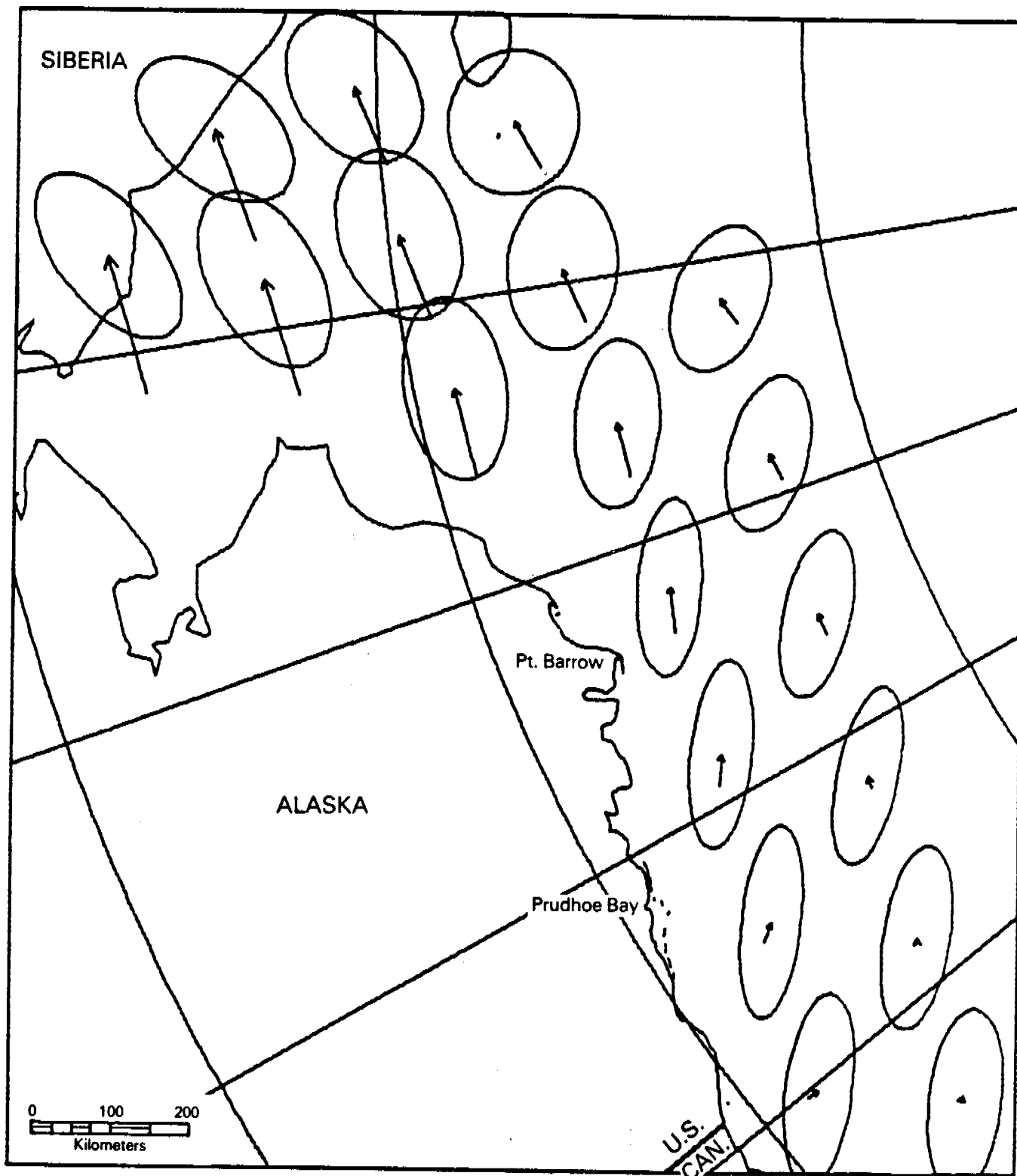
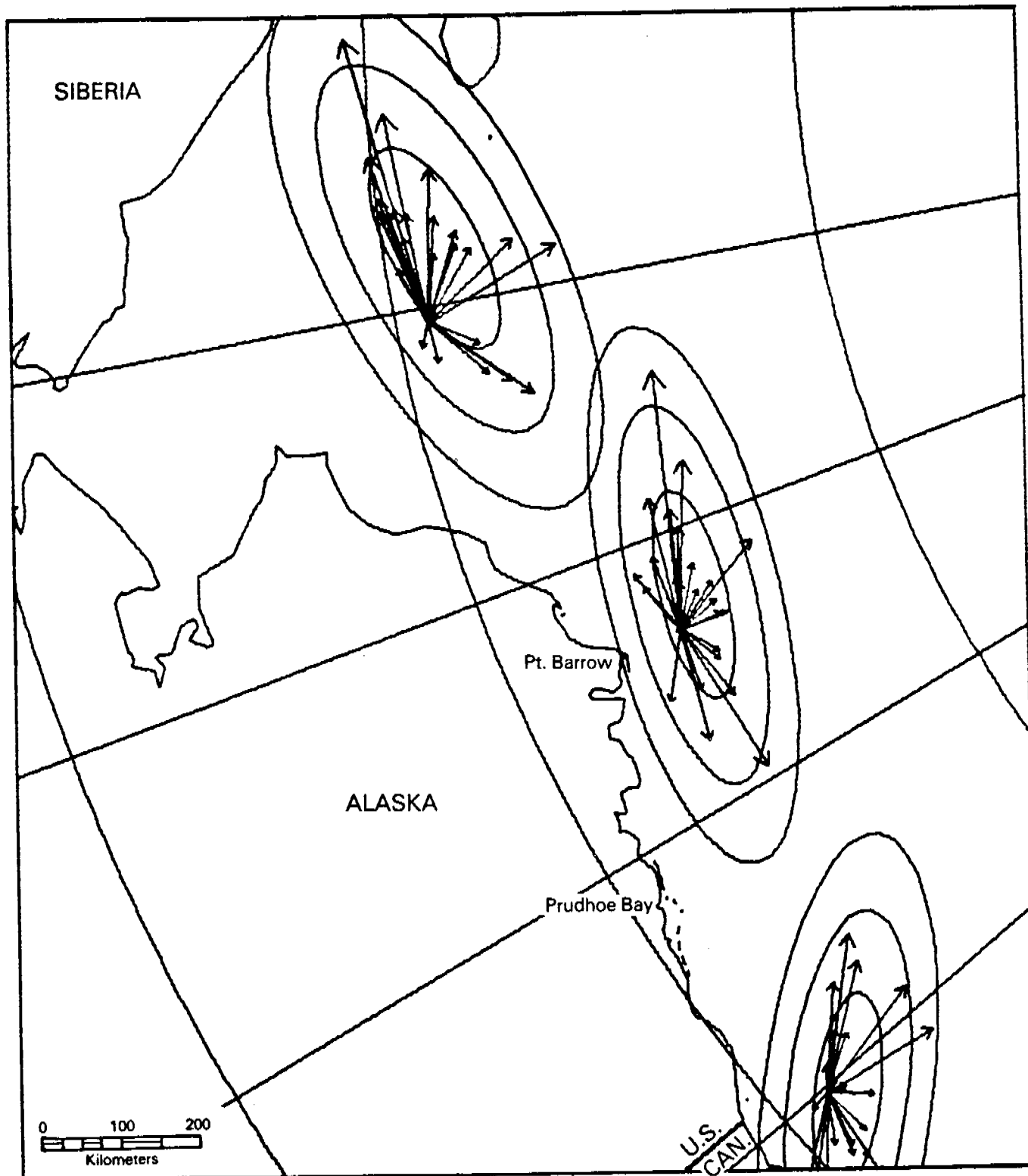
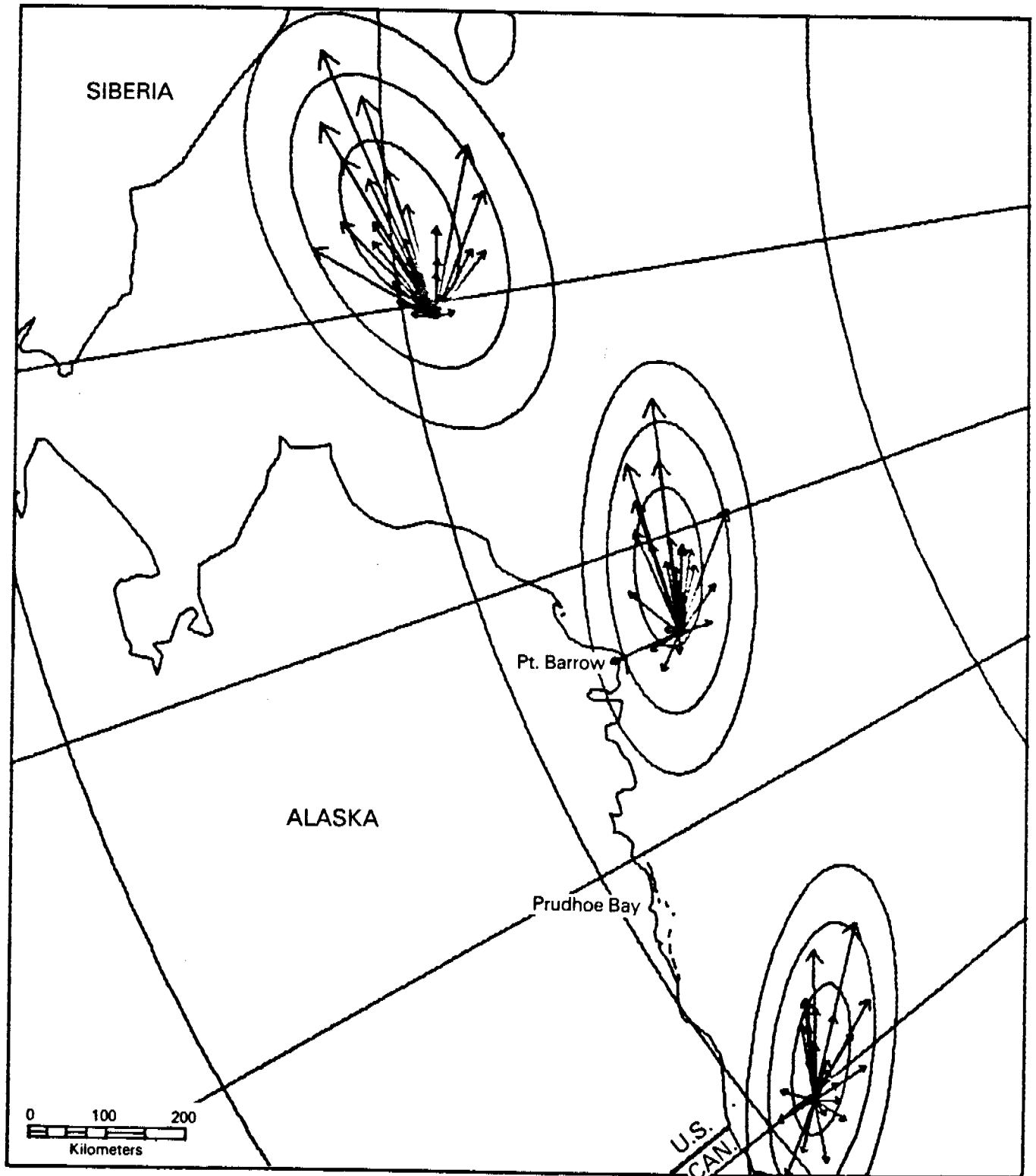


Figure 13. Mean Free Drift Ice Displacement and Mean Error Ellipses for December.



**Figure 14. Variation of Displacement During January Across the Beaufort/Chukchi Seas. Ellipses are 50-, 90- and 99 Percent Equi-Probability Ellipses.**



**Figure 15. Variation of Displacement During February Across the Beaufort/Chukchi Seas. Ellipses are 50-, 90- and 99 Percent Equi-Probability Ellipses.**

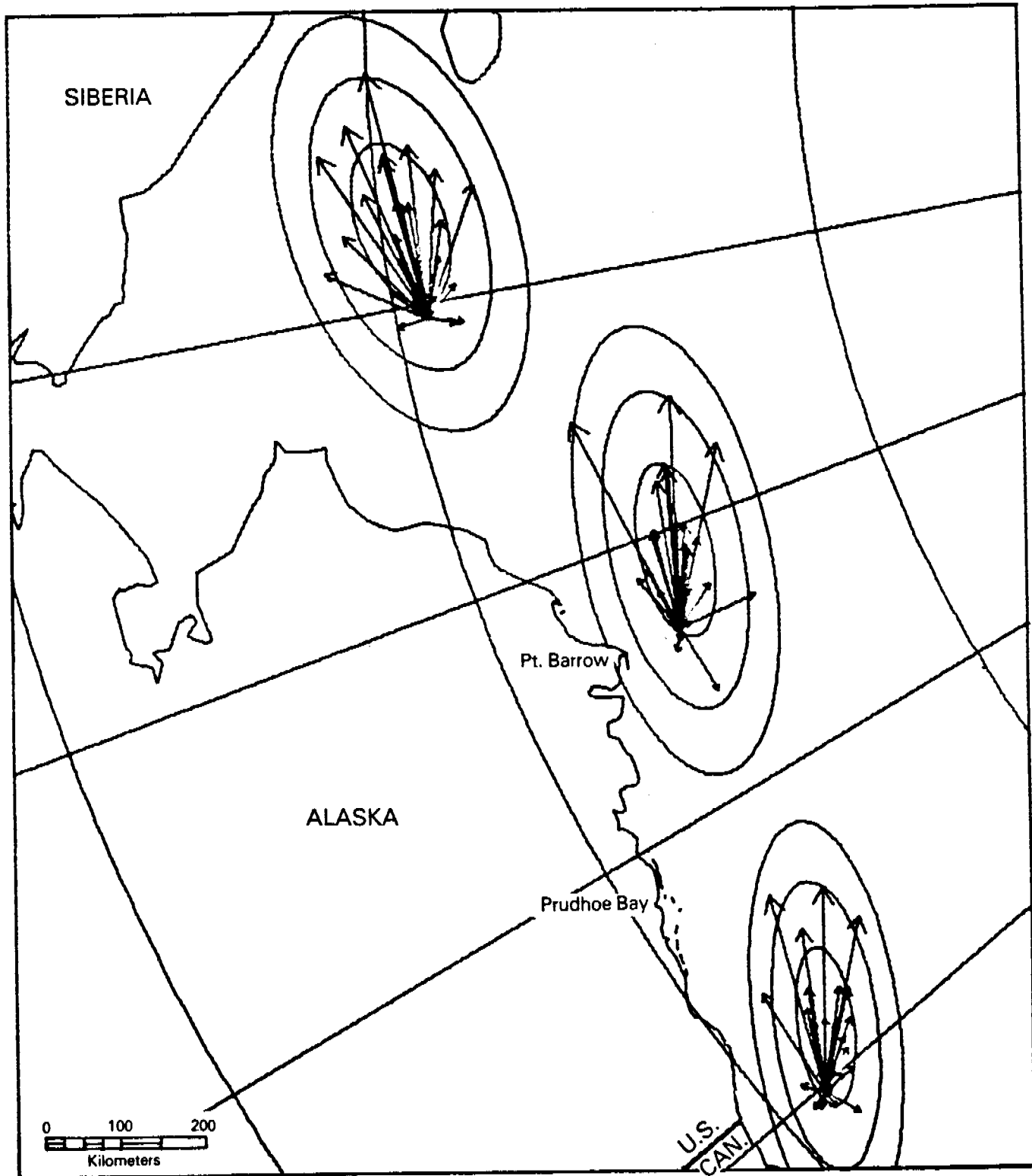


**Figure 16. Variation of Displacement During March Across the Beaufort/Chukchi Seas. Ellipses are 50-, 90- and 99 Percent Equi-Probability Ellipses.**

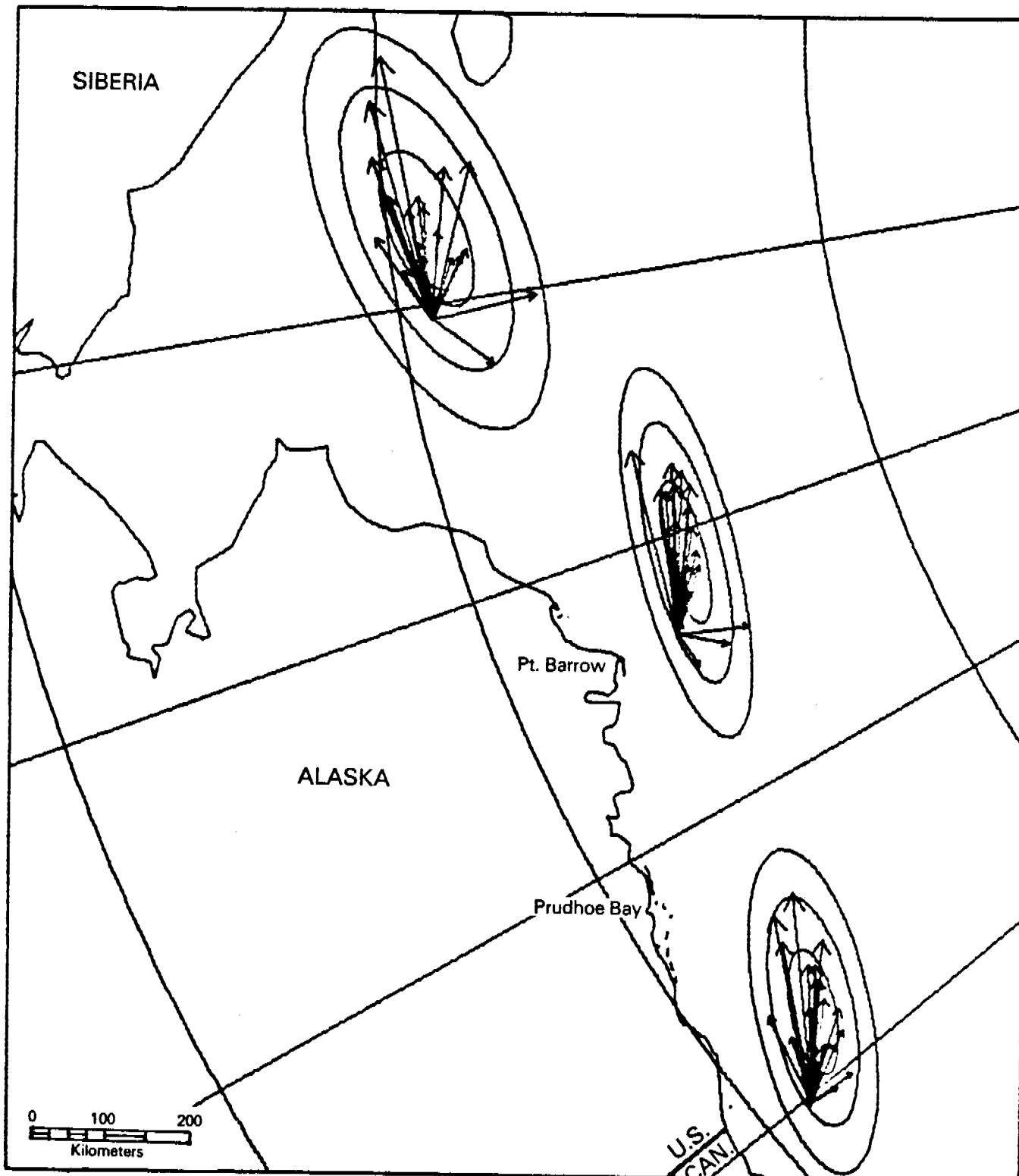


**Figure 17. Variation of Displacement During April Across the Beaufort/Chukchi Seas. Ellipses are 50-, 90- and 99 Percent Equi-Probability Ellipses.**

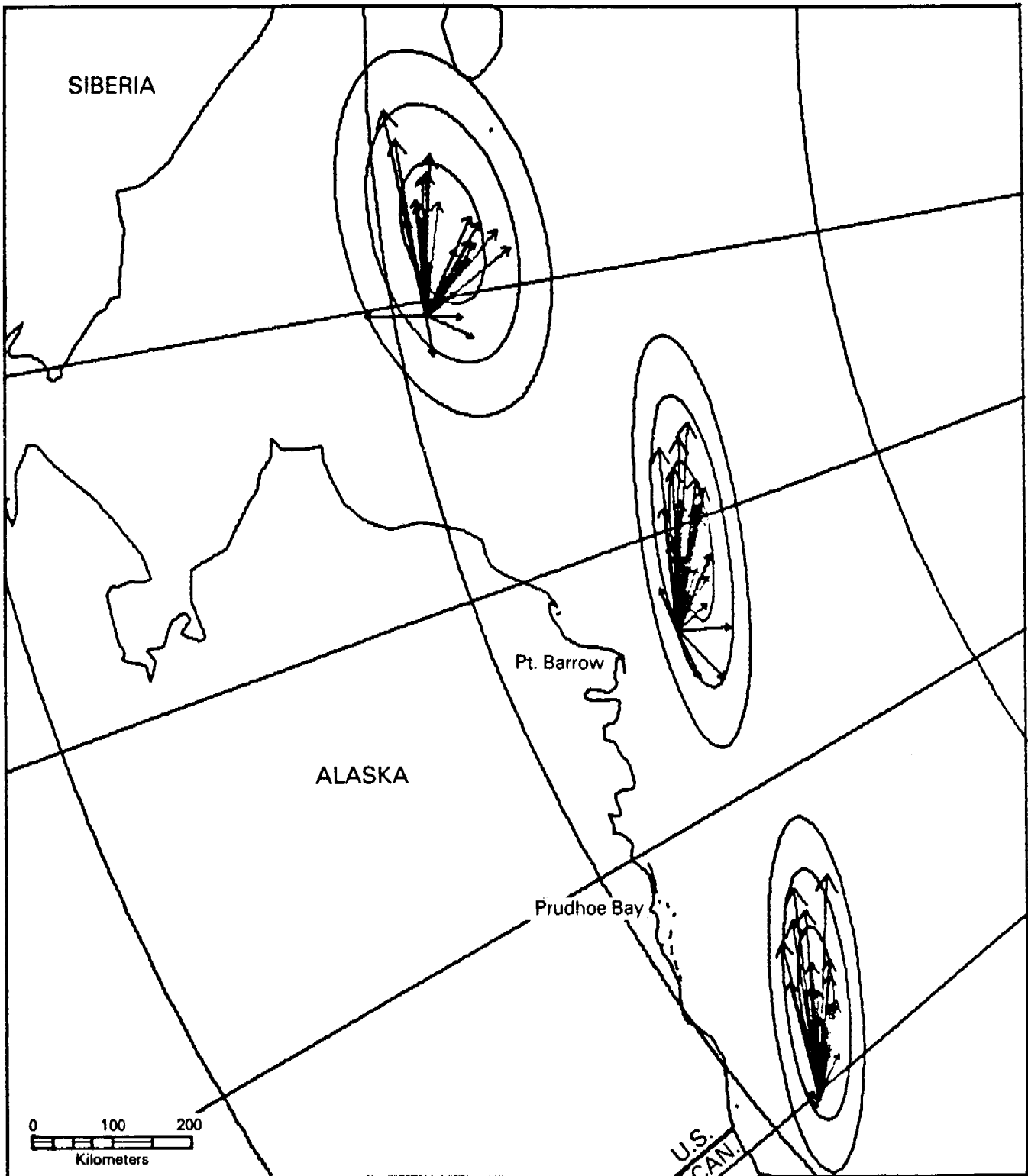


**Figure 18. Variation of Displacement During May Across the Beaufort/Chukchi Seas. Ellipses are 50-, 90- and 99 Percent Equi-Probability Ellipses.**

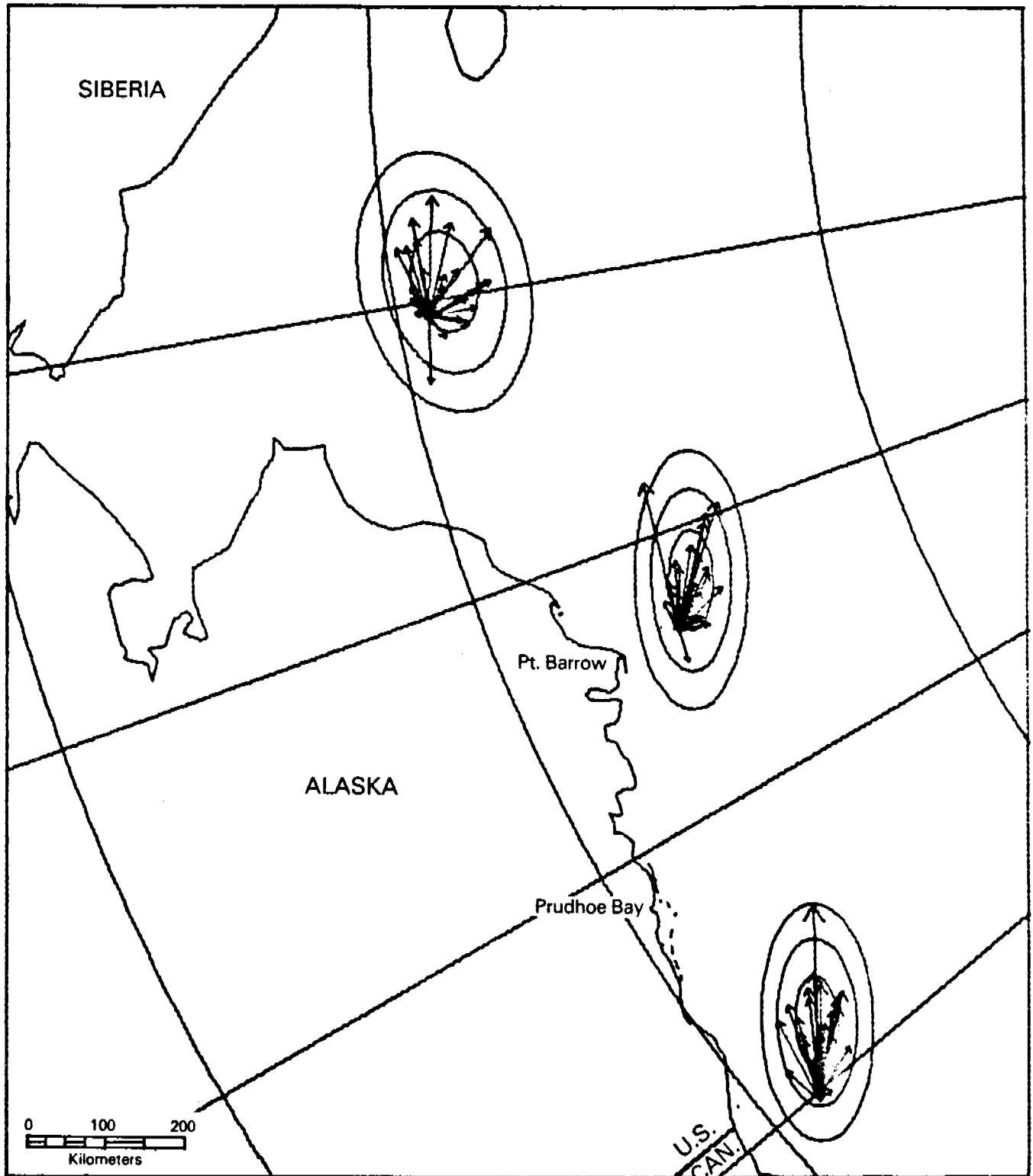


**Figure 19. Variation of Displacement During June Across the Beaufort/Chukchi Seas. Ellipses are 50-, 90- and 99 Percent Equi-Probability Ellipses.**

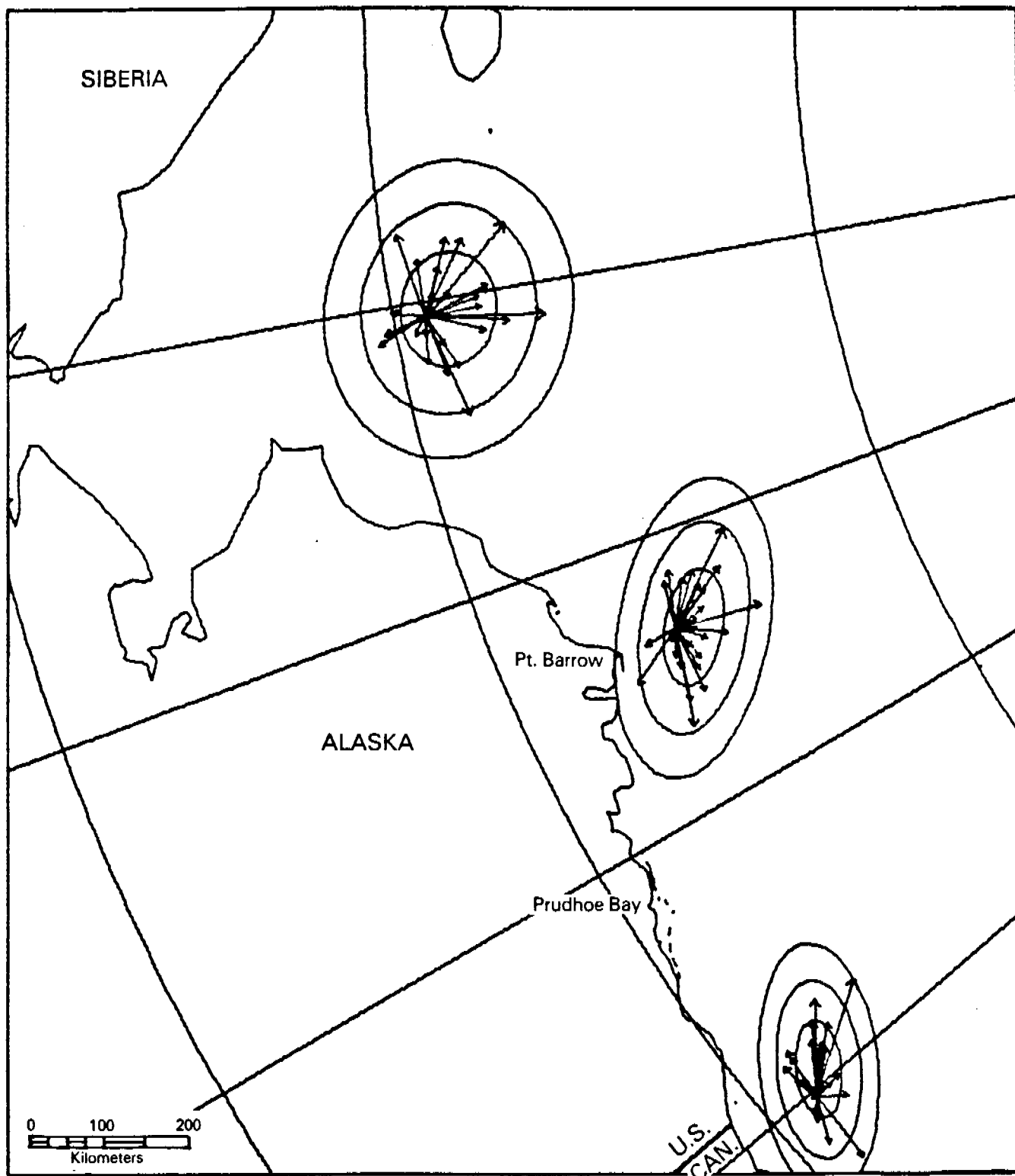


**Figure 20. Variation of Displacement During July Across the Beaufort/Chukchi Seas. Ellipses are 50-, 90- and 99 Percent Equi-Probability Ellipses.**



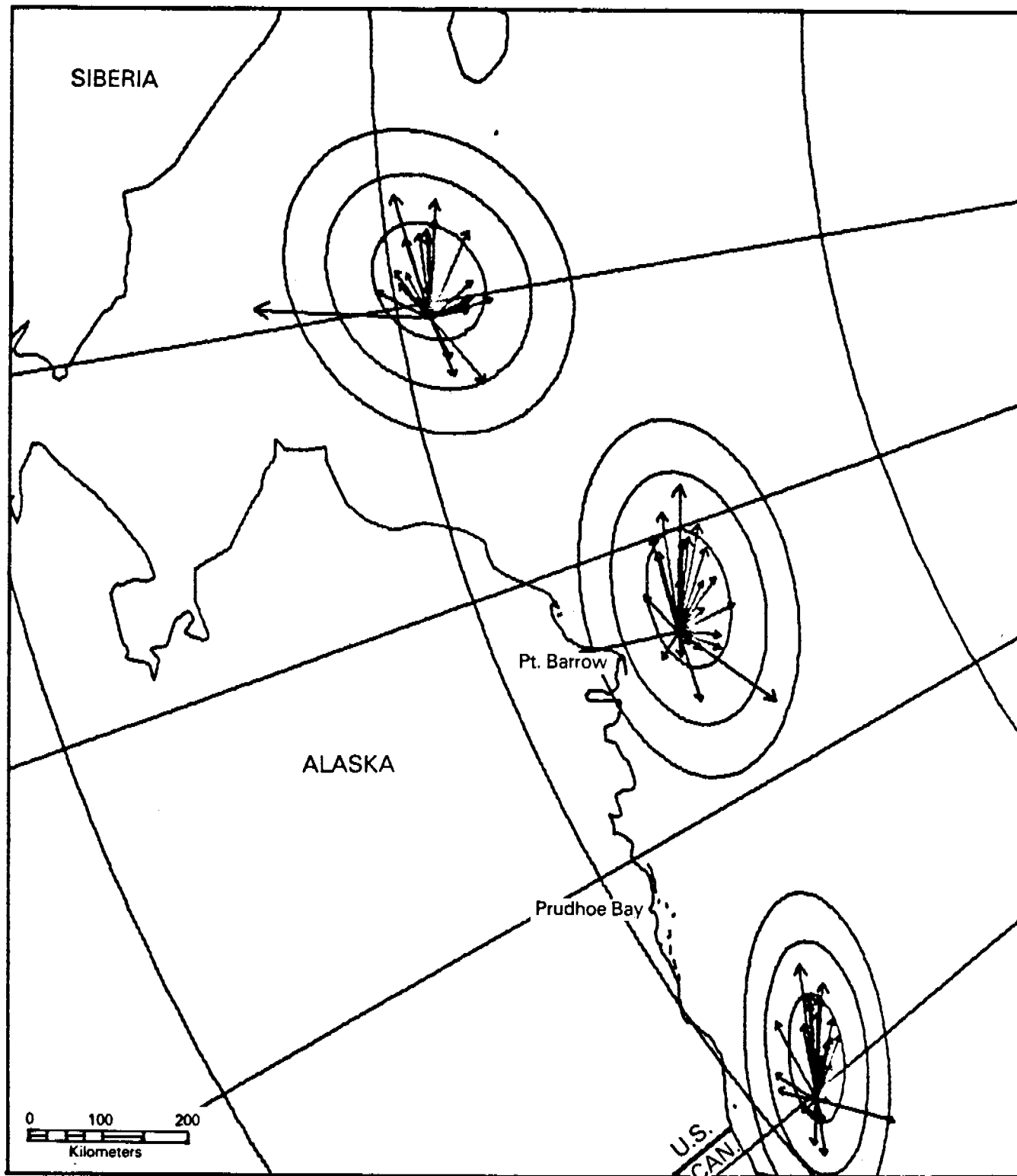


**Figure 21. Variation of Displacement During August Across the Beaufort/Chukchi Seas. Ellipses are 50-, 90- and 99 Percent Equi-Probability Ellipses.**

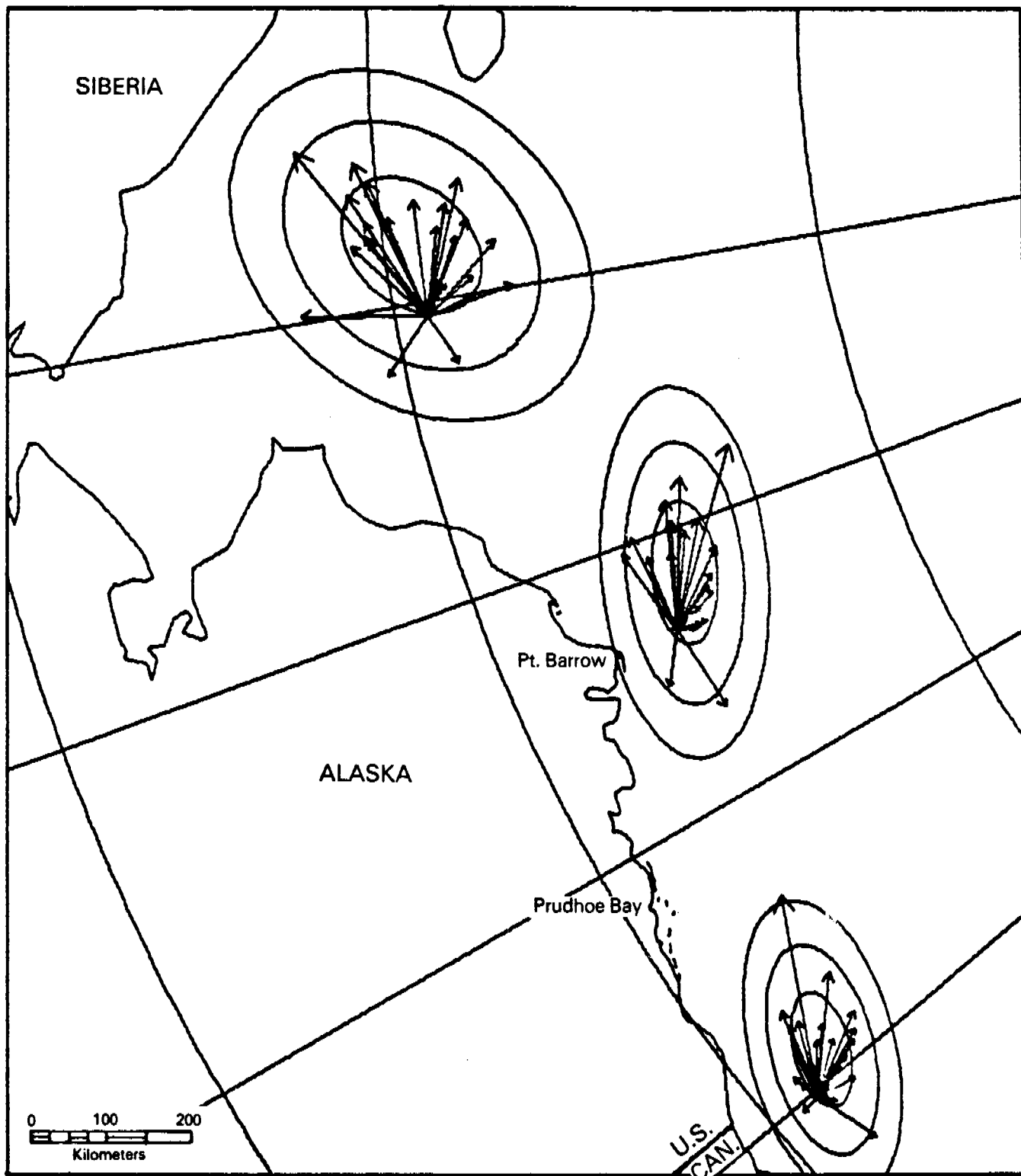


**Figure 22. Variation of Displacement During September Across the Beaufort/Chukchi Seas. Ellipses are 50-, 90- and 99 Percent Equi-Probability Ellipses.**

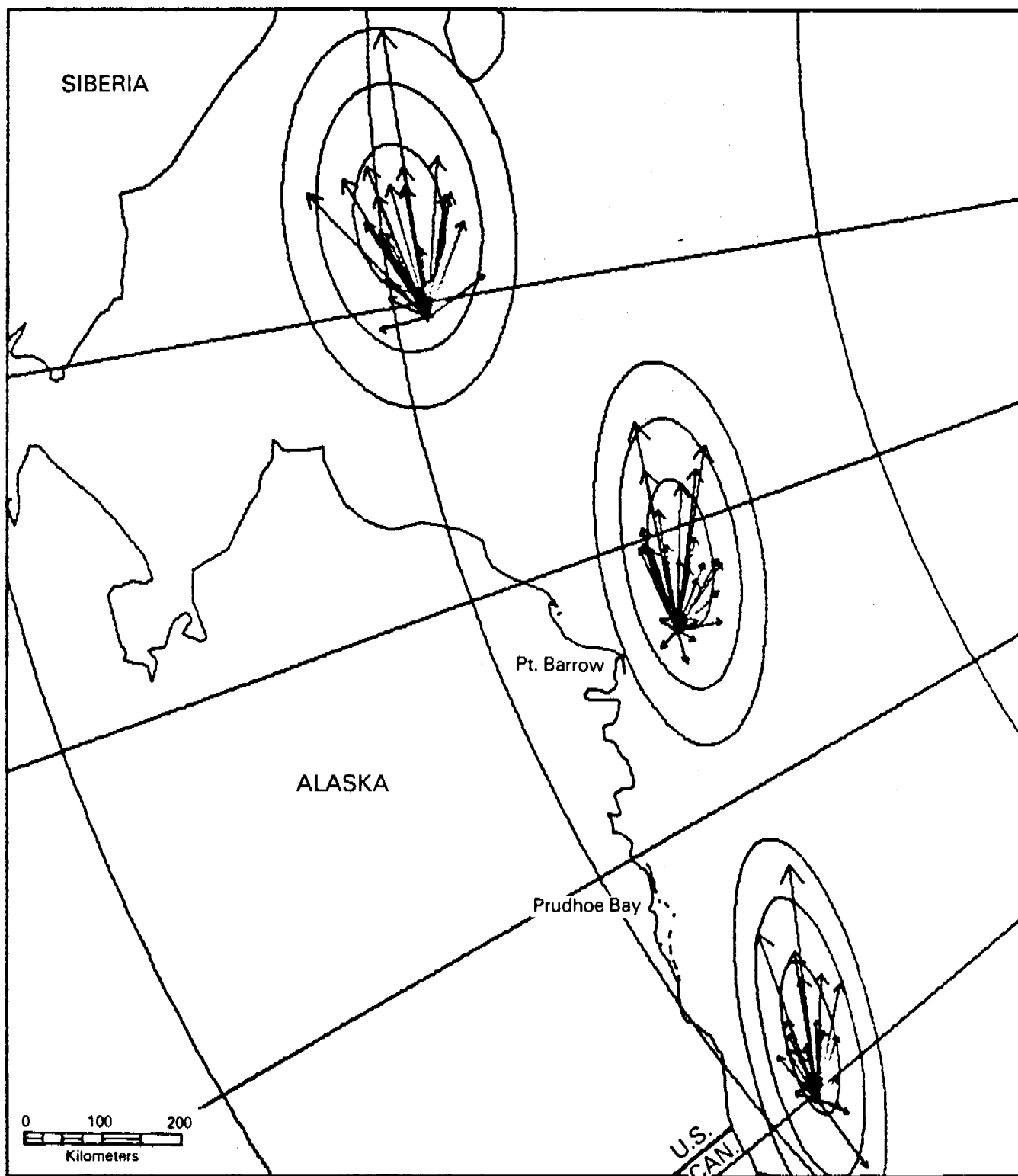


**Figure 23. Variation of Displacement During October Across the Beaufort/Chukchi Seas. Ellipses are 50-, 90- and 99 Percent Equi-Probability Ellipses.**

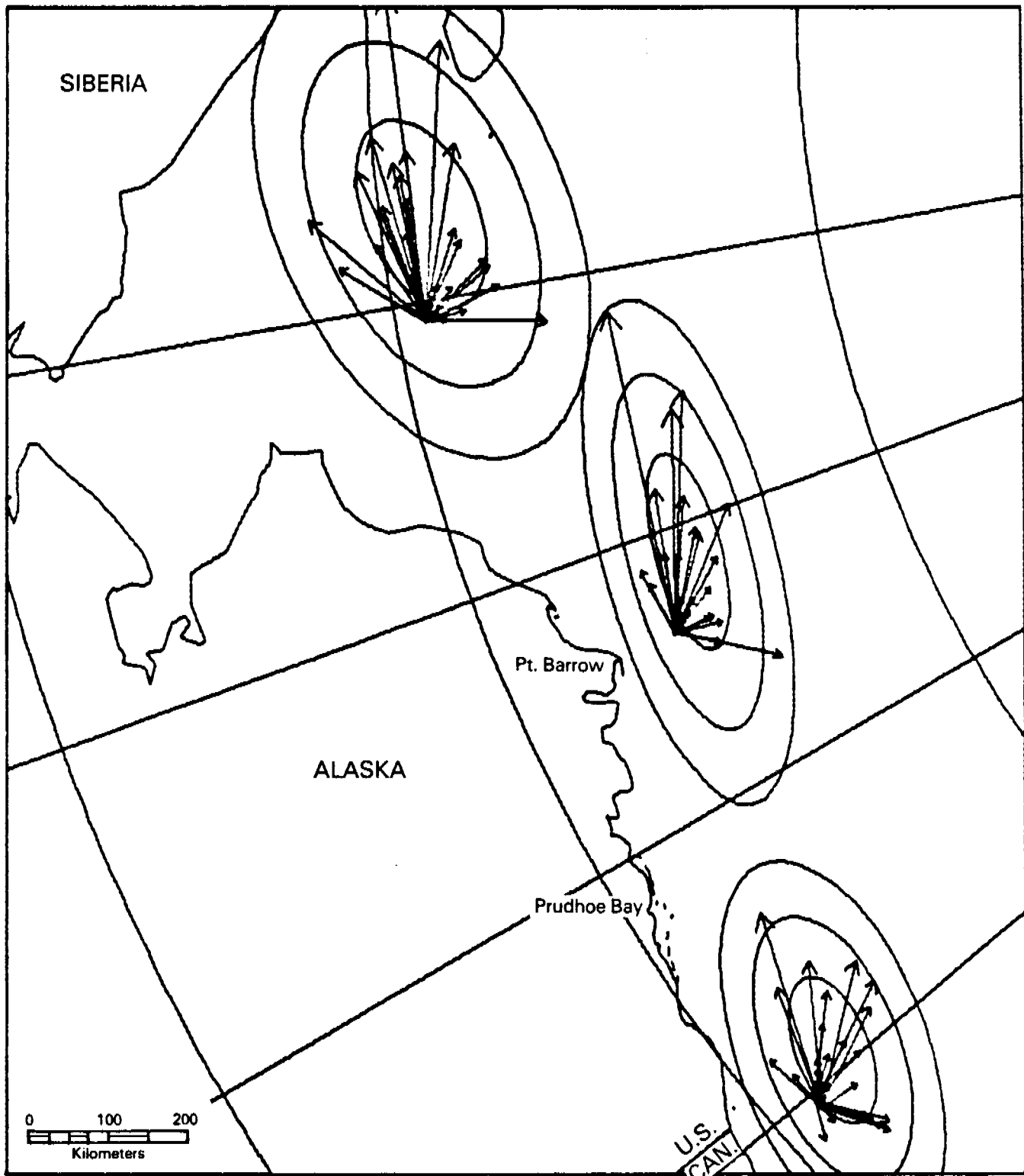


**Figure 24. Variation of Displacement During November Across the Beaufort/Chukchi Seas. Ellipses are 50-, 90- and 99 Percent Equi-Probability Ellipses.**

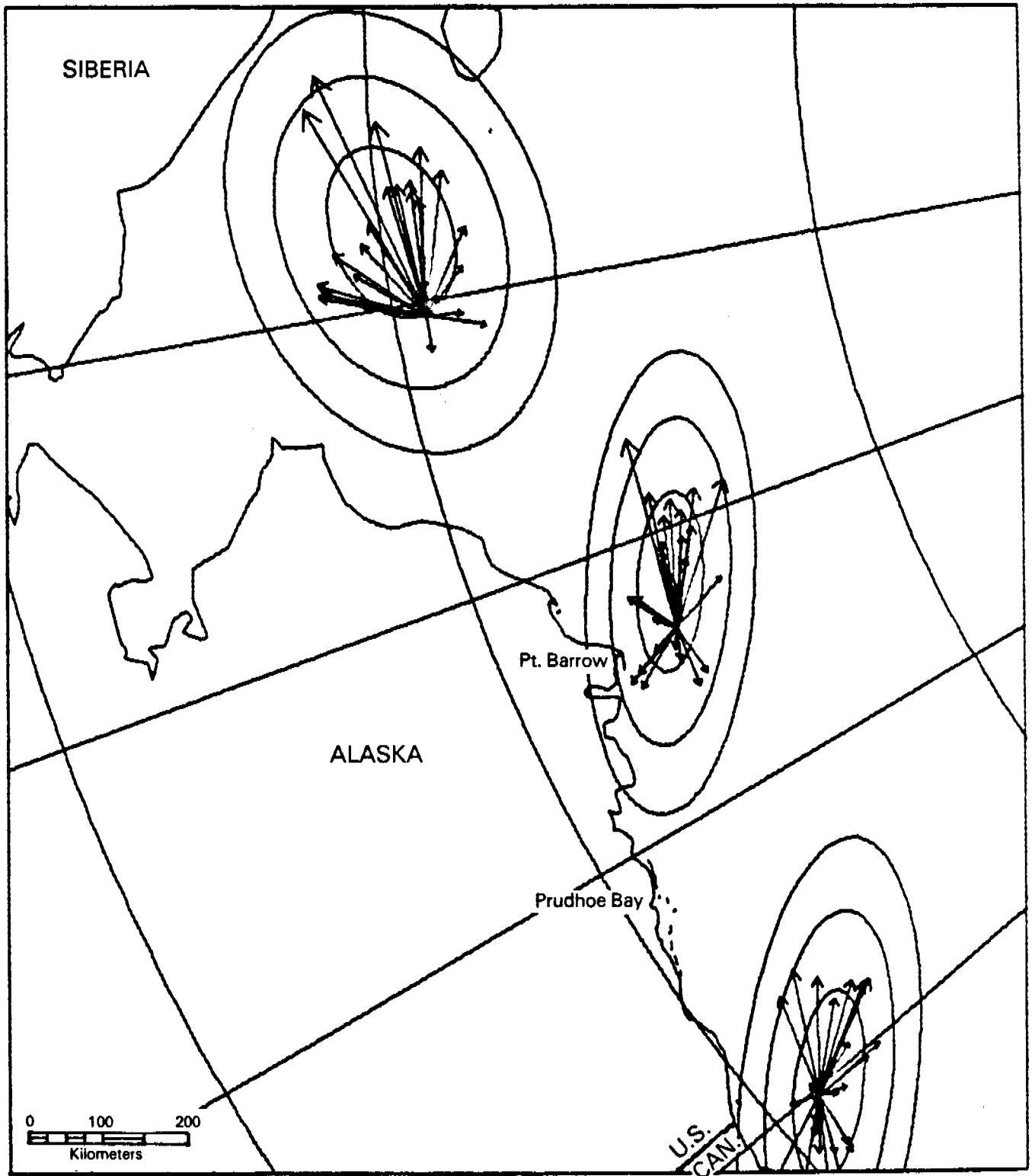


**Figure 25. Variation of Displacement During December Across the Beaufort/Chukchi Seas. Ellipses are 50-, 90- and 99 Percent Equi-Probability Ellipses.**

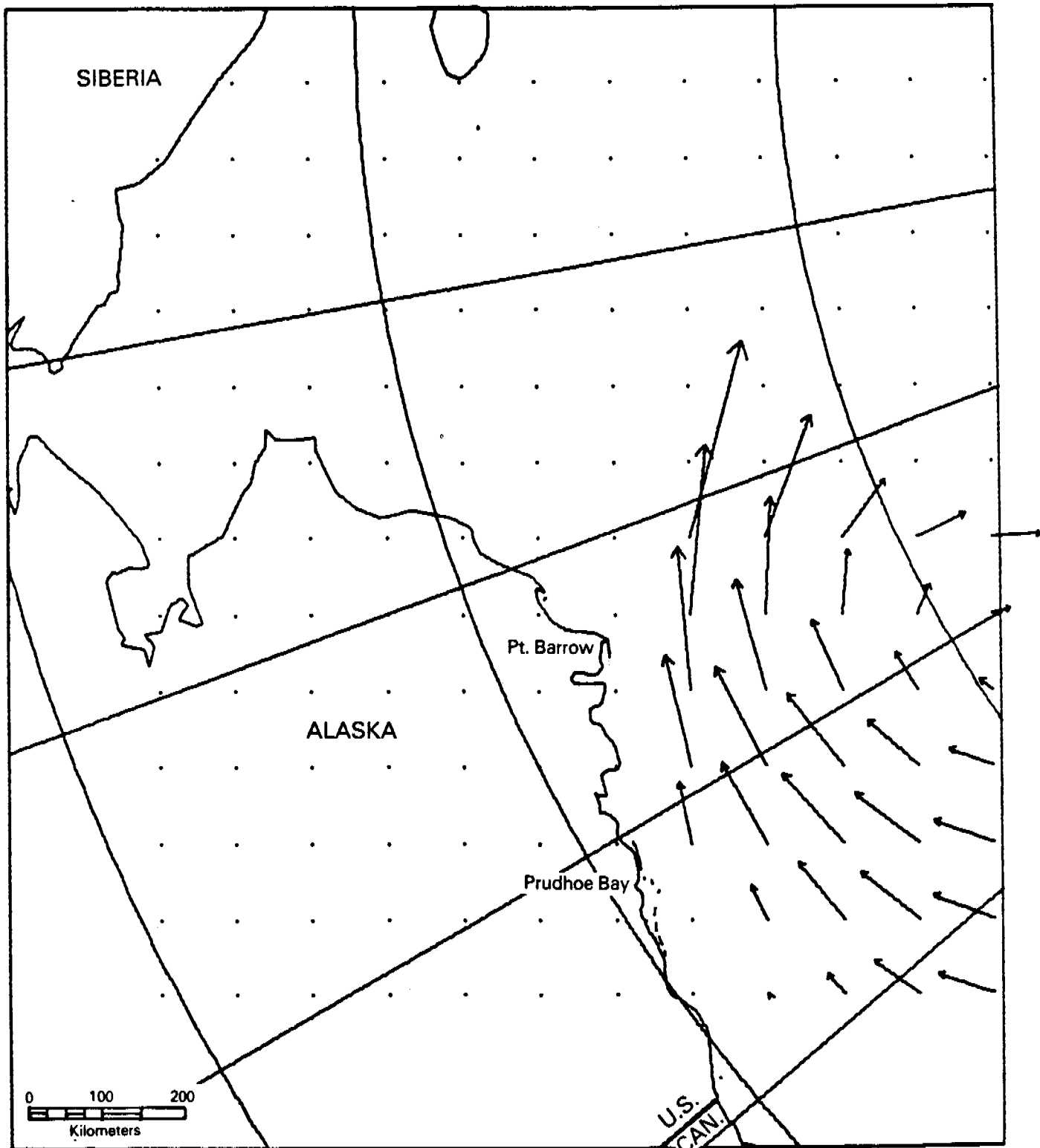


**Figure 26. Monthly Displacements Due to Geostrophic Ocean Currents in Central Beaufort Sea.**

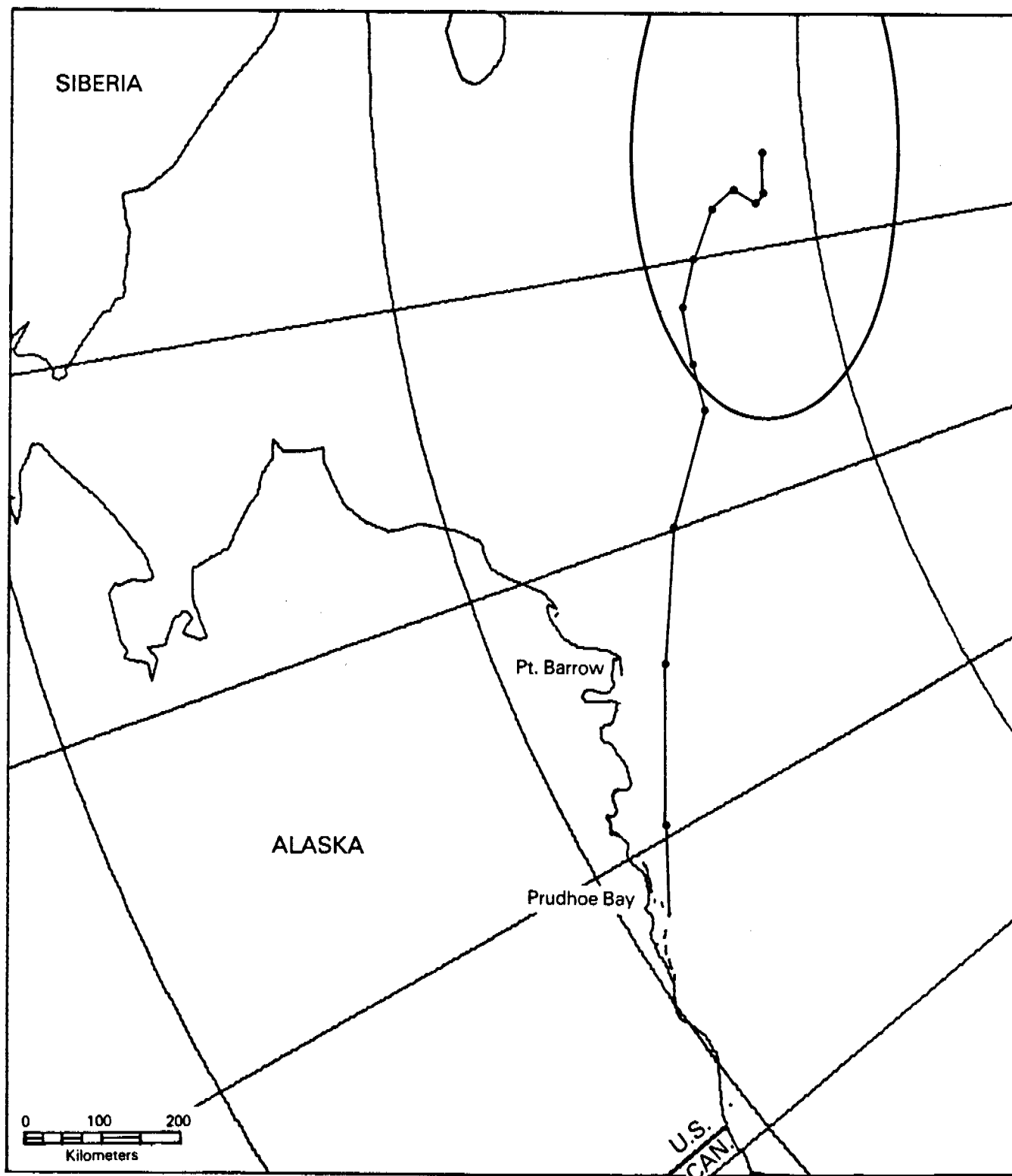


**Figure 27. Most Likely Twelve-Month Free Drift Ice Trajectory (Including Currents) and Approximate Mean Error Ellipse. Trajectory Begins at Prudhoe Bay, October 1st.**

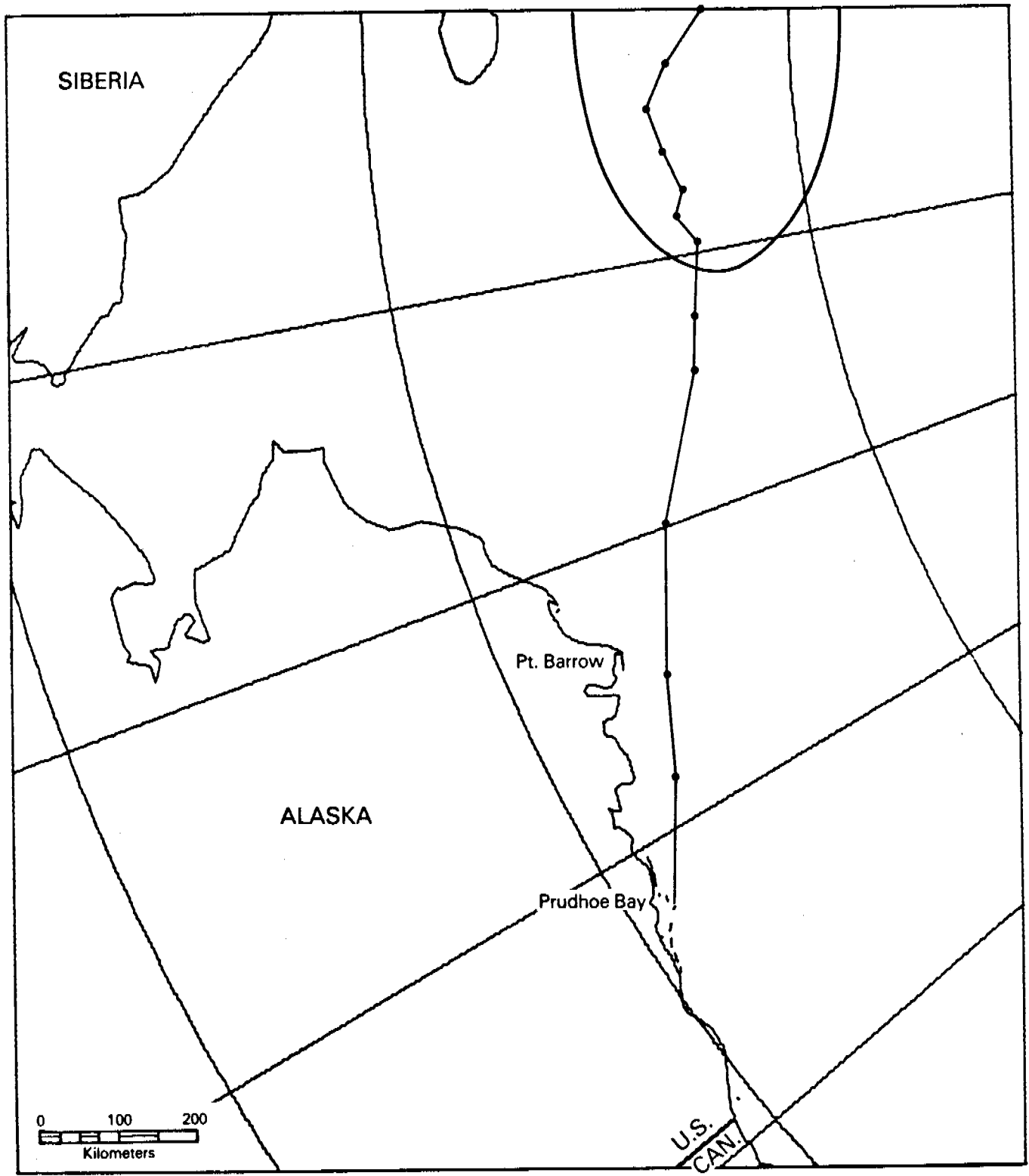


**Figure 28. Most Likely Twelve-Month Free Drift Ice Trajectory (Including Currents) and Approximate Mean Error Ellipse. Trajectory Begins at Prudhoe Bay, June 1st.**



## Appendix I. Daily Free Drift Model of Sea Ice.

Recently developed mathematical models, including the free drift model of sea ice dynamics have one day time resolution. This time scale has been shown to be meaningful for describing the large scale ice behavior. Furthermore, such models are compatible with barometric surface pressure data available to define the air stress. For the objectives of the study, however, it is monthly, not daily displacements that are needed. Therefore, in this section we will study the free drift model to learn if it may be used directly on a monthly time scale; or if it must be used to compute daily displacements with monthly values obtained by summing daily values. The crucial feature is linearity of the free drift model response. That is, is there a quantity, say air stress or geostrophic wind, which is linearly related to the daily ice motion? If the answer is positive, then the monthly means of these variables are also related. If the answer is negative, then daily values must be used to generate the monthly displacements. In addition, the free drift model is studied to estimate the effect of material parameter variations on ice drift.

During free drift, motion of the ice cover may be determined by considering momentum balance locally. The forces acting on the ice are air stress  $\tau_a$ , water stress  $\tau_w$ , Coriolis force  $-mfkXy$  and sea surface tilt  $-mg\sqrt{H}$ . Momentum changes then occur as

$$\dot{\vec{m}\vec{v}} = \tau_a + \tau_w - mf kXy - mg\sqrt{H} \quad (I.1)$$

where  $H$  is the dynamic sea surface height.

The air stress is determined from the geostrophic wind in the atmosphere as

$$\tau_a = \rho_a c_a \left| \vec{U} \right| B_a \vec{U} \quad (I.2)$$

where

$$B_a = \begin{pmatrix} \cos\alpha & -\sin\alpha \\ \sin\alpha & \cos\alpha \end{pmatrix} \quad (I.3)$$

and we have neglected the ice drift since it is two orders of magnitude smaller than the geostrophic wind. The geostrophic wind is determined from the surface barometric pressure field,  $P$  as

$$\vec{U} = -\frac{1}{\rho_a f} \vec{k} \times \nabla P \quad (I.4)$$

The water stress satisfies a quadratic drag law similar to the atmosphere

$$\vec{\tau}_w = \rho_w c_w \|\vec{v} - \vec{v}_g\| B(\vec{v} - \vec{v}_g) \quad (I.5)$$

where  $\vec{v}_g$  is the ocean geostrophic current and

$$B = \begin{pmatrix} \cos(\beta+\pi) & -\sin(\beta+\pi) \\ \sin(\beta+\pi) & \cos(\beta+\pi) \end{pmatrix} \quad (I.6)$$

The sea surface tilt defines the ocean geostrophic current in the form

$$mg \nabla H = -mf \vec{k} \times \vec{v}_g \quad (I.7)$$

The ice velocity may be determined at each point as a function of time whenever the barometric pressure field history is prescribed. Many authors have used the free drift relationships to analyze ice motions. Recently, McPhee (1977a) has used this model to simulate motion and deformation of the AIDJEX manned array during the summer of 1975.

The results sought have time resolution on the order of one day. For this case, inertia is negligible. Therefore, the analysis is performed for steady state conditions. When shorter time-scale results are desired the ice inertia may be included, but in this case McPhee (1977b) has shown that the inertia of the water column is also significant. Thus, the inertia contribution is not completely formulated. For both reasons we choose to neglect inertia completely and use the steady state equations. In this case, equation (I.1) becomes

$$\vec{\tau}_a + \vec{\tau}_w - mf \vec{k} \times \vec{v} - mg \nabla H = 0 \quad (I.8)$$

If the water stress and sea surface tilt terms are substituted into (I.8) then

$$\tau_{\sim a} + \rho_w c_w \left| \left| \underline{v} - \underline{v}_{\sim g} \right| \right| B(\underline{v} - \underline{v}_{\sim g}) - mf kX(\underline{v} - \underline{v}_{\sim g}) = 0 \quad (I.9)$$

But this force balance relates air stress  $\tau_{\sim a}$ , ocean currents  $\underline{v}_{\sim g}$  and ice drift in a special way, namely, the ice velocity and current always appear as a difference  $\underline{v} - \underline{v}_{\sim g}$ . Thus, if we introduce

$$\underline{G} = \underline{v} - \underline{v}_{\sim g} \quad (I.10)$$

then force balance becomes

$$\tau_{\sim a} + \rho_w c_w \left| \left| \underline{G} \right| \right| B \underline{G} - mf kX \underline{G} = 0 \quad (I.11)$$

This equation may be rewritten in terms of water stress if desired as

$$\tau_{\sim a} + \tau_{\sim w} - mf kX \underline{G} = 0 \quad (I.12)$$

$$\tau_{\sim w} = \rho_w c_w \left| \left| \underline{G} \right| \right| B \underline{G} \quad (I.13)$$

As a result of introducing  $\underline{G}$ , the ice velocity relative to deep ocean current, it is seen that it is this quantity that air stress affects. Therefore, contributions to ice drift due to air stress and to ocean current may be calculated separately. The air stress effect is found from equation (I.11) and the ocean current is added directly in the form

$$\underline{v} = \underline{G} + \underline{v}_{\sim g} \quad (I.14)$$

In the present work, our efforts shall be directed toward understanding the response of this model. The approach is to introduce nondimensional variables that show explicitly how all material constants affect solutions and to simplify our presentation and understanding of the results. The nondimensional variables have been determined by Pritchard and Thomas (1978) for the AIDJEX ice model.

Introduce nondimensional variables

for velocity,

$$\bar{v} = \frac{\rho_w c_w}{mf} v \quad (I.15)$$

$$\bar{U} = \frac{\rho_w c_w}{mf} U$$

$$\bar{G} = \frac{\rho_w c_w}{mf} G$$

for air and water stress,

$$\bar{\tau} = \frac{\rho_w c_w}{(mf)^2} \tau \quad (I.16)$$

and for pressure and position introduce arbitrary scaling,

$$\bar{P} = P/P_R$$

$$\bar{x} = x/x_R \quad (I.17)$$

Introduce the nondimensional numbers,

$$N_p = \frac{\rho_w c_w P_R}{\rho_a f m x_R}$$

$$N_a = \frac{\rho_a c_a}{\rho_w c_w}$$

and the steady state equation of motion then becomes

$$\bar{\tau}_a + ||\bar{G}||_{B\bar{G}} - k \times \bar{G} = 0 \quad (I.18)$$

where air stress satisfies

$$\bar{\tau}_a = N_a ||\bar{U}||_{B_a \bar{U}} \quad (I.19)$$

The geostrophic wind is

$$\bar{U} = -N_p k \times \bar{V} P \quad (\text{I.20})$$

The relationship between ice velocity and applied air stress has been described in a convenient form by Pritchard, Coon and McPhee (1977). If we modify that work by using the present nondimensional variables, then

$$\bar{U}_a = s Q \bar{G} \quad (\text{I.21})$$

where

$$s = (|\bar{G}|^2 + 2|\bar{G}|\sin\beta + 1)^{1/2} \quad (\text{I.22})$$

$$Q = \begin{pmatrix} \cos\delta & -\sin\delta \\ \sin\delta & \cos\delta \end{pmatrix}$$

where

$$\tan\delta = \tan\beta + \frac{1}{|\bar{G}|\cos\beta} \quad (\text{I.23})$$

The ice drift relative to geostrophic ocean currents is to the right of the air stress by angle  $\delta$ . The forces acting on the ice are shown in Figure I.1. The ice drift appears as a dashed arrow.

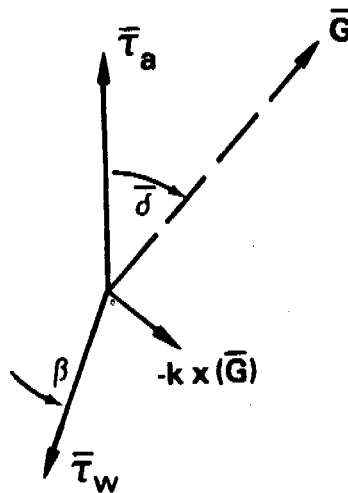


Figure I.1. Free Drift Force Balance and Ice Velocity.

The magnitude of air stress and ice drift are related by

$$||\bar{\tau}_a|| = s ||\bar{G}|| \quad (I.24)$$

which is displayed in Figure I.2. We have chosen to invert equation (I.24) for graphical representation since we anticipate  $\bar{\tau}_a$  to be given as input and ice drift calculated as output. The angle  $\delta$  also varies with air stress magnitude as may be seen by solving (I.23) and (I.24) simultaneously. In Figure I.3 we present the results. It is seen that the turning angle depends significantly on the oceanic boundary layer Ekman angle  $\beta$ . This is not true of ice speed which is insensitive to changes in  $\beta$ .

The ice speed is a nonlinear function of air stress magnitude and the turning angle depends on air stress magnitude too. Thus, the response is nonlinear and therefore the model cannot be used directly on monthly mean air stress.

To circumvent this problem, we look at the relationship between air stress magnitude and ice drift speed which is nearly parabolic. By introducing the quadratic atmospheric boundary layer model we seek a linear relationship between geostrophic wind and the ice drift. We find

$$N_a \|\bar{U}\| B_a \bar{U} = s Q \bar{G} \quad (I.25)$$

The wind and ice speed are related by

$$N_a \|\bar{U}\|^2 = s \|\bar{G}\| \quad (I.26)$$

This relationship is presented in Figure I.4. It is seen that the ice speed is nearly a linear function of the wind speed. This observation was noted by both M. G. McPhee and A. S. Thorndike (personal communications) and led them to prefer using geostrophic wind rather than air stress in their free drift analyses.

The angle between geostrophic wind and ice drift is controlled by  $B_a^T Q$  and since

$$N_a \|\bar{U}\| \bar{U} = s B_a^T Q \bar{G} \quad (I.27)$$

we see that the ice drift is oriented at angle  $\delta - \alpha$  to the right of the geostrophic wind. This relationship is shown in Figure I.5. It is seen that the turning angle depends strongly on wind speed. Therefore, the relationship is not linear and the monthly average geostrophic wind cannot be used directly to obtain the monthly ice motion. In practice, however, it is possible that a constant angle (say  $\delta = 45^\circ$ ) would provide a useful approximation to longer term drift.

Due to the nonlinearity in these relationships, the decision was made to process historical winds on a daily basis and sum up the daily ice displacements to obtain monthly values. The nondimensional formulation has simplified the task of determining the effect of material parameters, however. To estimate better these effects, consider the relationship between ice speed and geostrophic wind. The ice speed is nearly a linear function of geostrophic wind speed at higher values. If equation (I.26) is rewritten as

$$y^2 = (x^2 + ax + 1)^{\frac{1}{2}} x \quad (I.28)$$

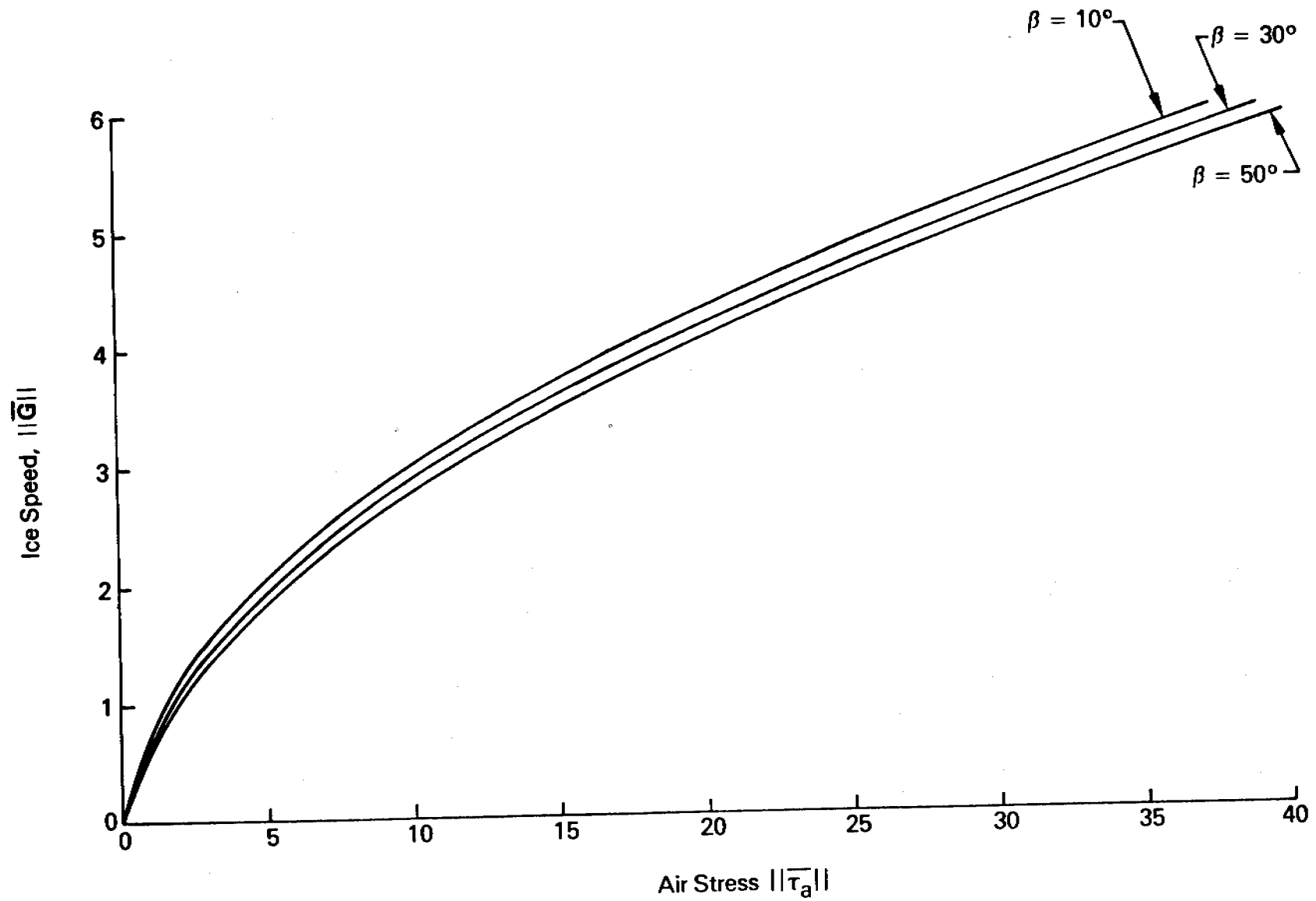


Figure I.2. Relationship Between Nondimensional Relative Ice Speed  $\|\bar{G}\|$  and Nondimensional Air Stress Magnitude  $\|\bar{\tau}_a\|$  for a Range of Oceanic Boundary Layer Turning Angles  $\beta$ .



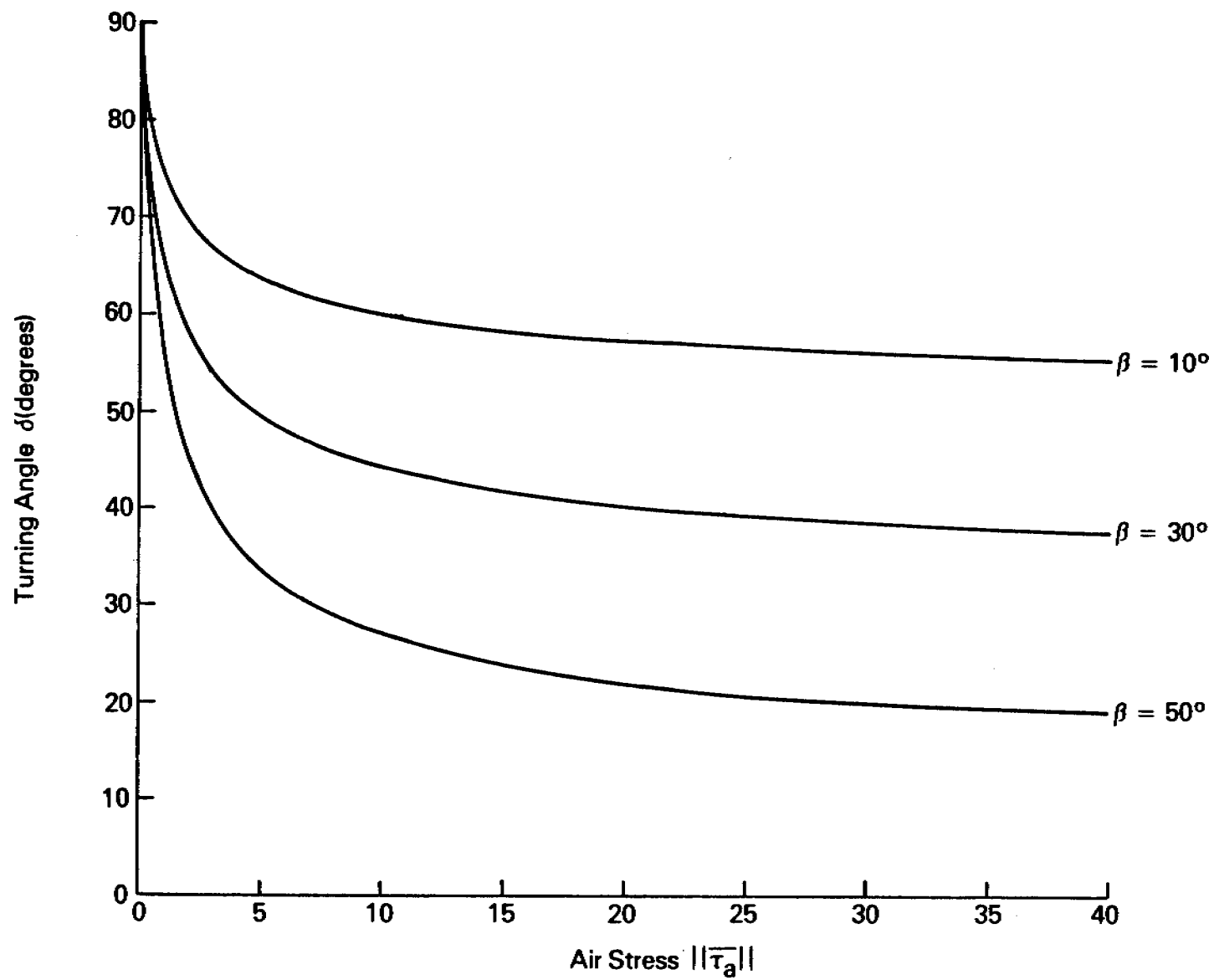


Figure 1.3. Relative Orientation  $\delta$  as a Fraction of Nondimensional Air Stress Magnitude  $||\bar{\tau}_a||$  for a Range of Oceanic Boundary Layer Turning Angles of  $\beta$ .

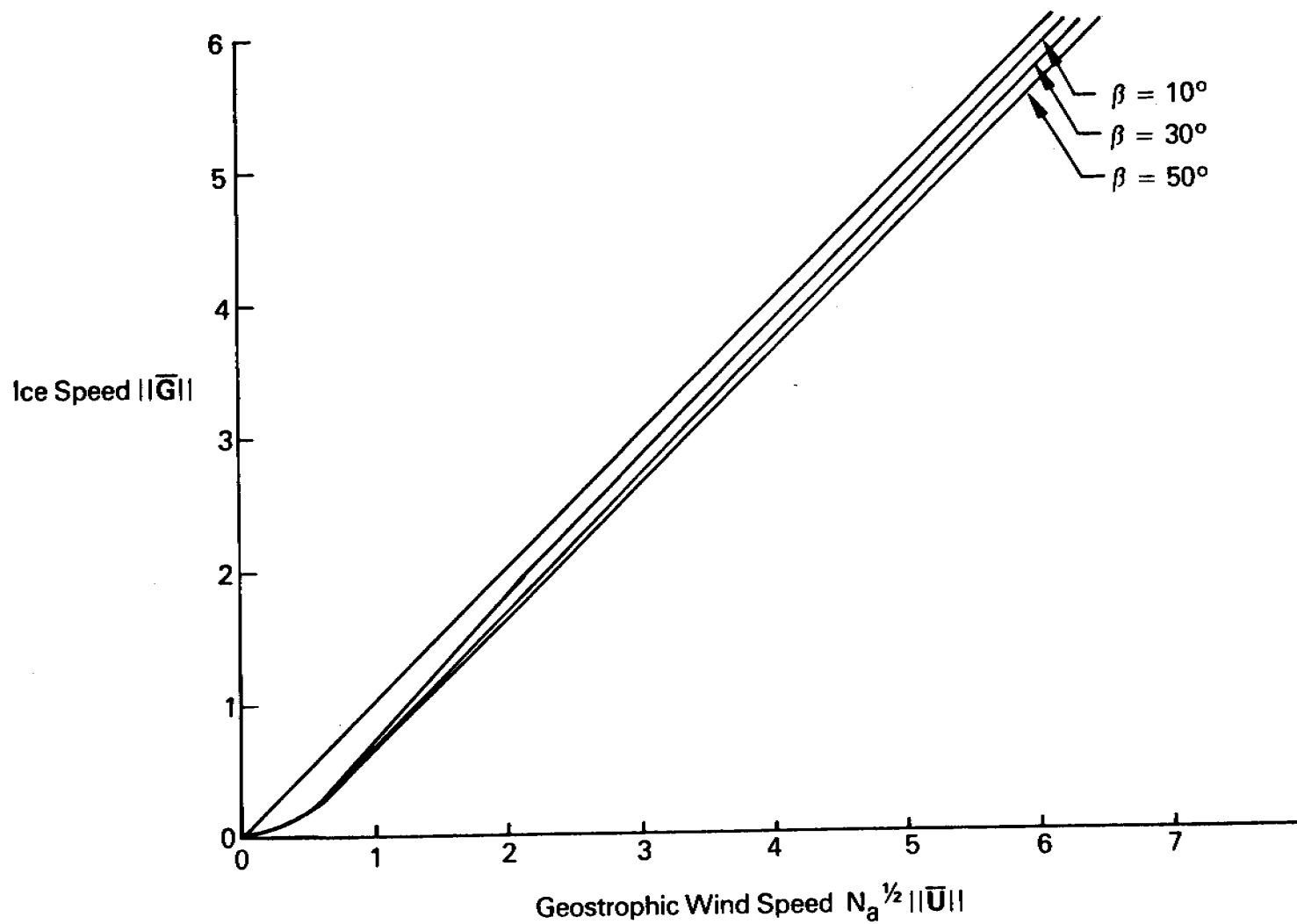


Figure I.4. Relationship Between Nondimensional Relative Ice Speed  $\|v - v_g\|$  and Nondimensional Geostrophic Wind speed  $N_a^{1/2} \|\bar{U}\|$  for Range of Oceanic Boundary Layer Turning Angles  $\beta$ .

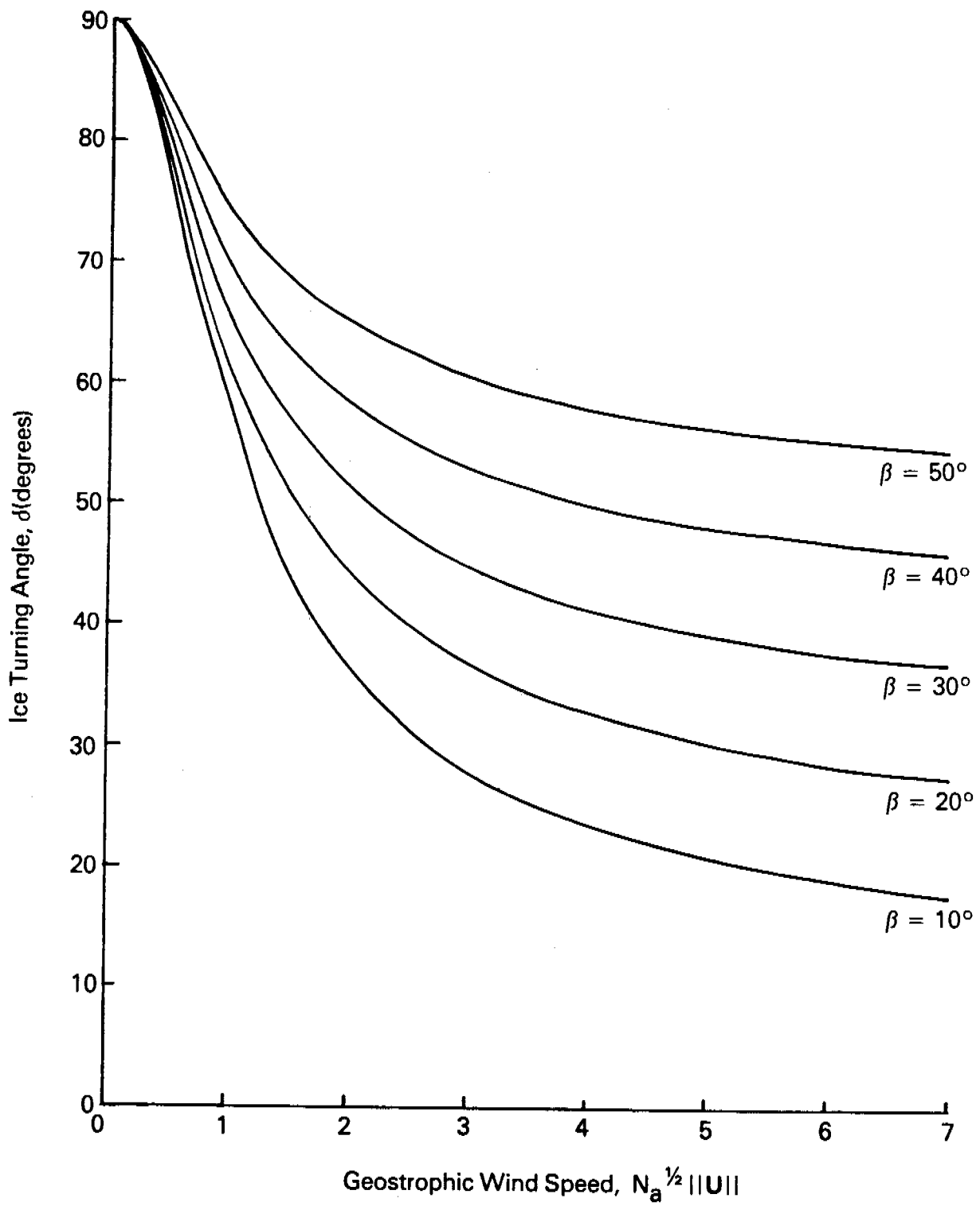


Figure I.5. Relative Ice Velocity Orientation  $\delta$  as a Function of Nondimensional Geostrophic Wind speed  $N_a^{1/2} ||\bar{U}||$  for Range of Oceanic Boundary Layer Turning Angles  $\beta$ .

where

$$y = N_a^{1/2} ||\bar{U}||, \quad x = ||\bar{G}|| \quad \text{and} \quad a = 2\sin\beta$$

are introduced for notational convenience, then an expansion may be made for large values of  $x$ .

$$y = (1 + ax^{-1} + x^{-2})^{1/2} x$$

and then

$$y = (1 + \frac{1}{2}ax^{-1} + \dots)x$$

Finally,

$$y = \frac{a}{4} + x + O(x^{-1}) \quad . \quad (I.29)$$

Returning to the original notation and inverting provides that

$$||\bar{G}|| \cong N_a^{1/2} ||\bar{U}|| - \frac{1}{2}\sin\beta \quad (I.30)$$

which provides the coefficients of the linear relationship. If the nondimensional solutions given by equations (I.23) and (I.30) are rewritten in terms of physical variables, then

$$||\bar{G}|| \cong N_a^{1/2} ||\bar{U}|| - \frac{mf}{2\rho_w c_w} \sin\beta \quad (I.31)$$

and

$$\tan\delta = \tan\beta + \frac{mf}{\rho_w c_w ||\bar{G}|| \cos\beta} \quad . \quad (I.32)$$

It is seen that the ice speed is insensitive to changes in mass  $m$  because it occurs only in the constant term, which is small. But the ratio of drag coefficients in the atmosphere and ocean,  $N_a$ , affects ice speed as a square root function. Therefore, all parameters have a modest affect on ice speed. However, in the range

of parameters anticipated, all can cause large changes in the turning angle. For example, increasing  $\beta$  from 20° to 30° increases the turning angle by about 10°. This is comparable to increasing the water drag or decreasing the mass density  $m$  by about 10 percent at higher speeds. The changes are smaller when winds are lower. The ratio of drag coefficients,  $N_a$ , affects the turning angle indirectly through the ice speed. If a 10 percent increase in  $N_a$  causes a 5 percent increase in  $||\underline{G}||$ , this in turn will cause about a 5° decrease in the turning angle.

Some consideration must be given to the special conditions that exist near the edge of the pack ice during summer when there is appreciable open water. In this case, the ice concentration is often low and the model has not been tested thoroughly under these conditions. The following argument, however, should eliminate serious concern. In the free drift model (equation I.11) the areal mass density is scaled down in proportion to the ice concentration. Similarly, the traction exerted by atmosphere and ocean on the ice in equations (I.2) and (I.11) should be proportional to the relative area covered by ice - but this is just the concentration. Therefore, each term in the free-drive momentum balance is changed by the same amount and the relationship between ice motion and geostrophic wind is unchanged.

#### Free Drift Simulation Parameters

The main driving force of the free drift model is the air stress. The air stress is computed from the geostrophic wind field as

$$\underline{\tau}_a = \rho_a c_a ||\underline{U}|| \underline{B}_a \underline{U} \quad (\text{I.1 bis})$$

$$\underline{B}_a = \begin{pmatrix} \cos\alpha & -\sin\alpha \\ \sin\alpha & \cos\alpha \end{pmatrix} \quad (\text{I.3 bis})$$

where  $c_a$  is a drag coefficient,  $\rho_a$  is the air density,  $\underline{U}$  is the geostrophic wind and  $\alpha$  is the angle of the air stress from the geostrophic wind. The geostrophic winds are computed from the surface pressure field as

$$\underline{U} = -\frac{1}{\rho_a f} \underline{k} \times \nabla P \quad (\text{I.4 bis})$$

where  $f$  is the Coriolis parameter.

Leavitt, et al. (1978a) have estimated  $c_{10}$ , the 10 meter drag coefficient to be 0.0025 using AIDJEX data presented by Leavitt, et al. (1978b). They believe

$c_{10}$  to be accurate to  $\pm 20$  percent. Albright (personal communication) has computed the ratio  $U_{10}/U$  to be 0.55 in summer, using the AIDJEX data set. Computing the drag coefficient as

$$c_a = \frac{U_{10}}{U}^2 c_{10}$$

and using the above values of  $U_{10}/U$  and  $c_{10}$  gives  $c_a = 0.0009$  for the summer. Albright (1978) also gives the summer value of  $\alpha = 24^\circ$ . The standard deviation of  $\alpha$  is  $13^\circ$  (Albright, personal communication).

The air density,  $\rho_a$ , is computed as the monthly average of all the densities computed from AIDJEX temperature data. The "within month" standard deviation of  $\rho_a$  is about 2 percent while the range of variation from month to month is about 12 percent.

Reliable data on the mean thickness of the ice for 1975 are not available. We used the computed mean thickness presented in Thorndike, et al. (1975) where an initial ice thickness distribution as measured by under-ice profile is followed through two years of known deformation and climatological thermodynamics. Table IV-1 gives the air density and ice thickness used in free drift simulations. One check point of these data appears during April 1976 when an under-ice profile was obtained by upward-looking, submarine-mounted sonar. Analysis of these data by Wadhams and Horne (1978) shows a mean draft of 3.7 m (average of two tracks if 200 km length crossing under camp Caribou). Converting mean draft to mean ice thickness is accomplished by multiplying by the ratio of ocean to water density to ice density  $\rho/p_i = 1.1$ . The mean ice thickness during April 1976 is observed to be 4.1 m. This observed value is about 5 percent larger than the April values calculated by Thorndike et al. (1975). It is likely that values in Table 1 for January through April are somewhat low since mean thickness should increase throughout winter. The history shown is probably dependent on initial conditions and the specific deformation history used by Thorndike et al. (1975). In any case, the values are reasonable and an uncertainty of 5 percent is acceptable.

Table I-1. Seasonal Variations in Ice Thickness and Air Density.

Month	$\bar{h}$ (cm)	$\rho_a$ (gm/cm <sup>3</sup> )
January	390	0.00147
February	390	0.00147
March	390	0.00145
April	390	0.00140
May	370	0.00136
June	355	0.00131
July	325	0.00129
August	295	0.00129
September	330	0.00133
October	370	0.00138
November	415	0.00144
December	405	0.00146

The Coriolis parameter is computed as

$$f = 2\Omega \sin\phi$$

where

$$\Omega = 7.29 \times 10^{-5} \text{ rad/sec}$$

$$\phi = \text{latitude}$$

The water stress is computed as

$$\tau_w = \rho_w c_w \left| \vec{v} - \vec{v}_g \right| B(\vec{v} - \vec{v}_g) \quad (\text{I.5 bis})$$

$$B = \begin{pmatrix} \cos(\beta+\pi) & -\sin(\beta+\pi) \\ \sin(\beta+\pi) & \cos(\beta+\pi) \end{pmatrix} \quad (\text{I.6 bis})$$

The water drag coefficient and turning angle used were  $c_w = 0.0055$  and  $\beta = 23^\circ$ , as given in McPhee (1977a). The geostrophic current  $\vec{v}_g$  was set to zero as previously explained.

## Appendix II. Temporal Averaging in Free Drift.

In Appendix I we have shown that the ice response to geostrophic wind direction is nonlinear while ice speed is nearly linearly related to wind speed at higher wind speeds. The air stress was also shown to be related nonlinearly to ice velocity, in both speed and direction. On the scale of one day we believe that using constant winds (and thus air stress) to compute ice velocity is a very good approximation. For time scales of a month, we believe that there is enough variability in the winds that the nonlinearities affect the ice response significantly.

It might be possible to adjust the drag coefficients and turning angles used in the model in order to make use of monthly (or other period) mean winds or air stress feasible. This would be desirable for computational reasons but no attempt has been made to do this. As an illustrative example though, we have computed the displacement of the grid point near Pt. Barrow during January using the mean January geostrophic wind and again using mean air stress. The free drift model used is the same one used for daily free drift, including the values of all parameters. Twenty-five years of data were processed.

In addition, we have computed the January displacement of the same grid point using Zubov's (1943) empirical estimate of ice motion; the ice moves 30 degrees to the right of the surface wind direction, at 1/50 the wind speed. Two methods are tried here. One method is to accumulate the daily drifts which are computed using Zubov's formula, and the other method is to apply Zubov's formula to the mean monthly surface winds. The difference in the monthly displacement between these two methods is due entirely to the spatial variation of the winds. This difference was small, averaging 4 percent in speed and a degree or two in direction so that it is not necessary to present the Zubov drift using monthly average winds. Surface winds were computed as 30 degrees to the left of and 55 percent of the speed of the geostrophic winds. These values of turning angle and wind speed ratio were computed from AIDJEX main experiment data (Albright, 1978, and Albright, personal communication).

The results of these several methods of computing free drift displacements are given in Table II-1. For comparison, the accumulation of daily free drift displacements as computed in the main body of this report are also given.

Using either monthly mean winds or monthly mean air stress in the free drift model produces an ice motion to the right of the daily free drift motion, just as



was predicted in Appendix I. The mean air stress produces an ice motion too large in magnitude while the mean winds produce a motion that is too small. Evidently a significant proportion of the monthly ice motion is brought about by lighter winds where the relationship between ice speed and wind speed is non-linear. Zubov's formula produces motion generally to the left of free drift and varying from year to year in being too small or too large in magnitude.

In Figure II.1a, we present the vector means of 25 years of January motions computed by each of the methods. The general observations made above apply to the means also. While it appears possible to tune the model or Zubov's formula to accurately estimate the mean motion of an ensemble of January's, the question of variation remains open and was not examined here. In Figures II.1b and II.1c, we show the motion for January 1975 and 1973 as examples of the year to year variation when the net motion was small and large, respectively.

Table II-1. Speed and Direction of Motion for January of Years 1953-1977  
 at Approximate Location 156.5° W. Longitude, 71.9° N. Latitude.  
 Distances are Given to the Nearest Kilometer, Direction to the  
 Nearest Degree.

Year	ΣF.D. (daily)		F.D. (monthly winds)		F.D. (monthly air stress)		Zubov's Formula	
	Distance	Direction	Distance	Direction	Distance	Direction	Distance	Direction
1953	101	87	41	67	142	55	87	120
1954	112	-74	51	-104	167	-93	96	-54
1955	155	70	112	51	214	63	150	90
1956	84	-95	42	-124	125	-105	89	-73
1957	150	-100	130	-123	239	-100	163	-84
1958	175	80	165	74	222	75	194	106
1959	77	33	50	21	104	25	90	68
1960	132	67	108	52	198	62	142	90
1961	220	65	221	54	283	63	236	85
1962	60	-53	30	-87	127	-39	73	-41
1963	61	15	24	-10	92	-5	64	47
1964	60	65	31	41	86	51	72	95
1965	87	55	62	34	135	47	100	80
1966	149	27	114	15	206	26	141	53
1967	66	-3	37	-33	98	-13	80	23
1968	66	-61	32	-93	94	-63	78	-39
1969	57	0	16	-31	87	-28	52	22
1970	73	107	40	96	96	115	100	131
1971	6	-164	1	-147	7	52	12	-92
1972	94	106	36	74	154	83	77	125
1973	210	-81	175	-98	250	-88	201	-61
1974	96	-122	43	-152	164	-139	96	-101
1975	56	43	13	-5	100	20	44	50
1976	66	70	32	39	108	57	70	95
1977	337	72	310	66	363	66	316	90

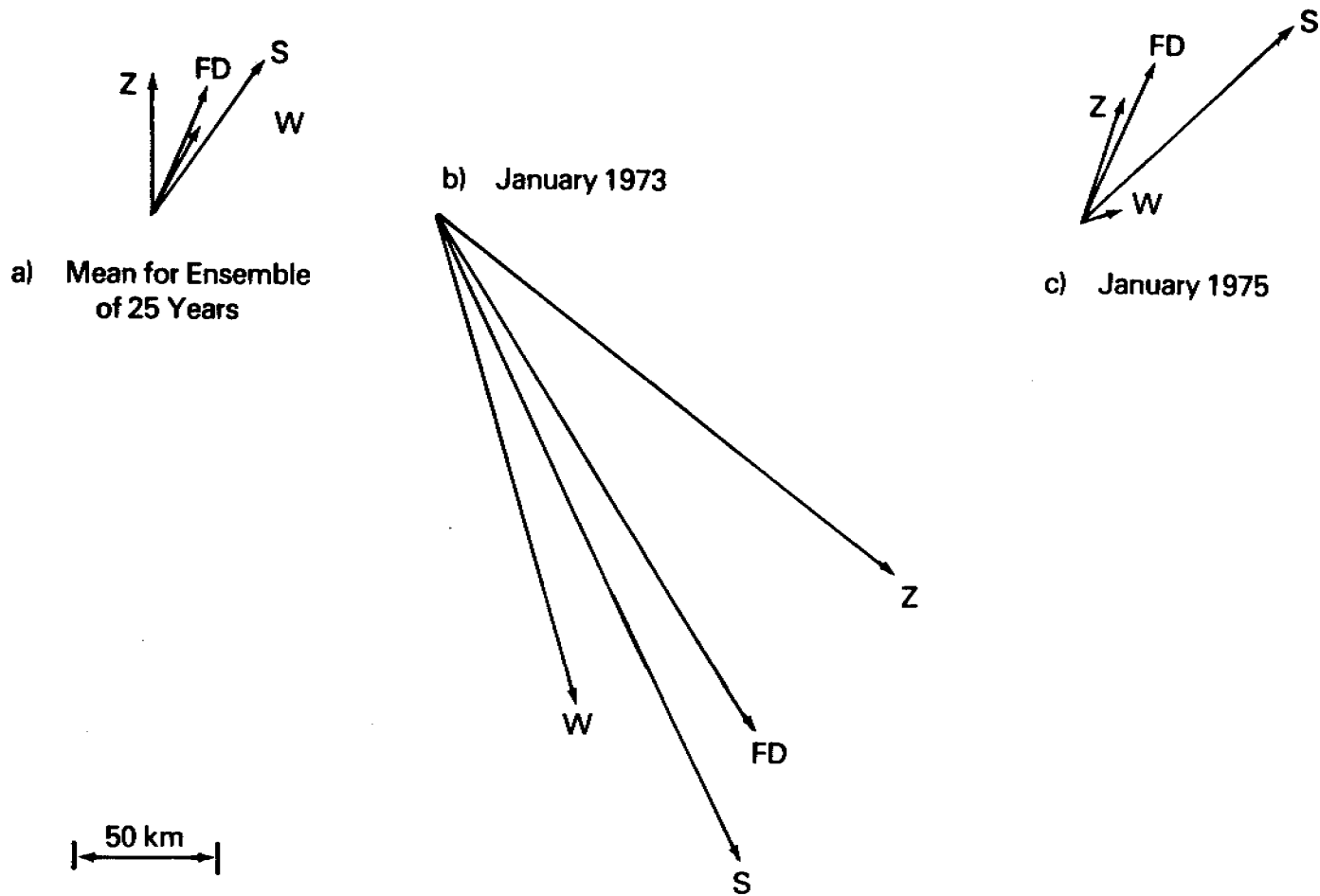


Figure II.1. (a) Mean of 25 Years Free Drift During January Computed by: 1) Summing Daily Displacements FD, 2) Using Monthly Mean Winds W, 3) Using Monthly Mean Air Stress S, and 4) Using Zubov's Empirical Formula Z. (b) Same Four Free Drift Calculations for January, 1975. (c) Same Four Free Drift Calculations for January, 1973.

### Appendix III. Observed Winter Ice Motion.

In general, winter ice dynamics are more complicated than summer ice dynamics due to the increased strength of the ice cover. We thought it likely that there would be less ice motion in the winter with a limit of no motion at times when ice strength is large enough to resist the applied air stress. This behavior was observed in February 1976 when the ice was strong enough to remain motionless during winds up to  $6 \text{ ms}^{-1}$  blowing over a long fetch (Pritchard, 1976). Of course, prior to that time the ice had been moving in response to the wind and at times winter ice motions must approach a state of free drift, depending on ice conditions, strength and direction of winds, and the recent history of the pack ice.

Although we expected the range of possible winter ice motions to be as large as the range in summer, we thought it possible that the typical winter ice motion would be small. To test this possibility, we examined the available drift station data for the Beaufort and Chukchi Sea regions for the months October through March. Unfortunately little of this observed motion is near shore, the region of primary interest, and the data concentration for any one year is sparse, except for the winter of 1975-76. This year is seen to be anomalous. The data sources, period observed and number of months of observed motions are given in Table III-1.

Table III-1. Source and Quantity of Winter Drift Station Data.

Source and Years	Oct	Nov	Dec	Jan	Feb	Mar
AIDJEX; 1975, 1976	3	6	9	14	14	14
AIDJEX; 1972	1	-	-	-	-	-
Russian Stations; 1964, 1970	1	1	-	-	-	-
Ice Island T3; 1959, 60, 62, 66	2	2	1	1	1	3
ARLIS 1&2; 1960, 1961	1	1	2	1	1	-
Total Observations:	8	10	12	16	16	17

Figures III.1 through III.6 show the monthly displacements (October through March) of the drift stations. The extremely large motion of the station near Pt. Barrow in January is associated with the Bering Strait breakout and is not considered with the rest of the data hereafter.

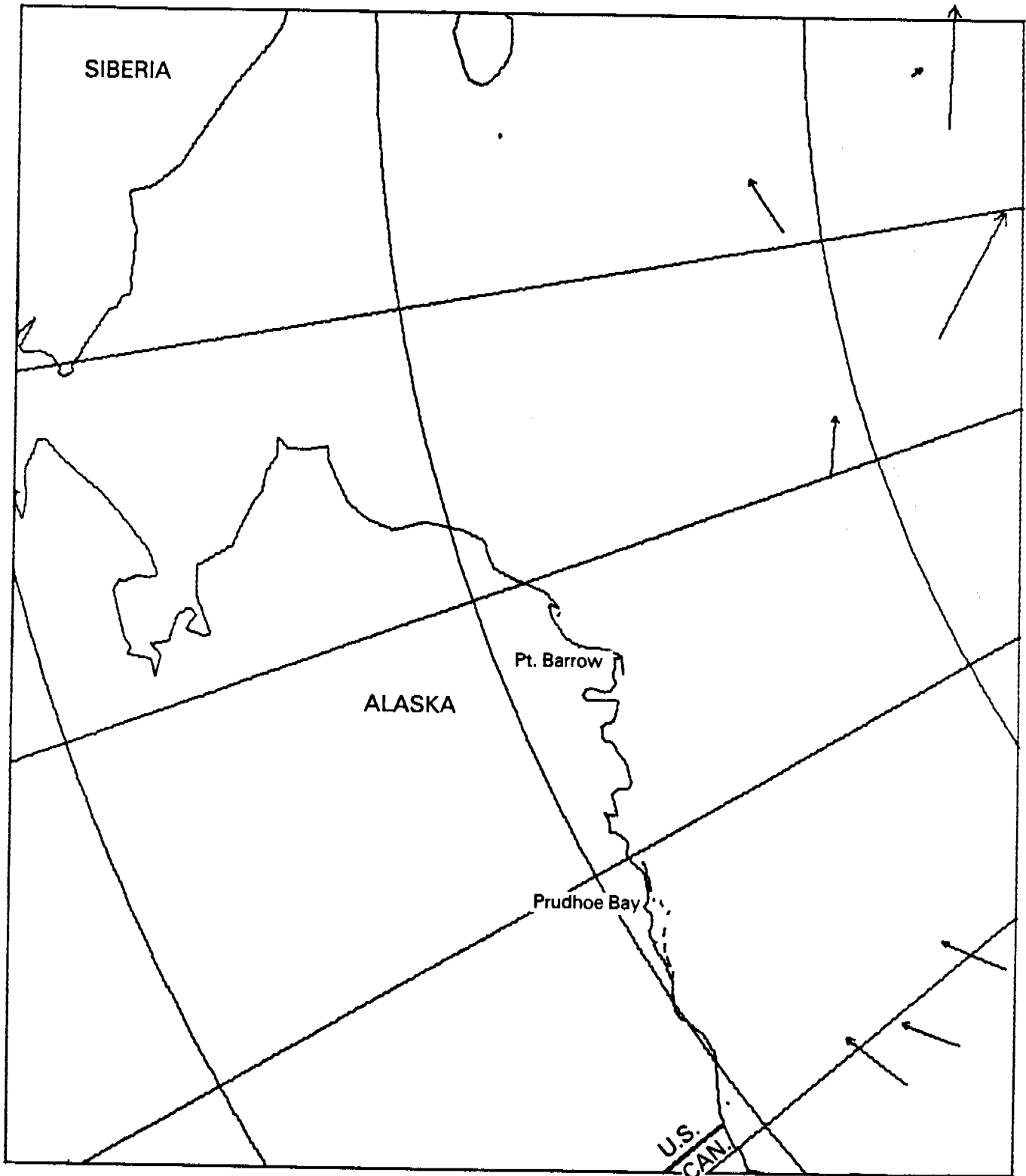


**Figure III.1. Observed Ice Station Displacements in Beaufort/Chukchi Seas for Month of October.**

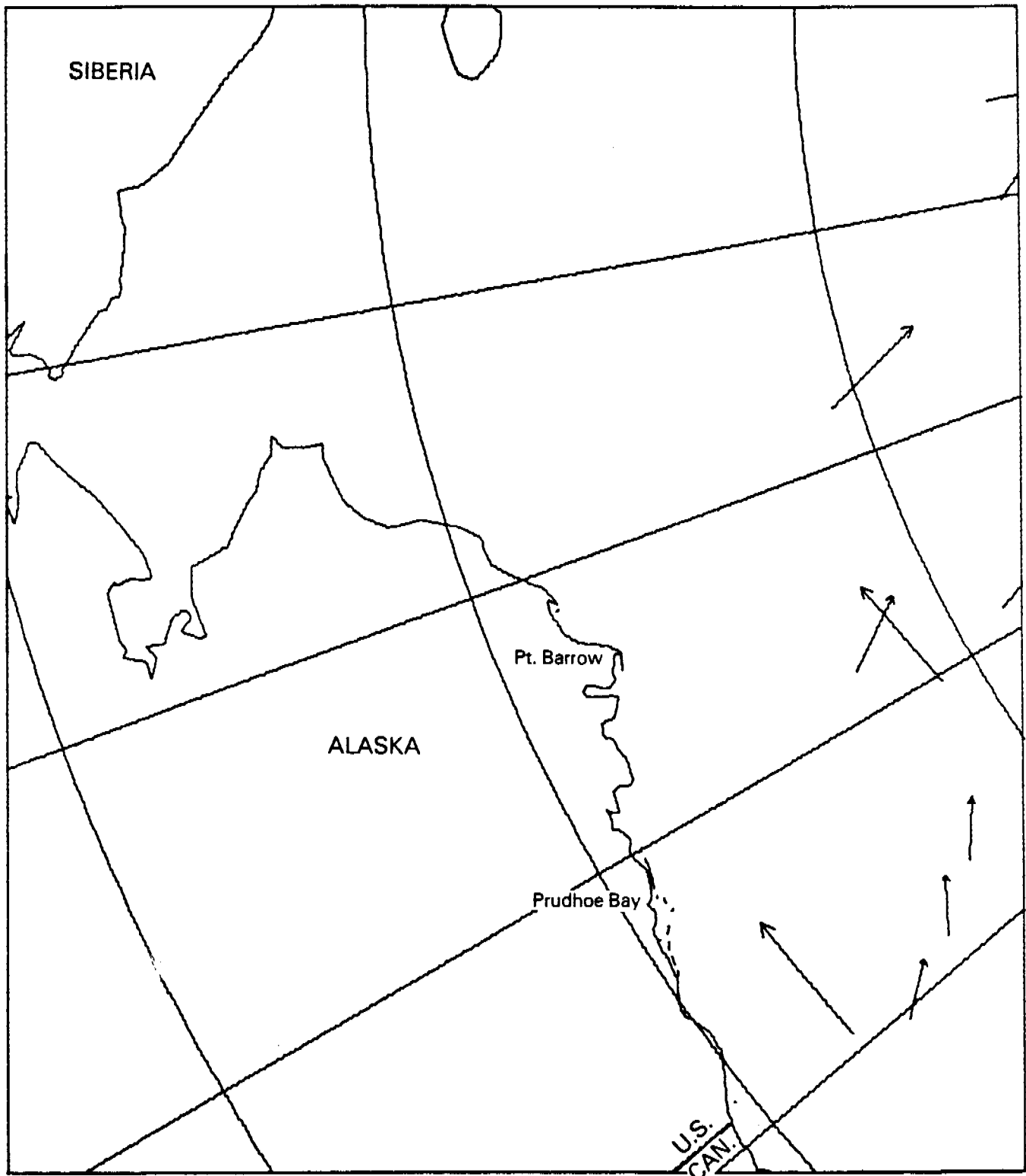


**Figure III.2. Observed Ice Station Displacements in Beaufort/Chukchi Seas for Month of November.**

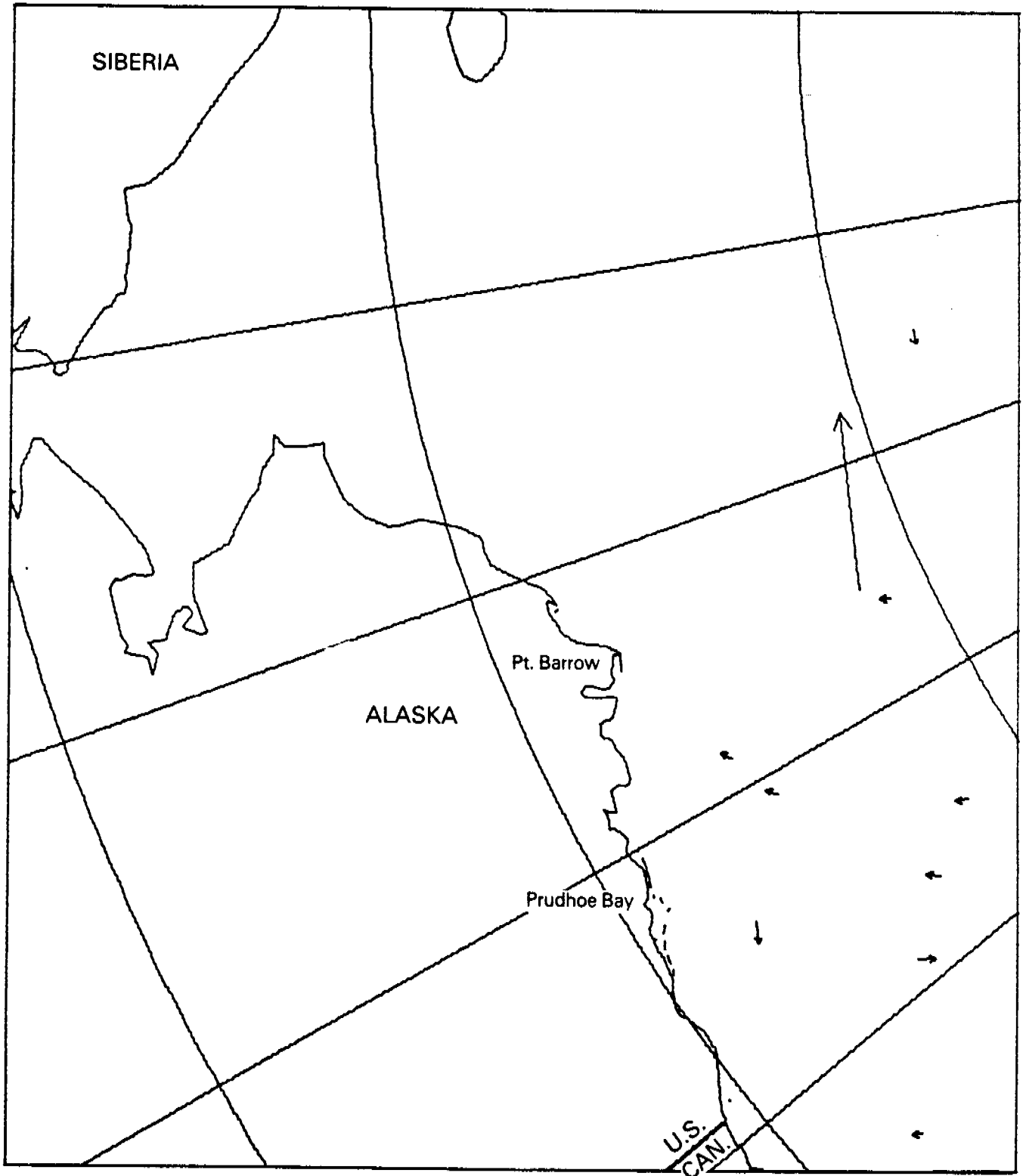


**Figure III.3. Observed ice Station Displacements in Beaufort/Chukchi Seas for Month of December.**

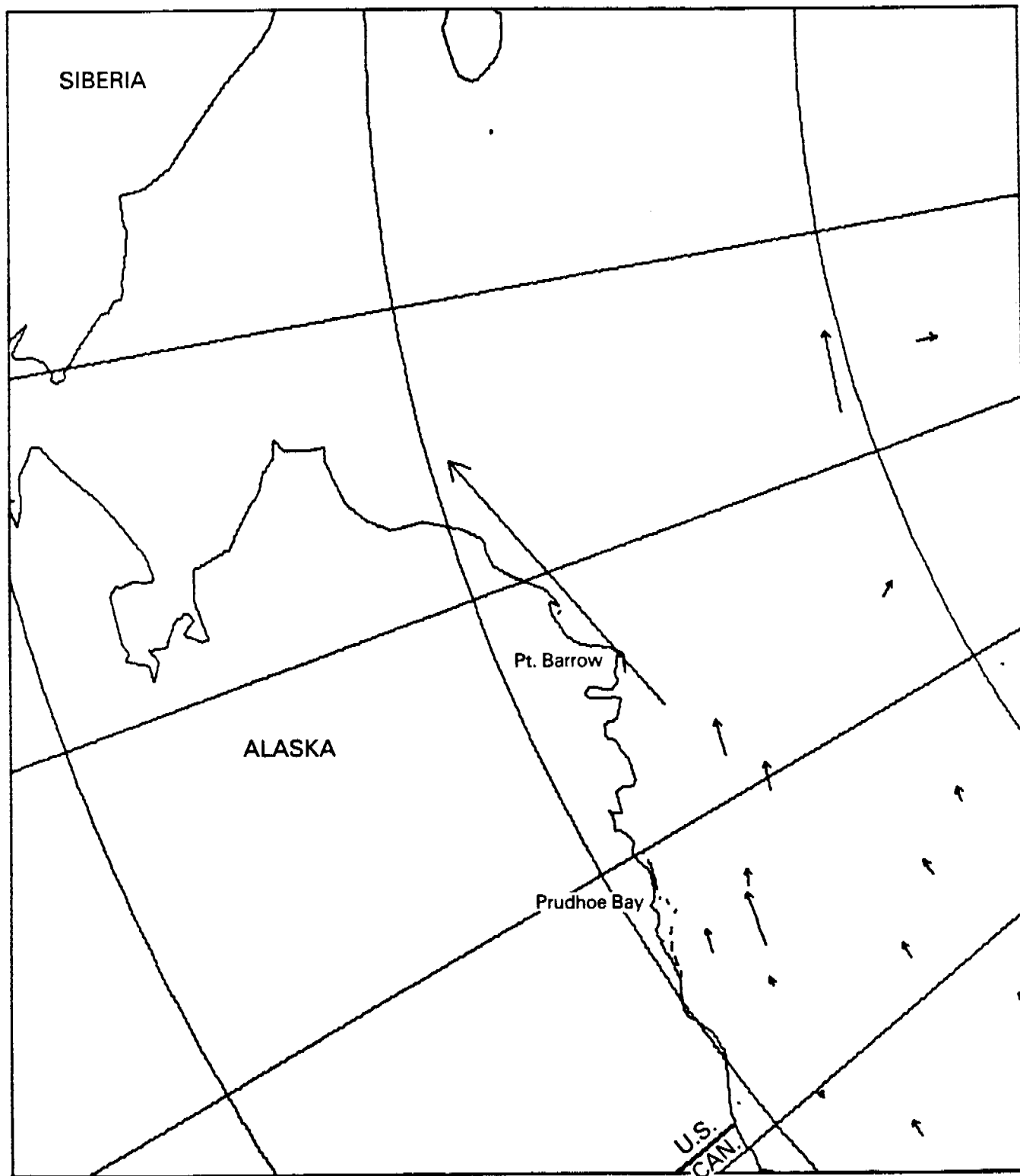


**Figure III.4. Observed Ice Station Displacements in Beaufort/Chukchi Seas for Month of January.**



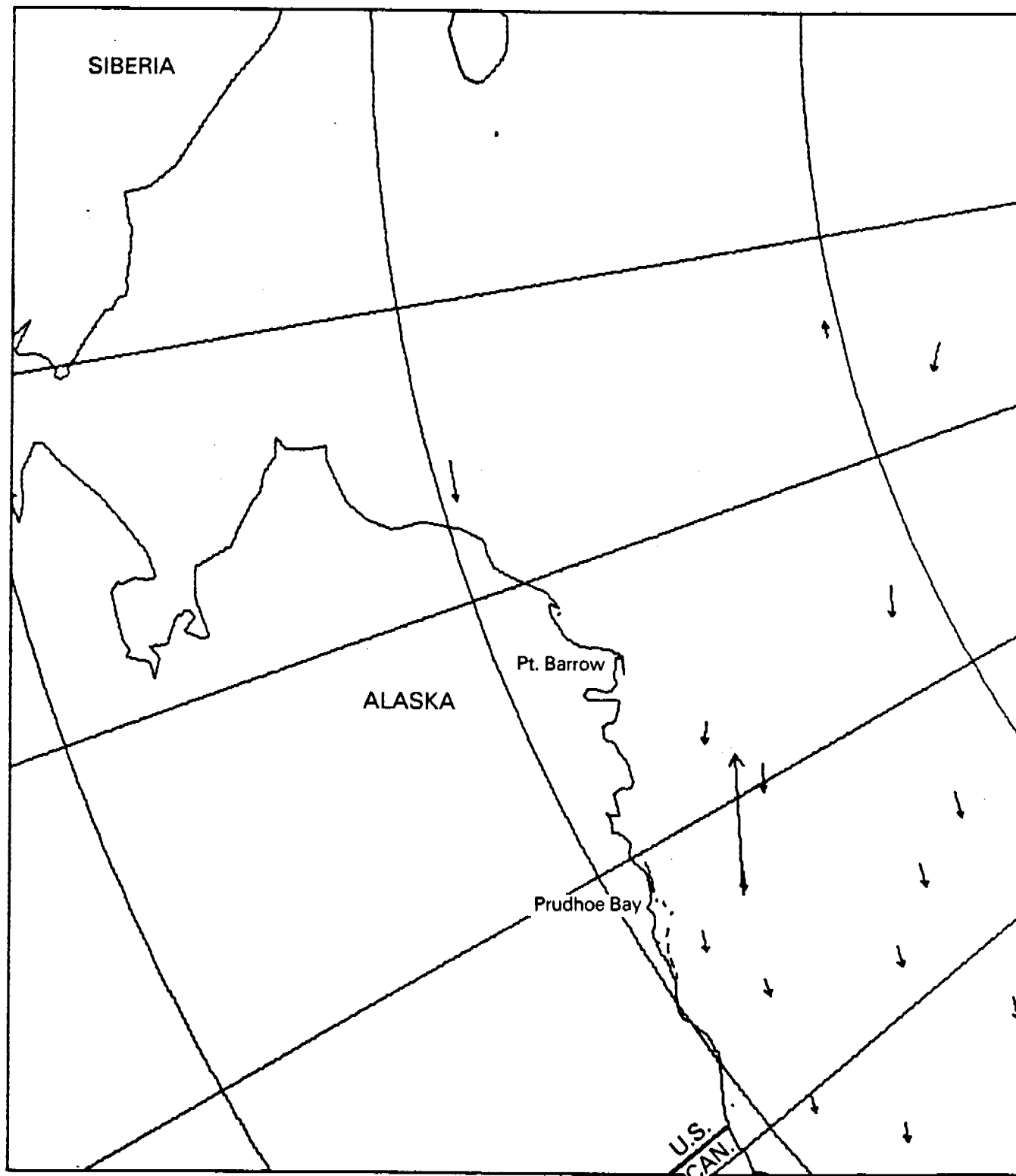


**Figure III.5. Observed Ice Station Displacements in Beaufort/Chukchi Seas for Month of February.**

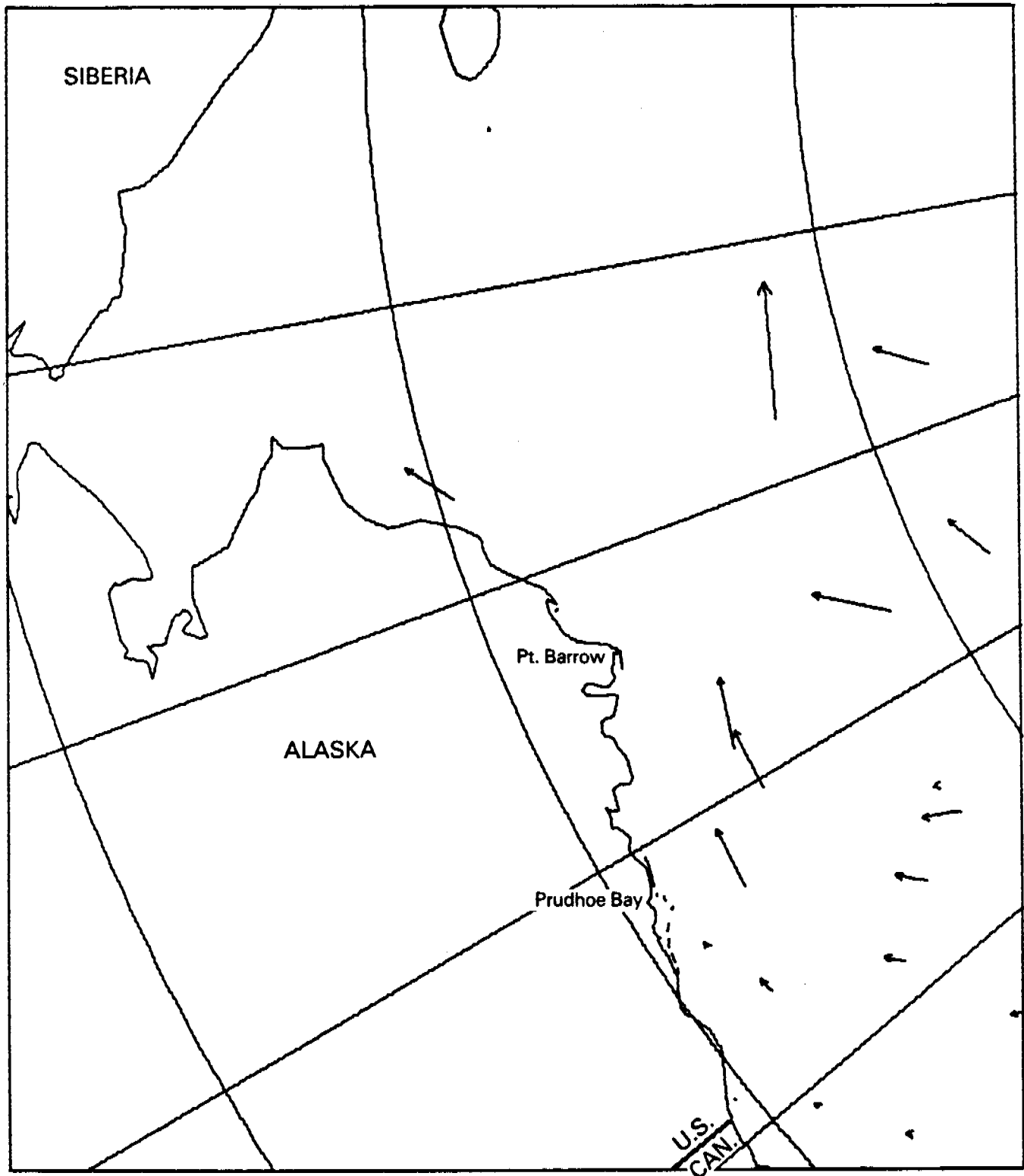


**Figure III.6. Observed Ice Station Displacements in Beaufort/Chukchi Seas for Month of March.**

It is obvious from Figures 1 through 6 that the range of winter motions is large. From December 1975 to March 1976 in the Eastern Beaufort Sea a period of little or no motion occurred, but generally it would be difficult to distinguish these from summer drift tracks. One cannot say that ice strength does not play an important role during winter, but the effect of ice strength is not obvious from looking at the individual drift tracks. Unfortunately the data density is much too low for computing reliable means and variability of observed drift. The observed range and typical values of displacement magnitude, by month, of the whole Southern Beaufort Sea area are presented in Table III-2.

Table III-2. Range and Typical Values of Observed Winter Drift in the Beaufort Sea.

Month	Range (km/month)	Typical Magnitude (km)
Oct	16-184	100
Nov	78-186	100
Dec	13-228	25
Jan	9-106	35
Feb	18-183	35
Mar	3-176	75

The typical values given in Table III-2 have no statistical significance; they are purely eyeball estimates. Furthermore, the drift data are heavily weighted toward one year, the winter of 1975-76. Displacements during that winter were generally much smaller than those occurring during other years.

It should be remembered that the free drift trajectories were computed using zero geostrophic ocean currents. It is expected that motions resulting from the currents alone are of approximately the same magnitude as the mean motion resulting from the air stress alone. The observed drift tracks include effects of the ocean currents. Since the direction of the currents is aligned with the general ice motion, the magnitude of the free drift trajectories will be increased by inclusion of currents, however, even when the ocean current contributions to free drift are considered, the range of observed motions still falls within the range of free drift motions. Therefore, we conclude that ice strength is important at times

during the winter season, but at other times free drift provides a reasonable approximation of the motion. Because of the small amount of observed drift data we have not tried to work out the actual distribution of winter motions. The most important conclusion, however, is that winter ice motions are not small enough so that they can be neglected. Instead they are closer to free drift estimates.

#### Appendix IV. Large Scale Free Drift.

During part of the year little open water is present in the Arctic and floes are connected by thin ice of up to two meters thickness. At these times, the inter-flow forces create a large scale stress that affects ice motion significantly, and the free drift model is inadequate. The quasi-steady momentum balance including the ice stress divergence,  $\nabla \cdot \underline{\sigma}$  is written by adding stress divergence to the free drift equation (I.12).

$$\underline{\tau}_a + \nabla \cdot \underline{\sigma} + \underline{\tau}_w(\underline{G}) - mfk \times \underline{G} = 0 \quad (\text{IV.1})$$

where the ice velocity relative to geostrophic current

$$\underline{G} = \underline{v} - \underline{v}_g \quad (\text{I.10bis})$$

has been introduced for convenience.

If we average the forces acting on the ice over some arbitrary region  $R$ , the form of the momentum balance equation remains the same but each term is averaged over region  $R$ . The average momentum balance becomes

$$\overline{\underline{\tau}}_a + \overline{f}_\sigma + \overline{\underline{\tau}}_w(\overline{\underline{G}}) - mfk \times \overline{\underline{G}} = 0 \quad (\text{IV.2})$$

$$\overline{\underline{G}} = \frac{1}{A} \int_R \underline{G} \, da, \quad \overline{\underline{\tau}} = \frac{1}{A} \int_R \underline{\tau} \, da, \quad \overline{f}_\sigma = \frac{1}{A} \int_R \nabla \cdot \underline{\sigma} \, da.$$

In this appendix, overbars are used to denote average quantities. This is different from Appendix I where overbars were used to denote nondimensional variables.

In a recent paper, Pritchard (1977) examined the AIDJEX plastic sea ice model (Coon, et al., 1974) and determined a bound for the average ice stress divergence  $\overline{f}_\sigma$  in equation (IV.2). For a circular area with diameter  $\ell$  and for a diamond yield surface with a compressive yield strength of  $p^*$  and shear strength of  $\tau^*$ , the magnitude of  $\overline{f}_\sigma$  is bounded as

$$\|\overline{f}_\sigma\| \leq \frac{4\sqrt{2}}{\pi} \frac{p^* + 2\tau^*}{\ell} \quad (\text{IV.3})$$

The average ice stress divergence bound depends upon the shape of the region  $R$ , the ice strength and shape of the yield surface, and is inversely related to the size of the region. For example, an ice strength of  $p^* + 2\tau^* = 2 \times 10^4 \text{ Nm}^{-1}$  and an  $\ell = 800 \text{ km}$ , limits the average stress divergence magnitude to less than  $0.04 \text{ Pa}$ . This is on the order of errors in the air stress.

How can we take advantage of this bound on  $\underline{f}_\sigma$ ? One method is to compute the velocity everywhere in  $R$  as the local free drift velocity

$$\underline{\tau}_a + \underline{\tau}_w(\underline{c}) - mfk \times \underline{c} = \underline{0} \quad . \quad (\text{IV.4})$$

Then, average the velocities over region  $R$

$$\bar{\underline{c}} = \frac{1}{A} \int_R \underline{c} \, da \quad (\text{IV.5})$$

so that  $\bar{\underline{c}}$  is the mean free drift response to local winds over region  $R$ . A second method of approximating  $\bar{\underline{c}}$  is to use the equation

$$\bar{\underline{\tau}}_a + \underline{\tau}_w(\underline{w}) - mfk \times \underline{w} = \underline{0} \quad (\text{IV.6})$$

where  $\underline{w}$  is the free drift response to the mean winds over region  $R$ .

Which of these methods is the more accurate? The first method seems to average the response more in the spirit of equation (IV.2) but requires more computation in practice. We note that in the case of free drift, when  $\nabla \cdot \underline{\sigma}$  is zero everywhere in  $R$ , the spatial average of equation (IV.4) is identical to equation (IV.2). In this case, the second method, equation (IV.6), produces an error in velocity due to the non-linear water stress term. A test of the two methods using AIDJEX air stress data and comparison with AIDJEX position data showed that the first method gave better results, but the improvement was modest. We choose to use equations (IV.4) and (IV.5) to approximate the large scale average velocity since computer costs are minimal for this test and we wish to eliminate all possible spurious differences.

The integral in equation (IV.5) is approximated as

$$\bar{\underline{c}} = \sum_{i=1}^n w_i \underline{c}(x_i, y_i) + \text{remainder} \quad (\text{IV.7})$$

following a method given by Abromowitz and Stegun (1965). The chosen algorithm has seven ( $n = 7$ ) points whose location and weights are shown in Figure IV.1.

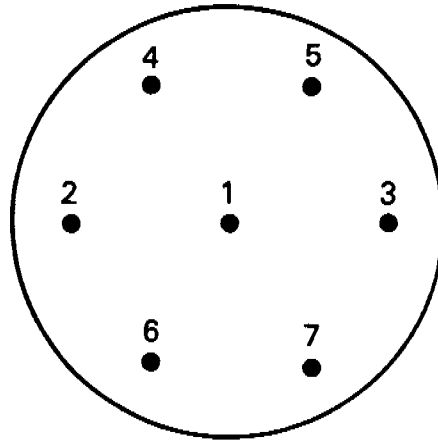


**Figure IV.1. Algorithm for Approximating Area Integral.**

Point	Location $(x_i, y_i)$ from center	Weight Factor, $w_i$
1	$(0,0)$	$1/4$
2,3	$(\pm \frac{\sqrt{2}}{3} r, 0)$	$1/8$
4,5,6,7	$(\pm \frac{\sqrt{1}}{6} r, \pm \frac{\sqrt{1}}{2} r)$	$1/8$

## Estimation of Errors in Drift Rates

To test the accuracy of large scale free drift calculations, some measure of error is required. Since we know the true drift (i.e., velocity) of some locations on the ice during the AIDJEX main experiment in 1975, we can define the "error" as the difference between the computed drift and the observed drift. During each month we expect the error to decrease, as the area over which we average increases until a limit is reached where spatial variations in driving forces are large enough to again increase errors. This minimum radius is expected to be small in summer and to grow larger as ice strength increases in fall and early winter. The radius of averaging is limited to no more than 400 km simply to stay within the region of interest and avoid averaging over land.

Two problems are immediately evident. How do we measure the difference in drift and what is the source of the error?

Errors may arise from several sources; errors in the observed ice drift, model parameters, geostrophic ocean currents, winds, spatial variations of driving forces, and neglect of internal ice stress. It is only this last mentioned source of error which will be affected by large scale averaging. Errors from observed ice drift and model parameters are expected to be small and are constant for all radii of averaging. The winds are also thought to be accurate and differences due to spatial variation of the winds will be very small. We therefore neglected these sources of error. Unfortunately, errors in geostrophic ocean currents are not expected to be small compared to errors from neglecting ice stress.

The geostrophic flow which has been used in the AIDJEX model is a modified version of the dynamic topography compiled from historical data by Newton (1973). The main feature is a high pressure dome resulting in anticyclonic flow in the Canada Basin. McPhee (1978a) observed that because of the anomalous drift patterns of the AIDJEX array during 1975 there is some question whether the historical topography is appropriate for this time. In addition, when we computed the daily average error between free drift and observed velocities, we could see some correlation between the error and geostrophic currents.

McPhee (1978b) presents some of the 1975-1976 AIDJEX oceanographic data. Because of instrument error he does not consider the 30 meter current measurements very reliable, but we used these data to estimate mean monthly currents. The



procedure was to plot the mean current/ice ratio, and angle, pick off average monthly ratios and angles from the plots, then use the mean monthly ice velocities to compute the current  $\vec{v}_g$ . These currents are approximations based upon probably inaccurate data but we felt they might better represent actual currents affecting the ice during 1975. These "measured" currents were smaller in magnitude than currents based upon the dynamic topography and with directions suggesting the gyre center was located further south. Using the "measured" currents in the free drift calculations reduces the average daily errors slightly.

Our conclusion is that we do not know the ocean currents accurately during 1975. We have estimated a bound on the error when currents are neglected entirely in the free drift calculations. McPhee (1977a) has shown that during the summer of 1975 the ice was in a free drift state and a point free drift model should accurately represent the ice motion. Since other errors are relatively small, the difference between computed relative ice motion (Appendix I) and observed ice motion will approximate the geostrophic current. The currents are seen to be small, less than 1 cm/sec in the central Beaufort Sea, but significant in terms of displacement since the currents are assumed steady over periods of many days. Unfortunately, our best estimate of the currents in the central Beaufort has speeds of 1 to 3 cm/sec. With that much possible error in the currents, we felt it best to neglect currents entirely and compute ice velocities relative to the deep currents.

How we measure the error in free drift is also important. When we compare the errors resulting from averaging over different size areas, a large and unknown error from some other source (i.e., ocean currents) can make the results inconclusive. Fortunately, as we show below, we have one error measure that is relatively uncontaminated by errors in ocean currents, even when currents are neglected entirely.

Errors in magnitude and direction are a common measure for vector quantities. Statistics on these error measures are not entirely satisfactory though. Mean errors in speed and direction bear no relation to the total displacement error because errors in direction will sometimes cancel when summed. Speed and directional errors may also be confounded with errors in the ocean currents.

We therefore chose the vector mean and standard deviation as our primary error measures. The standard deviation is not affected by cancellation of daily values and the mean error gives a direct indication of monthly displacement error. The standard deviation is seen to be especially useful because it is least affected by ocean currents.

Computation of the mean error and standard deviation of the error follows standard statistical definitions. Let  $\tilde{v}$  be calculated daily velocity, and  $\tilde{w}$  be observed daily velocity. Although we use no sub- or superscript, each variable is evaluated daily. The daily velocity error is

$$\tilde{e} = \tilde{v} - \tilde{w} \quad . \quad (\text{IV.8})$$

During a month the mean error is

$$\bar{\tilde{e}} = \frac{1}{N} \sum \tilde{e} \quad (\text{IV.9})$$

where  $N$  is the number of daily observations during the month. The standard deviation of the error is

$$s_e = \left( \frac{1}{N-1} \sum ||\tilde{e} - \bar{\tilde{e}}||^2 \right)^{\frac{1}{2}} \quad . \quad (\text{IV.10})$$

However, without accurate estimates of currents,  $\tilde{v}_g$ , we cannot compute  $\tilde{e}$  directly.

If we introduce the relative ice velocity  $\tilde{G}$  from equation (I.14) by separating the geostrophic current  $\tilde{v}_g$

$$\tilde{v} = \tilde{G} + \tilde{v}_g \quad (\text{I.14 bis})$$

then the error, mean error and standard deviation we have actually computed are

$$\tilde{\epsilon} = \tilde{G} - \tilde{w} \quad (\text{IV.11})$$

$$\bar{\tilde{\epsilon}} = \frac{1}{N} \sum \tilde{\epsilon} \quad (\text{IV.12})$$

$$s_\epsilon = \left( \frac{1}{N-1} \sum ||\tilde{\epsilon} - \bar{\tilde{\epsilon}}||^2 \right)^{\frac{1}{2}} \quad . \quad (\text{IV.13})$$

Combining equations (IV.8), (IV.11) and (I.14) we see that

$$\bar{e} = \bar{\epsilon} + \bar{v}_g \quad (\text{IV.14})$$

and it follows that when geostrophic ocean currents are included in calculating the ice drift, the mean daily error is

$$\bar{e} = \bar{\epsilon} + \bar{v}_g \quad (\text{IV.15})$$

and the standard deviation of the error  $\epsilon + v_g$  is

$$S_e = \left( S_\epsilon^2 + S_{v_g}^2 + 2 \text{cov}(\epsilon, v_g) \right)^{1/2} \quad (\text{IV.16})$$

where the covariance is bounded as

$$-S_\epsilon S_{v_g} \leq \text{cov}(\epsilon, v_g) \leq S_\epsilon S_{v_g} \quad (\text{IV.17})$$

When ocean currents are constant along the month-long trajectory, or nearly constant, then the mean and standard deviations of  $v_g$  are

$$\bar{v}_g \approx \bar{v}_g \quad \text{and} \quad S_{v_g} \approx 0 \quad (\text{IV.18})$$

The standard deviation of daily errors  $e$  becomes

$$S_e = S_\epsilon \quad (\text{IV.19})$$

If  $v_g$  does vary, we see from equations (IV.16) and (IV.17) that the standard deviation of the daily error is bounded by

$$S_e \leq S_\epsilon + S_{v_g} \quad (\text{IV.20})$$

which shows the range of influence that ocean current variations may have on standard deviation of the errors  $S_e$ .

Since we believe that the ocean currents are nearly constant along a month-long ice trajectory,  $S_{\tilde{v}_g}$  will be much smaller than  $S_{\tilde{e}}$  and equation (IV.19) will be correct. The mean current though is thought to be at least as large as the error measure  $\overline{\tilde{e}}$  and can possibly be in the opposite direction. Thus, the measured error  $\overline{\tilde{e}}$  is not a good approximation of  $\overline{e}$ , and in fact, depending on the direction of  $\overline{\tilde{v}_g}$ , can produce results contradictory to results had we been able to compute  $\overline{e}$  directly using accurate currents. Furthermore, directional errors tend to cancel out in the mean, but not in the standard deviation. For these reasons, the standard deviation is the preferred error measure.

### Accuracy of Large-Scale Free Drift

The AIDJEX data set provides valuable information to test how accurately a large scale free drift model can predict daily ice motions. The geostrophic and surface winds and the ice drift has been measured accurately during this period. Data from June through December 1975 were used for testing the large scale free drift model since this provides a variety of ice conditions; from spring when the ice still has considerable strength, summer when free drift is the expected mechanism, and fall and early winter when the ice is constantly gaining strength through freezing. Furthermore, the AIDJEX main experiment was located near the center of the Beaufort Gyre so that ocean currents are smaller than in other regions.

The free drift velocity is averaged over a circular area  $A$  of radius  $R$ . The radius was varied from  $R = 0$  (local free drift) to  $R = 400$  km, in increments of 100 km. The average velocity over  $A$  is approximated by the weighted average algorithm presented earlier in this appendix.

To measure how well the large scale free drift model performed, we compared the resulting daily velocities with observed velocities. The observed velocity was the daily average velocity of the average position of the three outer manned camps of AIDJEX array. This temporal and spatial averaging was a simple way of removing the high frequencies of the observed velocity. Comparisons of daily velocities were made for each one month period. Several different error measures were introduced in our attempts to quantify the error magnitudes and when possible to determine the cause of the errors.

Our primary error measures are the mean and standard deviation of the daily velocity vectors. These variables were introduced previously in this report. The mean ice drift error  $\bar{e}$ , equation (IV.15), depends on the average error due to winds and to the mean ocean current. We present  $\bar{\epsilon}$ , the average error due to winds, since we have no accurate measure of  $\bar{v}_g$ . The standard deviation of the daily velocity errors during each month, have been shown to depend on variations in error due to winds and to the variations in ocean currents. When ocean current variations are small during a month then standard deviation of ice motions is attributable almost entirely to errors in wind forcing of relative velocity  $\tilde{G}$ .

Errors in speed and direction between observed and simulated velocity vectors are studied. These appeared desirable because they are commonly used. However, we could not separate ocean current errors and this problem remains of concern. When  $\tilde{v}_g \approx 0$ , our previous analysis of free drift does indicate that speed errors are

caused by errors in wind speed and the ratio of drag coefficients, equation (I.31), and errors in direction are caused by errors in wind speed, in ocean boundary layer turning angle and in wind direction, equation (I.32). It should be pointed out that a possible error exists in computing  $\bar{\alpha}$ , the average direction error. When the winds are light and the ice is not wind driven, it is possible for the observed and computed winds to be in nearly opposite directions. In that case, it is possible for large negative and large positive angles to average out to near zero, an error of approximately 180 degrees. We did not do anything about this except observe that it rarely happened and would have little affect on  $\bar{\alpha}$ . Standard deviations of errors in speed  $E$  and  $\alpha$  were computed and studied, but are not presented since little additional information was found.

The total monthly displacement errors are also presented as examples of the errors we can expect. The displacement errors give no new information as an error measure since they are merely the mean daily velocity errors times the number of days in a month and a scaling factor.

The coefficient of meandering (Dunbar and Wittman, 1963), equal to the total distance traveled divided by the net distance traveled was also found to be useful. Generally, we would expect wind driven ice to wander about more (have a higher coefficient of meandering) than ice constrained by internal stress.

The velocity components for the month of October for radii of 0, 100, 200, 300 and 400 km are shown in Figure IV.2. In general it appears that free drift velocities, whatever the radius of large scale averaging, agree fairly well with observed velocities. That is, the free drift model does approximately the right thing at the right time. Differences can be seen in the free drift velocities between various radii, but quantitative judgment is difficult.

The ice trajectories for the months of September, October and November are shown in Figures IV.3, IV.4 and IV.5, respectively. The observed trajectory is plotted as a heavy line, point free drift trajectory as a light line and large scale average free drift trajectory (with radius = 300 km) as a dashed line. The trajectories for October and November are somewhat disappointing since this is the time of year when we hoped large scale free drift would be most useful. Position errors as large as 40 km occur at times although final position errors are 15 to 20 km. It does appear that large scale averaging improves the trajectory fit for October and November, but not overwhelmingly. The improvement in September is somewhat better.

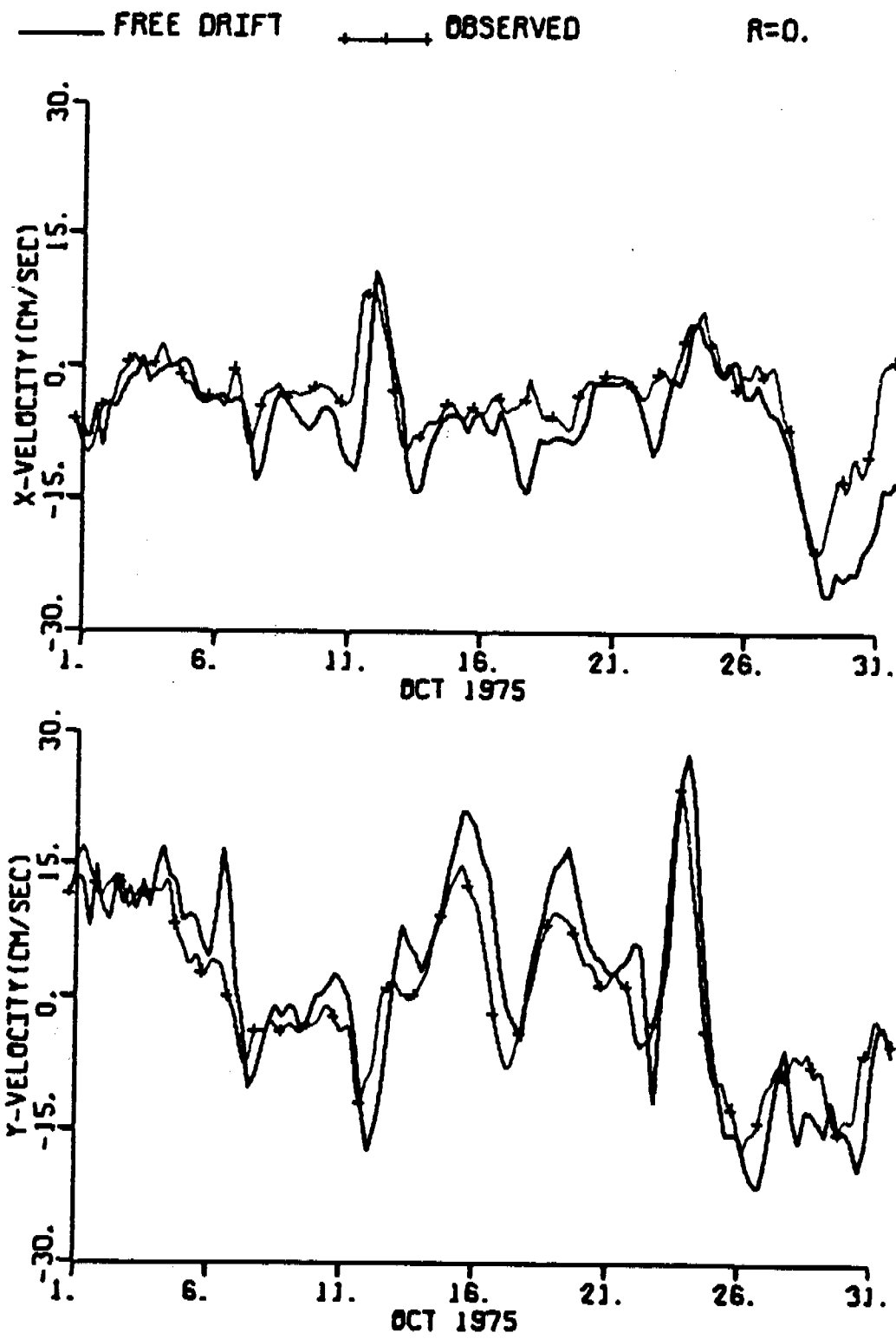


Figure IV.2a. Observed and Free Drift Velocity Components of AIDJEX Manned Camp Area for October, 1975. Area for Which Free Drift Velocity is Averaged is Circle of Radius:  $R = 0$  km.

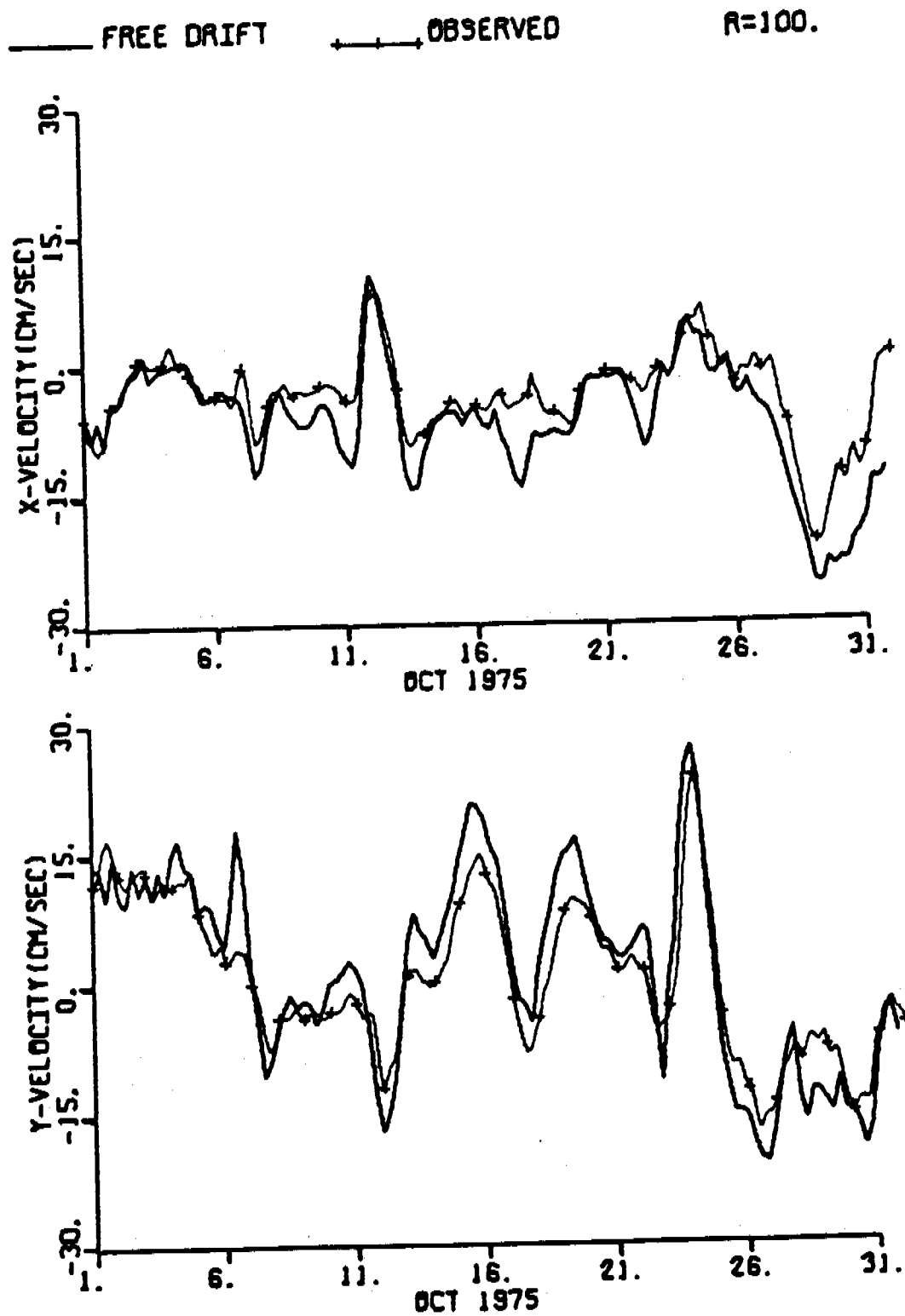


Figure IV.2b. Observed and Free Drift Velocity Components of AIDJEX Manned Camp Area for October, 1975. Area for Which Free Drift Velocity is Averaged is Circle of Radius:  $R = 100$  km.



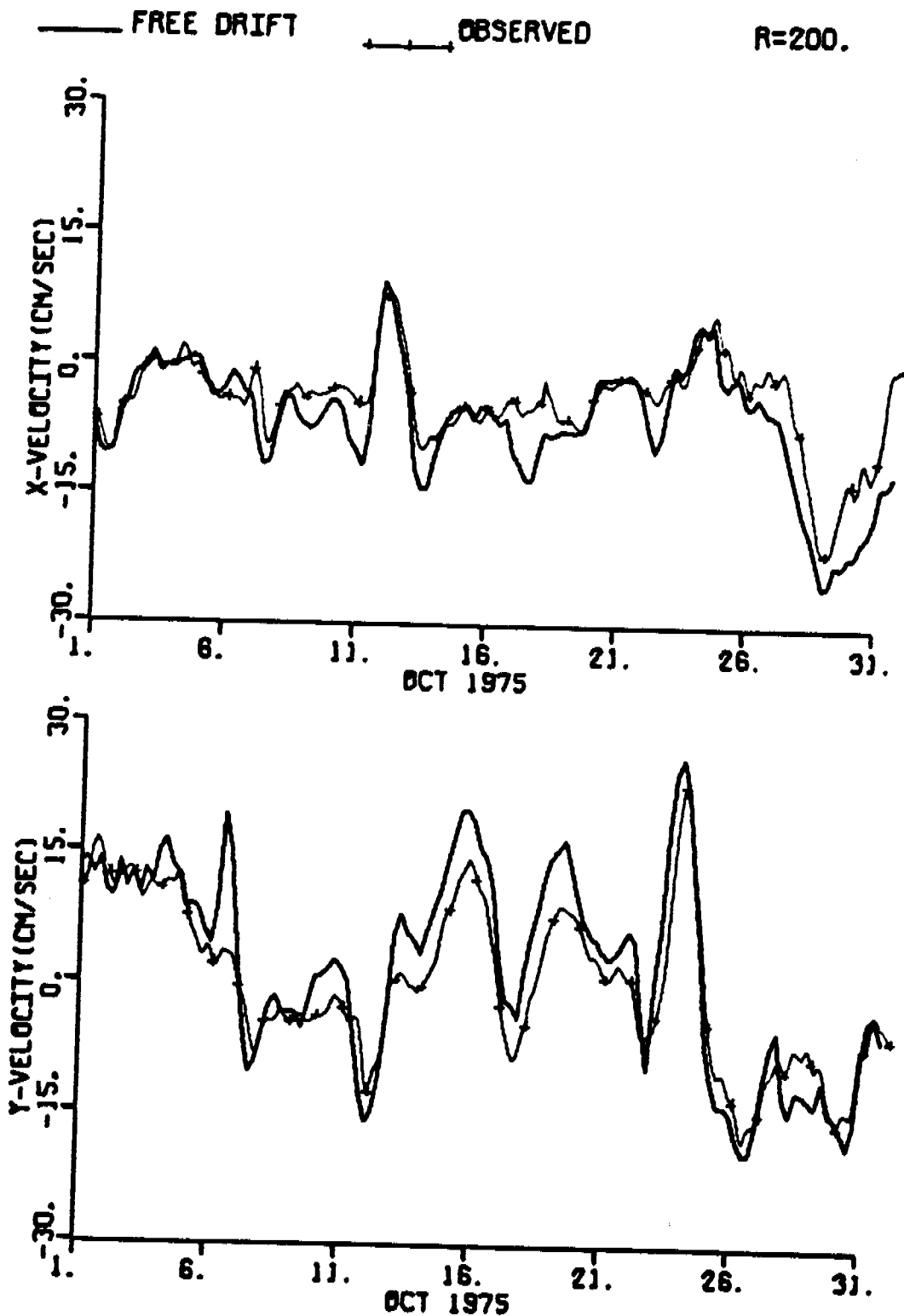


Figure IV.2c. Observed and Free Drift Velocity Components of AIDJEX Manned Camp Area for October, 1975. Area for Which Free Drift Velocity is Averaged is Circle of Radius:  $R = 200$  km.

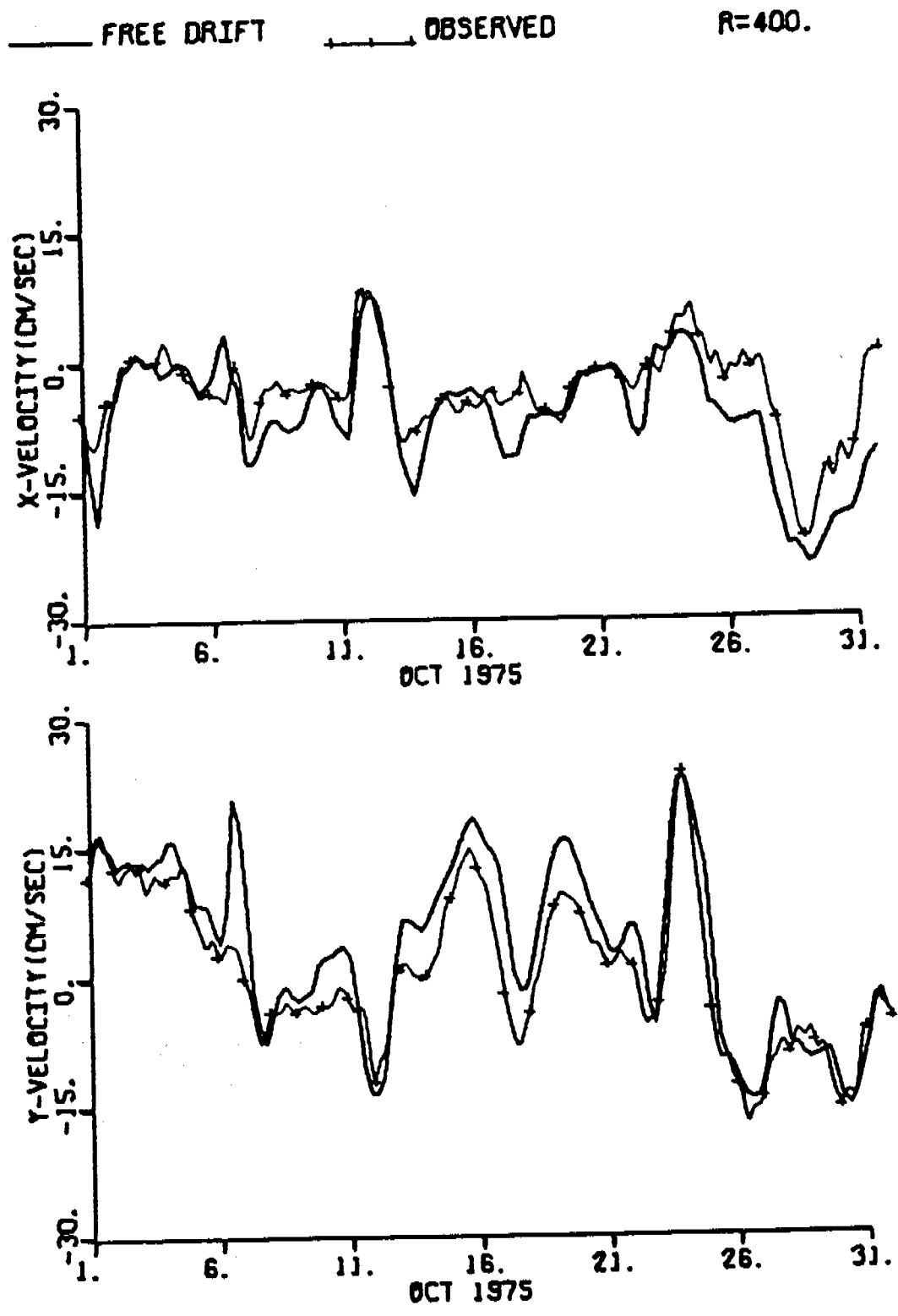
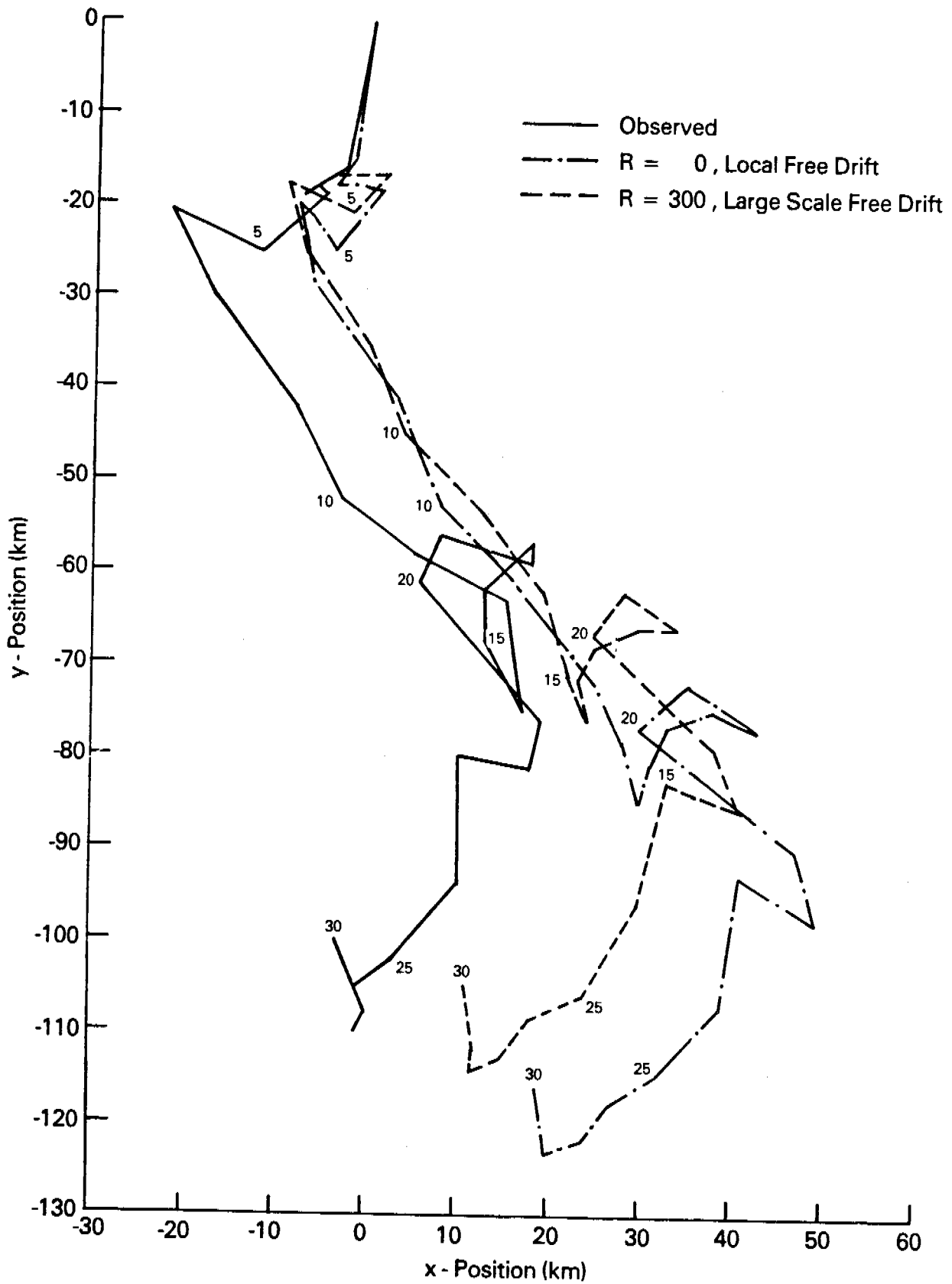


Figure IV.2d. Observed and Free Drift Velocity Components of AIDJEX Manned Camp Area for October, 1975. Area for Which Free Drift Velocity is Averaged is Circle of Radius:  $R = 400$  km.



**Figure IV.3. Ice Trajectory for September, 1975. Heavy Line - Observed, Broken Line - Free Drift, Dashed Line - Large Scale Average Free Drift (R = 300 km).**

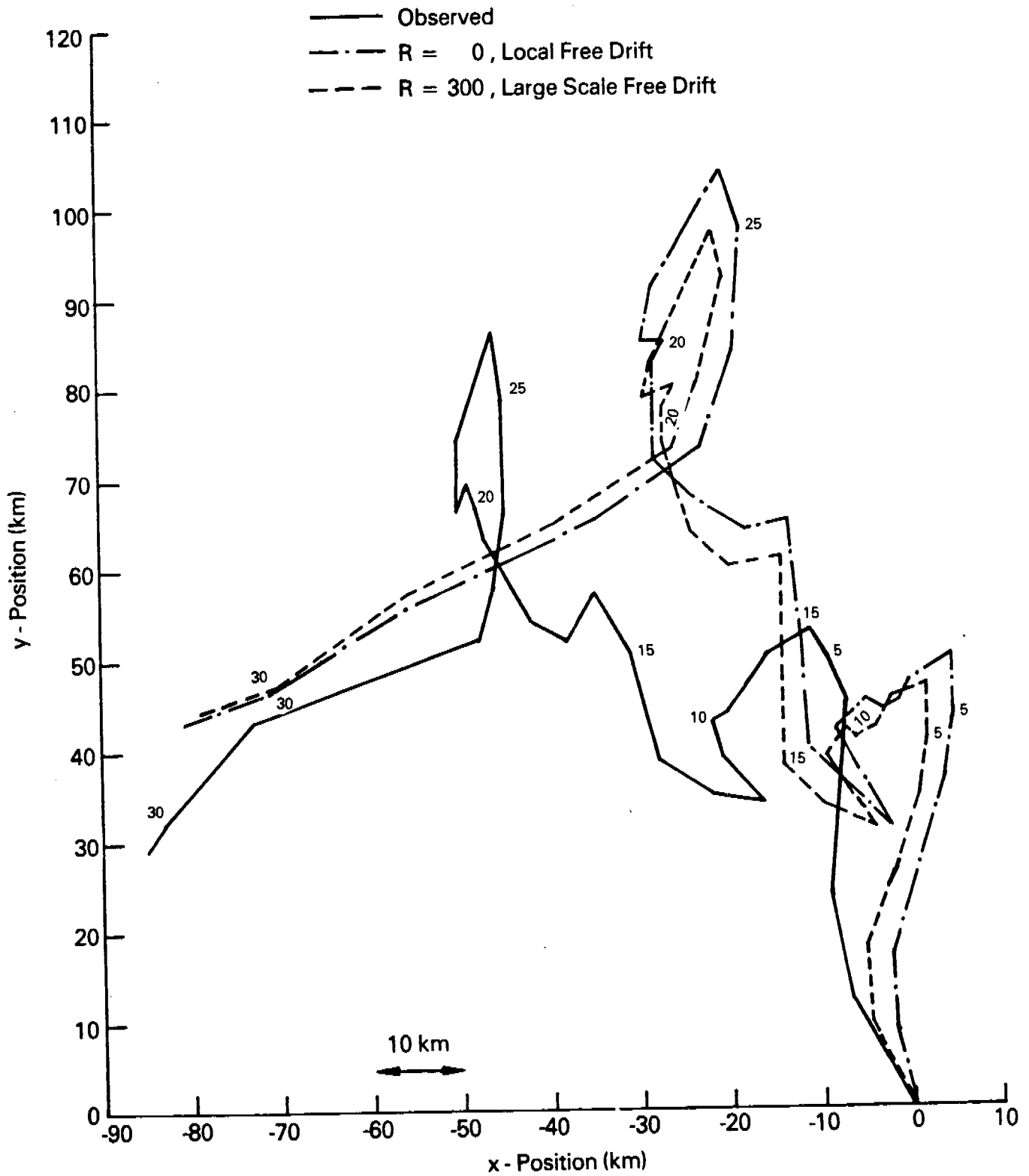


Figure IV.4. Ice Trajectory for October, 1975. Heavy Line - Observed, Broken Line - Free Drift, Dashed Line - Large Scale Average Free Drift (R = 300 km).

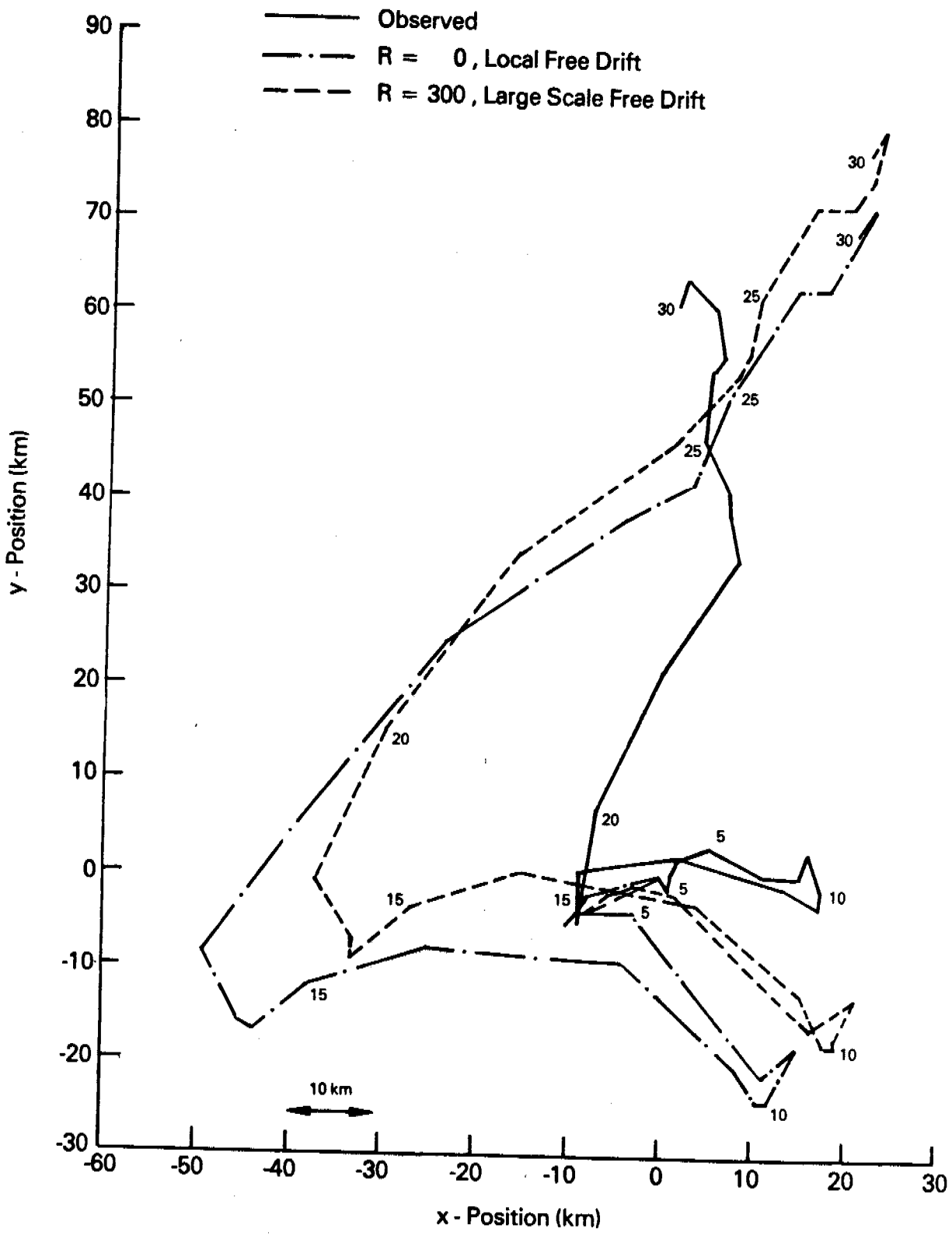


Figure IV.5. Ice Trajectory for November, 1975. Heavy Line - Observed, Broken Line - Free Drift, Dashed Line - Large Scale Average Free Drift (R = 300 km).

During September we observe that for the majority of days, the free drift velocity agrees fairly well in both speed and direction. The discrepancy in the trajectories seem to result from a poor fit around the 5<sup>th</sup> and again around the 15<sup>th</sup> day. One possible explanation for this is that the ice was not completely wind driven for the few days about those dates. Another explanation is inaccurate estimates of the winds during those periods.

Looking at the October trajectories there are no obvious periods of large disagreement between observed and free drift trajectories. Rather the free drift motions seem to be generally to the right of observed motions and the daily distances traveled to be too small at first and then too large. Increased ice strength would explain this, but inaccurate estimates of the driving forces cannot be ruled out.

For November, the free drift trajectories fit the observed worst of all. Not only are speed and direction off, but for the first five days there is no resemblance of trajectories at all. Again increasing ice strength would explain the discrepancy.

To see the effect of large scale averaging over the 7-month period, various error measures are listed in Table IV-2 by month and by radius of averaging. The quantities given in Table IV-2 are magnitude of the mean error velocity  $|\bar{\epsilon}|$ , standard deviation of the error velocity  $S_{\epsilon}$ , free drift coefficient of meandering, observed coefficient of meandering, mean daily difference in speed  $\bar{E}$ , and angle  $\bar{\alpha}$ , monthly displacement error and observed monthly displacement. Plots of several of these quantities are also shown in Figures IV.6, IV.7, IV.8, and IV.9.

The daily mean velocity errors are shown in Figure IV.6. For local free drift simulations, the errors are in the range 0.5 to 1.0 cm/sec, corresponding to a monthly displacement error of about 13 to 26 km. Looking back at the trajectories, Figure IV.5 (November) for instance, we see that during a 1-month period, displacement errors can be much larger than that.

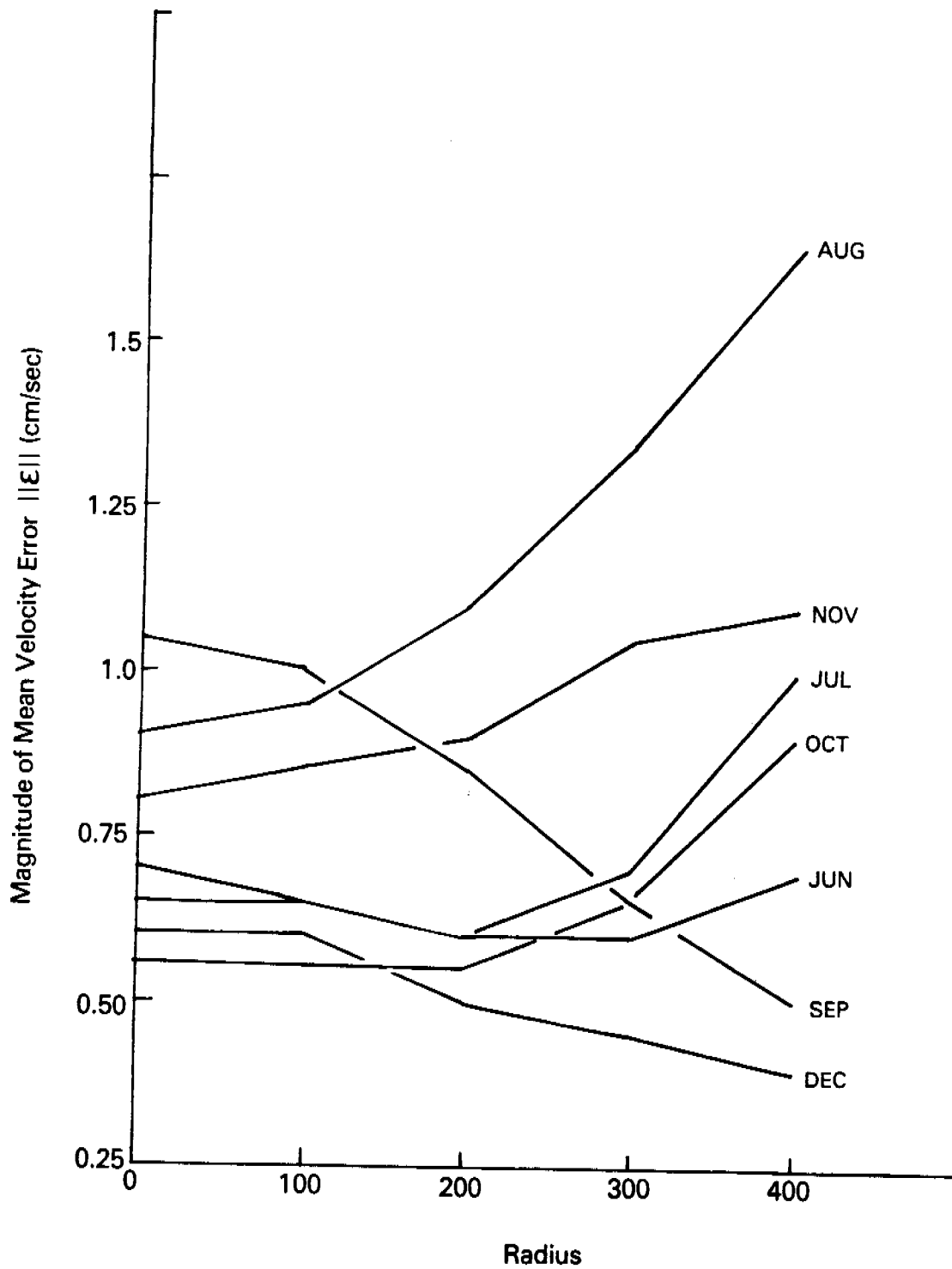


Figure IV.6. Mean Daily Velocity Errors for June Through December for Radii of 0, 100, 200, 300 and 400 km.

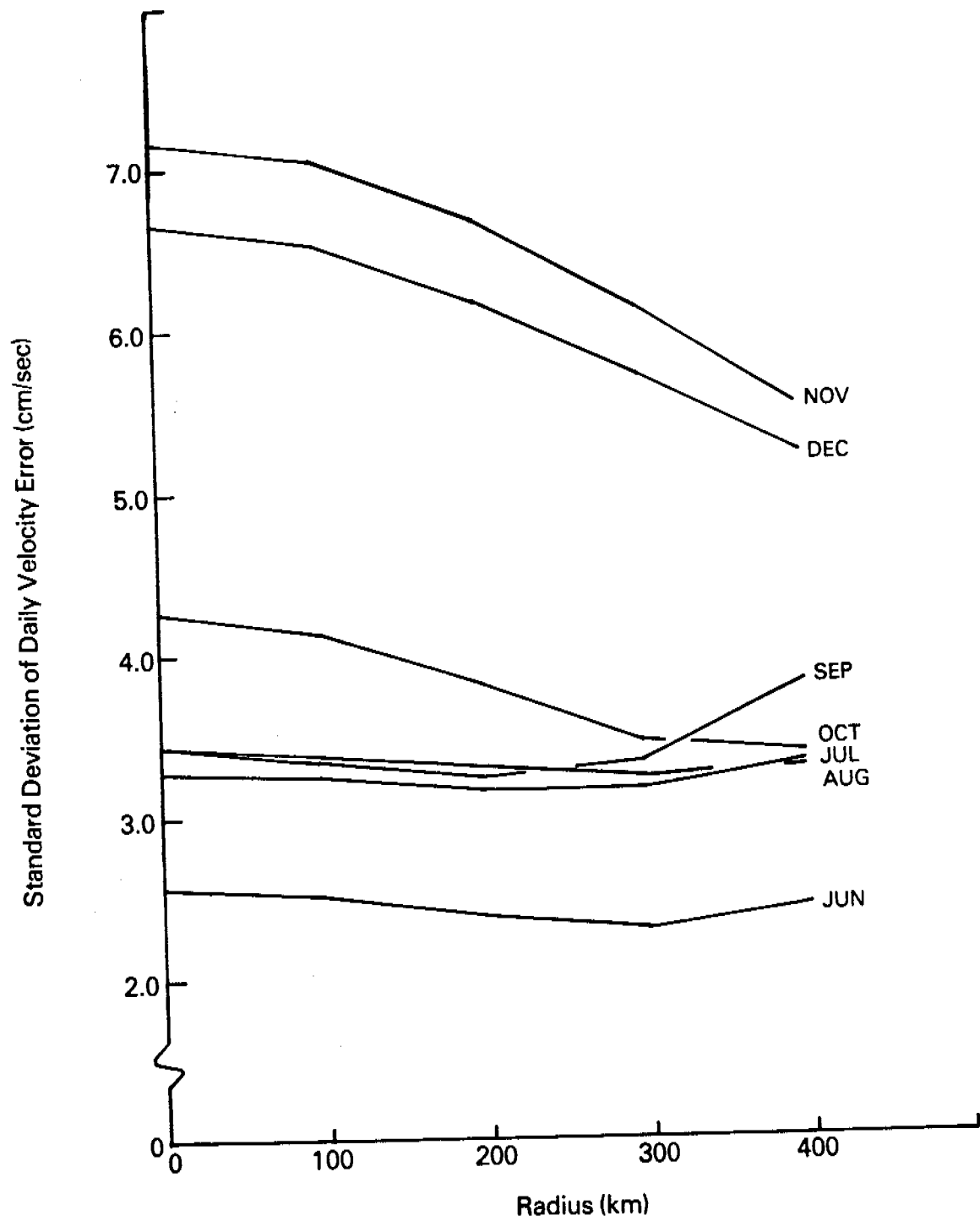


Figure IV.7. Standard Deviations of Daily Velocity Errors for June Through December for Radii of 0, 100, 200, 300 and 400 km.



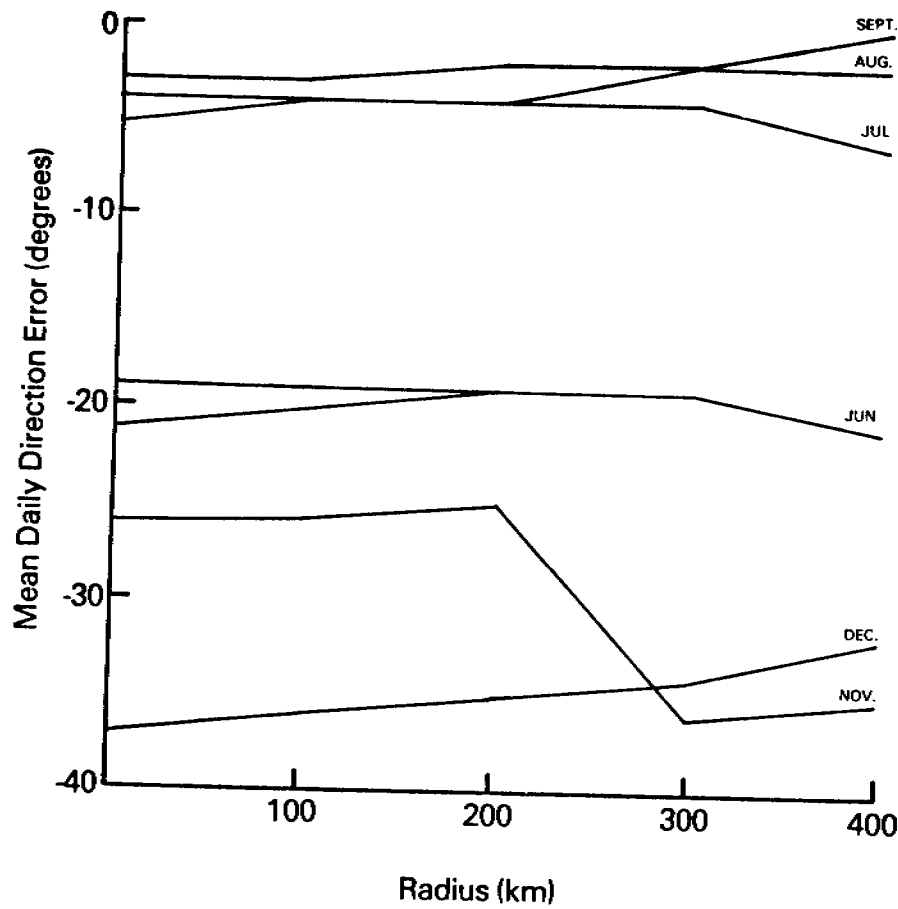


Figure IV.8. Mean Daily Error in Direction for June Through December for Radii of 0, 100, 200, 300 and 400 km.

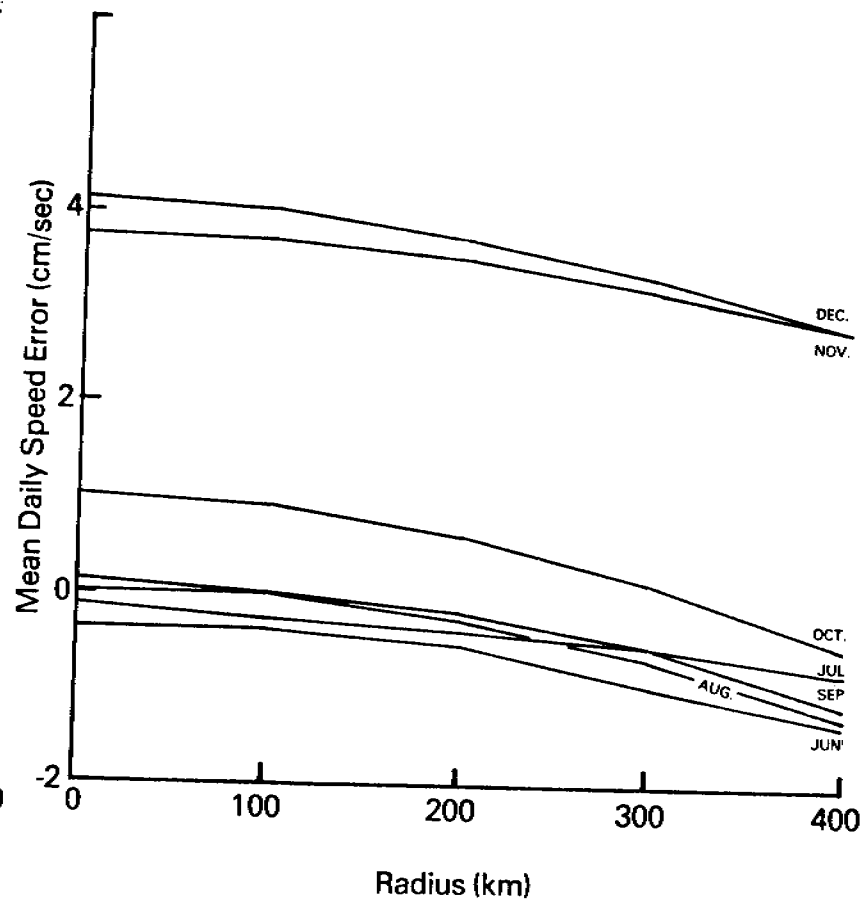


Figure IV.9. Mean Daily Error in Speed for June Through December for Radii of 0, 100, 200, 300 and 400 km.

Table IV-2. Large Scale Free Drift Error Measures.

Radius (km)	Error	June	July	Aug.	Sept.	Oct.	Nov.	Dec.
0	$ \bar{\epsilon} $ cm/sec	0.6	0.7	0.9	1.1	0.6	0.8	0.6
	$S_{\epsilon}$	2.5	3.3	3.4	3.4	4.3	7.2	6.6
	meandering	3.6	1.4	1.6	2.0	2.9	3.3	19.7
	(observed meandering)	(2.9)	(1.4)	(1.6)	(2.2)	(2.7)	(2.3)	(6.2)
100	$ \bar{\epsilon} $	0.6	0.7	0.9	1.0	0.5	0.8	0.6
	$S_{\epsilon}$	2.5	3.2	3.4	3.2	4.1	7.0	6.5
	meandering	3.5	1.4	1.6	2.0	2.9	3.3	20.2
200	$ \bar{\epsilon} $	0.6	0.6	1.1	0.9	0.5	0.9	0.5
	$S_{\epsilon}$	2.4	3.2	3.3	3.2	3.8	6.7	6.2
	meandering	3.1	1.4	1.7	2.0	2.8	3.1	20.9
300	$ \bar{\epsilon} $	0.6	0.7	1.3	0.7	0.6	1.0	0.5
	$S_{\epsilon}$	2.3	3.2	3.2	3.3	3.5	6.1	5.7
	meandering	2.7	1.5	1.7	2.1	2.7	2.8	21.2
400	$ \bar{\epsilon} $	0.7	1.0	1.7	0.5	0.9	1.1	0.4
	$S_{\epsilon}$	2.4	3.3	3.3	3.8	3.3	5.5	5.2
	meandering	2.2	1.5	1.7	2.1	2.5	2.6	20.4

Table IV-2. (Cont.)

Radius (km)	Error	June	July	Aug.	Sept.	Oct.	Nov.	Dec.
0	$\bar{E}$ cm/sec	-0.1	-0.3	1.5	0.2	1.1	3.8	4.2
	$\bar{\alpha}$ degrees	-19	-4	-3	-5	-21	-26	-37
	displacement error (km)	16.8	18.3	23.5	27.3	15.2	21.1	16.0
	(observed displacement)	(50.8)	(183.7)	(180.3)	(103.3)	(90.4)	(60.6)	(19.1)
100	$\bar{E}$	-0.2	-0.3	0.5	0.1	1.0	3.8	4.1
	$\bar{\alpha}$	-19	-4	-3	-4	-20	-26	-36
	displacement error	16.3	17.5	24.9	26.2	14.4	21.7	15.4
200	$\bar{E}$	-0.3	-0.5	-0.2	-0.1	0.7	3.6	3.8
	$\bar{\alpha}$	-19	-4	-3	-4	-19	-25	-35
	displacement error	15.3	16.3	29.2	22.5	14.3	23.8	14.0
300	$\bar{E}$	-0.5	-0.9	-0.6	-0.5	0.2	3.3	3.4
	$\bar{\alpha}$	-19	-4	-2	-2	-19	-36	-34
	displacement error	15.4	18.7	35.7	16.9	17.1	26.9	12.1
400	$\bar{E}$	-0.7	-1.3	-1.2	-1.1	-0.5	2.9	2.9
	$\bar{\alpha}$	-21	-6	-2	0	-21	-35	-32
	displacement error	18.1	26.8	44.5	12.7	23.5	29.1	10.3

Thus the size of the monthly displacement errors ( $< 26$  km) observed could be controlled by choosing a one month period rather than a shorter period. The result is not surprising since standard deviations are relatively large and our sample is small. Looking at the components of  $\bar{\epsilon}$  for the seven months (not presented here), the  $\bar{\epsilon}_y$  average to near zero while the  $\bar{\epsilon}_x$  are all positive and average to 0.65 cm/sec or about 17 km in the plus  $x$  direction (northeast). This bias could be partially explained by our having neglected the ocean currents.

One would expect local free drift ( $R = 0$ ) simulations to be most accurate for months when the ice is mostly wind-driven. For months when the ice has significant strength, averaging over a radius  $R > 0$ , but less than some critical value, should provide the most accurate simulations. The mean velocity errors shown in Figure IV.6 are somewhat confusing in that August, October and November have smallest errors at  $R = 0$ , June and July have minimum errors at 200 or 300 km radius and September and December have minimum errors at  $R \geq 400$  km radius. As we have pointed out though, the mean is not the most useful error measure to use.

The standard deviations of the error are shown in Figure IV.7. The most obvious fact from these plots is that November and December have standard deviations about twice as large as the other five months. While the mean errors for November and December shown in Figure IV.6 are not readily distinguishable from other months, there must be more large daily velocity errors during November and December. This agrees with our expectations that the free drift model is less accurate in winter than summer. October also has a larger standard deviation than June through September. The standard deviations for October, November and December all decrease with increasing radius of averaging as one would expect from the analyses of large scale average free drift. The months June through September also show a slightly decreasing standard deviation for radii of 200 or 300 km, but they are near enough to being constant so as not to contradict the expectation that local free drift is better than large scale free drift during this period.

A comparison of all error measures indicates that only standard deviations of the error vector are consistent at all times. It is our belief that  $S_{\epsilon}$  is the most important measure of the error to use to judge on the usefulness of large scale free drift. This is true because ocean current errors do not contaminate  $S_{\epsilon}$  as they do all other error measures. Most of our attention is thus focused on  $S_{\epsilon}$ .

Proceeding to the mean daily errors in direction and speed plotted in Figures IV.8 and IV.9 several observations can be made. For the summer months July, August and September, mean errors in speed and direction are small. From the September trajectory plotted in Figure IV.3 we see this to be true with the exception of two short periods of time where most of the error accumulates.

For the months June and October, the mean error in speed is small but the free drift velocities average  $20^{\circ}$  to the right of observed velocities. The October trajectory plotted in Figure IV.4 bears this out. The speed is in error about 1 cm/sec at radius zero but it decreases to near zero at radius 400 km. The directional error during November and December amounts to 25- to  $35^{\circ}$  and the error in speed is about 4 cm/sec, by far the worst errors observed in the study. The November trajectory in Figure IV.5 illustrates these errors very well.

Large scale averaging seems to have little affect on the error in direction. The large jump in  $\bar{\alpha}$  for November at  $R = 300$  km is due to one day's  $\alpha$  going from near  $+180$  at  $R = 200$  to near  $-180$  degrees at  $R = 300$ . The free drift ice speed is always reduced by increasing the area over which the velocity is averaged. This improves the fit for October, November, and December, but it makes the free drift speed too slow for June through September.

Table IV-2 shows the relationship of free drift and observed meandering. A value of the ratio greater than one means the free drift trajectory wandered about more than the observed trajectory did. Values much larger than one, such as the ratio for December at all radii, most probably occur when the ice has considerable strength and moves very little in response to the winds. Normal winds over a month will produce free drift motions in varying directions. During December the ice was observed to move only a short distance. December free drift motions, however, described a large loop, ending up near the starting point. Thus  $\bar{\epsilon}$  for December is small, but the coefficient of meandering for free drift is much too large. Other error measures ( $S_{\epsilon}$ ,  $\bar{E}$  and  $\bar{\alpha}$ ) are also large for December.

The coefficient of meanderings is also fairly large for small values of  $R$  in November. Looking at the trajectories in Figure 10, we see that the ice probably had considerable resistance due to ice strength in the x-direction, but much less strength in the y-direction. The free drift trajectories make much larger excursions in the x-direction than do the observed trajectory. Increasing the radius of averaging reduces these excursions which is reflected in the coefficient of meandering.

June and October also exhibit reduced free drift meandering for large scale free drift. Little change in free drift meandering is observed in July, August and September with increases in  $R$ . We conclude that large scale averaging tends to straighten out the kinks in the free drift trajectories.

From Figures IV.8 and IV.9 it appears that July, August, and September most nearly match the observed velocities in speed and direction and have reasonably small standard deviations of error velocities. November and December velocities match the observed velocities the poorest, while June and October are intermediate between the two groups. From this we conclude that July, August and September are wind-driven, June and October are nearly wind-driven or wind-driven part of the time and November and December are mostly not wind-driven. From the analysis of large scale free drift we would then expect the months in which free drift is an adequate approximation to have minimum errors at radii of zero or 100 km while months in which the ice is not completely wind-driven should show decreasing errors with increasing radius of averaging until a critical radius is reached, if it is less than or equal to 400 km.

To summarize the response in 1975-76, it appears that during the summer the ice experienced mostly wind-driven free drift. During late spring and early fall the ice was not quite wind-driven or was not wind-driven part of the time, but ice stress was small. In the winter, however, ice had enough strength to support some internal stress all the time. The large scale free drift model did improve the modeled ice motion when strength was reasonably low. The extent of this improvement for simulating 1975-76 behavior is less than was desired. There is not enough accurate data to check this model in other years when ice conditions might have been less severe. We have decided that the improvement is not worth the seven fold increase in cost due to the averaging algorithm so we will not pursue its use further. For cases when strengths are low enough, local free drift appears to give almost as good an approximation as large-scale free drift, and when strength is very high then the improvement is not substantial.

**Flow Research Report No. 133**  
**Beaufort and Chukchi Sea Ice Motion**  
**Part 2. Onset of Large Scale Chukchi**  
**Sea Ice Breakout**

**By**

**Ronald W. Reimer**  
**Robert S. Pritchard**  
**and**  
**Max D. Coon**

**March 1979**

**Flow Research Company**  
**A Division of Flow Industries, Inc.**  
**21414-68th Avenue South**  
**Kent, Washington 98031**  
**(206) 854-1370**

## Table of Contents

Page

1.	Physical Characteristics of Breakout	
1.1	Introduction	
1.2	Development of Arch and Propagation of Failure	
2.	Description of Data Set	
2.1	National Weather Service Pressure Maps	
2.2	NOAA-4 Satellite Images	
3.	Material Models of Breakout	
3.1	Wedge	
3.2	Restricted Channel	
3.3	Arch	
4.	Factors Controlling Breakout	
4.1	Onset of Breakout	
4.2	Large Scale Motion	
5.	Conclusions	
	References	
	Appendices	
I.	Ice Breakout in the Bering Strait	
II.	Circular Arches under Radial Loading	



## 1. Physical Characteristics of Ice Breakout in Strait

### 1.1 Introduction

The period of time during which sea ice is present in the Bering Strait region extends, in general, from mid-November to late June. During this time the ice pack undergoes numerous deformation cycles which at times are extensive enough to cause large scale flow of pack ice south through the Strait. Evidence taken from satellite images of the area indicates that this phenomenon is likely to occur at least once every winter. In order to understand when and why this occurs, it is necessary to learn which material properties of the ice pack control such breakout, as well as to understand the physical environment which influences the ice pack.

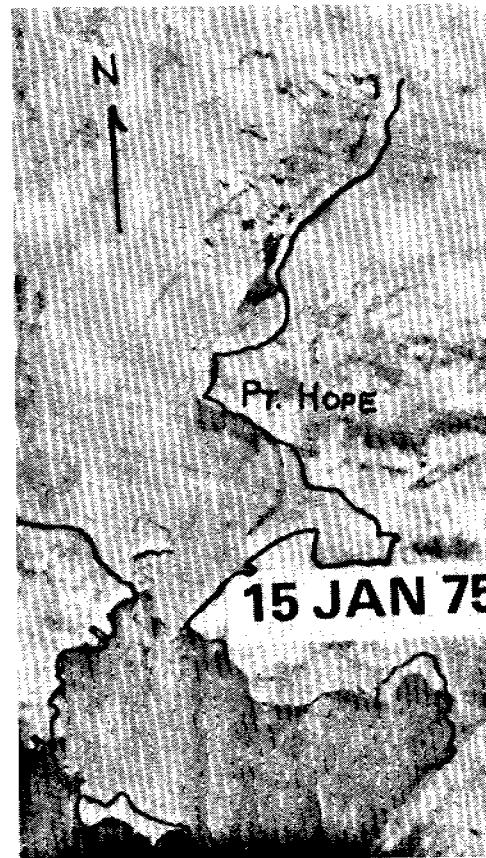
Sea ice responds to the influence of the atmosphere and ocean, as well as to the surrounding ice pack. If the material response of the ice is assumed to be rigid-perfectly plastic then it becomes possible to obtain some analytic solutions to the response of sea ice under various loads. This will be the approach used to model ice breakout through the Bering Strait. While there has been at least one previous attempt at such a model by Sodhi (1977), there exists, at the present time, a poor understanding of the critical driving forces and material properties to be modeled. A later section will review and compare all of the known existing solutions for ice flow through a restricted channel. The present work has taken advantage of the knowledge gained from these models, and so constructs a model which is sensitive to a number of material, as well as environmental conditions.

### 1.2 Development of Arch and Propagation of Failure

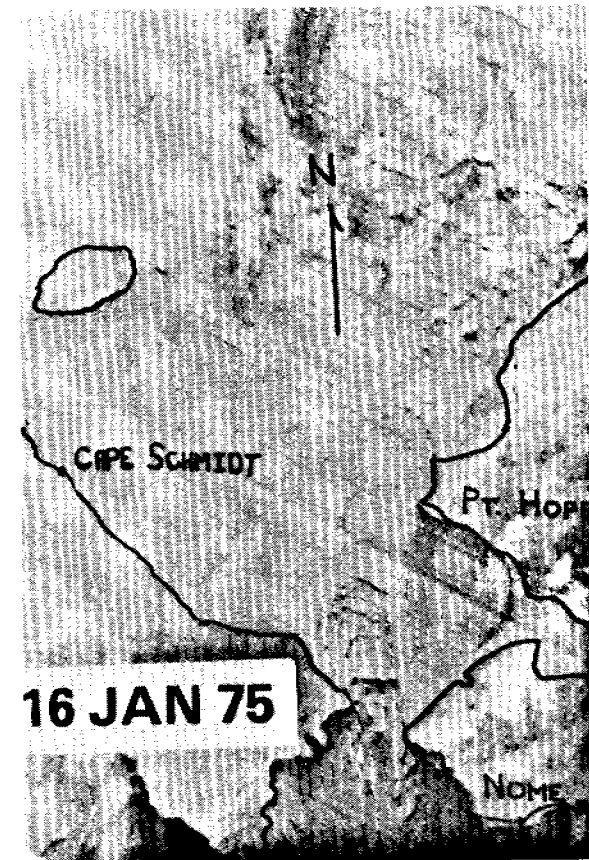
Breakout of ice through the Strait occurs after the persistence of some external load on the ice pack by the physical environment. It appears that the ice pack in the Strait is stable under this load up to a certain point, during which time the ice pack forms an arch across the Strait, preventing the passage of any significant amount of ice. If the load is intense enough the arch fails, or collapses, and the ice pack is free to move through the Strait, resulting in a breakout. An example of this may be seen in Figure 1a. If the existing conditions persist, repeated failures of arches may occur, until a channel of moving fractured ice, extending past Cape Lisburne, has been formed. This persistence of conditions is anomalous and is the reason that large scale breakout occurrences are infrequent. The time period shown in Figure 1, however, exhibits this persistence and in Figure 1c, four days after the initial arch became visible, a channel



a. Shows the Regional Ice Characteristics at Onset of Arch Formation.



b. Shows Failure of this Arch.



c. Shows Propagation of Failure to the Wainwright Region.

**Figure 1. Breakout Sequence Through the Bering Strait.**

of ice extends around Point Hope past Cape Lisburne. It happens in this case that the ice in the Wainwright area is also densely fractured, so that it is easily moved by the prevailing winds and internal ice stresses through the channel which has been opened to the Strait. This occurrence would be termed large-scale because deformations on the order of hundreds of kilometers become possible. Owing to the simultaneous occurrence of several unusual atmospheric and ice conditions, it appears possible that ice from Point Barrow might pass through the Strait in a relatively short time during this period in January 1975. If two such occurrences were to take place within a single winter, this likelihood would be enhanced. This was, in fact, the case in the winter of 1976 as will be discussed later.

An understanding of the scenario just described requires both a model of the arch which forms across the Strait, and the loads which act upon it. Much of this information must come from a knowledge of the physical environment of the Bering Strait. It is therefore unlikely that a data set describing breakout will be frequently available.

## 2. Description of Data Set

### 2.1 National Weather Service Pressure Maps

Since the present work models the response of sea ice to both the atmosphere and ocean, it is desirable to have data from both sources simultaneously. These are not available directly, however, owing to their scantiness, particularly with the latter.

Direct knowledge of the atmospheric system is available from National Weather Service surface maps. Pressure and wind conditions from six stations in the Bering Strait region have been obtained from these for the winters of 1975 and 1976. The air stress on the ice cover was calculated from the geostrophic winds through the Strait. This was felt to be as reliable as the surface winds, which cannot be read from the NWS maps without large errors. The geostrophic winds are also less likely to be influenced by local geographic features, which are not likely to influence breakout. The meteorological stations whose records were used are located at Cape Schmidt, Wrangel Island, Uelen, Nome, Kotzebue, and Barrow.

Knowledge of ocean currents through the Strait and in the Chukchi Sea is scant and no direct data were available to us for the time of concern. Past work in this area has shown some predominant patterns, and the work of Coachman, et al. (1975) was found particularly useful. An empirical formula relating transport of water through the Strait to atmospheric conditions, given by Coachman, et al., was used to obtain at least a qualitative understanding of the currents, and the effect they have on the ice cover. The accuracy of transport calculated from this formula is usually within 25 percent for the available data.

### 2.2 NOAA-4 Satellite Images

Perhaps the most useful source of data in this study has been NOAA-4 satellite images. These have been available to us since January 1975, thereby determining the time period under study. During the months of January and February these are available in only the infrared bands, but in March additional information becomes available with the visible band images. Features on the order of 15 to 20 km can frequently be followed on successive days. In this way large scale motions can be estimated. A very useful feature of these images has been their help with the formation of visual analogies of ice breakout with other types of plastic deformation. The most important use of these images, however, was the correlation of breakout with atmospheric conditions.

### 3. Material Models of Breakout

#### 3.1 Wedge

It should be emphasized that although models of arching are found in the literature, they are based on material properties different from those in the present model of sea ice. There is presently no way of making correlations between existing solutions and the material properties being modeled here. As an example of this, a model by Sodhi (1977) derives a value for the cohesion of pack ice, a quantity which has no analog on the yield surface used in our work. It is felt, therefore, that the derivation of a new solution based on material properties appropriate to the sea ice model is necessary. This section will summarize the results obtained by Sodhi, together with two arching solutions that have been obtained from our material model. The primary concern of each of these models is to give the collapse load of the material in the region just north of the Strait. The regions modeled by the three different authors are shown in Figure 2. Although individual authors used different notations, expressions for collapse loads have been made consistent.

The first solution, derived in Appendix I, is for a rigid-plastic material and assumes that stresses are constant in subregions of the wedge in Figure 2a. For a given region geometry and a specified failure mechanism, the stresses in each subregion are uniquely determined by the boundary tractions. In this model, failure of the wedge occurs by the loading at the top surface of the wedge from ice stresses transmitted internally. Hence, only the effect of the surrounding ice pack is modeled. The yield surface, shown in Figure 3a, is diamond shaped in principal stress space.

This solution contains a number of interesting features. First of all, the mechanism of failure is one where streamlines of the velocity field coincide with the outer boundaries of the wedge. This is an attractive feature in a model of channel flow since material is not forced to accumulate or disappear along the boundaries. Secondly, the model shows that as the depth of the wedge (parameterized by angle  $\beta$  in Figure 2a) increases to a certain point, the failure load increases. Beyond a critical depth, given by  $\beta = 45^\circ$  in Figure 2a, the failure load is constant. This is illustrated in the following

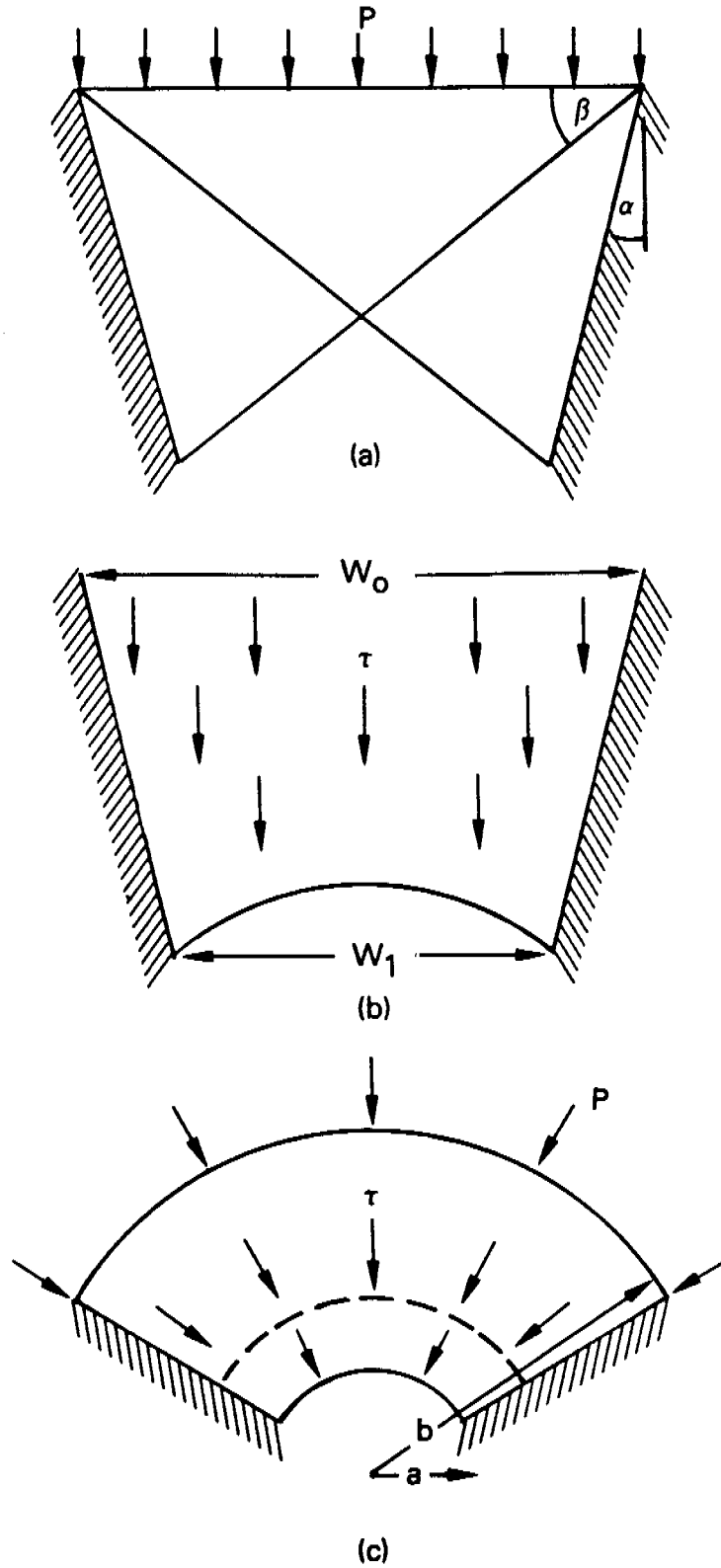


**Figure 2. Regions Modeled by Different Authors for Analyzing Breakout. Figures 2a, 2b and 2c are from the models of Appendix 1, Sodhi and Appendix 2, Respectively.**

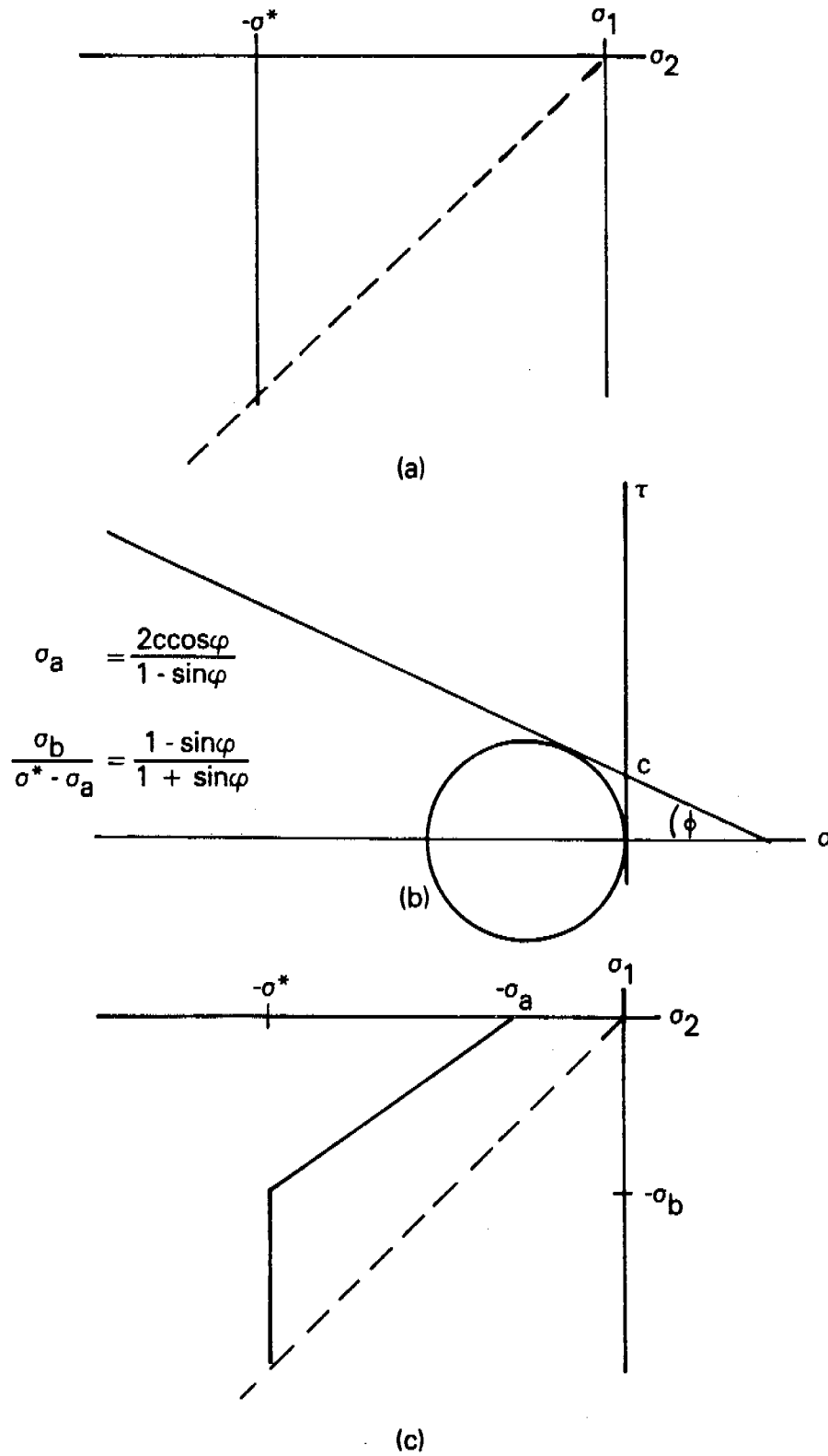


**Figure 3. Yield Surfaces Used by Different Authors for Analyzing Breakout. Figures 3a, 3b and 3c are From the Models of Appendix 1, Sodhi and Appendix 2, Respectively.**

equation, which specifies the traction which fails the wedge. The collapse load normalized by  $\sigma^*$  is

$$\frac{P}{\sigma^*} = \begin{cases} \left[ \frac{\bar{b}-1}{\bar{b}+1} \cot\alpha \right]^2 & \frac{\bar{b}-1}{\bar{b}+1} \cot\alpha < 1 \\ 1 & \text{Otherwise} \end{cases} \quad (1)$$

Here the wedge depth ( $\bar{b}$ ) has been rewritten in terms of the ratio of radii  $\bar{b} = b/a$  shown in Figure 2c. The half-angle subtended by the wedge is  $\alpha$ . This model predicts that an 18-knot wind requires a 1000 km fetch to fail the wedge and cause breakout for a yield strength of  $10^5 \text{ Nm}^{-1}$ .

Body forces can be accounted for indirectly in this model by calculating the total body force acting on the area of the wedge and distributing it across the top boundary. The accuracy of such an approach has not been determined.

### 3.2 Restricted Channel

A solution which accounts for body forces explicitly, but neglects boundary tractions, is given by Sodhi (1977). While the material in the previous model fails in plane stress, the material modeled by Sodhi deforms in plane strain. The modeled region is a restricted channel, shown in Figure 2b. Failure is assumed to be described by an uncapped Coulomb yield surface, as in Figure 3b.

The material properties appearing in the Sodhi solution are the angle of friction and cohesion. Substantial tensile stresses are permitted. These quantities do not have direct analogs in the sea ice solution of Appendix I, making comparison difficult. The minimum body force required to fail the restricted channel is given by

$$\frac{\tau}{\sigma_a} = \frac{c_2}{bc_1 \cos\alpha} \frac{\bar{b}^{c_1}-1}{\bar{b}^{c_2}-1} \quad (2)$$

Here  $c_1$  and  $c_2$  are material constants, introduced in subsection 3.3 for the circular arch solution. The quantity  $\sigma_a$  is the unconfined compressive strength of the material, which is defined below. On the basis of this equation, Sodhi predicts that an 11-knot wind will provide sufficient body force to cause breakout, using material properties found in that work.



### 3.3 Arch

Finally, the solution presented in Appendix II combines body forces and boundary tractions in a single model. For this case, loads from air and water stress as well as forces from internal ice stresses are considered simultaneously. The solution region is a circular arch, as in Figure 2c. The yield surface, shown in Figure 3c, generalizes the diamond yield surface of Figure 3a. It is parameterized by the unconfined compressive strength as  $\sigma_a$ , and we examine the effect of this quantity upon failure loads. As may be seen in Figure 3c, the unconfined compressive strength is the maximum allowable uniaxial stress. If  $\sigma_a = \sigma^*$ , the yield surfaces in Figures 3a and 3c are identical. The arch is taken to have outer and inner radii of  $b$  and  $a$  respectively, and the ratio of these is  $\bar{b}$ , used previously. The material constants  $c_1$  and  $c_2$  are taken from the yield surface for values of  $\sigma_a$  and  $\sigma_b$ :

$$c_1 = \frac{\sigma^* - \sigma_a - \sigma_b}{\sigma_b}$$

$$c_2 = c_1 - 1.$$

The failure load, in terms of two parameters, the traction  $P$  and the body force  $\tau$ , is

$$P + \frac{\tau b}{c_2} \left[ \bar{b}^{c_2} - 1 \right] = \frac{\sigma_a}{c_1} \left[ \bar{b}^{c_1} - 1 \right]. \quad (3)$$

The combinations of loads which cause failure for different values of the unconfined compressive strength ( $\bar{\sigma}_a = \sigma_a / \sigma^*$ ) is shown in Figure 4. The values  $\bar{b} = 5$  and  $\bar{\sigma}_b = 0.4$  were used in this calculation. It is interesting to note that for some ranges of the loads, the effect of unconfined compressive strength is very significant.

This solution may be compared with the previous ones in two limiting cases. If no boundary tractions are present ( $P = 0$ ), the body force which causes failure is given by

$$\frac{\tau}{\sigma_a} = \frac{c_2}{bc_1} \frac{\bar{b}^{c_1} - 1}{\frac{c_2}{\bar{b}} - 1}. \quad (4)$$

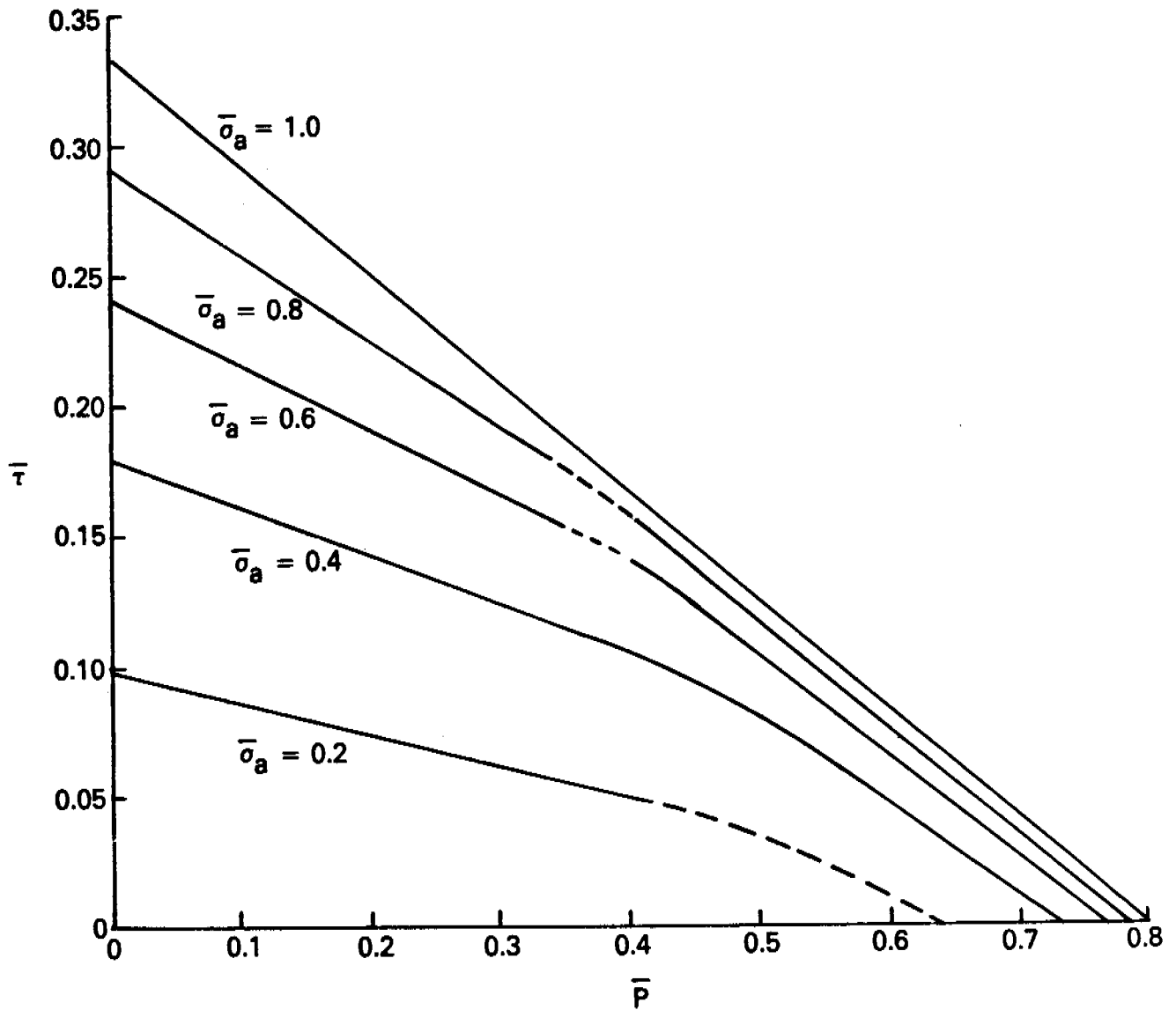


**Figure 4. Effect of Unconfined Compressive Strength on Arch Collapse Loads. These were Calculated Using the Model of Appendix 2 with  $\bar{b} = 5$  and  $\bar{\sigma}_b = 0.4$ .**

This differs from the Sodhi model in equation (2) by a factor  $\cos\alpha$ . The difference is assumed to be caused by radial loading. On the other hand, if no body forces are present, a boundary traction given by

$$\frac{P}{\sigma^*} = 1 - \frac{1 - \bar{\sigma}_b}{\bar{b}} \left[ 1 + \frac{c_1 \sigma_b}{\sigma_a} \right]^{\frac{1}{c_1}}$$

will fail the arch. If the value  $\sigma_a = \sigma^*$  is taken, so that comparison may be made with the first solution, the failure load is

$$\frac{P}{\sigma^*} = 1 - \frac{1}{\bar{b}}$$

This result is compared to Equation (1). For an arch of depth  $\bar{b} = 5$ , the wedge used in the first model agrees with this prediction to within 20 percent.

Figure 5 shows the effect of the parameter  $\bar{\sigma}_b$  on collapse loads. The values  $\bar{b} = 5$  and  $\bar{\sigma}_a = 0.6$  were taken for this calculation. It is noteworthy that  $\sigma_b$  has a smaller effect on collapse than does  $\sigma_a$ . Thus, although accurate knowledge of  $\sigma_a$  is not necessary if  $\bar{\sigma}_a > 0.6$ , it is very important when smaller. On the other hand, when  $\bar{\sigma}_a = 0.6$  there is small effect of  $\bar{\sigma}_b$  for any value.

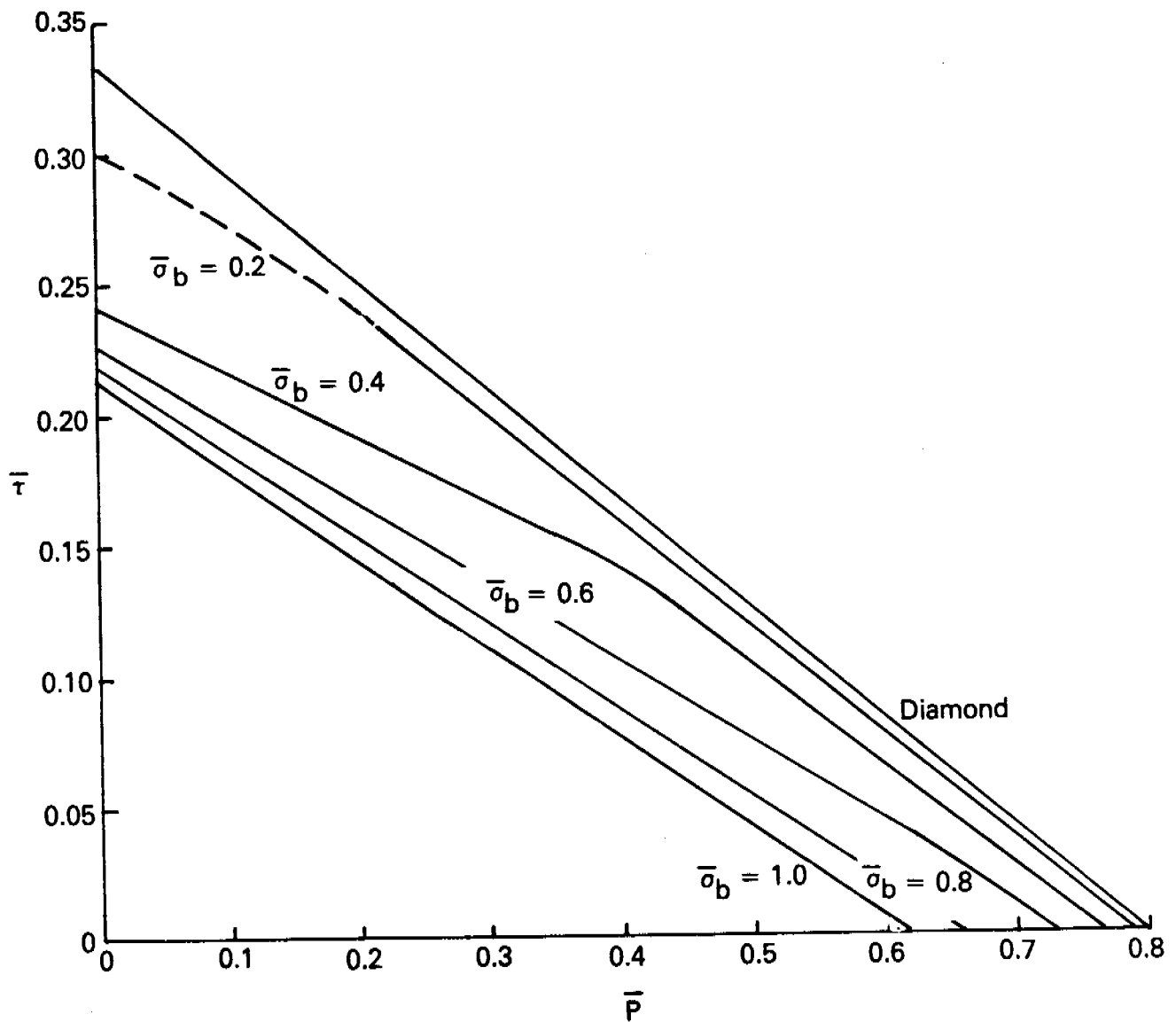


Figure 5. Effect of  $\bar{\sigma}_b$  on Arch Collapse Loads. These were Calculated Using the Model of Appendix 2, with  $\bar{b} = 5$  and  $\bar{\sigma}_g = 0.6$ .

#### 4. Factors Controlling Breakout

##### 4.1 Onset of Breakout

The question of what controls breakout through the Strait may be approached with some generality now that a model exists for a failure mode which combines the effects of both body forces and boundary tractions on a region of arbitrary depth. Examination of Figure 1, which provided a basis for the scenario described in Section 1, suggests that the mechanism for large scale breakout may be the continued failing of arches to produce a channel through which ice may flow. The arch model is able to analyze the failure of the individual arches.

Using National Weather Service maps, the pressure systems in the Bering Strait area have been inspected for anomalous conditions during breakout. The most obvious condition to associate with breakout is the occurrence of strong winds through the Strait. If these blow directly through the Strait, the isobars associated with the geostrophic wind will have their maximum gradient approximately 30 degrees to the right of the wind, owing to the turning angle of the geostrophic component. Figure 6 represents the surface atmospheric condition on 15 March 1976 and is a good example of the conditions leading to breakout. The combined effects of the high- and low-pressure systems enhance the pressure gradient in the proper direction.

It is not known to what extent the ocean currents through the Strait contribute to the body force on the ice pack. Even though the prevailing currents are northward, the occurrence of southerly flow is well documented. In fact, Coachman, et al. (1975) record 13 such incidents in the interval September 1956 to August 1957. These occurrences were concentrated in the fall, lasting between 1 and 9 days, but most commonly 2 to 5 days. Coachman, et al. record southerly currents in excess of 20 cm/sec.

The mechanism which has been proposed by Coachman, et al. as an explanation of this phenomenon is sea surface tilt. If a low pressure system persists in the southern Bering Sea, the sea level of the northern Bering Sea is lowered as the result of southward transport. As a consequence of this lower sea level, water from the Chukchi Sea is able to flow southward through the Strait. It should be noted that southward flow through the Strait will occur only until the equilibration process in the Bering Sea is completed. In other words, setting up the sea surface tilt in the Bering Sea creates a southerly flow through the Strait.

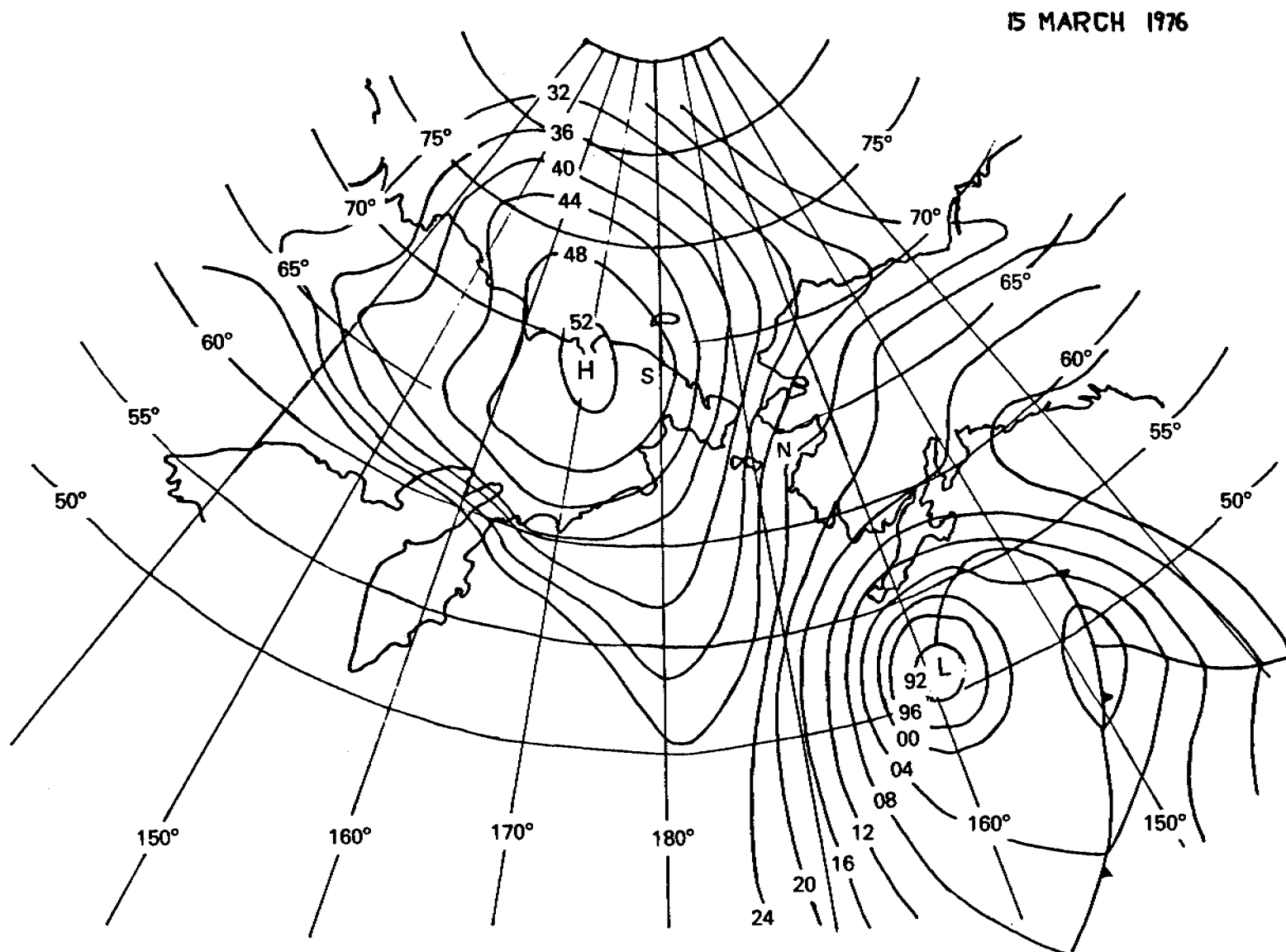


Figure 6. A Surface Pressure Map During the Breakout Sequence in March 1976.  
N and S Denote the Locations of Nome and Cape Schmidt, Respectively.

If these two mechanisms are indeed the factors controlling breakout then our model of breakout is simplified. For then, both the geostrophic wind and the southerly currents through the Strait are set up to act in concert by one atmospheric condition. In fact, the atmospheric condition on 15 March 1976, as shown in Figure 6, occurred at the onset of a major ice breakout through the Strait. Furthermore, a similar condition exists during nearly all breakouts which we have observed since 1975.

With this in mind, a time history of the pressure gradient between Nome and Cape Schmidt was prepared. A maximum pressure gradient in that direction leads to the maximum component of the geostrophic wind being directed through the Strait, as may be seen in Figure 6. This time history, shown in Figure 7, was obtained for portions of the winters of 1975 and 1976. The pressures were taken from synoptic readings at the meteorological stations at Nome and Cape Schmidt, as recorded on the NWS surface maps. During this same time, NOAA-4 satellite images were used to determine when breakout occurred through the Strait. With one exception, whenever the pressure difference between Nome and Cape Schmidt exceeded 20 mb for more than just a few days, an observable breakout occurred. It should be noted that while the short duration peaks in the pressure gradient may cause an initial failure of an arch across the Strait, it is the persistence of this condition which makes large scale breakout possible. The idea that the successive failure of several arches may control large scale breakout has its root in this observation.

By estimating the geostrophic wind in the Strait from the NWS maps, a value for the air stress, acting as a body force on the ice cover, was obtained. These are plotted for 1975 in Figure 8. At the same time, the body force arising from the ocean current was estimated by means of an empirical formula arrived at by Coachman, et al. (1975). This formula, based on 21 data points, is a correlation found between transport through the Strait and Nome atmospheric pressure of the previous day. This equation, thought to be accurate to 0.5 Sv is

$$T = 1.58 + 0.08(P_N - \bar{P})$$

where  $T$  is transport (in Sverdrups),  $P_N$  is Nome pressure (in millibars), and  $\bar{P}$  is mean pressure in the southern Chukchi. Using this, together with the assumption of uniform flow through the Strait, a crude estimate of current speed

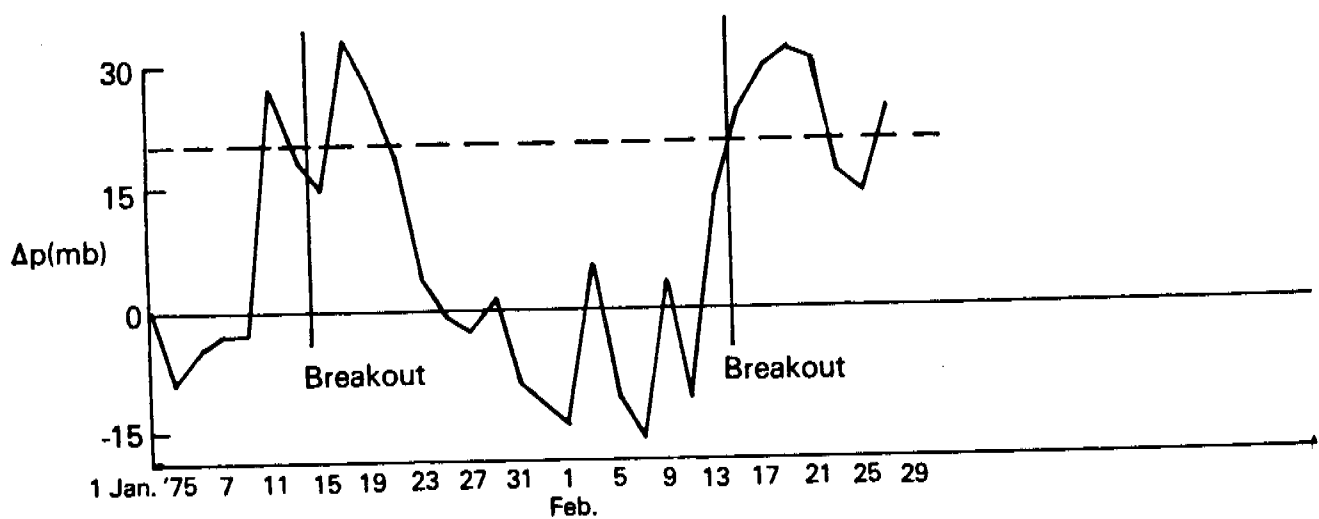
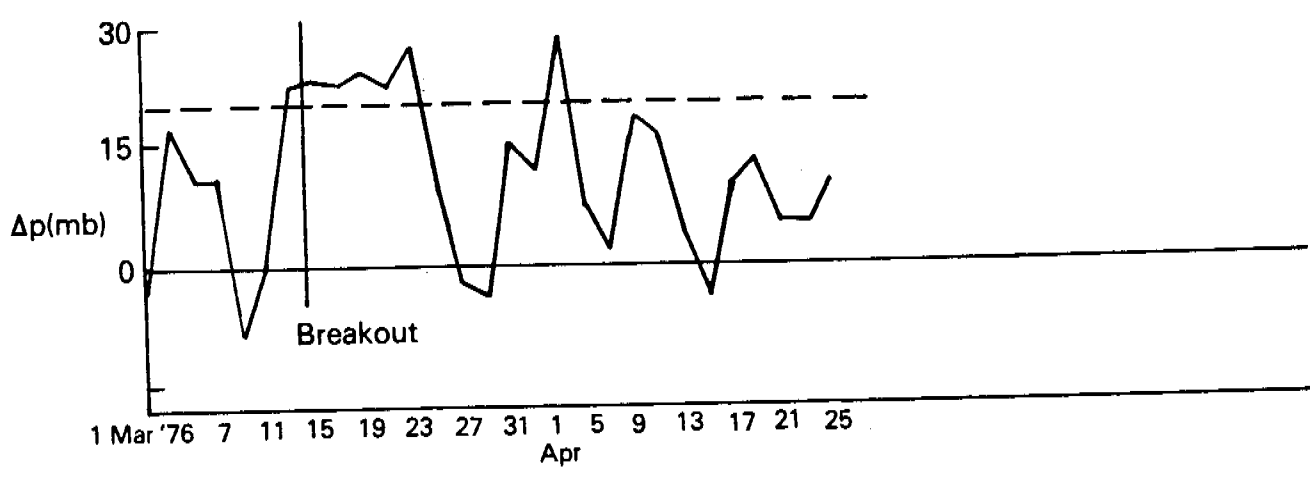
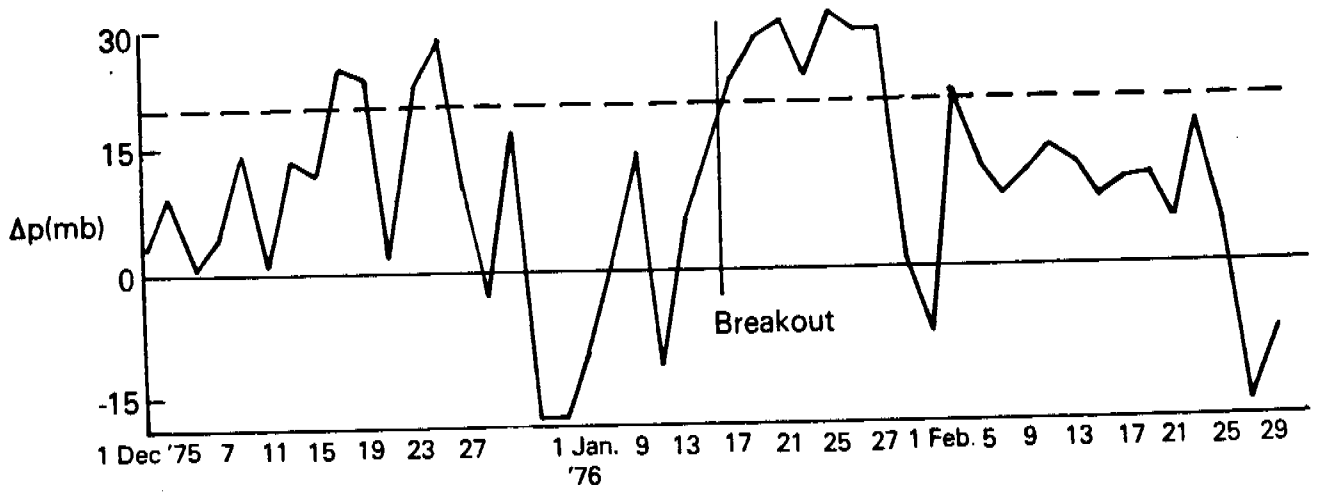


**Figure 7. Pressure Gradient Between Nome and Cape Schmidt.  $\Delta P$  = Pressure (Nome) - Pressure (Cape Schmidt) in Millibars. All Large Breakouts which Occured are Indicated.**



1975

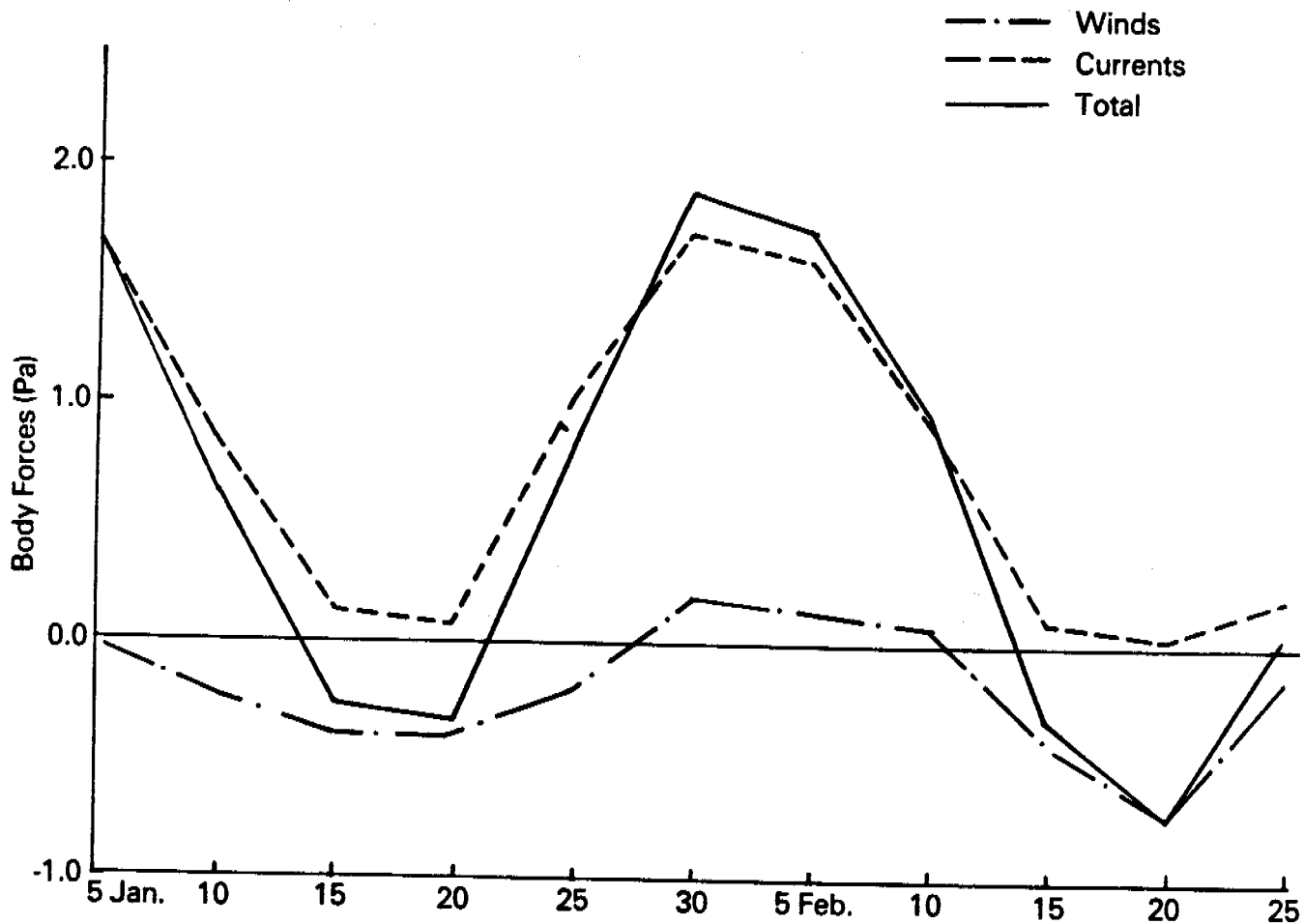


**Figure 8. Body Forces Acting on Ice Cover During the Winter of 1975. The Total Body Force (in Pascals) is the Sum of Wind Stress and Water Drag.**

was obtained. The water drag calculated from this (with quadratic law and a drag coefficient of 0.008) should be considered an estimate since currents are known to vary a great deal, even locally. The large values of water drag obtained for northward transport are not likely to provide a significant body force, as the Chukchi widens rapidly north of the Strait, and currents are likely to decrease rapidly. The total body force acting on the ice cover may be read from Figure 8.

The failure of large scale breakout to occur between 15-26 December 1975 is the one exception which has been found to the above rule. Two possible explanations exist. The first is that the pressure gradient does not persist for the full nine day period but drops very sharply between 20 December and 23 December. The Strait could have reconsolidated during this time. The second explanation, somewhat more interesting, is offered by the air stresses calculated during this time. They are approximately 50 percent lower than during other breakout occurrences. If the latter is the correct explanation, then it would be possible to obtain a bound on the ice strength.

A final important point to be made on body forces is that both the onset and termination of breakout correlated well with the 20 mb pressure gradient whenever cloud conditions permitted the observation of both.

Knowledge of sea ice indicates that tractions exerted by internal stress of the ice pack on the region which controls breakout should be of appreciable importance. In fact two of the solutions which have been presented model this phenomena. However, no correlation has been found between breakout occurrences and phenomena producing tractions on the modeled region. That this correlation would be harder to find is not surprising since it is an indirect one.

#### 4.2 Large Scale Motions

There seems to be some evidence that large scale motion results from the persistence of conditions which control the onset of breakout. This evidence is easily seen in the trajectory of a RAMS buoy deployed by AIDJEX in the vicinity of Barrow (Thorndike and Cheung, 1977). RAMS buoy R 534 (called Station 24 by Thorndike & Cheung) began transmitting position data on 26 December 1975, from approximately 100 km northeast of Barrow. On 22 January 1976, the buoy had not moved appreciably from its original position. However, by 24 January the buoy was 30 km north of Wainwright. There is little doubt that this motion was associated with the breakout occurring during this time (Figure 7). This direction

of motion continued through 31 January when the buoy was 130 km from Cape Lisburne. At that time, large scale motion ended and the buoy position remained relatively stable for several days. This trajectory, shown in Figure 9, exactly follows the channel which is evident in Figure 1.

It seems likely that this large scale deformation in the ice pack could be made possible by the continued failing of arches in the southern Chukchi. Hence, the duration of the 20 mb gradient, the onset of which seems to initiate breakout, controls the extent of breakout. The strength of this conclusion will require more study.

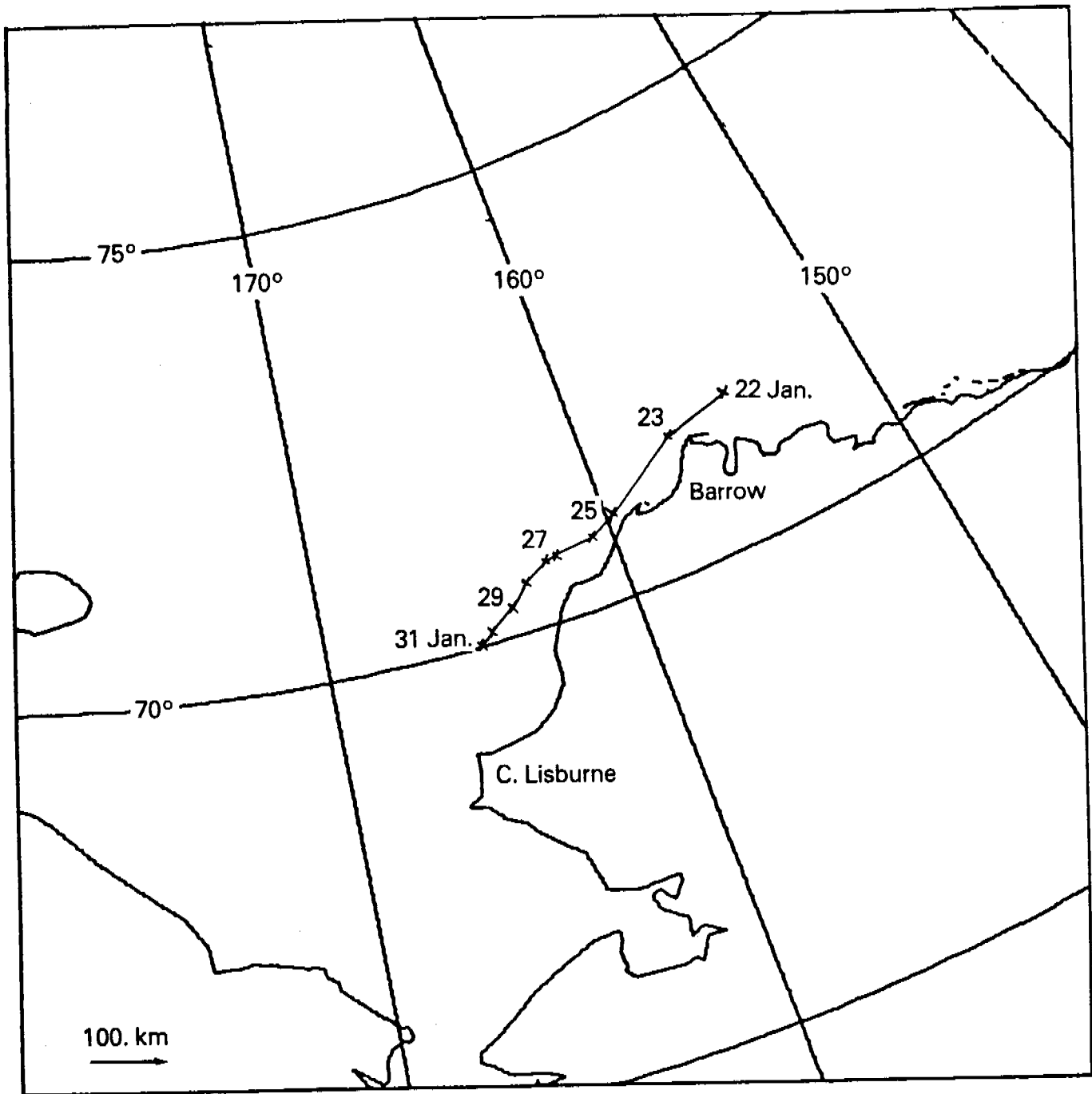


**Figure 9. The Trajectory of RAMS Buoy R 534 During the Breakout of January 1976. The Maximum Daily Displacement was 130 km.**

## 5. Conclusions

Three models of ice flow through the Bering Strait have been given. Among them, they model failure by boundary tractions, body forces, or combinations thereof. All three models are able to predict the winds required to cause breakout. If ocean currents were better understood, they could be included in the body forces used to arrive at these predictions. Apparently large scale breakout is such a complex phenomenon it requires the combination of several loads to adequately model it. None of these models predict the size of the region to be modeled. This information must be inferred from other data.

The solution in Appendix 2 was used for a parameter study of a yield surface. It was found that the unconfined compressive strength seems to be the most critical information modeled by the yield surface.

A good correlation has been found between ice breakout and the magnitude of body forces. This may indicate that body forces are relatively more important than boundary tractions in initiating breakout, since no correlation with tractions has yet been discovered. Using some results on ocean currents that were obtained by Coachman, et al., it seems likely that currents play an important role in starting breakout. It was found that the presence of large pressure gradients between Nome and Cape Schmidt is a condition associated with both strong southerly winds and southward ocean currents through the Strait. It is, therefore, expected that these two forces act in concert to initiate breakout.

The possibility of large scale ice flow through the Strait is a real one. When the condition causing breakout persists for several days, a channel of fragmented ice is formed between the Strait and the Wainwright area. This creates the possibility of daily motions on the order of a hundred kilometers. This magnitude of motion has been documented on several occasions. At the beginning of the breakout period of 16-30 January, an AIDJEX buoy was located approximately a hundred kilometers from Cape Lisburne. At the end of the breakout period the buoy was caught up in the shorefast ice north of the Cape Lisburne prominence. If the buoy's course had taken it slightly more to the west so that it could get around the promintory, then the breakout which occurred two months later, 13-25 March, would likely have transported the buoy through the Strait. Another documentation of the scale of motion has been made by Marco and Thompson (1976), who measure daily ice motions of 75 km in the Strait.

During the time period which was considered in this work there were four cases of large scale breakout, two each winter. The occurrence of a 20 mb

pressure gradient between Nome and Cape Schmidt coincided with each of these. There were a number of cases, 3 February 1976, for example, when the pressure gradient reached the critical value for one day only. Breakout may have occurred on a small scale during these times, but failure did not propagate beyond the Strait. A single case has been found where the 20 mb gradient persisted for ten days, but breakout did not occur. One explanation of this exception may be that the pressure gradient during this period, 15-26 December 1975, is actually two three-day peaks separated by three days. The ice pack may have strengthened during the intervening three-day period. However, the body forces calculated during this time are lower than during the other breakouts. If this was the actual reason breakout did not occur, then a lower bound could be placed on the ice pack strength. Another important inference may be drawn from this exception. Even though the 20 mb difference existed during much of 15-26 December 1975, the total air stress vector magnitude is lower than at other breakout times. This suggests that another component of air stress may also have been involved in breakout.

This work has placed the relative roles of body forces and boundary tractions in some perspective. Some circumstances seem to indicate that the anomalous southward ocean current through the Strait is critical to breakout. If this view is adopted, then a better understanding of these currents is required for estimates of the physical parameters of the model.

#### References

- Coachman, L. K., Aagaard, K., and Tripp, R. B. (1975) Bering Strait: The Regional Physical Oceanography. University of Washington Press: Seattle, WA.
- Coon, M. D. (1967a) "Rigid Plastic Analysis of Circular Arches," Int. J. Mech. Sci., 9, pp. 137-142.
- Coon, M. D. (1967b) "Reply to Comment by P. G. Hodge on 'Rigid Plastic Analysis of Circular Arches'," Int. J. Mech. Sci., 9, pp. 674-677.
- Marco, J. R., and Thompson, R. E. (1976) "Rectilinear Leads and Internal Motions in the Ice Pack of the Western Arctic Ocean," Journal of Geophysical Research, 82(6), pp. 979-987.
- Prager, W. (1959) An Introduction to Plasticity. Addison-Wesley Publishing Co., Inc., Reading, MA, pp. 38-42.
- Sodhi, D. S. (1977) "Ice Arching and the Drift of Pack Ice Through Restricted Channels," CRREL Report 77-18, Cold Regions Research and Engineering Laboratory, Hanover, NH, pp. 1-11.
- Thorndike, A. S., and Cheung, J. Y. (1977) "AIDJEX Measurement of Sea Ice Motion, 11 April 1975 to 14 May 1976." AIDJEX Bulletin, 35, University of Washington, Seattle, WA.

Appendix I. Ice Breakout in the Bering Strait

Ice Breakout in the Bering Strait

by

Ronald Wayne Reimer

A thesis submitted in partial fulfillment  
of the requirements for the degree of

Master of Engineering

University of Washington

1979

Approved by *D. Reid Pamuta*  
(Chairperson of Supervisory Committee)

Program Authorized  
to Offer Degree Aeronautics & Astronautics

Date *Feb 23, 1979*



Master's Thesis

In presenting this thesis in partial fulfillment of the requirements for a Master's degree at the University of Washington, I agree that the Library shall make its copies freely available for inspection. I further agree that extensive copying of this thesis is allowable only for scholarly purposes. *It is understood, however, that any copying or publication of this thesis for commercial purposes, or for financial gain, shall not be allowed without my written permission.*

Signature 

Date 23 Feb. 1979

University of Washington

Abstract

ICE BREAKOUT IN THE BERING STRAIT

By Ronald Wayne Reimer

Chairperson of the Supervisory Committee: Professor Reid Parmerter  
Department of Aeronautics  
& Astronautics

A rigid-plastic sea ice model developed by the AIDJEX modeling group is used to determine when large-scale ice flow may occur through the Bering Strait. Incipient flow is modeled as an arching problem of a two-dimensional granular material with no cohesive strength. For this analysis body forces on the ice pack and material hardening are neglected. Prediction of failure of an ice arch across the Strait is made in terms of a boundary traction which is related to the strength of winds blowing across the ice pack.

The method of solution is to parameterize a wedge-shaped region in the Bering Strait and to model the ice pack in this region as a rigid-plastic material. The choice of a region is based on a visual study of satellite photographs of actual breakout occurrences. A boundary value problem is defined in terms of approximate stress and velocity boundary conditions. Using Prager's theorems on limit analysis, it is shown that an upper and lower bound on a failure load can be calculated if the stresses are assumed constant within subregions of the modeled region. By picking a stress state associated with a kinematically admissible velocity field, a unique failure load is calculated. It is found that

for the Bering Strait the failure load is independent of the depth of the modeled region. A simple calculation shows that a wind creating a stress of 0.5 Pa requires a fetch of 200 km to cause breakout. The usefulness of the solution depends primarily on the accuracy of the stress boundary conditions which define the problem.

## TABLE OF CONTENTS

	Page
LIST OF FIGURES . . . . .	.
LIST OF SYMBOLS . . . . .	.
ACKNOWLEDGMENTS . . . . .	.
I. INTRODUCTION . . . . .	.
1. Motivation for Doing the Problem . . . . .	.
2. Description of Breakout . . . . .	.
3. Description of the Model . . . . .	.
II. MODEL . . . . .	.
1. Yield Surface . . . . .	.
2. Governing Equations . . . . .	.
3. Constant Stresses and Limit Analysis . . . . .	.
4. Stress Boundary Conditions . . . . .	.
III. STATICALLY ADMISSIBLE STRESS STATES IN A RIGID-PLASTIC WEDGE . . . . .	.
1. Parameterization and Equilibrium Conditions . . . . .	.
2. Stress States in Traction Space . . . . .	.
IV. KINEMATICALLY ADMISSIBLE VELOCITY FIELDS IN A RIGID-PLASTIC WEDGE . . . . .	.
1. Equations Governing the Velocity Field . . . . .	.
2. Positive Work . . . . .	.
3. Velocity Boundary Conditions and Physically Acceptable Velocity Fields . . . . .	.
V. A FAILURE MECHANISM FOR BERING STRAIT BREAKOUT . . . . .	.
1. Stress State in Invariant Space . . . . .	.

2. Principal Directions . . . . .

VI. CONCLUSIONS . . . . .

1. Results Pertaining to the Yield Surface . . . . .

2. Application to the Bering Strait . . . . .

VII. REFERENCES . . . . .

VIII. APPENDIX: Kinematically Admissable Velocity Fields . . . . .

## LIST OF FIGURES

Number	Page
1.	The yield surface and associated flow rule used in the sea ice model . . . . .
2.	The wedge and boundary tractions which parameterize the solution region . . . . .
3.	A representation of different failure mechanisms in traction space. Possible failures occur on or above line A. Figs. 3a and 3b are for $\beta$ less than and greater than $45^\circ$ , respectively . . . . .
4.	The location of each region of the wedge on the yield surface at incipient failure . . . . .
5.	The principal direction of each region of the wedge at incipient failure . . . . .
6.	The relationship between the fetch required to produce a failure load as a function of air stress when ice strength is $10^5$ N/m . . . . .
7.	The region thought to be critical in Bering Strait breakout. The Strait width is 60 km . . . . .
8.	Kinematically admissible velocity fields for $\beta$ equal to and less than $45^\circ$ , respectively . . . . .

## LIST OF SYMBOLS

$A, B$	linear coefficients of first-order partial differential equation
$b$	yield surface equation
$D$	strain-rate tensor
$\underline{l}$	left eigenvector of characteristic determinant
$P$	traction across top of wedge
$P^*$	ice strength
$Q$	traction along sides of wedge
$x, y$	spatial coordinates
$x_0$	horizontal coordinate of upper right-hand corner of wedge
$u, v$	velocity components
$\alpha$	half-angle subtended by wedge
$\beta$	angle defining constant stress partition
$\gamma$	angle of greater principal stress
$\xi$	characteristic direction
$\lambda$	flow rule parameter
$\phi$	yield surface
$\sigma_{ij}$	Cartesian stress tensor components
$\sigma_I, \sigma_{II}$	stress tensor invariants
$\tau_{\pm}$	characteristic roots

## ACKNOWLEDGMENTS

The author wishes to acknowledge the assistance of Robert S. Pritchard in all phases of this work. Numerous discussions with Reid Parmerter and Max Coon also helped clarify many of the difficult points in the analysis of this problem.

This study was supported by the Bureau of Land Management through interagency agreement with the National Oceanic and Atmospheric Administration, under which a multi-year program responding to the needs of petroleum development of the Alaskan continental shelf is managed by the Outer Continental Shelf Environmental Assessment Program (OCSEAP) Office.



## I. INTRODUCTION

### I.1 Motivation for Doing the Problem

The final sale of leases of the Continental Shelf of the Beaufort Sea for oil exploration is tentatively scheduled for December 1979. Environmental impact statements on the effect of oil spills in the Arctic environment will have to be filed before that time. An important element in these impact statements will be an attempt to describe the role of sea ice in offshore drilling operations. The fact that little can be done to cap a well blowout during the Arctic winter places an oil spill of several months duration within the realm of possibility. Since the spilled oil is not likely to be immediately recoverable, it may become incorporated in the ice pack. Arctic sea ice is known to travel as much as a thousand kilometers between freeze-up in the fall and spring thaw, so cleanup operations may be required at great distances from the actual spill site. The possibility exists that oil-bearing ice may be deposited in the Chukchi Sea, whence a storm of sufficient magnitude might blow the ice through the Bering Strait. This possibility is of special environmental concern because of the rich fishing areas in the Bering Sea.

This work is part of a larger study of the transport of oil spilled in and under sea ice. As a subtask in the larger study, this work will focus on the possibility of large-scale ice flow through the Bering Strait. Under normal circumstances this will be prevented by arching of ice flows across the Strait, but records indicate that at

times the arch fails and ice breaks out into the Bering Sea. The problem to be solved is the actual prediction of breakout. This will involve the determination of the properties of sea ice which control breakout. A separate study will determine when and how often the physical environment of the Bering Strait is such as to permit breakout.

### I.2 Description of Breakout

In the last few years there has usually been at least one well-defined case of large-scale ice breakout through the Strait every winter. The best way to observe the phenomenon is by examination of satellite photographs of the area. The onset of breakout is accompanied by the formation of regularly placed cracks in the ice cover which open to form leads at breakout. Since open water appears dark on both visible and infrared photographs, these features are easy to identify. As the intensity of ice motion builds up, the extent of the leads increases into the Chukchi Sea to the north of the Strait. After a period of several days the motion ceases and the ice cover resolidifies.

### I.3 Description of the Model

The geography of the Bering Strait plays an important role in selection of a model to describe breakout. At the southern boundary of the Chukchi Sea the Siberian and Alaskan shorelines come together to form a restricting channel which is a very good approximation to a two-dimensional hopper or chute. In the vein of this analogy, the Bering Strait is the outflow of the hopper. This suggests modeling flow through the Strait as two-dimensional flow of granular material

through a restricting channel. The forces driving the flow are the<sup>3</sup> atmospheric and oceanic drag on the ice cover. In addition to this, the Coriolis force will play an important role once the velocity of the ice becomes appreciable. The Chukchi Sea provides a large fetch over which winds may blow to produce ice stresses of sufficient magnitude to cause failure of any arch which may form across the outflow of the hopper. Flows of 25 km per day are a matter of record, and may continue for a number of days [1].

If breakout is to be modeled as the flow of material through a two-dimensional hopper, then a very important element of the model will be a constitutive relation for sea ice. The plastic model of pack ice developed by the AIDJEX modeling group [2] will be used in this study. In this model pack ice is represented as a continuum on length scales of tens of kilometers. On shorter scales, the micro-structure of the pack becomes important and the necessary assumptions about continuity and differentiability of field variables may not hold. There are several rationales for using a plastic constitutive law.

On this scale sea ice is a densely fractured material. The AIDJEX model does not consider the formation of cracks, but assumes they exist independently of the model. Deformation may occur in the ice cover by relative motions at the cracks, but the ice between the cracks is rigid. Relative motion at a crack may result in three types of local deformation: the crack can open to form a lead; it can close to eliminate a lead and perhaps form a pressure ridge; and, at the same time, it can shear without changing thickness distribution. The strongest argument, then, for a plastic model is that, despite

rather smooth variations in the atmospheric and oceanic forcing fields, local events such as ridging and lead formation are known to happen sporadically as though a critical stress state must be reached before deformation can occur. Thus, the concept of a critical or yield stress is natural to a pack ice model. 4

Parmeter and Coon [3], discussing the mechanism of ridge formation, conclude that most of the energy expended in building a ridge goes into doing work against gravity and thus appears as gravitational potential energy in the ridge. They argue that the total work does not depend on the rate at which the ridge is built. The rate independence, together with the irreversibility of the process, suggests plastic behavior.

A final argument for a plastic treatment is based on a strong visual similarity between the ice pack, as seen from high-altitude aircraft or satellites, and other materials, such as sands, gravels, clays, and fractured rocks, which have been modeled successfully as plastic materials.

Extensive work has been done in developing plasticity solutions for material passing through a restricting channel. A summary of some of the literature which applies to granular materials such as crushed ores and soils has been given by Pritchard and Reimer [4]. These solutions have in common that they model materials which deform in plane strain and that they are all two-dimensional models derived from a three-dimensional theory. The solution for a problem formulated in plane strain with a Coulomb-type yield surface may also be a solution for another type of problem--in plane stress, for example. However, a detailed comparison of the yield surfaces of the two

problems, together with the resulting flow rules, must be made in <sup>5</sup> order to understand how the results of one apply to the other. Lacking a solution to a constricting flow problem in plane stress, this comparison has not been possible. The only attempt to give a quantitative description of the plastic flow of sea ice through a restricting channel has been made by Sodhi [5]. This work is based on the assumptions of plane strain and incompressible flow. The present solution, therefore, should make possible some comparisons between the plane strain and plane stress solutions.

In order to formalize the description of pack ice as a plastic material, a yield surface, flow rule, and hardening law must be provided. Because of the length scales involved, sea ice is truly a two-dimensional material, and since all forces are exerted in the plane of the material, the system must be in a state of plane stress. The two-dimensional yield surface used by the AIDJEX modeling group is not derived from a three-dimensional surface (as in plane-strain problems in soil mechanics), but is taken two-dimensional by assumption. A desire to keep this analysis analytical requires that the yield surface used by the AIDJEX modeling group be approximated by a surface composed of flats and corners in stress space. The exact nature of the yield surface to be used will be discussed in a later section. While plastic models of soils have exhibited unphysical amounts of dilation with normal flow rules, there is no *a priori* reason to assume that sea ice should experience the same difficulty. A normal flow rule will be assumed in this work, if for no other reason than that there is no evidence to influence this assumption one way or the other. Finally, it will be assumed that pack ice does

not harden in the processes to be modeled.

While the AIDJEX model treats pack ice as an elastic-plastic material, this work will assume a rigid-plastic material. The problem with this assumption is that the stress state in rigid domains is not unique. This, however, does not preclude obtaining some useful bounds on the loads which cause failure. This may be done by using two theorems due to Prager [6]. Using the usual definitions, one statement of these theorems is that if a stable, statically admissible stress state exists, failure cannot occur. On the other hand, if a kinematically admissible velocity field exists, for which the rate of work done by the boundary tractions exceeds the internal plastic dissipation, then failure must occur. A restatement of these theorems, given by Schofield and Wroth [7], is that failure loads derived from statically admissible stress states are lower bounds on the actual failure load, while failure loads derived from kinematically admissible velocity fields are upper bounds. The proof of these theorems is based on Drucker's postulate, which holds for the present model, and proportional loading, which is taken to be the case in this model.

These results can be used to obtain a unique solution to a special type of problem. If a failure load is derived from a statically admissible stress state which has the special property that it admits a kinematically admissible velocity field, then that failure load is both a lower and upper bound. In this way a unique failure load is obtained for a rigid-plastic problem.

The complete model to be used for predicting breakout will include two first order quasilinear partial differential equations.

Chapter II will show how the method of characteristics can be used to obtain solutions to these equations. Also in Chapter II will be the details of the plastic model, including the yield surface and flow rule. Chapter III will give a parameterization of the solution region and will develop the stress solutions. Only those stress solutions which admit velocity fields, or failure mechanisms, can be solutions to the problem, as will be discussed in Chapters IV and V. Results and conclusions will be discussed in the final chapter. Finally, some explicit velocity solutions have been placed in an appendix.

## II. MODEL

### II.1 Yield Surface

Modeling sea ice as a plastic material requires a special yield surface. A review of some of the properties of sea ice is sufficient to establish that none of the commonly used failure criteria will suffice. Because the material being modeled consists of individual ice floes on the ocean surface, it is not expected that the material will support any tension. Hence, only compressive normal stresses may be allowed. Also, the AIDJEX model is for a material thought to be non-cohesive [2]. Since the von Mises and Tresca failure criteria apply to materials that fail independently of pressure, they are not expected to apply in the present model because sea ice is known to fail in compression. Another relevant feature that the yield surface must exhibit arises from observations that have been made by Pritchard [8], that the yielding strength of sea ice in shear is about half the yielding strength in compression.

The AIDJEX modeling group has found it convenient to use a yield surface which has coordinate axes rotated 45° from the principal directions. These stress variables, called  $\sigma_I$  and  $\sigma_{II}$ , are defined by

$$\begin{aligned}\sigma_I &= 1/2(\sigma_{xx} + \sigma_{yy}) \\ \sigma_{II}^2 &= \left[ \frac{(\sigma_{xx} - \sigma_{yy})}{2} \right]^2 + \sigma_{xy}^2\end{aligned}\tag{1}$$

However, since the problem is two-dimensional there are three unknown



stress components. The third stress variable is chosen to be the <sup>9</sup> direction of the greater principal stress, measured by a positive (counterclockwise) rotation from the x-axis, and designated by  $\gamma$ . In terms of Cartesian components, the tangent of twice this angle is defined by

$$\tan 2\gamma \equiv \frac{2 \sigma_{xy}}{\sigma_{xx} - \sigma_{yy}}$$

A yield surface of the form

$$\phi(\sigma_I, \sigma_{II}, P^*) = 0 \quad (2)$$

is then assumed.  $P^*$  is the yielding strength of the material. A desire to keep this calculation tractable forces some restrictions on  $\phi$ ; namely, that it consist of straight lines and the corners which form the intersection of these lines. Fig. 1 shows the surface to be used.

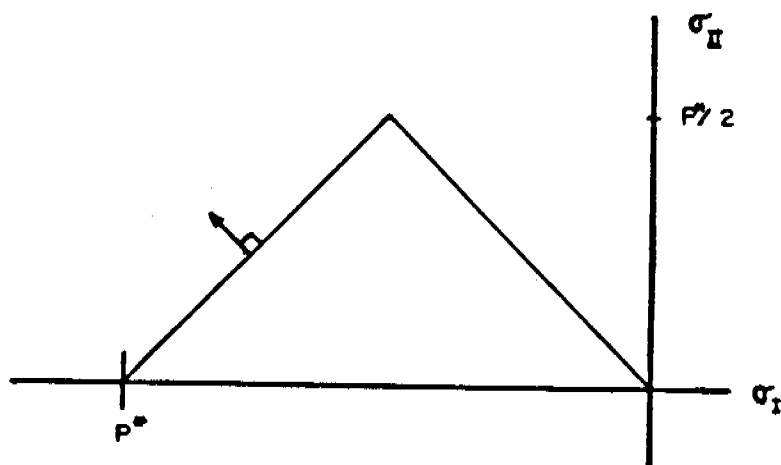


Fig. 1. The yield surface and associated flow rule used in the sea ice model.

The implications of the corners, apart from the usual indeterminacy<sup>10</sup> they imply in the flow rule, will become apparent when a characteristic analysis is performed on the governing equations. (2) may be written in a more explicit form:

$$\phi = \sigma_{II} - b(\sigma_I) \quad (3)$$

where  $b(\sigma_I)$  is the equation of either of the straight lines in Figure 1.

## II.2 Governing Equations

The principal directions of stress and strain-rate will be assumed to coincide so that the flow rule, written in terms of the strain-rate tensor  $\underline{D}$ , is

$$\underline{D} = \lambda \frac{\partial \phi}{\partial \sigma}, \quad \lambda > 0 \quad (4)$$

or, taking into account the possibility of intersecting lines at a corner,

$$\underline{D} = \lambda_1 \frac{\partial \phi_1}{\partial \sigma} + \lambda_2 \frac{\partial \phi_2}{\partial \sigma}, \quad \lambda_1, \lambda_2 > 0. \quad (5)$$

If the principal directions may be assumed given by the stress state, then (4) consists of three equations in two velocity components  $u$  and  $v$  and the unknown scalar  $\lambda$ . The latter quantity may be eliminated in favor of the velocity components, and in the case of (4) is

$$\frac{\lambda}{2} = \frac{u_y + v_z}{\sin 2\gamma} \quad (6)$$

The subscripts denote partial differentiation. Of the three equations

in (4), one equation has been used to determine the positive scalar  $\lambda$ . Using this result, (6), the other two equations may be written in a matrix form:

$$\underline{A} \underline{u}_x + \underline{B} \underline{u}_y = 0 \quad (7)$$

where

$$\underline{u}^T = (u \ v)$$

$$\underline{A} = \begin{bmatrix} 2 \sin 2\gamma & b' - \cos 2\gamma \\ 0 & b' + \cos 2\gamma \end{bmatrix} \quad (8)$$

$$\underline{B} = \begin{bmatrix} b' - \cos 2\gamma & 0 \\ b' + \cos 2\gamma & 2 \sin 2\gamma \end{bmatrix}$$

$\underline{A}$  and  $\underline{B}$  do not depend on the solution so (7) is linear.

In the case of (5) there are three equations in the two velocity components and two unknown scalars. The latter are found to be

$$\frac{\lambda_1}{2} = \frac{1}{\Delta} \left[ u_x (b_2' + \cos 2\gamma) - v_y (b_2' - \cos 2\gamma) \right] \quad (9)$$

$$\frac{\lambda_2}{2} = \frac{1}{\Delta} \left[ -u_x (b_1' + \cos 2\gamma) + v_y (b_1' - \cos 2\gamma) \right]$$

where

$$\Delta = 2(b_2' - b_1') \cos 2\gamma .$$

Here  $b_1'$  and  $b_2'$  are the slopes of the intersecting lines of the yield surface. The third of eqs. (5), with the help of (9), reduces to a simple statement of the alignment of principal directions:

$$\tan 2\gamma = \frac{u_y + v_z}{u_x - v_y} \quad (10)$$

To review briefly, the flow rule equations (4) and (5) which govern the velocity field are considered in two separate cases. In the first case, when the stress state lies on a flat of the yield surface (with a slope of  $b'$ ) the governing equations are the two equations in (7). In the second case, when the stress state lies at the intersection of two lines (with slopes  $b'_1$  and  $b'_2$ ), the single equation governing the velocity field is (10). In this case the velocity field may not be completely determined.

Discontinuities in the velocity field are to be expected in a model describing pack ice. Since the model is described by a boundary value problem, and the model equations are partial differential equations which may be parabolic or hyperbolic, it is natural to use characteristics as a means of obtaining and studying solutions. A characteristic analysis of the complete set of coupled stress and velocity equations describing the ocean-ice-atmosphere system has been made by Pritchard and Reimer [4]. The results used here can be found there or in most texts on partial differential equations [9].

Characteristic directions are directions in a solution region from which the solution of a partial differential equation cannot be extended uniquely, regardless of boundary conditions. For a system of first-order equations these directions are the roots of a characteristic determinant, given by

$$\left| \tau \underline{A} - \underline{B} \right| = 0 \quad (11)$$

where  $\underline{A}$  and  $\underline{B}$  are defined by (8). Each real  $\tau$  which is a solution of this equation represents a characteristic direction. Evaluating the characteristic determinant for the case of (7), obtained by substitut-

ing the given values of  $\underline{A}$  and  $\underline{B}$ , gives two roots called  $\tau_{\pm}$ , which are

$$\tau_{\pm} = \frac{\sin 2\gamma \pm \sqrt{1 - b'^2}}{b' - \cos 2\gamma}$$

Since the yield surface slope  $b'$  is either positive or negative unity (Figure 1), we obtain the result that, for this yield surface at most one distinct root (and hence one distinct characteristic direction) exists. The differential equation, (7), is therefore classified as parabolic. If this direction is called  $\xi$  then we have

$$\tan \xi = \frac{\sin 2\gamma}{\pm 1 - \cos 2\gamma} \quad (12)$$

which can be shown to give  $\xi = \gamma$  or  $\xi = \gamma + \pi/2$  for the plus and minus, respectively. The plus holds when the stress state lies on the yield surface cap and the minus applies along the tensile cutoff. [This  $\pm$  should not be confused with the  $\pm$  denoting the two roots of (11).]

The next step in the characteristic analysis is to find the differential equation which holds along characteristic curves. For a system of differential equations, this involves taking a linear combination of all the equations in such a way that all derivatives are in the characteristic direction. The eigenvector  $\underline{\xi}$  of each characteristic root of (11) accomplishes this [10]. The eigenvector associated with (12) is, within a normalizing constant,

$$\underline{\xi}^T = (1 \quad -\tan \xi) .$$

The linear combination of (7)

$$\underline{\xi}^T (\underline{A} \underline{u}_x + \underline{B} \underline{u}_y) = 0$$

then give the result

$$u_{\xi} - \tan \xi v_{\xi} = 0 . \quad (13)$$

This result, an ordinary differential equation, may be easily integrated in regions where the characteristic direction does not change.

Considering the case when the stress state is at a corner of the yield surface, only one equation, (10), governs the velocity field. A characteristic direction does not exist and no useful simplifications of the elliptic eq., (10), may be made.

The model description up to this point has provided a yield surface, and via the assumption of a flow rule, related the velocity field to the stress state. The equations governing the velocity field have been found, but these equations depend explicitly on the stress state. In the parabolic case, (13), this dependence is through the characteristic direction  $\xi$ , and in the elliptic case, (10), through the principal directions, which are assumed given through knowledge of the stress state. In order to complete the model description, the stress state must be discussed.

### II.3 Constant Stresses and Limit Analysis

The stress state in the modeled region will consist of constant stress regions by assumption. If a constant stress solution exists, there is no guarantee that it is unique, but if the solution is statically admissible, it will represent a lower bound on the particular boundary tractions. It must, therefore, be shown that the constant stress state satisfies equilibrium and continuity conditions, and nowhere lies outside the yield surface. The failure load calculated

from such a stress state will be unique if a kinematically admissible<sup>15</sup> velocity field, related to the stress state via the flow rule, can be shown to exist.

There are few guidelines to aid in the selection of constant stress regions. Some experimentation shows that there must be a constant stress region for each different boundary condition. Also, Cauchy's stress principal shows that for arbitrarily specified boundary tractions, a constant stress region can have at most three sides. Beyond these requirements one is guided only by a desire for simplicity. In the problem which has been solved here, it was found that the minimum number of regions, established by the number of stress boundary conditions, was sufficient to also allow an acceptable failure mechanism.

These concepts may be clarified by a list of steps in obtaining a complete problem solution.

1. Obtain a stress state which satisfies equilibrium and all stress boundary conditions.
2. Check that this particular stress state is everywhere on or within the yield surface. This may place restrictions on the allowable tractions.
3. Obtain at least one velocity field which satisfies the governing equations and velocity boundary conditions, and does positive work.

The last step guarantees the existence of a kinematically admissible velocity field and therefore completes the proof of the uniqueness of the failure load derived from the stress state.

#### II.4 Stress Boundary Conditions

Finally, to complete the model description, a boundary value problem must be defined. A more exact model of Bering Strait breakout than the present one would include the effect of body forces from ocean currents and winds on the ice cover. These would enter in the integration of the momentum balance equations, which have not been considered here because they are automatically satisfied by constant stresses when no body forces are present. This introduces the final model assumption. It will be assumed that breakout in the modeled region is caused by tractions along a boundary of the region, and the effect of body forces will not be considered. For regions so large that body forces are sure to be appreciable, this will limit the validity of a solution obtained.

The modeled region, picked to resemble the Bering Strait, will have one boundary perpendicular to the direction of the forces which cause breakout. The value of the traction along this boundary will determine the load which fails the entire region. Two of the sides of the region will be constricting at an angle which approximates the Bering Strait geography. Along these boundaries there will be two components of traction, one defined by the requirement of global equilibrium of the region, and the other specified by the condition of failure. The only velocity boundary condition will be specified along the constricting boundaries. As is usual in problems of bulk flow, these boundaries must be streamlines of the velocity field. Finally, when breakout occurs there must be an outflow of material, which assumes a traction-free boundary. The physical orientation of the four boundaries just described is shown in the next section.



### III. STATICALLY ADMISSIBLE STRESS STATES IN A RIGID-PLASTIC WEDGE

#### III.1 Parameterization and Equilibrium Conditions

Modeling incipient breakout of the ice pack through the Bering Strait involves finding the stress state in a two-dimensional restricting channel. This wedge-shaped region has tractions specified on all four boundaries and is to consist of constant stress regions. A solution will be attempted by guessing a stress solution and checking if it is statically admissible. Each of the constant stress regions must be separately statically admissible. The wedge is parameterized in Figure 2.

The angle subtended by the sides is assumed to be known and is designated  $2\alpha$ . The depth of the wedge is parameterized by the angle  $\beta$ , which also serves to define the constant stress and is assumed traction free.

The reactions between the triangular regions are defined by the conditions that each constant stress region be in equilibrium and by Newton's third law. These two conditions give a unique traction on each side of each triangular subregion. Cauchy's principle then gives a unique specification of the stress state within the constant stress region. Since Newton's third law constrains the reaction forces, the appropriate components of the stress tensor will be continuous across boundaries of subregions. The normal traction across the top of the wedge is designated  $2P$ , while the horizontal traction along the sides is called  $Q$ . The vertical tractions acting along the

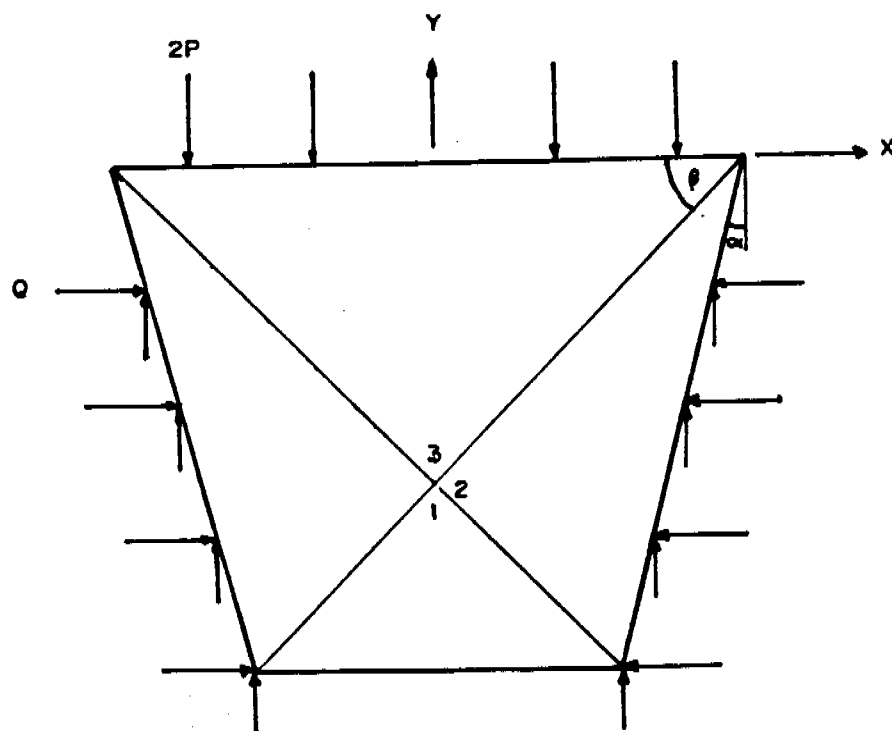


Fig. 2. The wedge and boundary tractions which parameterize the solution region.

sides of the wedge are defined by the condition of vertical equilibrium of the wedge. This completes the parameterization of the problem region, and the conditions of equilibrium may be obtained algebraically. These conditions provide a value for each of the reactions shown in Figure 2 in terms of  $P$  and  $Q$ . The Cauchy stress principal then gives the Cartesian components of the stress tensor, which may be related to the more convenient components defined by (1).

### III.2 Stress States in Traction Space

The material being modeled is assumed to have no tensile strength. It must, therefore, be assumed that all principal stresses are negative. The stress state in Region 1 of the wedge (see Figure 2), found by applying the previous conditions, is

$$\sigma_I^{(1)} = -\frac{1}{2} \left[ \frac{Q}{\cos \alpha} - P \cot^2 \beta (1 + \tan \alpha \tan \beta) \right]$$

$$\sigma_{II}^{(1)} = \left| \sigma_I^{(1)} \right|$$

$$\tan 2\gamma^{(1)} = 0,$$

and will be compressive only if

$$\frac{Q}{\cos \alpha} \geq P \cot^2 \beta (1 + \tan \alpha \tan \beta) \quad (14)$$

If we consider a traction space with  $Q$  and  $P$  as coordinate axes then condition (14) defines a solution region above line  $A$  as shown in Figure 3. When the equality of condition (14) is satisfied, then the tractions  $Q$  and  $P$  lie on line  $A$  in Figure 3.

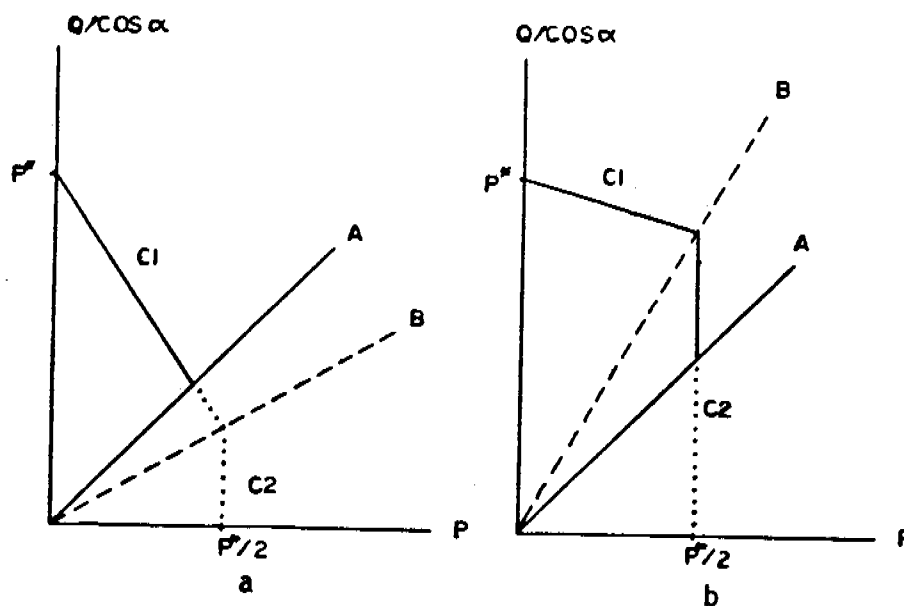


Fig. 3a,b. A representation of different failure mechanisms in traction space. Possible failures occur on or above line  $A$ . Figs. 3a and 3b are for  $\beta$  less than and greater than  $45^\circ$ , respectively.

The tensile cutoff of the yield locus (Figure 1) has a slope of minus one. Region 1 automatically falls on this line and Regions 2

3 must be required to lie on or to the left of this line. The stress state in Region 2 is

$$\begin{aligned}\sigma_I^{(2)} &= -\frac{1}{2} \left[ \frac{Q}{\cos \alpha} + P(1 - \tan \alpha \cot \beta) \right] \\ \sigma_{II}^{(2)} &= \frac{1}{2} \left[ \left( \frac{Q}{\cos \alpha} - P(1 + \tan \alpha \cot \beta) \right)^2 + 4 P^2 \cot^2 \beta \right]^{\frac{1}{2}} \\ \tan 2\gamma^{(2)} &= -\tan 2\beta\end{aligned}$$

Some algebra shows that condition (14) guarantees that Region 2 will lie on or to the left of the tensile cutoff. Hence, if the tractions lie on line A of Figure 3, then Region 2 will be plastic.

In Region 3 we find the stress state to be

$$\begin{aligned}\sigma_I^{(3)} &= -\frac{1}{2} \left[ \frac{Q}{\cos \alpha} + P \cot^2 \beta (1 - \tan \alpha \tan \beta) + 2P \right] \\ \sigma_{II}^{(3)} &= \frac{1}{2} \left| \frac{Q}{\cos \alpha} + P \cot^2 \beta (1 - \tan \alpha \tan \beta) - 2P \right| \\ \tan 2\gamma^{(3)} &= 0.\end{aligned}$$

Condition (14) places this state to the left of the tensile cutoff of the yield locus, but it must also lie on or to the right of the yield surface cap (Figure 1). The latter condition is more complicated than the former. If

$$\frac{Q}{\cos \alpha} > P \left[ 2 - \cot^2 \beta (1 + \tan \alpha \tan \beta) \right] \quad (15)$$

then the condition that Region 3 lie on the yield surface cap gives

$$\frac{Q}{\cos \alpha} = P^* - P \cot^2 \beta (1 - \tan \alpha \tan \beta) \quad (16)$$

whereas, if

21

$$\frac{Q}{\cos \alpha} < P \left[ 2 - \cot^2 \beta (1 + \tan \alpha \tan \beta) \right] \quad (17)$$

then the criterion for Region 3 is

$$P = \frac{P^*}{2} . \quad (18a)$$

Before this information may be plotted in Figure 2 its relationship to line *A* must be discovered. We find that this requires a separate consideration of  $\beta < \pi/4$  and  $\beta > \pi/4$ . Let us call the equation

$$\frac{Q}{\cos \alpha} = P \left[ 2 - \cot^2 \beta (1 + \tan \alpha \tan \beta) \right]$$

line *B*, and represent it by a dashed line in Figure 3. Now, if  $\beta < \pi/4$ , line *B* has a slope less than line *A*, whereas if  $\beta > \pi/4$ , the opposite is true. These two cases are shown in Figure 3a and 3b, respectively. We call the failure criterion of (17) line *C1* and that of (18a) line *C2*.

The analysis up to this point may be summarized briefly. The stress state in each region, found from equilibrium conditions and the Cauchy principle, is required to lie on or within the yield locus of Figure 1. This results in several relationships between tractions *Q* and *P*. These relationships are plotted in traction space and are represented by the lines in Figs. 3a and 3b. When the tractions acting on the wedge fall on any of these lines, a particular region becomes plastic. When the tractions fall on the intersection of lines then two or more regions become plastic. Possible tractions are on or

above line  $A$  of Figure 3.

Bearing in mind this last requirement, we examine some of the possible modes of plastic failure. When the tractions lie on line  $A$  at a point where this line intersects no other line, then Regions 1 and 2 are plastic and Region 3 is rigid. This corresponds to a mode of failure where Region 3 undergoes no deformation, but the sides and bottom of the wedge are failing. When the tractions lie along  $C1$  or  $C2$  at a point where these lines do not intersect line  $A$ , then Region 1 and 3 are plastic and Region 2 is rigid. Correspondence is made to a failure mechanism where the sides are rigid and the top and bottom undergo deformation. This failure mode will have material passing out of the bottom and top of the hopper. Finally, we make note of the mechanism represented by the intersection of line  $A$  with either  $C1$  or  $C2$ . The former occurs at a value of  $P$  less than  $P^*/2$ , while the latter occurs at  $P$  equal to  $P^*/2$ . These situations correspond to  $\beta$  less than  $45^\circ$  and greater than  $45^\circ$ , respectively. When this occurs all three regions of the wedge will be plastic and the equality of (14) holds simultaneously with either (16) or (18a), depending on  $\beta$ . When  $\beta$  is less than  $45^\circ$ , (14) and (16) together imply, upon elimination of  $Q$ , that

$$P = \frac{P^*}{2} \tan^2 \beta \quad (18b)$$

and if  $\beta$  is greater than  $45^\circ$ , (18b) specifies  $P$  independently of  $Q$ . The failure load for  $\beta$  greater than  $45^\circ$ ,

$$P = \frac{P^*}{2}$$

may be substituted in (14) to find  $Q$ .

We may note an important result at this time. Since  $\beta$  is a measure of the depth of the wedge, this analysis has shown that below a critical depth the load which fails the wedge depends on the depth of the wedge. However, above the critical depth, defined by  $\beta$  equal to  $45^\circ$ , the failure load is independent of  $\beta$  and hence of wedge depth.

#### IV. KINEMATICALLY ADMISSIBLE VELOCITY FIELDS IN A RIGID-PLASTIC WEDGE

##### IV.1 Equations Governing the Velocity Field

The traction across the top of the wedge-shaped region which causes failure is given in (18). This chapter will prove the uniqueness of the failure load by showing that the stress state from which (18) was derived admits a kinematically admissible velocity field. Attention should be drawn to the fact that the problem which has been uniquely solved is defined by the boundary conditions of Section II.4. The strength of the solution rests on how accurate a representation these boundary conditions are. We now identify the conditions to be satisfied by velocity fields.

The first requirement to be imposed on a velocity field is that it satisfy the flow rule equations. This will insure that the principal stretching directions are the same as the principal stress directions. In the case when the stress state of a region lies on a flat of the yield surface equation, (13) is the relevant equation. We have the constant stress assumption to help with the integration of this equation. (12) relates the principal directions, which are constant in a given region, to the characteristic direction. From Chapter III we have the result that

$$\gamma^{(2)} = \frac{\pi}{2} - \beta$$



$$\gamma^{(3)} = 0 \quad \beta > \frac{\pi}{4}$$

$$\gamma^{(3)} = \frac{\pi}{2} \quad \beta < \frac{\pi}{4}$$

which, with (12) and (13), gives

$$u^{(2)} - \tan \beta v^{(2)} = \text{constant}$$

$$u^{(3)} = u^{(3)}(y) \quad \beta > \pi/4 \quad (19)$$

$$v^{(3)} = v^{(3)}(x) \quad \beta < \pi/4 .$$

The two possibilities for Region 3 correspond to  $\beta > \pi/4$  and  $\beta < \pi/4$  as discussed in the paragraph below Figure 3 in Chapter III. Region 1 will be removed from consideration for the remainder of this work, since it is stress free and will not affect breakout directly.

Recalling the result at the end of Chapter III, that when  $\beta$  is  $45^\circ$  each region is at a corner of the yield surface, we consider this case separately. This is because, as already stated in Chapter II, the governing equations become elliptic and characteristic directions do not exist. In fact, the only equation governing the velocity field is the statement of coaxiality, (10). Starting with Region 3, Figure 4 places it at the isotropic corner of the yield surface when  $\beta$  is  $45^\circ$ . Here all directions are principal, so (10) is of no value. However, the requirement that the stretching vector lie within the bounds set by the normals of intersecting yield surfaces does place a restriction on the velocity field allowed in Region 3. Examination of Figure 1 shows that Region 3 may be in a stretching state which is uniaxial closing, isotropic closing, or any state intermediate between these two.

Region 2, at the shear corner of the yield surface, is constrained by (10). However, since the case  $\beta = 45^\circ$  is being considered, the left side of this equation is infinite so the requirement

$$u_x^{(2)} = v_y^{(2)}$$

follows.

#### IV.2 Postive Work

A further requirement set by the theory of plasticity is that all deformations result in positive work. This is known to be true whenever the scalar  $\lambda$ , first appearing in (4), is positive. Again, a distinction must be made between the parabolic and elliptic cases.

Considering the parabolic case first, an expression for  $\lambda$  has already been obtained, shown in (6). For Region 2, where  $\sin 2\gamma$  is positive this simply implies that shearing deformation occurs in a positive sense:

$$u_y^{(2)} + v_x^{(2)} > 0 \quad . \quad (20)$$

Region 3 is more complicated because both the denominator and numerator of (6) vanish when  $\gamma$  is zero or  $90^\circ$ . Recalling that both of these cases exist in Region 3, depending on whether  $\beta$  is greater than or less than  $45^\circ$ , we consider the two individually. From the defining equation, (4), we have

$$u_x = -\frac{\lambda}{2} (b' - \cos 2\gamma)$$

$$v_y = -\frac{\lambda}{2} (b' + \cos 2\gamma)$$

In Region 3 then, where  $b' = \pm 1$ , the result follows that if  $\beta < \pi/4$  <sup>27</sup>

$$\lambda = -u_x^{(3)} > 0 \quad (21a)$$

and if  $\beta > \pi/4$

$$\lambda = -v_y^{(3)} > 0 \quad (21b)$$

Hence, if the governing equations are parabolic ( $\beta \neq 45^\circ$ ), then (20) and (21) insure that positive work will be done by the velocity field.

In the elliptic case each region is at a yield surface corner and the positive work requirement must again be enforced in each region separately. At the isotropic corner (Region 3) one of the yield surface slopes is infinite (referring to Figure 1) while the other is +1. The appropriate limit of (9) when  $b_1' = \infty$  and  $b_2' = +1$  is

$$\frac{\lambda_1}{2} = -u_x^{(3)} \left[ \frac{1 + \cos 2\gamma}{2 \cos 2\gamma} \right] + v_y^{(3)} \left[ \frac{1 - \cos 2\gamma}{2 \cos 2\gamma} \right] > 0 \quad (22)$$

$$\frac{\lambda_2}{2} = \frac{u_x^{(3)} - v_y^{(3)}}{2 \cos 2\gamma} > 0$$

for Region 3.

At the shear corner (Region 2) difficulties arise in (9) because  $\beta$  is  $45^\circ$ , and therefore  $\cos 2\gamma$  vanishes. Taking the limit correctly, and using  $b_1' = -b_2' = 1$ , gives

$$\lambda_1 = \frac{u_y^{(2)} + v_x^{(2)}}{2} - u_x^{(2)} > 0$$

$$\lambda_2 = \frac{u_y^{(2)} + v_x^{(2)}}{2} + u_x^{(2)} > 0 \quad (23)$$

for Region 2.

The restrictions placed on the velocity field by the theory of plasticity, namely flow rule and positive work, are contained in (19) - (23). The conditions pertaining to the specific model of breakout are discussed next. These criteria will amount to physical features of the flow field such as flow direction and boundary conditions.

#### IV.3 Velocity Boundary Conditions and Physically Acceptable Velocity Fields

The failure mechanisms to be modeled are those which occur by sliding at the sides of the restricting channel. This assumption is embodied in the statement that the sides of the wedge are streamlines of the flow field. Defining a streamline through the differential equation

$$\frac{dy}{dx} = \frac{v}{u},$$

the parameterization of the wedge is such that the sides will be streamlines if

$$\left. \begin{array}{l} \underline{v}^{(2)} \\ \underline{u}^{(2)} \end{array} \right|_{y = (x - x_0) \cot \alpha} = \cot \alpha \quad (24)$$

Here  $x_0$  is the coordinate of the upper right hand corner of the wedge (see Figure 2).

It has been stated that the failure mechanism most likely to be of interest in predicting breakout is one in which the entire wedge

is plastic. This must be taken as a hypothesis in the present work. However, consideration of the velocity field can give some credibility to the hypothesis. There is no *a priori* reason for requiring that the normal velocity components be continuous between regions of the wedge since sea ice can thicken during deformation. However, if the model is not to have accumulation of material at region boundaries, then continuity of normal velocity components is required. This will be used in the following way. It is hypothesized that Region 2 of the wedge must be plastic if failure is to occur. The flow field for this failure will be a function of both spatial coordinates, and so, therefore, must be the flow field of Region 3 if normal velocity components are to match at the intervening boundary. The only way this may be is if Region 3 is plastic. The case for assuming a fully plastic wedge will be further strengthened in the next chapter. The discussion of velocity fields is concluded by noting the condition of continuity:

$$u^{(3)} \tan \beta - v^{(3)} \Big|_{\text{boundary}} = u^{(2)} \tan \beta - v^{(2)} \Big|_{\text{boundary}} \quad (25)$$

That a velocity field exists which satisfies all these criteria and is kinematically admissible is demonstrated in the appendix.

V. A FAILURE MECHANISM FOR  
BERING STRAIT BREAKOUT

V.1 Stress State in Invariant Space

The failure mechanism most likely to be of interest in the breakout problem is the one with all three regions plastic. This stress state occurs at the intersection of two lines in traction space and hence specifies uniquely, in terms of  $\beta$ , the tractions which fail the wedge. Knowledge of these permits determination of the location of each region on the yield surface in terms of the angle  $\beta$ . This result is shown in Figure 4.

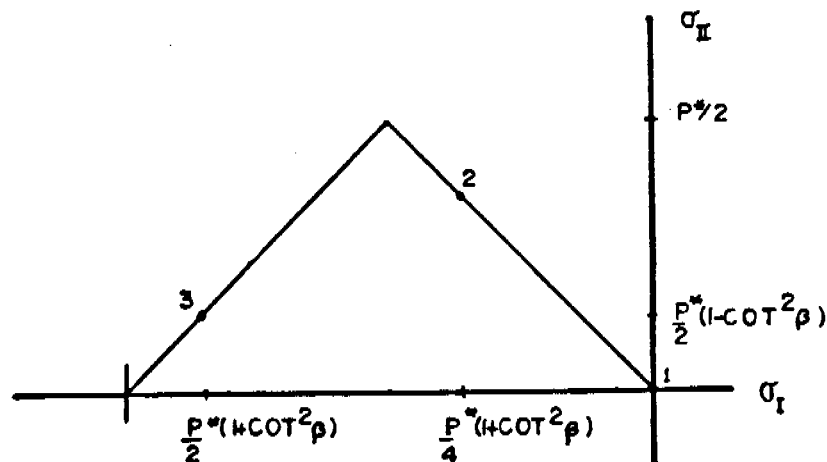


Fig. 4. The location of each region of the wedge on the yield surface at incipient failure.

Figure 4 shows the case  $\beta > \pi/4$ . When  $\beta < \pi/4$ , the replacement of  $\cot \beta$  with  $\tan \beta$  gives the correct result. When  $\beta = \pi/4$  each region

is at a corner of the yield surface.

## V.2 Principle Directions

Finally, we will need to know the principal direction in each region of the wedge. They are shown in Figure 5 when the wedge is at incipient failure.

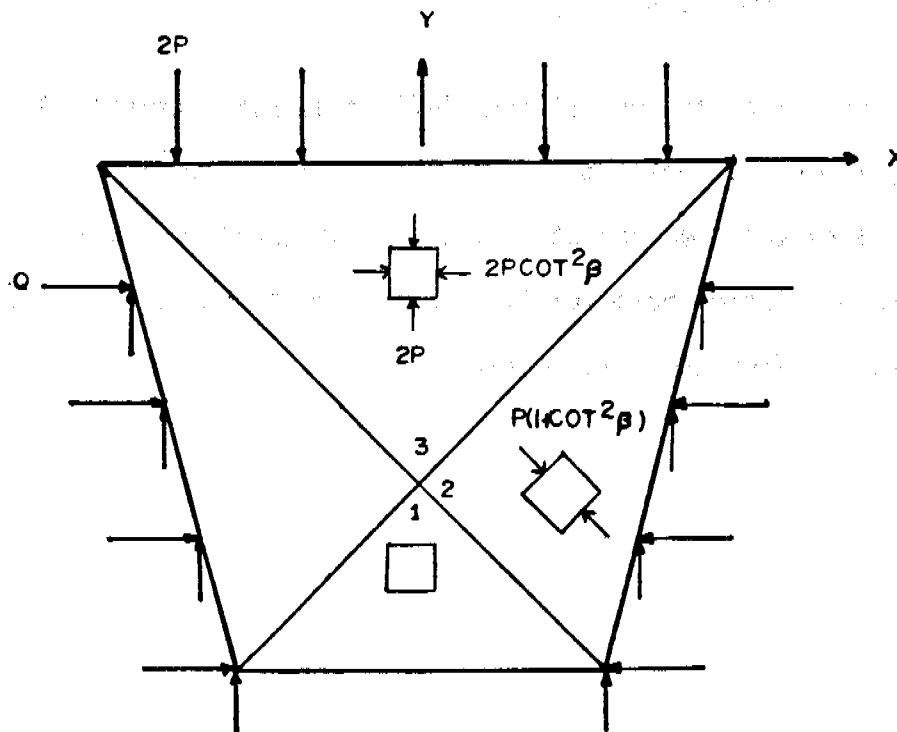


Fig. 5. The principal direction of each region of the wedge at incipient failure.

Apparently the size of  $\beta$  determines the greatest principal stress in Region 3. If  $\beta > \pi/4$  ( $\cot^2 \beta < 1$ ), then  $\sigma_{xx}$  is the greatest principal stress, and then  $\gamma^{(3)} = 0$ . On the other hand, if  $\beta < \pi/4$ , then  $\gamma^{(3)} = \pi/2$ . In Region 2 we have no *a priori* reason for choosing between  $\gamma^{(2)} = -\beta$  or  $\gamma^{(2)} = -\beta + \pi/2$  from information provided by the stress state. The infinitesimal material element in Region 2 (Figure 5) is in a state of uniaxial compression, and the choice of

the nonzero principal stress must be based on velocity considerations.<sup>32</sup> Recalling the condition in Chapter IV, that material should streamline along the wedge boundaries, we reach the conclusion that a stress state must have the compression taking place in such a way that material flows out of the bottom of the wedge. From the sense in which the greatest principal stress is measured, it follows that

$$\gamma^{(2)} = -\beta + \pi/2 .$$

Recalling the result from (12), the characteristic direction of each region may be found. In Region 3 the horizontal or vertical direction will be characteristic if  $\beta$  is smaller or larger than  $45^\circ$ . In Region 2 the characteristic direction is a clockwise rotation of  $\beta$  degrees from the horizontal.



## VI. CONCLUSIONS

### VI.1 Results Pertaining to the Yield Surface

The constant stress analysis of a rigid-plastic wedge has illuminated some of the important factors in breakout of ice through the Bering Strait. With the help of a yield surface of straight lines an exact solution has been obtained for a problem which otherwise could not be solved analytically. The nature of the solution is such that the various failure mechanisms of a rigid-plastic wedge with constant stress regions are defined, and the present work has selected one of those mechanisms as being the one likely to describe breakout. An important feature of this mechanism is that ice is not allowed to accumulate along the boundaries of the Strait during breakout. From the stress state which permits this particular failure, a failure load is derived. Even though the validity of the failure load is restricted by the approximate boundary conditions which define the problem, some insight is gained from the model which has been developed.

An important discovery regarding the yield surface has been that Region 2 of the wedge can fail only on the tensile cutoff or the shear corner of the yield surface. Region 3 can fail only on the cap or at the isotropic corner. From this it follows that a failure mode analyzed with an uncapped yield surface is indistinguishable from a failure mode which has Region 3 rigid. This result depends on the perfectly plastic assumption. A further conclusion which may be drawn

is that since Region 2 fails only along the tensile cutoff, which passes through the origin of stress space, this region becomes plastic at arbitrarily small loads. These results are not unexpected since a material modeled by an uncapped yield surface will not exhibit any dependence on ultimate yielding strength. Since breakout is a process which does not occur until after a certain amount of stress buildup, the choice of failure mechanisms in Chapter V, which requires each region of the wedge to be plastic, seems reasonable.

Another yield surface feature is that the slope of the tensile cutoff is not arbitrarily chosen. There is no proof that the bottom region of the wedge (called Region 1) must be plastic at incipient failure, but it is hard to conceive of a failure mode where it is not, it being the outflow of a constricting channel. Recalling a result from Chapter III, Region 1 always lies along a  $45^\circ$  line in stress space. If this is the case, as it must be under the constant stress assumption, then the only yield surface on which Region 1 may fall is one whose tensile cutoff has negative unit slope. This conclusion is of more limited validity, depending as it does on the constant stress assumption and the straight line yield surface.

## VI.2 Application to the Bering Strait

With these comments made, it is possible to make a prediction of breakout in the Bering Strait. To the extent that the model assumptions are correct, failure of ice arches in the Strait will not occur unless the entire wedge-shaped region is plastic. When the conditions causing breakout are well represented by the assumed boundary conditions, the breakout load across the top of the wedge is given by (18).

An interpretation of these equations may be given. The failure load increases with wedge depth up to a critical depth, beyond which it remains constant. The sense in which this is true is made clear by studying how the angle  $\beta$  parameterizes the wedge depth. When  $\beta$  exceeds  $45^\circ$ , by (18a), failure is independent of depth. For wedges shallower than  $45^\circ$  the failure load is given by (18b).

It is important to understand the meaning of the traction across the top of the wedge. The implication may be made that the effect of ice stresses in the ice pack surrounding the wedge are represented by the boundary tractions. While these stresses are likely to be the most important in precipitating failure, the effect of body forces on the wedge itself may also be appreciable. The present model is not able to account for body forces explicitly, but if an appropriate interpretation is given to the boundary tractions they may be approximated there. Hence, an appropriate forecast of failure is that if the combined effect of boundary tractions and a distribution of the effective force on the body across the top boundary result in a traction of  $P^*/2$ , then failure will occur. The value of the horizontal traction along the side of the wedge is unknown until failure occurs. At that time it is given by (14) with the appropriate value of  $P$ .

The application which will be made in this work is to select what is thought to be the wedge of importance in the Bering Strait. Visual features observed in satellite images of breakout will be the criteria used in this selection. Then the failure load is given by the above theory, and, neglecting body forces, a correlation may be made between the wind strengths and fetches which produce stresses leading to failure. If the pack ice in the Strait is taken to have a strength of

$10^5$  N/m [8], then an air stress (in Pascals) will create a force in the ice which increases as the fetch over which the wind blows. Figure 6 shows this relationship for the indicated strength.

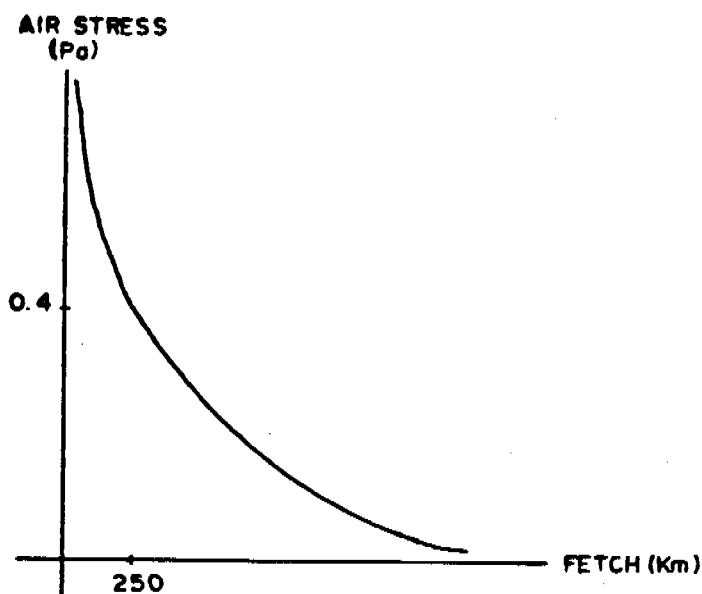


Fig. 6. The relationship between the fetch required to produce a failure load as a function of air stress when ice strength is  $10^5$  N/m.

Winds producing stresses greater than 0.5 Pa seldom have great frequency in the Arctic. Hence, a 200-km fetch, at the least, is required for winds of highest probable magnitude to cause breakout.

Breakout in the Bering Strait may usually be observed at least once every winter by studying NOAA satellite photographs of that region. When this condition occurs, open water appears in bands which symmetrically span the Strait and the region to the north of the Strait. The axis of symmetry of these bands should be taken as the axis of the wedge used to model breakout. In most cases the extent

of these bands continues up to Wrangell Island on the east side of the Chukchi Sea and at least to Point Hope on the west side. Figure 7 shows what appears to be a good selection by these criteria. Inspection of the angles shows that  $\beta$  is approximately  $45^\circ$ , so the failure load is  $P^*/2$ . The present work predicts that any wedge deeper than the indicated one will fail independently of depth.

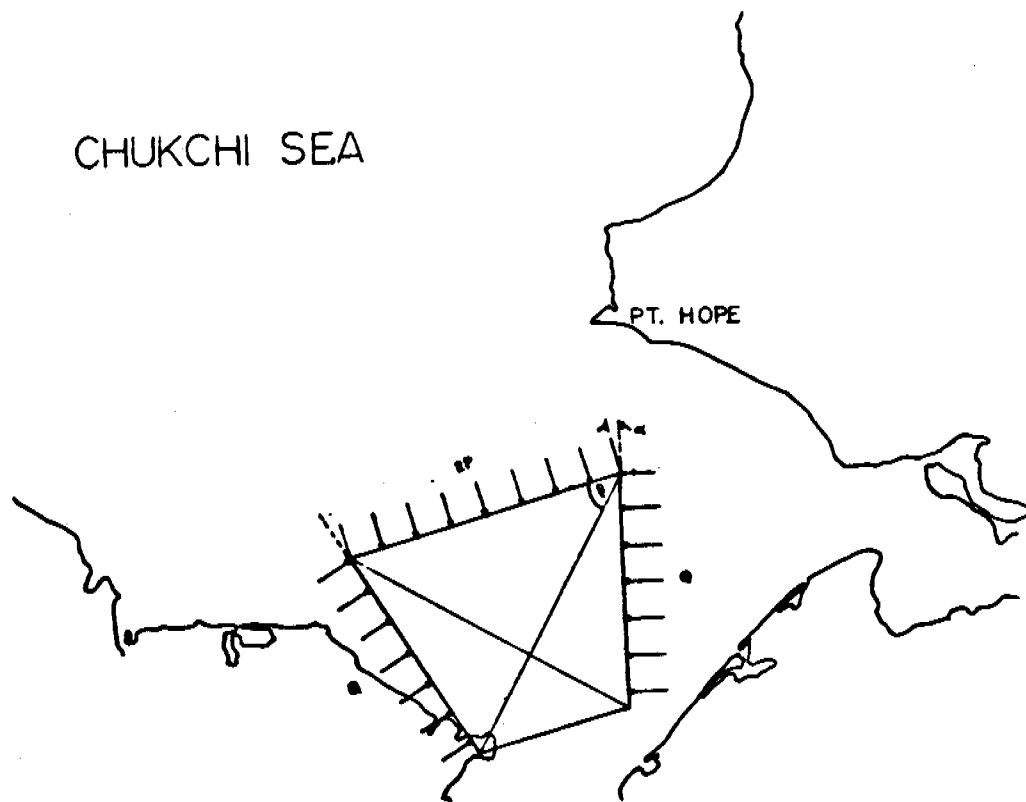


Fig. 7. The region thought to be critical in Bering Strait breakout. The Strait width is 60 km.

## VII. REFERENCES

- [1] Marco, J. R., and R. E. Thompson. 1976. "Rectilinear leads and internal motions in the ice pack of the western Arctic Ocean." Journal of Geophysical Research, 82(6), pp. 979-987.
- [2] Coon, M. D., G. A. Maykut, R. S. Pritchard, D. A. Rothrock, and A. S. Thorndike. 1974. "Modelling the pack ice as an elastic-plastic material." AIDJEX Bulletin, 24, pp. 1-106.
- [3] Parmenter, R. R., and M. D. Coon. 1973. "Model of pressure ridge formation in sea ice." AIDJEX Bulletin, 19, pp. 59-74.
- [4] Pritchard, R. S., and R. Reimer. 1978. "Mathematical characteristics of a plastic model of sea ice dynamics." AIDJEX Bulletin, 40, pp. 109-151.
- [5] Sodhi, D. S. 1977. "Ice arching and the drift of pack ice through restricted channels." CRREL Report 77-18, Cold Regions Research and Engineering Laboratory, Hanover, N.H., pp. 1-11.
- [6] Prager, W., and P. G. Hodge. 1951. Theory of Perfectly Plastic Solids. John Wiley:New York.
- [7] Schofield, A., and P. Wroth. 1968. Critical State Soil Mechanics. McGraw-Hill, Ltd.:Maidenhead, England.
- [8] Pritchard, R. S. 1976. "An estimate of the strength of Arctic pack ice." AIDJEX Bulletin, 34, pp. 94-113.
- [9] Courant, R., and D. Hilbert. 1962. Methods of Mathematical Physics, Vol. 2. Interscience Publishers:New York.

## VIII. APPENDIX

### KINEMATICALLY ADMISSABLE VELOCITY FIELDS

A kinematically admissible and physically acceptable velocity field must satisfy a number of requirements as discussed in the text. A brief summary of those requirements is made. That a velocity field must have a negative y-component is obvious from Figure 2. The horizontal component is expected to be symmetric about the center of the wedge, as well as to be zero there. As discussed in Chapter IV, the wedge sides must be streamlines of the flow field and this requirement is given by (24). The continuity of the velocity component normal to region boundaries will be satisfied if (25) is enforced.

The characteristic conditions and the condition of positive work are dependent on principal directions in each region, so the case when  $\beta$  is  $45^\circ$  (the elliptical case) is treated separately. The case of  $\beta < 45^\circ$  is considered first. For Region 3 the characteristic condition is (19) and the positive work condition is (21a). For Region 2 these two conditions are (19) and (6), respectively. A velocity field which satisfies all these criteria is:

$$u^{(3)} = -\frac{u_0 x}{x_0} (\cot \beta - \tan \alpha) \cot \beta$$

$$v^{(3)} = -2 u_0 (\cot 2\beta + \cot 2\alpha)$$

$$u^{(2)} = \frac{u_0}{x_0} \left[ \frac{(x - x_0) - y \tan \alpha}{\cot \beta - \tan \beta} \right] \cot \beta - u_0$$

$$v^{(2)} = \frac{u_0}{x_0} \left[ \frac{(x - x_0) - y \tan \alpha}{\cot \beta - \tan \beta} \right] \cot^2 \beta - u_0 \cot \alpha .$$

Here  $u_0$  is an arbitrary speed and  $x_0$  is the coordinate of the upper right-hand corner of the wedge. Figure 8a shows this flow field.

In the case when  $\beta = 45^\circ$  the condition of positive work in Region 3 is contained in (22). The characteristic condition is not applicable for the elliptic case. (23) is the condition of positive work for Region 2. An acceptable velocity field is given by

$$u^{(3)} = - \frac{u_0 x}{2x_0} \left[ \cot \alpha - \tan \alpha \right]$$

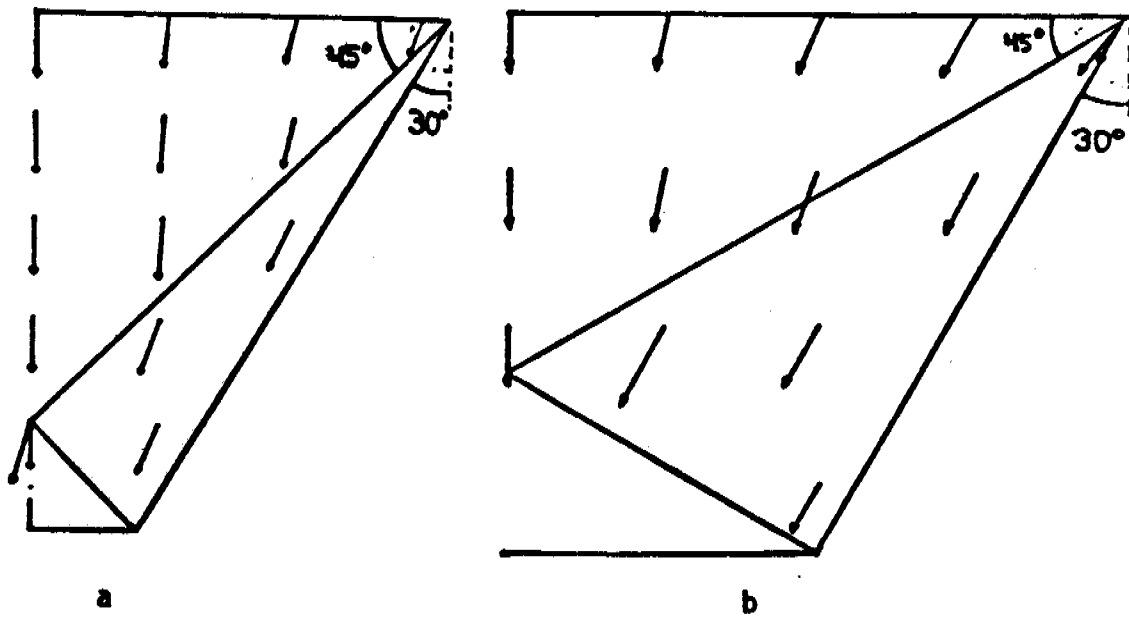
$$v^{(3)} = \frac{u_0}{x_0} \left[ x(\cot \alpha - \tan \alpha) - \frac{y}{2} (\cot \alpha - \tan \alpha) - x_0 \left( \frac{5}{2} \cot \alpha - \frac{3}{2} \tan \alpha - 1 \right) \right]$$

$$u^{(2)} = \frac{u_0}{x_0} [ y \tan \alpha - x ]$$

$$v^{(2)} = \frac{u_0}{x_0} \cot \alpha [ - y \tan \alpha + x - 2x_0 ]$$

Figure 8b shows this result.





- Fig. 8. Kinematically admissible velocity fields for  $\beta$  equal to and less than  $45^\circ$ , respectively.

## Appendix II. Circular Arches Under Radial Loading.

### Introduction

Flow of sea ice through a constriction is difficult to solve when realistic loading conditions and material models are treated. In this section, a circular region is analyzed under the combined system of body forces  $\tau$  from winds and currents and of boundary tractions  $P$  from internal ice stress (Figure II.1). The material model response is rigid-plastic with a general three-parameter yield surface as shown in Figure II.2. This yield surface is used

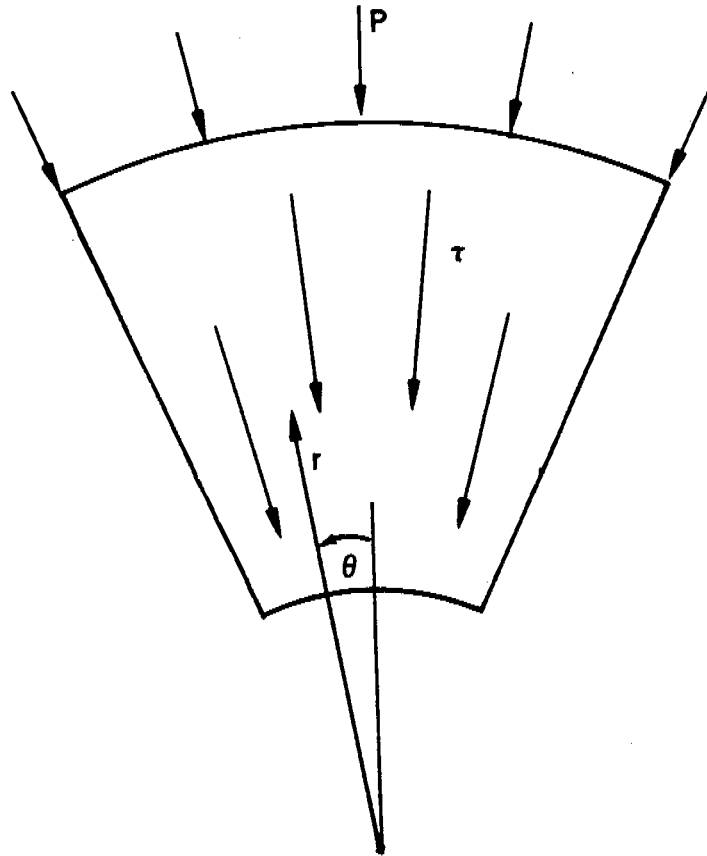


Figure II.1. Circular Arch.

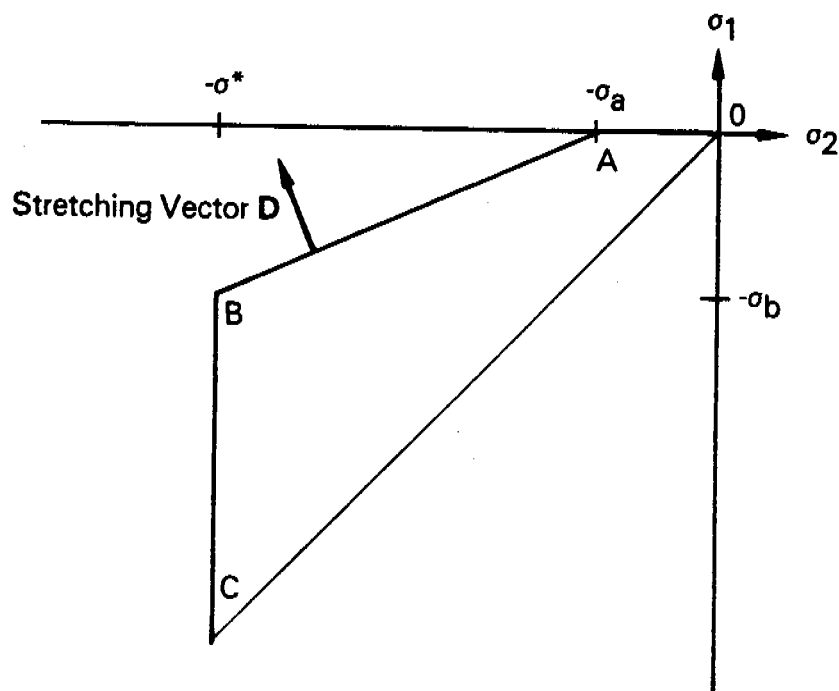


Figure II.2. Three-Parameter Yield Surface.

because it is desirable to learn what properties of the yield surface control the formation and collapse of arches in the constriction.

Although applied loads and material properties are rather general, it is necessary to make simplifying assumptions elsewhere in the problem to obtain analytical solutions. To this end, we follow Coon (1967a, b) and assume that the solution is axisymmetric. With this assumption, collapse loads may be found and the stress and velocity fields analyzed for various external loads, geometries and material properties.

Our approach is to determine separately the lower bound on collapse loads from an admissible stress field and an upper bound on collapse loads from an admissible velocity field. This approach is explained further in Appendix I where it is used to determine another approximate solution to the flow through a wedge-like constriction.

### Stress Fields and Collapse Load Lower Bound

The force balance in the  $r, \theta$  plane expressed in cylindrical coordinates is

$$\frac{\partial \sigma_{rr}}{\partial r} + \frac{1}{r} \frac{\partial \sigma_{r\theta}}{\partial \theta} + \frac{\sigma_{rr} - \sigma_{\theta\theta}}{r} - \tau = 0 \quad (\text{I.1})$$

$$\frac{\partial \sigma_{r\theta}}{\partial r} + \frac{1}{r} \frac{\partial \sigma_{\theta\theta}}{\partial \theta} + \frac{2}{r} \sigma_{r\theta} = 0$$

where  $\tau$  is the radial component of externally applied body force. If it is assumed that stress varies only with radial position  $r$ , then

$$\frac{d\sigma_{rr}}{dr} + \frac{\sigma_{rr} - \sigma_{\theta\theta}}{r} - \tau = 0 \quad (\text{II.1})$$

and

$$\sigma_{r\theta} = \frac{C}{r^2} \quad (\text{II.3})$$

where  $C$  is an arbitrary constant.

The boundary conditions specified on the stress tensor is that no traction is applied at  $r = a$

$$\sigma_{rr}(a) = 0 \quad (\text{II.4})$$

$$\sigma_{r\theta}(a) = 0$$

and that a normal component of  $-P$  is applied at  $r = b$  from the internal ice stress

$$\sigma_{rr}(b) = -P \quad (\text{II.5})$$

$$\sigma_{r\theta}(b) = 0 .$$

The shear component must then be identically zero to satisfy both boundary conditions and the axisymmetric assumption.

The stress state satisfying equation (II.2) is restricted to lie within or on the yield surface. To find the collapse load, we seek the case when the stress in some region lies on the yield surface. Furthermore, to simplify analysis we consider the case when the stress in the entire region  $a \leq r \leq b$  lies on the yield surface. The solution must be obtained by carefully considering the individual parts of the yield curve - i.e., line OA, AB and BC.

As a first step in determining the stress field, consider the boundary condition at  $r = a$  given by equation (II.4). Since  $\sigma_{rr}(a) = 0$ , the stress must lie on the yield surface somewhere along line OA and  $\sigma_1 = \sigma_{rr}$  at that point. Thus  $\sigma_{\theta\theta} \leq \sigma_{rr}$  and so  $\sigma_2 = \sigma_{\theta\theta}$ . Although the relative magnitude of  $\sigma_{rr}$  and  $\sigma_{\theta\theta}$  could switch for different values of  $r$ , the boundary condition specifies that hoop stress  $\sigma_{\theta\theta}$  be algebraically less than radial stress near  $r = a$ . To continue the analysis, consider several special cases. We present these cases in increasing order of complexity.

Case 1.

Let us first study the case when the stress lies along the sloped line AB of the yield surface. In Figure II.3, this segment is presented along with the equation relating principal stress components along AB. For our case where the boundary condition at  $r = a$  imposes  $\sigma_{\theta\theta} \leq \sigma_{rr}$ , the stress components satisfy

$$\frac{\sigma_{rr}}{-\sigma_b} = \frac{\sigma_{\theta\theta} + \sigma_a}{-\sigma^* + \sigma_a} \quad (II.6)$$

Substitute for  $\sigma_{\theta\theta}$  from equation (II.6) into the radial force balance equation (II.2) to obtain

$$\frac{d\sigma_{rr}}{dr} + \frac{m}{r} \sigma_{rr} = \tau - \frac{\sigma_a}{r} \quad (II.7)$$

where

$$m = \frac{-\sigma^* + \sigma_b + \sigma_a}{\sigma_b} \quad (II.8)$$

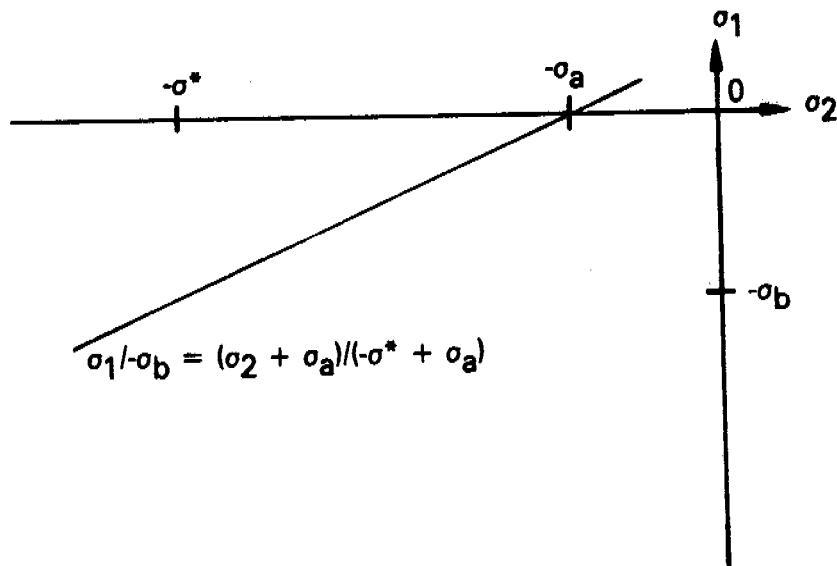


Figure II.3. Sloped Line Portion of Yield Surface, AB.

This ordinary differential equation may then be integrated to obtain a homogeneous solution of the form

$$\sigma_{rr}^h = Cr^{-m} \quad (\text{II.9})$$

where  $C$  is an arbitrary constant.

A particular solution is

$$\sigma_{rr}^p = C_1 + C_2 r \quad (\text{II.10})$$

where  $C_1 = -\frac{\sigma}{m}$  and  $C_2 = \frac{\tau}{m+1}$ . Adding these provides the general solution as

$$\sigma_{rr} = Cr^{-m} + C_1 + C_2 r \quad (\text{II.11})$$

Finally, if the boundary condition at  $r = a$  is used, equation (II.4), then the radial stress field is

$$\sigma_{rr} = \frac{\sigma_a \sigma_b}{\sigma^* - \sigma_b - \sigma_a} \left[ 1 - \left( \frac{r}{a} \right)^{\frac{\sigma^* - \sigma_b - \sigma_a}{\sigma_b}} \right] + \frac{\sigma_b \tau_a}{2\sigma_b + \sigma_a - \sigma^*} \left[ \frac{r}{a} - \left( \frac{r}{a} \right)^{\frac{\sigma^* - \sigma_b - \sigma_a}{\sigma_b}} \right]. \quad (\text{II.12})$$

It should be noticed that the stress field,  $\sigma_{rr}$  from equation (II.12) and  $\sigma_{\theta\theta}$  from equation (II.6), is determined without consideration of the boundary condition at  $r = b$ . This is not unusual in plastic analysis (Coon, 1967a). The point is that the stress field will be valid in the region where  $\sigma_{rr}(b)$ , given by equation (II.12), equals  $-P$ , the radial component of boundary traction. However, the form of equation (II.12) is complicated enough that it is difficult to know when  $\sigma_{rr}$  decreases monotonically and when it does not. Thus, it is insufficient to substitute  $-P = \sigma_{rr}(b)$  and assume that this is a collapse load. This process could provide stresses passing through a line containing points A and B, but outside the two points A and B. Our solution to this difficulty has been to plot the stress variations for a variety of material properties ( $\sigma^*$ ,  $\sigma_a$ ,  $\sigma_b$ ) to learn the conditions for which  $\sigma_{rr}$  is monotonic. From equation (II.12) it may be seen that useful nondimensional plots arise if  $\sigma_{rr}/\sigma^* = \bar{\sigma}_{rr}$  is plotted against  $r/a = \bar{r}$  with  $\tau_a/\sigma^* = \bar{\tau}$  as a parameter. This choice reduces the three material constants to two:  $\sigma_a/\sigma^* = \bar{\sigma}_a$  and  $\sigma_b/\sigma^* = \bar{\sigma}_b$ . The nondimensional formula is

$$\bar{\sigma}_{rr} = \frac{\bar{\sigma}_a \bar{\sigma}_b}{1 - \bar{\sigma}_b - \bar{\sigma}_a} \left[ 1 - (\bar{r})^{\frac{1 - \bar{\sigma}_b - \bar{\sigma}_a}{\bar{\sigma}_b}} \right] + \frac{\bar{\sigma}_b \bar{\tau} \bar{r}}{1 - 2\bar{\sigma}_b - \bar{\sigma}_a} \left[ (\bar{r})^{\frac{1 - 2\bar{\sigma}_b - \bar{\sigma}_a}{\bar{\sigma}_b}} - 1 \right]. \quad (\text{II.13})$$

In Figures II.4 through II.12, the stress variations are shown for a range of material properties. The typical result is that  $\bar{\sigma}_{rr}$  decreases from zero at  $\bar{r} = 1$  to a minimum value which is controlled by  $\bar{\tau}$ .

Whenever the stress field in  $1 \leq \bar{r} \leq \bar{b}$  lies within the points A and B on the yield surface, then the collapse load P must be the radial stress at  $\bar{r} = \bar{b}$ . The combined collapse load from internal ice stress and from body forces thereafter satisfies

$$\bar{P} + \frac{\bar{\sigma}_b \bar{\tau}}{2\bar{\sigma}_b + \bar{\sigma}_a - 1} \left[ \bar{b} - (\bar{b}) \frac{1 - \bar{\sigma}_b - \bar{\sigma}_a}{\bar{\sigma}_b} \right] = \frac{\bar{\sigma}_a \bar{\sigma}_b}{1 - \bar{\sigma}_b - \bar{\sigma}_a} \left[ 1 - (\bar{b}) \frac{1 - \bar{\sigma}_b - \bar{\sigma}_a}{\bar{\sigma}_b} \right] \quad (\text{II.14})$$

where  $\bar{P} = P/\sigma^*$ .

For the diamond yield surface (Figure II.4), the stress field approaches -1.0 for large  $\bar{b}$  when there is no body force  $\bar{\tau} = 0$ . Body forces cause lack of monotonicity and at large wedge depths cause tensile failures at the top surface  $\bar{r} = \bar{b}$ . It is seen that for a body force of  $\bar{\tau} = 0.3$  and a wedge depth of either 1.47 or 3.85 the collapse load is 0.2. This double valuedness led to careful evaluation of stress fields and their graphical presentation.

Another useful example is found in Figure II.7 for  $\bar{\sigma}_a = 0.4$ ,  $\bar{\sigma}_b = 0.4$  where radial stress exceeds  $\bar{\sigma}_b$  if  $\bar{\tau} = 0.1$ . This implies that for some  $\bar{\tau}$  the stress must lie along line BC of the yield surface. As  $\bar{\tau}$  increases, the minimum is increased algebraically (it becomes closer to positive) and the minimum occurs at a smaller radius. In fact there is a limit for which the stress everywhere for  $\bar{r} > 1$  is positive. This case shows tensile failure at the bottom or neck of the wedge and occurs at

$$\bar{\tau} = \bar{\sigma}_a.$$

Only when  $\bar{\tau}$  is less than this maximum value, can an arch of finite thickness  $\bar{b}$  exist.

The collapse loads determined for this case when stress lies along line AB of the yield surface are included in Figure 5 of the main text. Typically, the part of the curve where  $\bar{P}$  is small has been obtained from this analysis.



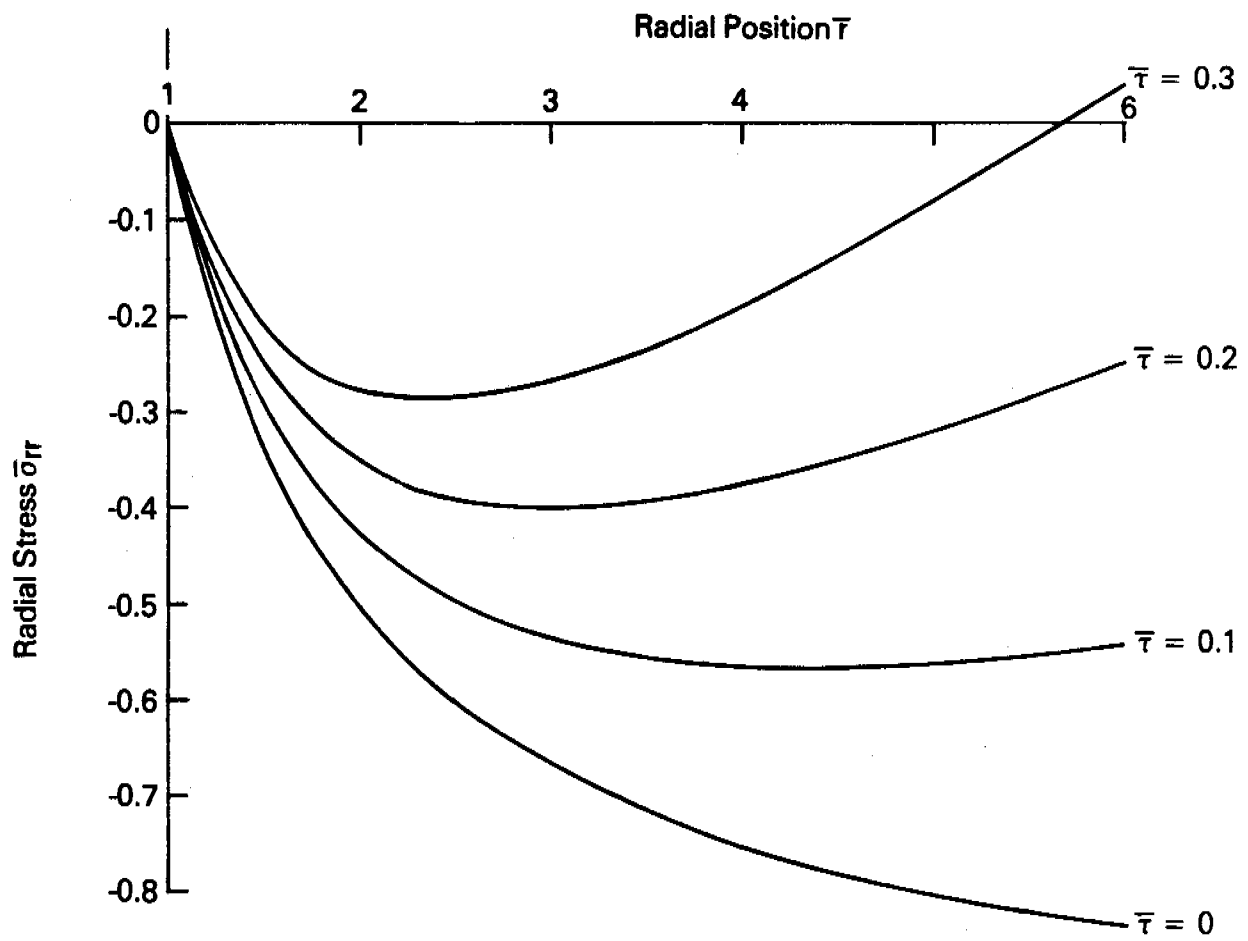


Figure II.4. Radial Stress Distribution for Diamond Yield Surface ( $\bar{\sigma}_a = 1$ ).

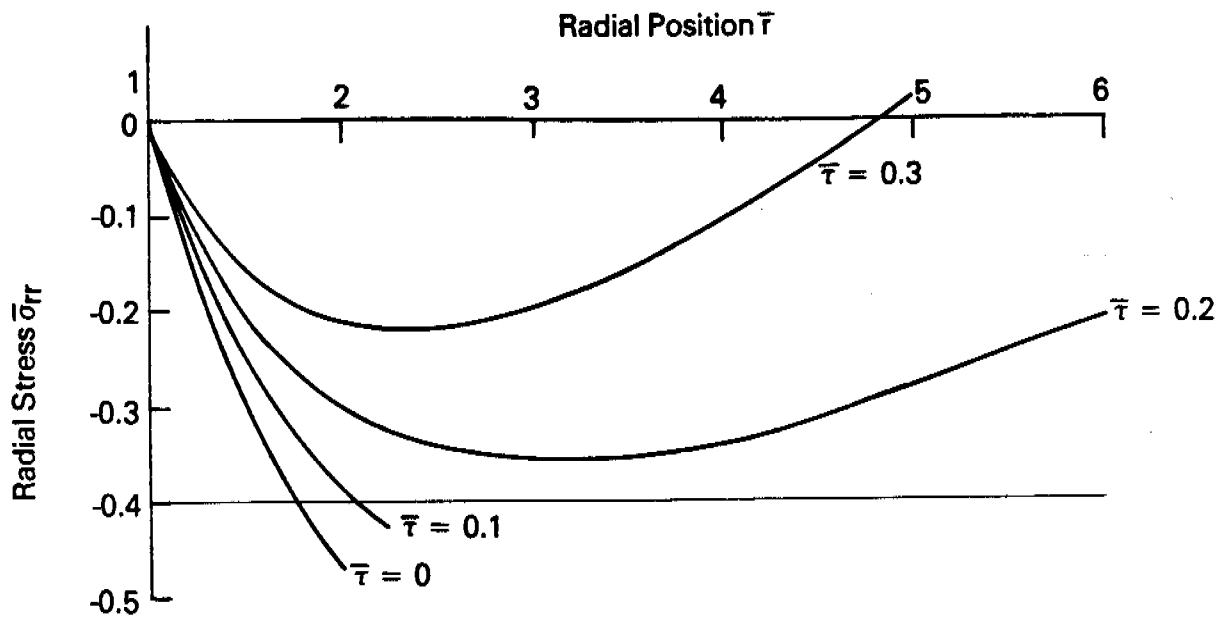


Figure II.5. Radial Stress Distribution for Yield Surface with  $\bar{\sigma}_a = 0.8$  and  $\bar{\sigma}_b = 0.4$ .

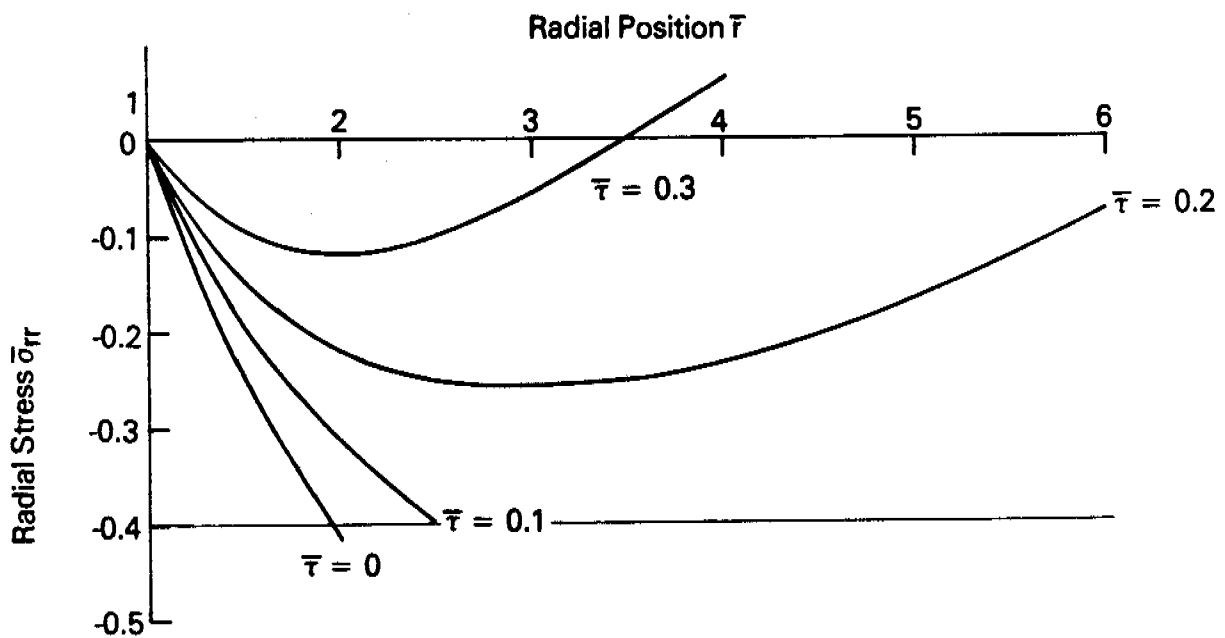


Figure II.6. Radial Stress Distribution for Yield Surface with  $\bar{\sigma}_a = 0.6$  and  $\bar{\sigma}_b = 0.4$ .

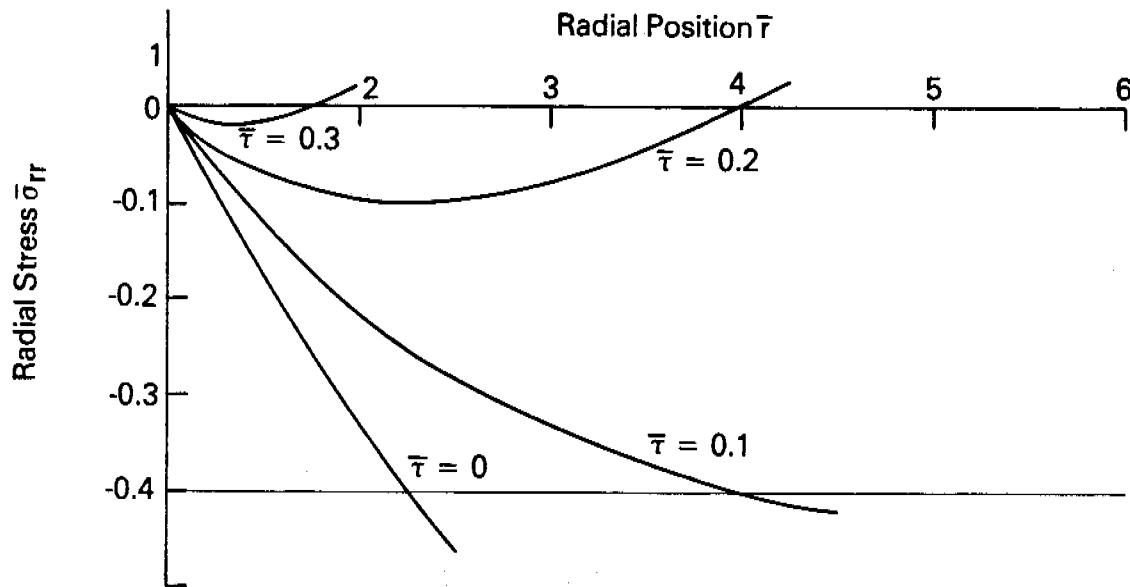


Figure II.7. Radial Stress Distribution for Yield Surface with  $\bar{\sigma}_a = 0.4$  and  $\bar{\sigma}_b = 0.4$ .

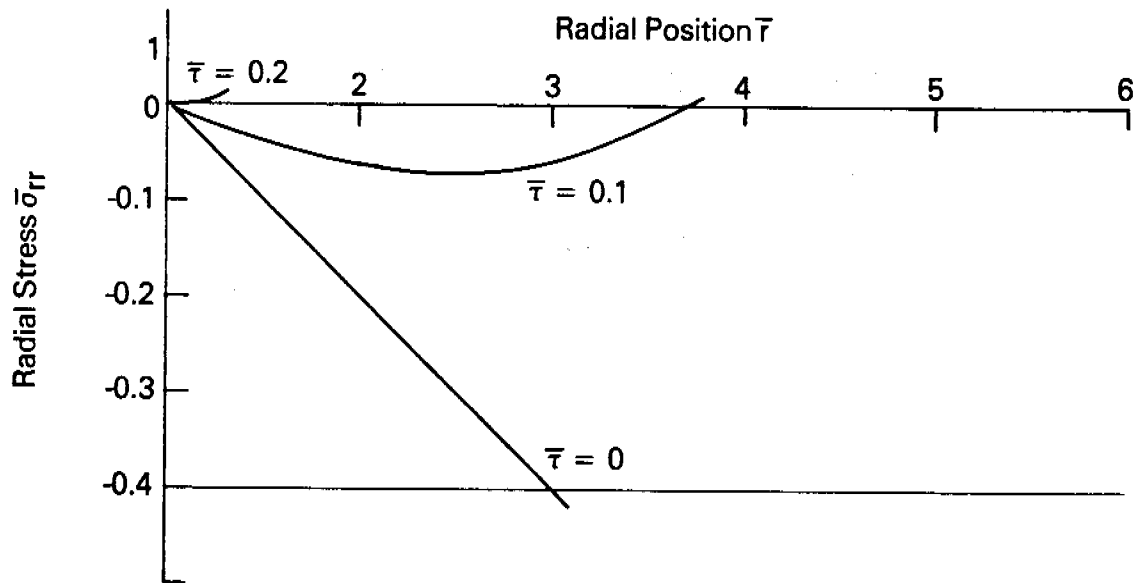


Figure II.8. Radial Stress Distribution for Yield Surface with  $\bar{\sigma}_a = 0.2$  and  $\bar{\sigma}_b = 0.4$ .

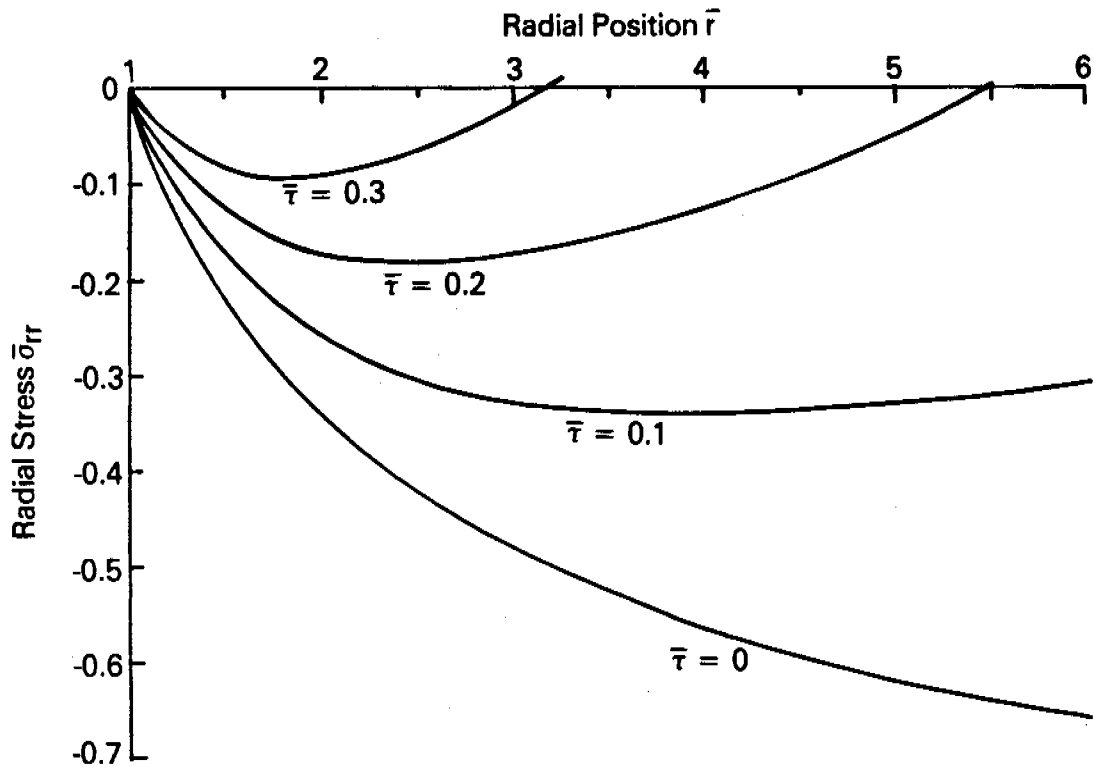


Figure II.9. Radial Stress Distribution for Yield Surface with  $\bar{\sigma}_a = 0.6$  and  $\bar{\sigma}_b = 1.0$ .

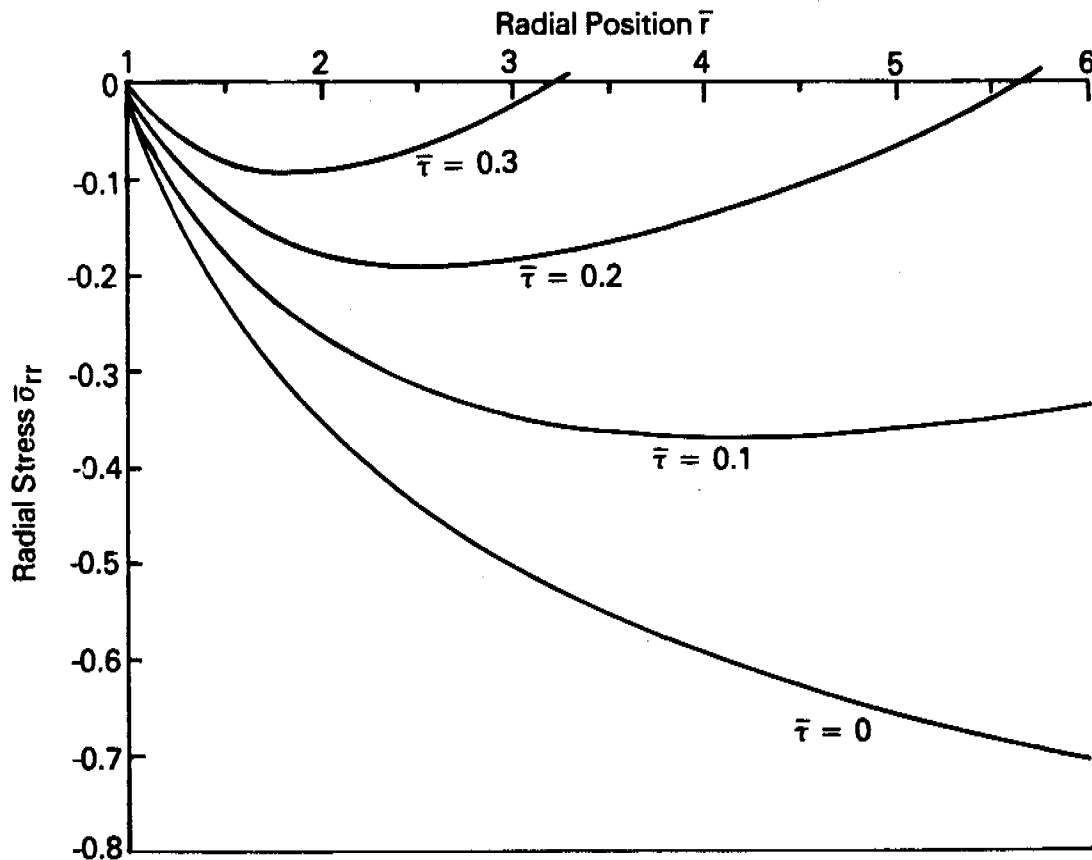


Figure II.10. Radial Stress Distribution for Yield Surface with  $\bar{\sigma}_a = 0.6$  and  $\bar{\sigma}_b = 0.8$ .

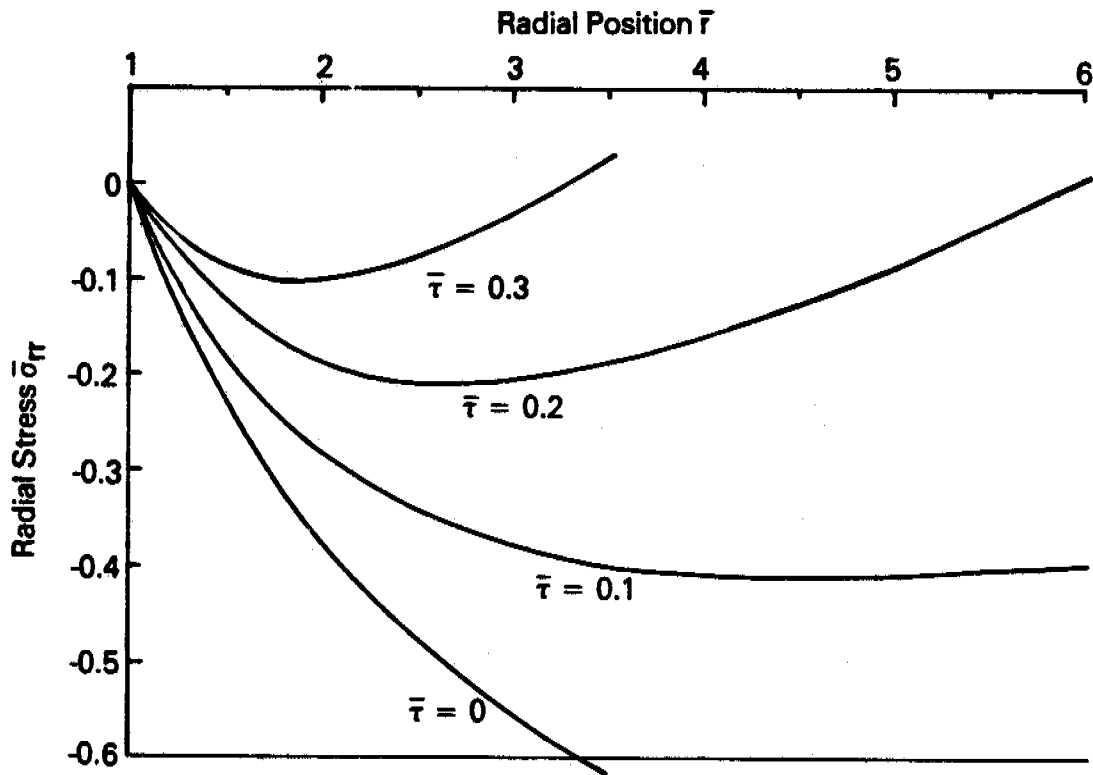


Figure II.11. Radial Stress Distribution for Yield Surface with  $\bar{\sigma}_a = 0.6$  and  $\bar{\sigma}_b = 0.6$ .

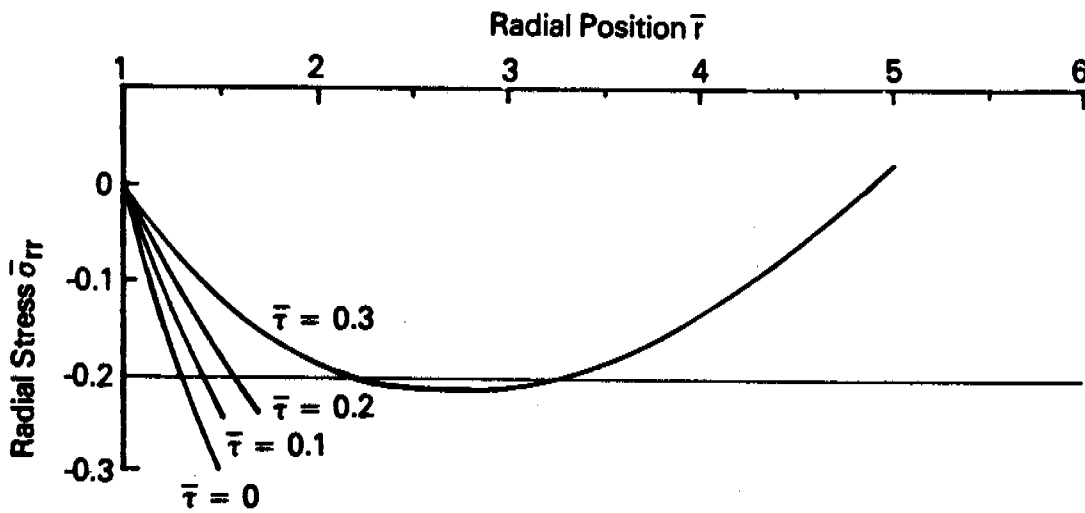


Figure II.12. Radial Stress Distribution for Yield Surface with  $\bar{\sigma}_a = 0.6$  and  $\bar{\sigma}_b = 0.2$ .

For each value of material properties, one cannot obtain collapse loads using this solution for collapse loads exceeding  $\bar{\sigma}_b$ . We note that even when  $\bar{P} < \bar{\sigma}_b$  it is possible for stress to exceed  $-\bar{\sigma}_b$  somewhere in the region. This is a more complicated case and has not been considered in this work.

Case 2

For the next special case, suppose there is a region  $a \leq r \leq c$  for  $c > a$  where the stress lies along line OA of the yield surface. For this to occur, we require that  $\sigma_{rr}(r) \equiv 0$  and  $\sigma_{\theta\theta} = \sigma_{\theta\theta}(r)$  be in the range  $(-\sigma_a, 0)$  from the boundary condition at  $r = a$  and the assumed stress distribution. From radial momentum balance this requires

$$\sigma_{\theta\theta} = -Tr \quad . \quad (II.15)$$

Although this stress field appears reasonable at first glance, it can be shown that having a finite region with constant radial stress is not acceptable. To complete the argument, introduce a straight line yield surface passing through the origin as shown in Figure II.13. The slope of the line is  $\epsilon$  which may be of either sign, but we are interested only in slopes near zero.

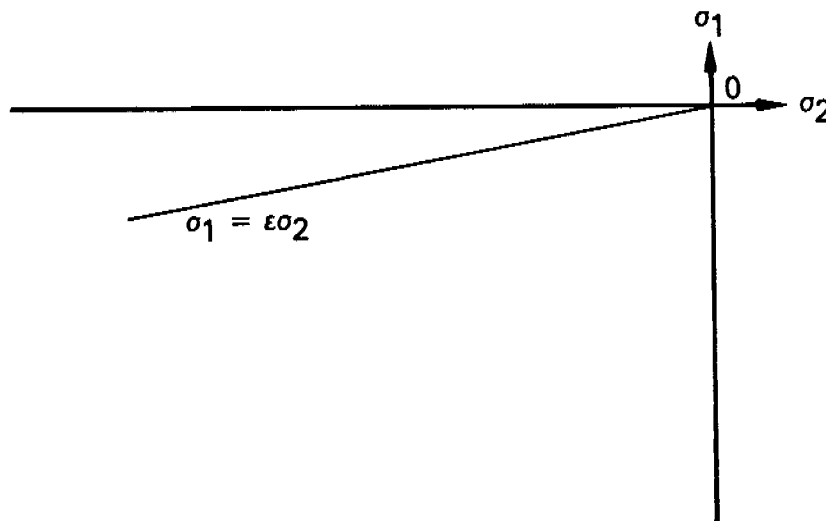


Figure II.13. Straight Line Yield surface Through Origin.

The radial stress distribution is found from Equation (II.13) to be

$$\bar{\sigma}_{rr} = \frac{\bar{\sigma}_b \bar{\tau} \bar{r}}{1-2\bar{\sigma}_b} \left[ \frac{1-2\bar{\sigma}_b}{\bar{\sigma}_b} (\bar{r}) - 1 \right] \quad (\text{II.16})$$

and collapse loads are found from equation (II.14) to be

$$\bar{P} + \frac{\bar{\sigma}_b \bar{\tau}}{2\bar{\sigma}_b - 1} \left[ \bar{b} - (\bar{b}) \frac{1-\bar{\sigma}_b}{\bar{\sigma}_b} \right] = 0 \quad (\text{II.17})$$

if the slope  $\epsilon$  is given by

$$\epsilon = \bar{\sigma}_b = \sigma_b / \sigma^* \quad (\text{II.18})$$

To aid our understanding of this relationship between collapse loads  $\bar{P}$  and  $\bar{\tau}$ , write

$$\bar{P} + K\bar{\tau} = 0 \quad (\text{II.19})$$

where

$$K = \frac{\epsilon \left[ \bar{b} - (\bar{b}) \frac{1-\epsilon}{\epsilon} \right]}{2\epsilon - 1} \quad (\text{II.20})$$

If  $1/2 > \epsilon > 0$ , then it can be seen that  $K > 0$  which eliminates the possibility of positive  $\bar{P}$  and  $\bar{\tau}$  occurring simultaneously. Therefore, arching cannot occur (i.e., no positive, finite loads  $\bar{P}$  or  $\bar{\tau}$  can be withstood) when the yield surface contains a line segment through the origin that lies within the third quadrant of stress space. On the other hand, if  $\epsilon < 0$  and the yield surface allows tensile stresses along this line, then  $K < 0$  and positive loads  $\bar{P}$  and  $\bar{\tau}$  may be applied to the arch.

If we consider the case of  $\epsilon = 0$  it is necessary to take the limit carefully. Using L'Hospital's rule it can be shown that

$$\lim_{\epsilon \rightarrow 0} K = \infty \quad (\text{II.21})$$

Therefore, as  $K$  blows up we must require that the applied body force be restricted to zero so that

$$\lim_{\epsilon \rightarrow 0} \bar{\tau} = 0 \quad (II.22)$$

Then since radial stress is also identically zero, there can be no load  $\bar{P}$  applied by continuity. As a result, we conclude that no finite part of our domain may have a stress distribution lying along the line segment OA of the yield surface.

We have found another important result and it is restated in summary. Namely, only materials with nonzero unconfined compressive strength  $\bar{\sigma}_a$  can withstand loads  $\bar{P}$  and  $\bar{\tau}$  and form an arch.

### Case 3

When loads from the internal ice stress are large,  $\bar{P} > \bar{\sigma}_b$  then the radial stress must lie along both line segments AB and BC. The boundary condition at  $r = a$  still requires the stress to be at state A and the condition at  $r = b$  requires the radial stress in part of the region to lie on line BC. To solve this problem we introduce two regions as shown in Figure II.14.

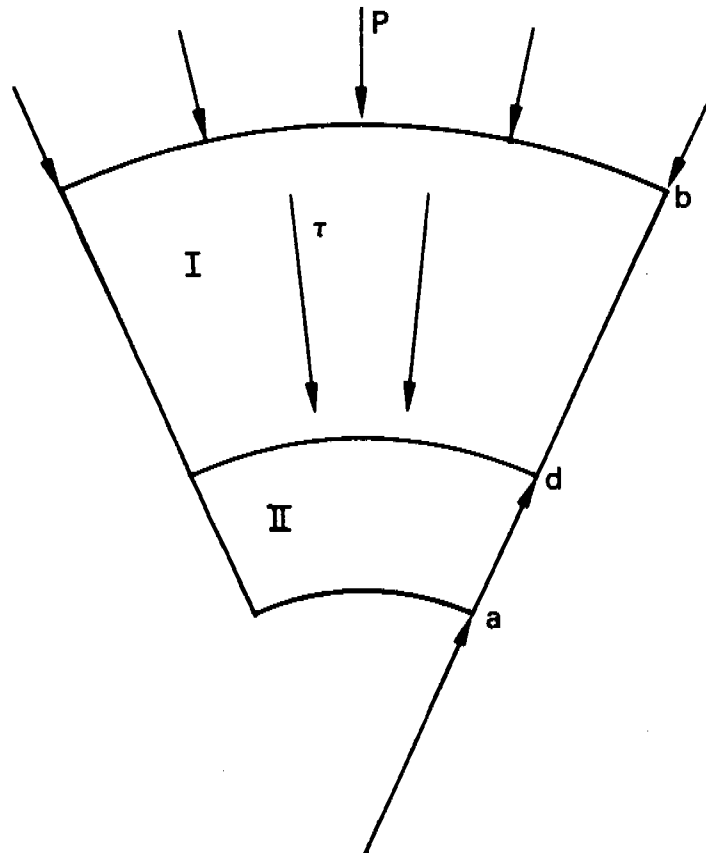


Figure II. 14. Two-Region Circular Arch Geometry.



It is assumed that the stress in subregion I lies along line segment AB of the generalized yield surface shown in Figure II.2 and the stress in subregion II lies along line segment BC. As before, the stress at  $r = a$  is at state A to satisfy the boundary condition there.

To determine the stress field, the radial force balance (equation II.2) is assumed to hold within each subregion  $a \leq r \leq d$  and  $d \leq r \leq b$  and the value of the radial stress component from each solution at  $r = d$  is assumed to be  $-\sigma_b$ , the value at state B. Under these assumptions, the radial stress solution in subregion I satisfies equation (II.13) and is identical to that obtained for Case 1, the single region solution. The only difference is that it holds in interval  $a \leq r \leq d$  where  $d < b$  rather than in the entire region  $a \leq r \leq b$ .

In subregion II, by continuity of stress components, the hoop stress remains algebraically less than the radial stress component. This assumption could possibly be violated under certain loading conditions (not considered in this work) for which radial stress decreases to isotropic state C and then increases after  $\sigma_{rr}$  and  $\sigma_{\theta\theta}$  reverse roles. The boundary conditions on the radial stress component are

$$\begin{aligned}\sigma_{rr}(d) &= -\sigma_b \\ \sigma_{rr}(b) &= -P\end{aligned}\tag{II.23}$$

so that the stress is at state B at  $r = d$  and must equal the applied boundary traction at  $r = b$ . The hoop stress along segment BC is constant (Figure II.2)

$$\sigma_{\theta\theta} = -\sigma^*\tag{II.24}$$

and radial stress then satisfies the differential equation obtained by substituting equation (II.24) into radial force balance, equation (II.2)

$$\frac{d\sigma_{rr}}{dr} + \frac{\sigma_{rr}}{r} = \tau - \frac{\sigma^*}{r}.\tag{II.25}$$

The general solution to this nonhomogenous ordinary differential equation is readily determined. One arbitrary constant appears and it is found by satisfying the radial stress boundary condition at the top surface of the arch,  $r = b$ . The radial stress field in subregion II then becomes

$$\bar{\sigma}_{rr} = -1 + (1-\bar{P}) \frac{\bar{b}}{r} + \frac{\bar{\tau} \bar{r}}{2} \left[ 1 - \left( \frac{\bar{b}}{r} \right)^2 \right] \quad (\text{II.26})$$

when expressed in terms of nondimensional variables as was the case in equation (II.13) for the stress field in subregion I.

The two expressions describing radial stress variations in subregions I and II (equations II.13 and II.26) must each be made to satisfy the stress continuity condition at  $r = d$  ( $\bar{r} = \bar{d} = d/a$ ). As part of this restriction the location of the interface must also be found. In nondimensional variables, both expressions for  $\bar{\sigma}_{rr}$  (given by equations II.13 and II.26) must satisfy

$$\bar{\sigma}_{rr}(\bar{d}) = -\bar{\sigma}_b \quad (\text{II.27})$$

By making this restriction, two relationships are obtained. These equations provide a definition of the collapse loads appropriate for the two-region solution. The result is

$$\frac{\bar{\sigma}_b \bar{\tau} \bar{r}}{1-2\bar{\sigma}_b-\bar{\sigma}_a} \left[ (\bar{r}) \frac{1-2\bar{\sigma}_b-\bar{\sigma}_a}{\bar{\sigma}_b} - 1 \right] + \bar{\sigma}_b = \frac{\bar{\sigma}_a \bar{\sigma}_b}{1-\bar{\sigma}_b-\bar{\sigma}_a} \left[ 1 - (\bar{r}) \frac{1-\bar{\sigma}_b-\bar{\sigma}_a}{\bar{\sigma}_b} \right] \quad (\text{II.28})$$

$$\bar{P} + \frac{\bar{\tau} \bar{b}}{2} \left[ 1 - \left( \frac{\bar{d}}{\bar{b}} \right)^2 \right] = 1 - (1 - \bar{\sigma}_b) \frac{\bar{d}}{\bar{b}} \quad .$$

This pair of equations relates  $\bar{P}$ ,  $\bar{\tau}$  and  $\bar{d}$  in terms of material properties  $\bar{\sigma}_a$ ,  $\bar{\sigma}_b$  and geometric property  $\bar{b}$ . Solutions to equations (II.28) define the combination of body force  $\bar{\tau}$  and boundary force  $\bar{P}$  at which collapse of the arch will occur. The results of equation (II.28) are presented graphically in Figures 4 and 5 of the main body of text. Typically that portion of the curve where  $\bar{P}$  is large (in excess of  $\bar{\sigma}_b$ ) is defined by the two-region solution.

#### Case 4

After obtaining collapse loads for the one- and two-region solutions defined as Cases 1 and 3, it was observed that a small portion of the failure curves was not defined. In these regions, the stress can be shown to lie along line segment AB at small values of  $r$ , to lie along line segment BC at larger values of

$r$  and then to again lie along line segment AB for the largest values of  $r$ . In theory, this three-region solution can be obtained by a direct extension of the present approach. However, this was not felt to be necessary for our purposes in this work.

### Velocity Field

Assume that a normal flow rule describes plastic flow of sea ice. Then, when the stress lies along a straight line segment of the yield surface, the ratio of principal stretching components is constant. This relationship is presented in Figure II.2. The yield surface along line segment AB is expressed as (see Figure II.2)

$$\phi = \frac{\sigma_1}{\sigma_b} - \frac{\sigma_2 + \sigma_a}{\sigma^* - \sigma_a} \quad (\text{II.29})$$

so that  $\phi < 0$  lies within the yield surface and the normal flow rule is

$$\tilde{D} = \lambda \frac{\partial \phi}{\partial \sigma} \quad (\text{II.30})$$

for positive scalar  $\lambda$  and stretching  $\tilde{D}$ .

Attempt to determine a simple velocity field by assuming radial flow. Then stretching components are

$$D_{rr} = \frac{du}{dr} \quad (\text{II.31})$$

$$D_{\theta\theta} = \frac{u}{r}$$

where  $u$  is the radial velocity component and other stretching components are zero. Then  $r, \theta$  are principal directions. We require that principal stretching components  $D_1, D_2$  satisfy  $D_1 = D_{rr} \geq D_{\theta\theta} = D_2$  so that the direction of larger (algebraic) principal stretching is radial. This requirement is consistent with the alignment of principal stresses in the previous section. Then

$$\frac{du}{dr} = \lambda \left( \frac{1}{\sigma_b} \right) \quad (\text{II.32})$$

$$\frac{u}{r} = \lambda \left( \frac{-1}{\sigma^* - \sigma_a} \right) .$$

Eliminate  $\lambda$  to find the equation defining  $u(r)$  to be

$$\frac{du}{dr} + \frac{\sigma^* - \sigma_a}{\sigma_b} \frac{u}{r} = 0 \quad (\text{II.33})$$

which may be integrated to

$$u(r) = - u_a \left(\frac{r}{a}\right)^{-\frac{\sigma^* - \sigma_a}{\sigma_b}} \quad (\text{II.34})$$

where  $u_a$  is the speed of motion through the neck of the constriction ( $r = a$ ). The negative sign arises because flow is downward, in the negative  $r$ -direction. Substituting the velocity solution, equation (II.34), back into the flow rule, equation (II.32), it can be seen that  $\lambda > 0$  is satisfied.

This velocity distribution has been derived for the special conditions (called Case 1 in determining stress distributions) where stresses lie along line segment AB. It can be extended to apply when conditions require stresses to lie along both line segments AB and BC (Case 3 in previous section). The speed variation in subregion I (Figure II.13) is unchanged and the speed at the interface  $r = d$  is

$$u(d) = - u_a \left(\frac{d}{a}\right)^{-\frac{\sigma^* - \sigma_a}{\sigma_b}} \quad (\text{II.35})$$

If we now consider the velocity distribution, equation (II.34) as  $\sigma_a \rightarrow \sigma^*$ , then the solution is applicable along the line segment BC of the yield surface. The resulting distribution is seen to be constant since the exponent to which  $r$  is raised is zero. By continuity, the speed must be  $u(d)$  given by equation (II.35). For this case, the material flows radially in the constriction at a constant speed (not rigid body because of assumed radial flow) and then increases monotonically to a maximum as it passes through the neck at  $r = a$ .

### Conclusion

By assuming that stress and velocity distributions are axisymmetric (independent of  $\theta$ ) in a circular wedge-like region, we have determined these fields for a wide variety of loading conditions. Externally applied forces from air and water stress as well as boundary traction at the top surface from internal ice stress are allowed. The combination of loads at which collapse of the circular arch occurs has been found for a wide range of material parameters.

It is shown that a nonzero unconfined compressive strength is required to allow circular arches to support externally applied body forces and boundary tractions. The collapse loads are presented for a three-parameter yield surface that allows variations in the unconfined compressive strength, a measure of shear strength and isotropic compressive strength. These collapse loads are in acceptable agreement with solutions found by different assumptions and analysis techniques.

## ARCTIC OIL SPILL SCENARIOS - OUTLINE

M. D. Coon  
Flow Research Company  
Kent, Washington

### I. Introduction

The purpose of this scenario set is to determine the possible fate of oil released into the sea ice in the Prudhoe Bay region. The behavior of oil released in the Arctic environment is quite different from the behavior in more temperate climates. The sea ice can act as a natural containment device reducing the areal coverage of a given volume of oil. However, when oil has been entrapped in sea ice, it can remain entrapped for many months before being released to ocean/atmospheric environment or clean up. During the period that the oil is in the ice, it can be transported long distances by the motion of the ice pack.

The studies required to understand the spreading of oil beneath sea ice and its subsequent entrapment and transportation by the sea ice are now being conducted. Therefore, at this point only a broad outline of the scenarios can be presented.

### II. Proposed Scenarios

Scenarios for twelve conditions will be considered. The conditions will include three separate ice configurations, two different times of year, and two different release volumes. Ice configurations will include smooth ice as would occur near shore, fixed but deformed ice as might occur further from shore, and deformed but moving ice representative of the conditions outside the shear zone. The scenarios will consider release of oil in the Fall, just before freeze up and in the Spring, just before the breakup of the shore fast sea ice. The release conditions to be considered are a release of 20,000 barrels of crude oil over a period of five days, and a much larger release of 50,000 barrels of oil per day for ninety days. All releases are to initiate in the Prudhoe Bay area.

### III. Scenario Inputs

The inputs for a scenario will include the location of the release, time of year, ice conditions, volume and type of oil, and ocean currents.

#### IV. Spreading and Entrapment of Oil

In this context spreading means the movement of the oil beneath the sea ice caused by ocean currents relative to the sea ice. In the case of fixed ice, the oil will spread due to ocean currents, however, in the case of the moving ice, spreading will depend on the difference between ocean currents and ice speed. The important output of this spreading consideration is the areal coverage that a given release will take before oil is entrapped in the ice.

#### VIA. Fast Ice

Laboratory studies are being conducted by ARCTEC, Incorporated to determine the spreading rates for oil beneath sea ice. The results from these experiments will be presented in a future OCS report. Preliminary conclusions from this work indicate that the spreading of oil is affected by its density, but not strongly by its viscosity. Furthermore, it has been shown that small (8-12 cm) relief on the bottom of sea ice will contain oil for ocean currents the order of 20 cm per second. The actual volume contained in such relief depend on the size and shape of the relief and the magnitude of ocean currents. Also it appears that large ridges will not be important in containing the oil. Field experiments in the Prudhoe Bay area are being conducted by CRREL to measure the ice thickness profile and subsequently determine the bottom relief. Tentative conclusions from these studies are that bottom relief, the order of 10-20 cm, is present even under what might be considered smooth ice.

Combining the tentative conclusions from the work at ARCTEC and CRREL, it appears that even the largest oil release to be considered in the present scenarios would spread to a size of only a few kilometers (5-10 kilometers) in diameter. Also it appears that the ridges will not appreciably increase the amount of oil entrapped or that is to say, not decrease appreciably the area over which the oil will spread.

#### IVB. Deforming Sea Ice

Considerations of the interaction of the spreading oil and deforming ice have not been considered at this time in the various studies.

## V. Ice Transport

The motion of sea ice in the Arctic Ocean is primarily caused by ocean currents and winds. The most likely and extreme sea ice motions are being studied by Flow Research Company and the results of that work are presented in a report by D. R. Thomas and Robert S. Pritchard entitled "Beaufort and Chukchi Sea Ice Motion - Part 1 Pack Ice Trajectories". This report was included in the Annual Report for Research Unit 567. To determine the most likely and extreme sea ice motions, the barometric pressure fields as determined by the U.S. Weather Service for twenty-five years were used to determine the winds and through a sea ice dynamics model, the subsequent sea ice motions. The results of this work are presented in twelve plots showing the mean motion for several locations in the Beaufort and Chukchi Seas together with their variation year-to-year. Each chart represents the mean and extreme motions for one calendar month. In these studies the motions due to the winds have been separated from those resulting from steady ocean current. The results of the sea ice motion study can be summarized by noting that for mean monthly sea ice motions, steady ocean currents are essentially as important as the winds driving the sea ice. The variations that may occur for a given month, year-to-year, are controlled by the variation of the winds.

With the results of the sea ice motion study, it is possible to build up a trajectory of ice motion suitable for any scenario. From the results on oil spreading, the oil will be confined in an area so small that it may be considered a point when considering sea ice trajectories. To illustrate how the results from the motion study can be used, two figures (Figures 27 and 28) from the report "Beaufort and Chukchi Sea Ice Motions" are included. In Figure 27 oil entrapped in the ice at Prudhoe Bay on October 1 and entering into the sea ice dynamics field at that time will follow the trajectory shown. In addition to the most likely trajectory with the location at the end of each month shown, a most probable ellipse enclosing the area that the oil might reach one year later is shown. A similar plot for oil entrapped in ice and leaving Prudhoe Bay in June followed for one year is shown in Figure 28. The ocean current data utilized in determining these trajectories is very sketchy in the Chukchi Sea and the motions in that region are controlled in the calculations by the winds. Future work should be done to better include ocean currents throughout the Beaufort and Chukchi Seas.



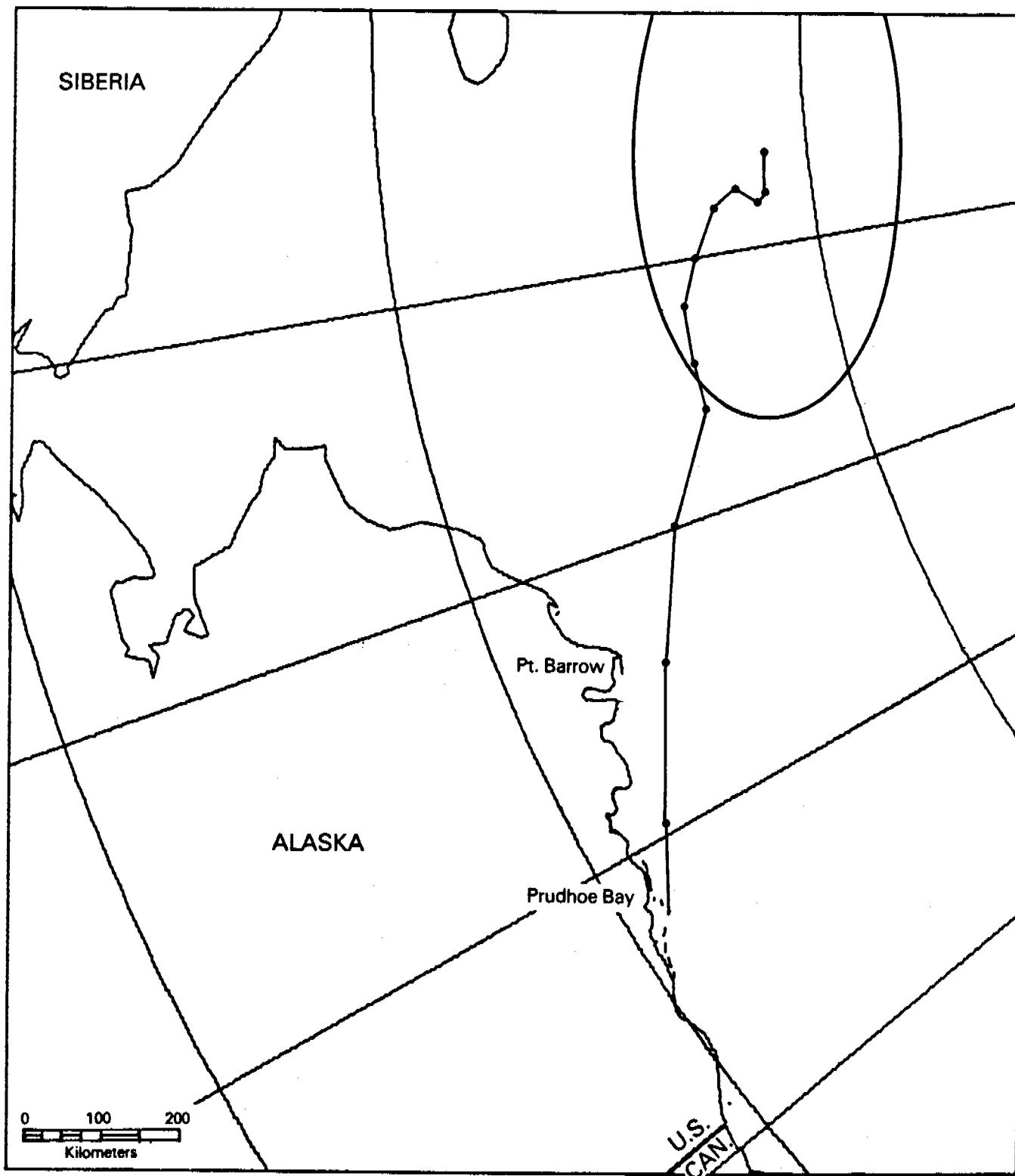


**Figure 27. Most Likely Twelve-Month Free Drift Ice Trajectory (Including Currents) and Approximate Mean Error Ellipse. Trajectory Begins at Prudhoe Bay, October 1st.**

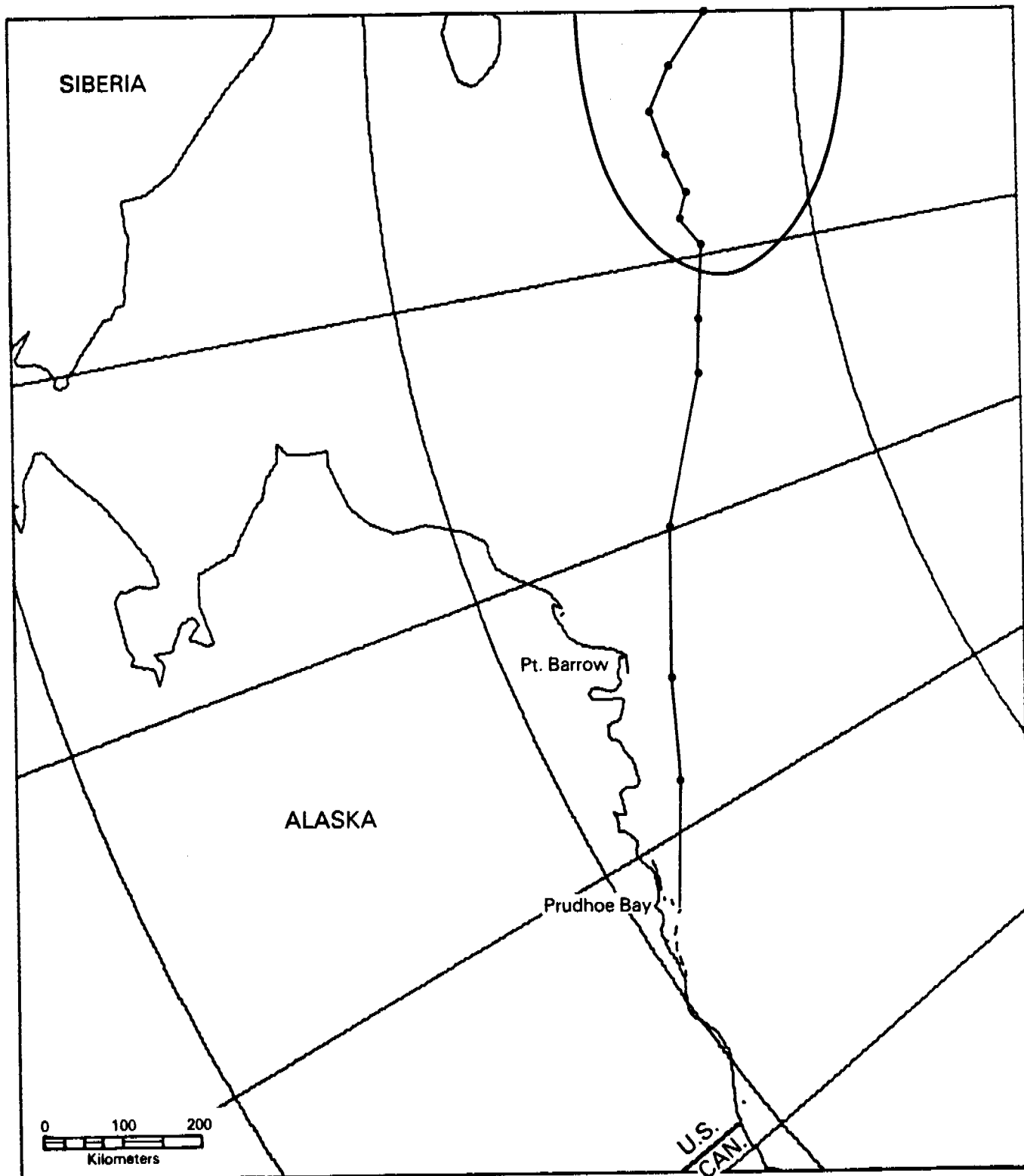


**Figure 28. Most Likely Twelve-Month Free Drift Ice Trajectory (Including Currents) and Approximate Mean Error Ellipse. Trajectory Begins at Prudhoe Bay, June 1st.**

ANNUAL REPORT

Contract: 03-78-B01-62  
Research Unit: 568  
Reporting Period: 1 May 1978-31 March 1979  
Number of Pages: 18

THE TRANSPORT AND BEHAVIOR OF OIL SPILLED

IN AND UNDER SEA ICE - TASK 1

L. A. Schultz and J. C. Cox

ARCTEC, Incorporated  
9104 Red Branch Road  
Columbia, Maryland 21045

26 March 1979

## 1. Summary of Objectives, Conclusions, and Implications with Respect to OCS Oil and Gas Development

The objective of this project has been to study the mechanisms of oil transport beneath and through an ice cover. The results of this project can be combined with the AIDJEX ice motion simulation to predict the long-term trajectory and disposition of oil spilled in the ice infested waters of the Arctic. Potential spill impact zones can then be identified, and appropriate environmental safeguards can be implemented. Additionally, the most promising oil spill clean-up procedures can be identified if a more precise knowledge of the oil-ice interaction is available.

The major conclusions and implications drawn from this work relative to OCS oil and gas development are as follows:

1. A typical threshold current velocity for the movement of oil beneath an ice sheet with only small roughness of 1 mm amplitude is 15 cm/sec.
2. A typical ice field has substantial oil spill containment capacity for even the largest conceivable spill volumes. Oil will be trapped within the under-ice roughness cavities of the ice and the areal coverage of the spill will be substantially less than that which would result from an open water spill.
3. Oil trapped upstream of a large ice obstruction can be flushed out at current velocities of 15 to 25 cm/sec, depending on the properties of the oil involved, but this oil is then trapped in the wake region downstream of the obstruction.
4. Vertical migration of oil trapped beneath ice will only occur in first year ice during the spring season. Multi-year ice is not porous enough to allow for the vertical migration of oil; the release of oil trapped beneath multi-year ice requires that the ice melt down to the oil.

## 2. Introduction

2.1 General Nature and Scope of Study - The purpose of the present study is to examine how oil from a spill will interact with the sea ice of the Beaufort and Chukchi Seas. The scope of the problem encompasses both the horizontal movement and the vertical migration of oil. The horizontal transport of oil has been studied in an ice covered laboratory flume. Conclusions on the vertical migration of oil in ice are based on observations made during both field and laboratory experiments. The results of these oil-ice interaction studies will be incorporated into the AIDJEX model of ice dynamics to provide a means for predicting the ultimate fate of oil spilled in ice infested waters.

2.2 Specific Objectives - As the problem was being formulated in more elementary terms, distinctions about oil trapping by ice ridges, roughness, or undulations were discarded in favor of definitions which only specified whether or not the oil is able to move beneath the ice. This type of specification is also the most compatible with the modeling requirements of the AIDJEX model. Three specific objectives for this project were then defined as follows:

1. Determine how and at what rates oil can migrate upward through an ice cover to the surface.
2. Determine the kinds of roughness and the range of ocean current velocities for which oil can be driven under sea ice of different underside roughness characteristics.
3. Determine the kinds of roughness and the range of ocean current velocities for which oil can be constrained beneath ice so that oil may become frozen into place or migrate into the ice and ultimately become incorporated therein.

2.3 Relevance to Problems of Petroleum Development - The continuing energy crisis, particularly the shortages of oil and natural gas, indicate that the petroleum reserves already found and expected to be found in the Alaskan offshore region will be developed in a timely manner. This increased petroleum industry activity related to the exploration, development, production, and transportation of Alaskan offshore oil and gas will increase the potential for accidental spills of oil in the region. The results of the present research will provide predictions of the extent of under-ice spreading of an offshore oil spill or blowout. In addition, when incorporated into the AIDJEX ice dynamics model, the likely long-term trajectory and fate of oil spilled in ice-infested waters can be predicted. Such predictions can be used to evaluate the possible impact of oil spills upon biological systems, and to aid in the selection of protective measures and the potentially most effective spill response methods.

### 3. Current State of Knowledge

Only limited research has been completed on the behavior of oil under ice. To date only two studies and one field observation have been made in reference to the horizontal transport and trapping of spilled oil beneath ice. Uzuner, et al. [1] presents slick speeds for current driven oil beneath a smooth ice sheet. Moir and Lau [2] study the containment of oil by a simulated ice ridge. In the field, NORCOR [3] qualitatively observed the spread of oil beneath a real ice cover. With reference to the vertical migration of oil, Martin [4] gives the most complete presentation on migration in first-year sea ice. An excellent discussion of the entire oil-ice interaction problem is presented by Lewis [5], who makes some strong and, as it appears, correct speculations on the behavior of the oil. These studies provide the available data on oil under ice behavior.

On the other hand, the dynamics of oil slicks in open water have been studied extensively. The major piece of work on open water slick behavior which can serve as a basis for the study of oil under ice is by Wilkinson [6, 7] who analytically treats oil contained by a floating boom. With suitable modification, his approach can be applied to oil trapping by ice roughness. In addition, the various theories for stratified flow may be used to approach the problem of oil spreading beneath rough ice.

#### 4. Study Area

Horizontal oil transport tests were performed in ARCTEC's glass walled Ice Flume. Fresh water ice was grown by a patented cryogenic process over 40 cm of water in the flume. With the pump running at full capacity, oil behavior for currents up to 35 cm/sec could be observed through the glass walls of the flume.

Observations on the vertical migration of oil were made in the laboratories of ARCTEC CANADA, Limited, and the University of Washington, and during a field test spill under ice in Balaena Bay, N.W.T.

#### 5. Sources, Methods, and Rationale of Data Collection

Data for this project comes from studies on the horizontal transport of oil performed in ARCTEC's Ice Flume, and from studies of the vertical migration of oil performed at ARCTEC CANADA, Limited, the University of Washington, and at Balaena Bay, N.W.T. These data include direct measurements of slick dimensions, speed, and shape, ice properties and roughness, and current speed. Measurements of the under-ice spreading and containment of oil are best made in the controlled environment of an ice flume. This eliminates the danger of creating a hazardous spill while in the process of studying one. It also allows for the level of detail in observations and measurement needed for a fundamental study which is not possible in the field. Vertical migration studies require both laboratory and field studies since laboratory grown ice cannot reproduce field formed brine channels precisely.

#### 6. Results

This study addresses four basic spill related phenomena, slick thickness, the motion of oil beneath smooth ice and ice having small roughness features, the motion of oil beneath ice having large roughness features, and the vertical migration of oil in ice. The results of the study will be presented according to each of these subdivisions.

6.1 Slick Thickness - The static slick thickness of oil is based upon a balance between the surface tension and buoyancy forces. For the four oil types tested in fresh water, the equilibrium slick thicknesses beneath

smooth ice were determined to be 0.52 cm for No. 2 oil, 0.94 cm for No. 4, 1.03 cm for No. 5 light, and 1.16 cm for No. 5 heavy. Treating the surface tension of all the oils as a constant, it was found that over the range of oil types tested the slick thickness could be empirically related to the relative oil density according to:

$$\delta = -8.50 (\rho_w - \rho_o) + 1.67$$

where  $\delta$  is the slick thickness in centimeters, and  $(\rho_w - \rho_o)$  is the relative density difference between water and oil in gm/cc. Additionally, it was found that the static thickness relation also applies to an unaccelerated moving slick.

6.2 Smooth Ice and Small Ice Roughness - For the purposes of this study, small ice roughness was less than the equilibrium slick thickness of the oil. For this series of tests, the primary interest was in determining the threshold velocity of the oil slick and the subsequent relationship between slick velocity and current velocity.

Figure 6.1 is a plot of the threshold velocity for oil slicks beneath smooth ice versus oil viscosity. As shown in the figure, the smooth ice threshold velocities for No. 2, No. 4, and No. 5 light oil were all found to be between 3 and 4 cm/sec. The threshold velocity for No. 5 heavy oil was substantially higher at 7 cm/sec. Based on the laboratory data, an empirical relationship between the smooth ice threshold velocity and the oil viscosity was obtained as follows:

$$U_{th} = \frac{305.79}{88.68 - \mu_o}$$

where  $U_{th}$  is the threshold velocity in cm/sec and  $\mu_o$  is the oil viscosity in poise.

Figure 6.2 is a plot of slick speed versus current speed for oils moving beneath a smooth ice cover. The slick speeds were found to follow a two step linear curve which was predicted by the theory. A first approximation of slick speed beneath smooth ice for any oil within the range of oils tested can be obtained from the best curve fit of the data for all the oils tested as follows:

$$U_s = 0.15 U_w - 0.60 \quad \text{for } U_w < 18 \text{ cm/sec,}$$

$$U_s = U_w - 15.6 \quad \text{for } U_w > 18 \text{ cm/sec,}$$

where  $U_s$  and  $U_w$  are the slick and current velocities, respectively, in cm/sec. Of most significance is the fact that the slope of the upper line is unity, indicating that for the higher current speeds, the oil slick is transported with the mean flow.

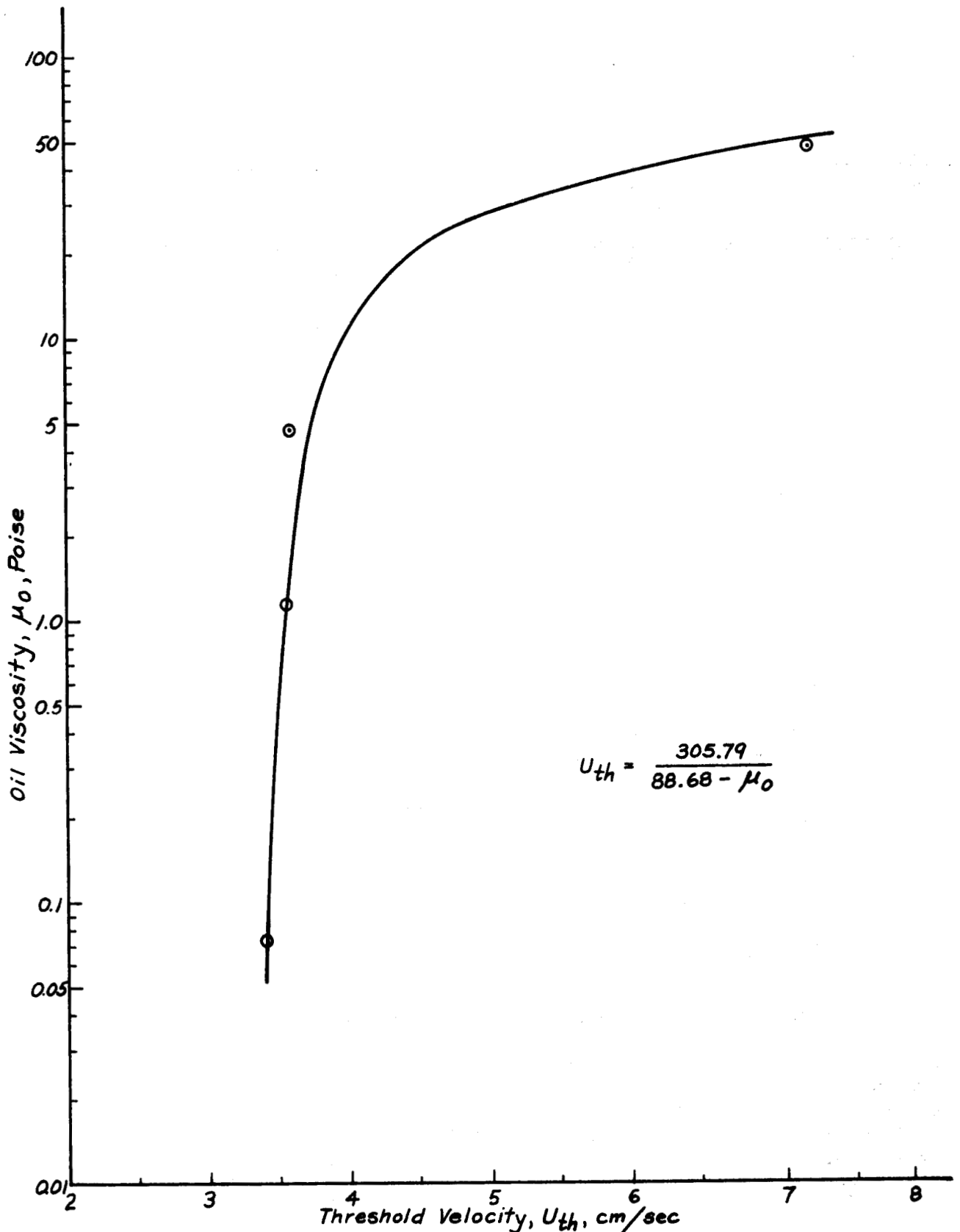


Figure 6.1 Plot of Oil Slick Threshold Velocity versus Oil Viscosity for Oil Beneath Smooth Ice



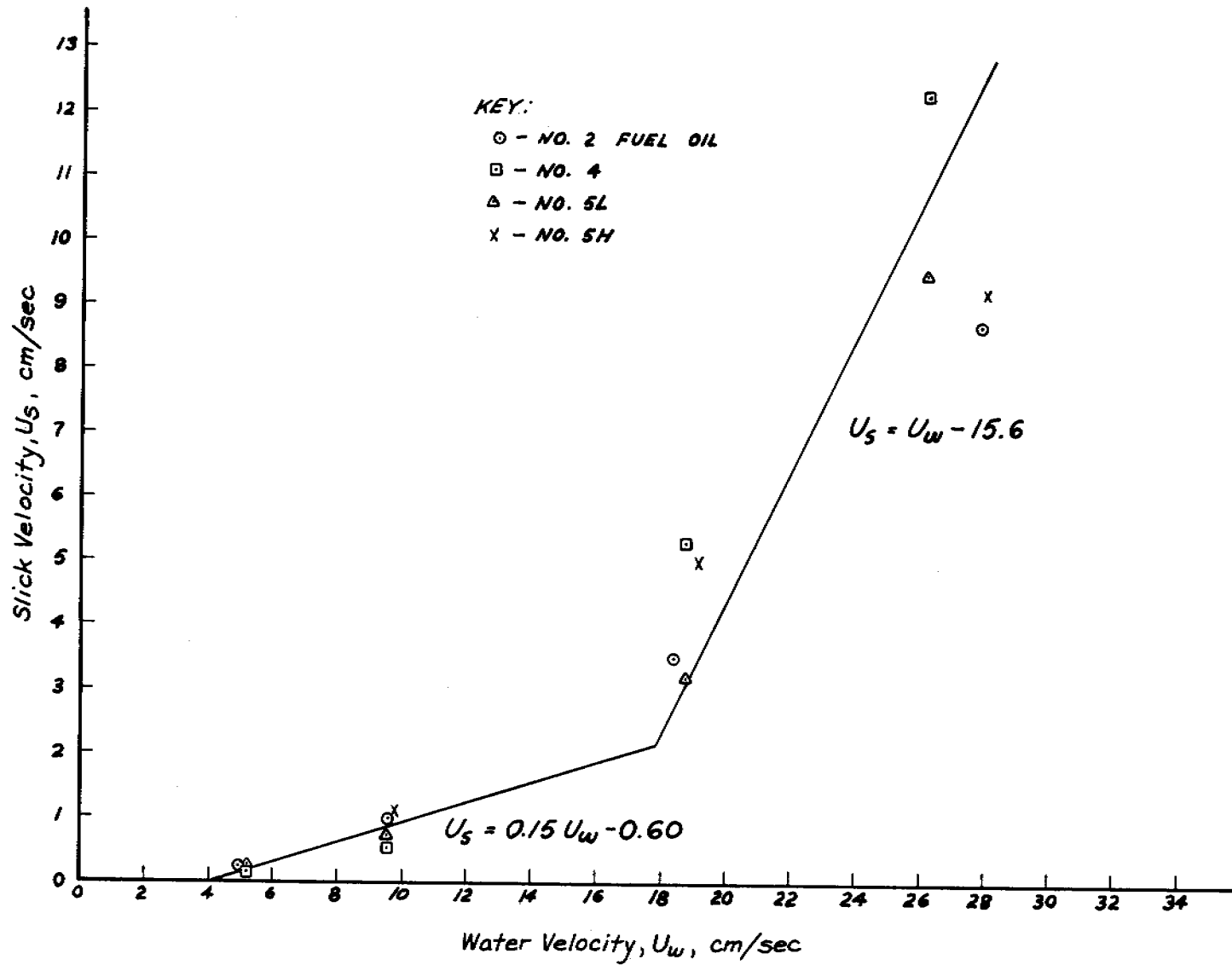


Figure 6.2 Plot of Oil Slick Velocity versus Current Velocity for the Horizontal Transport of Oil Beneath Smooth Ice Cover

When small scale roughness of 1 mm amplitude on 4 cm spacing was added to the under-ice surface, the threshold velocity for No. 4 oil increased from about 4 cm/sec to 12 cm/sec. When the roughness amplitude was further increased to 1 cm, the threshold velocity also increased to about 22 cm/sec. The threshold velocity for No. 5 heavy oil changed similarly. For a 1 mm amplitude roughness, the threshold velocity increased from about 7 cm/sec to 16 cm/sec; for a 1 cm amplitude roughness, the threshold velocity increased further to about 25 cm/sec. These results, shown graphically in Figure 6.3, reveal that even a slight amount of under-ice roughness causes a substantial increase in the threshold velocity of an under-ice oil slick.

For smooth and small roughness ice, a generalized slick speed relation has been developed in the form:

$$1 - \left( \frac{U_s}{U_w} \right)^2 = \frac{K}{0.115 F_s^2 + 1.105}$$

where  $F_s$  is a slick densimetric Froude Number equal to  $U_w/\sqrt{\Delta g \delta}$ ,  $\Delta$  is the density difference between water and oil divided by the water density,  $\delta$  is the slick thickness, and  $K$  is an amplification factor for the oil-ice friction factor. For smooth ice  $K$  is unity, while for ice of small roughness  $K$  is greater than unity. The limited data suggests that  $K$  for small roughness may follow the curve presented as Figure 6.4.

**6.3 Large Roughness Ice** - When the amplitude of ice roughness exceeds the equilibrium thickness of a slick, the roughness is defined as large roughness and has the potential of totally restraining an advancing slick up to some critical value of current velocity. The confined slick develops into the shape shown in Figure 6.5 with three distinct regions, a head region, a neck region, and a tail region. For a given oil, the dimensions of each of these features is a function of the current speed. Two types of failure, or oil release, can occur. The first is the result of the slick growing in volume to a point where its length and thickness exceed an equilibrium point prescribed by the flow. When this occurs, leakage from the tail region results until the equilibrium volume is restored. The second type of failure consists of the total flushing of the oil as a result of a Kelvin-Helmholtz instability in the slick which occurs at higher current velocities. In this case, the head wave is continually being rebuilt by the flow as oil is being torn away, and the slick gradually decreases in length until the slick is entirely flushed out.

Following the approach developed by Wilkinson [6], a generalized expression for the confined slick head thickness in finite water depths is given by:

$$F^2 = \Psi(2 - \Psi) \frac{(1 - \Psi)}{(1 + \Psi)}$$

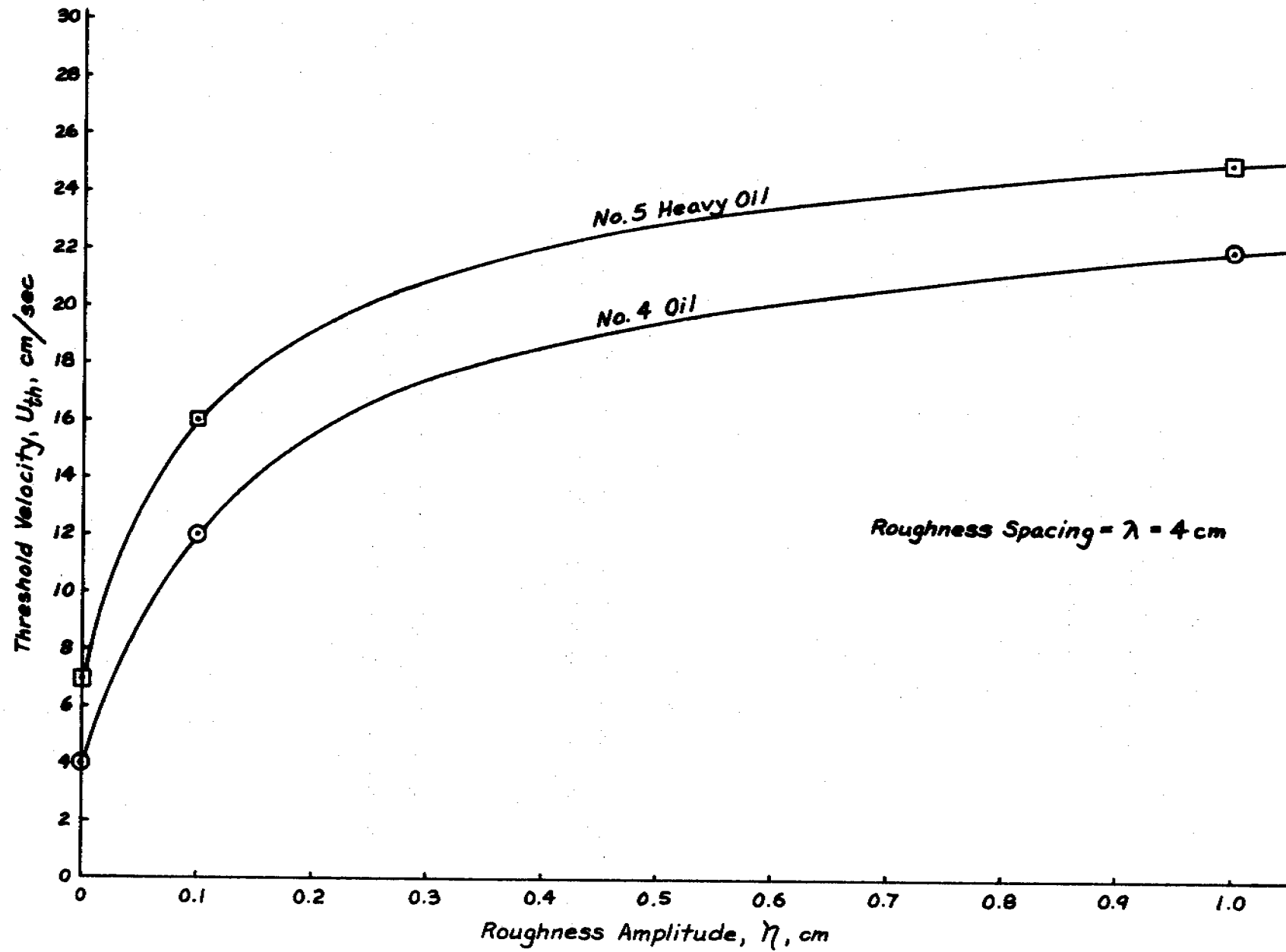


Figure 6.3 Variation of Under Ice Slick Threshold Velocity with Ice Surface Roughness

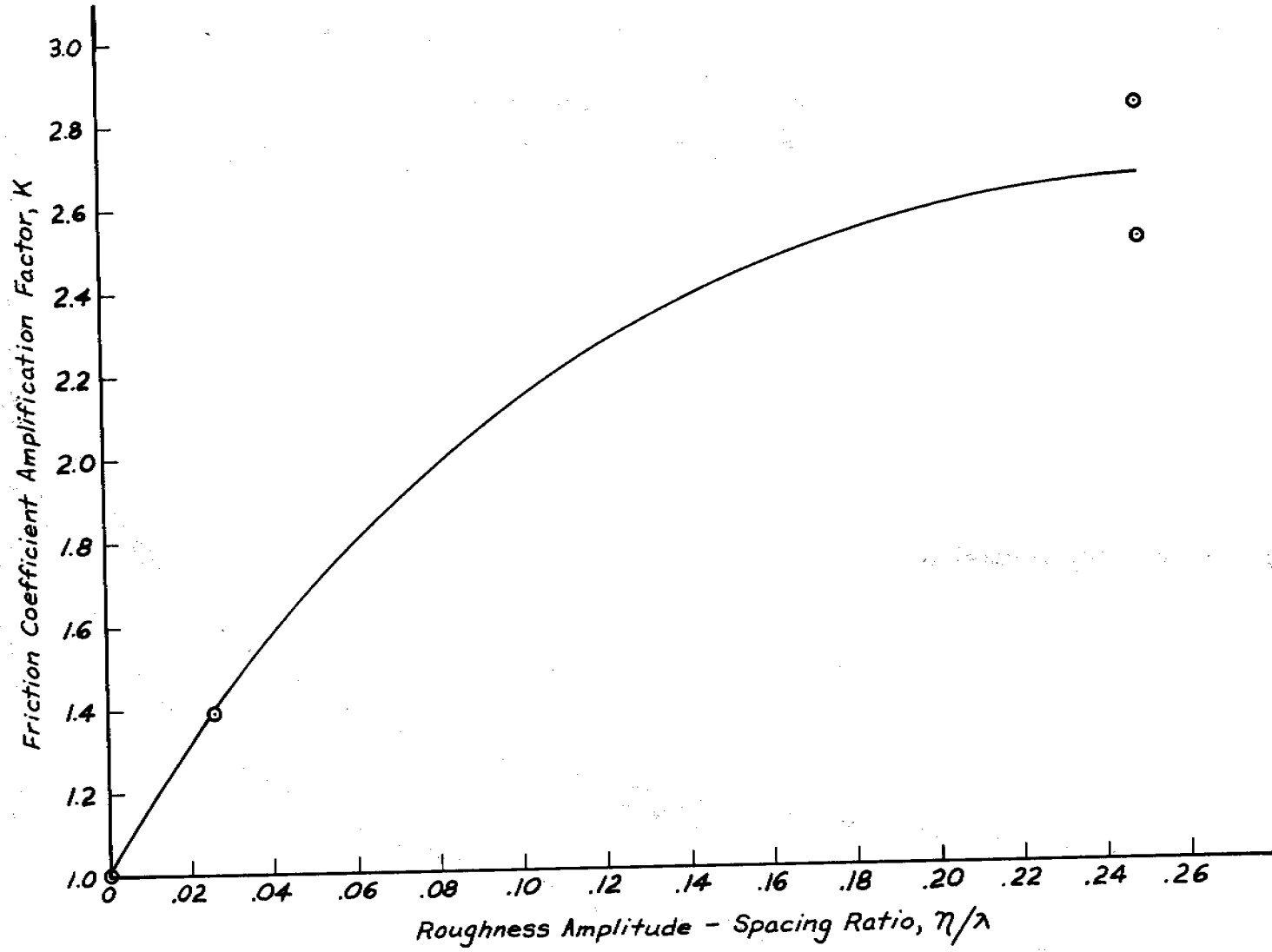


Figure 6.4 Projection of Friction Coefficient Amplification Factor as a Function of the Roughness Amplitude to Spacing Ratio

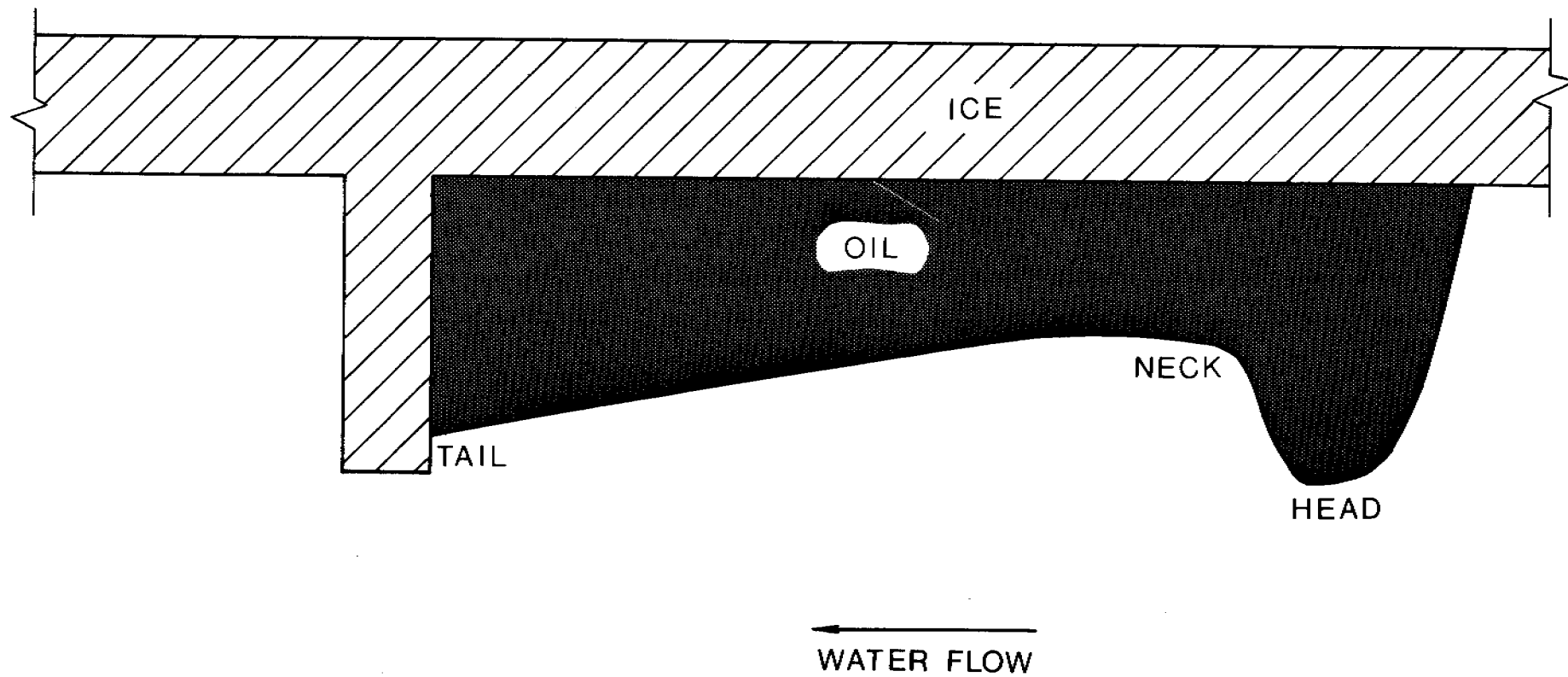


Figure 6.5 Sketch of the Shape Taken by a Slick Confined Behind a Large Roughness Element or Obstruction

where  $F$  is the free stream densimetric Froude number equal to  $U_w/\sqrt{\Delta g D}$ ,  $D$  is the water depth, and  $\Psi$  is the nondimensional slick thickness equal to  $\delta/D$ . This expression is plotted in Figure 6.6 to show that a maximum Froude number exists beyond which flushing of a slick must occur. In applying these results, the Froude number can be calculated given the current velocity, water depth, and oil and water densities. If the resulting Froude number is greater than 0.527, containment will fail and the oil will be flushed from the upstream side of the obstruction regardless of the depth of the obstruction. If the Froude number is less than the critical value of 0.527, there can be containment if the obstruction depth is great enough, i.e., in the range of  $\delta$  to  $\delta/2$ , since the neck thickness is typically taken as  $\delta/2$ . If the obstruction depth is less than  $\delta/2$ , containment will fail and the entire slick will clear from the upstream side of the obstruction.

While the volume of slick contained by the obstruction can be determined using the above approach, the general relationship is somewhat complex. For the deep water case of  $\Psi$  less than 0.01, the relationship simplifies considerably to:

$$\frac{\bar{V}}{w} = \frac{9}{16} \frac{U_w^4}{f_s (\Delta g)^2}$$

where  $\bar{V}/w$  is the volume contained per unit width and  $f_s$  is the slick-water interfacial friction factor determined to be 0.03 in this study.

For the range of parameters covered by the laboratory tests, the failure or flushing velocity is related to the difference between the oil and water densities as shown in Figure 6.7. The failure velocity was found to be independent of obstruction depth and obstruction angle.

Two different geometries of two dimensional large ice roughness were tested, one a vertical barrier and the other a wedge shaped barrier angled  $32^\circ$  from the horizontal. No differences were observed in the containment ability of each type. The buoyancy of the oil contributes strongly to its containment, so that even mild slopes present formidable barriers to any advance of the slick.

Oil which leaked or flushed beneath a large ice roughness element did not get picked up by the free stream and carried away, rather the strong buoyant forces caused the oil to rise into the wake region behind the roughness element. The oil was firmly captured in this region since it is a region of lower pressure. While the size of the region was not mapped in this program, other studies [8] indicate that it extends downstream seventeen times the barrier depth for Reynolds numbers based on barrier depth greater than 200. A schematic representation of this kind of behavior is shown in Figure 6.8.

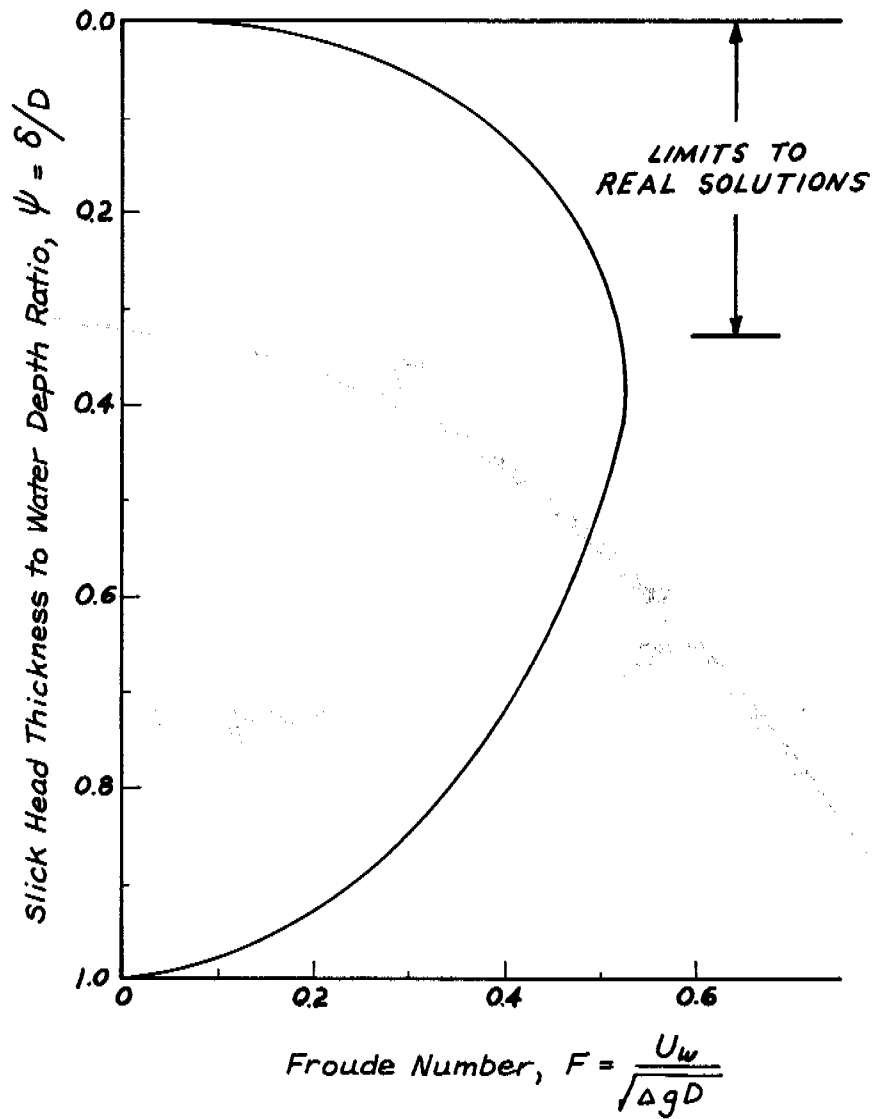


Figure 6.6 Slick Thickness Ratio versus Freestream Densimetric Froude Number for Large Roughness

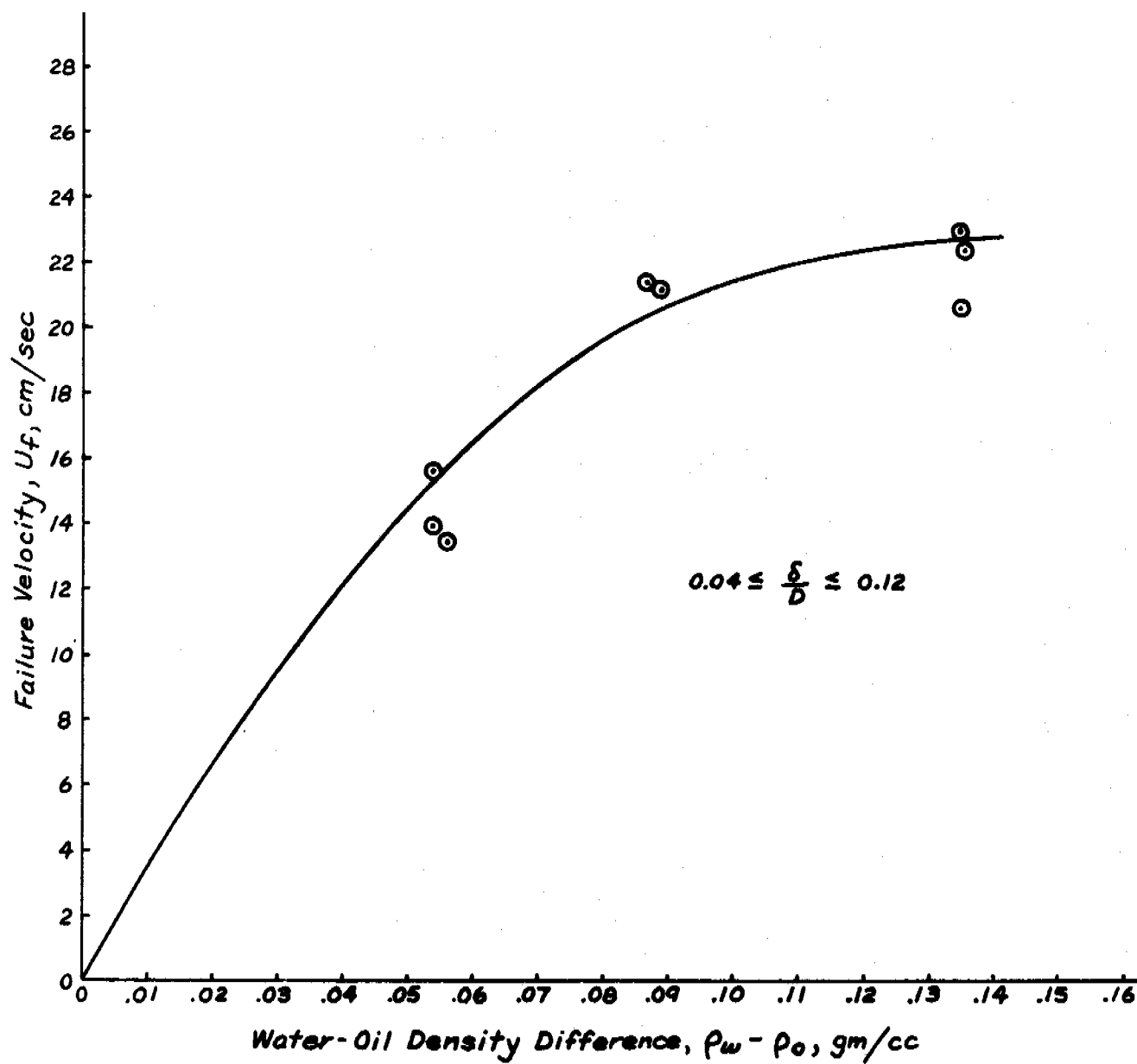


Figure 6.7 Relationship Between Failure Velocity and Water-Oil Density Difference for Containment of Oil Upstream of an Obstruction



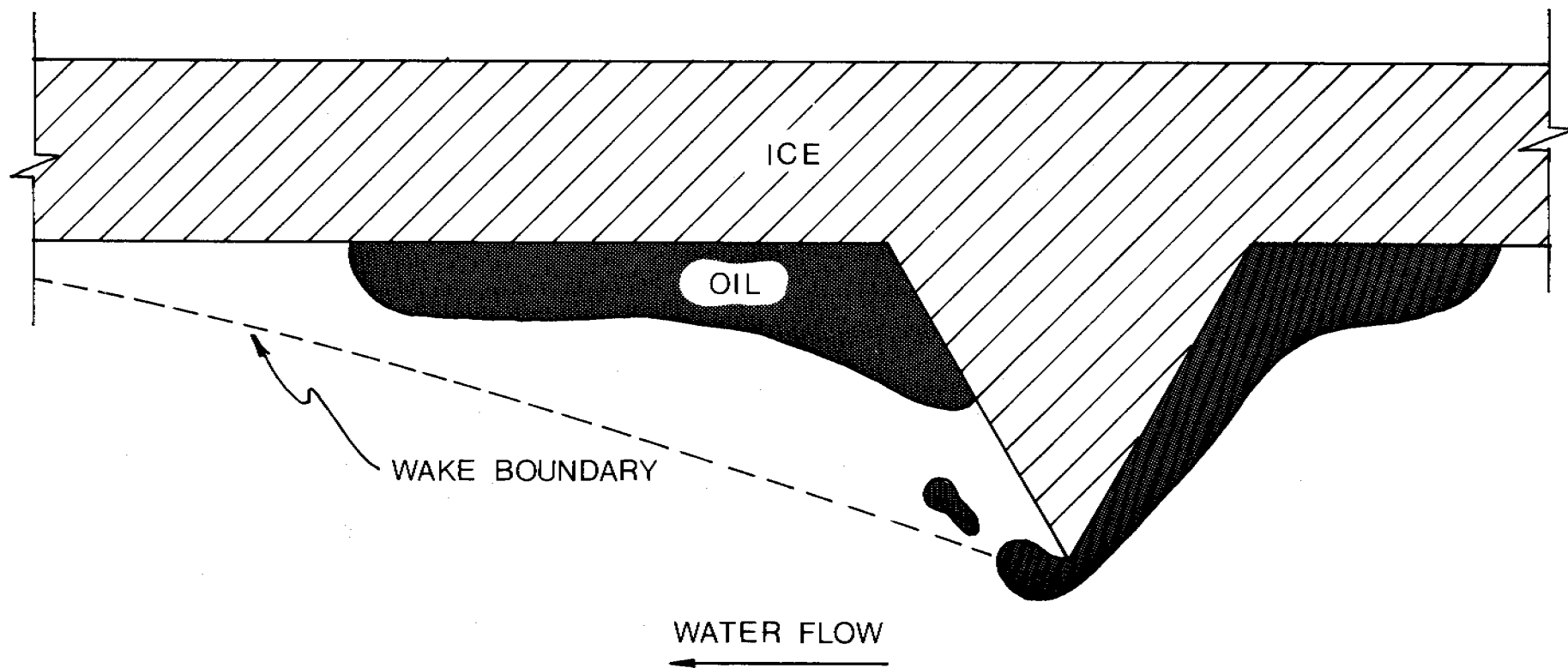


Figure 6.8 Sketch of Oil Leakage From Upstream of a Large Roughness Element to the Wake Region Behind the Element

6.4 Vertical Migration - In a recently published work, Martin [4] examined the vertical entrapment of oil by first year ice. The observations cited by Martin, and some laboratory work by Purvis [9], suggest that oil trapped beneath or within first year sea ice will begin to flow to the surface when the minimum ice interior temperature reaches  $-4^{\circ}\text{C}$ . The flow to the surface accelerates as the ice temperature continues to increase. In field observations made at a test spill in Balaena Bay, a vertical migration rate of 0.07 cm/sec was observed, and the spacing of the centers of the oiled areas varied from 0.1 to 0.5 m, which correlated with the typical brine channel spacing. In general, the vertical migration rate,  $\bar{u}$ , is predicted as:

$$\bar{u} = \frac{(\rho_w - \rho_o) g \delta d^2}{32 L \mu_o}$$

where  $(\rho_w - \rho_o)$  is the water density difference,  $\delta$  is the slick thickness,  $d$  is the brine channel diameter,  $L$  is the ice thickness, and  $\mu_o$  is the viscosity of the oil.

Once on the ice surface, the solar radiation absorbed by the oil will cause a melt pond to form which will eventually melt through the ice and cause the re-release of the oil into the ocean. In terms of time, oil will probably reach the surface of first year ice in May, and be released into the ocean in July or August.

In some limited studies by Martin [10] and Environment Canada [11], the vertical migration of oil on multi-year ice was found to be insignificant. The major reason is that the thermal reworking of multi-year ice has reduced its porosity, transforming it into essentially fresh water ice. The laboratory results indicate that only bulk melting of this ice from above and below provides a pathway to the oil. No signs of upward flow through brine channels were observed.

#### 6.5 References

1. Uzuner, Weiskopf, Cox, Schultz, "Transport of Oil Under Smooth Ice Cover," Environmental Protection Agency Report No. 670/3-78, 1978.
2. Moir and Lau, "Some Observations of Oil Slick Containment by Simulated Ice Ridge Keels," Prepared for the Frozen Sea Research Group by the Hydraulics Division of the Canada Centre for Inland Waters, March 1975.
3. Dickens, Overall, and Brown, "The Interaction of Crude Oil with Sea Ice," Beaufort Sea Project Technical Report No. 27, December 1975.

4. Martin, "The Seasonal Variation of Oil Entrainment in First Year Arctic Sea Ice: A Comparison of NORCOR/OCS Observations," Department of Oceanography, University of Washington Special Report No. 71, March 1977.
5. Lewis, "Oil in Sea Ice," Unpublished Manuscript, Pacific Marine Science Report No. 76-12, 1976.
6. Wilkinson, "Dynamics of Contained Oil Slicks," *Journal of the Hydraulics Division*, ASCE, June 1972.
7. Wilkinson, "Limitations to Length of Contained Oil Slicks," *Journal of the Hydraulics Division*, ASCE, May 1973.
8. Lin and Landweber, "On the Solution of the Lavrentiev Wake Model and Its Cascade," *Journal of Fluid Mechanics*, Vol. 79, Pt. 4, 1977.
9. Purves, "The Interaction of Crude Oil and Natural Gas with Laboratory Grown Saline Ice," Environment Canada, March 1978.
10. Martin, Personal Communication.
11. Brown, Personal Communication.

## 7. Discussion

The categories of small roughness and large roughness result in a division of the theories according to containment and noncontainment. The two theories are differentiated by the relationship of the slick thickness to the ice roughness amplitude. The results of the two theories do not necessarily merge when the ice roughness is exactly equal to the equilibrium oil thickness. This is a transition point where both containment phenomena and transport phenomena are occurring simultaneously. This one anomaly does not, however, limit the usefulness of the two theories.

## 8. Conclusions

This examination of the transport of spilled oil beneath and through sea ice has revealed these fundamental conclusions:

1. The thickness of an unaccelerating moving oil slick is equal to the static thickness of the slick, and for the oils tested ranged between 0.5 and 1.2 cm. Further, the slick thickness was found to be a linear function of the difference between water and oil density.

2. The threshold velocity of an oil slick beneath smooth ice cover varied from about 3 to 4 cm/sec for No. 2, No. 4, and No. 5 light oil to 7 cm/sec for No. 5 heavy oil.
3. The presence of the slightest roughness on the under-ice surface, even roughness having an amplitude of 1 mm, significantly increases the threshold velocity of the oil and decreases its transport rate.
4. Oil trapped upstream of a large roughness element can be flushed out at current velocities in the 15 to 25 cm/sec range for typical oils regardless of the depth of the roughness element.
5. In general terms, oil which cannot be trapped by a large roughness element on its upstream side will be captured within the wake region downstream of the roughness element.
6. Large roughness features such as pressure ridges are not likely to be major factors in the trapping of oil released beneath ice cover since a release of even the largest conceivable volume of oil will be confined to a relatively limited area by the normal under-ice surface roughness.
7. The seasonal vertical migration and release of trapped oil is likely in first year ice due to brine channel thawing. Bulk melting of the ice cover would be required to expose and release oil spilled beneath multi-year ice.

#### 9. Needs for Further Study

The two most important areas requiring additional laboratory tests have been identified as the interaction of oil with multiple large roughness elements, and the containment ability of large roughness wake regions. Tests in this first set of experiments treated only single large roughness elements. When multiple large roughness arrays are introduced the oil may interact with the ice in a totally different manner. Similarly, when the oil escapes beneath a large roughness element, it becomes trapped in the wake of the element. Additional tests are needed to determine the effective size of the wake region for high current velocity oil containment.

The findings of the laboratory test program and the projection of these results to field conditions should be verified to the greatest extent possible through the conduct of a limited field test program carried out in a region having substantial under-ice surface roughness, and water current velocities approaching the upper limit of what can be expected in the area.

10. Summary of Third Quarter Operations

A. SHIP OR LABORATORY ACTIVITIES

1) Ship or Field Trip Schedule

None

2) Scientific Party

None

3) Methods

Laboratory data gathered during the previous quarter was analyzed and compared against theory as reported above.

4) Sample Localities

Not Applicable

5) Data Collected or Analyzed

Not Applicable

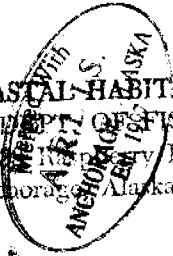
B. PROBLEMS ENCOUNTERED

None

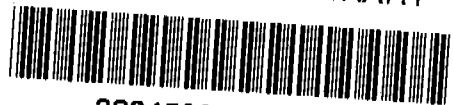
C. ESTIMATE OF FUNDS EXPENDED

As of 31 March 1979, it is estimated that approximately \$97,500 will have been expended for the work of Task 1. It is estimated that the work will be completed on budget.

MARINE & COASTAL HABITAT MANAGEMENT  
ALASKA DEPT. OF FISH & GAME  
3000 Aly Road  
Anchorage Alaska 99502



ADF&G HABITAT LIBRARY



32345000066333